ZAŠTITA MATERIJALA

EVROPSKA FEDERACIJA ZA KOROZIJU (EFC) SMATRA OVAJ ČASOPIS ZVANIČNOM PUBLIKACIJOM ZA OBJAVLJIVANJE IZVEŠTAJA I INFORMACIJA

EUROPEAN FEDERATION OF CORROSION (EFC) CONSIDERES THIS JOURNAL TO BE THE OFFICIAL PUBLICATION FOR PUBLISHING THE REPORTS AND INFORMATION

SADRŽAJ – CONTENT

ISTORIJAT INŽENJERSKOG DRUŠTVA ZA KOROZIJU

Inženjersko društvo za koroziju, koji je pravni naslednik Saveza inženjera i tehničara za zaštitu materijala Srbije i Crne Gore, je društveno stručna organizacija koja je član Saveza inženjera i tehničara Srbije. Savez inženjera i tehničara za zaštitu materijala Jugoslavije, kako se prvobitno zvalo Inženjersko društvo za koroziju, početke svog delovanja je imao još 1952. godine preko Komisije za zaštitu od korozije. Ova komisija je postojala u okviru Društva hemičara i tehnologa DIT-a , mada se neki koreni iz zaštite od korozije pominju i pre drugog svetskog rata. Inicijatori za oformljenje ove Komisije bili su dr.inž Frano Podbrežnik, prof.dr Blažon, prof.dr Milan Pajević i Sveta Živanović. Komisija je imala 15 aktivnih članova i radila je u tri potkomisije.

Januara 1953. godine ova Komisija prerasta u Centar za zaštitu od korozije sa osnovnim zadatkom da radi na antikorozionoj zaštiti svih materijala, uređaja, opreme i instalacija. Već u prvoj godini postojanja ovaj Centar je obrazovao svoju servisnu radionicu za fosfatiranje i pristupio izdavanju svojih stručnih publikacija.

Dalji rad Centra, do svog prerastanja u Društvo a kasnije u Savez, odvijao se u komisijama i servisnim radionicama preko kojih se intenzivno radilo na održavanju raznih kurseva i predavanja iz oblasti korozije materijala i zaštite od nje a, takođe, i na izradi projekata za korozionu zaštitu raznih objekata i opreme za mnoga preduzeća.

PREDSEDNIŠTVO IDK: Predsednik IDK prof.dr Časlav Lačnjevac Potpredsednik IDK Zoran Ivljanin, dipl.inž.tehn. Članovi Upravnog odbora – Srećko Stefanović, dipl. inž. tehn. – Dragan Petrović, dipl. elek. inž. – Momir Đurović, dipl. inž. tehn. Članovi Nadzornog odbora – Ljupče Milosavljević, dipl.inž.tehn. – Miodrag Jovanović, dipl.građ.inž. – Mirko Bačilović, dipl.ecc. Tehnički sekretar IDK – Srbislav Nešić, dipl.maš.inž.

Delatnost strukovnih udruženja (udruživanje u okviru profesije i tehničkih oblasti, uključujući i udruženja specijalista angažovanih u naučnoj delatnosti); – Obrazovanje odraslih (obrazovanje na seminarima, naučno-stručnim skupovima, specijalističkim kursevima i sl.); – Istraživanje procesa korozije i zaštite od korozije; – Izrada tehničke dokumentacije, ekspertiza i vršenje nadzora iz oblasti hidroizolacije, antikorozione zaštite i protivpožarne zaštite.

Inženjersko društvo za koroziju Republike Srbije je izdavač časopisa Zaštita materijala, počlo je sa radom daleke 1953. godine, kao deo Centra za zaštitu od korozije u okviru Saveza inženjera i tehničara za zaštitu materijala Jugoslavije. Iste godine, Društvo je pokrenulo časopis Zaštita materijala, koji i danas aktivno izlazi. Pridružite se bezbrojnim čitaocima koji su imali koristi od njegovog zanimljivog naučnog sadržaja.

Otvaranje naučnog skupa

Zaštita materijala je recenzirani časopis koji sadrži radove o originalnom eksperimentalnom ili teorijskom istraživanju i značajno unapređuju razumevanje u oblastima korozije i zaštite materijala, zaštite životne sredine, ekološkog inženjerstva i tehnologija, inženjerstva materijala (keramika, polimeri, kompoziti; biomaterijali, materijali za skladištenje i konverziju energije, itd.); nanomaterijala i nanotehnologija; hemijskog i biohemijskog inženjerstva, primenjene hemije, upravljanja tehnologijom, i obrazovanja o održivom razvoju. Časopis prihvata radove koji prikazuju eksperimentalne i teorijske naučne i inženjerske rezultate na osnovu dostavljenih podataka.

Naučni radovi za ZM moraju biti dostavljeni na engleskom jeziku i treba da sadrže rezime na engleskom i srpskom jeziku. Za autore van srpskog govornog područja, izdavač će obezbediti rezimee i naslove tabela i slika na srpskom jeziku. Časopis izlazi 4 puta godišnje.

Časopis je indeksiran u Scopus, DOAJ, International Scientific Indexing (ISI), Journalspedia (JPSA), Sherpa Romeo itd.

Digitalne kopije časopisa su arhivirane u repozitorijumu.

*Bhushan Kumar[1, *], Sahil Jangra[2], Subhankar Das[1], Manjeet Singh Goyat[2, 3]*

[1]*Cluster of Mechanical Engineering, School of Advanced Engineering, UPES, Dehradun, Uttarakhand-248007, India,* [2]*Cluster of Applied Sciences, School of Advanced Engineering, UPES, Dehradun, Uttarakhand-248007, India,* [3]*Smart Materials, Mads Clausen Institute, University of Southern Denmark, Alsion 2, Sønderborg 6400, Denmark*

State-of-the-art developments in mxenes: A comprehensive review

ABSTRACT

In recent years, two-dimensional (2D) materials have garnered significant attention because of their distinctive properties and potential applications in a wide range of applications. Among these materials, MXenes, a family of transition metal carbides, nitrides, and carbonitrides, have emerged as a prominent class of 2D materials with remarkable structural, electrical, thermal, optical, mechanical, and chemical properties. This review explores recent advancements in the synthesis techniques, properties, and diverse applications of MXenes in energy storage, electromagnetic interference (EMI) shielding, sensors, and environmental applications. Additionally, it provides a bibliometric overview, analyzing 10,957 research papers to assess global scientific trends and future research directions using Web of Science (WOS) data and VOSviewer software. This review aims to provide a comprehensive understanding of the state-of-the-art developments in MXene technology, offering insights into future directions and potential advancements in this rapidly evolving field.
Keywords: *2D materials; MXene; synthesis;applications; bibliometric analysis*

1. INTRODUCTION

Over the past 20 years, the discovery of the unique physical properties of single-layer graphene has sparked extensive research into two-dimensional (2D) materials [1]. In addition to graphene, materials such as transition metal dichalcogenides (TMDs) [2], boron nitride[3] and phosphorene [4], and their various derivatives have become some of the most extensively studied. While many of these materials continue to be of academic interest, several have gained significant attention due to their exceptional properties, which have paved the way for practical applications. Notably, carbides, nitrides, or carbonitrides of transition metals, collectively known as MXenes, have emerged as a rapidly expanding family of 2D materials [5]. MXene is derived from its 3D precursor known as the MAX phase, which has a general formula of $M_{n+1}AX_n$, (where n=1−3) [6]. In this formula, M represents a transition metal, A is typically the most commonelement in groups 13 and 14

and X is carbon and/or nitrogen, which are coupled by strong metallic, ionic, and covalent bonds [7]. MXenes, which are characterized by the general formula $M_{n+1}X_nT_x$, where T_x represents surface terminations such as hydroxyl (-OH), oxygen (=O), or fluorine (-F), result from the selective etching of the MAX phase[8]. The removal of the A element during synthesis introduces these surface terminations, which significantly influence the material's properties. The bonds between the constituent parts of the MAX are too strong to be broken mechanically, in contrast to inorganic graphene equivalents, in which the nanosheets are connected by weak Van der Waals force and may be easily delaminated. It is important to note that M and the X atom have mixed chemical bonds that include covalent, ionic, and metallic bonding[9].In contrast, the bonds between M and the A atoms are purely metallic [10]. Consequently, the metallic bond is weaker than the covalent bond. By selecting an appropriate etching reagent, it is possible to break the M–A bonds and effectively remove the elements of the A layer [11]. In 2011, Naguib et al. [12] successfully obtained exfoliated, loosely packed accordion-like Ti_3C_2 2D materials by selectively etching the Al atom layer from Ti_3AlC_2, a typical MAX phase.

*Corresponding author's: Bhushan Kumar
E-mail: bhushan.sid83@gmail.com

Unlike most other 2D materials, such as graphene, MXenes demonstrate remarkable versatility with a unique combination of properties. They exhibit high electrical conductivity (25,000 S/cmfor $Ti_3C_2T_x$ MXene) [13], surface hydrophilicity[14], robust mechanical strength (tensile strength up to 570 MPa for $Ti_3C_2T_x$) [15],Young's modulus up to 333 ± 13 GPa for $Ti_3C_2T_x$ [16], tunable surface functionality, with surface terminations including O, OH, H, F, Cl, S, Br, Te, NH, in addition to bare MXenes (without surface termination) [17],the ability to absorb electromagnetic waves[18], and a high negative zeta potential[19], which enables the formation of stable colloidal solutions in water. The hydrophilicity of MXenes, in clear contrast to graphene, arises from surface terminations like –O and –OH acquired during synthesis [20]. Additionally, the negative zeta potential is due to surface groups including –Cl, –F, –O, and –OH, which contribute to their colloidal stability and broad applicability in various technological fields [21]. Due to their unique properties, MXenes find diverse applications with outstanding performance in various fields. In the energy sector, they are employed as energy storage devices, such as supercapacitors [22–24] and batteries [25]. Additionally, MXenes are utilized in electromagnetic interference (EMI) shielding [26–29], where their layered structure and high conductivity play a crucial role. In the biomedical field, MXenes are used for drug delivery, bioimaging, and cancer therapy [30–32]. For water purification, MXenes are effective in removing heavy metals and organic pollutants [33–36]. They also find applications in electronic devices, coatings, and additives to improve the properties of composite materials[37]. Further applications for MXenes include sensors [38–41], and photocatalysis [42–44], in addition to many more applications. These wide-ranging applications underscore the versatility and significant impact of MXenes in advancing various technological and industrial solutions.

Owing to their outstanding properties and diverse applications, there has been exponential growth in the number of publications on MXenes since their inception. Figure 1 shows a schematic illustration of the yearly increment in the number of articles, it demonstrates the gradual emergence of the MXene study field with less than 1% of articles published in the first three years, 2012, 2013, and 2014. Due to recent developments in the synthesis of MXene as well as an upsurge in potential applications, there has been an exponential improvement in publications since 2018. Records indicated an increase of over 5000% from 2017 to 2023.
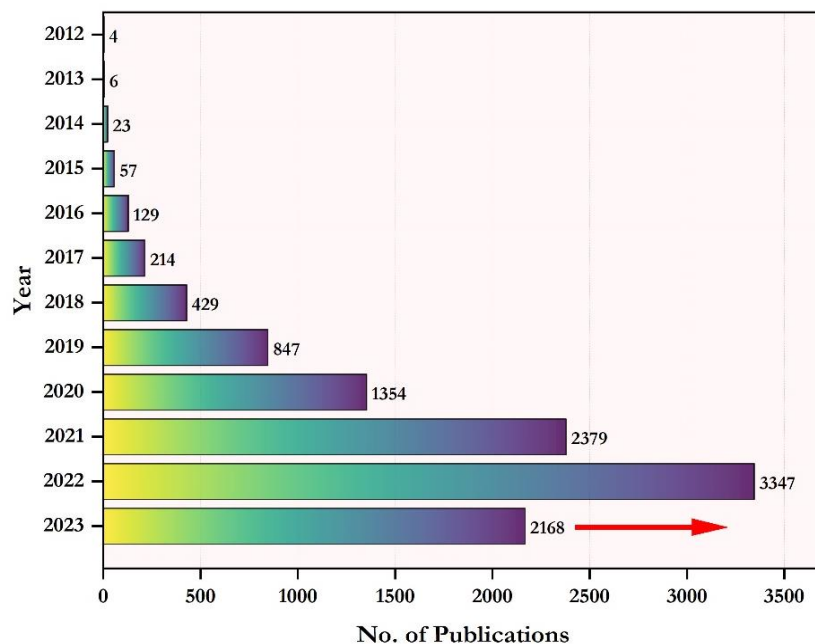
Figure 1. Exponential rise in MXene-based articles

This review article presents a comprehensive overview of the extensive family of 2D layered MXene materials, highlighting their unique structural features and remarkable properties that enable a wide range of applications. It discusses the various synthesis methods developed for producing 2D MXenes, along with their modifications. Finally, we describe various recent applications of MXenes, emphasizing their practical utility. To highlight the significance and impact of MXene research, we also include a bibliometric analysis. This analysis is crucial as it provides

insights into the research trends, key contributors, and the overall growth of the field, thereby underscoring the advancements and guiding future studies in MXene research.

2. SYNTHESIS OF MXENES

Two primary methods explored for synthesizing MXenes are the top-down and bottom-up approaches. In the top-down process of producing MXene, bulk materials are either reduced or parts of the overall composition are removed to produce micro to nano-size particles[10]. Selectively etching and exfoliation fall under top-down techniques, while chemical vapor deposition (CVD), and template methods are classified as bottom-up techniques [45]. The top-down approach is widely used for the preparation of multilayer since the first successful removal of aluminum from Ti_3AlC_2 to make multilayer Ti_3C_2 was accomplished using this process [12]. Wet chemical etching using HF acid yields multilayered MXenes of different compositions, including $Ti_3C_2T_x$, V_2CT_x, Ti_2CT_x, and Nb_2CT_x [46]. Despite HF being the main etchant in the MXene synthesis process, alternatives have been investigated because of its extremely volatile and hazardous nature [47]. Alternative etchants, such as electrochemical [48], halogen [49], molten salts [50], and hydrothermal [51], have broadened synthesis methods and resultant properties. Bifluorides of sodium [52], ammonium [53], and potassium [52] have been reported as alternative etchants for the selective removal of Al from Ti_3AlC_2. However, the synthesis of MXenes using HF leads to the intercalation of cations with fluoride or bifluoride salts, resulting in increased interlayer spacing. This interlayer spacing is further expanded when HF is used in combination with fluoride salts compared to using HF alone [52]. In-situ HF synthesis is carried out with reduced HF concentrations (5−10 wt%) within acid mixtures. To synthesize $Ti_3C_2T_x$[54], $Mo_3C_2T_x$ [55], and V_2C [56] MXenes from Ti_3AlC_2, Mo_3AlC_2, andV_2AlC MAX phases, a mixture of HCl and fluoride salts are utilized as the etchant. However, scaling of these techniques is challenging because unetched MXene remains during the exfoliation process [53]. The unetched MXene persists because the in-situ HF etching process may not uniformly penetrate all the layers, leading to incomplete removal of aluminum from some regions. This incomplete etching results from variations in the diffusion of HF through the multilayer structure and the limited access to inner layers, which is influenced by the MXene's intrinsic layer spacing and surface chemistry. Traditional HF aqueous solutions that are acidic cannot effectively etch nitride-based MAX phases. Consequently, producing nitride MXenes, like Ti_4N_3, requires selectively removing aluminum from Ti_4AlN_3 using molten salts. Although numerous studies still use HF or fluoride

sources as the preferred etchant for the MAX phase, this acid is extremely toxic and dangerous to handle, particularly for biological applications. Even a small amount of unreacted HF can cause cell death [57]. In humans, HF exposure can result in systemic toxicity that can be fatal [58]. Consequently, the direct use of HF or its in situ formation presents significant safety and environmental risks, impeding the progress of MXenes' applications [58]. Therefore, a fluorine-free etching technique is highly preferable for producing MXenes. Such an approach not only enhances safety and reduces environmental risks but also promotes the broader application and development of MXenes in various fields. There are several other methods for synthesizing MXenes without the use of HF. One alternative is using molten salts, such as molten chloride salts zinc chloride ($ZnCl_2$) [50] and copper chloride ($CuCl_2$) [59], to selectively etch the MAX phase. This method operates at high temperatures, which can enhance the efficiency of the etching process while avoiding the hazards associated with HF. Additionally, an electrochemical intercalation method was developed, where an electrolyte solution facilitates the removal of elements from the MAX phase through an electrochemical reaction, effectively producing MXenes without HF [48]. During the past several years, various bottom-up methods for synthesizing MXenes have emerged, including chemical vapor deposition (CVD) [60], the template method [61], and plasma-enhanced pulsed laser deposition (PEPLD) [62]. These approaches tend to produce higher quality MXenes than traditional top-down techniques, as they allow for greater control over atomic arrangements and surface properties. In 2015, ultrathin α-Mo_2C orthorhombic 2D crystals, just a few nanometers thick and with lateral sizes up to 100 μm, were successfully synthesized using CVD with methane on a copper foil bilayer substrate atop molybdenum foil [60]. This technique was also applied to create ultrathin tungsten carbide (WC) [63] and tantalum carbide (TaC) [64] crystals from tungsten and tantalum, respectively. However, despite these advancements, bottom-up methods have yet to achieve the synthesis of single-layer MXenes, resulting only in the formation of ultrathin films comprising multiple layers. This limitation underscores the challenges in manipulating atomic-scale interactions and achieving precise layer control in material synthesis.

The synthesis and application growth of MXenes, as illustrated in Figure 2a, is closely tied to advancements in their production methods since their discovery. These developments have enhanced the intrinsic properties of MXenes, such as their electrical conductivity, mechanical strength, and chemical stability, making them increasingly viable for a wide range of applications. The timeline

in Figure 2a highlights the correlation between synthesis breakthroughs and the expanding scope of MXene applications, underscoring the importance of continued research in refining synthesis methods to unlock the full potential of these versatile materials. Based on the number of atomic layers, MXenes are categorized into the following families: M_2X, M_3X_2, M_4X_3, and, most recently, M_5X_4, as shown in Figure 2b.
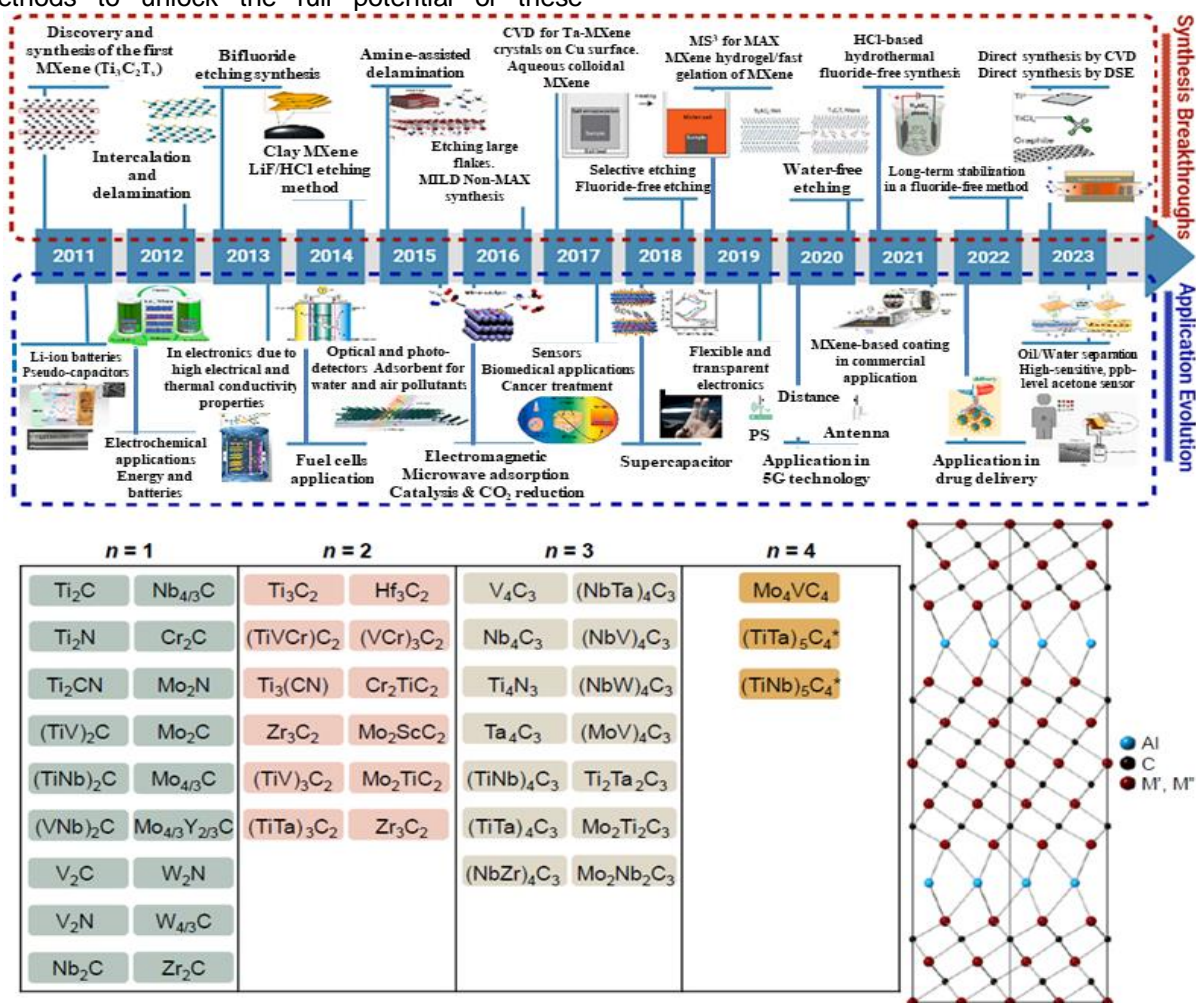
Figure 2. (a) Chronological overview of key synthesis advancements and emerging applications of MXenes from their discovery in 2011 to the present. Reproduced with permission from Reference [78]. © 2023 Elsevier. (b) List of MXenes Reported So Far, showcasing their structural diversity. Reproduced with permission from Reference [105]. © 2023 American Chemical Society

The constituents of MAX and MXene are shown in the periodic table (Figure 3a). The crystal structures of the 211, 312, and 413 MAX phases, along with the exfoliation process of MXene ($M_3X_2T_x$) from the MAX phase (M_3AX_2) to obtain free-standing nanosheets, are illustrated in Figure 3b. Following etching in the HF acid, the multilayered MXene particles exhibit an accordion-like structure (Figure 3d), which is different from the rock-like appearance of the MAX phase (Figure 3c)[53]. After intercalation with dimethyl sulfoxide (DMSO), which causes the layered structure to swell, the interlayer spacing of the expanded multilayer-MXene increases, and the interactions among the layers weaken[65]. When subjected to bath or tip sonication, the multilayer-MXene delaminates, producing smaller nanosheets due to the scissor effect of the sonic energy[66]. The corresponding SEM image is shown in Figure 3e. Figure 3f shows the XRD patterns of the Ti_3AlC_2 and $Ti_3C_2T_x$ powders, confirming the removal of the aluminum layer. The characteristic (104) peak at 39° associated with aluminum disappeared, additionally, the (002) peak at 9.8° shifted to a lower angle, indicating the delamination of MXene layers [67,68]. The water contact angle for the MAX phase was reported as 86°, whereas for MXene, it was 57.8°, indicating that the MXene film is hydrophilic.
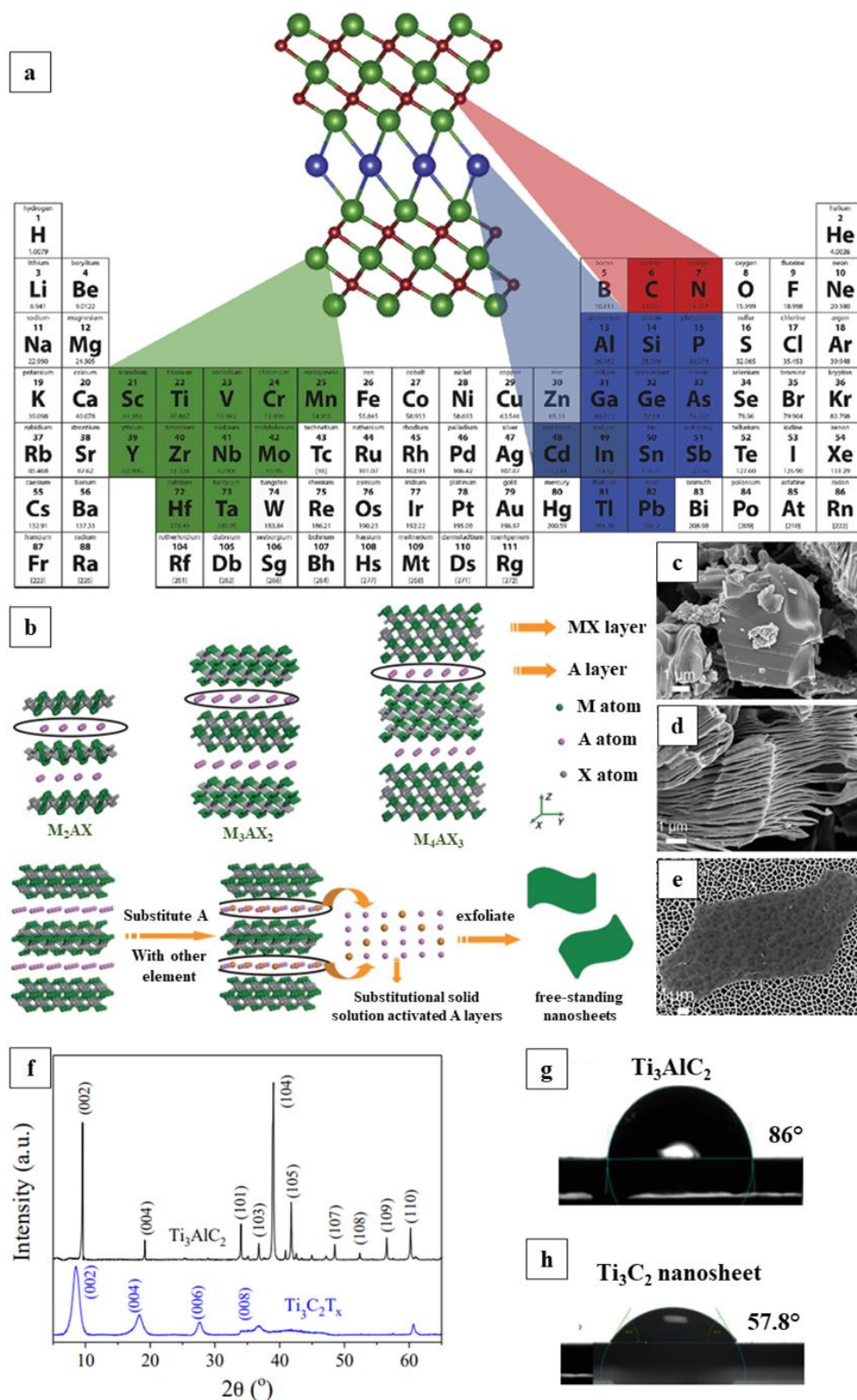
Figure 3. (a) The chemical components constituting MAX and MXenes. Reproduced with permission from Reference [5]. © 2019 Elsevier. (b) Schematic of the synthesis process of MXene. Reproduced with permission from Reference [106]. © 2013 Wiley. SEM images showing (c) MAX phase [66], (d) multilayered MXene. Reproduced with permission from Reference [66]. © 2020 Wiley, and (e) MXene in a delaminated state. Reproduced with permission from Reference [53]. © 2017 American Chemical Society. (f) XRD spectra of MAX and MXene [107]. contact angles of (g) MAX, and (h) MXene [108]

3. PROPERTIES

Over the past decade, 2D materials attracted significant attention owing to their unique properties distinct from their bulk forms. MXenes, in particular, combine metallic conductivity from their transition metal nitride, carbide, or carbonitride framework with hydrophilicity due to surface terminations. These materials exhibit diverse mechanical, electrical, electronic, magnetic, and optical properties. Their performance can be fine-tuned by adjusting their transition metals and surface terminations. A summary of MXene properties is shown in Figure4.
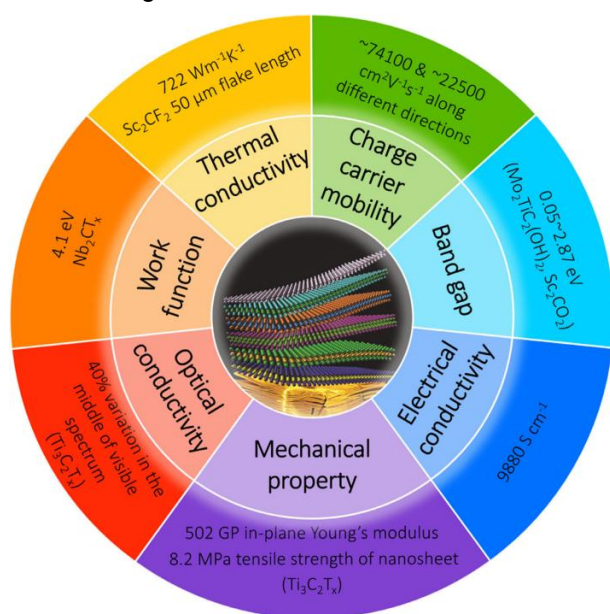
Figure 4. Summary of MXene properties, including thermal and electrical conductivity. mechanical property, work function, optical conductivity, band gap, and charge carrier mobility. Reproduced with permission from Reference [66]. © 2019 Wiley

3.1. Structural properties

In practical applications, MXene is typically enriched with surface termination groups like OH, F, and O following exfoliation from its 3D precursor MAX phase. OH, and O surface terminated MXenes are considered highly stable, as F terminations are swapped out for OH groups, whenever theyare rinsed or stored in water[69]. Studies have shown that metal adsorption or high-temperature procedures can change OH groups into O terminations [69]. Additionally, O-terminated MXene can break down into without surface-terminated MXene as well as metal oxides when exposed to metals like Ca, Mg, or Al[70].

3.2. Hydrophilic

MXenes are highly hydrophilic owing to their unique surface chemistry, which is dominated by the presence of various surface terminalgroups,

resulting in negatively charged surfaces [71]. These functional groups enhance their affinity for water and other polar solvents, making MXenes easily dispersible in aqueous solutions [72]. These groups are introduced during synthesis, typically involving selectively etching of A-layers from the MAX precursors using acidic solutions like HF acid[73]. This hydrophilic nature is advantageous in applications requiring dispersion in water-based solutions, such as in inks for printable electronics, humidity sensors, water purification, and composites for enhanced mechanical properties and EMI shielding, where uniform distribution within a matrix is crucial [74].

3.3. Electrical Property

MXenes exhibit exceptional electrical and electronic properties, primarily due to their unique structure and composition, which provide a high density of mobile charge carriers [75]. The layered structure of MXenes allows for efficient charge transport, akin to other well-known 2D materials like graphene[76]. Additionally, the transition metals in MXenes contribute d-electrons, which facilitate metallic conductivity[7]. The existence of conductive channels within the MXene layers and the relatively low energy barriers for electron movement result in high electrical conductivity[77]. This combination of features makes MXenes very well-suited for applications in energy storage devices, sensors, and EMI shielding, where excellent electrical performance is crucial[14].

3.4. Mechanical properties

The unique mechanical strength of MXenes is largely attributed to the robust M–X bond. Beyond bond strength, MXene nanosheets are held together by hydrogen bonds that are around six times higher than those found in graphite as well as MoS_2 sheets [78]. A particular study highlighted that the bare MXenes, which lack termination groups, possess interlayer binding energyas high as 3.3 J/m^2[79]. Earlier first-principles calculations had indicated that the elastic moduli of MXenes are at least double those of their parent 3D MAX phases and other 2D materials [80]. However, the interlayer mechanical characteristics and stiffnessof MXenes are influenced by surface-terminating groups andn-value in the $M_{n+1}X_n$.

3.5. Optical properties

In optics, MXenes have showcased intriguing attributes over recent years, such as optical transparency, efficient photothermal conversion, and plasmonic behavior. These capabilities to interact with light in diverse manners have profoundly influenced the research community[81]. The material's optical properties are predominantly dictated by its surface terminations, underscoring

their critical role in modulating how MXenes interact with light. This nuanced understanding is pivotal for leveraging MXenes in advanced optical applications, from transparent electrodes to photonic devices. The optical characteristics of MXenes differ based on their composition and the surrounding medium. Generally, MXenes exhibit minimal light absorption in the UV–Vis range (300–500 nm). However, a 5 nm thick film of $Ti_3C_2T_x$ is largely transparent within this range, with a transmittance of approximately 91% [66]. Variations in optical behavior among MXenes are notable; for instance, although Ti_3N_2 and Ti_3C_2 exhibit similar light reflectivity, Ti_3N_2 is a much better absorber. Conversely, Ti_3C_2 has a higher refractive index of 11.9 compared to 9.9 for Ti_3N_2[66].

4. APPLICATIONS OF MXENES

The distinctive blend of exceptional electrical conductivity and hydrophilicity in MXenes makes them excellent alternatives for a diverse array of applications.Their layered morphology allows for the intercalation of ions and molecules, further enhancing their versatility. Modifying their surface terminationsenables precise control over their electronic properties and chemical reactivity. Additionally, MXenes exhibit flexibility and outstanding mechanical strength making them appropriate for use in flexible electronics and composite materials.Figure 5 illustrates the diverse applications of MXenes, showcasing their broad spectrum, versatility, and effectiveness across multiple domains.
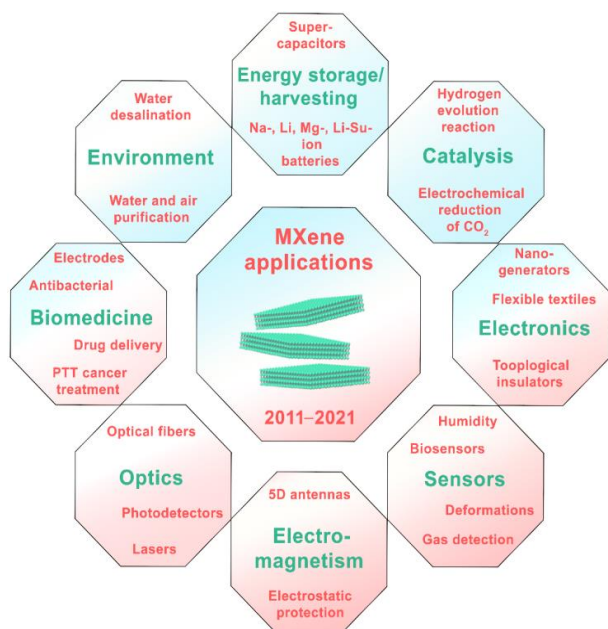
Figure 5. Overview of Various Applications of MXenes [14]

MXenes offer promising applications across diverse fields owing to their unique properties. Some key areas of potential include:

4.1. Energy Storage

Batteries, while widely used for energy storage in portable electronics and electric vehicles, are limited by their lower power densities, and degradation over time [82]. Due to their exceptional electrical conductivity and the ease with which ions can diffuse between their layers, MXenes have demonstrated significant potential as electrodes for sodium [83], potassium [84], aluminum [85], lithium [86], and zinc ion batteries [25]. Most research to date has predominantly focused on sodium and Lithium-ion batteries. For instance, multi-layered $Ti_3C_2T_x$ exhibits a capability of approximately 150 $mAhg^{-1}$ at 260 mA g^{-1} in Lithium-ion batteries [87] and nearly 100 mAh g^{-1} at 100 mA g^{-1} in Sodium-ion batteries [70]. However, electrodes constructed from predominantly single-layered, delaminated flakes are anticipated to achieve even higher capacities because of their increased surface area exposure to the electrolyte.

Supercapacitors offer an alternative for energy storage in electric vehicles and portable electronics but have lower energy densities than batteries[88]. Efforts to improve their energy density focus on increasing volumetric capacitance [89]. Supercapacitors are categorized into electrical double-layer capacitors, which accumulate charge via ion accumulation at the electrode and electrolyte interfaces, and pseudocapacitors, which utilize surface redox interactions for charge storage. While pseudocapacitors generally have higher volumetric capacitance, they often have poor cycling stability. Because of their 2D structure, vast surface area, and defined geometry, MXenes are promising materials for supercapacitor electrodes. The fast electron transport provided by the transition metallic core layers in MXenes enables exceptionally high rates of charge storage within the electrode [90]. Their surface, resembling transition metal oxides, offers redox-active spots essential for pseudocapacitive charge retention. This dual functionality makes MXenes highly suitable for high-performance batteries and ultrafast supercapacitors as electrode materials. Additionally, the ultrathin interlayer spacing among 2D sheets facilitates swift ion transport and intercalation. This spacing can be adjusted through techniques such as pillaring, pre-intercalation, and the creation of heterostructures or hybrids that utilize different 2D materials to accommodate ions of various sizes. Moreover, MXenes' surface terminations can be engineered to optimize specific redox reactions, enhancing their performance in electrochemical applications. MXene-based structures used in batteries as electrode materials are presented in Table 1. The capacitance and related characteristics of MXene as a supercapacitor electrode material are listed in Table 2.

Table 1. MXene-derived structures are employed as electrode materials in batteries

MXene Based Material	Battery type	Electrode	Initial Capacity (mAh·g^{-1})	Current Density	Capacity Retention (mAh·g^{-1})	No. of Cycles	Coulombic Efficiency (%)	Ref.
V_2CT_x	Al-ion	cathode	335	100 mA·g^{-1}	112	20	90	[111]
$Ti_3C_2T_x$	Na-ion	anode	110	30 mA·g^{-1}	73	70	100	[112]
Nb_2C	Li-ion	anode	780	0.5 C	420	100	≈100	[86]
V_2C	Li-ion	anode	467	1 C	291	20	98.6	[113]

Table 2. Electrochemical capabilities of MXene-based electrode materials in supercapacitors

MXene Based Material	Type of Electrode	Electrolyte	Rate	Capacity Retention F·g^{-1}	Cycle Number	Volumetric Capacitance F·cm^{-3}	Ref.
V_2CT_x	film electrode	seawater	2 A·g^{-1}	181.1	5000	317.8	[114]
$Ti_3C_2T_x$	three-electrode system	H_2SO_4 (3 M)	0.5 A·g^{-1}	351	10000	1142	[115]
Ti_2CT_x	porous	30 wt% KOH	1 A·g^{-1}	51	6000	-	[116]
Ta_4C_3	free-standing	0.1 M H_2SO_4	1 V·s^{-1}	481	2000	520	[88]
Ti_3C_2/CNT	hybrid films	KOH (6 M)	1 A·g^{-1}	134	10000	-	[117]

4.2. Electromagnetic Shielding

EMI is the term used to describe the disturbances generated by electronic circuits during their operation, which can adversely affect nearby circuits [91]. As the use of electrical and electronic equipment shows exponential growth in the commercial, industrial, and military sectors, the resulting increase in EMI necessitates effective shielding [92]. Ideal shielding materials must possess excellent electrical conductivity and magnetic permeability to attenuate electromagnetic waves efficiently [93]. Additionally, they should exhibit lightweight and flexible properties to integrate seamlessly into compact electronic devices [94]. Advanced materials like MXenes, with their high conductivity, mechanical flexibility, and tunable surface chemistry are emerging as promising contenders for EMI shielding solutions in modern electronics [95].

Table 3. Performance of various MXene-derived materials in terms of EMI shielding effectiveness.

Composition	Structure	Etchant for Mxene	Wt. %	Thickness [mm]	SE [dB]	Ref. No.
$Ti_3C_2T_x$	Pure	LiF/HCL	100	0.045	92	[118]
Ti_3CNT_x (annealing for 1 h at 350 °C)	Pure	/	/	0.045	116	[119]
$Ti_3C_2T_x$	Pure	LiF/HCL	100	0.000055	20	[120]
$Ti_3C_2T_x$/paraffin	Matrix Composite	HF	90	1	76.1	[121]
$Ti_3C_2T_x$/polystyrene	Matrix Composite	LiF/HCL	/	2	62	[122]
$Ti_3C_2T_x$/Ni/PVDF	Matrix Composite	LiF/HCL	10	0.003	52.6	[123]
$Ti_3C_2T_x$/rGO/Epoxy	Matrix Composite	LiF/HCL	3.3	/	55	[124]
$Ti_3C_2T_x$/ CNF	composite paper	LiF/HCL	50	0.047	25	[125]
$Ti_3C_2T_x$/CNT/CNF	composite paper	LiF/HCL	/	0.038	38.4	[126]
$Ti_3C_2T_x$/ANF	Composite film	LiF/HCL	80	0.0032	40.6	[127]

Figure 6a depicts the block diagram of a vector network analyzer (VNA) setup. Scattering parameters, measured through a VNA, characterize how the incident and transmitted waves interact with a shield, providing insights into its reflection and transmission properties. The possible EMI shielding mechanism is illustrated in Figure 6b. When incoming electromagnetic (EM) waves encounter the outermost layer of MXene ($Ti_3C_2T_x$)/PEDOT:PSS composite film, a portion of the EM waves is promptly reflected because of the abundance of the free electrons onto the highly conductive $Ti_3C_2T_x$ surface. Another portion of the radiation is absorbed by the material, leading to multiple internal reflections within the composite layers. This process enhances energy dissipation

and ultimately reduces the transmitted electromagnetic radiation, thereby effectively attenuating the incident waves. As illustrated in Figure 6c, MXenes derived from titanium (such as Ti_2CT_x, Ti_3CNT_x, $Ti_{1.6}Nb_{0.4}CT_x$, and $Ti_3C_2T_x$), as well as V_2CT_x, demonstrate electrical conductivity exceeding 1000 S cm^{-1}. In contrast, MXenes derived from niobium exhibit comparatively low electrical conductivity.

Figure 6d displays the total EMI shielding effectiveness (SE_T) for various MXene films with comparable thicknesses (5 ± 0.3 μm) across the X-band (8−12 GHz). Each film shows a nearly linear frequency-dependent trend, with SET values decreasing as the frequency increases. This pattern suggests that the MXenes under investigation share a similar conductive response to frequency variations. Table 3 lists the performance of pure MXene film and several MXene-based composites in terms of electromagnetic shielding effectiveness.
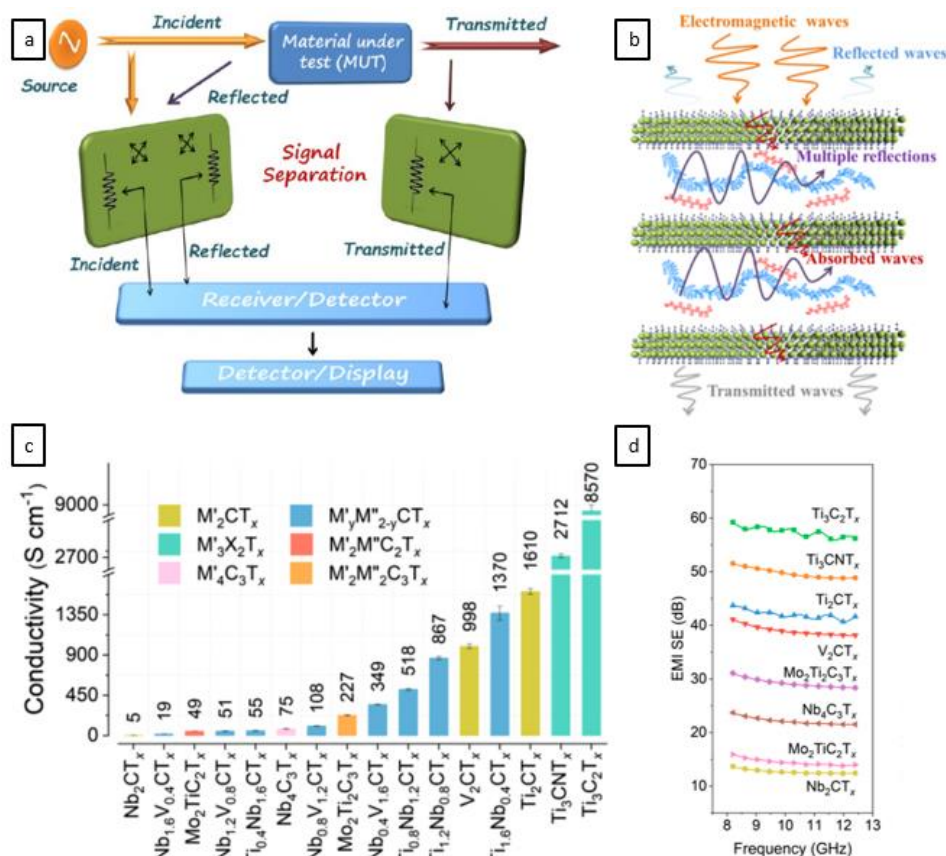
Figure 6. A schematic representation of the VNA. Reproduced with permission from Reference [109]. © 2022 American Chemical Society. (b) Schematic illustration of the EMI shielding mechanism of the MXene ($Ti_3C_2T_x$)/ PEDOT:PSS (composite film of 11.1 μm). Reproduced with permission from Reference [110]. © 2018 American Chemical Society. (c) Electrical Conductivity of Various MXenes [27]. (d) EMI shielding effectiveness of various MXene films in X-band frequency range. Reproduced with permission from Reference[27]. © 2020 American Chemical Society

4.3. Photocatalysis

Photocatalysis is a method that uses catalysts to transform solar energy into chemical fuels and remove pollutants from the surroundings [96]. Since 2014, MXenes have been extensively studied in photocatalysis, leading to a notable rise in research on MXene-based photocatalysts. Several factors contribute to the effectiveness of MXenes in photocatalytic applications: (i) The substantial functional groups that result from wet chemical exfoliation are beneficial for forming an intimate interface between the MXene and attached semiconductor material, (ii) the interfacial chemistry of MXenes can be adjusted to modify bandgap alignment, and (iii) the multilayer structure with high- conductive metal centers enhances metallic conductivity and electron-receiving capabilities [97]. Consequently, MXenes are considered a promising alternative to other 2D materials, being thoroughly investigated for various photocatalytic uses,including water splitting, CO_2 reduction, nitrogen fixation, and pollutant oxidation. In such applications, MXenes can enhance

photocatalytic performance by improving charge carrier separation and transfer, limiting photocatalyst size, providing robust support, and increasing reactant adsorption[98].

4.4. Sensing Technology

Materials with high conductivity, flexibility, ease offunctionalization, and prolonged stability are crucial for advanced self-powered sensors[99]. MXenes are employed in sensors for detecting gases, biomolecules, and pollutants, leveraging their unique electronic structure and surface chemistry to enable efficient charge transport and sensitivity, making them ideal candidates for advanced sensing technologies [100].

These diverse applications underscore MXenes' potential across scientific, technological, and environmental domains, driving ongoing research and development to harness their capabilities for practical and impactful solutions.

5. BIBLIOMETRIC ANALYSIS AND CURRENT DEVELOPMENTS IN MXENE RESEARCH

MXene isrecognized as a high-performance material with exceptional qualities. The bibliometric analysis is a useful tool for identifying uniqueness and promise in light of current trends in the evolution of current area studies [101]. For bibliometric research, reliable data must be obtained through a reputable database to assure the reliability of the findings and further the data used as input for the software. The databases that are readily accessible for data collection are Google Scholar, Web of Science, Dimensions, Microsoft Academic, IEEE Xplore, PubMed, and Scopus. Web of Science Core Collection database (https://www.webofscience.com) was selected as the primary information source for this study because of its extensive coverage and thorough content. Bibliometric software is utilized to assess individual performance and visualize publications based on their titles, institutions, authors, countries, and references [102]. VOSviewer has been used to construct and visualize authors, institutions, countries, keywords, journals, and relationships between co-authorship, citation, co-citation, co-occurrence, and bibliographic coupling. The data collection process started with a thorough search of MXene using the WOS search engine. 2012 to 2023 was chosen as the sample collecting period, and 10957 papers were found using the search engine.
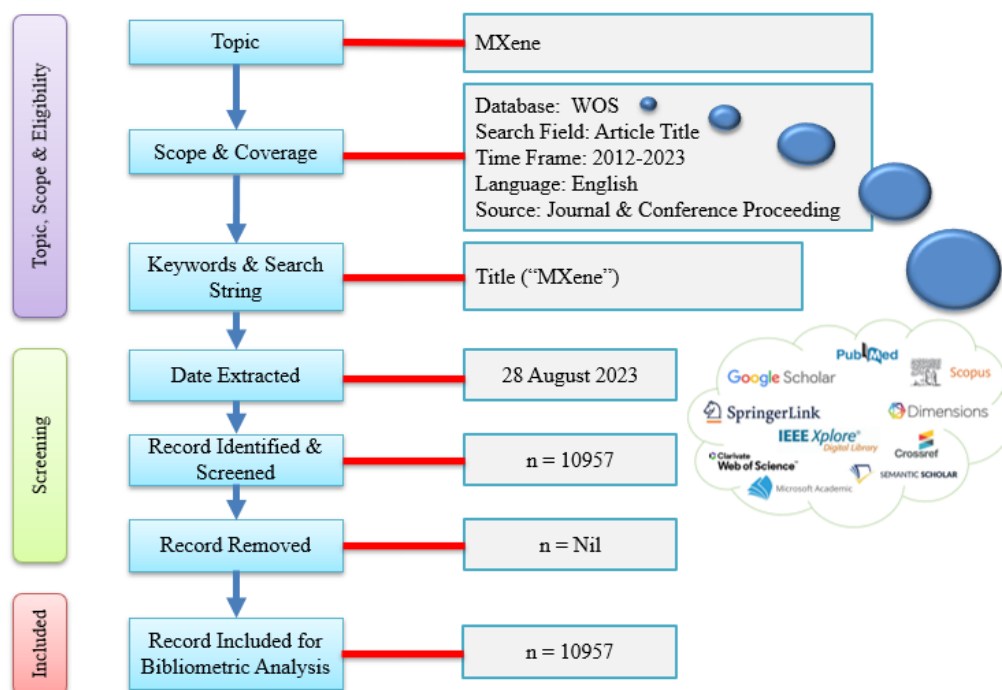
Figure 7. Flow chart of the search process

The whole search approach, including the search string and keywords, is presented in Figure 7. The field for searching was restricted to titles only to increase the accuracy of the outcomes because integrating additional search criteria like keywords and abstract raises the risk of including unrelated publications in our bibliometric analysis (false-positive results). Higher false-positive results necessitate longer pre-cleaning procedures. The methodology employed in the bibliometric analysis follows the approach outlined by Zakaria et al. [103], providing a structured and comprehensive evaluation of the research developments and contributions within the realm of MXene studies.

A statistical technique employed for identifying similar subjects is called cluster analysis. In VOSviewer, clusters do not overlap. Cluster numbers are used to identify clusters. Citation and co-occurrence analysis, which is based on the notion that citations signify the intellectual connections among publications that come from one publication citing another, is a fundamental approach to effective scientific mapping [104]. In this research, the citation count of an article has been used to estimate its effect. Therefore, taking advantage of citations, one may investigate the most significant works in an area to learn about the dynamics in that realm of knowledge.

5.1. Assessment based on participating nations

The nations participating in the MXene studies are ranked according to the number of papers published. About 33918 researchers from 90 different nations accounted for the publication of retrieved documents. China and the USA are the top two contributors to the MXene research domain. The top contributing countries for this research domain are shown in Table 4.

An effective way to evaluate the significance of the articles and the contributors is to look at the ratio of the total number of citations to the number of documents. The USA has an average of 103 citations per document followed by South Korea with 40 citations per document, compared to China with only 34 citations per document. However, China is the major contributor in terms of publications. It demonstrates the prominent level of quality output produced by the USA in terms of citations. Visualization of international collaboration among nations with a minimum output of five documents is displayed in Figure 8.

Table 4. The top contributing nations in the context of MXene publications

Ran-king	Country	Documents	Citations	Citations to documents ratio
1.	Peoples r China	8387	287113	34
2.	USA	1224	126004	103
3.	South Korea	622	24874	40
4.	India	528	8667	16
5.	Australi a	387	25649	66
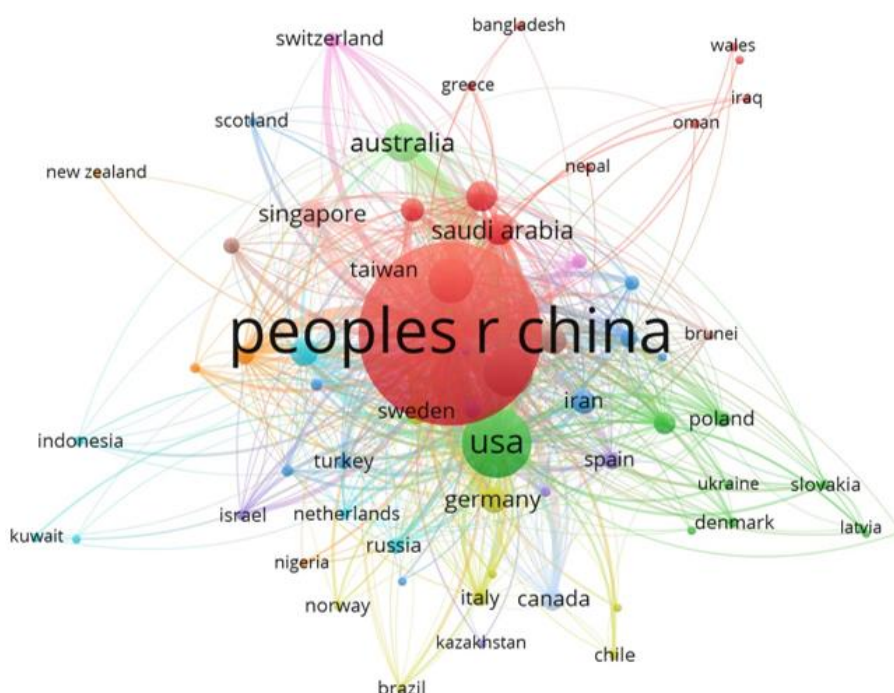
Figure 8. Cooperation among a number of nations

In bibliometric analysis using VOSViewer software, the size of individual nodes (representing nations, authors, or institutions) in a visualized network indicates their impact or contribution within the research field. Larger nodes signify higher levels of influence.

5.2. Assessment based on participating institutions

Chinese Acad Sci gained first place, followed by Drexel University, concerning the number of articles published. Chinese Acad Sci achieved 973 documents with 45709 citations. Despite being

ranked second, Drexel University still received a lot of citations (87562) while having less documents (457) as compared to Chinese Acad Sci. Additionally, as a result of the development of this field of study, institutions now place a greater emphasis on matters related to MXene materials. In the area of MXene research, 10 institutions contributed more than 200 articles as displayed in Table 5.

Table 5. Institutional rankings based on the number of articles published on MXene

Ranking	Organization	Documents	Citations	Citations to documents ratio
1.	Chinese acad sci	973	45709	47
2.	Drexel univ	457	87562	192
3.	Univ Chinese acad sci	328	16079	49
4.	Zhengzhou univ	297	13204	44
5.	Univ sci & technol China	254	10218	40
6.	Shenzhen univ	232	8373	36
7.	South China univ technol	213	10402	49
8.	Northwestern polytech univ	211	9166	43
9.	Sichuan univ	211	8335	40
10.	Jilin univ	210	9691	46

For Drexel University, the citations-to-publication ratio is calculated to be ~192, while it is only 47 for the Chinese Academy ofSciences. The ratio's difference demonstrates the significant contributions to this field's research. Overall, bibliometric analysis provides valuable insights into institutional collaboration within the scientific community, which can inform strategic decisions, funding allocations, and collaborative initiatives among research institutions. Figure 9 displays the collaboration networks of institutions.
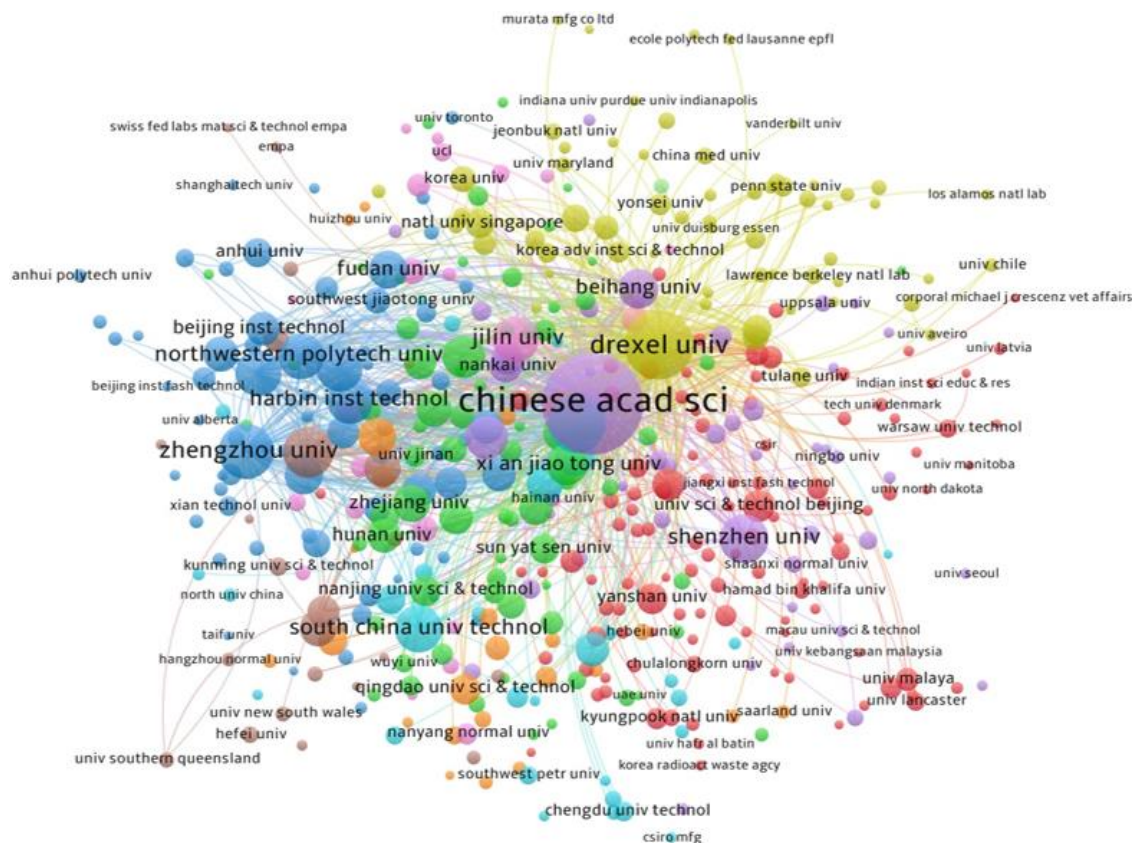
Figure 9. Cluster of institutional collaboration.

5.3. Assessment based on authors

The number of published articles and citations are used to rank the writers. Yuri Gogotsi was found to have the most articles (344) with 82506 citations, followed by Babak Anasori with 122 articles and 29532 citations and Michel W. Barsoum with 99 articles and 33834 citations. They are regarded as the leading researchers in this area. Table 6 presented the top 10 authors who had contributed more than 50 articles in the domain of MXene research.

Table 6. Authors rankings based on number of articles published on MXene.

Ranking	Author	Documents	Citations	Citations to documents ratio
1.	Yury Gogotsi	344	82506	240
2.	Babak Anasori	122	29532	242
3.	Michel W. Barsoum	99	33834	342
4.	Han Zhang	75	3850	51
5.	Michael Naguib	69	22395	325
6.	Lei Wang	68	3393	50
7.	Aiguo Zhou	67	6778	101
8.	Peng Zhang	66	4107	62
9.	Husam N. Alshareef	64	6652	104
10.	Wei Zhang	62	1520	25

Visualization of international collaboration among authors is displayed in Figure 10.
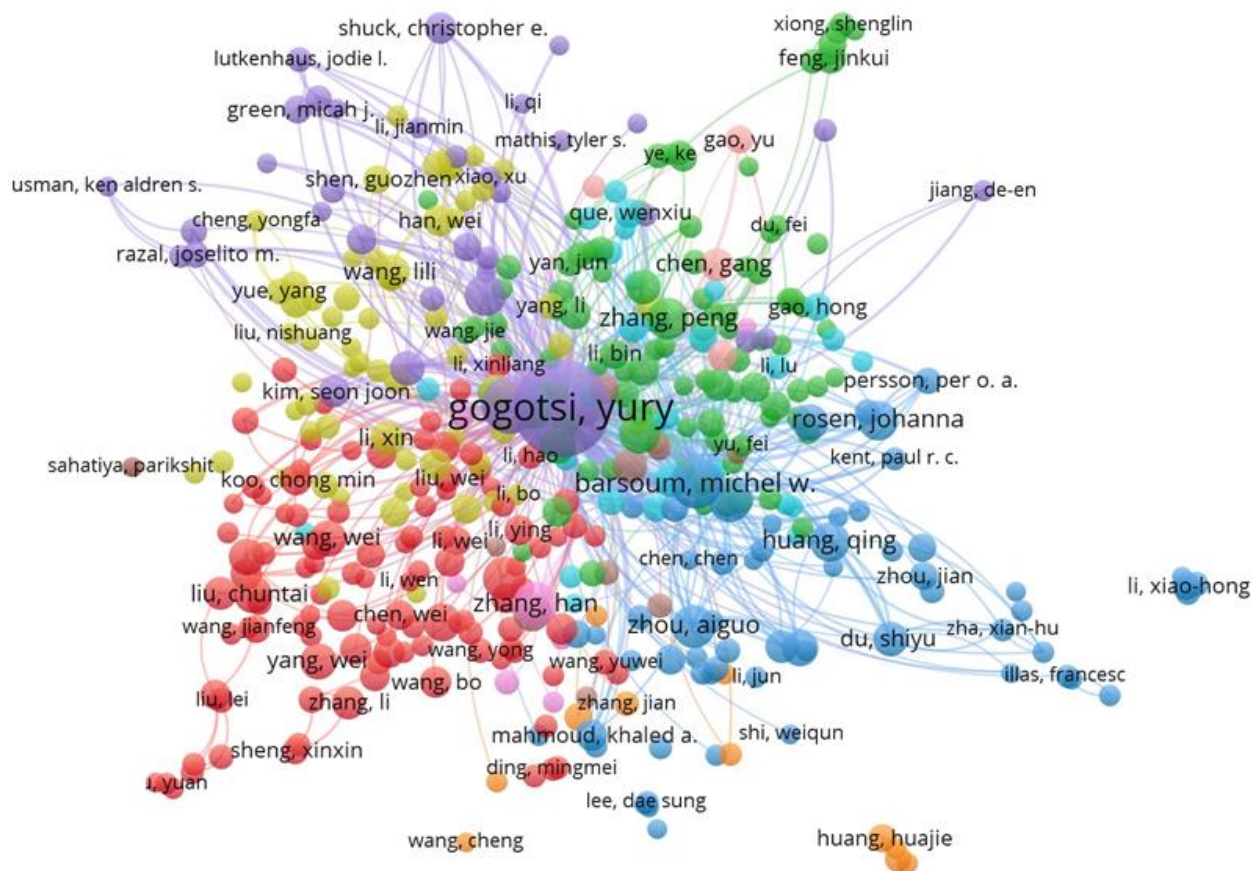
Figure 10. An illustration of the authors contributions to scientific publications in the MXene field

5.4. Assessment based on publications of articles based on MXene

The well-known publications that publish in this area of research have been found through a literature review of the many MXene-based research articles. The ranking of journals is shown in Table 4 according to the quantity of published documents, which was chosen as the ranking criterion. The top ranked journals, according to the quantity of papers published, are Chemical Engineering Journal followed by ACS Applied Materials & Interfaces, and ACS Nano. Table 7 lists the 8 journals that published more than 200 publications in the MXene research field.

The average number of citations per document for the ACS nano journal is 19586 with 317 publications, which is the highest among all other journals. In bibliometric analysis, a cluster typically refers to a grouping of related documents. Research on MXene is being published in all prestigious publications, and Figure 11 shows the clustering patterns.

Table 7. Journal rankings based on number of articles published on MXene

Ran-king	Journal name	Documents	Citations
1.	Chemical engineering journal	535	17949
2.	ACS applied materials & interfaces	479	21580
3.	ACS nano	317	39658
4.	Journal of materials chemistry A	304	17206
5.	Applied surface science	283	7330
6.	Advanced functional materials	266	21451
7.	Journal of alloys and compounds	227	3363
8.	Ceramics international	208	4979
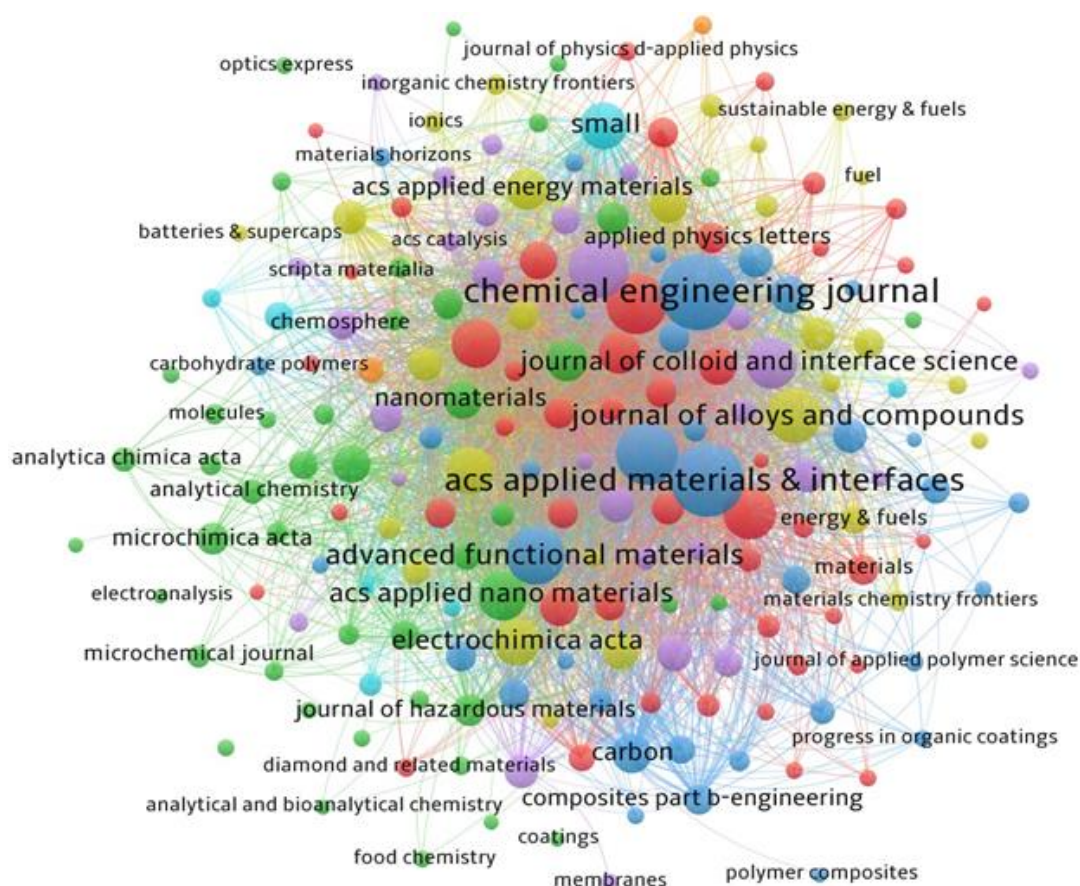
Figure 11. An illustration of the Journals contributions to scientific publications in the MXene field

5.5. Assessment based on Keywords

The use of relevant and appropriate keywords has a significant impact on the operation and efficacy of document searches. The keyword serves as a vital link that separates the reference sources from the wide range of readily available

papers. MXene, performance, and Nanosheets are the top three keywords, appearing 4834, 1955, and 1548 times respectively. It is evident to utilize the precise keyword or phrase for quick and accurate document identification. 15 keywords that appear in the MXene research field most frequently (more than 500 times) are listed in Table 8.

The growth of international research in the area of MXene research has been emphasised by this bibliometric analysis. A thorough analysis of the clustering structure gave more information on the teams that collaborated and the caliber of the research articles. The outcomes shown throughout the study period (2012-2023) unmistakably demonstrated the development and continued expansion of MXene as a research area.

A cluster of significant keyword occurrences is displayed in Figure 12.

Table 8. lists keywords in order of occurrence.

Ranking	Keyword	Occurrences
1.	mxene	4834
2.	performance	1955
3.	nanosheets	1548
4.	graphene	1468
5.	mxenes	978
6.	nanoparticles	924
7.	composite	839
8.	composites	813
9.	carbon	774
10.	intercalation	718
11.	ti_3c_2	696
12.	nanocomposites	690
13.	$ti_3c_2t_x$ mxene	673
14.	transition-metal carbides	536
15.	graphene oxide	508
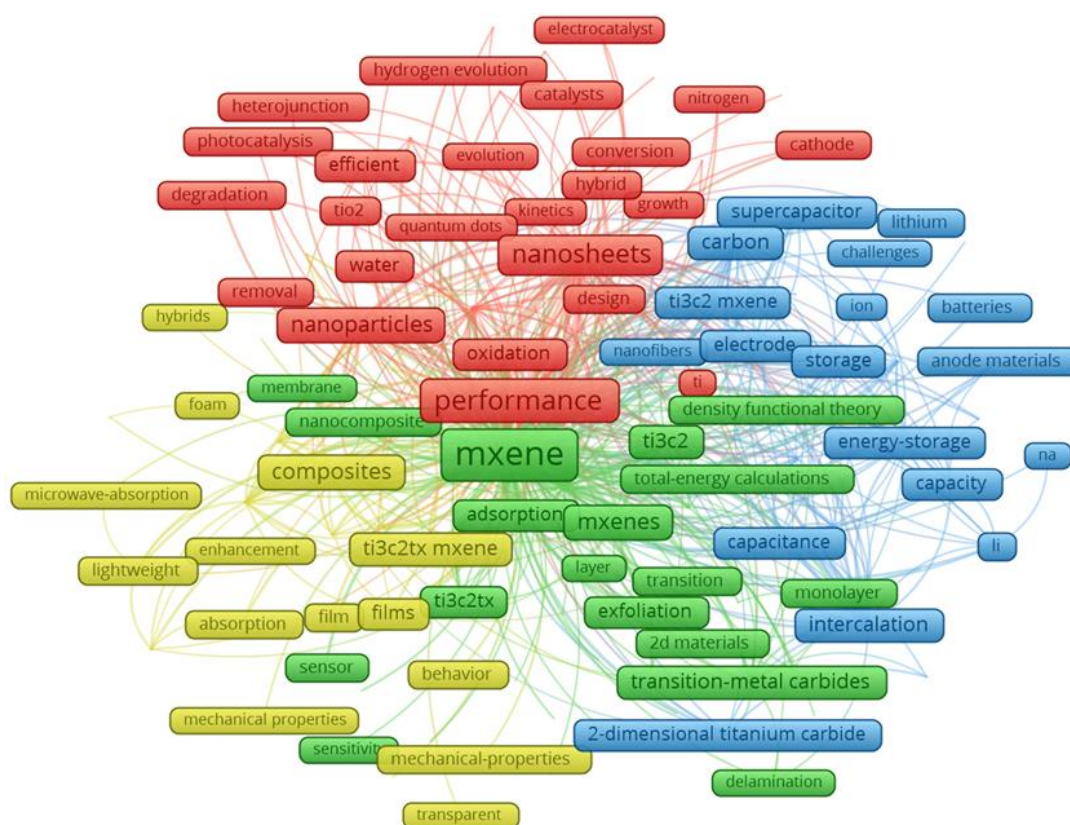
Figure 12. An illustration displaying the co-occurring assessment of keywords in studies on MXene that have been published

6. CONCLUSIONS AND OUTLOOK

Following their discovery, MXenes rapidly gained recognition as a highly promising class of 2D materials, demonstrating significant potential for a variety of scientific and technological applications. The synthesis techniques for MXenes have seen considerable advancements, enabling better control over their properties and expanding

their research scope. This progress has facilitated precise tuning of electronic and optical properties through surface terminations and compositional adjustments, allowing for enhanced performance in various applications. MXenes are perfect for energy storage applications since their interlayer spacing can be adjusted to maximize ion transit. The distinctive blend of metal-like conductivity and hydrophilicity in MXenes also offers exciting opportunities for creating EMI shielding materials.As the understanding of their fundamental physical properties deepens, MXenes continue to stimulate revolutionary research directions and innovative experimental techniques, further driving innovation and exploration in the field. Looking ahead, future research will likely focus on advanced synthesis methods, new functionalization strategies, the development of hybrid materials, and the exploration of emerging applications. However, challenges remain, including synthesis complexity, stability issues, environmental and health impacts, and the high production cost. Addressing these challenges through targeted research and innovation will be crucial for the successful commercialization and integration of MXenes into next-generation technologies.

Bibliometric analysis is essential in shaping scientific research, guiding decision-making, and promoting knowledge dissemination and collaboration. The bibliometric analysis employed in this literature underscores the notable expansion of global research in MXene. Our bibliometric investigation indicates that research on MXene is still actively ongoing. A substantial dataset from the Web of Science was systematically analyzed, focusing on research growth across nations, institutions, authors, journals, and keywords. The analysis revealed China as the leading contributor with 8,387 articles, followed by the USA with 1,224 publications. Notably, the USA has a higher average citation count per document (103)compared to China (34), highlighting the quality of US research output. The two largest contributing institutions were the Chinese Academy of Sciences and Drexel University, while Yuri Gogotsi, Babak Anasori, and Michel W. Barsoum were the most prolific authors. The Chemical Engineering Journal and ACS Applied Materials & Interfaces were the most favored journals. Certainly, it is crucial to highlight that despite the comprehensive investigation, this research has notable limitations. For instance, the reliance on data from the Web of Science, although recognized as one of the most reliable and trustworthy sources of information, introduces a potential limitation. The observed patterns and conclusions may vary when data is obtained from different search platforms.

7. REFERENCES

[1]   Y. Gogotsi, B. Anasori (2019) The rise of MXenes. ACS Nano, 13, 8491–8494, https://doi.org/10.1021/acsnano.9b06394.

[2]   K.S. Novoselov, D. Jiang, F. Schedin, T.J. Booth, V. V Khotkevich, S. V Morozov, A.K. Geim (2005) Two-dimensional atomic crystals. PNAS, 102(30),10451–10453, https://doi.org/10.1073/pnas.050284810.

[3]   H. Zhang (2015) Ultrathin two-dimensional nanomaterials. ACS Nano, 9, 9451–9469, https://doi.org/10.1021/acsnano.5b05040.

[4]   H. Liu, A.T. Neal, Z. Zhu, Z. Luo, X. Xu, D. Tománek, P.D. Ye (2014) Phosphorene: An unexplored 2D semiconductor with a high hole mobility. ACS Nano, 8, 4033–4041, https://doi.org/10.1021/nn501226z.

[5]   R.M. Ronchi, J.T. Arantes, S.F. Santos (2019) Synthesis, structure, properties and applications of MXenes: Current status and perspectives. Ceram Int, 45, 18167–18188, https://doi.org/10.1016/j.ceramint.2019.06.114.

[6]   R. Riedel, I.-Wei. Chen (2010) The Mn+1AXn phases and their properties.Ceramics science and technology: materials and properties,2, 1–510, https://doi.org/10.1002/9783527631971.

[7]   M. Naguib, V.N. Mochalin, M.W. Barsoum, Y. Gogotsi (2014) 25th anniversary article: MXenes: A new family of two-dimensional materials. Advanced Materials, 26, 992–1005 https://doi.org/10.1002/adma.201304138.

[8]   Y. Gogotsi, Q. Huang (2021) MXenes: two-dimensional building blocks for future materials and devices. ACS Nano, 15, 5775–5780, https://doi.org/10.1021/acsnano.1c03161.

[9]   Z. Zhang, X. Duan, D. Jia, Y. Zhou, S. van der Zwaag (2021) On the formation mechanisms and properties of MAX phases: A review. J Eur Ceram Soc, 41, 3851–3878 https://doi.org/10.1016/j.jeurceramsoc.2021.02.002

[10]   M. Naguib, O. Mashtalir, J. Carle, V. Presser, J. Lu, L. Hultman, Y. Gogotsi, M.W. Barsoum (2012) Two-dimensional transition metal carbides. ACS Nano, 6, 1322–1331 https://doi.org/10.1021/nn204153h.

[11]   Z. Xiao, S. Ruan, L.B. Kong, W. Que, K. Zhou, Y. Liu, T. Zhang (2020) MXenes and MXenes-based composites. Springer international publishing, Cham, 8, 1-404, https://doi.org/10.1007/978-3-030-59373-5.

[12]   M. Naguib, M. Kurtoglu, V. Presser, J. Lu, J. Niu, M. Heon, L. Hultman, Y. Gogotsi, M.W. Barsoum (2011) Two-dimensional nanocrystals produced by exfoliation of Ti3AlC 2. Advanced Materials, 23, 4248–4253 https://doi.org/10.1002/adma.201102306.

[13]   Q. Zhang, R. Fan, W. Cheng, P. Ji, J. Sheng, Q. Liao, H. Lai, X. Fu, C. Zhang, H. Li (2022) Synthesis of large-area MXenes with high yields through power-focused delamination utilizing vortex kinetic energy. Advanced Science, 9, 2202748, https://doi.org/10.1002/advs.202202748.

[14]   M. Pogorielov, K. Smyrnova, S. Kyrylenko, O. Gogotsi, V. Zahorodna, A. Pogrebnjak (2021) MXenes—a new class of two-dimensional materials: Structure, properties and potential applications. Nanomaterials, 11,3412 https://doi.org/10.3390/nano11123412.

[15]   J. Zhang, N. Kong, S. Uzun, A. Levitt, S. Seyedin, P.A. Lynch, S. Qin, M. Han, W. Yang, J. Liu, X. Wang, Y. Gogotsi, J.M. Razal (2020) Scalable manufacturing of free-standing, strong Ti3C2Tx MXene films with outstanding conductivity. Advanced Materials, 32, 2001093 https://doi.org/10.1002/adma.202001093.

[16]   A. Lipatov, H. Lu, M. Alhabeb, B. Anasori, A. Gruverman, Y. Gogotsi, A. Sinitskii (2018) Elastic properties of 2D Ti3C2Tx MXene monolayers and bilayers. Sci Adv, 4,1-7, https://doi.org/10.1126/sciadv.aat0491

[17]   V. Kamysbayev, A.S. Filatov, H. Hu, X. Rui, F. Lagunas, D. Wang, R.F. Klie, D. V. Talapin (2020) Covalent surface modifications and super-conductivity of two-dimensional metal carbide MXenes. Science, 369, 979–983, https://doi.org/10.1126/science.aba8311.

[18]   J. Liu, H. Bin Zhang, R. Sun, Y. Liu, Z. Liu, A. Zhou, Z.Z. Yu (2017) Hydrophobic, flexible, and lightweight MXene foams for high-performance electromagnetic-interference shielding. Advanced Materials, 29, 1702367 https://doi.org/10.1002/adma.201702367.

[19]   S. Nahirniak, A. Ray, B. Saruhan (2023) Challenges and future prospects of the MXene-based materials for energy storage applications. Batteries, 9, 126, https://doi.org/10.3390/batteries9020126.

[20]   O. Salim, K.A. Mahmoud, K.K. Pant, R.K. Joshi (2019) Introduction to MXenes: synthesis and characteristics. Mater Today Chem, 14, 100191, https://doi.org/10.1016/j.mtchem.2019.08.010.

[21]   B. Anasori, M.R. Lukatskaya, Y. Gogotsi (2017) 2D metal carbides and nitrides (MXenes) for energy storage. Nat Rev Mater, 2, 16098, https://doi.org/10.1038/natrevmats.2016.98.

[22]   Y. Wang, Y. Wang (2023) Recent progress in MXene layers materials for supercapacitors: high-performance electrodes. SmartMat, 4, e1130, https://doi.org/10.1002/smm2.1130.

[23]   A. Sohan, P. Banoth, M. Aleksandrova, A. Nirmala Grace, P. Kollu (2021) Review on MXene synthesis, properties, and recent research exploring electrode architecture for supercapacitor applications. Int J Energy Res, 45, 19746–19771, https://doi.org/10.1002/er.7068.

[24]   A.S. Etman, J. Halim, J. Rosen (2021) Mo1.33CTz–Ti3C2Tz mixed MXene freestanding films for zinc-ion hybrid supercapacitors. Mater Today Energy, 22, 100878 https://doi.org/10.1016/j.mtener.2021.100878.

[25]   M.S. Javed, A. Mateen, S. Ali, X. Zhang, I. Hussain, M. Imran, S.S.A. Shah, W. Han (2022) The emergence of 2D MXenes based Zn-Ion batteries: recent development and prospects. Small, 18, 2201989, https://doi.org/10.1002/smll.202201989.

[26]   J. Cheng, C. Li, Y. Xiong, H. Zhang, H. Raza, S. Ullah, J. Wu, G. Zheng, Q. Cao, D. Zhang, Q. Zheng, R. Che (2022) Recent advances in design strategies and multifunctionality of flexible electromagnetic interference shielding materials. Nanomicro Lett, 14, 80 https://doi.org/10.1007/s40820-022-00823-7.

[27]   M. Han, C.E. Shuck, R. Rakhmanov, D. Parchment, B. Anasori, C.M. Koo, G. Friedman, Y. Gogotsi (2020) Beyond Ti3C2Tx: MXenes for electromagnetic interference shielding. ACS Nano, 14, 5008–5016 https://doi.org/10.1021/acsnano.0c01312.

[28]   A. Iqbal, P. Sambyal, C.M. Koo (2020) 2D MXenes for electromagnetic shielding: A review. Adv Funct Mater, 30, 2000883, https://doi.org/10.1002/adfm.202000883.

[29]   S. Geetha, K.K.S. Kumar, C.R.K. Rao, M. Vijayan, D.C. Trivedi (2009) EMI shielding: methods and materials - A review. J Appl Polym Sci, 112, 2073–2086, https://doi.org/10.1002/app.29812.

[30]   J. Huang, Z. Li, Y. Mao, Z. Li (2021) Progress and biomedical applications of MXenes. Nano Select, 2, 1480–1508, https://doi.org/10.1002/nano.202000309

[31]   H. Li, R. Fan, B. Zou, J. Yan, Q. Shi, G. Guo (2023) Roles of MXenes in biomedical applications: recent developments and prospects. J Nanobiotechnology, 21, 1-39, https://doi.org/10.1186/s12951-023-01809-2.

[32]   A. Zamhuri, G.P. Lim, N.L. Ma, K.S. Tee, C.F. Soon (2021) MXene in the lens of biomedical engineering: synthesis, applications and future outlook. Biomed Eng Online, 20, 1-24, https://doi.org/10.1186/s12938-021-00873-9.

[33] R. Alfahel, R.S. Azzam, M.A. Hafiz, A.H. Hawari, R.P. Pandey, K.A. Mahmoud, M.K. Hassan, A.A. Elzatahry (2020) Fabrication of fouling resistant Ti3C2Tx (MXene)/cellulose acetate nanocomposite membrane for forward osmosis application. Journal of Water Process Engineering, 38,101551, https://doi.org/10.1016/j.jwpe.2020.101551.

[34] I. Ihsanullah (2020) Potential of MXenes in water desalination: current status and perspectives. Nanomicro Lett, 12, 1-20, https://doi.org/10.1007/s40820-020-0411-9.

[35] Y.A.J. Al-Hamadani, B.-M. Jun, M. Yoon, N. Taheri-Qazvini, S.A. Snyder, M. Jang, J. Heo, Y. Yoon (2020) Applications of MXene-based membranes in water purification: A review. Chemosphere, 254, 126821, https://doi.org/10.1016/j.chemosphere.2020.126821.

[36] S. Jangra, A. Raza, B. Kumar, J. Sharma, S. Das, K. Pandey, Y.K. Mishra, M.S. Goyat (2025) MXene decorated ZnO-tetrapod for efficient degradation of Methyl Orange, Methylene Blue, and Rhodamine B dyes. Materials Science and Engineering: B, 311, 117832, https://doi.org/10.1016/j.mseb.2024.117832.

[37] R. Giménez, B. Serrano, V. San-Miguel, J.C. Cabanelas (2022) Recent advances in MXene/epoxy composites: Ttends and prospects. Polymers (Basel), 14(6), 1170, https://doi.org/10.3390/polym14061170.

[38] K. Khan, A.K. Tareen, M. Iqbal, Z. Ye, Z. Xie, A. Mahmood, N. Mahmood, H. Zhang (2023) Recent progress in emerging novel MXenes based materials and their fascinating sensing applications. Small, 19, 2206147, https://doi.org/10.1002/smll.202206147.

[39] Z.U.D. Babar, B. Della Ventura, R. Velotta, V. Iannotti (2022) Advances and emerging challenges in MXenes and their nanocomposites for biosensing applications. RSC Adv, 12, 19590–19610, https://doi.org/10.1039/d2ra02985e.

[40] H. Liao, X. Guo, P. Wan, G. Yu (2019) Conductive MXene nanocomposite organohydrogel for flexible, healable, low-temperature tolerant strain sensors. Adv Funct Mater, 29, 1904507, https://doi.org/10.1002/adfm.201904507.

[41] S. Hroncekova, T. Bertok, M. Hires, E. Jane, L. Lorencova, A. Vikartovska, A. Tanvir, P. Kasak, J. Tkac (2020) Ultrasensitive Ti3C2TX MXene/chitosan nanocomposite-based amperometric biosensor for detection of potential prostate cancer marker in urine samples. Processes, 8(5), 580 https://doi.org/10.3390/PR8050580.

[42] X. Li, Y. Bai, X. Shi, N. Su, G. Nie, R. Zhang, H. Nie, L. Ye (2021) Applications of MXene (Ti3C2T:X) in photocatalysis: A review. Mater Adv, 2, 1570–1594. https://doi.org/10.1039/d0ma00938e.

[43] Y. Sun, X. Meng, Y. Dall'Agnese, C. Dall'Agnese, S. Duan, Y. Gao, G. Chen, X.F. Wang (2019) 2D MXenes as Co-catalysts in photocatalysis: synthetic methods. Nanomicro Lett, 11, 1-22, https://doi.org/10.1007/s40820-019-0309-6.

[44] T. Haneef, K. Rasool, J. Iqbal, R. Nawaz, M. Raza Ul Mustafa, K.A. Mahmoud, T. Sarkar, A. Shahzad (2023) Recent progress in two dimensional Mxenes for photocatalysis: a critical review. 2d Mater, 10,012001, https://doi.org/10.1088/2053-1583/ac9e66.

[45] C.E. Shuck, A. Sarycheva, M. Anayee, A. Levitt, Y. Zhu, S. Uzun, V. Balitskiy, V. Zahorodna, O. Gogotsi, Y. Gogotsi (2020) Scalable synthesis of Ti3C2Tx MXene. Adv Eng Mater, 22, 1901241, https://doi.org/10.1002/adem.201901241.

[46] S.T. Mahmud, M.M. Hasan, S. Bain, S.T. Rahman, M. Rhaman, M.M. Hossain, M. Ordu (2022) Multilayer MXene heterostructures and nanohybrids for multifunctional applications: A review. ACS Mater Lett, 4, 1174–1206, https://doi.org/10.1021/acsmaterialslett.2c00175.

[47] J. Halim, M.R. Lukatskaya, K.M. Cook, J. Lu, C.R. Smith, L.Å. Näslund, S.J. May, L. Hultman, Y. Gogotsi, P. Eklund, M.W. Barsoum (2014) Transparent conductive two-dimensional titanium carbide epitaxial thin films. Chemistry of Materials, 26, 2374–2381, https://doi.org/10.1021/cm500641a.

[48] W. Sun, S.A. Shah, Y. Chen, Z. Tan, H. Gao, T. Habib, M. Radovic, M.J. Green (2017) Electrochemical etching of Ti2AlC to Ti2CT:X (MXene) in low-concentration hydrochloric acid solution. J Mater Chem A Mater, 5, 21663–21668, https://doi.org/10.1039/c7ta05574a.

[49] R.A. Vaia, A. Jawaid, A. Hassan, G. Neher, D. Nepal, R. Pachter, W. Joshua Kennedy, S. Ramakrishnan (2021) Halogen etch of Ti3AlC2 MAX phase for mxene fabrication. ACS Nano, 15, 2771–2777, https://doi.org/10.1021/acsnano.0c08630

[50] M. Li, J. Lu, K. Luo, Y. Li, K. Chang, K. Chen, J. Zhou, J. Rosen, L. Hultman, P. Eklund, P.O.Å. Persson, S. Du, Z. Chai, Z. Huang, Q. Huang (2019) Element replacement approach by reaction with Lewis Acidic molten salts to synthesize nanolaminated MAX phases and MXenes. J Am Chem Soc, 141, 4730–4737, https://doi.org/10.1021/jacs.9b00574.

[51] L. Wang, H. Zhang, B. Wang, C. Shen, C. Zhang, Q. Hu, A. Zhou, B. Liu (2016) Synthesis and electrochemical performance of Ti3C2Tx with hydrothermal process. Electronic Materials Letters, 12, 702–710, https://doi.org/10.1007/s13391-016-6088-z.

[52] A. Feng, Y. Yu, Y. Wang, F. Jiang, Y. Yu, L. Mi, L. Song (2017) Two-dimensional MXene Ti3C2 produced by exfoliation of Ti3AlC2. Mater Des, 114, 161–166, https://doi.org/10.1016/j.matdes.2016.10.053.

[53] M. Alhabeb, K. Maleski, B. Anasori, P. Lelyukh, L. Clark, S. Sin, Y. Gogotsi (2017) Guidelines for synthesis and processing of two-dimensional titanium carbide (Ti3C2Tx MXene). Chemistry of Materials, 29, 7633–7644, https://doi.org/10.1021/acs.chemmater.7b02847.

[54] T. Zhang, L. Pan, H. Tang, F. Du, Y. Guo, T. Qiu, J. Yang (2017) Synthesis of two-dimensional Ti3C2TxMXene using HCl+LiF etchant: Enhanced

exfoliation and delamination. J Alloys Compd, 695, 818–826, https://doi.org/10.1016/j.jallcom.2016.10.127.

[55] B. Unnikrishnan, C.W. Wu, A. Sangili, Y.J. Hsu, Y.T. Tseng, J. Shanker Pandey, H.T. Chang, C.C. Huang (2022) Synthesis and in situ sulfidation of molybdenum carbide MXene using fluorine-free etchant for electrocatalytic hydrogen evolution reactions. J Colloid Interface Sci, 628, 849–857, https://doi.org/10.1016/j.jcis.2022.07.176.

[56] F. Liu, A. Zhou, J. Chen, J. Jia, W. Zhou, L. Wang, Q. Hu (2017) Preparation of Ti3C2 and Ti2C MXenes by fluoride salts etching and methane adsorptive properties. Appl Surf Sci, 416, 781–789, https://doi.org/10.1016/j.apsusc.2017.04.239.

[57] K. Huang, Z. Li, J. Lin, G. Han, P. Huang (2018) Two-dimensional transition metal carbides and nitrides (MXenes) for biomedical applications. Chem Soc Rev, 47, 5109–5124, https://doi.org/10.1039/c7cs00838d.

[58] S.Y. Pang, Y.T. Wong, S. Yuan, Y. Liu, M.K. Tsang, Z. Yang, H. Huang, W.T. Wong, J. Hao (2019) Universal strategy for HF-free facile and rapid synthesis of two-dimensional MXenes as multifunctional energy materials. J Am Chem Soc, 141, 9610–9616, https://doi.org/10.1021/jacs.9b02578.

[59] J. Chen, Q. Jin, Y. Li, H. Shao, P. Liu, Y. Liu, P.L. Taberna, Q. Huang, Z. Lin, P. Simon (2023) Molten salt-shielded synthesis (MS3) of MXenes in air.Energy and environmental Materials, 6, 1-6, https://doi.org/10.1002/eem2.12328.

[60] D.C. Geng, X.X. Zhao, Z.X. Chen, W.W. Sun, W. Fu, J.Y. Chen, W. Liu, W. Zhou, K.P. Loh (2017) Direct synthesis of large-area 2D Mo2C on in situ grown graphene. Advanced Materials, 29, 1700072, https://doi.org/10.1002/adma.201700072.

[61] J. Jia, T. Xiong, L. Zhao, F. Wang, H. Liu, R. Hu, J. Zhou, W. Zhou, S. Chen (2017) Ultrathin N-doped Mo2C nanosheets with exposed active sites as efficient electrocatalyst for hydrogen evolution reactions. ACS Nano, 11, 12509–12518, https://doi.org/10.1021/acsnano.7b06607.

[62] Z. Zhang, F. Zhang, H. Wang, C. Ho Chan, W. Lu, J.Y. Dai (2017) Substrate orientation-induced epitaxial growth of face centered cubic Mo2C superconductive thin film. J Mater Chem C Mater, 5, 10822–10827, https://doi.org/10.1039/c7tc03652c.

[63] J. Li, Y. Luo, M. Cui, Z. Zhao, X. Liu, X. Chen, L. He, F. Sun (2023) Preparation ultrafine WC based on the new tungsten metallurgy system of "no ammonia transformation - no hydrogen reduction." Int J Refract Metals Hard Mater, 113, 106212, https://doi.org/10.1016/j.ijrmhm.2023.106212.

[64] D. Nakamura, K. Shigetoh, A. Suzumura (2017) Tantalum carbide coating via wet powder process: From slurry design to practical process tests. J Eur Ceram Soc, 37, 1175–1185, https://doi.org/10.1016/j.jeurceramsoc.2016.10.029

[65] O. Mashtalir, M. Naguib, V.N. Mochalin, Y. Dall'Agnese, M. Heon, M.W. Barsoum, Y. Gogotsi (2013) Intercalation and delamination of layered carbides and carbonitrides. Nat Commun, 4, 1-7, https://doi.org/10.1038/ncomms2664.

[66] C. Zhang, Y. Ma, X. Zhang, S. Abdolhosseinzadeh, H. Sheng, W. Lan, A. Pakdel, J. Heier, F. Nüesch (2020) Two-dimensional transition metal carbides and nitrides (MXenes): synthesis, properties, and electrochemical energy storage applications. Energy and environmental materials, 3, 29–55, https://doi.org/10.1002/eem2.12058.

[67] A.C. Khot, T.D. Dongale, J.H. Park, A.V. Kesavan, T.G. Kim (2021) Ti3C2-based MXene oxide nanosheets for resistive memory and synaptic learning applications. ACS appl mater Interfaces, 13, 5216–5227, https://doi.org/10.1021/acsami.0c19028

[68] M. Naguib, M. Kurtoglu, V. Presser, J. Lu, J. Niu, M. Heon, L. Hultman, Y. Gogotsi, M.W. Barsoum (2011) Two-dimensional nanocrystals produced by exfoliation of Ti3AlC 2. Advanced Materials, 23, 4248–4253, https://doi.org/10.1002/adma.201102306

[69] Y. Xie, M. Naguib, V.N. Mochalin, M.W. Barsoum, Y. Gogotsi, X. Yu, K.W. Nam, X.Q. Yang, A.I. Kolesnikov, P.R.C. Kent (2014) Role of surface structure on li-ion energy storage capacity of two-dimensional transition-metal carbides. J Am Chem Soc, 136, 6385–6394, https://doi.org/10.1021/ja501520b.

[70] Y. Xie, Y. Dall'Agnese, M. Naguib, Y. Gogotsi, M.W. Barsoum, H.L. Zhuang, P.R.C. Kent (2014) Prediction and characterization of mxene nanosheet anodes for non-lithium-ion batteries. ACS Nano, 8, 9606–9615, https://doi.org/10.1021/nn503921j.

[71] X. Li, Z. Huang, C.E. Shuck, G. Liang, Y. Gogotsi, C. Zhi (2022) MXene chemistry, electrochemistry and energy storage applications. Nat Rev Chem, 6, 389–404 https://doi.org/10.1038/s41570-022-00384-8.

[72] Y. Zhang, J. Wu, L. Jia, D. Jin, B. Jia, X. Hu, D. Moss, Q. Gong (2024) Advanced optical polarizers based on 2D materials. Npj Nanophotonics, 1:28, 1-17, https://doi.org/10.1038/s44310-024-00028-3.

[73] K.R.G. Lim, M. Shekhirev, B.C. Wyatt, B. Anasori, Y. Gogotsi, Z.W. She (2022) Fundamentals of MXene synthesis. Nature Synthesis, 1, 601–614, https://doi.org/10.1038/s44160-022-00104-6.

[74] S. Kumar, N. Kumari, Y. Seo (2024) MXenes: Versatile 2D materials with tailored surface chemistry and diverse applications. Journal of Energy Chemistry, 90, 253–293, https://doi.org/10.1016/j.jechem.2023.11.031.

[75] S. Palei, G. Murali, C.H. Kim, I. In, S.Y. Lee, S.J. Park (2023) A Review on Interface Engineering of MXenes for Perovskite Solar Cells. Nanomicro Lett, 15, 123, https://doi.org/10.1007/s40820-023-01083-9.

[76] M.B. Bahari, C.R. Mamat, A.A. Jalil, N.S. Hassan, N.F. Khusnun, M.H. Sawal, N.M. Izzudin, A.H. Hatta, S.H. Zein, V.G. Le (2023) Advances in MXene-based photoanodes for water-splitting. Journal of Electroanalytical Chemistry, 947, 117750, https://doi.org/10.1016/j.jelechem.2023.117750.

[77] A.A.P.R. Perera, K.A.U. Madhushani, B.T. Punchihewa, A. Kumar, R.K. Gupta (2023) MXene-based nanomaterials for multifunctional applications. Materials, 16(3), 1138, https://doi.org/10.3390/ma16031138.

[78] T.A. Oyehan, B.A. Salami, A.A. Abdulrasheed, H.U. Hambali, A. Gbadamosi, E. Valsami-Jones, T.A. Saleh (2023) MXenes: synthesis, properties, and applications for sustainable energy and environment. Appl Mater Today, 35, 101993, https://doi.org/10.1016/j.apmt.2023.101993.

[79] T. Hu, M. Hu, Z. Li, H. Zhang, C. Zhang, J. Wang, X. Wang (2016) Interlayer coupling in two-dimensional titanium carbide MXenes. Physical Chemistry Chemical Physics, 18, 20256–20260, https://doi.org/10.1039/c6cp01699e.

[80] M. Kurtoglu, M. Naguib, Y. Gogotsi, M.W. Barsoum (2012) First principles study of two-dimensional early transition metal carbides. MRS Commun, 2, 133–137, https://doi.org/10.1557/mrc.2012.25.

[81] K. Chaudhuri, M. Alhabeb, Z. Wang, V.M. Shalaev, Y. Gogotsi, A. Boltasseva (2018) Highly Broadband Absorber Using Plasmonic Titanium Carbide (MXene). ACS Photonics, 5, 1115–1122, https://doi.org/10.1021/acsphotonics.7b01439.

[82] S.C. Lee, Y.H. Kim, J.H. Park, D. Susanto, J.Y. Kim, J. Han, S.C. Jun, K.Y. Chung (2024) Mechanical activation of graphite for Na-Ion battery anodes: unexpected reversible reaction on solid electrolyte interphase via X-Ray analysis. Advanced Science, 11(28), 2401022, https://doi.org/10.1002/advs.202401022.

[83] M.Q. Zhao, X. Xie, C.E. Ren, T. Makaryan, B. Anasori, G. Wang, Y. Gogotsi (2017) Hollow MXene spheres and 3D macroporous MXene frameworks for Na-Ion storage. Advanced Materials, 29, 1702410, https://doi.org/10.1002/adma.201702410.

[84] M. Naguib, R.A. Adams, Y. Zhao, D. Zemlyanov, A. Varma, J. Nanda, V.G. Pol (2017) Electrochemical performance of MXenes as K-ion battery anodes. Chemical Communications, 53, 6883–6886, https://doi.org/10.1039/c7cc02026k.

[85] E. Lee, A. Vahidmohammadi, Y.S. Yoon, M. Beidaghi, D.J. Kim (2019) Two-dimensional Vanadium carbide MXene for gas sensors with ultrahigh sensitivity toward nonpolar gases. ACS Sens, 4, 1603–1611, https://doi.org/10.1021/acssensors.9b00303.

[86] O. Mashtalir, M.R. Lukatskaya, M.Q. Zhao, M.W. Barsoum, Y. Gogotsi (2015) Amine-assisted delamination of Nb2C MXene for li-ion energy storage devices. Advanced Materials, 27, 3501–3506, https://doi.org/10.1002/adma.201500604.

[87] D. Sun, M. Wang, Z. Li, G. Fan, L.Z. Fan, A. Zhou (2014) Two-dimensional Ti3C2 as anode material for Li-ion batteries. Electrochem Commun, 47, 80–83, https://doi.org/10.1016/j.elecom.2014.07.026.

[88] R. Syamsai, A.N. Grace (2019) Ta4C3 MXene as supercapacitor electrodes. J Alloys Compd, 792, 1230–1238 https://doi.org/10.1016/j.jallcom.2019.04.096.

[89] Q. Dou, H.S. Park (2020) Perspective on high-energy carbon-based supercapacitors. Energy and environmental materials, 3, 286–305, https://doi.org/10.1002/eem2.12102.

[90] S. Jangra, B. Kumar, J. Sharma, S. Sengupta, S. Das, R.K. Brajpuriya, A. Ohlan, Y.K. Mishra, M.S. Goyat (2024) A review on overcoming challenges and pioneering advances: MXene-based materials for energy storage applications. J Energy Storage, 101, 113810, https://doi.org/10.1016/j.est.2024.113810.

[91] M.K. Aswathi, A. V Rane, A.R. Ajitha, S. Thomas, M. Jaroszewski (2019) EMI shielding fundamentals. Wiley Semiconductors,1-9, https://doi.org/10.1002/9781119128625.ch1.

[92] M.H. Al-Saleh, W.H. Saadeh, U. Sundararaj (2013) EMI shielding effectiveness of carbon based nanostructured polymeric materials: A comparative study. Carbon N Y, 60, 146–156, https://doi.org/10.1016/j.carbon.2013.04.008.

[93] V.K. Sachdev, S.K. Sharma, M. Tomar, V. Gupta, R.P. Tandon (2016) EMI shielding of MWCNT/ABS nanocomposites in contrast to graphite/ABS composites and MWCNT/PS nanocomposites. RSC Adv, 6, 45049–45058, https://doi.org/10.1039/c6ra04200g.

[94] P. Banerjee, Y. Bhattacharjee, S. Bose (2020) Lightweight epoxy-based composites for EMI shielding applications. J Electron Mater, 49, 1702–1720, https://doi.org/10.1007/s11664-019-07687-5.

[95] X. Yang, J. Luo, H. Ren, Y. Xue, C. Yang, T. Yuan, Z. Yang, Y. Liu, H. Zhang, J. Yu (2023) Simultaneously improving the EMI shielding performances and mechanical properties of CF/PEKK composites via MXene interfacial modification. J Mater Sci Technol, 154, 202–209, https://doi.org/10.1016/j.jmst.2023.01.020.

[96] F. Raziq, A. Hayat, M. Humayun, S.K. Baburao Mane, M.B. Faheem, A. Ali, Y. Zhao, S. Han, C. Cai, W. Li, D.C. Qi, J. Yi, X. Yu, M.B.H. Breese, F. Hassan, F. Ali, A. Mavlonov, K. Dhanabalan, X. Xiang, X. Zu, S. Li, L. Qiao (2020) Photocatalytic solar fuel production and environmental remediation through experimental and DFT based research on CdSe-QDs-coupled P-doped-g-C3N4 composites. Appl Catal B, 270, 118867, https://doi.org/10.1016/j.apcatb.2020.118867.

[97] Z. Li, Y. Wu (2019) 2D early transition metal carbides (MXenes) for catalysis. Small, 15, 1804736, https://doi.org/10.1002/smll.201804736.

[98] P. Kuang, J. Low, B. Cheng, J. Yu, J. Fan (2020) MXene-based photocatalysts. J Mater Sci Technol, 56, 18–44, https://doi.org/10.1016/j.jmst.2020.02.037.

[99] R. Bhardwaj, A. Hazra (2021) MXene-based gas sensors. J Mater Chem C Mater, 9, 15735–15754, https://doi.org/10.1039/D1TC04085E.

[100] H. Riazi, G. Taghizadeh, M. Soroush (2021) MXene-based nanocomposite sensors. ACS Omega, 6, 11103–11112, https://doi.org/10.1021/acsomega.0c05828.

[101] M. Kamali, D. Jahaninafard, A. Mostafaie, M. Davarazar, A.P.D. Gomes, L.A.C. Tarelho, R. Dewil, T.M. Aminabhavi (2020) Scientometric

analysis and scientific trends on biochar application as soil amendment. Chemical Engineering Journal, 395, 125128, https://doi.org/10.1016/j.cej.2020.125128.

[102] P. Saravanan, S. Rajeswari, J.A. Kumar, M. Rajasimman, N. Rajamohan (2022) Bibliometric analysis and recent trends on MXene research – A comprehensive review. Chemosphere, 286, 131873 https://doi.org/10.1016/j.chemosphere.2021.131873

[103] R. Zakaria, A. Ahmi, A.H. Ahmad, Z. Othman (2021) Worldwide melatonin research: a bibliometric analysis of the published literature between 2015 and 2019. Chronobiol Int, 38, 27–37, https://doi.org/10.1080/07420528.2020.1838534.

[104] F.P. Appio, F. Cesaroni, A. Di Minin (2014) Visualizing the structure and bridges of the intellectual property management and strategy literature: a document co-citation analysis. Scientometrics, 101, 623–661, https://doi.org/10.1007/s11192-014-1329-0.

[105] M. Downes, R.W. Lord, M. Anayee (2023) M5X4-A family of MXenes venture capital view project senior design project for hemolife View project. ACS Nano, 17, 17158–17168, https://doi.org/10.26434/chemrxiv-2023-v6m0k.

[106] X. Zhang, J. Xu, H. Wang, J. Zhang, H. Yan, B. Pan, J. Zhou, Y. Xie (2013) Ultrathin nanosheets of MAX phases with enhanced thermal and mechanical properties in polymeric compositions: Ti3Si0.75Al 0.25C2. Angewandte Chemie – International Edition, 52, 4361–4365, https://doi.org/10.1002/anie.201300285.

[107] L. Chen, X. Shi, N. Yu, X. Zhang, X. Du, J. Lin (2018) Measurement and analysis of thermal conductivity of Ti3C2Tx MXene films. Materials, 11(9), 1701, https://doi.org/10.3390/ma11091701.

[108] H. Liu, N. Li, Y. Jiang, Q. Wang, Z. Peng (2019) Plasma treated MXene/Ag-based humidity sensor with ultrahigh sensitivity for gesture tracking. in: IOP Conf Ser Mater Sci Eng, Institute of Physics Publishing, 563, 022046, https://doi.org/10.1088/1757-899X/563/2/022046.

[109] L. Omana, A. Chandran, R.E. John, R. Wilson, K.C. George, N.V. Unnikrishnan, S.S. Varghese, G. George, S.M. Simon, I. Paul (2022) Recent advances in polymer nanocomposites for electromagnetic interference shielding: A review. ACS Omega, 7, 25921–25947, https://doi.org/10.1021/acsomega.2c02504.

[110] R. Liu, M. Miao, Y. Li, J. Zhang, S. Cao, X. Feng (2018) Ultrathin biomimetic polymeric Ti 3 C 2 T x MXene composite films for electromagnetic interference shielding. ACS Appl Mater Interfaces, 10, 44787–44795, https://doi.org/10.1021/acsami.8b18347.

[111] A. Vahidmohammadi, A. Hadjikhani, S. Shahbazmohamadi, M. Beidaghi (2017) Two-dimensional Vanadium carbide (MXene) as a high-capacity cathode material for rechargeable Aluminum batteries. ACS Nano, 11, 11135–11144, https://doi.org/10.1021/acsnano.7b05350.

[112] A. Gentile, C. Ferrara, S. Tosoni, M. Balordi, S. Marchionna, F. Cernuschi, M.H. Kim, H.W. Lee, R. Ruffo (2020) Enhanced functional properties of Ti3C2Tx MXenes as negative electrodes in Sodium-ion batteries by chemical tuning. Small Methods, 4(9), 2000314, https://doi.org/10.1002/smtd.202000314.

[113] F. Liu, J. Zhou, S. Wang, B. Wang, C. Shen, L. Wang, Q. Hu, Q. Huang, A. Zhou (2017) Preparation of high-purity V2C MXene and electrochemical properties as Li-Ion batteries. J Electrochem Soc, 164, A709–A713, https://doi.org/10.1149/2.0641704jes.

[114] H. He, Q. Xia, B. Wang, L. Wang, Q. Hu, A. Zhou (2020) Two-dimensional vanadium carbide (V2CTx) MXene as supercapacitor electrode in seawater electrolyte. Chinese Chemical Letters, 31, 984–987, https://doi.org/10.1016/j.cclet.2019.08.025.

[115] Z. Fan, Y. Wang, Z. Xie, X. Xu, Y. Yuan, Z. Cheng, Y. Liu (2018) A nanoporous MXene film enables flexible supercapacitors with high energy storage. Nanoscale, 10, 9642–9652, https://doi.org/10.1039/c8nr01550c.

[116] R.B. Rakhi, B. Ahmed, M.N. Hedhili, D.H. Anjum, H.N. Alshareef (2015) Effect of postetch annealing gas composition on the structural and electrochemical properties of Ti2CTx MXene electrodes for supercapacitor applications. Chemistry of Materials, 27, 5314–5323, https://doi.org/10.1021/acs.chemmater.5b01623.

[117] L. Yang, W. Zheng, P. Zhang, J. Chen, W.B. Tian, Y.M. Zhang, Z.M. Sun (2018) MXene/CNTs films prepared by electrophoretic deposition for supercapacitor electrodes.Journal of Electroanalytical Chemistry, 830–831, 1–6, https://doi.org/10.1016/j.jelechem.2018.10.024.

[118] F. Shahzad, M. Alhabeb, C.B. Hatter, B. Anasori, S.M. Hong, C.M. Koo, Y. Gogotsi (2016) Electromagnetic interference shielding with 2D transition metal carbides (MXenes). Science, 353, 1137–1140, https://doi.org/10.1126/science.aag2421.

[119] A. Iqbal, F. Shahzad, K. Hantanasirisakul, M.-K. Kim, J. Kwon, J. Hong, H. Kim, D. Kim, Y. Gogotsi, C. Min Koo (2020) Anomalous absorption of electromagnetic waves by 2D transition metal carbonitride Ti3CNTx (MXene). Science, 369, 446–450, https://doi.org/10.1126/science.aba7977.

[120] T. Yun, H. Kim, A. Iqbal, Y.S. Cho, G.S. Lee, M.K. Kim, S.J. Kim, D. Kim, Y. Gogotsi, S.O. Kim, C.M. Koo (2020) Electromagnetic shielding of monolayer MXene assemblies. Advanced Materials, 32(9), 1906769, https://doi.org/10.1002/adma.201906769.

[121] M. Han, X. Yin, H. Wu, Z. Hou, C. Song, X. Li, L. Zhang, L. Cheng (2016) Ti3C2 MXenes with modified surface for high-performance electromagnetic absorption and shielding in the X-Band. ACS Appl Mater Interfaces, 8, 21011–21019, https://doi.org/10.1021/acsami.6b06455.

[122] R. Sun, H. bin Zhang, J. Liu, X. Xie, R. Yang, Y. Li, S. Hong, Z.Z. Yu (2017) Highly conductive transition metal carbide/carbonitride (MXene)@po-

lystyrene nanocomposites fabricated by electro-static assembly for highly efficient electromagnetic interferenceshielding. Adv Funct Mater, 27(45), 1702807, https://doi.org/10.1002/adfm.201702807.

[123] L. Liang, R. Yang, G. Han, Y. Feng, B. Zhao, R. Zhang, Y. Wang, C. Liu (2020) Enhanced electromagnetic wave-absorbing performance of magnetic nanoparticles-anchored 2D Ti3C2Tx MXene. ACS Appl Mater Interfaces, 12, 2644–2654, https://doi.org/10.1021/acsami.9b18504.

[124] P. Song, H. Qiu, L. Wang, X. Liu, Y. Zhang, J. Zhang, J. Kong, J. Gu (2020) Honeycomb structural rGO-MXene/epoxy nanocomposites for superior electromagnetic interference shielding performance. Sustainable Materials and Technologies, 24, e00153, https://doi.org/10.1016/j.susmat.2020.e00153.

[125] W.T. Cao, F.F. Chen, Y.J. Zhu, Y.G. Zhang, Y.Y. Jiang, M.G. Ma, F. Chen (2018) Binary strengthening and toughening of MXene/Cellulose nanofiber composite paper with nacre-inspired structure and superior electromagnetic interference shielding properties. ACS Nano, 12, 4583–4593, https://doi.org/10.1021/acsnano.8b00997.

[126] W. Cao, C. Ma, S. Tan, M. Ma, P. Wan, F. Chen (2019) Ultrathin and flexible CNTs/MXene/Cellulose nanofibrils composite paper for electromagnetic interference shielding. Nanomicro Lett, 11 (72), 1-17, https://doi.org/10.1007/s40820-019-0304-y.

[127] C. Weng, T. Xing, H. Jin, G. Wang, Z. Dai, Y. Pei, L. Liu, Z. Zhang (2020) Mechanically robust ANF/MXene composite films with tunable electromagnetic interference shielding performance. Compos Part A Appl Sci Manuf, 135, 105927, https://doi.org/10.1016/j.compositesa.2020.105927.

IZVOD

NAJSAVREMENIJI RAZVOJI U MKSENES-U: SVEOBUHVATAN PREGLED

Poslednjih godina, dvodimenzionalni (2D) materijali su privukli značajnu pažnju zbog svojih karakterističnih svojstava i potencijalne primene u širokom spektru primena. Među ovim materijalima, MKSenes, porodica karbida, nitrida i karbonitrida prelaznih metala, pojavili su se kao istaknuta klasa 2D materijala sa izuzetnim strukturnim, električnim, termičkim, optičkim, mehaničkim i hemijskim svojstvima. Ovaj pregled istražuje nedavna dostignuća u tehnikama sinteze, osobinama i različitim primenama MKSenes-a u skladištenju energije, zaštiti od elektromagnetnih smetnji (EMI), senzorima i primenama u životnoj sredini. Pored toga, pruža bibliometrijski pregled, analizirajući 10.957 istraživačkih radova za procenu globalnih naučnih trendova i budućih pravaca istraživanja koristeći podatke Veb of Science (VOS) i softver VOSviever. Ovaj pregled ima za cilj da pruži sveobuhvatno razumevanje najsavremenijeg razvoja u MKSene tehnologiji, nudeći uvid u buduće pravce i potencijalne napretke u ovoj oblasti koja se brzo razvija.

Ključne reči: *2D materijali; MKSene; sinteza; aplikacije; bibliometrijska analiza*

Bhushan Kumar: https://orcid.org/0009-0006-8870-5962
Sahil Jangra: https://orcid.org/0009-0004-6217-9496
Subhankar Das: https://orcid.org/0000-0002-1724-2722
Manjeet Singh Goyat: https://orcid.org/0000-0002-0668-6512

Alaeddine Kaouka[1,], Khedidja Benarous[2], Mourad Keddam[3]*

[1]*Laboratory of Applied Sciences and Didactic, Higher Normal School of Laghouat, Laghouat, Algeria;* [2]*Laboratoire de Science Fondamentales, University of Laghouat, Laghouat, Algeria,* [3]*Laboratoire de Technologie des Matériaux, USTHB BP 32 El-Alia 16111 Algiers, Algeria*

Electrochemical evaluation of natural extracts as effective corrosion inhibitors and surface treatments on metal substrates

ABSTRACT

Corrosion is a serious problem encountered in the industry, protection from it is more than necessary using inhibitors and treatments. These treatments can effectively ease the problem on the surface of the material substrate, particularly the metal substrate for being easily etched during usage and being unable to withstand abrasion. Experimental results showed that the extracts are effective inhibitors of corrosion. Polarization tests indicate that the inhibitors are of mixed nature and the corrosion mechanism does not change after their addition to the solution. The electrochemical impedance spectroscopy confirmed that inhibitory quality and surface treatments improved corrosion resistance. Surface analysis revealed that the surface of the sample for the control solution was covered and protected. However, for the inhibited solutions the presence of oxides was not observed.

Keywords*: corrosion protection, inhibitor, surface treatments*

1. INTRODUCTION

Corrosion is well known as the result of a chemical or electrochemical action of an environment on materials such as metals and alloys. It is a scourge that affects the materials used in many industrial fields: petroleum, electrical, chemical, nuclear industries, port facilities, environment, civil engineering, agrifood, and health. The ramifications are significant in many domains, but particularly in the industry: production halts, component replacements for corroded parts, pollution hazards, and accidents are common occurrences with occasionally severe financial repercussions. Corrosion causes significant economic losses, estimated at around US$2.5 trillion per year globally (Koch et al., 2016) [1, 2], which is approximately 3.4% of the worldwide gross domestic product (GDP). In the United States alone, corrosion costs 875 billion dollars per year according to the National Association of Corrosion Engineers (NACE).

The reactivity of industrial materials to their environments is reflected in corrosion.

We distinguish two main processes of corrosion [3]:

- The electrochemical corrosion (or wet corrosion);
- The corrosion dryers. (or high-temperature gas corrosion).

The fundamental study of corrosion phenomena in the middle-wet falls primarily into electrochemistry, while their study is an applied field of science of materials that includes at the time the concepts of chemistry and physics. The corrosion phenomena take place on the surface of metallic materials exposed to an environment chemically aggressive. Not only is the priming of the corrosion but also its propagation; essentially a surface process both chemical and electrochemical.

Also, to study these mechanisms, electrochemical techniques are essential.

Thus, all this is likely to deteriorate: Corrosion is the permanent damage that a metal sustains from a chemical or electrochemical reaction with its surroundings. It can take many different forms, such as uniform, localized, etc., and it changes the properties of materials.

Regarding anti-corrosion measures, actions can be taken against the material itself (e.g.,

selecting appropriate constraints based on application requirements, painting, coating, applying various surface treatments, etc.) or the environment that comes into contact with the material to be protected.

Today, protection against corrosion consists of a variety of treatments such as metallic coating or surface treatment, cathodic protection, or even the modification of the corrosive medium by adding inhibitors of corrosion. These latter ones constitute an original way to fight against corrosion. These are substances that, when added at low concentrations in corrosive media, reduce or even prevent the reaction of the metal within its environment. The trend today is the combination of two or more of these means of protection. The modified cerium seal PEO pretreatment significantly enhances the corrosion protection of 2A14 Al alloy by creating a robust duplex coating system. This system combines a cerium-based PEO coating with an epoxy layer, resulting in improved adhesion and long-term corrosion resistance. [3-5].

Among the methods, the most used one to protect the structural steel industry is coatings loaded with corrosion inhibitors. The paint additives known for their inhibitory effectiveness against corrosion are chromates, molybdates, tungstates, vanadates, phosphates, and polyphosphates [4]. However, these compounds are characterized by their significant toxicity (for chromates) and/or a detrimental effect on the environment. LDH (Layered double hydroxide) coatings contain a variety of inhibitors that are intercalated and may offer persistent corrosion protection. It illustrates the inhibitor release kinetics of LDHs as well as corrosion prevention mechanisms [6]. The inhibiting action of these pigment particles in paints relies on their dissolution in water, allowing inhibiting ions to diffuse to the metal surface and ions with the properties of inhibition must diffuse and reach the surface of the metal to repair and inhibit the phenomenon of corrosion. Corrosion inhibition performances of zinc were studied by potentiodynamic measurements and electrochemical impedance spectroscopy [7]. Several studies have shown that the salts soluble in the base of cerium, lanthanum, yttrium [8], and calcium [9] can be considered as inorganic inhibitors [10].

The materials capable of fulfilling the role of the corrosion inhibitor are of the lamellar type. Their structure consists of a stack of sheets, generally of inorganic nature. The latter can be either neutral such as metal sulphides MPS 3 (M = Mn, Zn, Cd), or anionic types of double lamellar hydroxides (HDL) or basic salts of hydroxides, or either cationic such as clay minerals of smectite types.

Heavy metals found in the water by industrial pollution and agricultural processing as well as the corrosion of the distribution piping, accumulate in food chains. Even at low concentrations, these heavy metals are very toxic.

For this, different electrode materials are studied and proposed by different researchers, as needed:

- To enhance the rate of electrochemical oxidation, various electro-catalytic metals, such as Pt and Au, as well as their alloys and compounds like Ti/Pt, have been utilized. Their main problem during oxidation at a constant potential, despite their high activity, is the loss of catalytic activity as a consequence of the formation of the species that block the surface of the anode. Also, these activated electrodes promote electrochemical conversion more than incineration and are very expensive, which limits their industrial applications.

- To reduce the costs of these processes, various anodes that are cheaper and available were proposed as steel or carbon materials such as carbon graphite or glassy carbon [11, 12]. In general, these electrodes have much lower catalytic activity and chemical and/or electrochemical corrosion problems.

- The boron-doped diamond anode (Boron-Doped-Diamond, BDD) has received a lot of attention in these recent years. Due to its great potential of Oxygen Evolution Reaction (OER) the reaction of oxygen release, it has a very high efficiency (100%) in the combustion of organic compounds in aqueous medium and its extreme stability (chemical and electro-chemical). Therefore, the high costs of manufacture as well as their great fragility constitute negligible drawbacks.

- Scientific research is directed to the Metal Oxide Electrodes of Dimensionally Stable Anode (DSA) to try to solve all the problems associated with the previous electrodes. This is due to the enormous instability of metal oxides when optimizing electro-catalytic properties, the stability and the prices of the electrodes, by appropriate selection of various metallic elements, and the ability to prepare and file various media by simple and inexpensive techniques.

When the electrode is brought to a potential higher than that of the evolution of oxygen, competitive reactions that consume electrons, such as the formation of peroxide compounds, can limit the direct oxidation of the organic compounds present in the solution.

However, these oxidizing species can react with organic compounds to oxidize them in turn.

Not all electrode materials produce these oxidants, and in particular hydroxyl radicals, with the same efficiency. Much research has been devoted in recent years to the study of the treatment of wastewater polluted by organic compounds; the most efficient materials are those that have a high potential for the release of oxygen.

The comparison of the oxygen evolution potentials shows that the metal oxides and the boron-doped diamond have much larger electrochemical windows than platinum. This entails, under positive polarization in the region of the oxidation of water, the possibility of producing very oxidizing species that are very little adsorbed, and therefore particularly active for oxidation. Overall, this results in a remarkable electro-catalytic activity in organic compounds. In other words, the potential for oxygen evolution increases with the decrease in the adsorption force of hydroxyl radicals on the electrode; for example, the boron-doped diamond electrode has lower adsorption properties than the platinum.

The researchers worked in the field of Dimensionally Stable Anode (DSA) studied in depth, from the preparation to the characterization of these electrodes to understand and improve their electro-catalytic properties and their stability. Although the first RuO_2- based DSA electrodes are emerging for their application in the Cl_2 -NaOH industry. The following years gave a step to the appearance of new electrode materials which are based on the original concept of DSA to find new applications.

Thus, in addition to the generation of Cl_2, in most cases, the anodes of DSA are used against the electrode of a cathode of interest in several processes (production of hydrogen, electrodeposition of metals, electro galvanizing, protection against corrosion, etc.) wherein the anodic reaction in aqueous solution is mainly the OER. The most commonly used anode in these applications is Ti / IrO_2 [13].

However, over the past 20 years, DSA electrodes have experienced massive growth in the oxidation of organic and inorganic compounds. In particular, in the treatment of industrial water [14, 15], for which scientists have prepared and characterized other electrodes made of metal oxides.

RuO_2 and IrO_2 were the most studied metal oxides. These two oxides have some points in common, such as good conductivity (metal type) and a crystalline structure like rutile. However, this crystal structure is adopted by many dioxides of several metals, belonging to the p block (Sn, Pb, Ge, Te, and Si) as transition metals of the 3d, 4d, and 5d series (Ti, Cr, Mn, Nb, Ru, Rh, Ta, Ir, Pt, and some others).

In practice, the big problem is centered on the loss of coating due to the dissolution of the active metal oxide. The chemical dissolution is favored when the ligands involved in the electrolyte (NH_3, CN^-, OH^- and others that can form the complexes) or activators of the corrosion (Cl^- or F^- for example) [18]. The dissolution or the electrochemical corrosion can occur at potentials at which the coating is not stable, being oxidized and forming soluble species.

Erosion of the coating can occur, especially if the adhesion between the particles and the coating is not good and too porous, the evolution of gas can separate the particles and remove them. One deactivation mechanism occurs during the anodic process when chemical changes alter the electrode's conductive properties. For example, it has been proposed that the SnO_2 electrodes are deactivated by the formation of a passivating layer from the hydration of the outer layer.

The deactivation by passivation of the base metal is different from known mechanisms on all electrodes which operate at high current densities. It can happen in three ways:

- When the ions go through the pores and cracks of the coating, with the support, by reacting and/or the remover in a way that it causes a loss of adhesion and therefore local coating losses (stripping);
- With the formation of an insulating layer (for example TiO_2), added to the active material, formed during the heat treatment, due to the migration of ions and electrons at the support/oxide interface (the poorly adherent layer may also cause a coating loss);
- When the TiO_{2-x} oxide, is formed during heat treatment [15, 16], it loses its non-stoichiometric conductive conformation and changes to its insulating stoichiometric configuration (TiO_2), due to the migration of O_2 species through the coating.

Given the different deactivation mechanisms, several strategies have been proposed in the bibliography to extend the useful life of this type of electrode:

- Choice of support.
- Control of the coating thickness
- The use of the stable conductive interlayer.
- Doping of the coating with stabilizers (mixed oxide).

Regarding the choice of support, Vercesi et al. [17] carried out a detailed study on the corrosion of the different valve metals used as supports. For information, a "valve metal" is a metal that is

covered with a thin layer of protective oxide when it is oxidized (passivation) and which does not. passes the current that is under a cathodic potential. They concluded that the best base metal was the tantalum, Ta. However, the Ti was the one used at an industrial scale because its properties, as a substrate, lower than Ta, are good enough and the price is much lower.

Another way to prevent or delay the formation of the insulating oxide is the addition of an oxide capable of creating solid solutions (interlayer) conductors with TiO_2, such as iridium which forms mixed oxides of type of $Ir_xTi_{(1-x)}O_2$. The deactivation of this type of mixed oxide electrodes occurs by the migration of the noble metal from the substrate/oxide layer interface to the outer oxide layer.

After much research, researchers found that the most stable electrode for OER in an acidic environment is Ti / IrO_2 (70%) - Ta_2O_5 (30%) [18]. So, to improve performance both in OER and in other electrochemical reactions, they studied the properties of several mixed oxides, with one active species (which provides catalytic activity) and other inactive species (which provides stability).

For the basic medium, the most stable and catalytic electrodes in the OER have been those based on cobalt spinel [19]. However, these electrodes do not exhibit strong activity in the oxidation of aromatic organic compounds. In this way, and since the vast majority of studies on electrode optimization have been designed for use in the acidic medium, it is necessary to further study the stability and deactivation in the basic medium with new electrodes that have good performance for their use in this medium.

2. MATERIALS AND METHODS

Corrosion resistance is not an intrinsic property of a given metal, but rather a property of the metal / medium interface. Hence, the characterization of the chemical composition of the microstructure of the metal as well as its electrochemical behavior is required. In addition, the corrosion behavior depends on the various stresses to which the material is subjected, whether they are physico chemical, thermal, or mechanical. One inferred that any means of action to prevent and/or fight against corrosion concerns one of the three elements of the system studied even its whole.

The inhibitors of corrosion constitute an original way of combating the corrosion of metals and alloys. The originality comes from that the anticorrosion treatment should not be done on the metal itself (choice of intrinsically corrosion-resistant material) but by the intermediary of the corrosive medium. It does this not, however, to change the kind of the medium, but to add the inhibitor formulation (isolated molecule, mixture of molecules) in small amounts to the corrosive environment.

Natural extracts have emerged as an eco-friendly and sustainable solution for mitigating metal corrosion, offering a viable alternative to conventional synthetic inhibitors, which are often toxic and environmentally harmful. These extracts are typically derived from plant sources such as leaves, seeds, fruits, barks, and roots, and they contain a rich blend of organic compounds with diverse chemical structures. The primary constituents responsible for corrosion inhibition include alkaloids, flavonoids, tannins, saponins, terpenoids, and essential oils. These compounds possess functional groups like hydroxyl (-OH), carbonyl (C=O), carboxyl (-COOH), and nitrogen or sulfur-containing groups that can adsorb onto the metal surface, forming a protective barrier that isolates the metal from corrosive agents such as oxygen, chloride ions, and moisture. This adsorption process often follows Langmuir or Temkin isotherms, indicating the formation of a monolayer of inhibitor molecules on the metal surface.

For instance, the extract of Lawsonia inermis (henna), which is rich in lawsone and tannins, has demonstrated high corrosion inhibition efficiency on mild steel, often exceeding 90% under optimal conditions. Similarly, extracts from Allium sativum (garlic) containing sulfur-rich compounds like allicin have shown significant inhibition effects on copper corrosion. Another example is the use of green tea extract, derived from Camellia sinensis, which is abundant in catechins and polyphenols that exhibit strong antioxidant properties, thereby reducing the anodic and cathodic reactions responsible for metal dissolution and hydrogen evolution. The mechanism of action generally involves the adsorption of active compounds onto the metal surface, forming a physical and chemical barrier that decreases the metal's exposure to corrosive environments, thus reducing the corrosion current density and shifting the corrosion potential in electrochemical tests.

Electrochemical techniques such as potentio-dynamic polarization (PDP) and electrochemical impedance spectroscopy (EIS) are widely used to evaluate the efficacy of natural extracts as corrosion inhibitors. Potentiodynamic polarization provides information on the reduction in corrosion current density and the nature of inhibition, whether predominantly anodic, cathodic, or mixed. EIS, on the other hand, measures the charge transfer resistance (Rct) and the capacitance of the double layer, offering insights into the integrity and stability

of the protective film formed by the inhibitor. For instance, the impedance spectra of metals treated with pomegranate peel extract, rich in polyphenols and tannins, often reveal a significant increase in charge transfer resistance, indicating the formation of a robust protective layer.

Despite their numerous advantages, including biodegradability, non-toxicity, and cost-effectiveness, the use of natural extracts as corrosion inhibitors faces certain challenges. The complex and variable composition of plant extracts can lead to inconsistencies in inhibition performance, and their stability under harsh conditions may be limited. Moreover, the presence of multiple active components can make it difficult to pinpoint the exact compound responsible for the inhibition, complicating efforts to optimize and standardize their use. Nonetheless, ongoing research aims to address these limitations by exploring synergistic effects between different plant extracts, improving extraction techniques to enhance the concentration of active compounds, and developing formulations that improve their stability and efficiency in various corrosive environments. Overall, natural extracts hold significant promise as a green and sustainable approach to corrosion control, aligning with global efforts to reduce environmental impact and promote the use of renewable resources.

- In order to provide a unique form of protection, an inhibitor or a combination of inhibitors can be used. This can be done either permanently, allowing the use of metallic materials (unalloyed ferrous, for example) under acceptable conditions of corrosion resistance, though installation monitoring is necessary [20]. In this situation, it will be easier to predict the inhibitor's behavior in the short term, and, in theory, the system control will be more straightforward. Either as temporary protection during a period when the workpiece or the installation is particularly sensitive to corrosion (storage, stripping, and cleaning).

- An inhibitor or an inhibitor mixture may be combined with other means of protection: protection by adding a coating surface of paint, grease, oil, etc...

The inhibitor is a chemical substance added to the corrosion system at a concentration chosen for its effectiveness, which causes a decrease in the corrosion rate without changing significantly the concentration of the corrosive agent contained in the aggressive environment. Generally, an inhibitor should reduce the rate of corrosion of a metal, without affecting the physic-chemical characteristics, particularly the mechanical strength (e.g., risk of embrittlement by the hydrogen in an acid

medium). An inhibitor must be stable in the presence of the constituents of the medium, in particular, vis-à-vis the oxidants. An inhibitor must be stable at temperatures of use. An inhibitor should be effective at low concentrations. An inhibitor must be compatible with the standards for non-toxicity. An inhibitor should be inexpensive.

3. RESULTS

Corrosion is the irreversible deterioration of a metal caused by a chemical or electrochemical interaction within its surroundings. It can take many different forms, such as uniform, localized, etc., and changes the properties of the materials in question.

Regarding corrosion prevention, actions can be taken against the material itself (e.g., by applying corrosion inhibitors), on the material's surface (coating, painting, surface treatment of any kind), or on the environment the material comes into contact with (choice-wise, forms adapted constraints in the function of applications...) [20–22].

However, prevention against corrosion must be considered from the design phase of an installation. The preventative measures taken in good time allow to avoid many problems when it comes to ensuring a certain time of life for an object, especially for industries such as nuclear, chemical, or aeronautics, where the risk of accident can have particularly serious consequences for people and the environment.

Other researchers [21] show that alkylamines are strongly chemisorbed on the surface of iron, with the sharing of electrons between nitrogen and the atoms of the metal. This then results in a very good inhibition of the corrosion of iron in an acidic medium. It should be noted, however, that the alkylamines, classified as fairly strong bases, adsorb, preferentially, at the surface of ferrous and ferric oxides and hydroxides (considered as strong acids), which may explain the poor protection of the underlying metal.

There are more complex compounds such as aminobenzimidazole act as mixed inhibitors for the protection of brass (Cu / Zn alloy) where they inhibit corrosion by blocking the anodic and cathodic sites by the formation, on the surface of the brass, of a protective film consisting of complexes of Cu (II) and Zn (II). Aminobenzimidazole acts as a metal-coordinated bidentate ligand through nitrogen from the amino group (> C = NH) and nitrogen from the cyclic azole group (= C-NH) [22].

The amines that regulate the pH or the alkalinization of the medium are intended to react chemically with the acidic species to neutralize

them. These properties tend to be operated to lower the activity of protons in the corrosive solution: neutral medium at temperature ordinarily the increase of the pH causes the metal in a region where the corrosion is slowing down (please revise the meaning of this sentence in red). Contrary to amine filaments, amine neutralizing will not protect against corrosion due to the presence of oxygen dissolved in the electrolyte [23].

Amines are considered to be a very efficient functional group against the corrosion of ferrous metals due to the combination of weak base properties with adsorption properties. In some cases, their inhibition can be further enhanced when combined with other types of molecules, such as carboxylic acids [24].

The hydrolysis of aluminum dihydrogen triphosphate (ATP), produces H + protons [25], which could neutralize the hydroxyl ions resulting from the reduction of dissolved oxygen on the metal substrate, thus prolonging the life of the organic coatings [26]. The protective performance using ATP as a pigment was investigated by Dongdong Song [27], under full immersion conditions, of a water-based acrylic paint, applied to steel. The data obtained have permitted to provide the following protection mechanism: the specific pigments used in the paint formulation showed the release of phosphates that form a protective on the metal substrate, which interfere with the result, access of aggressive species on the surface of the substrate and will prevent the corrosion reaction thus protecting the substrate.

Moreover, it is only recently that the first successful implementation of nanocomposite orthophosphate of zirconium/polyurethane (α-ZrP / PU), for protection against corrosion, has been published [28]. A-ZrP / PU nanocomposite films are PU-based with different ZrP contents from 0.5 to 5% by weight. The results revealed that α-ZrP was dispersed very well in PU films with improved moisture barrier properties of α- ZrP / PU films and that no substantial agglomeration occurred, comparing a series of measures of electrochemical potential for corrosion (E corr) , the strength of polarization (Rp), the current of corrosion (i corr) and of the spectroscopy impedance electrochemical performed on the coatings ZrP / PU and PU pure, applied on the electrodes in cold rolled steel. The inhibition of zinc corrosion in NaCl medium has been the subject of numerous studies in which different chemical compounds have been used. We cite here those whose results were more striking.

The use of other cationic type of inhibitors such as Ce 3+ and La 3+ could be put to the point [29]

and gave satisfaction with the efficiencies of the order of 91.2 % and 93.9 % respectively. The mode of protection in this case is provided by the formation, on the cathodic sites, of thick layers of Ce (OH) 3, Ce 2 O 3, or La (OH) 3 and La 2 O 3, which provide cathodic protection. Zinc, in addition to the formation of small amounts of Zn (OH) 2 and ZnO which have a barrier effect against the diffusion of oxygen as previously reported. Corrosion protection of bronze in a 3% NaCl solution. Potentiodynamic polarization curves were used to determine the anodic and cathodic behavior, indicating the effectiveness of the extract as a mixed-type inhibitor. The study also quantifies the phenolic content through HPLC analysis, which highlights the role of rutin, quercetin, and gallic acid in the inhibition process [30].

Recently, the inhibition by the organic molecules as the tricine [N- (Tri (hydroxymethyl) methyl) glycine (phrase incomplete , à revoir). It comes out that the latter can be considered as an inhibitor anode, of corrosion of zinc in the solutions of chloride neutral. An effective inhibitory of about 90.4 % has been registered in the presence of 10 mM. Tricine in a solution NaCl 0.5 M. This inhibition was the result of the adsorption of the inhibitor molecules through the atom of oxygen and/or an atom of nitrogen on the active centers in the area of the electrode, forming a barrier that blocks the process of anode corrosion [31].

In various fields, the production of coatings from nanostructures makes it possible to endow the surface with new functionalities in terms of appearance, hardness, adhesion, corrosion resistance, and wettability and permits to increase their performance and thermal or electrical conductivity. mechanical, chemical, or thermal resistance, etc ... while limiting production costs. Moreover, these materials are often multifunctional, making it possible to couple various functions at the same time.

In the field of optics, the structuring of the surface brings several functionalities to the surface. It reduces reflection and increases the absorption capacity of incident light [32, 33]. In addition, it also allows to provide coloration to a material without the use of dye [34]. Beyond its effects, the surface structuring can present very selective characteristics in wavelength and/or polarization. This property gives these devices the ability to behave like an optical filter [35] that can be adjusted by controlling the geometric parameters of the surface patterns.

In the field of tribology, one crucial factor that determines how well a mechanical contact performs is its surface structure. It affects not only the amount of lubricant transported but also the

quality of surface separation, which in turn affects wear and friction [36]. In the field of medical applications, the surface micro and nanostructuring of implants is a parameter to be taken into account in the cellular response. Positive bone reactions have been observed on dental implants, linked with their nanostructuring [37-39].

In the field of anti-corrosion coating applications, surface nanostructuring can provide other interesting properties to the material concerning protection against corrosion: mechanical properties such as flexibility and solidity, and therefore impact resistance. This is the case with the coating produced by Greer et al. with Caltech having on the surface nanopillars 100 nm in diameter of metallic glass rich in zirconium (Zr 35 Ti 30 Co 6 Be 29) [40].

In the field of self-cleaning coatings, neoculturation of the surface is essential. Corrosion and contamination of metallic structures can cause loss of their functionality as well as aesthetic values, self-cleaning, and anti-corrosion surfaces for metallic structures. [41-43]. Many works have tried to artificially reproduce the surface of the lotus leaf which is covered with micro/nano textures. Therefore, at this surface topography water does not fill the space between surface textures and relies on air. This configuration allows the drop of water to roll without adhering to the surface, which gives it the ability to wash away the dust present on the surface, hence the designation of a self-cleaning surface. Nanostructured materials at the surface constitute a class of nanomaterials that combine both properties at the nanometer scale as well as their synergy to either amplify exciting ones or create new ones. The synergy between the properties of the patterns at the surface results both from the size of the patterns, from their organization, and the physical couplings between the patterns. According to the preparation methods mentioned in this chapter, a control of the size, the morphology and the spacing between the patterns is possible, and this is via the technical parameters of each of the methods. In the case of techniques using a mask, the properties (size, morphology, and spacing between patterns) of the textures prepared depend on those of the mask. On the other hand, for the techniques not using a mask, the properties of the textures are imposed by the parameters of the technique and the processing conditions. The hydrophobic systems can be prepared in one step by creating a surface roughness from a material having low surface energy such as perfluorinated compounds (tetrafluoroethylene…) [44,45], silicon [46-49], organic materials (polystyrene, alkylketene dimers,

polyamide, etc…) [50- 59], inorganic materials (ZnO, TiO $_2$ and SnO $_2$) [50-55]. According to the work of Ralph Hulseman of Hoowaki, nanostructured surfaces have been developed and were shaped in the form of small pillars of polymers such as silicone [56] on metal surfaces such as aluminum or steel. The first function is hydrophobicity with drop angles exceeding 150 ° (super-hydrophobic). This results in an anti-wetting effect, favorable against pathogens and atmospheric corrosion, but above all an oleophilic property resulting in reduced friction. In fact, on the one hand, a smaller quantity of oil is necessary, and on the other hand, in the event of a drop of oil falling on the substrate, it will be able to spread and thus reduce the risk of default.

Most hydrophobic systems are prepared in two stages: the first stage consists of forming a rough surface and the second of depositing on this surface a molecular film with low surface energy of the Teflon type [57]. The synergy of the two steps makes it possible to obtain optimal hydrophobicity. To obtain superhydrophobic surfaces, molecules of SiO $_2$ or silanes are chemically deposited by vapor phase (CVD) on various surfaces, the drop angles obtained are very high, greater than 170 ° and the deposition time is less than one minute. We can also cite examples of adsorption of Thiols on noble metals such as Ag [58].

Hydrophobic surfaces can be a solution against corrosion, as the wetting time is considerably reduced [59]. In this context, the work of GK Kannarpady et al. has shown that coatings composed of tungsten or aluminum nanorods from 25 to 75 nm provide the anti-icing property, which is highly sought after in aeronautics [60,61]. The functionalization of these nanostructured coatings by "Teflon-like" silanes brings to the surface a superhydrophobic behavior (164 ° +/- 3 °). This protection can be used in drinking water pipes against corrosion.

Law and Zhao of the Xerox company [62] have shown that PTFE (Teflon) certainly has superhydrophobic but oleophilic properties. By adding super oleophobic character to surfaces, better performance is obtained. In addition, their work confirms that high hydrophobicity is not necessarily a sign of low adhesion and that the sliding angle of a drop of water can be high even for a surface with a high contact angle. To ensure the oleophobicity, tests were carried out on etched silicon to obtain pads 7 µm high, 3 µm in diameter, and with a spacing of 6 µm, on which is deposited by phase molecular deposition vapor (MVD: molecular vapor deposition).

TiO$_2$ also exhibits photo-induced super-hydrophobicity, that is to say, a contact angle θ between the surface and water of about zero degrees under UV exposure [63]. This property has been widely studied for anti-fog applications. The vapor easily blurs the view through a mirror or glass due to the many water droplets that condense on the solid surface. In the case of a TiO$_2$ coating exposed to UV, the water does not settle in the form of drops but is spread on the superhydrophobic surface. The opposite option aimed at eliminating water drops from the surface by playing on super-hydrophobic properties has also been proposed. However, this alternative does not make it possible to eliminate the mist deposited on the surface without the water drops being removed by an external intervention: the force of the wind, vibration, or manual intervention. Conversely, under practical conditions, vision is never disturbed by the spreading of water on a superhydrophilic surface [64].

It is interesting to note that the photoinduced super hydrophilicity enters into synergy with the photocatalytic activity of TiO$_2$ because the two phenomena occured under UV irradiation. Thus, surface contamination can be totally or partially reduced (or made less toxic) by photocatalysis and the photodecomposition residues (partially mineralized elements) can be removed by a simple operation of rinsing with water, without the need for detergent. The combination of these two properties leads to the self-cleaning application. Over the past decade, self-cleaning devices have demonstrated their many benefits. In particular, they can be installed in outdoor or even indoor atmospheres, since UV rays do not only form part of the solar spectrum (typically 5%) but are also emitted by many indoor lighting devices, albeit in quantity much lower than solar radiation (typically 1 µW / cm ^{2}, i.e. 10 times less). Because of these arguments, many self-cleaning products have been marketed in Japan, USA, Europe, and many other countries [65].

In a general manner, there is a variety of protective inhibitors that effectively addresses corrosion for every type of material. In neutral, alkaline, or acidic conditions, there are a wide range of corrosion inhibitors available for iron metal research. It has been established how carbon steel behaves electrochemically when alkyl imidazoles which are present in a NaCl solution [66]. It is observed that the number of atoms in the chain alkyl as well as the concentration of each organic substance examined both affect the effectiveness of corrosion inhibition. With 11 carbon atoms, the corrosion has been effectively and maximally inhibited. The organic chemicals are adsorbed on the metal surface at low concentrations. An adsorption molecule is then "flat" on the electrode and acts on the process cathode as a result. An additional layer forms at high concentrations, enabling the inhibitor to cover the website's anode as well. The process anode and/or cathode mechanisms are altered in the two scenarios.

The behavior of mild steel in the presence of the triazole derivative 3,5-bis (4-methylthiophenyl) - 4H- 1,2,4-triazole) has been studied in acidic media, HCl (1 M) and H$_2$SO$_4$ (0.5 M). The results indicate that the inhibitory efficacy can reach values of the order of 99% and 80%, respectively [67]. The corrosion inhibition effect of *Calotropis procera* extract on 304 stainless steel in a 2 M HCl solution. Electrochemical methods such as electrochemical impedance spectroscopy (EIS), potentiodynamic polarization (PP), and electrochemical frequency modulation (EFM) were used to analyze the adsorption behavior, which followed the Langmuir adsorption isotherm. Surface morphology was also evaluated using various techniques [68]. The primary process of inhibition was caused by the molecules of triazole derivatives adhering to the steel surface. The latter turned out to be the Langmuir isotherm that was impacted by two modes: adsorption of the derivative of triazole with the doublets free of atoms of sulfur and/or of nitrogen or well of electrons the nucleus aromatic which act with orbital of vacancies of iron and adsorption of anions from the medium to the surface of the iron (Cl - SO 4 2- ...) which will attract the forms protonated derivative of triazole.

The characterizations of the corrosion products reveal the presence of a protective layer of iron III heptanoate on the metal surface while the impedance measurements indicate the great improvement in the corrosion protection of the steel in NaCl (0. 1 M). This efficacy has been attributed to the release of progressive heptanoate clay on the one hand, and its fibrous morphology enhancing the barrier properties of the coating polymer on the other hand. In general, the molecules inhibiting the most commonly employed and the least toxic are the amines or even the salts of carboxylic acids, which are also present in the inhibitor zirconium orthophosphates, and are extensively studied because of their physico chemical properties. The main properties of these minerals are their ability to exchange their cations by exchange reactions thanks to their high cation exchange capacity; and their intercalation property of organic entities of different sizes. These qualities give them the name of the reservoir of cations or organic compounds.

The study of the cation exchange properties has also been completed with varying degrees of success by exchanging the labile protons of Zr orthophosphate by the Ca 2+, Mg 2+, and Zn 2+ ions which present an interest in the field of inhibiting aqueous metallic corrosion. The conditions of ion exchange were explored by varying the temperature, by keeping in touch directly the dispersion of α-ZrP with the solutions of salts of metal corresponding (Ca (NO 3) 2 .4H 2 O, Zn (NO 3) 2 .6H 2 O, Mg (NO 3) 2 .6H 2 O) or by neutralizing them with the corresponding bases in the case of exchange by Ca 2+ (Ca (OH) 2) or by passing through the sodium form of α-ZrP (Na + -ZrP). The different characterizations of structural, microstructural, thermal, and spectroscopic performed on the compounds derived CaZr (PO 4) 2, 4H 2 O (Ca 2+ -ZrP) MgZr (PO 4) 2, 4H 2 O (Mg 2+ -ZrP), and ZnZr (PO 4) 2, 4H 2 O (Zn 2+ -ZrP) agree to demonstrate the successful intercalation of the different cations within the interfoliar spaces of α-ZrP causing their expansion of 0.98 nm for Ca 2+ -ZrP, and 0.96 nm for Mg 2+ -ZrP, and Zn 2+ -ZrP. However, it is important to note that less crystallized α-ZrP prepared under reflux (α-ZrP-R) is ready better to exchange cation than the highly crystallized synthesized by the hydrothermal way α-ZrP-H. Of more, intercalation of the cation metal into the compound α- ZrP-R is easy in the order given: Ca 2+> Mg 2+> Zn 2+. The study of inhibitory effect of corrosion zinc electrodes and mild steel has been extensively studied by different electrochemical techniques: measurement of corr, polarization, and spectroscopy impedance electrochemical for α-ZrP and Ca 2+ -ZrP because of the ease of intercalation Ca 2+ into the interleaving space of α-ZrP. Also, thanks to their properties of acid-base, the dispersions of materials to the base of α-ZrP alter the pH of a corrosive solution such as NaCl (0.1 M) exchange internal protons in the case of α-ZrP or exchange of protons of the area in the case of Ca 2+ -ZrP. Thus, in the context of inhibition of the corrosion process, they act as inhibitors to corrosion by buffering the pH at the surface of the zinc and avoiding any increase of the pH due to the corrosion. In this sense, the best performance was achieved with Ca 2+ -ZrP which provides the terms chemically interesting to interface the electrochemical of zinc. The results of the analysis of metal surfaces by XRD and SEM, after the electrochemical tests, showed the formation of layers protective against corrosion. In fact, in the presence of Ca 2+ - ZrP, a layer of zinc oxide (ZnO) and calcium phosphate was developed on bare zinc, while the presence of α-ZrP leads to the formation of zirconium, and zinc phosphates. For the corrosion inhibitor and the release of the latter

the second time, which was easily confirmed by obtaining, after the electrochemical test, from the stage sodium of α-ZrP after the replacement of entities organic by Na + cations, as well as by the formation of different protective layers as in the case of Cs-ZrP, where a very thin layer of zinc hydroxy heptanoate [Zn 5 (OH) 8 (C 7 -) 2] precipitated on bare zinc.

In addition, the products formed on the surface also have the effect of limiting the diffusion of oxygen and corrosive ions towards the metal surface, thus reducing the rates of corrosion. For the two parts, the orthophosphates of zirconium modified either by way of exchange cationic or by reactions acid-base have been used as fillers in the resin alkyd to test their electrochemical behavior on zinc and/or steel. The assessment of the inhibitory action of these loads (5 mass%) was achieved through spectroscopy electrochemical impedance (EIS) in a solution of NaCl (0.5 M).

As regards the corrosion of zinc, the sample RA-ZrP shows a performance of important protection that remains almost constant between 99 and 98 % during 768 hours of immersion of zinc. It should be noted that the organic coatings containing fillers based on α-ZrP and used as corrosion inhibitors exhibit an inhibitory efficiency that is better or at least comparable to that of ATP. This is explained by their laminated microstructure which improves the "barrier" properties of the coating. Also, these compounds act as mini tanks through their ability to release corrosion inhibitors over time and conferring the coating self-healing properties and ensuring the longevity of protection.

4. CONCLUSIONS

The fight against corrosion of materials, in a medium of hydrochloric acid of concentration 1M, by inhibitors of extracts. From the polarization tests, it appears that these three inhibitors are of mixed nature and the corrosion mechanism was not changed after their addition to the solution. Other analytical methods were used to further investigate the study, using the concentrations considered. The electrochemical impedance spectroscopy (EIS), allowed us to confirm the inhibitory quality and also to identify the corrosion mechanism, which takes place by charge transfer as well as the mode of inhibition by adsorption of the inhibiting molecules. This model assumes that the corrosion inhibition is due to the formation of a monolayer on the metal surface, reducing contact with the electrolyte, and that the interactions between the adsorbed particles are negligible. Tests on the influence of temperature, in the range of 25-60 ° C, on the inhibitory power have shown that the increase in temperature decreases the

inhibitory effectiveness of the compounds considered. This suggests that their adsorption to the sample surface is electrostatic. Therefore, the determination of thermodynamic activation parameters confirmed this. Scanning electron microscopy showed the presence of a uniform protective layer covering the entire surface of the steel. Surface analysis revealed that the surface of the sample for the control solution was covered with iron oxide (Fe_2O_3). However, in the inhibited solutions, no presence of oxides was observed, which indicates that the steel surface is perfectly isolated from the solution by the adsorbed protective film.

Natural extracts serve as effective green corrosion inhibitors due to their rich composition of bioactive compounds capable of adsorbing onto metal surfaces and forming protective barriers against corrosive agents. Alkaloid-based inhibitors like quinine from *Cinchona* bark, nicotine from tobacco (*Nicotiana tabacum*), and berberine from *Berberis* species reduce corrosion by interacting with the metal surface through nitrogen atoms. Flavonoids such as quercetin from onions and tea, catechin from green tea (*Camellia sinensis*), and rutin from citrus fruits inhibit corrosion by chelating metal ions and forming stable complexes. Tannin-rich inhibitors like tannic acid from tea and oak bark, and ellagic acid from pomegranate, form insoluble layers that protect the metal. Terpenoids like limonene from citrus peels, thymol from thyme, and menthol from mint provide hydrophobic protection, while sulfur-containing compounds such as allicin from garlic and sulforaphane from broccoli disrupt corrosion reactions at the metal surface. Essential oil components like eugenol from clove, carvacrol from oregano, and cinnamaldehyde from cinnamon enhance corrosion resistance by forming antioxidant-rich films. Additionally, lawsone from henna (*Lawsonia inermis*), curcumin from turmeric (*Curcuma longa*), and azadirachtin from neem (*Azadirachta indica*) exhibit excellent inhibition efficiency through both physical and chemical adsorption, making natural extracts a promising, sustainable alternative to conventional synthetic inhibitors.

It has been demonstrated that the inhibitors function mostly as mixed inhibitors. The findings regarding the effect of concentration indicated that, at a concentration of 0.04 g/L, the highest efficiency was attained, with 96% of the saffron and 95% of the turmeric at that concentration. The anode and cathode current densities decreased as the concentration increased, according to the polarization curves. For all concentrations examined, impedance diagrams have demonstrated that this is a mechanism of charge transfer over a heterogeneous surface. A capacitive loop, which is typically thought to be a representation of the charge transfer resistance at the metal/electrolyte contact, is included in the diagrams. Variations in concentration have an impact on the amplitude of the diagrams, as the concentration rises, so does the capacitive loop's size.

Future research in corrosion inhibition and surface treatments on metals is poised to focus on the development of green and sustainable inhibitors, particularly those derived from natural extracts, agricultural waste, and bio-based polymers, which offer eco-friendly alternatives to traditional toxic inhibitors. However, challenges remain in optimizing their chemical composition, improving their long-term stability, and understanding their adsorption mechanisms at the molecular level. The advancement of multifunctional surface treatments, such as nanostructured coatings, graphene-based films, and metal-organic frameworks (MOFs), is also a key area of exploration, with emphasis on enhancing properties like self-healing, antibacterial resistance, and mechanical robustness. Despite their potential, these advanced materials face challenges in scalability, cost-effectiveness, and durability under extreme conditions, such as high temperatures, salinity, and acidic environments, commonly encountered in industries like marine, oil and gas, and aerospace. Additionally, there is a critical need to deepen our understanding of corrosion mechanisms at the nanoscale through the use of advanced characterization techniques, such as atomic force microscopy and in situ transmission electron microscopy, to develop predictive models that link nanoscale behavior to macroscopic performance. The integration of machine learning and artificial intelligence offers a promising pathway for accelerating the discovery of new inhibitors and optimizing surface treatments, though the lack of standardized datasets and interpretable models remains a significant barrier. Moreover, research efforts must address the long-term performance and durability of corrosion inhibitors and coatings, emphasizing field testing and real-world applications to bridge the gap between laboratory results and practical use.

Conflicts of Interest

The author declared no conflict of interest.

5. REFERENCES

[1] R.Mohammadi, J.Wassink, A.Amirfazli (2004) Effect of Surfactants on Wetting of Super-Hydrophobic Surfaces , Langmuir, 20 , 9657-9662.

[2] J.-Y.Shiu, C.-W.Kuo, P.Chen, C.-Y.Mou (2004) Fabrication of Tunable Superhydrophobic Surfaces by Nanosphere Lithography, Chemistry of materials, 16 , 561-564.

[3] S. Zhang, Y. Ma, S. Zhao, W. Dai, B. Liu (2024) Enhanced coating system corrosion protection of 2A14 Al alloy by modified cerium seal PEO pretreatment, Corrosion Science, 235, 112203.

[4] H.Yabu, M.Shimomura (2005) Single-Step Fabrication of Transparent Superhydrophobic Porous Polymer Films, Chemistry of materials, 17, 5231-5234.

[5] S. Agarwal, S. Horst, M. Bognitzki (2006) Macromolecular materials and engineering, 291, 592-601.

[6] A.A. Aghzzaf, B. Rhouta, E. Rocca, A. Khalil, J. Steinmetz (2014) Corrosion Inhibition of Zinc by Calcium Exchanged Beidellite Clay Mineral: A New Smart Corrosion Inhibitor. 80 , 46-52.

[7] [7] K. Aramaki (2001) The Inhibition Effects of Chromate-Free, Anion Inhibitors on Corrosion of Zinc in Aerated 0.5 M NaCl. Corrosion Science., 43, 591-604.

[8] J. Aslam, R. Aslam, S.H. Alrefaee, M. Mobin, A. Aslam, M. Parveen, C.M. Hussain (2020) Gravimetric, Electrochemical, and Morphological Studies of an Isoxazole Derivative as Corrosion Inhibitor for Mild Steel in 1M HCl Arabian Journal of Chemistry., 13 , 7744-7758.

[9] S.Bag, S.Chakraborty, A.Roy, B.Chaudhuri (1996) Aminobenzimidazole as Corrosion Inhibitor for 70-30 Brass in Ammonia. British Corrosion Journal Chaudhuri, British Corrosion Journal ., 31, 207-212.

[10] Y.Bai, H.Yu, Z.Li, R.Amal, G.Lu, L.Wang (2012) In Situ Growth of a ZnO Nanowire Network within a TiO2Nanoparticle Film for Enhanced Dye-Sensitized Solar Cell Performance. Advanced Materials., 24, 5850-5856.

[11] E. Balaur, J.M. Macak, L. Taveira, P. Schmuki (2005) Tailoring the Wettability of TiO2 Nanotube Layers. Electrochemistry Communications. 7, 1066-1070.

[12] R. Berenguer, A. La Rosa-Toro, C. Quijada, E. Morallón (2008) Origin of the Deactivation of Spinel CuxCo3−XO4/Ti Anodes Prepared by Thermal Decomposition. The Journal of Physical Chemistry C., 112, 16945-16952.

[13] B. Bhushan, Y.C. Jung, K. Koch (2009) Micro-, Nano- and Hierarchical Structures for Superhydrophobicity, Self-Cleaning and Low Adhesion. Philosophical transactions of the Royal Society of London. Series A: Mathematical, physical, and engineering sciences., 367, 1631-1672.

[14] D. Bose, O. Mehra, C. Gupta (1985) Preparation of Rare Earth-Silicon-Iron Alloy by Metallothermic Reduction. , J. of the Less Common Metals., 110, 239-242.

[15] C. Comninellis, A. De Battisti (1996) Electrocatalysis in Anodic Oxidation of Organics with Simultaneous Oxygen Evolution, Journal de chimie physique., 93 , 673-679.

[16] C. G. Dariva, F.Alexandre (2014) Corrosion Inhibitors: Principles, Mechanisms and Applications , Developments in corrosion protection., 16 , 365-378.

[17] P. de Lima-Neto, A.P. de Araujo, W.S. Araujo, A.N. Correia (2008) A. N. Study of the Anticorrosive Behaviour of Epoxy Binders Containing Non-Toxic Inorganic Corrosion Inhibitor Pigments, Progress in Organic Coatings., 62 , 344-350.

[18] C. Deya, G. Blustein, B. Del Amo, R. Romagnoli (2010) Evaluation of Eco-Friendly Anticorrosive Pigments for Paints in Service Conditions. Progress in Organic Coatings., 69, 1-6.

[19] Y. Feng, S. Chen, J. You, W. Guo (2007) Investigation of Alkylamine Self-Assembled Films on Iron Electrodes by SEM, FT-IR, EIS, and Molecular Simulations. Electrochimica acta., 53, 1743-1753.

[20] Z. Guo, F. Zhou, J. Hao, W. Liu (2005) Stable Biomimetic Super-Hydrophobic Engineering Materials, Journal of the American Chemical Society., 127, 15670-15671.

[21] B. Hinton, L. Wilson (1989) The Corrosion Inhibition of Zinc with Cerous Chloride, Corrosion., 29, 967-985.

[22] D. Jang, C.T. Gross, J.R. Greer (2011) Effects of Size on the Strength and Deformation Mechanism in Zr-Based Metallic Glasses , International Journal of Plasticity, 27 858-867.

[23] F. Jianqing, Y. Huipin, Z. Xingdong (1997) Promotion of Osteogenesis by a Piezoelectric Biological Ceramic Biomaterials., 18 , 1531-1534.

[24] A. Kaouka, O. Alaoui (2019) Characterization and Corrosion Resistance of Boride Layers on Carbon Steel. IOP Conference Series: Materials Science and Engineering, IOP Publishing, , p. 012029.

[25] A. Kaouka, O. Allaoui, M. Keddam (2013) Growth kinetics of the boride layers formed on SAE 1035 steel , Matériaux & Techniques, 101 705.

[26] A. Kaouka, K. Benarous (2019) Electrochemical Boriding of Titanium Alloy Ti-6Al-4V Journal of Materials Research and Technology, 8 6407-6412.

[27] M.T. Khorasani, H. Mirzadeh, Z. Kermani (2005) Wettability of Porous Polydimethylsiloxane Surface: Morphology Study Applied surface., 242 , 339-345.

[28] G. Koch (2017) Trends in oil and gas corrosion research and technologies, p.3-30.

[29] B.K. Körbahtı, B. Salih, A. Tanyolaç (2001) Electrochemical Conversion of Phenolic Wastewater on Carbon Electrodes in the Presence of NaCl., Journal of Chemical Technology & Biotechnology: International Research in Process, Environmental & Clean Technology., 77 , 70-76.

[30] D. Kasapović, L. Klepo, J. Ostojić , F. Bikić, F. Korać (2023) Effect of polka raspberry (Rubus idaeus L.) extract on corrosion inhibition of bronze, Zastita Materijala, 64 (4) 383 - 307

[31] X.-y. Li, Y.-h. Cui, Y.-j. Feng, Z.-m. Xie, J.-D. Gu (2005) Reaction Pathways and Mechanisms of the

Electrochemical Degradation of Phenol on Different Electrodes. Water research, 39 , 1972-1981.

[32] Z. Li, Y. Qu, X. Zhang, B. Yang (2009) Bioactive Nano-Titania Ceramics with Biomechanical Compatibility Prepared by Doping with Piezoelectric BaTiO3 , Acta biomaterialia ., 5 , 2189-2195.

[33] Q.-h. LU, Y.-h. HU (2012) Synthesis of Aluminum Tri-Polyphosphate Anticorrosion Pigment from Bauxite Tailings., Transactions of Nonferrous Metals Society of China ., 22 , 483-488.

[34] X. Lu, C. Zhang, Y. Han (2004) Low-Density Polyethylene Superhydrophobic Surface by Control of Its Crystallization Behavior, Macromolecular rapid communications., 25 , 1606-1610.

[35] X. Lu, Y. Zuo, X. Zhao, Y. Tang (2013) The Influence of Aluminum Tri-Polyphosphate on the Protective Behavior of Mg-Rich Epoxy Coating on AZ91D Magnesium Alloy. Electrochimica acta ., 93, 53-64.

[36] G. Martelli, R. Ornelas, G. Faita (1994) Deactivation Mechanisms of Oxygen Evolving Anodes at High Current Densities, Electrochimica acta,. 39, 1551-1558.

[37] H. Nady (2017) Tricine [N- (Tri (Hydroxymethyl) Methyl) Glycine] – a Novel Green Inhibitor for the Corrosion Inhibition of Zinc in Neutral Aerated Sodium Chloride Solution , Egyptian Journal of Petroleum, 26 , 905-913.

[38] D.-M. Shin, S.W. Hong, Y.-H. Hwang(2020) Recent Advances in Organic Piezoelectric Biomaterials for Energy and Biomedical Applications, Nanomaterials, 10 , 123.

[39] C. Silvestre, D. Duraccio, S. Cimmino (2011) Food Packaging Based on Polymer Nanomaterials. P . Progress in polymer science . 36 , 1766-1782.

[40] D. Song, J. Gao, L. Shen, H. Wan, X. Li (2015) The Influence of Aluminum Tripolyphosphate on the Protective Behavior of an Acrylic Water-Based Paint Applied to Rusty Steels , J. of Chemistry., ID 618971,

[41] M. Tabish, G. Yasin, M.J. Anjum, M.U. Malik, J. Zhao, Q. Yang, S. Manzoor, H. Murtaza, W.Q. Khan (2021) Reviewing the Current Status of Layered Double Hydroxide-Based Smart Nanocontainers for Corrosion Inhibiting Applications. J. of Mater. Res. and Techno., 10, 390-421.

[42] P.J. Thomas, D. Carpenter, C. Boutin, J.E. Allison (2014) Effects on Germination and Growth of Selected Crop and Native Plant Species. Chemosphere ., 96 , 57-66.

[43] G. Vercesi, J. Rolewicz, C. Comninellis, J. Hinder(1991) Characterization of DSA-Type Oxygen Evolving Electrodes. Choice of Base Metal , Thermochimica acta, 176 , 31-47.

[44] X. Wu, Z. Chen (2018) A Mechanically Robust Transparent Coating for Anti-Icing and Self-Cleaning Applications, Journal of materials chemistry. A, Materials for energy and sustainability. 6 , 16043-16052.

[45] S.H. Yoo, Y.W. Kim, K. Chung, N.-K. Kim, J.-S. Kim (2013) .Corrosion Inhibition Properties of Triazine Derivatives Containing Carboxylic Acid and Amine Groups in 1.0 M HCl Solution. Industrial &

Engineering Chemistry Research . 52 , 10880-10889.

[46] N. Zhao, Q. Xie, L. Weng, S. Wang, X. Zhang, J. Xu (2005) Superhydrophobic Surface from Vapor-Induced Phase Separation of Copolymer Micellar Solution., Macromolecules . 38 , 8996-8999.

[47] S. Zheng, C. Li, Y. Zhang, T. Xiang, Y. Cao, Q. Li, Z. Chen (2021) A General Strategy towards Superhydrophobic Self-Cleaning and Anti-Corrosion Metallic Surfaces: An Example with Aluminum Alloy. Coatings (Basel) . 11 788.

[48] B. Zhmud, B. Pasalskiy(2013) Nanomaterials in Lubricants: An Industrial Perspective on Current Research., Lubricants. 1 , 95-101.

[49] F. Zucchi 1997 Organic Inhibitors of Corrosion Metals

[50] G.Zhang, E. Jiang, L. Wu, W.Ma, H. Yang, A. Tang, F.Pan (2021) Corrosion Protection Properties of Different Inhibitors Containing PEO/LDHs Composite Coating on Magnesium Alloy AZ31. Scientific Reports ., 11 (1)

[51] S.S. Latthe, B.A. Gurav, Sh.C. Maruti, Sh. Vhatkar (2012) Recent Progress in Preparation of Superhydrophobic Surfaces: A Review. J. of Surf. Eng.Mater. and Adv. Techno.. 02, 76–94

[52] E.E.Meyer, K. Rosenberg, J. Israelachvili (2006) Recent progress in understanding hydrophobic interactions. Proceedings of the National Academy of Sciences, 103 (43), 15739-15746.

[53] Y.Li, et al. (2022) Measuring the relationship between morphological spatial pattern of green space and urban heat island using machine learning methods. Applied Geography, 139, 102643.

[54] F.Pan, et al. (2019) Tuning Superhydrophobic Materials with Negative Surface Energy. Nanomaterials, 9(12), 1734.

[55] S.Kumar, et al. (2020). A review on the fabrication of superhydrophobic surfaces: From fundamentals to applications. Materials Today: Proceedings, 21, 1345-1350.

[56] R.Hulseman (2014) Innovative approach for the nano micro texturing of metallic surfaces. Doctoral thesis, (in French).

[57] E.Vazirinasab, R. Jafari, G. Momen (2018) Application of superhydrophobic coatings as a corrosion barrier: A review. Materials Chemistry and Physics, 207, 1-12.

[58] M.A. Mohamed Adel, A. Aboubakr, Y. Nathalie (2015) Corrosion behavior of superhydrophobic surfaces: A review. Chemical Engineering Transactions, 43, 61-66.

[59] M.Khan, et al. (2022) The new trends in corrosion control using superhydrophobic surfaces. Corrosion Reviews, 40(1), 1-20.

[60] G.Kannarpady, et al. (2023) Icephobic properties of tungsten and aluminum nanorod coatings for aircraft applications. Journal of Materials Science, 58(3), 1234-1245.

[61] D.Zeng, Y. Li, H. Liu, Y. Yang, L. Peng, C. Zhu, N. Zhao (2023) Superhydrophobic coating induced anti-icing and deicing characteristics of an airfoil. Colloids and Surfaces A: Physicochemical and Engineering Aspects, 648, 129068.

[62] K.Law, H. Zhao (2016) Surface wetting: characterization, contact angle, and fundamentals.

[63] S.Banerjee, D.Dionysiou, S. Pillai (2015) Self-cleaning applications of TiO2 by photo-induced hydrophilicity and photocatalysis. Journal of Photochemistry and Photobiology A: Chemistry, 317, 1-12.

[64] Y.Zhao, et al. (2023) Design of superhydrophobic surfaces for enhanced anti-fogging and anti-icing properties. Nature Communications, 14(1), 1234.

[65] S.Banerjee, D. Dionysiou, S. Pillai (2015) Self-cleaning applications of TiO₂ by photo-induced hydrophilicity and photocatalysis. Journal of Photochemistry and Photobiology C: Photochemistry Reviews, 25, 1-29.

[66] A.Ahmed, M. El-Sayed, H. Abdo, E. Gad (2021) Ethanedihydrazide as a Corrosion Inhibitor for Iron in 3.5% NaCl Solutions. ACS Omega, 6(24), 15734-15744.

[67] I.Merimi, R. Benkaddour, H. Lgaz, N.Rezki, M. Messali, F.Jeffali, H.Oudda, B. Hammouti (2021) Insights into corrosion inhibition behavior of a 5-Mercapto-1,2,4-triazole derivative for mild steel in hydrochloric acid solution: Experimental and DFT studies. Lubricants, 9 (12), 122

[68] A. S. Fouda, A. A. El-Hossiany, H. M. Ramadan (2017) Calotropis Procera Plant Extract as a Green Corrosion Inhibitor for 304 Stainless Steel in Hydrochloric Acid Solution, Zastita materijala, 58 (4), 541 - 555.

IZVOD

ELEKTROHEMIJSKA PROCENA PRIRODNIH EKSTRAKATA KAO EFIKASNIH INHIBITORA KOROZIJE I POVRŠINSKIH TRETMANA NA METALNIM PODLOGAMA

Korozija je ozbiljan problem sa kojim se susrećemo u industriji i zaštita od nje je više nego neophodna upotrebom inhibitora i tretmana. Ovi tretmani mogu efikasno da ublaže problem na površini materijalne podloge, posebno metalne podloge jer se lako urezuje tokom upotrebe i ne može da izdrži abraziju. Eksperimentalni rezultati su pokazali da su ekstrakti efikasni inhibitori korozije. Polarizacioni testovi pokazuju da su inhibitori mešovite prirode i da se mehanizam korozije ne menja nakon njihovog dodavanja u rastvor. Spektroskopija elektrohemijske impedanse je potvrdila da su inhibitorni kvalitet i površinski tretmani poboljšali otpornost na koroziju. Površinskom analizom utvrđeno je da je površina uzorka za kontrolni rastvor pokrivena i zaštićena. Međutim, za inhibirane rastvore nije primećeno prisustvo oksida.

***Ključne reči**: zaštita od korozije, inhibitor, površinski tretmani.*

Alaeddine Kaouka: https://orcid.org/0000-0002-1118-7603.
Khedidja Benarous: https://orcid.org/0000-0001-9112-6730
Mourad Keddam: https://orcid.org/0000-0002-6014-4482

Ali Akbar[1], Abhilekha Sharma[2], Abhirup Mitra[3,4],
Richa Saxena[5]*, Dipti Bharti[6], Richa Sharma[7]

[1]Department of Chemistry,Government Engineering College, Jehanabad, Bihar,India, [2]Department of Chemistry, JIMS Engineering Management Technical Campus, Greater Noida, India, [3]Department of Agriculture, Invertis University, Bareilly, U.P.,India, [4]Department of Food Process Engineering, NIT Rourkela, Odisha, India, [5]Department of Biotechnology, Invertis University, Bareilly, U.P.,India, [6]Departmentof Applied Science & Humanities, Darbhanga College of Engineering, Darbhanga, Bihar, India, [7]Department of Microbiology, Mahatma Gandhi University of Medical Sciences and Technology, India.

Novel strategies in carbon capture and utilization: A chemical perspective

ABSTRACT

The escalating threat of climate change demands innovative approaches to mitigate carbon emissions, and Carbon Capture and Utilization (CCU) has emerged as a promising paradigm. The article begins with an overview of the current carbon emission landscape, underscoring the critical role of CCU in climate change mitigation. Catalysts play a pivotal role in CCU, and the review discusses cutting-edge developments in catalytic materials and design, offering mechanistic insights into catalyzed reactions. Biological strategies, such as bioenergy with carbon capture and storage (BECCS) and microbial carbon capture, are explored alongside genetic engineering for enhanced carbon assimilation. Life cycle assessment and techno-economic analysis are scrutinized to evaluate the environmental and economic aspects of CCU. It concludes with a forward-looking perspective, outlining future prospects and research directions in CCU. This review aims to provide a valuable resource for researchers, policymakers, and industry professionals working towards a sustainable and low-carbon future.
Keywords: Sustainable chemistry; electrochemical reduction; industrial carbon utilization; nanotechnology in CCU

1. INTRODUCTION

The contemporary era, the escalating specter of climate change, driven by the unremitting surge in global carbon dioxide (CO_2) emissions, has propelled environmental sustainability to the forefront of global discourse [1].

Amidst this exigency, Carbon Capture and Utilization (CCU) emerges as a beacon of promise, providing a multifaceted strategy to not only mitigate the impacts of climate change but also ingeniously repurpose CO_2 as a valuable resource. This review embarks on an exhaustive exploration of the chemical intricacies and innovative strategies that underscore the evolving landscape of CCU. The urgency of addressing climate change necessitates a comprehensive understanding of the intricate mechanisms involved in the capture and subsequent utilization of carbon.

At the chemical forefront of CCU, absorption and adsorption techniques play a pivotal role [2,3]. These methods, leveraging solvents, solid absorbents, as well as porous materials and molecular sieves, form the bedrock for capturing CO_2 emissions from a spectrum of sources, including industrial processes and power generation [4,5]. The review meticulously dissects these techniques, providing insights into their mechanisms and applications. Moreover, it delves into the realm of chemical reactions driving CO_2 capture, extending the discourse beyond traditional amine-based processes to explore advanced and nuanced methodologies.

Catalysis emerges as a cornerstone in the chemical transformation of captured carbon, steering the conversion of CO_2 towards valuable end products [6]. The review embarks on an in-depth exploration of catalytic research, shedding light on cutting-edge materials, innovative designs, and mechanistic insights that fuel the efficiency of carbon utilization processes. This section illuminates the dynamic interplay between catalyst development and the expanding landscape of applications, ranging from sustainable fuels to high-

value chemicals. Simultaneously, electrochemical approaches represent a vanguard in CCU, offering a sustainable pathway for CO_2 conversion. The intricate exploration of electrochemical reduction mechanisms and advances in electrocatalysis underscores the transformative potential of renewable energy integration in CCU strategies.

The chemical perspective extends its embrace into the realm of biology, where living organisms become instrumental in carbon capture and utilization. Bioenergy with carbon capture and storage (BECCS) and microbial carbon capture present bio-inspired solutions, showcasing the marriage of biological processes with chemical ingenuity.

Biological processes for carbon assimilation play a pivotal role in the carbon capture and utilization (CCU) landscape. Photosynthetic organisms, such as microalgae and cyanobacteria, are among the most efficient natural systems for carbon fixation, converting atmospheric CO_2_22 into organic compounds through the Calvin-Benson-Bassham cycle. These microorganisms can be engineered to enhance their carbon capture efficiency, optimize growth rates, and produce valuable bio-based products, such as biofuels, bioplastics, and other high-value chemicals.

Additionally, non-photosynthetic microbial systems, such as chemoautotrophic bacteria, utilize CO_2_22 as a carbon source through pathways like the reductive acetyl-CoA pathway and the 3-hydroxypropionate bicycle. Advances in synthetic biology have enabled the reprogramming of these organisms to integrate novel pathways and improve carbon assimilation capabilities. These biological processes complement chemical and electrochemical approaches, offering

sustainable, scalable, and economically viable solutions for mitigating carbon emissions and addressing global climate challenges.

As CCU technologies continue to advance, the review navigates through emerging trends that hold the promise of enhancing efficiency and expanding the scope of carbon utilization [8]. Membrane-based separation processes and nanotechnology applications represent frontiers that have the potential to revolutionize the efficiency and selectivity of CCU processes. Among technologies for carbon assimilation, **artificial photosynthesis systems** mimic natural photosynthesis to convert CO_2_22 into energy-rich compounds using light as an energy source. Similarly, **bioelectrochemical systems**, such as microbial electrosynthesis, utilize electrogenic microorganisms to fix CO_2_22 into organic molecules, leveraging renewable electricity to drive the process.

Moreover, **enzyme-based catalysis** employs highly specific enzymes, such as carbonic anhydrase, to facilitate CO_2_22 conversion with exceptional selectivity and lower energy demands. **Hydrogenotrophic microbial systems**, which utilize hydrogen gas as an energy source, are also emerging as efficient methods to convert CO_2_22 into value-added chemicals.

Concurrently, life cycle assessment and techno-economic analysis provide critical lenses through which the environmental and economic viability of these CCU strategies are scrutinized, adding depth to our understanding of the broader impact of these technologies. These diverse approaches showcase the versatility of carbon assimilation technologies and their potential to transform CCU into a cornerstone of sustainable industrial practices [9].
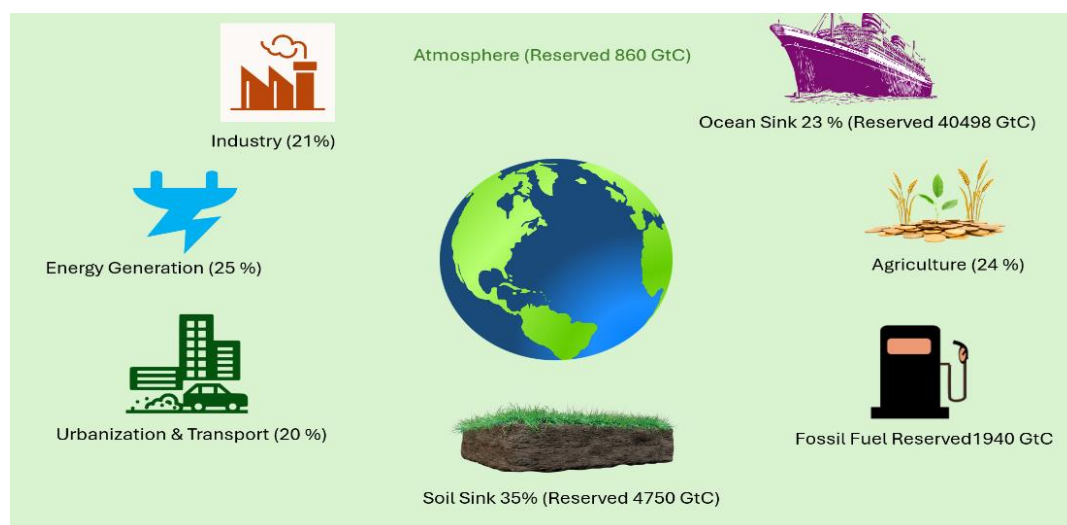
Figure 1. Schematic diagram of carbon cycle, Gigatonnes of carbon (GtC) represents the reserved carbons [80]

Yet, navigating the landscape of CCU is not solely a scientific endeavor; it is entwined with intricate policy and regulatory frameworks that shape its implementation. This review illuminates global initiatives, governmental incentives, and regulatory challenges, highlighting the complex interplay between technological innovation and the socio-political landscape. Real-world case studies drawn from industrial applications offer tangible insights into the successes, challenges, and potential scalability of CCU technologies, underscoring the need for a harmonious integration of technology and policy.

2. INTRODUCTION TO CARBON CAPTURE AND UTILIZATION (CCU):

In the contemporary epoch, the burgeoning challenge of climate change stands as an urgent and omnipresent global concern. The main culprit behind this predicament is the unabated release of carbon dioxide (CO_2) into the atmosphere, primarily from anthropogenic activities such as industrial processes and the burning of fossil fuels [10, 11]. As atmospheric CO_2 concentrations reach unprecedented levels, the repercussions for global climate patterns, sea levels, and biodiversity become increasingly profound.

Overview of the Current State of Carbon Emissions:

To appreciate the imperative of Carbon Capture and Utilization (CCU), it is essential to understand the current state of carbon emissions. As of the latest assessments, global CO_2 emissions continue to surge, with an ever-expanding industrial landscape and escalating energy demands contributing to this upward trajectory [12]. The repercussions of this unabated release of CO_2 extend beyond mere environmental concerns; they pose a direct threat to the delicate equilibrium of Earth's climate systems. The rise in average global temperatures, changes in precipitation patterns, and the intensification of extreme weather events serve as tangible manifestations of the burgeoning climate crisis.

Industrial activities, including energy production, manufacturing, and transportation, remain major contributors to the escalating carbon emissions. Fossil fuel combustion, a mainstay in the global energy mix, releases vast amounts of CO_2, amplifying the greenhouse effect and propelling climate change [13]. This stark reality necessitates a paradigm shift in our approach to carbon management — one that extends beyond emissions reduction to include innovative strategies

for actively removing and repurposing CO_2 from the atmosphere.

Importance of CCU in Mitigating Climate Change:

In this context, Carbon Capture and Utilization (CCU) emerges as a compelling and multifaceted strategy to address the dual challenge of reducing emissions and actively mitigating the impact of existing atmospheric CO_2. Unlike traditional carbon capture and storage (CCS) methods that focus solely on sequestering CO_2 underground, CCU introduces a transformative approach by converting captured CO_2 into valuable products, thus turning a greenhouse gas into a resource [14,15].

The significance of CCU in the broader climate change mitigation landscape lies in its potential to break the linear link between economic growth and carbon emissions. By capturing CO_2 emissions at their source and converting them into usable products, CCU provides a pathway for industries to decouple their growth from environmental degradation. This not only aligns with sustainability goals but also fosters a circular carbon economy where carbon is treated as a valuable commodity rather than a waste product [16].

Furthermore, CCU offers a pragmatic solution to the intermittency challenge of renewable energy sources. As the world transitions to a low-carbon energy system, the intermittent nature of renewable energy generation poses challenges for meeting constant energy demands. CCU can act as a complementary strategy by providing a means to store excess renewable energy in the form of converted carbon-based products, creating a more resilient and adaptable energy infrastructure.

3. CHEMICAL MECHANISMS OF CARBON CAPTURE:

The pursuit of effective carbon capture strategies is at the forefront of efforts to mitigate anthropogenic carbon dioxide (CO_2) emissions [17]. Understanding the chemical mechanisms underlying carbon capture is pivotal for developing efficient and scalable technologies. This section explores the diverse chemical pathways employed in carbon capture, encompassing absorption techniques, adsorption methods, and a spectrum of chemical reactions designed for CO_2 capture [18]. The Carbon Capture and Utilization (Figure 1) represents a comprehensive overview of the stages involved in capturing and utilizing carbon dioxide (CO_2) to mitigate anthropogenic emissions. The diagram outlines key steps and chemical pathways crucial for developing efficient and scalable carbon capture technologies.
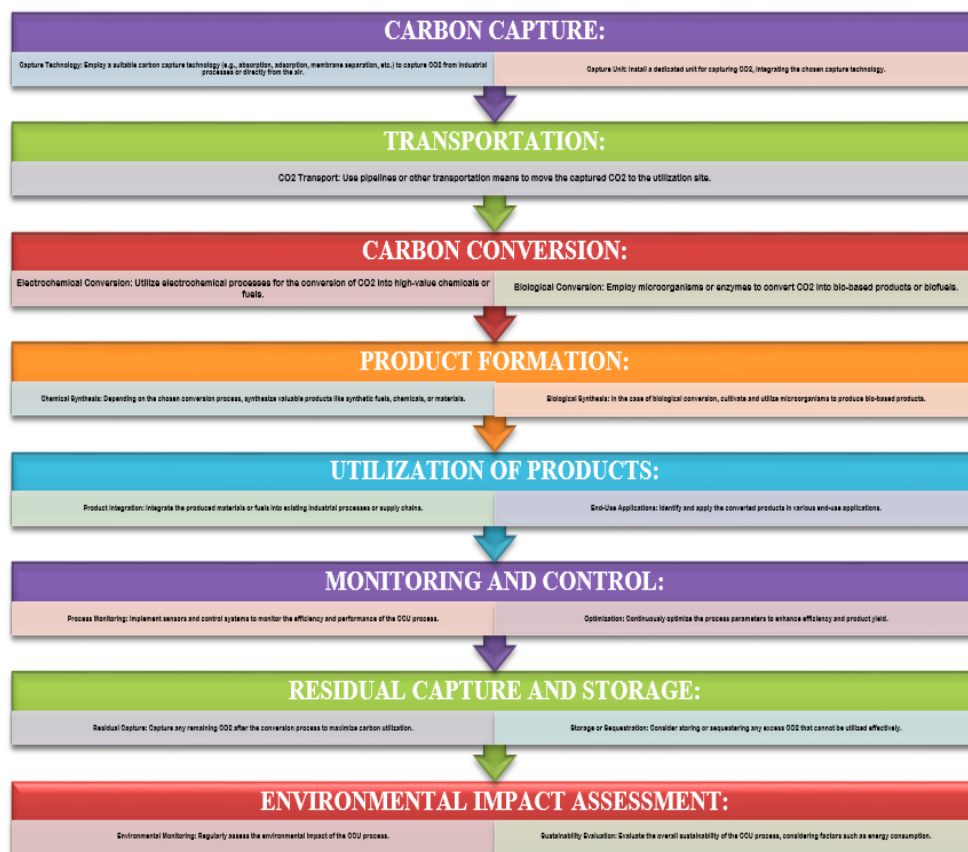
Figure 2. Pathways to sustainability: carbon capture and utilization process flow

Absorption Techniques:

Solvent-Based Absorption: Solvent-based absorption is a cornerstone of traditional carbon capture methods. In this approach, flue gases rich in CO_2 are brought into contact with a liquid solvent that selectively captures and binds with CO_2 [19]. Commonly used solvents include amines, which form stable compounds with CO_2. The resultant solution can then be processed to release the captured CO_2 for storage or utilization [20]. While effective, challenges such as solvent degradation and energy-intensive regeneration processes have prompted ongoing research into innovative solvent systems.

Solid Absorbents: Advancements in absorption techniques have led to the exploration of solid absorbents as alternatives to liquid solvents. Porous materials, such as metal-organic frameworks (MOFs) and zeolites, exhibit high surface areas and tunable chemical properties, making them effective candidates for CO_2 capture [21]. These materials adsorb CO_2 through physical and chemical interactions, and their regenerability makes them promising for repeated use. The development of novel solid absorbents with enhanced selectivity and capacity is a focal point for researchers seeking to improve the efficiency of absorption-based carbon cap.

Adsorption Methods:

Porous Materials: Adsorption methods rely on porous materials with a high affinity for CO_2 molecules. Porous materials, including activated carbons and zeolites, provide a structured environment where CO_2 molecules can adhere to the surface [22]. The porous nature of these materials facilitates high adsorption capacities, and their selectivity for CO_2 over other gases is finely tuned through material design. Advances in nanoporous materials and the synthesis of designer adsorbents contribute to the evolution of adsorption-based carbon capture technologies.

Molecular Sieves: Molecular sieves are crystalline materials with well-defined pores that selectively adsorb molecules based on size and shape. Tailoring molecular sieves for CO_2 adsorption involves precise control over pore size and functionalization. This adsorption method offers advantages in terms of scalability, stability, and regenerability [23, 24]. The exploration of novel molecular sieve architectures and the incorporation of sustainable materials enhance the efficacy of molecular sieve-based carbon capture.

Chemical Reactions for CO₂ Capture:

Amine-Based Processes: Chemical reactions provide an avenue for capturing CO_2 by forming stable chemical compounds. Amine-based processes involve the reaction of CO_2 with amines to produce stable carbamate compounds [25]. These reactions typically occur in liquid solvents and can be reversible through controlled changes in temperature or pressure. While widely employed, challenges such as energy-intensive regeneration and solvent degradation have spurred research into improving the efficiency and sustainability of amine-based carbon capture.

Beyond Amine-Based Processes: Innovations in chemical reactions for CO_2 capture extend beyond traditional amine-based processes [26, 27]. Researchers are exploring alternative reaction pathways, including the use of switchable solvents, metal-based catalysts, and hybrid approaches that combine chemical reactions with physical adsorption. These endeavors aim to overcome the limitations of conventional processes, such as high energy requirements and material degradation, opening avenues for more sustainable and economically viable carbon capture solutions [28].

In summary, the chemical mechanisms of carbon capture encompass a rich array of techniques ranging from traditional solvent-based methods to emerging adsorption strategies and innovative chemical reactions. Ongoing research in this realm seeks to enhance the efficiency, sustainability, and scalability of carbon capture technologies, addressing the imperative of reducing CO_2 emissions in the face of global climate challenges.

Innovative Catalysts for CO₂ Conversion:

The quest for sustainable solutions to mitigate carbon dioxide (CO_2) emissions has spurred intensive research into innovative catalysts for CO_2 conversion [29]. This section delves into cutting-edge developments in catalytic materials, novel catalyst design, and synthesis methods, along with the mechanistic insights thatunderpincatalyzed reactions aimed at transforming CO_2 into valuable products. (Figure 2) provides a detailed exploration of cutting-edge developments in catalytic materials, novel catalyst design, synthesis methods, and the mechanistic insights that form the foundation of catalyzed reactions aiming to transform CO_2 into valuable products.

Figure 3. Advancements in Catalytic CO₂ Conversion: A Visual Exploration of Innovative Catalysts and Reaction Mechanisms

Catalytic Materials for CO₂ Reduction:

Catalysts in CO₂ Reduction: The catalytic reduction of CO_2 involves the transformation of carbon dioxide into compounds with higher value, such as fuels or chemicals, through chemical reactions. Catalysts play a central role in facilitating these reactions by lowering the activation energy and providing reaction pathways that lead to desired products [30]. Traditional catalysts include metals like copper, silver, and gold, but recent advancements extend to a diverse range of materials, including metal oxides, nanoparticles, and complex nanostructured materials. These innovative catalysts exhibit enhanced activity, selectivity, and stability in CO_2 conversion processes.

Integration of Nanomaterials: Nanomaterials, characterized by their unique properties at the nanoscale, have gained prominence in CO_2 reduction catalysis. Nanocatalysts offer high surface areas, tunable reactivity, and unique electronic structures, all of which contribute to their exceptional catalytic performance. Materials such as metal nanoparticles, metal-organic frameworks (MOFs), and carbon-based nanomaterials have demonstrated remarkable efficacy in driving CO_2 reduction reactions [31]. The tailored design of nanocatalysts allows for precise control over catalytic activity, enabling the optimization of product selectivity.

Novel Catalyst Design and Synthesis:

Tailoring Catalysts for Specific Reactions:

The design of catalysts for CO_2 conversion is evolving towards tailoring materials for specific reactions, aiming to maximize the production of desired products. Rational catalyst design involves a deep understanding of the reaction mechanisms and the identification of active sites on the catalyst surface. Computational methods, such as density functional theory (DFT), aid in predicting catalytic performance and guiding the design of catalysts with enhanced reactivity [32]. The integration of machine learning algorithms further accelerates the discovery of novel catalysts by analyzing vast datasets of material properties and catalytic performance.

Synthesis Methods and Scalability:

Innovative catalyst design is coupled with advanced synthesis methods that enable the fabrication of catalytic materials with controlled structures and compositions. Techniques such as sol-gel, co-precipitation, and chemical vapor deposition facilitate the synthesis of nanoscale catalysts with tailored properties. Scalability is a crucial consideration, and efforts are underway to develop synthesis approaches that are not only efficient in the laboratory but also amenable to large-scale production for industrial applications [33]. Continuous-flow synthesis and template-assisted methods exemplify strides toward scalable catalyst fabrication.

Mechanistic Insights into Catalyzed Reactions:

Probing Reaction Mechanisms: A profound understanding of the mechanistic intricacies of catalyzed reactions is essential for optimizing catalyst performance. Mechanistic studies involve characterizing intermediate species, reaction pathways, and the role of various catalyst components during CO_2 conversion [34]. Advanced spectroscopic and imaging techniques, such as in-situ X-ray absorption spectroscopy and operando microscopy, provide real-time insights into catalyst behavior under reaction conditions. These studies deepen our comprehension of the complex interplay of factors influencing catalytic activity and guide the refinement of catalyst design.

Dynamic Reaction Kinetics: Mechanistic insights extend to dynamic reaction kinetics, unraveling the temporal evolution of catalyzed reactions. Kinetic studies elucidate the rate-determining steps, reaction intermediates, and the influence of reaction conditions on overall performance [35]. This knowledge enables the optimization of reaction parameters to enhance reaction rates and selectivity, crucial for the practical implementation of catalytic processes.

4. ELECTROCHEMICAL APPROACHES IN CARBON CAPTURE AND UTILIZATION (CCU):

The realm of electrochemical approaches in Carbon Capture and Utilization (CCU) represents a frontier where innovative technologies converge to address the dual challenges of reducing carbon dioxide (CO_2) emissions and harnessing renewable energy sources [36]. This section explores the electrochemical reduction of CO_2, recent advances in electrocatalysis for CO_2 conversion, and the pivotal integration of renewable energy sources in electrochemical CCU.

Electrochemical Reduction of CO₂:

Fundamentals of Electrochemical Reduction:

Electrochemical reduction involves the use of an external electrical potential to drive the conversion of CO_2 into value-added products. This approach offers a versatile and selective means to transform CO_2 into various chemical compounds, including hydrocarbons, alcohols, and formic acid. At the heart of the electrochemical reduction process are electrodes, typically composed of metals or other conductive materials, thatcatalyze the reduction reactions. The ability to tailor reaction conditions, electrode materials, and catalysts contributes to the flexibility and efficiency of electrochemical CO_2 conversion.

Selectivity and Product Diversity: One of the distinguishing features of electrochemical CO_2 reduction is the ability to control the selectivity of the reaction [37]. Through careful design of electrode materials and catalytic surfaces, researchers can steer the electrochemical process towards the production of specific products. Fine-tuning the reaction conditions allows for the generation of a diverse range of chemical compounds, providing opportunities for the synthesis of fuels, chemicals, and intermediates with high economic value.

Advances in Electrocatalysis for CO_2 Conversion:
Catalytic Enhancements for Improved Efficiency:

Electrocatalysis plays a pivotal role in dictating the efficiency and selectivity of CO_2 conversion. Advances in electrocatalysis aim to overcome the inherent challenges associated with sluggish kinetics and competing side reactions [38]. Catalyst design involves the development of materials with tailored properties, such as high surface area, active sites, and enhanced stability. Noble metals, metal oxides, and complex nanostructured materials are among the evolving repertoire of electrocatalysts that demonstrate improved performance in driving CO_2 conversion reactions.

Single-Atom and Nanoparticle Catalysts: Recent breakthroughs in electrocatalysis include the exploration of single-atom catalysts and nanocatalysts. Single-atom catalysts exhibit exceptional catalytic activity due to their precisely defined active sites, while nanocatalysts leverage the unique properties of nanoparticles to enhance reactivity [39]. These advancements contribute to the quest for catalysts that are not only highly efficient but also economically viable and sustainable for large-scale implementation.

Integration of Renewable Energy Sources in Electrochemical CCU:
Symbiosis with Renewable Energy:

An integral aspect of sustainable electrochemical CCU is the integration of renewable energy sources to power the electrochemical reduction of CO_2. By leveraging electricity generated from renewable sources such as solar or wind, electrochemical processes can operate with a significantly reduced carbon footprint [40]. The intermittent nature of renewable energy sources is addressed through smart system design and energy storage solutions, ensuring a continuous and reliable power supply for electrochemical CO_2 reduction.

Electrolyzer Technologies: Renewable energy integration is closely tied to the development of efficient and scalable electrolyzer technologies. Electrolyzers facilitate the electrochemical splitting of water into hydrogen and oxygen, with the generated hydrogen serving as a valuable reducing agent in CO_2 conversion. Proton-exchange membrane (PEM) electrolyzers and solid oxide electrolyzers are key technologies that continue to evolve, enhancing the overall efficiency and feasibility of renewable energy-integrated electrochemical CCU [41].

5. BIOLOGICAL STRATEGIES FOR CARBON CAPTURE AND UTILIZATION

Harnessing biological processes for Carbon Capture and Utilization (CCU) introduces an innovative and sustainable approach to mitigate carbon dioxide (CO_2) emissions(42). This section explores three key biological strategies: Bioenergy with Carbon Capture and Storage (BECCS), Microbial Carbon Capture and Utilization, and Genetic Engineering for Enhanced Carbon Assimilation.

Table 1. Electrochemical Approaches in Carbon Capture and Utilization (CCU): Examples

Electrochemical Approach	Description
Electrochemical Reduction of CO_2	Utilizing electrical energy to convert CO_2 into value-added chemicals or fuels such as methane, ethylene, ethanol, etc.
Carbon Capture via Electrochemical Processes	Electrochemically capturing CO_2 from industrial flue gases or ambient air using specialized electrodes or membranes.
Electrochemical Conversion of CO_2 to Carbonates	Converting CO_2 into stable carbonates through electrochemical reactions, which can be used in various industrial processes or as raw materials.
Direct Air Capture (DAC)	Utilizing electrochemical methods to directly capture CO_2 from the atmosphere, offering potential solutions for combating climate change.
Electrochemical Reduction of Carbonates	Reversing the process of carbonate formation through electrochemical means, potentially releasing CO_2 for further utilization or sequestration.
Electrochemical Conversion of CO_2 into Value-added Chemicals	Generating high-value chemicals like formic acid, carbon monoxide, or syngas from electrochemical reduction of CO2, offering sustainable alternatives to conventional synthesis routes.
Electrocatalytic Conversion of CO_2	Using electrocatalysts to enhance the efficiency and selectivity of CO_2 conversion reactions, enabling more sustainable production processes.

Bioenergy with Carbon Capture and Storage (BECCS):

Overview of BECCS: Bioenergy with Carbon Capture and Storage (BECCS) is a comprehensive strategy that integrates bioenergy production with carbon capture and storage technologies [43]. It involves the cultivation of biomass, such as energy crops or forestry residues, which absorb CO_2 during their growth. The biomass is then used for bioenergy production through processes like combustion or gasification. The resulting CO_2 emissions are captured and stored, preventing their release into the atmosphere. BECCS thus achieves negative emissions by actively removing CO2 from the air.

Sustainable Energy Generation: BECCS not only contributes to carbon capture but also addresses energy needs in a sustainable manner. By relying on renewable biomass resources, BECCS mitigates the use of fossil fuels, reducing overall greenhouse gas emissions [44]. The captured CO_2 can be stored underground or utilized in various industrial processes, contributing to the circular carbon economy.

Microbial Carbon Capture and Utilization:

Harnessing Microorganisms for Carbon Capture: Microbial carbon capture and utilization leverage the metabolic activities of microorganisms, such as bacteria and algae, to capture and convert CO_2 into valuable products. Algae, for instance, are adept at photosynthesis, where they absorb CO_2 and convert it into organic compounds in the presence of sunlight. Similarly, certain bacteria can fix carbon by assimilating CO_2 into their biomass.

Bioproducts and Bioremediation:

Microbial CCU holds promise for the production of bioproducts, such as biofuels, bioplastics, and biochemical [9]. Additionally, some microorganisms possess the ability to enhance soil fertility through the release of organic compounds, contributing to sustainable agriculture practices. Microbial carbon capture not only facilitates CO_2 removal but also offers a pathway to create valuable bio-based materials.

Genetic Engineering for Enhanced Carbon Assimilation:

Tailoring Organisms for Carbon Assimilation: Genetic engineering empowers scientists to tailor the genetic makeup of organisms to enhance their capacity for carbon assimilation. This involves modifying key metabolic pathways to optimize carbon fixation and utilization [45]. For instance, researchers are exploring ways to enhance the photosynthetic efficiency of plants or algae, allowing them to capture more CO_2 and convert it into biomass.

Synthetic Biology Approaches: Synthetic biology techniques enable the design of custom genetic circuits and pathways that optimize carbon assimilation in microorganisms [46]. This includes introducing novel enzymes or modifying existing ones to enhance their efficiency in fixing carbon. The aim is to create engineered organisms that can serve as efficient carbon sinks or be employed in biotechnological processes for carbon utilization.

6. EMERGING TRENDS IN CARBON CAPTURE TECHNOLOGIES:

The evolving landscape of carbon capture technologies is marked by innovative approaches that extend beyond traditional methods. This section explores three prominent emerging trends: Membrane-based separation processes, Nanotechnology applications in Carbon Capture and Utilization (CCU), and the Integration of CCU with industrial processes [47]. The (Table 1) provides a concise overview of various carbon capture technologies, their descriptions, and key advancements, offering a comparative perspective on their development.

Table 2. Advancements in Carbon Capture Technologies: A Comparative Overview

Carbon Capture Technology	Description	Advantages	Challenges
Absorption	Involves the use of solvents to absorb CO2 from flue gases or other sources.	- Mature technology - High capture efficiency - Applicable to various industries	- High energy consumption - Solvent degradation - Large footprint
Adsorption	Relies on solid sorbents to adsorb CO_2 molecules from gas streams.	- Can operate at ambient conditions - Potential for regeneration and reuse of sorbents - Suitable for low CO_2 concentration streams	- Limited sorbent capacity - Costly regeneration processes - Susceptible to impurities

Membrane Separation	Utilizes semi-permeable membranes to selectively separate CO_2 from gas mixtures.	- Energy-efficient - Compact and modular design - Scalable for various applications	- Limited by membrane selectivity - Vulnerable to fouling and degradation - Capital-intensive
Cryogenic Separation	Involves cooling gas mixtures to very low temperatures to separate CO_2 as a solid or liquid.	- High purity CO_2 capture - Well-established technology - Effective for high-pressure streams	- High energy consumption - Complex and expensive equipment - Requires large infrastructure
Direct Air Capture	Captures CO_2 directly from ambient air using chemical reactions or absorbents.	- Potential for carbon-negative emissions - Independent of CO_2 sources - Suitable for decentralized deployment	- Energy-intensive - Costly compared to point source capture - Limited by air CO_2 concentration

Membrane-Based Separation Processes:

Overview of Membrane-Based Carbon Capture: Membrane-based separation processes represent a paradigm shift in carbon capture, providing a more energy-efficient and economically viable alternative to traditional methods. Membrane technologies involve the use of selectively permeable membranes that allow the separation of CO_2 from other gases. These membranes can be designed to selectively transport CO_2, enabling its capture while allowing the passage of other gases [48]. This approach is particularly promising for point-source emissions, such as those from industrial facilities and power plants.

Advantages of Membrane-Based Capture:

Membrane-based carbon capture offers several advantages, including lower energy requirements, reduced footprint, and modular scalability. By sidestepping the need for energy-intensive solvent regeneration or adsorbent replacement, membrane technologies contribute to more sustainable and cost-effective carbon capture. Ongoing research focuses on developing high-performance membranes with enhanced selectivity and durability, thereby optimizing their application in diverse industrial settings.

Nanotechnology Applications in CCU:

Nanoparticles and Nanostructured Materials:

Nanotechnology presents innovative solutions for enhancing the efficiency and selectivity of carbon capture and utilization processes. Nanoparticles and nanostructured materials exhibit unique properties that can be harnessed for CO_2 adsorption, catalysis, and the design of advanced materials [49]. Metal-organic frameworks (MOFs), nanocatalysts, and engineered nanoparticles are examples of nanomaterials that hold promise for improving the performance of CCU technologies. Nanoscale Catalysis for CO_2 Conversion:

Nanotechnology applications in CCU extend to catalysis, where nanocatalysts facilitate the conversion of captured CO_2 into valuable products [50]. The high surface area and tunable properties of nanocatalysts enable precise control over reaction pathways and product selectivity. Additionally, the integration of nanocatalysts with electrode materials in electrochemical CCU enhances overall efficiency. This convergence of nanotechnology and CCU represents a frontier for developing sustainable and economically viable carbon transformation processes.

Integration of CCU with Industrial Processes:

Symbiotic Integration of CCU:

The integration of CCU with industrial processes exemplifies a holistic and symbiotic approach to carbon management. Rather than treating CO_2 as a waste product, industries are exploring ways to incorporate CCU into their operations, thereby converting CO_2 into valuable resources [51]. This integration not only reduces the environmental impact of industrial activities but also creates a circular economy where carbon becomes a feedstock for the production of fuels, chemicals, and materials.

Combined Heat and Power (CHP) Systems:

The integration of CCU with Combined Heat and Power (CHP) systems exemplifies the synergy between carbon capture and energy generation [52,53]. CHP systems, which simultaneously produce electricity and useful heat, can utilize captured CO_2 in various processes. This integration enhances the overall energy efficiency of industrial operations while providing an avenue for sustainable carbon utilization.

These emerging trends in carbon capture technologies signify a dynamic shift toward more efficient, sustainable, and integrated approaches. Membrane-based separation processes offer a breakthrough in energy-efficient carbon capture, nanotechnology applications enhance the precision and effectiveness of CCU processes, and the integration of CCU with industrial processes exemplifies a synergistic approach toward a circular carbon economy. These trends underscore the ongoing efforts to revolutionize carbon capture and utilization, contributing to the imperative of mitigating climate change while fostering sustainable industrial practices.

7. LIFE CYCLE ASSESSMENT AND TECHNO-ECONOMIC ANALYSIS IN CARBON CAPTURE AND UTILIZATION (CCU):

The deployment of Carbon Capture and Utilization (CCU) technologies necessitates a comprehensive evaluation of both its environmental impact and economic feasibility. Life Cycle Assessment (LCA) and Techno-Economic Analysis (TEA) are two crucial methodologies employed to scrutinize these aspects [54,55]. This section explores the role of LCA and TEA in the context of CCU processes, highlighting their significance in assessing environmental impacts, economic feasibility, and making comparisons with traditional Carbon Capture and Storage (CCS).

Environmental Impact Assessment through Life Cycle Assessment (LCA):
LCA Methodology:

Life Cycle Assessment (LCA) is a holistic approach that evaluates the environmental impact of a product or process throughout its entire life cycle — from raw material extraction and manufacturing to use and disposal. In the context of CCU processes, LCA plays a pivotal role in quantifying the carbon footprint and identifying potential environmental hotspots associated with each stage of the process [56]. This includes assessing impacts on climate change, resource depletion, ecosystem quality, and human health.

Environmental Benefits and Trade-offs:

LCA enables a nuanced understanding of the environmental benefits and trade-offs associated with CCU. While CCU processes aim to mitigate CO_2 emissions by converting them into valuable products, LCA helps to quantify the net reduction in greenhouse gas emissions and assess other potential environmental impacts. Additionally, LCA can highlight areas for improvement and guide the optimization of CCU technologies to minimize their overall environmental footprint [57].

Economic Feasibility and Challenges through Techno-Economic Analysis (TEA):
TEA Methodology:

Techno-Economic Analysis (TEA) assesses the economic feasibility of a technology or process by evaluating the costs and benefits throughout its life cycle [58]. In the context of CCU, TEA considers factors such as capital and operating costs, revenue generation from products, and the overall economic viability of the technology. TEA helps stakeholders, including investors and policymakers, make informed decisions by quantifying the financial implications of implementing CCU processes.

Economic Challenges and Uncertainties:

TEA identifies economic challenges and uncertainties associated with CCU, helping stakeholders navigate potential risks [59]. Economic challenges may include the initial high capital costs of implementing CCU technologies, uncertainties in product markets, and fluctuations in energy prices. By incorporating sensitivity analyses and scenario assessments, TEA provides insights into the robustness of CCU processes under varying economic conditions.

Comparison with Traditional Carbon Capture and Storage (CCS):
Environmental and Economic Contrasts:

LCA and TEA facilitate a comprehensive comparison between CCU and traditional Carbon Capture and Storage (CCS). While both approaches aim to mitigate CO_2 emissions, they differ in their end goals and outputs [60]. CCU focuses on converting captured CO_2 into valuable products, contributing to a circular carbon economy, whereas CCS primarily involves the capture and storage of CO_2 underground [61]. LCA and TEA assist in evaluating the environmental and economic contrasts between these approaches, considering factors such as energy requirements, economic viability, and the potential for revenue generation from CCU-derived products.

Policy and Market Dynamics:

The comparison between CCU and CCS is influenced by policy frameworks, market dynamics, and societal preferences. LCA and TEA provide valuable insights into how each approach aligns with sustainability goals, regulatory frameworks, and economic incentives [57]. Assessing the environmental and economic performance of CCU and CCS helps inform policy decisions and industry strategies in the pursuit of a low-carbon future.

The integration of Life Cycle Assessment and Techno-Economic Analysis provides a comprehensive framework for evaluating the environmental

and economic dimensions of Carbon Capture and Utilization processes [54,60]. These methodologies contribute crucial insights to enhance the sustainability and economic viability of CCU technologies, fostering informed decision-making in the transition towards a carbon-neutral and circular economy [62,63]. Additionally, the comparison with traditional Carbon Capture and Storage offers valuable perspectives on the relative merits and challenges of different carbon mitigation approaches.

8. POLICY AND REGULATORY LANDSCAPE IN CARBON CAPTURE AND UTILIZATION (CCU)

The policy and regulatory landscape plays a pivotal role in shaping the implementation and success of Carbon Capture and Utilization (CCU) technologies [64,65]. This section explores key aspects of the global initiatives, government incentives, and regulatory challenges in the field of CCU, along with potential solutions.

Global Initiatives and Agreements:

Paris Agreement and Climate Targets:

The Paris Agreement, a landmark international accord, sets the framework for global efforts to combat climate change [66]. Within this agreement, countries have committed to limiting global temperature increases to well below 2 degrees Celsius above pre-industrial levels. CCU aligns with the goals of the Paris Agreement by providing a means to actively reduce and repurpose carbon dioxide emissions. International collaborations and initiatives under the Paris Agreement serve as catalysts for advancing CCU technologies on a global scale.

Mission Innovation and Breakthrough Energy:

Mission Innovation, a global initiative, brings together countries committed to doubling their investments in clean energy research and innovation [67]. CCU technologies fall within the purview of these investments, aiming to accelerate the development and deployment of breakthrough solutions. Complementary to this, initiatives like Breakthrough Energy Ventures, a private investment fund led by Bill Gates, focus on supporting and scaling innovations, including those in CCU, to address climate challenges.

Government Incentives for CCU Implementation:

Financial Incentives and Funding Programs:

Governments worldwide are instituting financial incentives and funding programs to stimulate the implementation of CCU technologies. This includes grants, subsidies, and tax credits to incentivize research, development, and commercial deployment of CCU projects [68]. Financial support

fosters collaboration between industry and research institutions, encouraging innovation and the integration of CCU into existing industrial processes.

Carbon Pricing Mechanisms:

Carbon pricing, through mechanisms like carbon taxes or cap-and-trade systems, can create economic incentives for industries to adopt CCU [69,70]. By assigning a cost to carbon emissions, governments provide a financial motive for industries to invest in technologies that capture and utilize CO_2 [71]. This economic signal aligns market forces with environmental goals, driving the adoption of CCU as part of broader carbon mitigation strategies. Recent government initiatives for carbon capture and utilization (CCU) demonstrate a global commitment to advancing these technologies. In the United States, the Department of Energy allocated \$3.5 billion under the Bipartisan Infrastructure Law to establish Regional Direct Air Capture Hubs, aiming to scale CO_2_22 removal solutions. Similarly, India's NITIAayog launched a comprehensive CCUS Policy Framework, emphasizing innovative financing mechanisms like clean energy cesses and bonds, and promoting sector-specific CO_2_22 storage hubs for industries such as cement and steel. Incentives like the Production-Linked Incentive (PLI) scheme further encourage low-carbon product development. Meanwhile, the European Union supports projects like the Rotterdam CCS Cluster, integrating industrial CCU solutions for large-scale implementation.

Regulatory Challenges and Potential Solutions:

Uncertain Regulatory Frameworks:

One of the challenges in the regulatory landscape for CCU is the uncertainty surrounding standards and regulations. As CCU technologies evolve, regulatory frameworks may lag behind, posing challenges for permitting and compliance. Clear and adaptive regulatory guidelines are essential to provide a stable environment for industry stakeholders and to ensure that CCU technologies are deployed efficiently.

Cross-Border Regulatory Harmonization:

CCU projects often involve cross-border collaborations and the transport of captured CO_2 for utilization or storage [72]. Regulatory differences between regions can create barriers to the development of international CCU projects. Efforts to harmonize regulations and establish international standards can facilitate the smooth implementation of CCU technologies on a global scale.

Stakeholder Engagement and Public Perception:

CCU projects may face regulatory hurdles associated with stakeholder engagement and public perception. Transparency, effective communication, and public engagement are crucial for building trust and addressing concerns related to safety, environmental impact, and the socio-economic implications of CCU projects [73]. Regulatory frameworks that incorporate meaningful stakeholder participation can contribute to the social license needed for successful CCU deployment.

9. CASE STUDIES AND INDUSTRIAL APPLICATIONS OF CARBON CAPTURE AND UTILIZATION (CCU) TECHNOLOGIES:

Success Stories in CCU Implementations:

Carbon Cure Technologies (Concrete Industry):

Carbon Cure Technologies has successfully implemented CCU in the concrete industry. By injecting recycled CO_2 into the concrete mix during production, they not only reduce the carbon footprint of concrete but also enhance its strength [74]. This innovative approach has been adopted by numerous concrete producers globally, demonstrating the commercial viability of CCU in construction materials.

Carbon Clean Solutions (Industrial Emissions): Carbon Clean Solutions has developed and implemented CCU technologies for capturing CO_2 emissions from industrial processes. Their modular carbon capture units are designed to be cost-effective and scalable, making them suitable for integration into various industries. This approach has been demonstrated in applications such as natural gas processing and biogas upgrading.

Challenges Faced by Industries in Adopting CCU
High Capital Costs and Initial Investments:

One of the major challenges faced by industries in adopting CCU technologies is the high capital cost associated with the installation of carbon capture infrastructure [75]. The initial investments required for implementing CCU projects can be a barrier for industries, especially for small and medium-sized enterprises. Addressing this challenge often requires supportive government policies, incentives, and financial mechanisms to ease the burden on businesses.

Market and Product Acceptance:

The successful implementation of CCU is contingent on market demand for products derived from captured CO_2. Industries may face challenges in creating a market for CCU-derived products, especially when competing with traditional alternatives. Building consumer awareness and acceptance is crucial for establishing the market viability of CCU products.

Lessons Learned from Real-World Applications:

Integration with Existing Processes:

Real-world applications highlight the importance of integrating CCU technologies seamlessly into existing industrial processes. Retrofitting existing facilities to accommodate carbon capture units requires careful planning and engineering to ensure minimal disruption to ongoing operations [76]. Lessons learned emphasize the need for a comprehensive understanding of the host process and collaboration between technology providers and industrial stakeholders.

Sustainability Metrics and Reporting: CCU projects often involve sustainability goals beyond carbon capture, such as resource efficiency and circular economy principles. Lessons learned underscore the importance of developing robust metrics and reporting mechanisms to track and communicate the broader environmental and social impacts of CCU implementations. Transparent reporting enhances stakeholder engagement and facilitates compliance with sustainability standards.

Collaboration and Knowledge Sharing: Successful CCU implementations often involve collaboration between industry players, research institutions, and technology providers. Lessons learned emphasize the value of knowledge sharing, collaboration on research and development, and the creation of industry-specific networks. This collaborative approach accelerates the learning curve, fosters innovation, and facilitates the scale-up of CCU technologies.

10. FUTURE PROSPECTS AND RESEARCH DIRECTIONS IN CARBON CAPTURE AND UTILIZATION (CCU):

Technological Advancements on the Horizon:

Advanced Materials and Catalysts: Future prospects in CCU involve the development of advanced materials and catalysts with enhanced selectivity, stability, and efficiency. Innovations in materials science, such as the design of novel nanomaterials and catalysts, will play a critical role in improving the performance of CCU processes [77]. This includes the exploration of new classes of materials and the optimization of existing ones for enhanced CO_2 capture, conversion, and utilization.

Electrochemical and Photocatalytic Technologies:

Technological advancements are expected in the realm of electrochemical and photocatalytic technologies for CO_2 reduction. Improvements in

electrode materials, catalyst design, and reactor configurations will contribute to the efficiency and scalability of electrochemical CCU. Similarly, developments in photocatalysis, driven by renewable energy sources, hold promise for sustainable and energy-efficient CO_2 conversion.

Key Challenges and Opportunities for Further Research:

Scalability and Integration with Industrial Processes: One of the key challenges is to enhance the scalability of CCU technologies and their seamless integration with existing industrial processes. Research in this direction should address the engineering and logistical aspects of scaling up CCU, considering factors such as continuous operation, modular design, and compatibility with diverse industrial settings.

Economic Viability and Market Adoption: Research needs to focus on improving the economic viability of CCU technologies to ensure their widespread adoption. This includes cost reduction strategies, optimization of energy consumption, and the development of market-driven incentives. Understanding and overcoming the barriers to market adoption, such as creating demand for CCU-derived products, will be crucial for the success of these technologies.

Sustainability Assessment Beyond Carbon Footprint: While CCU primarily addresses carbon mitigation, future research should expand the sustainability assessment to include broader environmental, social, and economic dimensions. Life cycle assessments should encompass a comprehensive evaluation of the environmental impact of CCU processes, considering factors such as resource use, ecosystem impact, and social implications.

The Role of CCU in a Sustainable Future:

Circular Carbon Economy and Resource Efficiency: CCU plays a pivotal role in transitioning towards a circular carbon economy, where carbon is considered a valuable resource rather than a waste product [78]. Research should further explore how CCU can contribute to resource efficiency, circularity, and the creation of closed-loop systems within various industries.

Integration with Renewable Energy Sources: The integration of CCU with renewable energy sources is critical for achieving a sustainable future. Future research should explore synergies between CCU and renewable energy technologies, including the use of excess renewable energy for electrochemical CO_2 reduction and the development of integrated systems that combine CCU with renewable energy production.

Policy Frameworks and International Collaboration: To unlock the full potential of CCU, there is a need for supportive policy frameworks and international collaboration. Research should contribute to the development of policies that incentivize CCU adoption, streamline regulatory processes, and foster collaboration between governments, industries, and research institutions on a global scale [79].

In summary, the future of CCU is marked by exciting technological advancements, ongoing research to address challenges, and a crucial role in contributing to a sustainable future. The interdisciplinary nature of CCU research, spanning chemistry, materials science, engineering, and policy studies, underscores the need for collaborative efforts to drive innovation and bring about transformative changes in the way we approach carbon management.

11. CONCLUSION

In the exploration of Carbon Capture and Utilization (CCU), key findings reveal a dynamic landscape marked by technological advancements, successful implementations, challenges, and the pivotal role of policy frameworks. The synthesis of information yields critical insights that shape the path forward for CCU.

Key Findings:

Technological Advancements: The field of CCU is witnessing significant strides in technological advancements, particularly in materials science, catalysis, and electrochemical and photocatalytic processes. Innovations in advanced materials and catalysts are poised to enhance the efficiency and selectivity of CO_2 capture and conversion.

Successful Implementations: Success stories from companies like CarbonCure Technologies and Carbon Clean Solutions demonstrate the practical application of CCU across diverse industries, including concrete production and industrial emissions reduction. These implementations underscore the commercial viability of CCU technologies.

Challenges and Opportunities: Challenges faced by industries include high capital costs, market acceptance, and uncertainties in regulatory frameworks. Opportunities lie in addressing these challenges through financial incentives, market creation, and adaptive regulatory approaches. The circular carbon economy and resource efficiency present promising avenues for further research.

Policy and Regulatory Landscape: Global initiatives, such as the Paris Agreement and Mission Innovation, provide a framework for international collaboration. Government incentives,

including financial support and carbon pricing mechanisms, play a crucial role in driving CCU adoption. Regulatory challenges, including uncertain frameworks and cross-border harmonization, require attention for the seamless deployment of CCU technologies.

Recommendations for Future Research and Development:

Advanced Materials and Catalysts: Future research should focus on the development of advanced materials and catalysts with improved properties for CO_2 capture and conversion. This includes exploring nanomaterials, innovative catalyst designs, and scalable synthesis methods.

Scalability and Integration: Addressing the challenge of scalability is critical for the widespread adoption of CCU. Research should emphasize engineering solutions that enhance scalability and seamless integration with diverse industrial processes.

Economic Viability: Research should target strategies for improving the economic viability of CCU technologies. This includes cost reduction measures, optimization of energy consumption, and creating market demand for CCU-derived products.

Sustainability Assessment: Expand the scope of sustainability assessments beyond carbon footprints. Research should encompass comprehensive evaluations of the environmental, social, and economic impacts of CCU processes.

Circular Carbon Economy: Further exploration is needed on how CCU can contribute to the development of a circular carbon economy, promoting resource efficiency and closed-loop systems within various industries.

Renewable Energy Integration: Investigate synergies between CCU and renewable energy sources. This includes utilizing excess renewable energy for electrochemical CO_2 reduction and developing integrated systems that combine CCU with renewable energy production.

Policy Frameworks: Research should contribute to the development of supportive policy frameworks that incentivize CCU adoption. This includes streamlining regulatory processes, fostering international collaboration, and aligning policies with sustainability goals.

In conclusion, the future of CCU is dynamic and holds immense potential for contributing to a sustainable and low-carbon future. The recommendations for future research and development outlined here provide a roadmap for harnessing this potential, addressing challenges, and advancing CCU technologies towards broader adoption and impact. The collaborative efforts of researchers, industry stakeholders, and policy makers are essential in realizing the transformative potential of CCU for mitigating climate change and creating a more sustainable industrial landscape.

REFERENCES

[1] C. Merchant(2021) The Anthropocene and the humanities: from climate change to a new age of sustainability, Environment and History:New Haven and London: Yale University, 27(3), 499–501. doi: 10.3197/096734021X16076828553647.

[2] Y. Jinyue, Z. Zhang (2019) Carbon capture, utilization and storage (CCUS), Applied Energy, 235, 1289-1299 doi: 10.1016/j.apenergy.2018.11.019.

[3] S. M. Ashraf, S.A. Jitan, D. Bahamon, L. F. Vega, G. Palmisano (2021) Current and future perspectives on catalytic-based integrated carbon capture and utilization," Science of the Total Environmet, 790, 148081. doi: 10.1016/j.scitotenv.2021.148081.

[4] G.A. Ozinand,J.Y.Loh(2022) Energy Materials Discovery: Enabling a Sustainable Future, Royal Society of Chemistry,p.118, doi: 10.1039/9781839163838.

[5] M.S.Alam, T.W. Agung, K. Nakaso, J. Fukai (2010) Predictions of O_2/N_2 and O2/CO2 mixture effects during coal combustion using probability density function,"EVERGREEN Joint Journal of Novel Carbon Resource Sciences & Green Asia Strategy, 2, 12-16. doi: ncrs.cm.kyushu-u.ac.jp/ncrs2/index.html.

[6] Y.Zang, P. Wei, H. Li, D. Gao, G. Wang (2022) Catalyst design for electrolytic CO2 reduction toward low-carbon fuels and chemicals, Electrochemical Energy Reviews, 5(1), 29-36, doi.org/10.1007/s41918-022-00140-y.

[7] S. Ranjbar, F.X. Malcata (2022) Is genetic engineering a route to enhance microalgae-mediated bioremediation of heavy metal-containing effluents, Molecules , 27(5),1473. doi.org/10.3390/molecules27051473.

[8] M.A. Rahim, M. A. Rahman, M .M. Rahman, A.T. Asyhari, M.Z.A. Bhuiyan, D. Ramasamy (2021) Evolution of IoT-enabled connectivity and applications in automotive industry: A review,Vehicular Communications , 27, 100285. doi.org/10.1016/j.vehcom.2020.100285.

[9] M.Laughlin, Hope, A. A. Littlefield, M. Menefee, A. Kinzer, T. Hull, B. K. Sovacool, M. D. Bazilian, J.Kim, S. Griffiths (2023)Carbon capture utilization and storage in review: Sociotechnical implications for acarbon reliant world, Renewable and Sustainable Energy Reviews ,177, 113215. doi.org/10.1016/j.rser.2023.113215.

[10] A. Srivastav, N. Srivastav (2019) The science and impact of climate change, Singapore: Springer, p.111-146, doi.org/10.1007/978-981-13-0809-3.

[11] J. E. Aldy, R. Zeckhauser (2020) Three prongs for prudent climate policy, Southern Economic Journal , 87(1), 3-29, doi.org/10.1002/soej.12433.

[12] J.Santosa, A.H. Kuncoro, A. Dwijatmiko, N. W. Hesty, A. Darmawan (2023) The Role of Nuclear Power Plants in Indonesia towards Net Zero Emissions (NZE) in 2060 with a Multi Regions Approach, EVERGREEN Joint Journal of Novel Carbon Resource Sciences & Green Asia Strategy, 10(3), 1660-1673, doi.org/10.5109/7151715.

[13] A.Sudradjat, I. Syafri, M. Burhannudinnur (2022) The Geyser Type Mud Volcano Eruption in Sidoarjo, East Java, Indonesia, EVERGREEN Joint Journal of Novel Carbon Resource Sciences & Green Asia Strategy, p.108-113, doi.org/10.5109/5909074.

[14] M.N. Anwar, A. Fayyaz, N. F. Sohail, M. F. Khokhar, M. Baqar, A. Yasar, K. Rasool (2020) CO_2 utilization: Turning greenhouse gas into fuels and valuable products, Journal of environmental management, 260, 110059 doi.org/10.1016/j.jenvman.2019.110059.

[15] A. Alok, R. Shrestha, S.Ban, S.Devkota, B. Uprety, R. Joshi (2022) Technological advances in the transformative utilization of CO_2 to value-added products, Journal of Environmental Chemical Engineering, 10(1), 106922. doi.org/10.1016/j.jece.2021.106922.

[16] M. Kaur, N. Mittal, A. Charak, A.P. Toor, V. Singh (2023) Rice Husk derived Activated Carbon for the Adsorption of Scarlet RR an Anionic Disperse Dye, EVERGREEN Joint Journal of Novel Carbon Resource Sciences & Green Asia Strategy,10(1), 438-443.doi.org/10.5109/6782146.

[17] A.E. Creamer, B.Gao (2015) Carbon dioxide capture: an effective way to combat global warming, Springer Cham Heidelberg New York Dordrecht London , 62, 17-49,doi: 10.1007/978-3-319-17010-7

[18] J. Sekera, A. Lichtenberger (2020) Assessing carbon capture: public policy, science and societal need, Biophysical Economics and Sustainability, 5 (3), 1-28, doi.org/10.1007/s41247-020-00080-5.

[19] R.Singh, M.S.Samuel, M.Ravikumar, S.Ethiraj, V.S.Kirankumar, M.Kumar, R. Arulvel, S. Suresh (2023) A novel approach to environmental pollution management/remediation techniques using derived advanced materials, Chemosphere, 344, 140311 doi.org/10.1016/j.chemosphere.2023.140311.

[20] S.Zhang, Y. Shen, L. Wang, J. Chen,Y. Lu (2019) Phase change solvents for post-combustion CO_2 capture: Principle, advances, and challenges, Applied energy,p.876-897, doi: 10.1016/j.apenergy.2019.01.242

[21] C. A. Trickett, A.Helal, B.A. Al-Maythalony, Z. H. Yamani, K. E. Cordova, O.M. Yaghi (2017) The chemistry of metal–organic frameworks for CO_2 capture, regeneration and conversion, Nature Reviews Materials, 2(8),1-16, doi.org/10.1038/natrevmats.2017.45.

[22] D.D.Zhou, X.W. Zhang, Z.W. Mo, Y.Z. Xu, X.Y. Tian, Y.Li, X. M. Chen, J.P.Zhang (2019) Adsorptive separation of carbon dioxide: From conventional porous materials to metal–organic frameworks, EnergyChem, 13, 100016. doi.org/10.1016/j.enchem.2019.10001.

[23] H.Wang, M.Wang, X.Liang, J.Yuan, H.Yang, S.Wang, Y.Ren, H.Wu, F.Pan, Z.Jiang (2021) Organic molecular sieve membranes for chemical separations, Chemical Society Reviews, 50(9), 5468-5516. doi.org/10.1039/D0CS01347A.

[24] Z.Xu, Z. Fan, C. Shen, Q. Meng, G. Zhang, C. Gao (2022) Porous composite membrane based on organic substrate for molecular sieving: Current status, opportunities and challenges, Advanced Membranes, 2, 100027. doi.org/10.1016/j.advmem.2022.100027.

[25] R.E. Siegel, S. Pattanayak, L. A. Berben (2022) Reactive capture of CO_2: opportunities and challenges, ACS Catalysis, 13(1), 766-784. doi.org/10.1021/acscatal.2c05019.

[26] Z. Liang, K. Fu, R. Idem, P. Tontiwachwuthikul (2016) Review on current advances, future challenges and consideration issues for post-combustion CO_2 capture using amine-based absorbents, Chinese journal of chemical engineering, 24 (2), 278-288. doi.org/10.1016/j.cjche.2015.06.013.

[27] S.A. Pratiwi, A. Zulys, F. Yulia, N. Muhadzib (2021) Preliminary Study of Bio-Metal Organic Frameworks (Bio-MOFs) Based Chromium-Citric Acid for CO_2 Adsorption Application, EVERGREEN Joint Journal of Novel Carbon Resource Sciences & Green Asia Strategy, 8(4), 829-834,doi.org/10.5109/4742128.

[28] T.D. Moshood, G. Nawanir, F. Mahmud, F. Mohamad, M. H. Ahmad, A. AbdulGhani (2022) Sustainability of biodegradable plastics: New problem or solution to solve the global plastic pollution, Current Research in Green and Sustainable Chemistry, 5, 100273. doi.org/10.1016/j.crgsc.2022.100273.

[29] J. Wu, T.Sharifi, Y. Gao, T. Zhang, P. M. Ajayan (2019) Emerging carbon-based heterogeneous catalysts for electrochemical reduction of carbon dioxide into value-added chemicals, Advanced Materials, 31 (13), 1804257. doi.org/10.1002/adma.201804257.

[30] Y. Zheng, A.Vasileff, X. Zhou, Y. Jiao, M. Jaroniec, S. Z. Qiao (2019) Understanding the roadmap for electrochemical reduction of CO_2 to multi-carbon oxygenates and hydrocarbons on copper-based catalysts, Journal of the American Chemical Society, 141(19), 7646-7659, doi.org/10.1021/jacs.9b02124.

[31] M.A. Tekalgne, H. H. Do, A. Hasani, Q. Van Le, H. W. Jang, S. H. Ahn, S. Y. Kim (2020) Two-dimensional materials and metal-organic frameworks for the CO_2 reduction reaction, Materials Today Advances, 5, 100038. doi.org/10.1016/j.mtadv.2019.100038.

[32] B. Guan, H. Jiang, Y. Wei, Z. Liu, X. Wu, H. Lin, Z. Huang (2021) Density functional theory researches

for atomic structure, properties prediction, and rational design of selective catalytic reduction catalysts: Current progresses and future perspectives, Molecular Catalysis , 510, 111704. doi.org/10.1016/j.mcat.2021.111704.

[33] P. A. Julien, C. Mottillo, T. Friščić (2017) Metal–organic frameworks meet scalable and sustainable synthesis, Green Chemistry, 19 (12), 2729-2747, doi.org/10.1039/C7GC01078H.

[34] R. Lu, X. Zhang, H. Shi, Z. Zhao, M. Li, X. Zhang (2023) Wettability Control in Electrocatalytic CO_2 Reduction: Effects, Modulations and Mechanisms, Applied Catalysis B: Environmental, (341), 123293 doi.org/10.1016/j.apcatb.2023.123293.

[35] L. Che, J. Guo, Z. He, H. Zhang (2022) Evidence of rate-determining step variation along reactivity in acetylene hydrogenation: a systematic kinetic study on elementary steps, kinetically relevant (s) and active species, Journal of Catalysis, 414(29), 336-348,doi.org/10.1016/j.jcat.2022.08.023.

[36] E.A. Benalcázar, H. Noorman, R. M. Filho, J. A. Posada (2022) Decarbonizing ethanol production via gas fermentation: Impact of the $CO/H_2/CO_2$ mix source on greenhouse gas emissions and production costs, Computers & Chemical Engineering, 159, 107670. doi.org/10.1016/j.compchemeng.2022.107670.

[37] W. Ju, A. Bagger, G.P. Hao, A. S. Varela, I. Sinev, V. Bon, B. R. Cuenya, S. Kaskel, J. Rossmeisl, P. Strasser (2017) Understanding activity and selectivity of metal-nitrogen-doped carbon catalysts for electrochemical reduction of CO_2, Nature communications, 8(1), 944-925. doi.org/10.1038/s41467-017-01035-z.

[38] S. Das, J. P. Ramírez, J. Gong, N. Dewangan, K. Hidajat, B. C. Gates, S. Kawi (2020) Core–shell structured catalysts for thermocatalytic, photo-catalytic, and electrocatalytic conversion of CO_2, Chemical Society Reviews , 49 (10), 2937-3004, doi: 10.1039/C9CS00713J.

[39] Z. Li, S. Ji, Y. Liu, X. Cao, S. Tian, Y. Chen, Z. Niu, Y. Li (2019) Well-defined materials for hetero-geneous catalysis: from nanoparticles to isolated single-atom sites, Chemical reviews, 120(2), 623-682, doi.org/10.1021/acs.chemrev.9b00311.

[40] M.A. Sabri, S. A. Jitan, D. Bahamon, L. F. Vega, G. Palmisano (2021) Current and future perspectives on catalytic-based integrated carbon capture and utilization," Science of the Total Environment, 790, 148081. doi.org/10.1016/j.scitotenv.2021.148081.

[41] A.A.Adam, M. A. Shahein, A.E. EL-Kholy, H.A. Moneib (2023) Cofiring of Oil and Gaseous Fuels Through an Innovative Coaxial, Double Swirl Burner, EVERGREEN Joint Journal of Novel Carbon Resource Sciences & Green Asia Strategy,9, 79-85, doi.org/10.5109/7157952.

[42] E.B. Daneshvar, J. Wicker, P.L. Show, A. Bhatnagar (2022) Biologically-mediated carbon capture and utilization by microalgae towards sustainable CO_2 biofixation and biomass

valorization–A review," Chemical Engineering Journal, 427, 130884. doi.org/10.1016/j.cej.2021.130884.

[43] F. Taufany, M.J. Pasaribu, B.Y.S. Romaji, Y. Rahmawati1 , A. Altway, Susianto, S. Nurkhamidah, J.G. Anfias, Y. Mursidah, D. Fujanita, S. Yulianti, D. Rahmawati, G.Stellarosari (2022) The Synthesis of Activated Carbon from Waste Tyre as Fuel Cell Catalyst Support, EVERGREEN Joint Journal of Novel Carbon Resource Sciences & Green Asia Strategy, 9(2), 412-420, doi.org/10.5109/4794166.

[44] S. García-Freites, C. Gough, M. Röder (2021) The greenhouse gas removal potential of bioenergy with carbon capture and storage (BECCS) to support the UK's net-zero emission target, Biomass and Bioenergy, 151, 106164. doi.org/10.1016/j.biombioe.2021.106164.

[45] G. Li, W. Xiao, T. Yang, T.Lyu (2023) Optimization and process effect for microalgae carbon dioxide fixation technology applications based on carbon capture: A comprehensive review, C — Journal of Carbon Research, 9 (1), 10035. doi.org/10.3390/c9010035.

[46] P.F. Xia, H. Ling, J.L. Foo, M.W. Chang (2019) Synthetic biology toolkits for metabolic engineering of cyanobacteria, Biotechnology journal, 14 (6), 1800496.doi.org/10.1002/biot.201800496.

[47] C. Shah, S. Raut, H. Kacha, H. Patel, M. Shah (2021) Carbon capture using membrane-based materials and its utilization pathways, Chemical Papers, 75 (9), 4413-4429, doi.org/10.1007/s11696-021-01674-z.

[48] Y. Zhang, J. Sunarso, S. Liu, R. Wang (2013) Current status and development of membranes for CO_2/CH_4 separation: A review, International Journal of Greenhouse Gas Control, p.84-107, doi.org/10.1016/j.ijggc.2012.10.009.

[49] Z. Zhang, Y. Zheng, L. Qian, D. Luo, H. Dou, G. Wen, Aiping Yu, Z. Chen (2022) Emerging Trends in Sustainable CO_2-Management Materials, Advanced Materials, 34(29), 2201547. doi.org/10.1002/adma.202201547.

[50] Y.L. Zheng, H. C. Liu, Y. W. Zhang, (2020) Engineering heterostructured nanocatalysts for CO_2 transformation reactions: advances and perspectives, ChemSusChem , 13(23), 6090-6123, doi.org/10.1002/cssc.202001290.

[51] E.I. Koytsoumpa, C. Bergins, E. Kakaras (2018) The CO_2 economy: Review of CO_2capture and reuse technologies, The Journal of Supercritical Fluids,45, 3-16, doi.org/10.1016/j.supflu.2017.07.029.

[52] M. Costa, R. Maka, F. S. Marra, A. Palombo, M. V. Prati (2023) Assessing techno-economic feasibility of cogeneration and power to hydrogen plants: A novel dynamic simulation model, Energy Reports ,p.1739-1752,doi.org/10.1016/j.egyr.2023.08.013.

[53] N. Z. Zaini, N. B. Kamaruzaman, U. Abidin (2021) Magnetic microbeads trapping using microfluidic and permanent magnet system, EVERGREEN Joint

Journal of Novel Carbon Resource Sciences & Green Asia Strategy,8 (1),156-162, doi.org/10.5109/4372272 .

[54] H. Sosiati, N.D. M. Yuniar, D. Saputra, S. Hamdan (2022) The Influence of Carbon Fiber Content on the Tensile, Flexural, and Thermal Properties of the Sisal/PMMA Composites, EVERGREEN Joint Journal of Novel Carbon Resource Sciences & Green Asia Strategy, 9(1), 32-40, doi.org/10.5109/4774214.

[55] L.Cremonese, T. Strunge, B. Olfe-Kräutlein, S.Jahilo, T. Langhorst, S. McCord, L. Müller (2022) Making Sense of Techno-Economic and Life Cycle Assessment Studies for CO_2 Utilization, Global CO2 Initiative, doi.org/10.7302/4202.

[56] G. Garcia-Garcia, M. C. Fernandez, K. Armstrong, S. Woolass, P. Styring (2021) Analytical review oflife-cycle environmental impacts of carbon capture and utilization technologies, ChemSusChem, 14(4), 995-1015,doi.org/10.1002/cssc.202002126.

[57] A.J. K. Newman, P. Styring (2023) The pursuit of methodological harmonization within the holistic sustainability assessment of CCU projects: A history and critical review, Frontiers in Sustainability, 3, 1057476. doi.org/10.3389/frsus.2022.1057476.

[58] R. Mahmud, S.M. Moni, K. High, M. Carbajales-Dale (2021) Integration of techno-economic analysis and life cycle assessment for sustainable process design–A review, Journal of Cleaner Production, 317, 128247
doi.org/10.1016/j.jclepro.2021.128247.

[59] A.W. Zimmermann, J. Wunderlich, L. Müller, G. A. Buchner, A. Marxen, S. Michailos, K. Armstrong (2020) Techno-economic assessment guidelines for CO2 utilization, Frontiers in Energy Research, (8)5, 0005.doi.org/10.3389/fenrg.2020.00005.

[60] Q.H. Phung, K. Sasaki, Y. Sugai, K. Maneeintr, B. Tayfun (2010) Numerical simulation of CO2 enhanced coal bed methane recovery for a Vietnamese coal seam, EVERGREEN Joint Journal of Novel Carbon Resource Sciences & Green Asia Strategy, 2, 1-7, doi: ncrs.cm.kyushu-u.ac.jp/ncrs2/index.html.

[61] P. Tcvetkov, A. Cherepovitsyn, S. Fedoseev (2019) The changing role of CO2 in the transition to a circular economy: Review of carbon sequestration projects," Sustainability, 11(20), 5834. doi.org/10.3390/su11205834.

[62] V. Sick, K. Armstrong, G. Cooney, L. Cremonese, A. Eggleston, G. Faber, G. Hackett (2020) The need for and path to harmonized life cycle assessment and techno-economic assessment for carbon dioxide capture and utilization, Energy technology, 8(11), 1901034. doi.org/10.1002/ente.201901034.

[63] R. Liang, X. Zheng, P. H. Wang, J. Liang, L. Hu (2023) Research Progress of Carbon-Neutral Design for Buildings, Energies, 16(16), 5929. doi.org/10.3390/en16165929.

[64] F. Swennenhuis, V. de Gooyert, H. de Coninck (2022) Towards a CO2-neutral steel industry:

Justice aspects of CO2 capture and storage, biomass-and green hydrogen-based emission reductions, Energy Research & Social Science, 88, 102598. doi.org/10.1016/j.erss.2022.102598.

[65] H. Mc. Laughlin, A.A. Littlefield, M. Menefee, A. Kinzer, T. Hull, B. K. Sovacool, M. D. Bazilian, J. Kim, S. Griffiths (2023) Carbon capture utilization and storage in review: Sociotechnical implications for a carbon reliant world, Renewable and Sustainable Energy Reviews , 177, 113215. doi.org/10.1016/j.rser.2023.113215.

[66] H. Naims, E. Eppinger (2022) Transformation strategies connected to carbon capture and utilization: A cross-sectoralconfigurational study," Journal of cleaner production, 351,131391. doi.org/10.1016/j.jclepro. 2022.131391.

[67] J. Depledge (2016) The Paris Agreement: A significant landmark on the road to a climatically safe world, Chinese Journal of Urban and Environmental Studies, 4(1), 1650011. doi.org/10.1142/S2345748116500111.

[68] H. Liu, D. Liang (2013) A review of clean energy innovation and technology transfer in China, Renewable and Sustainable Energy Reviews, 18, 486-498. doi.org/10.1016/j.rser.2012.10.041.

[69] N. Wang, K. Akimoto, G. F. Nemet (2021) What went wrong? Learning from three decades of carbon capture, utilization and sequestration (CCUS) pilot and demonstration projects, Energy Policy, 158, 112546. doi.org/10.1016/j.enpol.2021.112546.

[70] J.D. Filippo, J. Karpman, J. R. DeShazo (2019) The impacts of policies to reduce CO2 emissions within the concrete supply chain," Cement and Concrete Composites, p.67-82, doi.org/10.1016/j.cemconcomp.2018.08.003.

[71] H.A. Umar, S. A. Sulaiman, M. A. B.A Majid, M. A. Said, A. Gungor, R. K. Ahmad (2021) An outlook on tar abatement, carbon capture and its utilization for a clean gasification process, EVERGREEN Joint Journal of Novel Carbon Resource Sciences & Green Asia Strategy,8(4), 717-731, doi.org/10.5109/4742115.

[72] A.Y. Ku, P. J. Cook, P. Hao, X. Li, J.P. Lemmon, T.Lockwood, N. M. Dowell, S. P. Singh, N. Wei, W. Xu (2020) Cross-regional drivers for CCUS deployment, Clean Energy, 4(3), 202-232, doi.org/10.1093/ce/zkaa008.

[73] J.A.E. Nielsen, K. Stavrianakis, Z. Morrison (2022) Community acceptance and social impacts of carbon capture, utilization and storage projects: A systematic meta-narrative literature review, PLoSone , 17(8), 2409. doi.org/10.1371/journal.pone.0272409

[74] D. Jianning, O. Eljamal (2023) Hydrogen production of anaerobic digestion: A review, EVERGREEN Joint Journal of Novel Carbon Resource Sciences & Green Asia Strategy,9, 247-252, doi.org/10.5109/7157979.

[75] E. Kawai, A. Ozawa, B. D. Leibowicz (2022) Role of carbon capture and utilization (CCU) for decarbonization of industrial sector: A case study of Japan, Applied Energy, 328, 120183 doi.org/10.1016/j.apenergy.2022.120183.

[76] A. Wahid, R. Mustafida, A. Husnil (2020) Exergy analysis of coal-fired power plants in ultra supercritical technology versus integrated gasification combined cycle, EVERGREEN Joint Journal of Novel Carbon Resource Sciences & Green Asia Strategy, 7 (1), 32-42, doi.org/10.5109/2740939.

[77] M.A.Sabri, S.A. Jitan, D. Bahamon, L. F. Vega, G. Palmisano (2021) Current and future perspectives on catalytic-based integrated carbon capture and utilization, Science of the Total Environment , 790, 148081.doi.org/10.1016/j.scitotenv.2021.148081

[78] K. Sankaran (2023) Turning black to green: Circular economy of industrial carbon emissions," Energy for Sustainable Development , 74, 463-470, doi.org/10.1016/j.esd.2023.05.003.

[79] A.Nurdiawati, F. Urban (2021) Towards deep decarbonisation of energy-intensive industries: A review of current status, technologies and policies, Energies, 14 (9), 2408. doi.org/10.3390/en14092408.

[80] R. Sharifian, R. M. Wagterveld, I. A. Digdaya, C. Xiang, D. A. Vermaas (2021) Electrochemical carbon dioxide capture to close the carbon cycle, Energy Environ. Sci., p.781-814, doi.org/10.1039/DOEE03382K.

IZVOD

NOVE STRATEGIJE U UPOTREBI I KORIŠĆENJU UGLJENIKA: HEMIJSKA PERSPEKTIVA

Sve veća pretnja od klimatskih promena zahteva inovativne pristupe za ublažavanje emisija ugljenika, a hvatanje i korišćenje ugljenika (CCU) se pojavilo kao paradigma koja obećava. Članak počinje pregledom trenutnog pejzaža emisije ugljenika, naglašavajući kritičnu ulogu CCU u ublažavanju klimatskih promena. Katalizatori igraju ključnu ulogu u CCU, a pregled razmatra najsavremenije razvoje u katalitičkim materijalima i dizajnu, nudeći mehaničke uvide u katalizovane reakcije. Biološke strategije, kao što su bioenergija sa hvatanjem i skladištenjem ugljenika (BECCS) i mikrobno hvatanje ugljenika, istražuju se zajedno sa genetskim inženjeringom za poboljšanu asimilaciju ugljenika. Procena životnog ciklusa i tehno-ekonomska analiza se ispituju da bi se procenili ekološki i ekonomski aspekti CCU. Završava se perspektivom koja je okrenuta budućnosti, izlažući buduće izglede i pravce istraživanja u CCU. Ovaj pregled ima za cilj da pruži vredan resurs za istraživače, kreatore politike i profesionalce iz industrije koji rade na održivoj budućnosti sa niskim sadržajem ugljenika.
Ključne reči: održiva hemija; elektrohemijska redukcija; Industrijsko korišćenje ugljenika; nanotehnologija u CCU.

Ali Akbar: https://orcid.org/0009-0002-9155-7308
Abhilekha Sharma: https://orcid.org/0000-0003-0153-1340
Abhirup Mitra: https://orcid.org/0000-0002-2696-7223
Richa Saxena: https://orcid.org/0000-0002-9229-9235
Dipti Bharti: https://orcid.org/0000-0001-5658-2749
Richa Sharma: https://orcid.org/0000-0001-9747-0700

*Safa Jabbar[1], Shaymaa Abbas Abdulsada[2] ***

[1, 2]*Department of Materials Engineering, Faculty of Engineering, University of Kufa, Iraq*

Investigating the effect of biomaterial coating deposited electrophoretically on titanium and its alloys substrates: A review

ABSTRACT

The current study discusses the value of improved biomaterials, particularly coatings for titanium and its alloys employed in surgicalsettings. Demonstrates how coating processes like electrophoretic (EPD) can be used to enhance mechanical and biological qualities of these materials. Because titanium is lightweight and resistant to corrosion, it is a preferred material for medical implants used in tissue repair and fracture treatment. The study also analyzes the use of ceramic coatings like hydroxyapatite and TiO_2 in promoting bone regeneration, as well as issues with biocompatibility and tissue adhesion that arise in metallic implants. Positive outcomes indicate that advancements in biomaterials can enhance treatment results and augment the efficacy of medical implants, hence augmenting patients' quality of life.
***Keywords**:Bio-coating, Titanium, Anti-corrosion alloys,Electrophoretic deposition.*

1. INTRODUCTION

The use of bio-active metallic materials in medical treatments can be traced back to nearly twenty years ago.About 70 to 80% of the devices used in the medical field are made from bio-compatible materials. Metallic bio-materials are of great importance in fracture fixation, bone repair, and the treatment of damaged tissues, especially hard tissues, which contributes to improving the quality of life for patients. This is due to its great strength, durability, and toughness. The need for bio metallic materials with superior mechanical properties is significantly increasing due to the growing number of elderly people worldwide, as older adults face a higher risk of hard tissue failure [1].

In the early stages of developing metal implants, there were challenges related to corrosion and reduced strength. The choice of the type of metal used in biomedical applications depends on the specific uses of these implants. Table 1 provides a summary of the different types of metals commonly used in various classifications of implants [2].

*Corresponding author: Shaymaa Abbas Abdulsada
E-mail: shaymaa.radhi@uokufa.edu.iq

Due to their high strength, durability, and low wear rate within the body, implant materials such as titanium, stainless steel, cobalt, and their alloys are frequently used in orthopedic and dental applications [3]. Figure 1 shows many typical applications for metal implants [4].

Titanium alloys are widely used in dental implants and bone grafting, as well as in other devices such as plates and screws, thanks to a range of distinctive properties, including good bio-compatibility, resistance to corrosion and wear, excellent mechanical properties, and effective osseointegration. Porous titanium alloys have been developed as an alternative to orthopaedics materials, providing good biological fixation through the growth of bone tissue within the porous network [5].

Despite the numerous benefits that titanium materials offer, there are concerns regarding their adequate stability and ability to resist corrosion in the body's fluid environment, especially in the long term. The release of corrosion products can lead to metallosis, which in turn may cause loosening of the implant or deterioration of its properties [6]. Furthermore, rejection of some internal prosthetics by the recipient may occur shortly after surgery due to an allergic reaction [7].

In addition, the implant should have a suitable micro-structure that enhances the formation of a permanent bond between the tissue interface and the implant [8].

Table 1. Classification of implants and types of metals used [2]

Division	Example of implants	Type of metal
Cardiovascular	Stent Artificial valve	316L SS; CoCrMo; Ti Ti6Al4V
Orthopaedics	Bone fixation (plate, screw, pin) Artificial joint	316L SS; Ti; Ti6Al4V CoCrMo; Ti6Al4V; Ti6Al7Nb
Dentistry	Orthodontic wire Filling	316L SS; CoCrMo; TiNi; TiMo AgSn(Cu) amalgam, Au
Craniofacial	Plate and screw	316L SS; CoCrMo; Ti; Ti6Al4V
Otorhinology	Artificial eardrum	316L SS
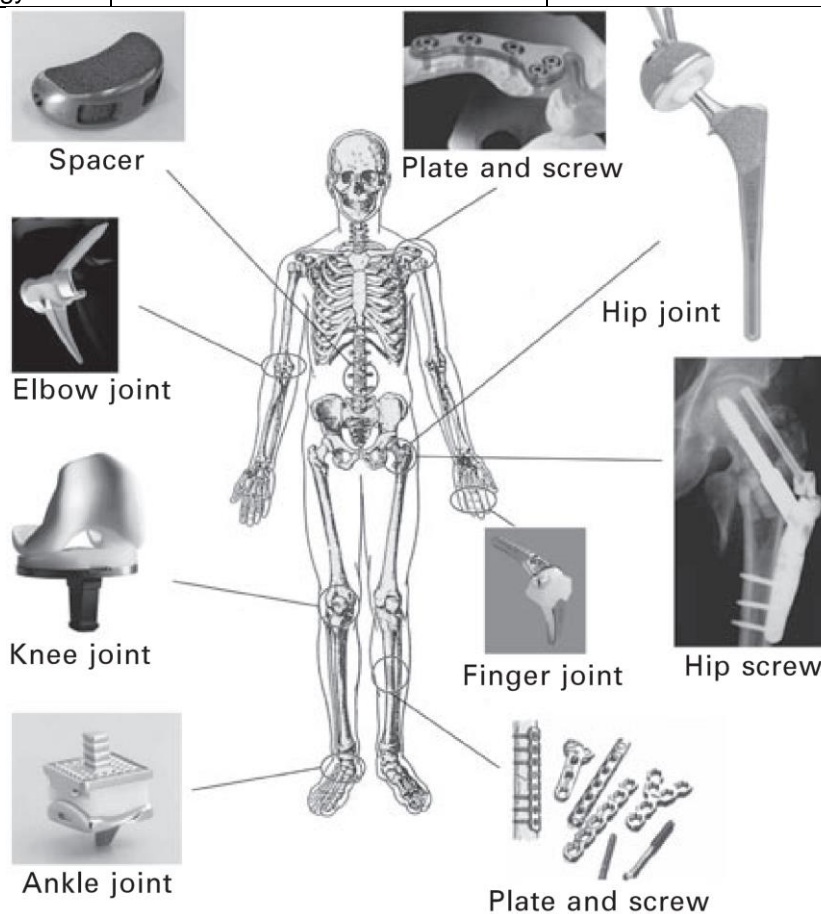
Figure 1. Biomaterials for human application [4]

Based on what has been mentioned earlier, methods are being explored to modify the surface of metal implants in order to meet these requirements, particularly concerning long-term aspects. The following methods that have already been used can be identified: thermal plasma spraying [9], plasma spray [10], physical vapor depo-sition[11], sol–gel [12], ano-dic oxidation (AO) [13], micro-arc oxida-tion (MAO) [14], and electro-phoretic deposition (EPD) [15].

The last three methods mentioned fall under the category of electro chemical methods, which are characterized by their simplicity and relatively low cost compared to the other methods mentioned. Furthermore, this process contributes to facilitating the production of coatings with diverse structures, roughness, crystallization, chemical composition, and wettability, in addition to properties such as corrosion resistance and mechanical characteristics on materials of various shapes. The equipment used in this context is also considered cost-effective [16].

The popularity of electrophoretic deposition (EPD) is increasing as an effective method for processing biomaterials, especially in the field of bio active coatings and nano structures used in

medicine[17].HA has been an attractive option for a long time as a partial alternative to bone, due to its similarity to the mineral component of natural bone.The synthetic hydroxyapatite (HA) material has shown excellent biocompatibility in the laboratory with cultured osteoblasts, as well as other cell types, which grow easily on HA compounds or surfaces coated with it. Hydroxyapatite (HA) is considered a bioactive ceramic that promotes bone growth; however, it suffers from relatively weak mechanical properties [18].

To improve the mechanical properties of hydroxyapatite (HAp) and to produce coatings with better bio-activity and enhanced mechanical properties, another type of bio-ceramic material is combined with HAp, such as titanium dioxide (TiO2), which is considered one of the other inactive bioceramics.

Titania is characterized by exceptional corrosion resistance in body fluids, as well as high fracture strength and significant load-bearing capacity, with a sufficient level of wear resistance [19,20]. Also it is a bio compatible material that is compatible with living organisms and is characterized by its biological activity, as it possesses antibacterial activity and effective properties against fungi [21].

2. TITANIUM AND TITANIUM ALLOYS

Titanium (Ti) is a shiny metal with a silver color. It is characterized by a high strength of up to 430 MPa and a low density of 4.5g/cm^3, while iron has a strength of 200 MPa and a density of 7.9 g/cm^3. Therefore, titanium has the highest strength-to-density ratio among all other metals. Furthermore, titanium is characterized by a relatively high melting point exceeding (1650°C or 3000 °F), and it is also a paramagnetic material with relatively low

electrical and thermal conductivity. This metal exists in two different crystalline forms known as body-centered cubic (bcc) and hexagonal close-packed (hcp) structures, as shown in Figures 2 (a) and (b), respectively [22].

a)   *b)*
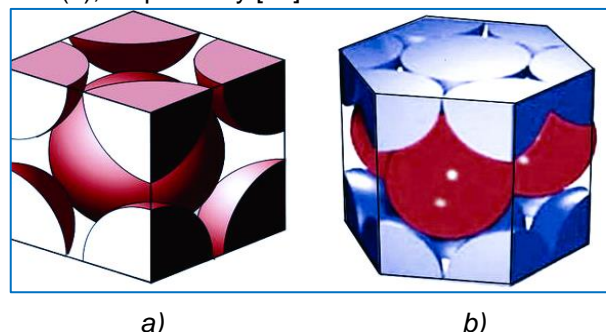
Figure 2. Crystalline state of titanium: (a) bcc, and (b) hcp [22]

At low temperatures, pure titanium is characterized by a close-packed hexagonal structure known as alpha titanium (α titanium).At high temperatures, the stable structure is the body-centered cubic (bcc) structure, known as titanium β [23].

2.1. Effect of alloying elements on titanium properties

In titanium alloys, three types of alloying elements are generally utilized: neutral elements, α-stabilizers, and β-stabilizers. In titanium alloys, elements like N, Al, O, and C are referred to as α-stabilizers because they generate the α phase [24-26].While components that yield the β phase are categorized as β-stabilizers. β-stabilizers can be classified into β-eutectoid and β-isomorphous elements according to the alloying elements that are added to titanium.
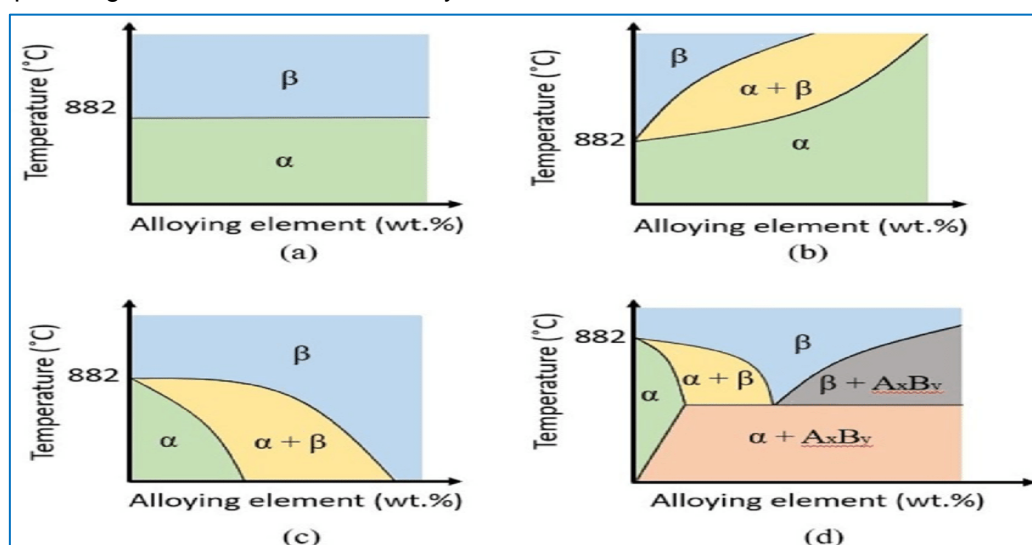
Figure 3. Different titanium alloy stabilizer types (a) neutral, (b) α-stabilizing, (c) β-stabilizing (isomorphous) and (d) β-stabilizing (eutectoid) [27]

As shown in Figure 3 isomorphs elementssuch as tantalum (Ta), molybdenum (Mo), vanadium (V), and niobium (Nb) are highly soluble in titanium. Nevertheless, eutectoid elements—manganese (Mn), chromium (Cr), silicon (Si), iron (Fe), cobalt (Co), nickel (Ni), and copper (Cu)—show extremely little solubility in titanium and are more likely to form intermetallic compounds with other elements. Conversely, elements with almost little influence on the α/β phase border, such as tin (Sn), hafnium (Hf), and zirconium (Zr), are regarded as neutral elements [27-32].

Titanium alloys are predominantly recommended for implant fabrication due to their exceptional corrosion performance. Table 2 shows the different stabilizing elements added to titanium alloy to stabilize particular structure and improve properties of titanium alloys [33-38].

Table 2. Titanium alloy stabilizer with its effects and different properties [38]

Stabilizing elements	Impact on transition temperature	Effects on properties of Ti
α-stabilizer :Fe, Mo, Ni, V, Cr, Nb	Increase	Hardening
β-stabilizers : N, Al, O, C	Decrease	Grain refiners
Neutral elements: Zr and Sn	No noticeable impact	Hardening

3. CORROSION RESISTANCE OF TITANIUM AND TITANIUM ALLOYS

The natural breakdown of metals and alloys brought on by interactions with the environment that are chemical, biological, and electrochemical in nature. Conditions that might cause corrosion include high pressure, heat, humidity, oxygen, inorganic and organic acids, and chlorides [39].

Metals are destroyed by corrosion, which turns them into oxides or other corrosion products. Because corrosion causes parts or buildings to become unusable, it reduces the amount of earth's material resources that can be used to replace them, which has an impact on the world's metal supply [40]. The high corrosion resistance of titanium alloys is due to the presence of a thin oxide layer that adheres to their metallic surface. This film naturally forms when titanium alloy is exposed to air or oxygen-rich environments, due to the close relationship between titanium and oxygen. Due to this fact, the oxide film can be easily repaired even in the presence of oxygen at low partial pressures (ppm) when it is subjected to damage. Although the oxide layer that covers titanium and its alloys has a high level of stability, when these materials are used in agriculture, electrochemical reactions may occur with physiological fluids. These reactions are exacerbated by the interplay between corrosion and mechanical stresses and/or wear [41].

4. SURFACE MODIFICATION TECHNIQUES

It has become extremely necessary to prevent the corrosion of biomaterials, especially to address the infections and allergic reactions that may arise from the implantation of these materials in the human body.Due to the issue of corrosion, a set of techniques has been adopted to modify the surface with the aim of improving corrosion behavior. The introduction of surface modifications on biocompatible metals is considered the "optimal solution" so far to enhance corrosion resistance performance, as well as to achieve superior biocompatibility and promote bone integration of biocompatible metals and alloys. Biocompatible metals include processes such as coating deposition, the development of a passivation oxide layer, and ion beam surface modification [42].

The acceptance of the biomaterial by the human body is the primary criterion for selection. When the material is implanted, it shouldn't have any negative side effects—such as allergies, inflammation, or toxicity—either right away during surgery or in the following[43]. Biomaterials can be modified via a variety of commonly employed surface modification techniques, including covalent grafting, surface coatings and synthetic films, plasma treatment, and self-assembled monolayers (SAMs) [44].

4.1. Coatings for titanium and its alloys in biomedical applications

Metal implants may sometimes fail in surgical procedures due to several factors, including insufficient biocompatibility, high degradation rates (as seen with magnesium alloys), inflammatory response, infection, inertness (such as with stainless steel, titanium, and cobalt-chromium alloys), as well as low wear resistance, mismatch in elastic modulus, excessive wear, and the presence of hidden stress. Therefore, it is important to address this issue by developing a method that contributes to improving the vital functions of metallic implant surfaces, by modifying the surface and shape of the materials without affecting the mechanical properties of the metallic implants as shown in Figure 4.
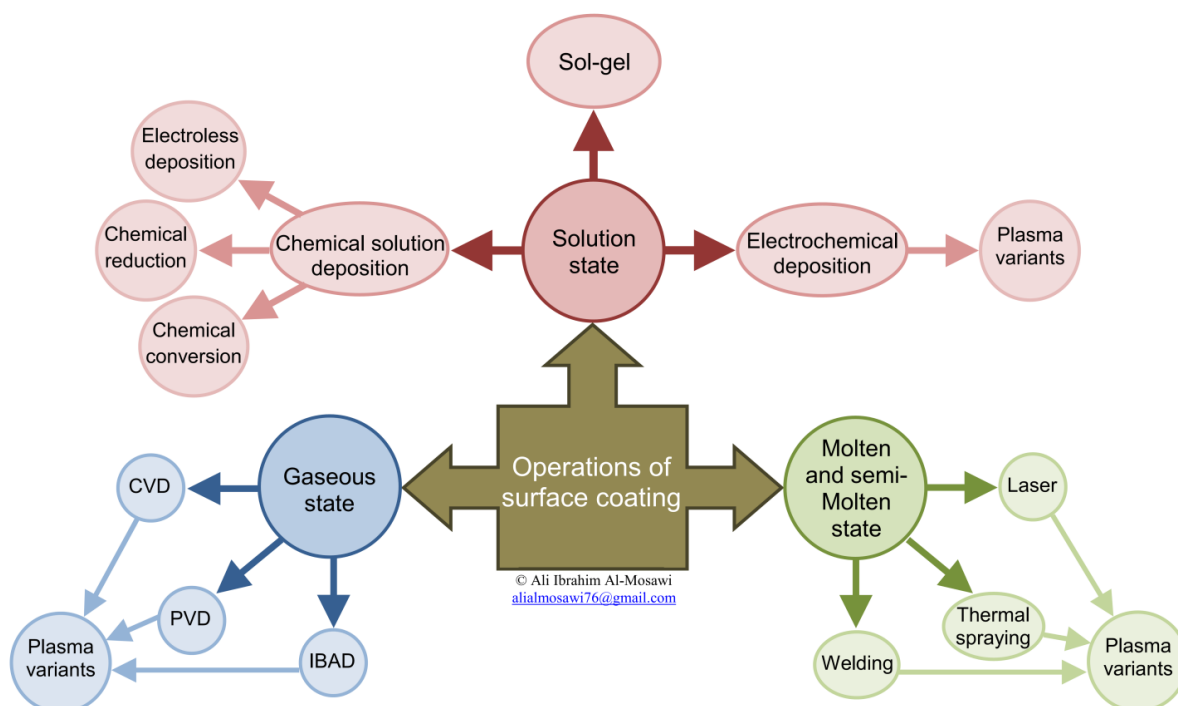
Figure 4. A broad division of surface engineering methods

The process of surface modification of metals through the use of coatings is considered one of the effective methods for enhancing the performance of implant materials, among the many available techniques [45]. By virtue of their reliability and efficiency, ceramic coatings are considered the optimal choice for activating implants that come into direct contact with bones and tissues. This is due to their unique properties that enhance bone compatibility and provide high stability [46,47]. The surface modification process using coatings can enhance the antibacterial activity of biomaterials. Coated surfaces contribute to improving the attachment of peptides to cells, directing changes in host cells, as well as extracellular matrix (ECM) proteins and tissue growth, leading to further improved acceptance of biomaterials. Coating of Ceramics on biomaterials show promising results in the field of orthopedic surgery, as they play an important role in enhancing bone regeneration and repair [48].

4.1.1. Hydroxyapatite Coating

Hydroxyapatite (HAp) is a natural mineral form of calcium apatite, characterized by the chemical formula $Ca_5(PO_4)_3(OH)$. It is often expressed in the formula $Ca_{10}(PO_4)_6(OH)_2$ to indicate that the crystal unit cell consists of two molecules. The HAp crystal structure unit cell, which is made up of Ca, PO_4, and OH groups densely packed together, is depicted in Figure 5 [49].
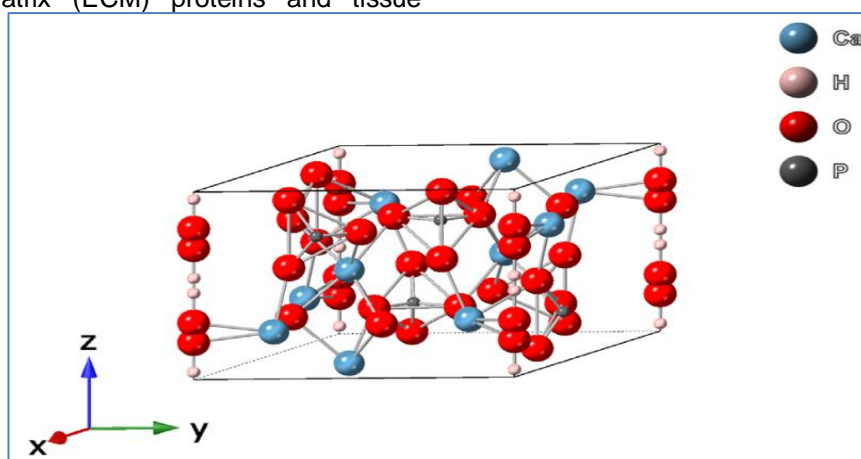
Figure 5. The hydroxyapatite molecular structure: a unit cell perspective on the hexagonal crystal structure [49]

Hydroxyapatite is the main component in the structure of tooth enamel and bone minerals, contributing to their hardness. Hydroxyapatite is used in many fields due to its excellent biocompatibility and active properties. In the field of medicine, it is used in orthopedics and dental implants due to its structural similarity to the minerals found in bones [50].

4.1.2. Titanium Oxide Coating

The oxide of titanium that occurs naturally is called titanium dioxide (TiO_2). It is sometimes referred to as titania. One of the most widely used ceramic materials in applications including sensors, photovoltaics, self-cleaning glass, water purification, photo-catalyst, and corrosion protection coatings is titania in its several crystalline forms. Titania is utilized so effectively in all these industries as a thin or thick coating film primarily due to its high chemical durability and thermal stability [51].

Titania exists in three primary crystalline phases: rutile, anatase, and brookite. These phases can exist as nanomaterials, and the grain size affects how stable they are. Whereas anatase titania is commonly utilized as spherical particles with a diameter of about 20 nm, rutile is regularly employed as a white pigment in polymers with particles size ranging from 200 to 300 nm [52].

All polymorphs, as illustrated in Figure 6 feature distorted TiO_6 octahedral formed by titanium cations six-fold coordinated to oxygen anions. These structures are connected by sharing the octahedral edges (some also have corner sharing). TiO_6 octahedral building block arrangement reveals the crystal formations of titania [53].
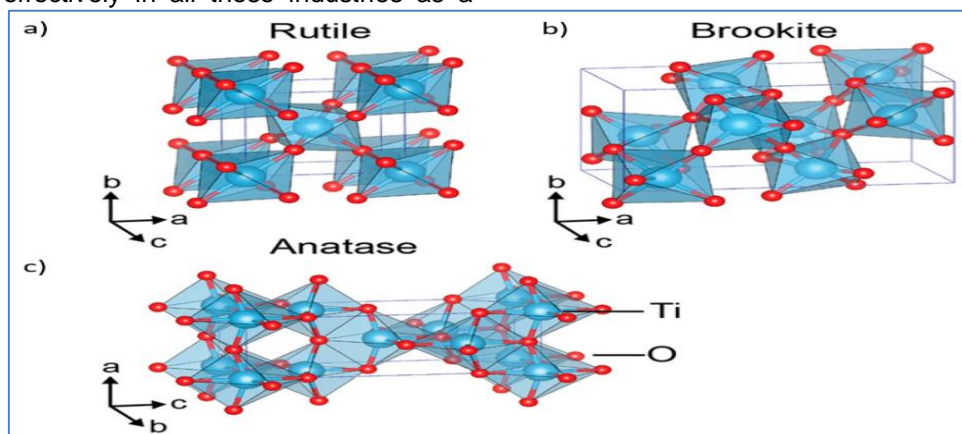
Figure 6. Polymorphs of TiO_2 crystal structures:(a) Rutile, (b) Brookite and (c) Anatase [53]

5. ELECTROPHORETIC DEPOSITION METHOD

EPD is a bridge that connects two processes: deposition and electricity [53].The EPD method is a versatile approach that may be used to deposit a wide range of materials, including composites, metals, ceramics, glasses, and polymers. This is an economical solution that doesn't require expensive equipment. The EPD's widespread use can be attributed to its simplicity in regulating the morphology and thickness of the coatings it forms by accurately adjusting process parameters [55, 56].

The EPD process includes fundamentally three steps [57]:

Creating a steady particles suspension.

- The particles move towards the deposited pole by the effect of the electric field.
- The deposition of particles on the surface of the electrode.

Figure 7 illustrates a graph that shows these steps in the EPD process.
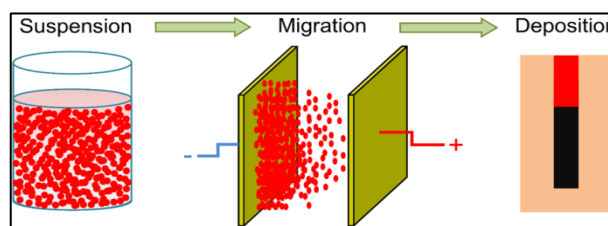
Figure 7. The EPD steps are depicted schematically [57]

The main difference between the electrophoretic deposition (EPD) process and the electrochemical deposition (ELD) process is that the former relies on the presence of suspended particles in a solvent, while the latter depends on the use of a solution containing salts., i.e. The positive and negative ions [58]. There are two basic types of EPD processes: cathodicEPD and anodic EPD. CathodicEPD is the process by which positive charges are deposited on the cathode (negative electrode).and anodic EPDis the accumulation of negative charges on the anode, or positive electrode. As depicted in Figure 8 [59].
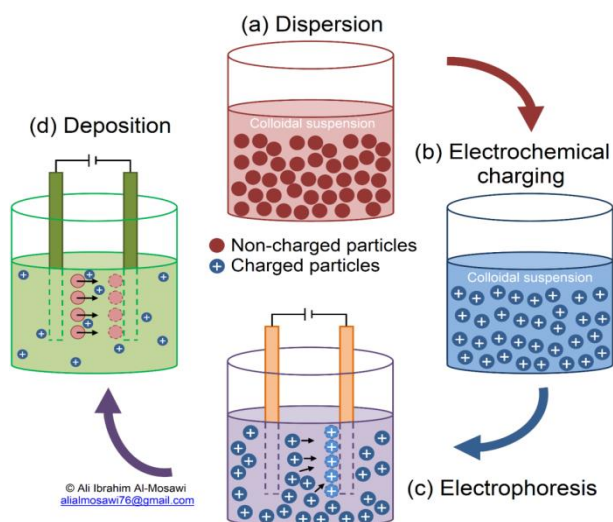
Figure 8. Schematic of the procedure for electrophoretic deposition [59]

6. BIOCOATINGSEFFECTS ON BONE REGENERATION, TISSUE ADHESION AND BIOCOMPATIBILITY OF TITANIUM ALLOYS IMPLANTS

The primary criteria for choosing a coating material are (a) sufficient mechanical dependability, adhesion strength, and fracture toughness to endure the applied forces; (b) resistance to corrosion in bodily fluid environments; and (c) biocompatibility and absence of inflammation, toxicity, or other undesirable effects. Biomedical coatings can be categorised into three primary classes based on how well they function in the organism: bioinert, bioactive, and bioresorbable. Bioactive coatings, as opposed to bioinert, are biomaterials that have the ability to promote the regeneration of surrounding tissue and cells around the foreign graft and the release of bioactive chemicals to eliminate post-operative problems. Absorbable (bioresorbable) coatings are made to dissolve electrochemically in the human body and then be metabolised by tissue and cells [60-65].

Improving the metal implant surface's osteo-conductive, osteo-inductive, and osteogenic pro-perties is the primary goal of applying a biocompatible coating. Osteo-inductivity is the ability of the surface to promote the differentiation of precursor (stem) cells into osteoblasts, whereas osteo-conductivity is the coating's capacity to serve as a scaffold for the production of extracellular bone matrix where osteoblasts can adhere and multiply. In order to calcify the collagen matrix of the freshly produced bone structure, osteoblasts are alloyed to produce calcium nodules [66-70].

Because of its strong mechanical qualities, antibacterial and catalytic activity, and long-term durability against chemical and photocorrosion,

TiO_2 is a valuable material for biomedical applications. When immersed in SBF solution, TiO_2 can encourage the surface to develop calcium phosphate or bone-like apatite, making it appro-priate for bone replacement and reconstruction. Furthermore, it was discovered that the anodisation of TiO_2 coating on the surface of Ti substrates was a successful technique for lowering the implant's temperature rise during microwave diathermy treatment, which could offer a potential rehabili-tation option for internal bone fracture fixation. Like TiO_2, tantalum oxide (Ta_2O_5) may promote the quick attachment of soft tissue and bone and aid in the creation of bone-like apatite. The magnesium alloy's in vitro biocompatibility and early-stage corrosion resistance were both improved by tanta-lum oxide made by reactive magnetron sputtering. When coated using a twin-gun magnetron sputtering method, a Ta_2O_5 coating containing 12.5%Ag demonstrated both good cellular biocom-patibility with skin fibroblast cells and enhanced antibacterial activity against S. aureus [71-73].

Since different metal ions (Ca^{2+}, Sr^{2+}, Mg^{2+}, etc.) have been shown to have the ability to enhance osseointegration, grafting metal ions and compounds is another popular technique to increase the osteogenic ability of oxide coatings. Figure 9 provides an example of how different metallic ions affect the numerous processes involved in bone repair [74].
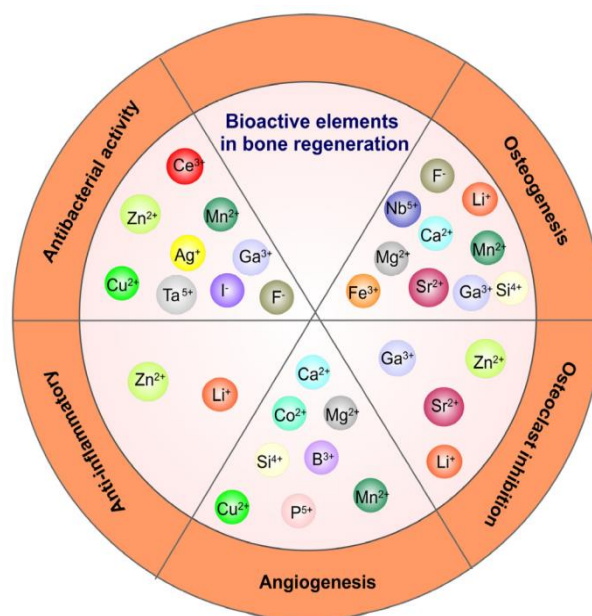
Figure 9. Some ions' therapeutic effects include angiogenic, osteogenic, anti-inflammatory, and antibacterial action [60]

Various photosensitisers can be used to alter the surface of TiO_2 in order to produce reactive

oxygen species (ROS) that will kill bacteria when exposed to near-infrared (NIR) light. To increase biocompatibility, hydrothermally generated MoSe2 nanosheets were placed on the surface of porous micro-arc oxidation (MAO) -prepared TiO_2 coatings, and chitosan was applied by electrostatic bonding. Chitosan enhanced the hybrid coating's hydrophilicity and biocompatibility, promoting osseointegration even in the presence of infection under NIR light. Under NIR irradiation, the coatings showed excellent in vivo and in vitro antibacterial properties against S. mutans due to the synergistic effect of hyperthermia and ROS generation. To alter the surface of composite collagen/polydopamine/TiO_2 coatings on Ti implants made by MAO and hydrothermal treatment, Han and co-authors choose MoS_2 because of its broad spectrum response [75-80].

## 7. CONCLUSIONS

This review provides a complete analysis to the properties of titanium and its alloys, as well as the impact of surface modification on medical implants used in orthopedic and dental implants and other applications. The analysis focuses on how these modifications extend the life of the implant in the body, achieve biocompatibility, and enhance osseointegration. This is done by coating these alloys with hydroxyapatite and titanium dioxide, as these coatings are characterized by their high corrosion resistance and excellent biocompatibility.

Electrophoretically deposition is one of the most popular methods due to its versatility, simplicity and low cost. The electrophoretic process is affected by a number of factors, including the deposition time, the type of solution, and the voltage used in the deposition process. Biomaterials have several difficulties, such as biocompatibility, durability, and corrosion. Comprehending the ways in which these variables impact the overall functionality of implants might facilitate the creation of novel materials that satisfy the requirements of patients. Biomaterials have several difficulties, such as biocompatibility, durability, and corrosion. Comprehending the ways in which these variables impact the overall functionality of implants might facilitate the creation of novel materials that satisfy the requirements of patients. This research is very important for the future since collaboration between scientists and engineers in this field can lead to tremendous progress in enhancing the quality of life for patients. In summary, the findings show that in order to satisfy the increasing demand, further research in the area of biomaterials is required, with an emphasis on developing coating and surface modification methods.

8. REFERENCES

[1] W.S.W.Harun et al. (2018) A comprehensive review of hydroxyapatite-based coatings adhesion on metallic biomaterials. Ceramics International, 44(2), 1250-1268.

[2] Z. Albaraqaawee, S. A. Abdulsada, A. I.Al-Mosawi (2024) Analysis of coated samples containing hydroxyapatite/multiwalled carbon nanotubes on 2205 DSS substrate, Full., Nano. C. Nano., 32(6), 1-8
https://doi.org/10.1080/1536383X.2024.2309943

[3] Z. Albaraqaawee, S. A. Abdulsada, (2024) Surface morphology and corrosion properties of 2205 DSS substrate modified by a deposited coating layer of hydroxyapatite/Multiwall carbon nanotubes composite, Fullerenes, Nanotubes and Carbon Nanostructures, 32, 1, 68-77.
https://doi.org/10.1080/1536383X.2023.2263106

[4] Z. Albaraqaawee, S. A. Abdulsada(2022) Optimisation of surface characteristics of standard duplex stainless for bio-applications by using electrophoretic deposition: A brief review. KOM – Corrosion and Material Protection Journal, 66, 1, 96-102. https://doi.org/10.2478/kom-2022-0013

[5] S. A. Abdulsada, A. I.Al-Mosawi, (2023) Analysis of corrosion rate, inhibition efficiency, and economic cost of XD3 reinforced concrete related to inhibitor and plasticiser types, Eng. Res. Exp., 5, 035032.
https://doi.org/10.1088/2631-8695/acee46

[6] X.Zhan, S.Li, Y.Cui, et al. (2020) Comparison of the osteoblastic activity oflow elastic modulus Ti-24Nb-4Zr-8Sn alloy and pure titanium modi-fied by physical and chemical methods. MaterSciEng C Mater BiolAppl. 113, 111018.
doi:10.1016/j.msec.2020.111018 .

[7] RC Rocha, AG Galdino, S.N.da Silva, M.Machado (2018) Surface microstructural, and adhesion strength investigations of a bioactivehydroxyapatite-titanium oxide ceramic coating applied to Ti-6Al-4Valloys by plasma thermal spraying. Mater Res. 21, e20171144.
doi:10.1590/1980-5373-mr-2017-1144.

[8] MN Timofeev, VA Koshuro, SYPichkhidze. (2021) Optimization of parame-ters of plasma spraying of titanium and hydroxyapatite powders.Biomed Eng (NY). 55,121-125. doi:10.1007/s10527-021-10084-0

[9] OA. Hammadi(2020) Effects of extraction parameters on particle size of titanium dioxide Nanopowders prepared by physical vapor deposition technique. Plasmonics. 15, 1747-1754.
doi:10.1007/s11468-020-01205-8 .

[10] A.Jaafar, C.Hecker, P.Arki, Y.Joseph(2020) Sol-gel derived hydroxyapatitecoatings for titanium implants: a review. Bioengineering. 7, 127.
doi:10.3390/bioengineering704012

[11] Y.Li, Y.You, B.Li, et al. (2019) Improved cell adhesion and Osseointegrationon anodic oxidation modified titanium implant surface. J Hard TissueBiol. 28, 13-20.

[12] B Engelkamp, B Fischer, K.Schierbaum(2020) Plasma electrolytic oxidationof titanium in H2 SO 4– H 3 PO4 mixtures. Coatings. 10, 116-125.

doi:10.3390/coatings10020116 .

[13] M.Bartmanski, L.Pawłowski, G.Strugała, A. Mielewczyk- Gryn, A. Zielinski(2019) Properties of nanohydroxyapatite coatings doped with nanocopper, obtained by electrophoretic deposition on Ti13Zr13Nballoy. Materials. 12, 3741-3749. doi:10.3390/ma12223741.

[14] B.Makurat-Kasprolewicz, A.Ossowska (2023) Recent advances in electro-chemically surface treated titanium and its alloys for biomedicalap-plications: a review of anodic and plasma electro-lytic oxidationmethods. Mater Today Commun.;34, 105425. Doi: 10.1016/j.mtcomm.2023.105425 ,

[15] Y. Y. Shi, M. Li, Q. Liu, Z. J. Jia, X. C. Xu, Y. Cheng and Y. F. Zheng (2016) Electrophoretic deposition of graphene oxide reinforced chitosan–hydroxy-apatite nanocomposite coatings on Ti substrate, J. Mater. Sci.: Mater. Med., 27, 1–13.

https://doi.org/10.1007/s10856-015-5634-9.

[16] K.Lawton, et al. (2019) Carbon nanotube reinforced hydroxyapatite nanocomposites as bone implants: Nanostructure, mechanical strength and biocompatibility. International journal of nanomedicine, 33, 7947-7962.

[17] S. A. Abdulsada, A. I.Al-Mosawi (2024) Surface Characteristics and Corrosion Tendency of TIG-Welded Low Carbon Steel Sheet Affected Cold Galvanizing and Processed by Immersion in Sodium Chloride Solution,Journal of Bio- and Tribo-Corrosion, 10(2), 34. DOI:10.1007/s40735-024-00838-0

[18] D. Qiu, L. Yang, Y. Yin, A. Wang (2011) Preparation and characterization of hydroxyapatite/titania composite coating on NiTi alloy by electrochemical deposition, Surface & Coatings Technology, 205(10), 3280– 3284.

[19] L. Mohan, D. Durgalakshmi, M. Geetha, T. S. N. S. Narayanan, R. Asokamani(2021) Electrophoretic deposition of nanocomposite (HAp + TiO2) on titanium alloy for biomedical applications, Ceramics International, 38, 4, 3435-3443.

[20] A. I.Al-Mosawi, S.A. Abdulsada(2024) Biopolymer-based coatings for anti-corrosion of Ti-alloys used in biomedical applications: A review, Polymer Engineering and Science, 64(5), 1905–1920. DOI: 10.1002/pen.26681.

[21] Veiga, C., Davim, J. P., &Loureiro, A. J. R. (2012). Properties and applications of titanium alloys: a brief review. Rev. Adv. Mater. Sci, 32(2), 133-148.

[22] Fazel-Rezai, Reza (ed.). Biomedical engineering: from theory to applications. BoD–Books on Demand, 2011.

[23] M.A.Baker, S.Assis, O.Higa, I.Costa (2009). Nanocomposite hydroxyapatite formation on a Ti–13Nb–13Zr alloy exposed in a MEM cell culture medium and the effect of H_2O_2 addition. Acta Biomaterialia, 5(1), 63-75.

[24] E. Carlos Nelson, et al. (2015). Mechanical properties, surface morphology and stability of a modified commercially pure high strength titanium alloy for dental implants. Dental Materials, 31.2: e1-e13.

[25] R. Majumda, J. Dutta; I.Manna (2015) Laser surface engineering of titanium and its alloys for improved wear, corrosion and high-temperature oxidation resistance. In: Laser Surface Engineering. Woodhead publishing, p.483-521.

[26] T.Mahender (2021) On the optimization of temperature and cooling rate to maximize strength and ductility of near α titanium alloy IMI 834. Materials Science and Engineering: A, 827: 142052.

[27] L.Xiaofei(2017) Microstructure, texture evolution and mechanical properties of VT3-1 titanium alloy processed by multi-pass drawing and subsequent isothermal annealing. Metals, 7(4), 131.

[28] M. Candrew, R.Anthony (2018) A literature review of Ti-6Al-4V linear friction welding. Progress in Materials Science, 92, 225-257.

[29] G. Xin (2018) Electrochemicalbehaviour of passive film formed on the surface of Ti-6Al-4V alloys fabricated by electron beam melting. Corrosion Science, 145, 80-89.

[30] S. Idambe, T. Alfred (2014) Biocompatibility of advanced manufactured titanium implants—A review. Materials, 7(12), 8168-8188.

[31] Y. Zhang, J.Hu, W.Zhang, S.Yu, Z.Yu, Y.Zhao, L.Zhang (2019) Discontinuous core-shell structured Ti-25Nb-3Mo-3Zr-2Sn alloy with high strength and good plasticity. Mater Charact 147, 127–13

[32] C. Liang, Y. ZHANG, L. Chang(2020) Recent development in beta titanium alloys for biomedical applications. Metals, 10(9), 1139.

[33] F.Amaechi, et al. (2021) Biomedical materials: A review of titanium based alloys. Proceedings of the Institution of Mechanical Engineers, Part C: Journal of Mechanical Engineering Science, 235(19), 3792-3805.

[34] P.Fernandes, et al. (2016) Improvement of microstructure, mechanical and corrosion properties of biomedical Ti-Mn alloys by Mo addition. Materials & Design, 110, 414-424 .

[35] E. Marin, A. Lanzutti (2023) Biomedical applications of titanium alloys: a comprehensive review. Materials, 17(1), 114.

[36] D. Correa, et al. (2014) The effect of the solute on the structure, selected mechanical properties, and biocompatibility of Ti–Zr system alloys for dental applications. Materials Science and Engineering: C, 34, 354-359.

[37] A. Farrah Noor; H. ZUHAILAWATI (2020) A brief review on the properties of titanium as a metallic biomaterial. Int. J. Electroactive Mater, 8, 63-67.

[38] P. Pralhad; B. Shivprakash(2023) A review—metastable β titanium alloy for biomedical applications. Journal of Engineering and Applied Science, 70(1), 25.

[39] B. Popov (2015) Corrosion engineering: principles and solved problems, Elsevier.

[40] E.McCafferty (2010) Introduction to corrosion science, Springer Science & Business Media.

[41] R. I. M. Asri, W. S. W. Harun, M. Samykano, N. A. C. Lah, S. A. C. Ghani, F. Tarlochan, M. R. Raza, (2017) Corrosion and surface modification on biocompatible metals: A review, Materials Science and Engineering C, 77, 1261-1274.

[42] A. Mosas, K.Kirubaharan, et al. (2022) Recent advancements in materials and coatings for biomedical implants. Gels, 8(5), 323

[43] M. Idrees, A.Z. Jebakumar (2014) A review on corrosion scenario of bio implants in the human body. Am J Biol Pharm Res., 1(3), 100-104.

[44] H. Xi, et al. (2023) Surface modifications of biomaterials in different applied fields. RSC advances, 13(30), 20495-20511.

[45] P. Kazimierczak, A. Przekora (2020) Osteoconductive and Osteoinductive Surface Modifications of Biomaterials for Bone Regeneration: A Concise Review. Coatings, 10, 971. doi: 10.3390/coatings10100971.

[46] M. Akhtar, S. Uzair (2022) The Improvement in Surface Properties of Metallic Implant via Magnetron Sputtering: Recent Progress and Remaining Challenges. Front. Mater.,8, 602. doi: 10.3389/fmats.2021.747169.

[47] H. Ahirwar, Y. Zhou, C. Mahapatra (2020) Materials for Orthopedic Bioimplants: Modulating Degradation and Surface Modification Using Integrated Nanomaterials. Coatings.10, 264.doi: 10.3390/coatings10030264.

[48] S.Uahbl; H. Aris, L. Blaney (2017) Evaluation of animal manure composition for protection of sensitive water supplies through nutrient recovery processes. In: Chemistry and water. Elsevier, p.469-509.

[49] F. Diana, et al. (2022) Current development in biomaterials—hydroxyapatite and bioglass for applications in biomedical field: a review. Journal of Functional Biomaterials, 13(4), 248.

[50] R. Mamunur; F.TAVČER(2021) Influence of titanium dioxide nanoparticles on human health and the environment. Nanomaterials, 11(9), 2354.

[51] F.Morteza (2018) Effect of Tris and acetic acid on the stability of titania nanoparticles in different alcohols and their electrophoretic deposition process. Processing and Application of Ceramics, 12(1), 56-65.

[52] F. Rehman, et al. (2016) Biomedical applications of nano-titania in theranostics and photodynamic therapy. Biomaterials science, 4(1), 40-54.

[53] B.Metka, et al. (2020) Crystallized TiO_2 nano-surfaces in biomedical applications. Nanomaterials, 10(6), 1121

[54] P. Sarkar, P. Nicholson (1996) Electrophoretic deposition (EPD): mechanisms, kinetics, and application to ceramics. Journal of the American Ceramic Society. 79(8), 1987-2002.

[55] A.Pouya, et al. (2015) Electrophoretic deposition (EPD): Fundamentals and applications from nano-to micro-scale structures. Handbook of Nano-electrochemistry, Springer International Publishing Switzerland.

[56] B. Ammara, et al. (2021) A brief insight to the electrophoretic deposition of PEEK-, chitosan-, gelatin-, and zein-based composite coatings for biomedical applications: recent developments and challenges. Surfaces, 4(3), 205-239.

[57] L. Oakes(2016) Controlling Nanomaterial Assembly to Improve Material Performance in Energy Storage Electrodes, Ph.D. Thesis, Vanderbilt University, United State.

[58] B. Laxmidhar; L.Meilin(2007) A review on fundamentals and applications of electrophoretic deposition (EPD). Progress in materials science, 52(1), 1-61.

[59] S. Magdalena, et al. (2020) Electrophoretic deposition of chitosan coatings on the Ti15Mo biomedical alloy from a citric acid solution. RSC advances, 10(23), 13386-13393.

[60] M. Nikolova, M. Apostolova (2023). Advances in Multifunctional Bioactive Coatings for Metallic Bone Implants.Materials, 16(1), 183. https://doi.org/10.3390/ma16010183

[61] Y. Cao, Q. Zhao(2020) Enhanced visible light photocatalytic activity of Fe2O3 modified TiO2 prepared by atomic layer deposition. Sci. Rep., 10, 1–10.

[62] X. He, G. Zhang(2020) Cu and Si co-doped microporousTiO_2 coating for osseointegration by the coordinated stimulus action. Appl. Surf. Sci., 503, 144072.

[63] Z. Hua, C. Zhang,Y. Xu(2019) Efficiently reduced heat rise in TiO_2 coating Ti-based metallic implants using anodic oxidation method. Surf.Coat. Technol., 363, 75–79.

[64] W. Jin, G. Wang, Z. Lin(2017) Corrosion resistance and cytocompatibility of tantalum-surface-functionalized biomedical ZK60 Mg alloy. Corros. Sci., 114, 45–56.

[65] H. Huang, Y. Chang, H. Chen, H. Chou (2014) Antibacterial properties and cytocompatibility of tantalum oxide coatings with different silver content. J. Vac. Sci. Technol. A, 32, 02B117.

[66] N. Xu, J. Fu(2020) Biofunctional Elements Incorporated Nano/Microstructured Coatings on Titanium Implants with Enhanced Osteogenic and Antibacterial Performance. Adv. Healthc. Mater., 9, 2000681.

[67] M. Sun, Y. Wu, C. Yang, J. Bao(2020) Enhanced osteogenic activity and antibacterial ability of manganese–titanium dioxide microporous coating on titanium surfaces. Nanotoxicology, 14, 289–309.

[68] Y. Zheng, T. Wen, R. Zhang(2021) Osteogenic capability of strontium and icariin-loaded TiO_2 nanotube coatings in vitro and in osteoporotic rats. J. Biomater. Appl., 35, 1119–1131.

[69] B. Zhang, B. Gao, S. Li, Y. Cao, R. Cheng, et al. (2020) Y-doped TiO2 coating with superior bioactivity and antibacterial property prepared via plasma electrolytic oxidation. Mater.Des., 192, 108758.

[70] K. Liu, S. Xue, Y. Zhang, L. Han(2019) A superparamagnetic Fe3O4–TiO2 composite coating

on titanium by micro-arc oxidation for percutaneous implants. J. Mater. Chem. B, 7, 5265–5276.

[71] Q. Feng, T. Huang, D. Liu, P. Lin, P. Wu (2019) Antibacterial and hydroxyapatite-forming coating for biomedical implants based on polypeptide-functionalized titaniananospikes. Biomater. Sci., 8, 278–289.

[72] E. Dini, C. Cordeiro, J.M.Ricomini-Filho(2019) Visible-Light-Induced Photocatalytic and Antibacterial Activity of TiO_2Codoped with Nitrogen and Bismuth: New Perspectives to Control Implant-Biofilm-Related Diseases. ACS Appl. Mater. Interfaces, 11, 18186–18202.

[73] I. Hengel, J. Tierolf(2020) Self-defending additively manufactured bone implants bearing silver and copper nanoparticles. J. Mater. Chem. B, 8, 1589–1602.

[74] T. Yetim(2016) Corrosion Behavior of Ag-doped TiO_2 Coatings on Commercially Pure Titanium in Simulated Body Fluid Solution. J. Bionic Eng. 2016, 13, 397–405.

[75] M. Ferraris, C. Balagna (2012) Silver nanocluster/silica composite coatings obtained by sputtering for antibacterial applications. IOP Conf. Series: Mater. Sci. Eng., 40, 012037.

[76] M. Chai, M. Zhang(2021) Construction of a TiO2/MoSe2/CHI coating on dental implants for combating Streptococcus mutans infection. Mater. Sci. Eng. C Mater., 129, 112416.

[77] X. Han,G.Zhang, M. Chai, X. Zhang(2021) Light-assisted therapy for biofilm infected micro-arc oxidation TiO2 coating on bone implants. Biomed. Mater., 16, 025018.

[78] G.Zhang, Z.Wu,Y.Yang, et al. (2022) A multifunctional antibacterial coating on bone implants for osteosarcoma therapy and enhanced osteointegration. Chem. Eng. J., 428, 131155.

[79] B. Li, L. Zhang, D. Wang(2021) Thermosensitive - hydrogel-coated titania nanotubes with controlled drug release and immunoregulatory characteristics for orthopedic applications. Mater. Sci. Eng. C Mater., 122, 111878.

[80] K. Su,L.Tan, X. Liu, Z. Cui, et al. (2020) Rapid Photo-Sonotherapy for Clinical Treatment of Bacterial Infected Bone Implants by Creating Oxygen Deficiency Using Sulfur Doping. ACS Nano 2020, 14, 2077–2089.

IZVOD

ISTRAŽIVANJE UTICAJA PREMAZA BIOMATERIJALA NANEŠENOG ELEKTROFORETSKI NA PODLOGE TITANIJUMA I NJEGOVIH LEGURA: PREGLED

Sadašnja studija govori o vrednosti poboljšanih biomaterijala, posebno premaza za titanijum i njegove legure koji se koriste u hirurškim postavkama. Demonstrira kako se procesi oblaganja kao što je elektroforetski (EPD) mogu koristiti za poboljšanje mehaničkih i bioloških kvaliteta ovih materijala. Pošto je titanijum lagan i otporan na koroziju, on je poželjan materijal za medicinske implantate koji se koriste u popravci tkiva i lečenju preloma. Studija takođe analizira upotrebu keramičkih premaza poput hidroksiapatita i TiO2 u promovisanju regeneracije kostiju, kao i probleme sa biokompatibilnošću i adhezijom tkiva koji se javljaju kod metalnih implantata. Pozitivni rezultati ukazuju na to da napredak u biomaterijalima može poboljšati rezultate lečenja i povećati efikasnost medicinskih implantata, čime se povećava kvalitet života pacijenata.
***Ključne reči:** biopremaz, titanijum, antikorozivne legure, elektroforetsko taloženje*

Shaymaa Abbas Abdulsada: https://orcid.org/0000-0001-7006-2950
Safa Jabbar: https://orcid.org/0009-0004-4836-7925

Ravi Ranjan[1], Madhulata Shukla[1]*

[1]*Department of Chemistry, Gram Bharti College, Ramgarh, Kaimur, Veer Kunwar Singh University, India*

Synthesis of copper (II) oxide nanoparticle: A promising material for photocatalysis

ABSTRACT

Copper oxide (CuO) nanoparticles have gained significant attention due to their unique properties and wide range of applications. Various methods have been developed to synthesize CuO nanoparticles (NP), including physical, chemical, and biological methods. These nanoparticles find applications in various fields, including electronics, energy storage, photocatalysis, medical, and materials science. This paper reports a facile and quick synthesis of CuOnanoparticles for the first time using curcumin as a stabilizing agent and sodium borohydride as a reducing agent. Synthesized nanoparticle is characterized using UV-visible spectrum measurement and X-ray diffraction techniques.Synthesized catalyst was used to study the photocatalytic degradation of the very hazardous organic pollutant para-nitrophenol. (PNP)The study wascarried out in acidic and basic medium under dark and visible light irradiation. In a basic environment, the degradation of PNP remains almost insignificant whether in the presence or absence of light. However, in an acidic environment, degradation of PNP occurs at a slow pace when there is no light, but the process accelerates significantly when exposed to light. Density Functional Theory calculation indicates a strong interaction between curcumin and CuO moiety. It indicates that curcumin stabilizes the CuO nanoparticles and will be quite stable for a long time. Also, it will facilitate the easy transfer of electrons from curcumin to CuO NP by lowering the band gap and enhancing the catalytic property of NP.
Keywords: Nanoparticles, CuO, photocatalysis, DFT calculation

1. INTRODUCTION

Copper (II) oxide (CuO) nanoparticles have gained significant attention due to their unique properties and their wide range of applications in various fields [1-4]. This paper provides an overview of CuO nanoparticle synthesis and its application in various fields. Over the past twenty years, copper oxide nanoparticles (CuO NPs) have become a popular alternative to gold and silver nanoparticles. Their affordability, widespread availability, and strong antibacterial characteristics have made them a favored choice in various applications [5-7]. Copper oxide nanoparticles (CuO NPs) stand out among metal oxides as an effective catalyst for the degradation of organic pollutants.

Their distinctive qualities, including a low band gap of 1.2–3.5 eV, low toxicity, abundance, and a cost-effective synthesis process, make them an excellent choice for this application [8,9]. Synthesis of CuO Nanoparticles can be carried out via several methods including physical, chemical, and biological methods [10]. The choice of synthesis method depends on the desired properties and the desired shape and size of the nanoparticles.One common physical method to synthesize CuO nanoparticles is through hydrothermal processing. In this method, copper oxide precursors are dissolved in a suitable solvent, which is then subjected to heat and pressure in a sealed container. The high temperatures and prolonged reaction times result in the formation of CuO nanoparticles.Another widely used method to synthesize CuO nanoparticles is through chemical routes.

One common chemical method involves the reduction of copper ions with a suitable reducing agent, such as sodium borohydride. The resulting reaction leads to the formation of CuO nanoparticles.Biological methods have also been

*Corresponding author: MadhulataShukla

E-mail: madhu1.shukla@gmail.com

employed to synthesize CuO nanoparticles. For example, blue-green algae such as Nostoc sp. can be used to synthesize CuO nanoparticles [11]. The algae secrete a reducing agent, which reacts with copper ions to form CuO nanoparticles. This paper will cover a facile and quick synthesis of copper oxide (CuO) nanoparticles using curcumin and sodium borohydride. The synthesis process involves chemical reduction method in which sodium borohydrideacts as a reducing agent, curcumin acts as stabilizing agent and it also enhances the catalytic activity of synthesized CuO by decreasing the band gap between Highest Occupied Molecular Orbital and Lowest Unoccupied Molecular Orbital, as stated by us in our previous report for Cu_2O nanoparticle [12]. This synthetic process is useful, as it require very less time to synthesize and require cheap chemicals to synthesize and also the particle size obtained is low.CuO nanoparticles have gained significant attention due to their unique properties and potential applications in various fields, such as catalysis, energy storage, and sensing [3,10,13-17]. CuO nanoparticles have been used to fabricate electronic devices, such as sensors and transistors. Their high electrical conductivity and tunable surface properties make them suitable for various applications in electronics. CuO nanoparticles have been investigated for their potential in energy storage applications. They have shown excellent energy storage capacities, making them potential candidates for energy storage devices such as batteries and supercapacitors [18,19]. CuO nanoparticles exhibit photocatalytic properties, making them suitable for applications in the field of photocatalysis. They can be used for the degradation of pollutants, water splitting, and solar energy conversion. CuO nanoparticles have shown potential in medical applications, such as drug delivery and cancer treatment [19,20].

Their unique properties, such as high biocompatibility and antibacterial activity, make them attractive candidates for biomedical applications.CuO nanoparticles have been explored for their potential in various materials applications. They can improve the properties of materials, such as strength, conductivity, and corrosion resistance, making them suitable for applications in coatings, composites, and catalysis. Nanoparticles have become increasingly prevalent in the food industry for producing antibacterial films [21].

Current research aims to create antimicrobial packaging materials using a variety of nanoparticles, including CuO. These innovative nanopackaging techniques can be utilized in food products through methods such as wrapping, dipping, brushing, or spraying. The goal is to establish a specialized barrier against gas, moisture, and dissolved materials, while also providing protection against physical damage [22].

Several literatures are available explaining the photocatalytic degradation of organic pollutants, this encourages us to carry out a photodegradation study of 4-nitrophenol (PNP) in our study using CuO-synthesized nanoparticles [23-25]. Copper oxide (CuO) nanoparticles are increasingly recognized for their effectiveness as a catalyst in the breakdown of nitrophenol, particularly 4-nitrophenol (PNP). Through a process known as catalytic reduction, these nanoparticles can transform PNP into the far less harmful 4-aminophenol (4-AP). Their high surface area and strong catalytic properties position them as a promising and environmentally friendly alternative for treating wastewater. It has been reported by Fan et al that the photodegradation of 4-nitrophenol using CuO adhered to pseudo-first-order kinetics, and the catalyst demonstrated the ability to be reused six times without any loss in its effectiveness [26].

2. MATERIALS REQUIRED

Materials required for the synthesis of CuO nanoparticles were Copper (II) nitrate (copper nitrate trihydrate) $(Cu(NO3)2 \cdot 3H_2O)$(Merck), Curcumin (Sigma Aldrich), sodium hydroxide (NaOH) (Merck), Sodium borohydride (NaBH4) (Merck) and ethanol (Merck). All reagents were used as received without further purification.

3. EXPERIMENTAL PROCEDURE

2 g of copper nitrate trihydrate $(Cu(NO3)2 \cdot 3H_2O)$ dissolved in 100 mL of distilled water in a 250 mL round bottom flask.Stir the solution on a magnetic stirrer until the $Cu(NO3)2$ is completely dissolved and a transparent blue color solution is obtained.1 g of NaOHdissolved in 100 mL of distilled water to prepare the alkaline solution.Stir the alkaline solution to dissolve it completely.20 mL of NaOH solution was added slowly to $Cu(NO3)2$ solution with stirring at room temperature. After that 1gNaBH4 dissolved in 20mLdistilled water and added slowly to alkaline $Cu(NO3)2$ solution. 9.15 g curcumin powder was dissolved in 5mL of prepared NaOH solution and after that water was added to obtain 25mL homogeneous curcumin solutions. The prepared curcumin solution was added to alkaline $Cu(NO3)2$ solution dropwise. P^H of reaction maintained around 10-11. Temperature was increased to 70-80 ºC. A schematic diagram to synthesize CuO NP from copper nitrate trihydrate has been shown in Figure 1.Stirring was done for 2h and mixture was characterized using UV-visible spectra analysis after every 30-minute interval. A broad hump around 500-600 nm region explains the synthesis

of CuO nanoparticles. After the 2h, let the mixture cool to room temperature. Then separate the precipitate by centrifugation at 15000 rpm.Wash the obtained CuO nanoparticles with distilled water four times and finally with acetonitrile two times to remove any residual reagents. Dry the CuO nanoparticles under a vacuum for 48h.
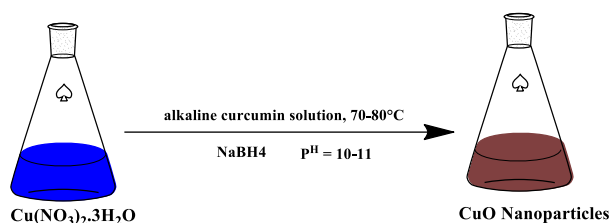
Figure 1. Schematic diagram to synthesize CuO NP from copper nitrate trihydrate

4. CHARACTERIZATION

4.1. UV-Vis Spectroscopy

UV-Vis spectroscopy is a powerful technique to analyze the optical properties of nanoparticles.The UV-visible spectrum of synthesized sample of CuO is shown in Figure 2. The broad absorption hump of CuO nanoparticles occurs at around 500-600 nm, indicating the formation of nanoparticles.
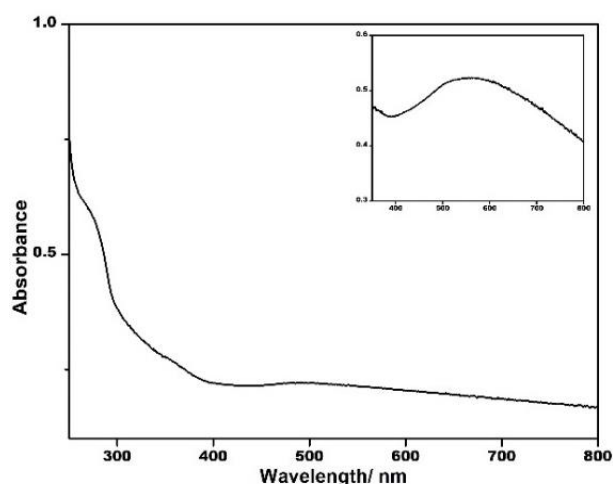
Figure 2. UV-visible spectrum of synthesized CuO NP. An expanded region of 500-600 nm hump is also shown

4.2. XRD Analysis

Figure 3 shows the X -ray diffraction pattern of the powdered CuO NPs samples. Eleven prominent peaks were observed at 32.47, 35.53, 38.78, 48.95, 53.59, 58.33, 61.61, 66.31, 68.10, 72.44, and 75.21 which correspond to {110}, {002}, {111}, {-202}, {020}, {202}, {-113}, {-311}, {113}, {311}, and {-222} reflections respectively of monoclinic Copper (II) Oxide **(**CuO) (JCPDSICDD No. 652309).
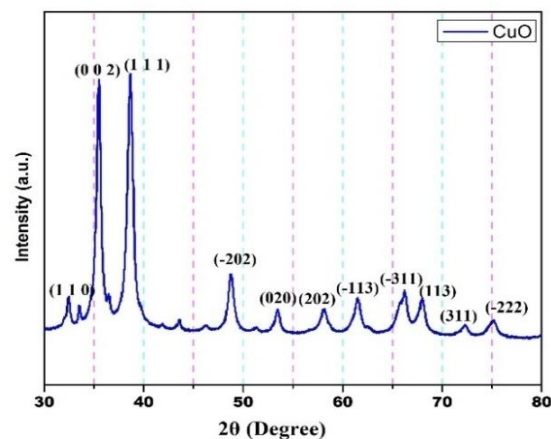
Figure 3.XRD spectrum of Copper (II) Oxide

4.3. Scanning Electron Microscopy (SEM)

SEM is a high-resolution imaging technique that provides a magnified view of the nanoparticles. It is used to determine the size and shape of the CuO nanoparticles. SEM images usually show spherical particles with a variable size distribution ranging from 11 to 70 nm.SEM image of CuO nanoparticle synthesized using curcumin has been shown in Figure 4a. The particle size distribution graph is shown in Figure 4b.

a)

b)
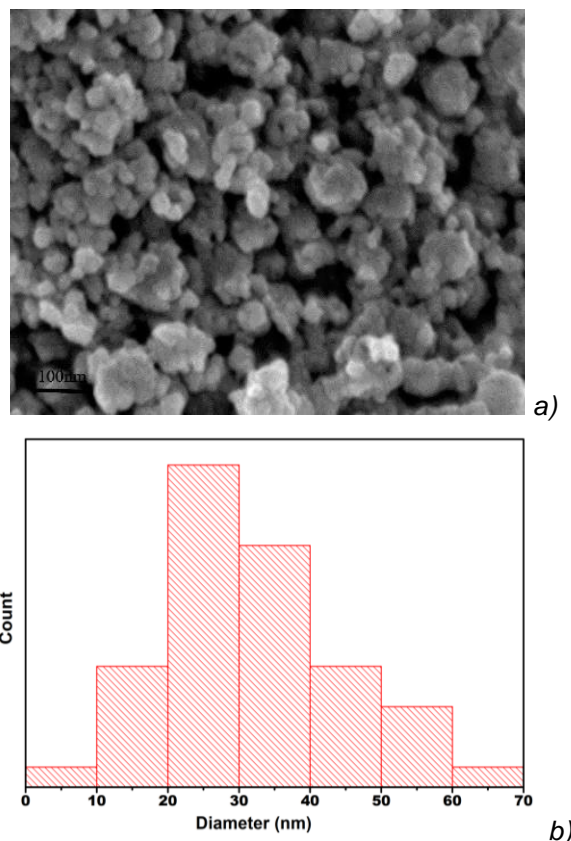
Figure 4. (a)SEM image of CuO nanoparticle synthesized using curcumin (b) Particle size distribution graph of CuO NP

5. 5. Photocatalytic Application of CuO nanoparticle:

The photocatalytic activity of synthesized CuO samples was investigated by application of these nanoparticles as photocatalysts for the photo-degradation of very hazardous organic pollutant 4-nitrophenol(PNP) under dark and visible light irradiation and also under acidic and basic mediums. The UV-visible spectrum of 4-nitrophenol mainly consists of characteristic absorption peaks at 314 nm in an acidic medium and 400 nm in basic medium (due to the phenolate ion). Figure5(a) and (b)represent the UV-visible spectra of an aqueous solution of PNP in the presence of CuO NP, hydrogen peroxide and sodium hydroxide in dark and visible light irradiation conditions respectively.

a)

b)
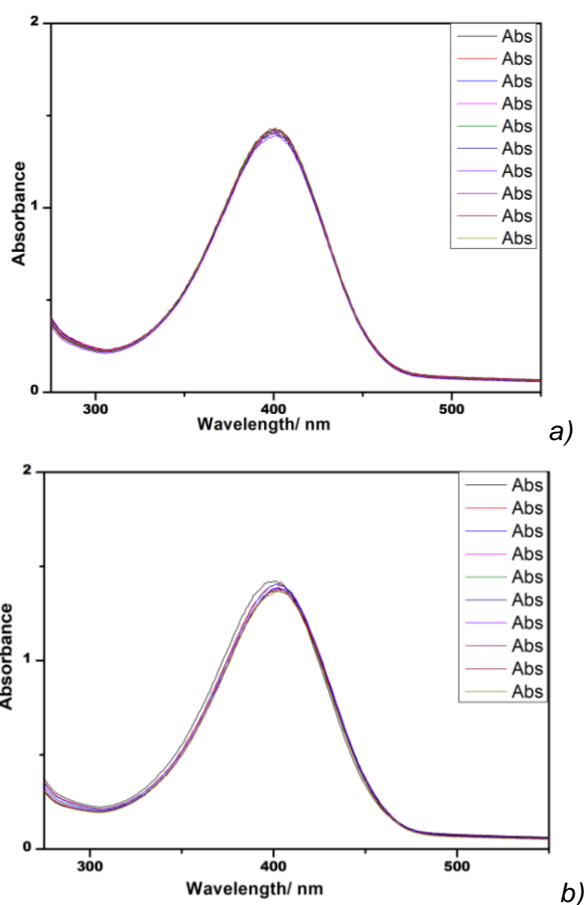
Figure 5. The photocatalytic reaction of CuO nanoparticle in the basic medium in (a) in absence of light (b) in the presence of LED light

Degradation of PNP was not observed in the basic medium in either dark or light conditions. Hence synthesized catalyst doesn't work for the degradation of PNP in a basic medium. Figure 6 (a) and (b) represent the UV-visible spectra of an aqueous solution of PNP in the presence of CuO NP, hydrogen peroxide, and hydrochloric acid in dark and visible light irradiation conditions respectively. Spectra were recorded for 90 minutes

but degradation was observed to be lesser in the absence of light as compared to visible light medium. It is clear from Fig. 5(a) &(b) that degradation of PNP is almost negligible in the absence and presence of light in the basic medium. The synthesized CuO demonstrated limited catalytic activity in alkaline conditions. This was primarily caused by the dissociation of PNP, which increased the repulsion between CuO and the PNP anions, as reported in earlier literature [26]. Whereas it shows slow degradation of PNP in the acidic medium in the absence of light and rapid degradation in the presence of light.

Initially, the degradation of PNP was studies in dark and found to show slow rate of degradation. Whereas when the reaction mixture was kept in the photocatalytic chamber under a cool white LED with visible light radiation, the reaction speeds up. A steady decrease in the intensity of peaks, on prolonged exposure to visible light, indicates gradual degradation of PNP with time. Photocatalytic activity of CuO was recorded for 90min in both conditions and irradiated condition, PNP was found to be almost fully degraded to simpler ions. Hence the rate of degradation of PNP organic pollutants using CuO nanoparticlesis higher in visible light irradiated conditions in an acidic medium.

a)

b)
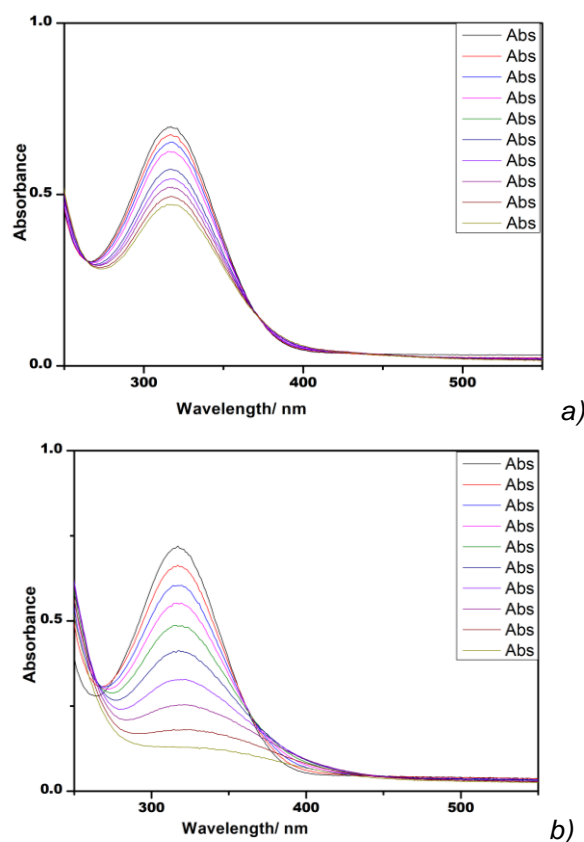
Figure 6. The photocatalytic reaction of CuO nanoparticle in the acidic medium (a) in the absence of LED light & (b) in the presence of LED light

6. DENSITY FUNCTIONAL THEORY CALCULATION

Geometry optimization of CuO-curcumin carried out using Density Functional Theory (DFT) calculation using Gaussian 16 [27] program at B3LYP level [28] and using the LaNL2DZ basis set. The molecular optimized structure of CuO-curcumin moiety is shown in Figure 7(a). The distance between curcumin and CuOnanocluster was found to be 2.50Å indication strong interaction between CuO and curcumin moiety. Mulliken charge analysis of CuO-curcumin moiety was done at the same level of calculation and using a similar basis set and shown in Figure 7 (b). It was observed that the inner copper atoms are electropositive as shown by the light green color whereas outer copper atoms are less electropositive as compared to inner copper atoms. Oxygen atoms carry a negative charge as represented by a brown color or red color in Figure 7 (b). Mulliken charge distribution shows that the curcumin actives the outer layer of the nanocluster to enhance the rate of photocatalytic degradation in light by decreasing the band gap in CuO catalyst.

Figure 8. Electrostatic potential charge distribution on CuO-Curcumin

Figure 9 represents the frontier molecular orbital pictures of highest occupied molecular orbital (HOMO) and lowest unoccupied molecular orbital (LUMO). HOMO is localized mainly on curcumin moiety (π of Benzene and non-bonding orbitals of Oxygen), whereas LUMO is localized on π* of benzene and d-orbital of copper atoms of CuOnanoclusters.

HOMO

LUMO
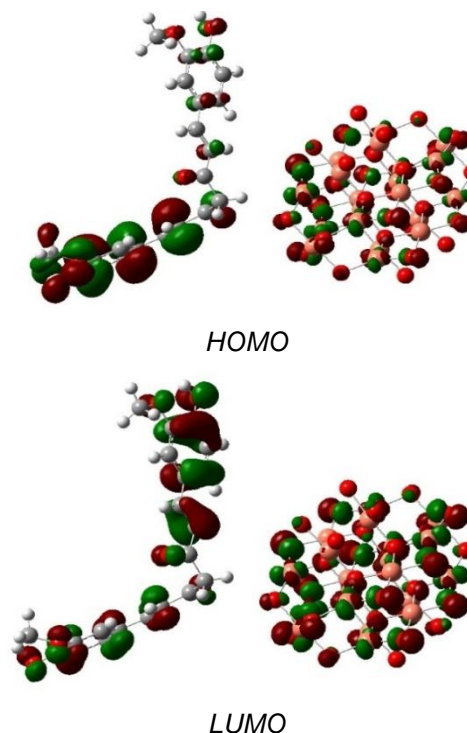
Figure 9. Frontier Molecular Orbital picture of CuO-Curcumin

a)

b)

Figure 7. Optimized structure and Mulliken charge analysis of CuO-curcumin moiety

Figure 8 represents the electrostatic potential charge distribution on CuO-Curcumin moiety. It indicates that strong interaction is present between curcumin and CuOnanocluster, as the potential charge is distributed all over the molecule. The orange color represents the electronegative and the yellowish-green color represents the electropositive charge distribution on the molecules.

7. CONCLUSION

Copper oxide (CuO) nanoparticles have garne red considerable attention due to their unique properties and diverse range of applications. Researchers have developed various methods for synthesizing CuO nanoparticles, spanning physical, chemical, and biological approaches. These nanoparticles play a crucial role in fields such as electronics, energy storage, photocatalysis, medicine, and materials science. This

study presents a simple and rapid method for synthesizing CuO nanoparticles using curcumin and sodium borohydride. Synthesized CuO nanoparticle was used to study the photocatalytic degradation of PNP to 4-aminophenol. Photo-catalytic degradation of the organic pollutant 4-nitrophenol under different conditions, such as acidic and basic environments, with and without visible light irradiation has been studied. The findings reveal that in a basic environment, the degradation of p-nitrophenol remains minimal regardless of the presence of light. On the other hand, in an acidic environment, the degradation process occurs slowly in the absence of light, but significantly accelerates when exposed to light. CuO nanoparticles transform PNP into less harmful 4-aminophenol (4-AP). DFT calculation explains the charge distribution and interaction between curcumin and CuOnanocluster.

Acknowledgment

Conflict of interests

The authors declare that they have no conflict of interest.

8. REFERENCES

[1] A. M. Al-Fa'ouri, M. H. Abu-Kharma, A. M. Awwad, M. K. Abugazleh (2023) Investigation of optical and structural properties of copper oxide nanoparticles synthesized via green method using Bougainvillea leaves extract," Nano-Structures & Nano-Objects, 36, 101051, doi:https://doi.org/10.1016/j.nanoso.2023.101051.

[2] S. Faisal et al. (2021) Curcuma longa Mediated Synthesis of Copper Oxide, Nickel Oxide and Cu-Ni Bimetallic Hybrid Nanoparticles: Characterization and Evaluation for Antimicrobial, Anti-Parasitic and Cytotoxic Potentials," Coatings, 11, 849, doi: 10.3390/coatings11070849.

[3] S. Aroob et al. (2023) Green Synthesis and Photocatalytic Dye Degradation Activity of CuO Nanoparticles," 13, 502, doi.org/10.3390/catal13030502

[4] S. Naz, A. Gul, M. Zia, R. Javed (2023) Synthesis , biomedical applications , and toxicity of CuO nanoparticles," Appl. Microbiol. Biotechnol., 107, 1039, doi: 10.1007/s00253-023-12364-z.

[5] M. Shukla, S. Pal, I. Sinha (2022) Ionic Liquid Functionalized Cu 2 O nanoparticles, 1262, 132961, doi: 10.1016/j.molstruc.2022.132961.

[6] P. Ramesh, A. Rajendran (2023) Photocatalytic dye degradation activities of green synthesis of cuprous oxide nanoparticles from Sargassum wightii extract, 6, 100208, https://doi.org/10.1016/j.chphi.2023.100208

[7] J. H N, K. G. Chandrappa, S. Fakrudeen, (2023) Green synthesis of CuO nanoparticles: A promising material for photocatalysis and electrochemical sensor, Sensors Int., 5, 100254, doi: 10.1016/j.sintl.2023.100254.

[8] H. Saha et al., (2024) Photocatalytic performance of CuO NPs: An experimental approach for process parameter optimization for Rh B dye, Results Mater., 24, 100614, doi: https://doi.org/10.1016/j.rinma.2024.100614.

[9] B. Coşkuner Filiz, (2020) The role of catalyst support on activity of copper oxide nanoparticles for reduction of 4-nitrophenol, Adv. Powder Technol., 31, 3845, doi: 10.1016/j.apt.2020.07.026.

[10] M. E. Grigore, E. R. Biscu, A. M. Holban, M. C. Gestal, A. M. Grumezescu, (2016) Methods of Synthesis, Properties and Biomedical Applications of CuO Nanoparticles, Pharmaceuticals, 9, 75, doi: 10.3390/ph9040075.

[11] R. S. Hamida, M. A. Ali, A. Redhwan, M. M. Bin-Meferij (2020) Cyanobacteria - A Promising Platform in Green Nanotechnology: A Review on Nanoparticles Fabrication and Their Prospective Applications., Int. J. Nanomedicine, 15, 6033, doi: 10.2147/IJN.S256134.

[12] R. Ranjan, M. Shukla (2025) Curcumin-mediated synthesis of cuprous oxide nanoparticles and its photocatalytic application," Next Mater., 6, 100481, doi: 10.1016/J.NXMATE.2024.100481.

[13] C. Yang, F. Xiao, J. Wang, X. Su (2014) Synthesis and microwave modification of CuO nanoparticles: crystallinity and morphological variations, catalysis, and gas sensing., J.Colloid Interface Sci., 435, 34-42, doi: 10.1016/j.jcis.2014.08.044.

[14] M. Ahamed, R. Lateef, M. J. Akhtar, P. Rajanahalli (2022) Dietary Antioxidant Curcumin Mitigates CuO Nanoparticle-Induced Cytotoxicity through the Oxidative Stress Pathway in Human Placental Cells," Molecules, 27, 7378, doi: 10.3390/molecules27217378.

[15] A. Mathew, A. Parveen, K. N. Pathade, A. Dhote, A. K. Nakkella, (2022) Green Synthesis And Pharma-cological Potential Of Curcumin," 13, 6090, doi: 10.47750/pnr.2022.13.S10.753.

[16] P. C. Okoye, S. O. Azi, T. F. Qahtan, T. O. Owolabi, T. A. Saleh, (2023) Synthesis, properties, and applications of doped and undoped CuO and Cu2O nanomaterials," Mater. Today Chem., 30, 101513, doi: https://doi.org/10.1016/j.mtchem.2023.101513.

[17] H. T. Berede, et al. (2024) Photocatalytic activity of the biogenic mediated green synthesized CuO nanoparticles confined into MgAl LDH matrix," Sci. Rep., 14, 2314, doi: 10.1038/s41598-024-52547-w.

[18] K. P. Jithul, K. S. Samra, (2022) Cupric Oxide based Supercapacitors: A Review," J. Phys. Conf. Ser., 2267, 012120, doi: 10.1088/1742-6596/2267/1/012120.

[19] M. Devaraji, P. V Thanikachalam, K. Elumalai, (2024) The potential of copper oxide nanoparticles in nanomedicine: A comprehensive review, Biotechnol. Notes, 5, 80, doi: https://doi.org/10.1016/j.biotno.2024.06.001.

[20] M. J. Woźniak-Budych, K. Staszak, M. Staszak, (2023) Copper and Copper-Based Nanoparticles in Medicine-Perspectives and Challenges., Molecules, 28, 6687, doi: 10.3390/molecules28186687

[21] H. Onyeaka, P. Passaretti, T. Miri, Z. T. Al-Sharify (2022) The safety of nanomaterials in food production and packaging, Curr. Res. Food Sci., 5, 763. doi: https://doi.org/10.1016/j.crfs.2022.04.005.

[22] A. A. Gvozdenko, et al., (2022) Synthesis of CuO nanoparticles stabilized with gelatin for potential use in food packaging applications, Sci. Rep., 12, 12843, doi:10.1038/s41598-022-16878-w

[23] A. Bhattacharjee, M. Ahmaruzzaman (2016) CuO nanostructures: facile synthesis and applications for enhanced photodegradation of organic compounds and reduction of p-nitrophenol from aqueous phase, RSC Adv., 6, 41348, doi: 10.1039/C6RA03624D.

[24] I. Hasan, C. Shekhar, I. I. Bin Sharfan, R. A. Khan, A. Alsalme (2020) Ecofriendly Green Synthesis of the ZnO-Doped CuO@Alg Bionanocomposite for Efficient Oxidative Degradation of p-Nitrophenol, ACS Omega, 5, 32011, doi: 10.1021/acsomega.0c04917.

[25] K.Dulta, G.Koşarsoy Ağçeli, P.Chauhan, R. Jasrotia, P.K.Chauhan, J.O.Ighalo (2022) "Multifunctional CuO nanoparticles with enhanced photocatalytic dye degradation and antibacterial activity," Sustain. Environ. Res., 32, 2. doi: 10.1186/s42834-021-00111-w.

[26] Y. Fan, et al. (2022) Effective photodegradation of 4-nitrophenol with CuO nano particles prepared by ionic liquids/water system,"Green Chem. Eng., 3, 15. doi: https://doi.org/10.1016/j.gce.2021.07.009.

[27] M. J. Frisch, G. W. Trucks, H. B. Schlegel, G. E. Scuseria, M. A. Robb, J. R. Cheeseman, G. Scalmani, V. Barone, G. A. Petersson, H. Nakatsuji, X. Li, M. Caricato, A. V. Marenich, J. Bloino, B. G. Janesko, R. Gomperts, B. Mennucci, H. P. Hratchian, J. V. Ortiz, A. F. Izmaylov, J. L. Sonnenberg, D. Williams-Young, F. Ding, F. Lipparini, F. Egidi, J. Goings, B. Peng, A. Petrone, T. Henderson, D. Ranasinghe, V. G. Zakrzewski, J. Gao, N. Rega, G. Zheng, W. Liang, M. Hada, M. Ehara, K. Toyota, R. Fukuda, J. Hasegawa, M. Ishida, T. Nakajima, Y. Honda, O. Kitao, H. Nakai, T. Vreven, K. Throssell, J. A. Montgomery, Jr., J. E. Peralta, F. Ogliaro, M. J. Bearpark, J. J. Heyd, E. N. Brothers, K. N. Kudin, V. N. Staroverov, T. A. Keith, R. Kobayashi, J. Normand, K. Raghavachari, A. P. Rendell, J. C. Burant, S. S. Iyengar, J. Tomasi, M. Cossi, J. M. Millam, M. Klene, C. Adamo, R. Cammi, J. W. Ochterski, R. L. Martin, K. Morokuma, O. Farkas, J. B. Foresman, D. J. Fox (2016) Gaussian, Inc., Wallingford CT.

[28] A. D. Becke (1993) Density-functional thermochemistry. III. The role of exact exchange," J. Chem. Phys., 98, 5648. doi: 10.1063/1.464913.

IZVOD

SINTEZA NANOČESTICA BAKAR (II) OKSIDA: OBEĆAVAJUĆI MATERIJAL ZA FOTOKATALIZU

Nanočestice bakarnog oksida (CuO) privukle su značajnu pažnju zbog svojih jedinstvenih svojstava i širokog spektra primene. Razvijene su različite metode za sintezu nanočestica CuO (NP), uključujući fizičke, hemijske i biološke metode. Ove nanočestice nalaze primenu u različitim oblastima, uključujući elektroniku, skladištenje energije, fotokatalizu, medicinu i nauku o materijalima. Ovaj rad izveštava o lakoj i brzoj sintezi CuOnanočestica po prvi put koristeći kurkumin kao stabilizator i natrijum borohidrid kao redukciono sredstvo. Sintetizovana nanočestica je okarakterisana pomoću merenja UV-vidljivog spektra i tehnika difrakcije rendgenskih zraka. Sintetizovani katalizator je korišćen za proučavanje fotokatalitičke degradacije veoma opasnog organskog zagađivača para-nitrofenola. (PNP) Studija je sprovedena u kiseloj i baznoj sredini pod tamnim i vidljivim zračenjem. U osnovnom okruženju, degradacija PNP ostaje gotovo beznačajna, bilo u prisustvu ili odsustvu svetlosti. Međutim, u kiseloj sredini, degradacija PNP se odvija sporim tempom kada nema svetlosti, ali se proces značajno ubrzava kada je izložen svetlosti. Proračun funkcionalne teorije gustine ukazuje na snažnu interakciju između kurkumina i CuO dela. To ukazuje da kurkumin stabilizuje nanočestice CuO i da će biti prilično stabilan dugo vremena. Takođe, to će olakšati lak prenos elektrona sa kurkumina na CuO NP smanjenjem pojasnog pojasa i poboljšanjem katalitičkih svojstava NP.
Ključne reči: *nanočestice, CuO, fotokataliza, DFT proračun*

Madhulata Shukla: https://orcid.org/0000-0002-4060-8729
Ravi Ranjan: https://orcid.org/0009-0004-3720-4514

Salsabeel Kareem Burhan[1,2,], Zoalfokkar Kareem Alobad[1], Ammar Emad Al-kawaz[1]*

[1]*Faculty of Materials Engineering, Department of Polymer Engineering and Petrochemical Industries, University of Babylon, Babylon, Iraq,* [2]*Technical Institute of Babylon, Al-Furat Al-Awsat Technical University (ATU), Iraq.*

Disulfide bonds modified epoxy resins: mechanical, adhesion and wear properties

ABSTRACT

Epoxy occupiesan important place in many engineering applications, so it is necessary to improveits properties such as adhesion strength, wear resistance, and toughness. In this study,epoxy was modified by incorporation of disulfide bonds. A coating layer was prepared by adding ethanol disulfideto epoxy resin at various weight percent: 0.5, 1.5, 2.5 and 3.5 wt.%. Fourier-transform infrared spectroscopywas employed to investigate any chemical interaction. Differential scanning colometry (DSC) analysis provides valuable information aboutthermal behaviour of the prepared epoxy coating. Tensile, hardness, impact, fracture toughness, and adhesion properties were tested. Wear behaviour was investigated by pin-on-disc device. Results show that epoxy containing disulfide bonds (EP+SS) offering excellent impact resistance with good fracture toughness compared to neat epoxy. Additionally, contact angle test results show an enhancement of wettability between the modified epoxy coating layer and steel substrate. Adhesion strength of epoxy layeenhanced by incorporating ethanol disulfide into epoxy resin reaching a superior value. Comparisonto neat epoxy, the coefficient of friction of (EP+SS) highly decreased reaching about 89% and wear rate decreased by 76% as the percentage of the added ethanol disulfide increases.
A tough superior adhesive epoxy coating layer was synthesised by incorporation of the ethanol disulfide compound into epoxy resin.
Key words: disulfide, epoxy, wear, adhesion, dynamic bonds.

1. INTRODUCTION

Epoxy resins have become ubiquitous in modern civilisation, appearing in everything from automobiles to aeroplanes, indoor decoration to household appliances, and biological technology to factory equipment [1-3]. Therefore, it is necessary to improve the properties of epoxy, such as mechanical properties, adhesion, and wear resistance [4-7]. Disulfide bond-modifying epoxy resins have attracted a lot of interest because of their distinctive characteristics, which include mechanical strength and the ability to heal themselves. Disulfide linkages are usually added to the epoxy network, which increases its flexibility and permits dynamic exchange processes [8].

Dutta and Karak showed that because the disulfide bonds are dynamic, epoxy vitrimers containing disulfide show remarkable elongation at break and self-healing efficiencies of up to 71.48% [9]. Similar to this, Zhang et al. found that epoxy with different disulfide bond contents had better mechanical properties [10]. With a remarkable 98% healing efficiency, Li et al. further highlighted the importance of disulfide bonds in improving self-healing performance under mild conditions [11]. Achieving strong adhesion at polymer/metal interfaces is a major challenge in interface engineering, as it is necessary for many technical applications.Tsai et. al. (2020) tried to improve the adhesive properties of epoxy by using epoxy containing aromatic disulfide links as adhesives. The disulfide system comprised bis (4-glycidyloxyphenyl) disulfide (BGPDS) and dithiodianiline (DTDA) as the epoxy monomer and diamine hardener, respectively. Exchangeable disulfide bond-epoxy resins have improved mechanical and thermal resilience.

A high density of disulfide bonds was incorporated to speed up the exchange process, which increased the chance of bond cleavage and rearrangement and improved adhesion [12]. Krishnakumar et. al. showed how to create epoxy vitrimers containing graphene oxide (GO) and 2-aminophenyldisulfide (2-AFD) assisted polydimethylsiloxane (PDMS) that show a decrease in glass transition temperature and storage modulus with an increase in flexural strain [5]. Luzuriaga et. al. chose 4-aminophenyldisulfide (AFD) as a dynamic hardener for epoxy resin. The "dynamic" epoxy resin used to manufacture fiber-reinforced polymer composites exhibits good mechanical strength along with recycling, and re-processability [13]. Henriksen et. al. added a bio-based disulfide additive (2-hydroxyethyldisulfide) to a commercial epoxy, the result was a cross-linked polymer that is safe for the environment to fractionate. In addition, it was shown that, when compared to commercial epoxy, modified epoxy matrices with minimal addition concentrations have comparable mechanical and thermal properties [14].

This study seeks to enhance the properties of epoxy by incorporating ethanol disulfide as a modifying compound. The effect of adding ethanol disulfide to epoxy resin on the mechanical, adhesion, and wear properties was investigated. Ethanol disulfide represents an alternative cheap disulfide bond-containing compound compared to the expensive amino phenyl disulfide compound.

2. EXPERIMENTAL PART

2.1 Materials

The selected epoxy resin and hardener for this study was Sikadur 52 bis phenol-A liquid epoxy resin and its aliphatic amine hardener, mixing ratio: 2:1, which purchased from Sikadur company, Turkey. 2-Hydroxyethyldisulfideor as known 2,2′-Dithiodiethanol or Bis(2-hydroxyethyl) disulfide, has linear formula: $HOCH_2CH_2SSCH_2CH_2OH$ with molecular weight of 154,25 g/mol. It has a clear, viscous liquid appearance with dark yellow colour.Melting point range: 25 - 27 °C, boiling point and boiling range158 - 163 °C and flash point at 112 °C. 2-Hydroxyethyldisulfide was made in Switzerland and purchased by Sigma-Aldrich.

2.2. Characterization and test methods

2.2.1. Fourier-transform infrared spectroscopy (FTIR)

FTIR spectroscopydetermines the distinct wavelengths at which a sample absorbs infrared radiation, enabling the identification of the sample's functional groups. FTIR was employed to characterize the chemical composition of the prepared specimens and investigate any chemical interaction using instrument type (IR Affinity-1, Japan) with spectra range 400-4000 cm^{-1}.Using a mortar and pestle, a small amount of the epoxy compositions was ground into an extremely fine powder, the sample was then transferred to potassium bromide (KBr) discs. The two discs were pressed together to create a film, plate holders were used to support the disc in the spectrometer and snugly fitted into spectrometer and fitted directly into the path of the infrared radiation. Finally, FTIR spectrum was presented in a diagram between the transmittance intensity (T%) and wavelengths (cm^{-1}).

2.2.2. Differential Scanning Calorimetry (DSC)

DSC analysis is a powerful thermo-analytic technique that provides valuable information aboutthermal behaviour and properties of materials. It provides quantitative measurement of heat flow associated with phase transitions and chemical reactions in the sample such as glass transition temperature (T_g) and curing process. A small sample (10 mg) was placed in a closed crucible, then the crucible was inserted into a temperature-controlled cell along with an empty reference crucible. The sample underwent a controlled heating, and the heat flow was monitored and analysed. DSC test was done using the SH1MADZ-4 DSC-60 device. The operating conditions were: 25- 250 $^{\circ}$C temperature range with10 $^{\circ}$C/min heating rate under argon gas environment.

2.2.3 Scanning Electron Microscope (SEM)

The American SEM device, FEI model, was employed to investigate the microstructure of coatings and the fracture surface of tensile specimens. The epoxy samples must be coated with ultrathin gold layer to be conductive.

2.2.4. Tensile test

The WDW-5E electronic universal testing machine was used for tensile strength test, using a 5 N load cell and a 5 mm/min cross headon ASTM D-638-14 [15]. Figure 1 shows the test process and specimen dimensions. The sample was firmly clamped by the machine grips to prevent any slippage during the test then the sample was subjected to a gradually increased axial force until rapture. The applied load and the corresponding deformation were continuously recorded to get the stress-strain curve [16]. The values of stress, strain, and modulus of elasticity were calculated according to the following equations:

$$\sigma = P/A \qquad\qquad (1)$$

$$\varepsilon = \Delta L/L \qquad\qquad (2)$$

$$E = \sigma_2 - \sigma_1 / \varepsilon_2 - \varepsilon 1 \qquad\qquad (3)$$

Where: σ: tensile strength (MPa), *P*: applied load (N), *A*: cross-sectional area (mm^2), E: modulus of elasticity (MPa).

a)   *b)*
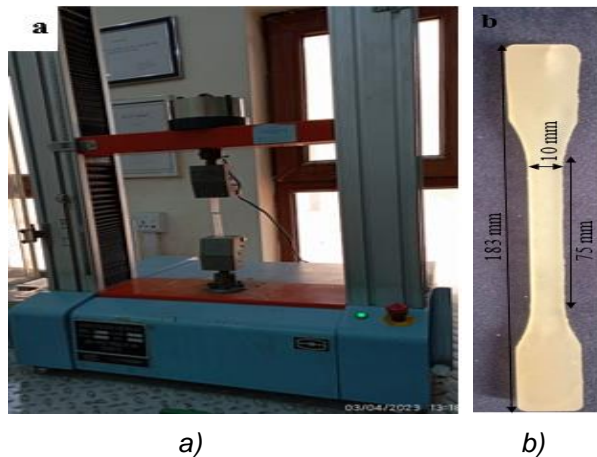
Figure 1. a) tensile strength test, b) specimen dimensions

2.2.5. Hardness test

A hardness test measures a material's resistance to indentation. The device is made-up of instrument with a calibrated and an indenting probe. The probe with conical-shaped tip is made of hardened steel or carbide. By perpendicular pressing the durometer probe on to the specimen surface, the device measures the depth of interpenetrating trace to get the value of hardness ranging from 0 to 100. A Shore D durometer instrument (TIME 5431 model, China) was used to test cylindrical specimens with at least 3 mm thickness, following ASTM (D2240) standards [17]. The surface of each specimen was tested six times, with the final hardness being an average of the results.

2.2.6. Fracture toughness test

A single edge-notched three-point bending test (SENB) was conducted on V-shaped notch bars of 53 mm long, 9 mm wide, 8 mm thickness with 36 mm support span length and 10 mm/min loading rate, using a universal testing machine type (WDW/5E) at 5 KN, following the ASTM D5045-14 procedure. Three accurate measurements were taken to confirm data dependability, and critical stress intensity factors (K$_{IC}$) were analysed.

(a)   *(b)*
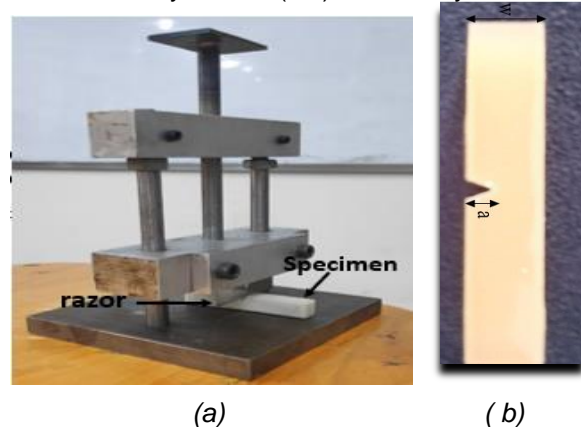
Figure 2. a) The process of creating incisions within SENB fracture toughness specimen, (b) SENB specimen

Before testing, the specimens should be pre-cracked at the tip of v-sectionand the so called " sharp crack introduced by the razor" was created by applying a weight with hand force on the razor at the tip of v-section as shown in figure 2. Finally, the stress intensity (K$_{IC}$) was calculated by Eq.4:

$$KIC = \frac{P}{B\sqrt{W}}\, f\left(\frac{a}{W}\right) \qquad (4)$$

$$f\left(\frac{a}{w}\right) = \frac{\left(2+\frac{a}{w}\right)\left\{0.886 + 4.64\left(\frac{a}{w}\right) - 13.32\left(\frac{a}{w}\right)^2 + 14.72\left(\frac{a}{w}\right)^3 - 5.6\left(\frac{a}{w}\right)^4\right\}}{\left(1-\frac{a}{w}\right)^{3/2}} \qquad (5)$$

Where: K$_{IC}$: fracture toughness (Stress Intensity Factor in Mode I) (MPa · m$^{1/2}$), P: maximum load (N), B: thickness of the specimen (mm), W: width of thespecimen (mm), a: crack length (mm) and *f* (a/w): shape factor.

2.2.7. Impact test

The WP 400 model, a German machine from HAMBURG, was used to test the impact strength of specimens using the Charpy test method basing on ISO 179. A rectangular bar was horizontally supported by two anvils then the pendulum of the machine test was released to a highest height and free felled to hit the specimen causing fracture. Then the energy absorbed by the specimen during fracture was measured.The impact strength (a$_{cU}$) was determined by calculating the necessary

energy for fracture using a formula on an unnotched specimen (Eq. 6). Figure 3 shows the dimensions of specimen required for impact test.

$$acU = \frac{W_B}{bh} * 10^3 \qquad (6)$$

Where: a$_{cU}$: impact strength (J/mm^2), h: thickness (mm), b: width (mm), W$_B$: energy at break (joule).
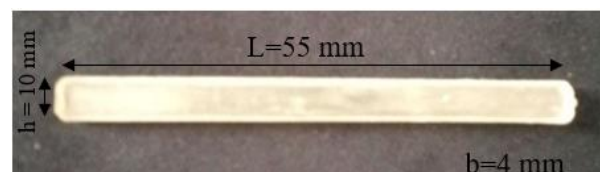
Figure 3. The dimensions of specimen required for impact test

2.2.8. Wear test

Using a pin-on-disk device, ASTM G99-17 describes the test method outlines of laboratory process for assessing material wear during sliding [18]. Wear test was accomplished utilizing a pin-on-disc machine (U.S.A. MT4003, version 10) where under a load of 15N, a disc of epoxy specimen (40 mm diameter and 4mm thickness) was rotated in a circular path with 250 rpm speed, sliding distance of approximately 235 m for 30 minutes on a stationary steel pin (6 mm diameter, HRC 56 hardness and 3.2 surface roughness) as shown in figure 4. Wear rate was calculated by Eq. 7.

$$Wear\ rate\% = \left(\frac{\Delta w}{w^\circ}\right)*100 \qquad (7)$$

Where:

Δw : weight difference of a specimen before and after wear test (g).

w° : weight of a specimen before wear test(g).
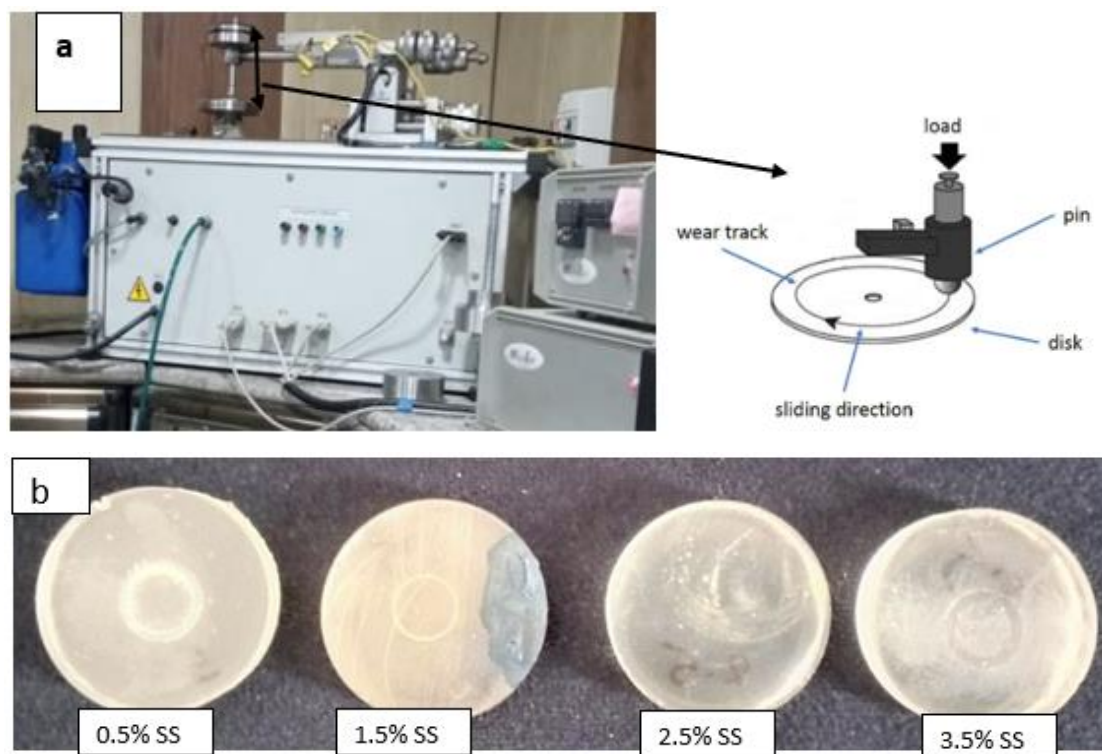
Fig.4: a) pin-on-disc wear test, b) EP+SS samples

2.2.9. Contact angle test

Microliter-sized droplets are applied to a sample surface in order to determine the contact angle (C.A.). A surface's wettability is determined by the contact angle, which is the angle produced at the droplet's boundary. Additionally, contact angle measurement can provide a useful information about surface free energy, surface tension, and work of adhesion. C.A of neat epoxy coating (EP) and that of epoxy-ethanol disulfide coatings (EP+SS) on steel surfaces was measured. Additionally, C.A between water droplet and those coatings was measured. Vino for contact angle meter, China, device was used.

2.2.10. Pull-off strength test

A typical technique for evaluating coating and adhesive quality is the pull-off test, which involves gluing a dolly to a substrate (metal), as illustrated by ASTM D-4541. Next, by drawing perpendicular to the surface, the dolly and the adhesive or coating are removed from the substrate then the required force to pull-off the coating from the substrate surface divided by the contact area represents the pull-off strength (adhesion strength) of coating. The surface of a steel screws with a diameter of 17 mm was prepared by grinding and cleaning well with acetone to adhere well to the coating layer. A sufficient vertical pulling force was applied to remove the coating layer from the surface of steel substrate using the tension device (WDW-5E electronic universal testing machine), then the adhesion force was calculated. Figure 5 shows the test technique.

$$Adhesion\ strength = \frac{f}{contact\ area} \qquad (8)$$

Where: f: pulling force (KN).

Contact is the contact area between dolly surface and coating layer (227 mm^2).

The adhesion strength and percentage improvement of adhesion strength were calculated according to Eq. 8 and 9, respectively.

$$Improvement\% = \left(\frac{Sm - S_0}{S_0}\right) * 100 \qquad (9)$$

Where: Sm :adhesion strength of modified epoxy (MPa) and S_0: adhesion strength of neat epoxy (MPa).
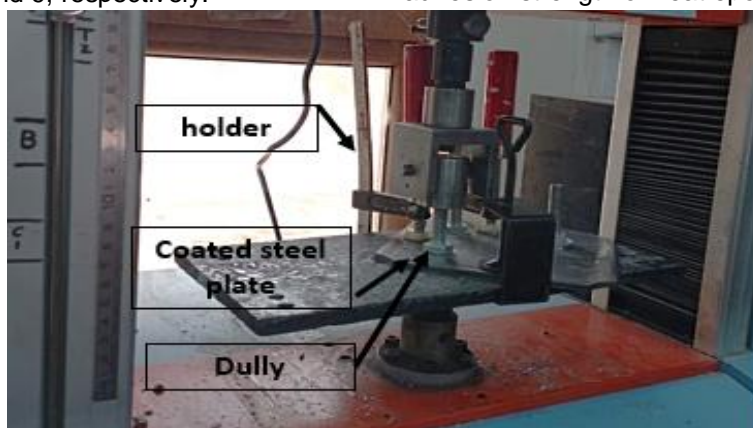
Figure 5. the pull-off test

3. RESULTS AND DISCUSSION

3.1. Fourier-Transform Infrared Spectroscopy (FTIR)

From analysing FTIR spectrum (Figure 6: a), it is clear that a complete curing of epoxy was satisfied by disappearance of peak at 910 cm^{-1}, which corresponded to C-O stretching in oxirane ring and 3056 cm^{-1} for C-H stretching of the oxirane ring, that served as a sign that the curing process was finished [13]. Additionally, FTIR spectroscopy was used to characterise all EP+SS with varying ethanol disulfide concentrations. Comparing with the spectrum of the reference sample (neat epoxy), we notice the emergence of a peak at 509 cm^{-1} for the epoxy samples modified with the addition of ethanol disulfide. This may indicate the incorporation of the S-S bond into epoxy structure [19]. Furthermore, it is possible to conclude that increasing the intensity of FTIR peaks for EP+SS samples represents an increment of functional groups or interaction between the functional groups.

The additives should have at least two functional groups, that can operate as affective nucleophiles, e.g., amines, alcohols, carboxylic acids and so on. 2-hydroxyethyldisulfide(ethanol disulfide) has two functional sites, or reaction sites, at the OH group as illustrated in Figure 6b.
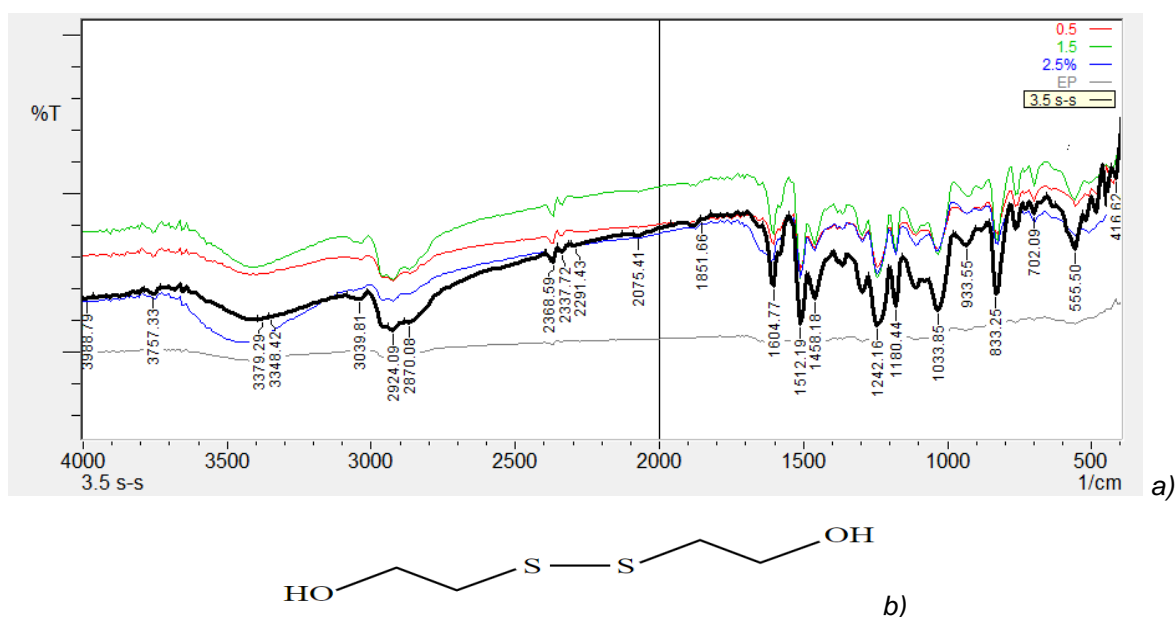
Figure 6. a) FTIR spectrum, b) chemical structure of 2-hydroxyethyldisulfide

3.2. Differential Scanning Calorimeter (DSC)

The polymer network's cross-linking density rises in tandem with the degree of cure, limiting molecular mobility and thus increasing the measured T_g. From analysing the results of DSC test, it is found that a high regression of T_g values of EP+SS compared to neat epoxy (see Table 1).

Table 1. DSC thermograms for the neat epoxy and EP+SS.

Sample	0	0.5	1.5	2.5	3.5
Tg (ºC)	80	65.5	63.4	64	63.6

3.3. Mechanical Properties

Figure 7 shows the change of the epoxy mechanical properties when different percentages of ethanol disulfide were added to it. It is clear that a regression of tensile and hardness properties has been occurred, whereas a raising of toughness properties has been occurred. It is found that as ethanol disulfide content increases up to 3.5%, the tensile strength of epoxy decreases by about 26%. The percentage elongation of neat epoxy reaches to 2%, whereas it reaches to 22% at 3.5 wt.% of ethanol disulfide adding. Epoxy hardness decreases by about 19 to 45% when 0.5% to 3.5% of ethanol disulfide were added to epoxy resin.
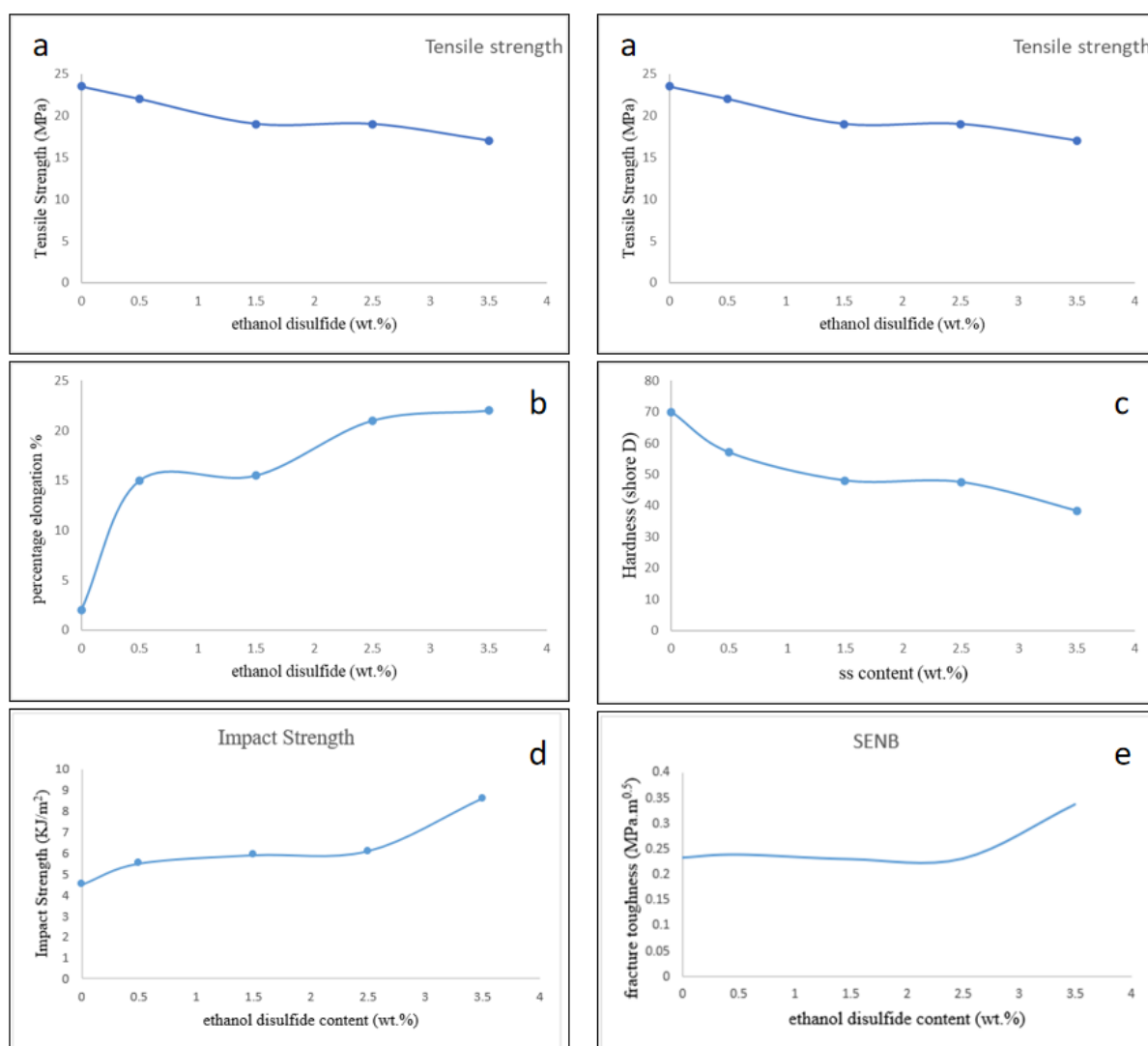
Figure 7. The principle mechanical properties of epoxy containing ethanol disulfide: a) tensile strength, b) percentage elongation at break, c) shore D hardness, d) impact strength and e) SENB

The primary disadvantage of cured epoxy is its extreme brittleness, which demonstrates low fracture toughness or low resistance to crack initiation and propagation. Epoxy using in various industries needing high fracture strengths, including matrix resins for composites, has been

restricted due to their intrinsic brittleness. Therefore, ethanol disulfide is used as modifier to improve toughness property of epoxy.

For neat epoxy, the values of impact resistance and K_{IC} are found as ~449.7 J/m^2 and ~0.234 MPa.m$^{1/2}$, respectively. For EP+SS containing a 3.5 wt.% of ethanol disulfide, the impact strength and K_{IC} are satisfied a maximum value reaching about 857.8 J/m^2 and 0.409 MPa.m$^{1/2}$ that are 91% and 75% higher than that of neat epoxy, respectively.

From the above results, the plasticizing effect of adding ethanol disulfide to epoxy resin is clear. As mentioned in paragraph regarding the results of DSC test, adding ethanol disulfide to the epoxy leads to a decrease in T_g values. This means that the structure becomes more flexible. Ethanol disulfide has no steric hindrance in the epoxy structure because it doesn't have aromatic or bulk groups. The material becomes less brittle as it softens, making it less susceptible to flaws or defects. The improved ductility is probably caused by the crack tip reducing before the crack propagates so this enhances the fracture strength and toughness of epoxy modified by ethanol disulfide adding. Additionally, disulfide bonds (S-S) undergoes reversible cleavage and reformation processes under mechanical shear leading to dynamic flexible structure [13,20].

Furthermore, SEM microscopic photo (figure 8) study approves the plasticising effect of adding ethanol disulfde on the mechanical behaviour of EP+SS system.
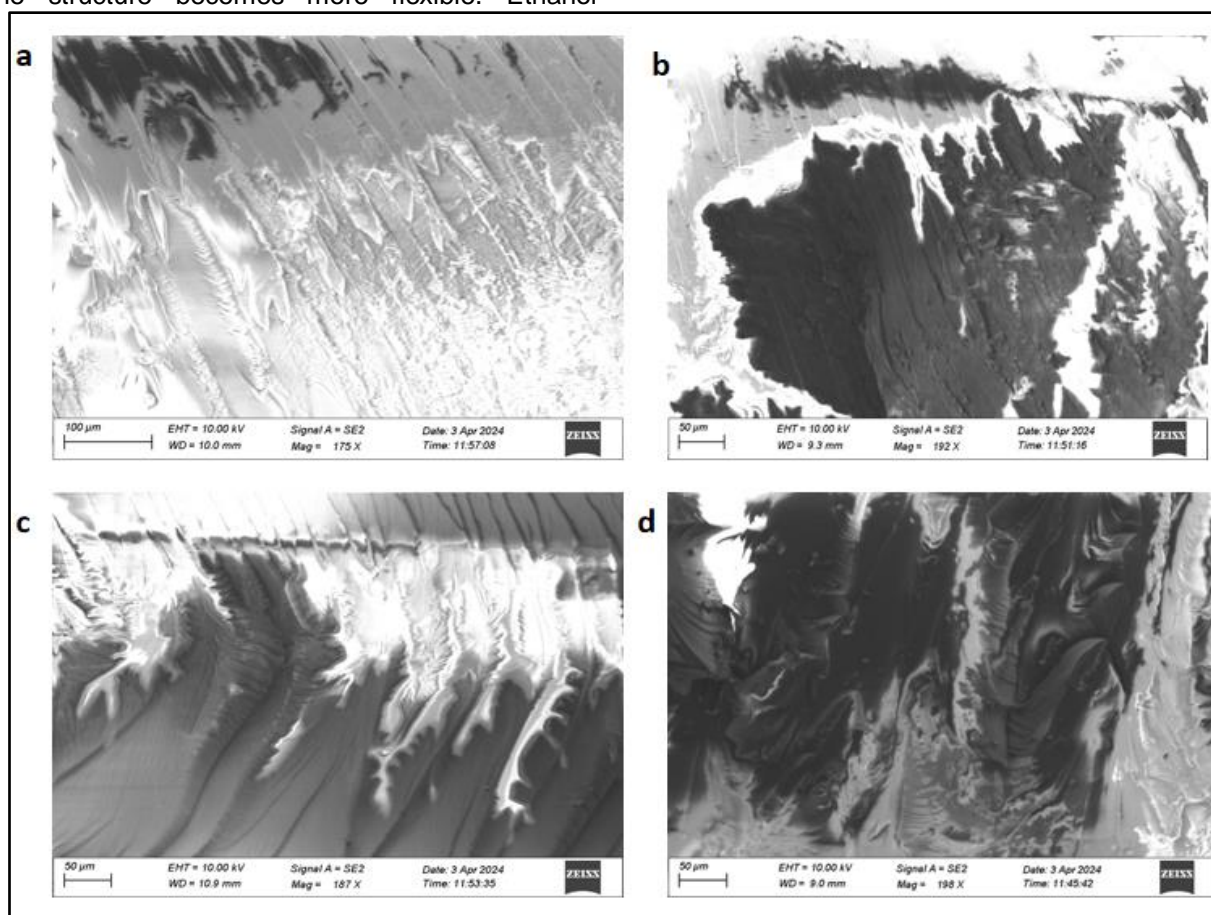
Figure 8. Micrographs from SEM of fracture surface of tensile specimens of: a) neat epoxy, b) 0.5%, c) 1.5%, d) 2.5% EP+SS

3.4. Pull-Off Adhesion Strength

The effect of adding ethanol disulfide compound, at various weight percentages, on the adhesion strength between epoxy coating and steel substrate was estimated by pull-off test. The results are summarised in Table 2 and Figure 9.

The wettability between epoxy coating layer and steel surface was evaluated basing on the values of free surface energy (SFE), contact angle (CA) and work of adhesion from the test of CA. From Figures 10 and 11 and Table 3, it is clear that CA values decrease, but the work of adhesion increases leading to enhanced wettability.

Table 2. the summarised results from pull-off test for neat epoxy and the modified epoxy coatings

Ethanol disulfide content (wt.%)	Adhesion strength (MPa)	Improvement%
0	3.3	-
0.5	8.3	152
1.5	7.66	133
2.5	7.44	127
3.5	6.16	88

Table 3. the value of CA, surface free energy (SFE) and work adhesion (WA) from contact angle test

SS,%	CA,(º)	SFE, (mJ/m^2)	WA,(mJ/m^2)^2
0	47.7	55	121.6
0.5	54.1	51.34	115.4
1.5	39.7	59.45	128.66
2.5	45.9	56.06	123.3
3.5	39.6	59.54	128.7
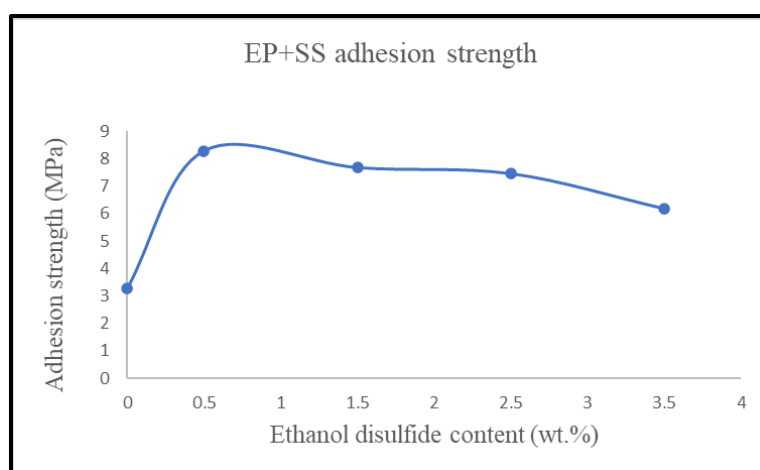
Figure 9. The graphical representation illustrates the correlation between the adhesive strength and the concentration of ethanol disulfide within the epoxy-based protective coating
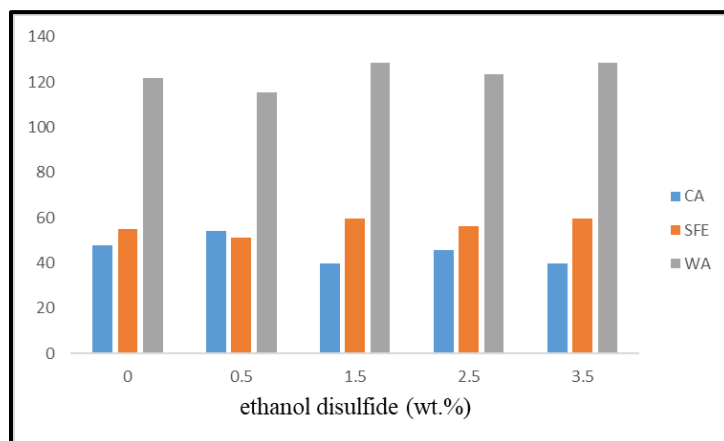
Figure 10. A chart represents the values of CA, surface free energy (SFE) and adhesion work from contact angle test according to content of ethanol disulfide within epoxy coating

From the obtained results, it is clear that an improvement of adhesion strength of epoxy coating is satisfied by incorporating ethanol disulfide into epoxy resin reaching a superior value. Adhesion failure mode, as shown in Figures 12 and 13, is glue-failure where failure occurs at glue-coating interface, at the same time there is no adhesion failure at coating-substrate interface. Epoxy resins inherently generate strong covalent bonds due to its hydroxyl groups [21]. The epoxy formulations containing a compound containing disulfide bonds show enhancedand superior adhesion to the metal surface due to the disulfide bonds which may experience reversible cleavage and reformation during the epoxy curing process. As a result, more covalent connections can be formed by the disulfide groups across the coating-substrate interface.

a) 0 %

b) 0.5%

c) 1.5%

d) 2.5%

e) 3.5%
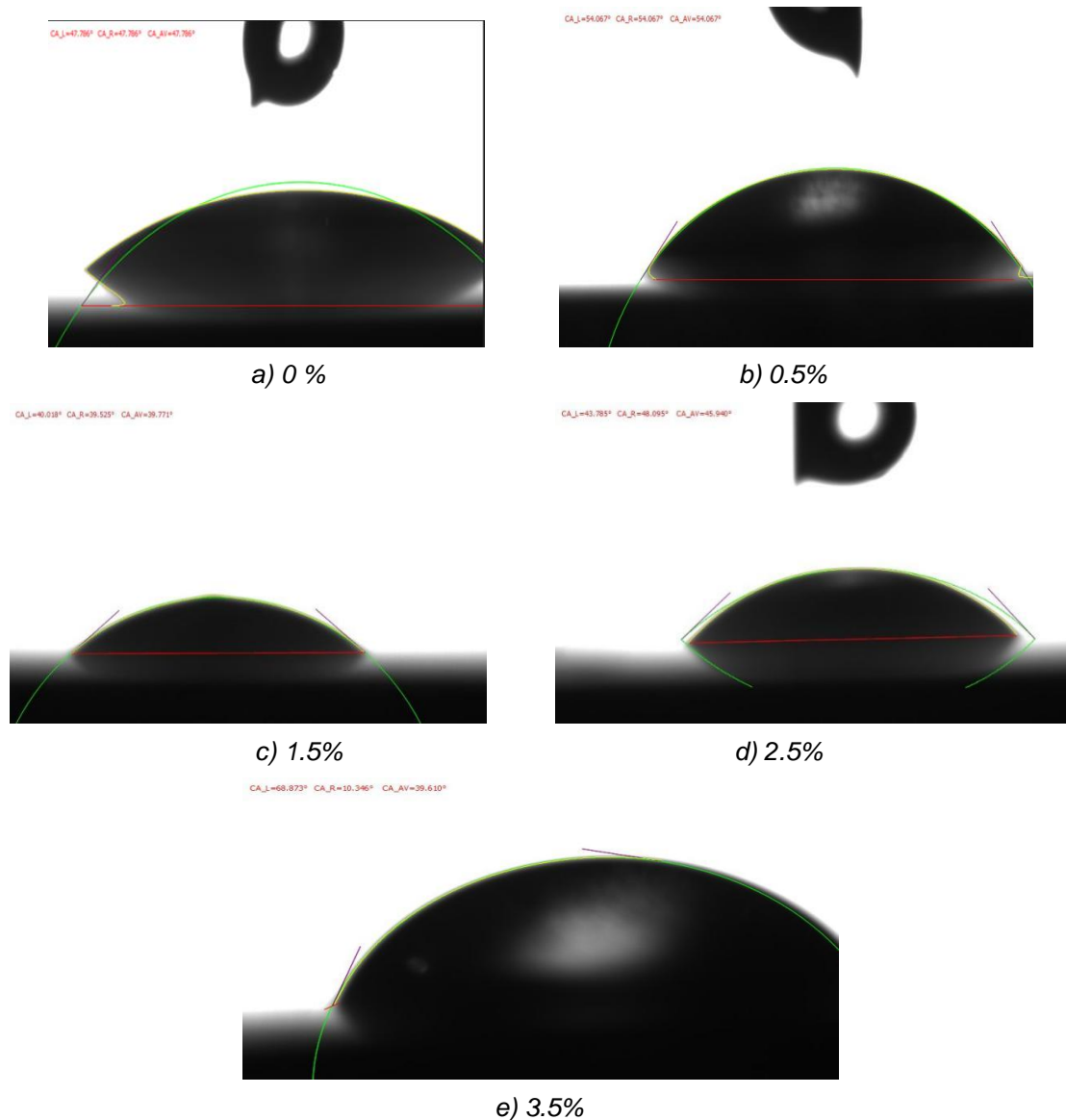
Figure11. measurements of contact angle between the modified epoxy micro-droplet and steel surface
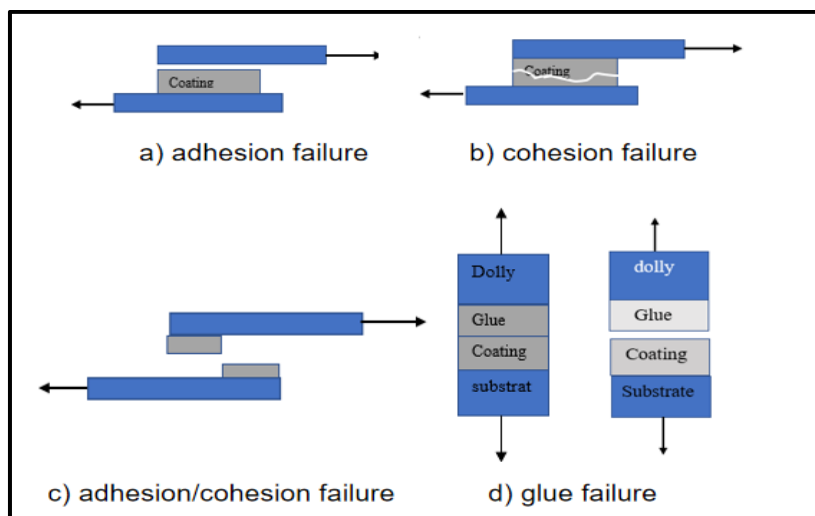
Figure 12. Diagram illustrates failure mode of coating
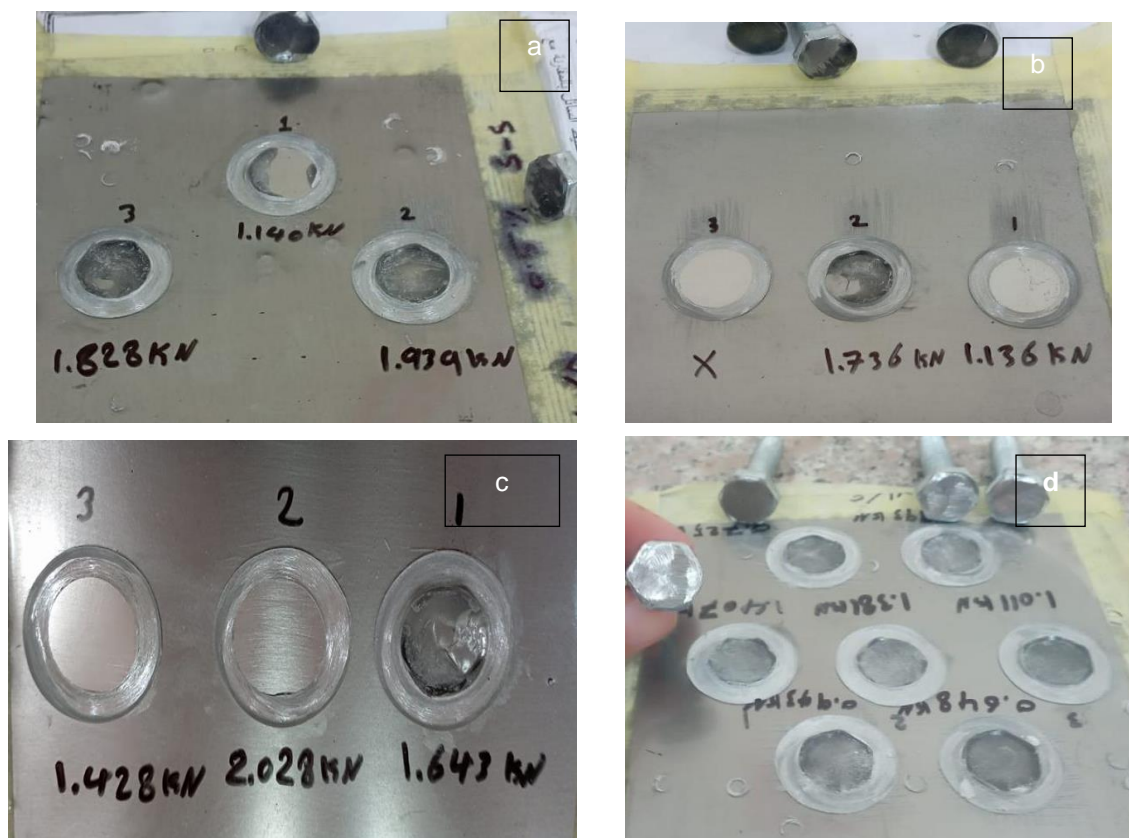
Figure13. photographic pictures for pull-off test specimens: a) 0.5%, b) 1.5%, 2.5% and 3.5% ethanol disulfide containing epoxy coatings

3.5. Wear Properties

Coefficient of friction (COF), wear rate, and plasticity index for neat EP and disulfide containing epoxy are planned in Figure 14 and presented in Table 4. Comparison to neat epoxy, the coefficient of friction of disulfide containing epoxy (EP+SS) highly decreases reaching about 89% when ethanol disulfide content increased up to 2.5 wt.%. Concurrently, as the percentage of ethanol disulphide increases, the rate of wear reduces. The wear rate decreased by 76% compared to the wear rate of pure epoxy. This means a significant improvement in the wear resistance of the epoxy as a result of adding ethanol disulfideto it.

Table 4. The data pertains to the wear rate, coefficient of friction, and plasticity index for the EP+SS coatings

Sample	Wear rate	Improvement%	Coefficient of friction	Improvement%	Plasticity index
0	0.037	-	0.56	-	4.519
0.5	0.01	62	0.54	4	3.859
1.5	0.014	73	0.27	52	2.916
2.5	0.01	76	0.06	89	3.578
3.5	0.009	76	0.12	79	4.177

Because the contacting surfaces' asperities are being removed, there is a noticeable rise in the coefficient of friction during the wear process' early stages. As test progresses, wear track is formed so decreasing COF. We note that the plasticity index (E/H) of EP+SS is lower than that for neat epoxy, and as previously mentioned in the study of the effect of adding ethanol disulfide to epoxy on mechanical properties, the effect of ethanol disulfide as a plasticizer increases the flexibility and toughness of the epoxy structure, thus the resistance to the growth of micro-cracks increases. This enhances material resistance to removal from contacting surfaces. To support this interpretation, we note from SEM microscopic graphs of wear truck in figure 15 that wear truck is blurred and invisible compared to that for neat epoxy. It is also believed that a continuous thin lubricating film forms between the rubbing surfaces, isolating them from each other and reducing direct contact

between the surfaces, thus reducing the friction coefficient and wear rate.

It is believed that the disulfide bonds absorb the heat resulting from friction because they are dynamic bonds that are affected by heat, so these bonds cleavage and reorganize themself, thus enhancing the cohesion and integrity of the structure resulting in enhancing resistance for material removal at contact area.
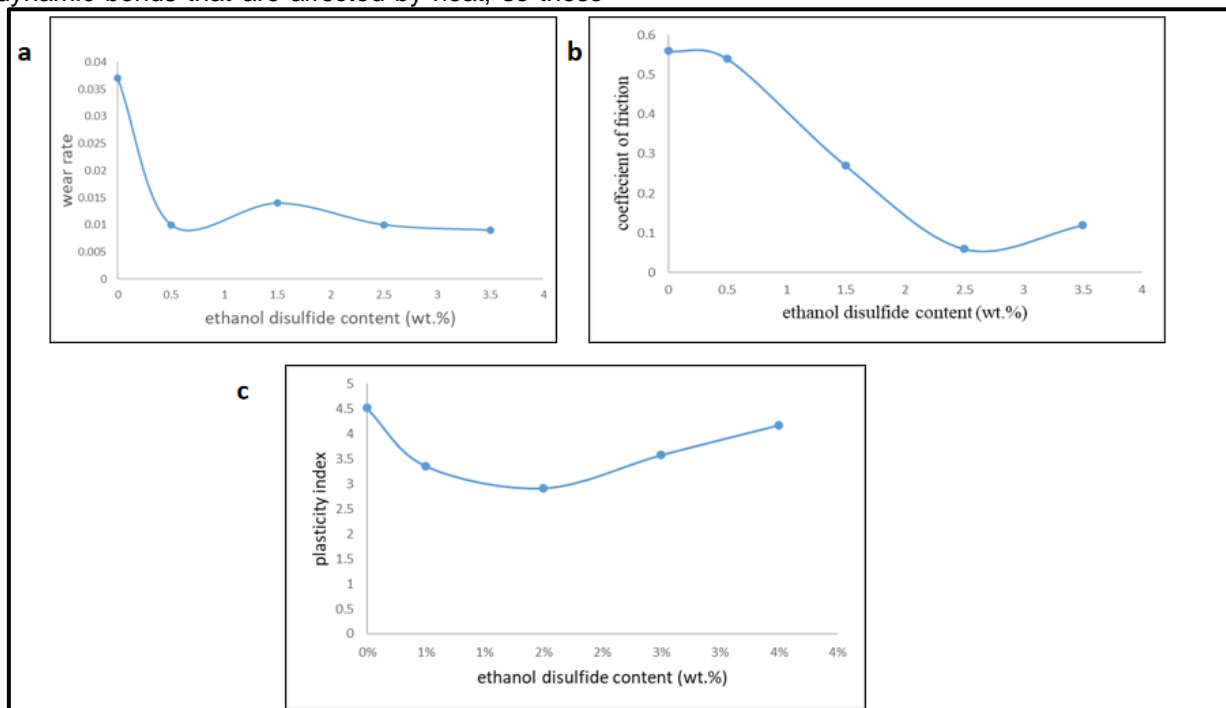
Figure 14. the changes of (a) Coefficient of friction (COF), (b) rate of wear, and (c) plasticity index as a function of ethanol disulfide content in epoxy resin
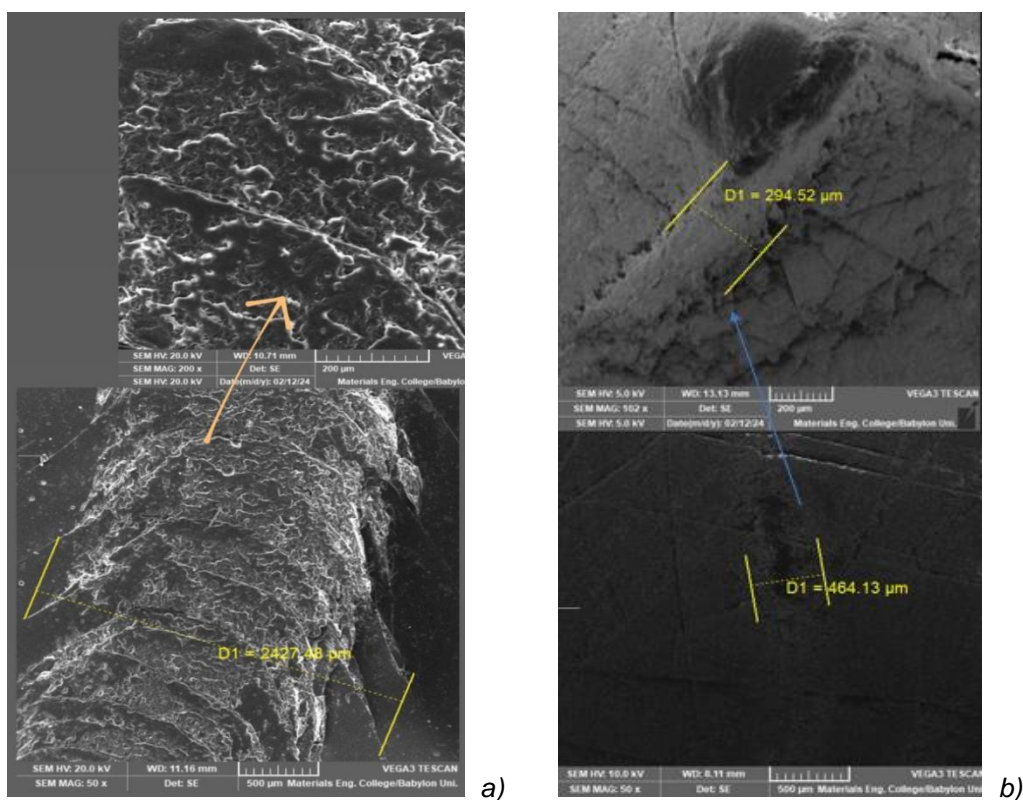
Figure 15. SEM micrographs of wear track of: a) neat and b) EP+SS coatings

4. CONCLUSIONS

Adding ethanol disulfide to epoxy resin has significant effects on epoxy properties. DSC analysing results show that a high regression of T_g values of EP+SS compared to neat epoxy.The tensile strength of epoxy decreases by about 26% whereas percentage elongation reaches to 22% at 3.5 wt.% of ethanol disulfide adding and the impact strength and K_{IC} are satisfied at a maximum value reaching about 857.8 J/m^2 and 0.409 MPa.m$^{1/2}$ that are 91% and 75% higher than that of neat epoxy, respectively. Additionally, hardness decreases by about 45%. This indicates improved epoxy toughness and reducingbrittleness with increasing the percentage of the additive. Adding ethanol disulfide to epoxy enhanced the modified epoxy's wear resistance of the modified epoxy, where the friction coefficient wasreduced by 89% and wear ratereduced by 76% for 2.5 wt.% of ethanol disulfide adding. Pull-off strength highly increased and glue-failure mode occurred. Finally, A tough superior adhesive epoxy coating layer was synthesised by incorporation of the ethanol disulfide compound. Using ethanol disulfide for improving the adhesion, wear and mechanical properties of the epoxy coating represents an excellent alternative compound compared to the very expensive amino phenyl disulfide compound.

5. REFERENCES

[1]   A. A. Naser and B. M. Fahad (2018) Adhesion test for epoxy reinforcing using waste materials applied on concrete surfaces," IOP Conf. Ser. Mater. Sci. Eng., 433(1), 012004.   doi: 10.1088/1757-899X/433/1/012004.

[2]   S. Saadatmandi, M. Asghari, B. Ramezanzadeh (2019) Effective epoxy composite coating mechanical/fracture toughness properties improvement by incorporation of graphene oxide nano-platforms reduced by a green/biocompataible reductant,J. Ind. Eng. Chem., 75, 271–284, doi: 10.1016/j.jiec.2019.03.038.

[3]   T. Prasad, S. Halder, S. S. Dhar, M. S. Goyat(2021) Epoxy/imidazole functionalized silica epoxy nanocomposites: Mechanical and fracture behaviour," Express Polym. Lett., 15(3), 203–223, doi: 10.3144/expresspolymlett.2021.19.

[4]   A. Abdelhussien, G. Yang, E. K. Hussein, L. Li, H. Al-Abboodi, B. Mohamad (2023) Analysis of The Mechanical Characteristics of Date Seed Powder-Based Composite Carbon Fiber Reinforced Polymers,Facta Univ. Ser. Mech. Eng.

[5]   B. Krishnakumar et al.(2020)Disulfide exchange assisted self-healing epoxy/PDMS/graphene oxide nanocomposites," Nanoscale Adv., 2(7), 2726–2730, 2020, doi: 10.1039/d0na00282h.

[6]   Yeasmin, F., Mallik, A. K., Chisty, A. H., Robel, F. N., Shahruzzaman, M., Haque, P., Ihara, H. (2021). Remarkable enhancement of thermal stability of epoxy resin through the incorporation of mesoporous silica micro-filler. Heliyon, 7(1).e05959DOI: 10.1016/j.heliyon.2021.e05959

[7]   M. Nawaz, N. Naeem, R. Kahraman, M. F. Montemor, W. Haider, R. A. Shakoor (2021) Effectiveness of epoxy coating modified with yttrium oxide loaded with imidazole on the corrosion protection of steel," Nanomaterials,. 11(9), 1–16, 2021, doi: 10.3390/nano11092291.

[8]   D. Martinez-Diaz, A. Cortés, A. Jiménez-Suárez, S. G. Prolongo (2022) Hardener Isomerism and Content of Dynamic Disulfide Bond Effect on Chemical Recycling of Epoxy Networks," ACS Appl. Polym. Mater., 4(7), 5068–5076, doi: 10.1021/acsapm.2c00598.

[9]   K. Dutta and N. Karak (2024) Exchangeable disulfide bond containing highly flexible epoxy vitrimers with shape-memory, self-healing, and UV shielding attributes," Polym. Adv. Technol., 35(1), e6286.

[10] X. Zhang, H. Lin, Y. Hu, D. Ding, F. Cai, Y. Wu (2023) Electric tree intrinsic self-healing epoxy insulating materials based on disulfide bond," Polym. Degrad. Stab., 218, 110567.

[11] Z.Li, J.Zhong, M.Liu, J.Rong, K.Yang, J.Zhou, H.He (2020) Investigation on self-healing property of epoxy resins based on disulfide dynamic links. Chinese Journal of Polymer Science, 38, 932-940.

[12] H. Y. Tsai, Y. Nakamura, T. Fujita, M. Naito (2020) Strengthening epoxy adhesives at elevated temperatures based on dynamic disulfide bonds," Mater. Adv., 1(9), 3182–3188, doi: 10.1039/d0ma00714e.

[13] A.de Luzuriaga, R.Martin, N.Markaide, A.Rekondo, G.Cabañero, J.Rodríguez, I.Odriozola (2016). Epoxy resin with exchangeable disulfide crosslinks to obtain reprocessable, repairable and recyclable fiber-reinforced thermoset composites. Materials Horizons, 3(3), 241-247.

[14] M. L. Henriksen, J. B. Ravnsbæk, M. Bjerring, T. Vosegaard, K. Daasbjerg, M. Hinge (2017) Epoxy Matrices Modified by Green Additives for Recyclable Materials," ChemSusChem, 10(14), 2936–2944, doi: 10.1002/cssc.201700712.

[15] S. K. Burhan (2017) Investigation of Mechanical and Thermal Behavior of Composite Material Filled Rice Husk Ash," Iraqi J. Mech. Mater. Eng., 17(4), 012009, DOI 10.1088/1757-899X/433/1/012009

[16] Z. A. R. A. H. Al Saadi, Z. K. Alobad, M. A. Akraa (2024) Effect of Modification With Polyether Polyol and Liquid Silicon Rubber on the Mechanical Properties of Epoxy System," Kufa J. Eng., 15(3), 170–185, doi: 10.30572/2018/KJE/150310.

[17] A. Q. Saeed, Z. K. M. Al-Obad (2023) Investigates the Effect of MgO, h-BN, and Hybrid Nano Fillers on the Thermal, Electrical Properties and Hardness of an Epoxy Polymer," AIP Conf. Proc., 2830(1),030025, doi: 10.1063/5.0157171.

[18] S.Burhan, M.Abed, M.Salih (2019). Rice Husk Ash as a nano-filler to synthesize thermosetting polymer nanocomposites and evaluation of its tribological behavior. Kufa Journal of Engineering, 10(1), 78-91.

[19] B.Wang, Z.Li, X.Liu, L.Li, J.Yu, S.Li, Y.Dai (2023). Preparation of epoxy resin with disulfide-containing

curing agent and its application in self-healing coating. Materials, 16(12), 4440.

[20] Z.Li, J.Zhong, M.Liu, J.Rong, K.Yang, J.Zhou, H.He (2020). Investigation on self-healing property of epoxy resins based on disulfide dynamic links. Chinese Journal of Polymer Science, 38, 932-940.

[21] A.Horton (2014). Zinc Metallizing for External Corrosion Control of Ductile Iron Pipe. In Pipelines 2014: From Underground to the Forefront of Innovation and Sustainability. p. 1307-1318.

IZVOD

DISULFIDNE VEZE MODIFIKOVANE EPOKSIDNE SMOLE: MEHANIČKA, ADHEZIJA I SVOJSTVA HABANJA

Epoksid zauzima važno mesto u mnogim inženjerskim primenama, pa je neophodno poboljšati njegova svojstva kao što su čvrstoća prijanjanja, otpornost na habanje i žilavost. U ovoj studiji, epoksid je modifikovan ugradnjom disulfidnih veza. Sloj prevlake je pripremljen dodavanjem etanol disulfideto epoksidne smole u različitim težinskim procentima: 0,5, 1,5, 2,5 i 3,5 tež.%. Infracrvena spektroskopija sa Furijeovom transformacijom je korišćena za istraživanje bilo kakve hemijske interakcije. Analiza diferencijalne skenirajuće kolometrije (DSC) pruža vredne informacije o termičkom ponašanju pripremljenog epoksidnog premaza. Ispitivana je zatezna, tvrdoća, udarna žilavost, žilavost loma i svojstva adhezije. Ponašanje pri habanju je ispitano pomoću pin-on-disc uređaja. Rezultati pokazuju da epoksid koji sadrži disulfidne veze (EP+SS) nudi odličnu otpornost na udar sa dobrom otpornošću na lom u poređenju sa čistim epoksidom. Pored toga, rezultati ispitivanja kontaktnog ugla pokazuju poboljšanje vlaženja između modifikovanog sloja epoksidnog premaza i čelične podloge. Čvrstoća adhezije epoksidnog sloja je poboljšana ugradnjom etanol disulfida u epoksidnu smolu koja dostiže superiornu vrednost. U poređenju sa čistim epoksidom, koeficijent trenja (EP+SS) je veoma smanjen i dostigao je oko 89%, a stopa habanja je smanjena za 76% kako se povećava procenat dodatog etanol disulfida.
Čvrsti superiorni adhezivni sloj epoksidnog premaza sintetizovan je ugradnjom jedinjenja etanol disulfida u epoksidnu smolu.
Ključne reči: *disulfid, epoksid, habanje, adhezija, dinamičke veze.*

Salsabeel Kareem Burhan: https://orcid.org/0000-0001-8879-8296
Zoalfokkar Kareem Alobad: https://orcid.org/0000-0002-2545-4960
AmmarEmad Al-kawaz: https://orcid.org/0000-0001-9289-2023

Sahil Jangra[1,], Bhushan Kumar[2], Jaishree Sharma[1],
Subhankar Das[2], Manjeet Singh Goyat[1,3]*

[1]*Cluster of Applied Sciences, School of Advanced Engineering, UPES,
Dehradun, India, [2]Cluster of Mechanical Engineering, School of
Advanced Engineering, UPES, Dehradun, India, [3]Mads Clausen
Institute, NanoSYD, University of Southern Denmark (SDU), Denmark*

MXenes: Synthesis, properties, and applications in advanced energy storage technologies

ABSTRACT

MXenes have emerged as highly promising materials in the field of advanced energy storage technologies, owing to their distinctive properties and versatile applications. This review offers a comprehensive analysis of MXenes, focusing on their synthesis methods, fundamental properties, and applications in rechargeable batteries and supercapacitors. In response to increasing global energy demands, MXenes present compelling solutions due to their exceptional electrical and electrochemical characteristics. These include high conductivity, large surface area, hydrophilicity, and a unique two-dimensional structure comprising metal carbides, nitrides, and carbonitrides. Additionally, this review incorporates a detailed bibliometric analysis using computational tools such as VOSviewer, which examines the global landscape of MXene research spanning from 2012 to 2024. This analysis identifies collaborative trends among different countries, institutions, authors, and journals, highlighting leading research areas. Overall, this review underscores the significant potential of MXenes in advancing energy storage technologies. It provides insights into future research directions and practical applications that could effectively meet the growing energy demands driven by electric vehicles and portable electronics.
Keywords:*MXene, 2D materials,energy storage, supercapacitor, bibliometric analysis*

1. INTRODUCTION

The reliance on fossil fuels for energy production presents significant challenges to the global economy and environment [1]. The depletion of these resources and the effects of climate change are pressing issues for modern society. To meet the growing energy demand sustainably, it is essential to develop efficient and affordable energy production and storage technologies. Unlike geo-thermal energy, which is limited to specific loca-tions, tidal and wave energy sources offer more consistent and abundant resources due to their steady flow [2.3]. However, the collection and transmission of this energy remain major obstacles. Renewable sources like wind and solar energy are often inconsistent, making energy storage crucial for capturing and utilizing excess power. Resear-chers are therefore focusing on developing advan-ced energy storage systems with high capacity and superior cyclic performance. Supercapacitors and

high-density batteries are expected to be pivotal in powering portable electronics such as smart-phones, tablets, laptops, and hybrid vehicles [4,5]. Recently, two-dimensional (2D) materials have garnered significant research interest due to their exceptional electrical properties compared to bulk materials [6]. While graphene has been extensively studied for its mechanical stability and high conductivity, other 2D materials like transition metal dichalcogenides (TMDs), hexagonal boron nitride, and metal oxides are also being investigated for their potential in flexible electronics and energy storage applications [7-10].

MXenes, a novel class of 2D materials composed of early transition metal carbides and/or nitrides, were first identified about a decade ago at Drexel University [11-13]. Fig. 1(a) shows the periodic table with MAX phases and MXene compositions [14]. These materials are notable for their versatile properties, including metal-like conductivity, high mechanical strength, and hydrophilicity, which stem from their surface-terminated functional. MXenes are produced by chemically etching the A element from their 3D MAX phase precursorsas depicted in Fig. 1(b), where M-X bonds are much stronger than M-A

bonds.Fig. 1(c) displays the three atomic structures of MXenes—M_2X, M_3X_2, and M_4X_3—demonstrating their potential for a wide range of applications. Their distinctive properties underscore their significant potential across various fields [14-18].

A bibliometric assessment of such promising 2D materials serves as a reference for identifying their uniqueness and potential for future developments and can act as a guiding resource in the evolution of research on trending materials[19].Bibliometricstudies employ statistical techniques to evaluate sources including books, papers, and other publications. Bibliometric software was used to analyse individual performance and visualise publications using information such as titles, dates, authors, addresses, and references.VOSviewer software has potential to create and visualise organisations, nations, authors, keywords, journals; including bibliographic coupling, co-citation, and co-authorship relationships.
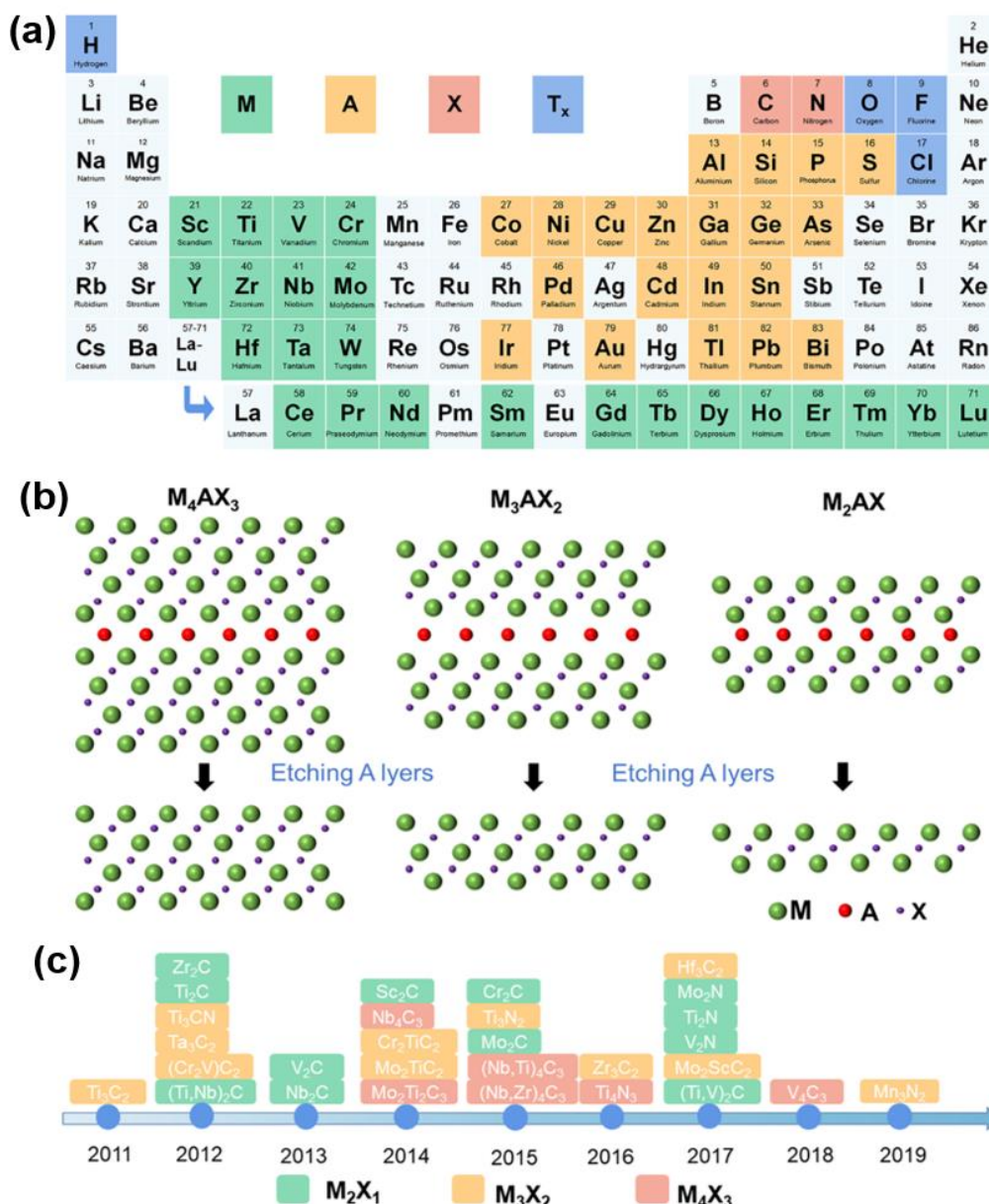
Figure 1. (a) Periodic table showing MAX phases and MXene compositions. (b) Schematic of etching MAX phases to produce three types of MXenes: M_2X, M_3X_2, and M_4X_3. (c) Timeline of advancements in MXene synthesis. (a-c) (Reprinted with permission from Ref. [14].Biosensors, © 2023 MDPI).

Despite significant progress in MXene-based energy storage research, a comprehensive scientometric study has been lacking. To fill this gap, this review utilizes VOSviewer software to

perform an in-depth scientometric analysis of the field. The analysis examines data from diverse sources—such as countries, organizations, and authors—to uncover key research trends and focus areas. The review provides a thorough overview of MXenes, including their synthesis, properties, and applications in supercapacitors and rechargeable batteries. With their exceptional electrical and physical properties, such as high conductivity and large surface area, MXenes offer promising solutions for addressing the increasing global energy needs. The bibliometric analysis spans research from 2012 to 2024, revealing collaboration patterns and leading research themes. This review highlights MXenes' potential to advance energy storage technologies and suggests future research directions and practical applications to support the development of electric vehicles and portable electronics.

2. SYNTHESIS OF MXENES

MXenes are generally derived from their parent MAX phases, which have the formula $M_{n+1}AX_n$ (where M is an early transition metal, A is an A-group element, and X is either carbon or nitrogen)[20]. The main synthesis methods for MXenes includes:

2.1. Hydrofluoric acid (HF) etching

The most common technique involves treating the MAX phase with hydrofluoric acid (HF) to selectively remove the A layer. The MAX structure has interconnected "A" layers. MXenes are produced by etching Al from the MAX phases, which are typically easy to handle and store (Fig. 2(a-c)).Forinstance, etching Ti_3AlC_2 with HF results in $Ti_3C_2T_x$MXene. To perform HF etching, the MAX phase is added to a hydrofluoric acid solution and continuously stirred. The resulting suspension is then repeatedly washed with deionized water until the black supernatant remains stable after centrifugation (Fig. (2d)). Finally, the sediment is dissolved in deionized water and sonicated for an hour[21].SEM images reveal the structure of Ti_3AlC_2 (MAX) powder Fig.(2e) and the multilayered morphology of $Ti_3C_2T_x$ after etching Fig.(2f). Additionally, MXene flakes derived from a colloidal solution of MILD-$Ti_3C_2T_x$ are also shown in Fig.(2g). A recent study found that low HF concentration leaves A-layer atoms unetched, while high HF concentration destroys or dissolves the MAX phase. Due to the toxicity and corrosiveness of HF, researchers are exploring alternative MXene synthesis methods [22].

2.2. In-situ HFetching

To eliminate the need for direct handling of HF, a combination of a fluoride salt (such as LiF) and hydrochloric acid (HCl) is used to generate HF in situ. This method enhances safety and provides better control over the etching process. Fig. 2(h) illustrates the synthesis of Ti_3CNT_xMXene, which was achieved by selectively etching the Ti_3AlCN MAX phase using aHCl and LiF etching process. Following the etching process, the aluminum layers were successfully removed, resulting in a multilayered, accordion-like Ti_3CNT_x structure, as shown in the SEM image (Fig.2i) [23]. In earlier research, a one-step etching and intercalation method was employed, utilizing MXene's affinity for cations. $Ti_3AlC_2$was gradually added to HCl mixed with LiF and stirred at 40°C for 45 hours. The precipitate was washed, centrifuged to increase its pH, yielding a monolayer of MXene. This clay paste can be molded for electrodes and supercapacitors[24]. Additionally, HCl and KF were used to etch the MAX phase of Ti_2AlN, allowing K^+ and H_2O to intercalate the Ti_2Nnanosheets, resulting in well-spaced and uniform Ti_2NMXene. This one-step process is simpler, gentler, and safer for obtaining monolayer MXenes[25].

2.3. Molten Salt Method

In this method, the MAX phase is etched with molten salts such as $ZnCl_2$ at elevated tempera-tures. This approach produces MXenes with fewer defects and enhanced crystallinity. The process is highly efficient, typically finishing within half an hour. However, the need for high temperatures can be a disadvantage[26]. Recently, large batches of $Ti_3C_2T_x$MXene (20 g and 60 g) were synthesized from its MAX phase using a Lewis acid molten $CuCl_2$/NaCl/KCl mixture at 700°C in a muffle furnace under acn air atmosphere [27].

2.4. Electrochemical Etching

This approach uses an electric current in a fluoride-containing electrolyte to precisely control the etching process. Recently, electrochemical etching has emerged as a key method for producing MXene from the MAX phase by selectively removing nanolaminate contents like carbide-derived carbon (CDC) and carbon/sulfur. In Ti_3AlC_2, applying a constant potential allows chloride ions (Cl^-) to bind with Al, breaking Ti–Al bonds and forming $AlCl_3$, which opens grain boundaries for Cl^- penetration and other species intercalation. However, protective CDC layers limit large-scale production. Using intercalants like tetramethyl ammonium ion can help, but their toxicity is a concern. To address this, thermally assisted electrochemical etching has been proposed[28]. This method is used to synthesize MXenes such as Ti_2CT_x, Cr_2CT_x, and V_2CT_xin HCl electrolyte, offering an environmentally friendly approach[29].

2.5. Chemical Vapor Deposition (CVD)

Chemical Vapor Deposition (CVD) is a novel technique for synthesizing MXenes, offering precise control over their composition and thickness. This involves introducing volatile precursors into a reaction chamber, where they decompose or react on a substrate to form MXene structures [30]. CVD produces high-quality, uniform MXene films with excellent crystallinity and minimal defects. The properties of MXenes can be finely tuned by adjusting parameters like temperature, pressure, and precursor flow rates, making CVD ideal for developing advanced MXenes for electronics and energy storage. Recently, α-Mo_2C

was prepared by CVD from methane over a bi-layer copper foil substrate on molybdenum foil. CVD is effective for fabricating monolayer carbides and transition metal nitrides, producing MXenes with greater crystallinity than those made by etching. It also allows for the creation of MXene heterostructures and various stoichiometries[31]. The template method is another approach for preparing MXenes, yielding larger quantities. For instance, N-doped Mo_2C sheets were prepared using MoO_2 as a template, achieving perfect crystallinity and morphology by calciningMoO_2 at 700°C with dicyandiamide, introducing C and N atoms to form N-doped Mo_2C sheets [32].
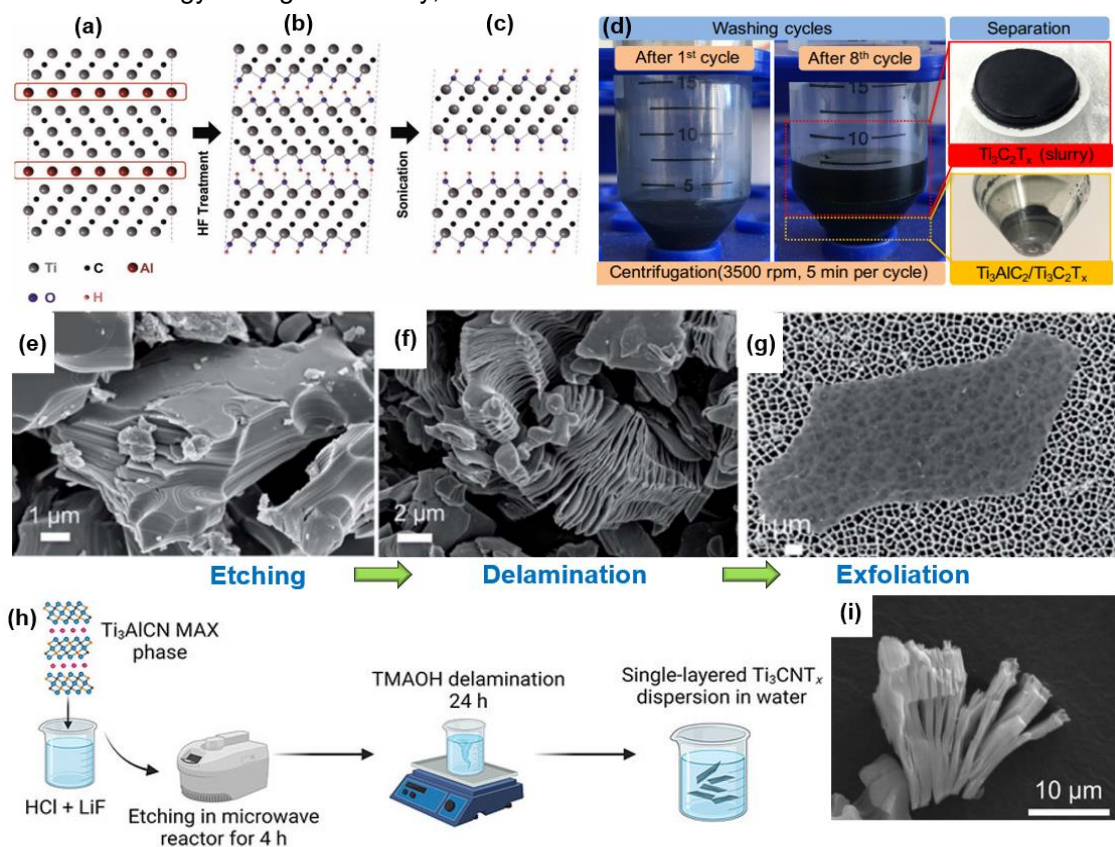
Figure 2. Exfoliation of Ti_3AlC_2: a) Ti_3AlC_2structure, b) OH replacing Al after HF reaction, c) Nanosheets separating after sonication. (a-c)(Reprinted with permission from Ref. [70]Advanced materials, Copyright © 2011, Wiley-VCH);(d) MILD-$Ti_3C_2T_x$powder post first and eighth wash cycles; SEM images show (a) Ti_3AlC_2 (MAX) powder with a compact layered structure and (b) multilayered $Ti_3C_2T_x$; (g) MXene flakes obtained from a colloidal solution of MILD- $Ti_3C_2T_x$. (d-g)(Reprinted with permission from Ref.[71] Chemistry of Materials, © 2017 American Chemical Society); (h) Ti_3CNT_xMXene synthesis diagram (i) Accordion-like Ti_3CNT_x layers. (h-i)(Reprinted with permission from Ref.[23]. Applied Materials & Interfaces, © 2023 American Chemical Society).

3. PROPERTIES

MXenes are two-dimensional materials known for their exceptional properties, making them highly versatile for various applications. They exhibit metallic-level electrical conductivity, high mechanical strength, flexibility, and excellent

thermal conductivity. Their hydrophilic surfaces can be functionalized with different attributes chemical groups, enhancing their adaptability. These make MXenes ideal for energy storage devices, sensors, electromagnetic interference shielding, and catalysis. Fig. 3(a) illustrates a summary of MXeneproperties[33].
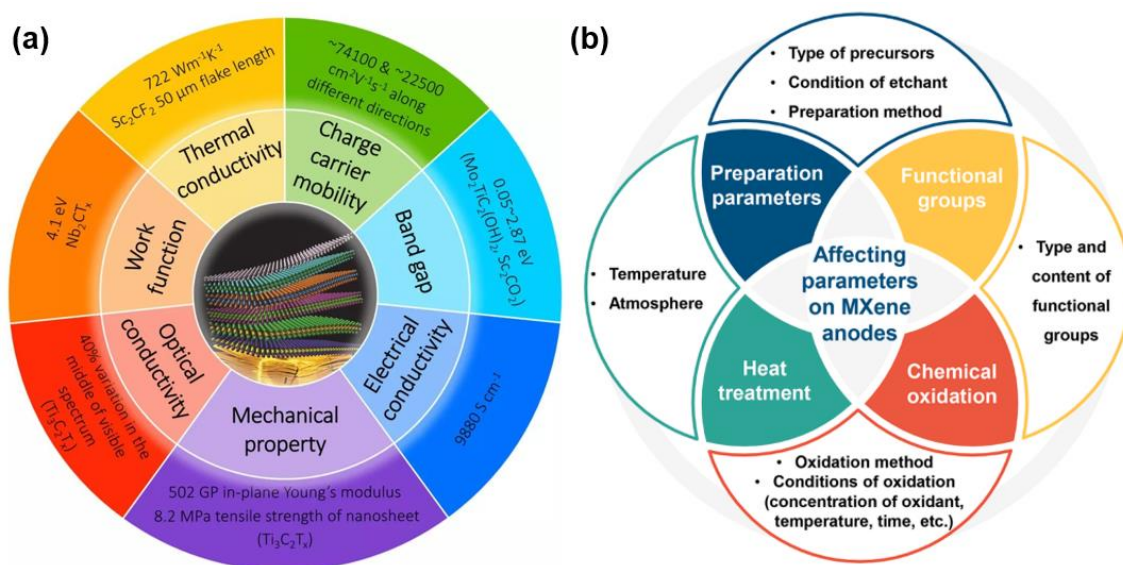
Figure 3. Overview of MXene properties (Reprinted with permission from Ref. [33]; (a) Energy & Environmental materials, Copyright © 2019, Wiley-VCH) (b) Overview of the factors influencing the electrochemical performance of MXene anodes. (b) (Reprinted with permission from Ref. [52]. Journal of Energy Storage, Copyright © 2022, Elsevier).

3.1. Surface termination

Density functional theory (DFT) indicates that MXenes are completely terminated with functional groups, with strong negative energy reflecting a robust bond to transition metals. MXenes produced by etching MAX phases in fluoride-containing acids feature –OH, –F, and –O– groups. Research also found significant energy for –Cl and –S groups. Fluoride-free synthesis of Ti_3C_2 was achieved via anodic corrosion of Ti_3AlC_2. Functional groups can attach in three ways: on top of metals, in hollow sites on top, and in hollow sites within stacked X layers. Bond lengths for Ti–H, Ti–O, and Ti–F are 0.97, 1.9, and 2.1 Å, respectively, with –O– termination showing the highest adsorption energy of 7.7 eV. Synthesizing MXenes without terminations remains challenging despite various methods. Techniques like X-ray photoelectron spectroscopy, NMR, Raman spectroscopy, surface acoustic probing, and neutron scattering are used to examine MXene surface terminations.

3.2. Conductivity of MXene

MXenes exhibit exceptional electrical conductivity, surpassing all synthetic 2D materials and being about ten times higher than reduced graphene oxide (rGO). Their conductivity, ranging from 1 to 15,000 S cm^{-1}, can be tailored by adjusting synthesis methods, post-etching conditions, ultrasonication, storage environments, and surface chemistry [34]. Understanding these factors is essential for producing high-conductivity MXene materials. MXenes' electrical conductivity can be improved by modifying their surface functional groups or elemental composition [35]. The electrical conductivity of functional group-terminated MXenes$Ti_3C_2T_x$ exhibit metal-like properties and electrical conductivities as large as 4600 S cm^{-1}[36].

3.3. Optical properties of MXenes

Excellent candidates for optical devices include 2D materials and their heterostructures. Additionally, they offer a great platform to improve light-matter interactions due to their efficient integration with nanophotonic structures and inherent polaritonic resonances [37]. First-principles density functional theory has been used in the study of optical properties of Ti_3C_2MXene. The outcomes demonstrate the significant impact of surface functionalization affecting the optical characteristics of MXene[38]. By varying the types and ratios of surface functional groups, MXenes' optical characteristics can be changed. The thickness, size, and modification process of MXenes all have a significant impact on the amount of UV-Visible light they absorb. Light transmittance of 5 nm $Ti_3C_2T_x$MXene films achieved 91.2% in the 300–500 nm range; as the thickness of film increase to 70 nm, light transmittance decreased to 43.8% [39]. Other applications have been proven using MXenes' optical properties, including effective light to heat conversion, surface enhance Raman scattering (SERS) [40], plasmonic broadband absorber, and photonic diodes [41]. The optical properties of other

MXenes have not yet been researched; however, titanium carbide, $Ti_3C_2T_x$, has been the MXene that has been explored the most in the majority of these investigations.

3.4. Magnetic Properties of MXenes

MXenes exhibit a wide range of chemical and structural variations, making them highly promising for intrinsic 2D magnetism. The d-orbitals of transition metals in MXenes can occupy bonding (σ) or antibonding (σ*) states formed by M-X and M-T bonds. Typically, bonding states are filled and antibonding states remain empty, assuming minimal oxidation. The magnetic behavior is attributed to electrons in the nonbonding d-orbitals [42]. Khazaei et al. [43] were the first to predict ferromagnetic ground states in pure $Cr_2C$and Cr_2NMXenes, which are particularly valuable for spintronics applications. While covalent M-X and M-T bonds generally lead to nonmagnetic ground states due to their strength, some studies have discovered intrinsic magnetism in both unfunctionalized and functionalized MXenes, including Ti_2C and Ti_2N [44]. MXenes are promising candidates for 2D magnetic materials that can operate in ambient conditions, offering significant magnetic anisotropy, intrinsic and controllable magnetic ordering, and thermal stability. Despite advancements in predicting the magnetic properties of MXenes, there remain many intriguing challenges and opportunities in this field[45].

4. ENERGY STORAGE APPLICATION

MXenes, a family of two-dimensional transition metal carbides and nitrides, have attracted significant attention recently due to their exceptional electrical conductivity, high surface area, and customizable chemical properties [46–48]. These unique attributes make MXenes highly suitable for various energy storage applications, including supercapacitors and batteries[49]. Compared to other materials like graphene, metal oxides, and conducting polymers, MXenes exhibit superior ion intercalation and diffusion capabilities, essential for high-per formance energy storage[50]. Their ability to intercalate various ions, combined with excellent mechanical flexibility and chemical stability, facilitates the development of high-performance, durable energy storage devices[51]. Moreover, the versatile surface chemistry of MXenes allows for functionalization, further enhancing their electrochemical properties. Fig. 3(b) illustrates various factors affecting the electrochemical performance of MXene anodes [52]. As research advances, MXenes are poised to revolutionize energy storage, providing sustainable and efficient solutions for future energy needs.

4.1. Supercapacitor

Supercapacitors offer high power output, rapid charging, and long cycle life [53]. They are mainly classified into Electrochemical Double-Layer Capacitors (EDLCs), which store energy through ion accumulation, and pseudocapacitors, which rely on reversible Faradaic reactions [54]. MXenes, known for their mechanical flexibility, high energy density, and excellent electrochemical performance, have become popular electrode materials [55]. Research on MXenes has surged, especially in 2021, with a focus on MXene-based composites such as conductive polymers, metal oxides, and carbon nanostructures. About 34-38% of these studies aim to improve cycle life, energy density, and oxidation resistance while addressing MXene stacking issues [56].

The energy storage performance of MXene-based materials is influenced by various factors[55]. One key factor for supercapacitors is the sheet size of MXenes synthesized through the etching process. Larger MXene sheets are generally suitable as electrode materials; however, their longer etching times lead to lower capacitance values, typically between 10-20 Fg^{-1}[57]. Smaller MXene sheets improve supercapacitor performance by providing more electrochemically active sites during charge-discharge cycles. However, the smaller size increases the risk of oxidation at the sheet edges [28]. A recent study explored how the size of Ti_3C_2MXene flakes affects supercapacitor performance. The flakes, produced via sonication and density gradient centrifugation, had lateral sizes from 0.1 to 5 μm. By employing centrifugation, they produced MXene sheets with various lateral sizes into monodisperse fractions. The best capacitance value, 290 Fg^{-1} at 2 mV/s, was achieved with MXene flakes approximately 1 μm in size, demonstrating that lateral size significantly impacts performance [57].

The performance of supercapacitors depends on the electrolyte used. Electrolytes can be aqueous, organic, ionic, or solid [58]. Each type affects the potential window and overall performance. In acidic environments, MXene-based materials exhibit higher pseudocapacitance, leading to greater volumetric capacitance. Sulfate-based electrolytes like Na_2SO_4 and K_2SO_4promote EDLCbehavior, though they are less suitable for practical devices. Gel electrolytes such as PVA/Na_2SO_4 are often used but can suppress the voltage window and reduce electrochemical performance [59, 60]. Organic electrolytes, which dissolve well in solvents like acetonitrile, can improve the potential window but are costly, toxic, and flammable. Ionic electrolytes, such as EMI-TFSI, enhance supercapacitor performance by

interacting with pores and adjusting interlayer spacing. Studies have shown that MXene interlayer spacing decreases under positive potential and increases under negative potential, influenced by the intercalation and deintercalation of ions [28,61]. A recent study showed clay-like $Ti_3C_2T_x$MXenesupercapacitor electrodes in H_2SO_4achieved 245 Fg^{-1} at 2 mV/s and retained capacitance after 10,000 cycles at 10 A/g[62].

MXenes' rich chemistry and surface functionalization boost electrochemical activity but worsen self-discharge in supercapacitors. Researchers are focusing on MXene-based

composites to enhance performance [34].Enhancing capacitance and rate performance in flexible supercapacitors' carbon-based electrodes is vital. $Ti_3C_2T_x$MXene/CNF electrodes were made via electrospinning and carbonization Fig.4(a-d). Fig. 4(e) shows medium-sized MXene/CNF with a porous, network-like structure formed by nanoscalefibers. $Ti_3C_2T_x$MXene/CNF electrodes achieved 90 Fg^{-1}at 300 mV/s, 2.3 times larger than pure PAN-derived CNF. Fig.4(f) also showed 98% retention after 10,000 cycles and excellent flexibility. These MXene/CNF electrodes hold promise for flexible electronics [63].
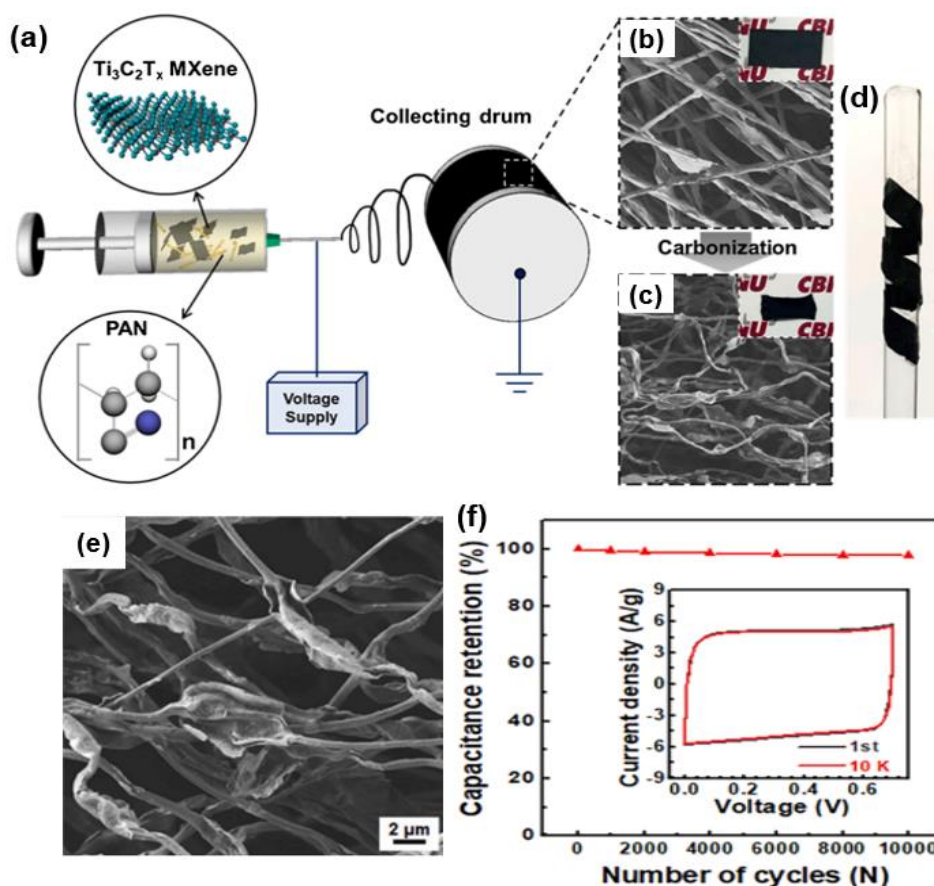
Figure 4. (a) Electrospinning schematic, (b) and (c) show nanofibers post-spinning and carbonization with TEM insets, (d) flexible electrode wrapped around a glass rod; (e) Morphology of electrospun medium-sized $Ti_3C_2T_x$MXene/carbon nanofibers; (f) Cyclic stability. (a-f) (Reprinted with permission from Ref. [63]. Applied surface science, Copyright © 2021, Elsevier).

Metal oxides are of great interest for their pseudocapacitive behavior and high performance. Nanocrystalline ε-MnO_2 whiskers were synthesized on MXene surfaces to create nanocomposite electrodes for aqueous pseudocapacitors Fig. 5(a). A specific capacitance of 212 Fg^{-1} was achieved for the composite (Fig. 5b). These ε-MnO_2/MXene supercapacitors showed ~88% capacitance retention after 10,000 cycles (Fig. (5c)), leveraging

MnO_2's high capacitance and MXenes' conductivity and stability[64].

Furthermore, though conjugated polymers like polyaniline and polypyrrole are used in flexible supercapacitors for their high pseudocapacitance and flexibility, their structural instability limits practicality. A new approach combines PDT with MXene ($Ti_3C_2T_x$) to form a freestanding hybrid film, enhancing cycling performance (Fig. 5d). This

hybrid layer shows a dense, granular structure on Ti₃C₂Tₓ-FTO (Fig. 5e). The supercapacitor exhibits good charge-discharge symmetry (Fig. 5f) and flexibility, with 10,000 cycles of 0–90° bending (Fig. 5g). PDT enhances charge transport and stability through strong bonds with Ti₃C₂Tₓ[65].
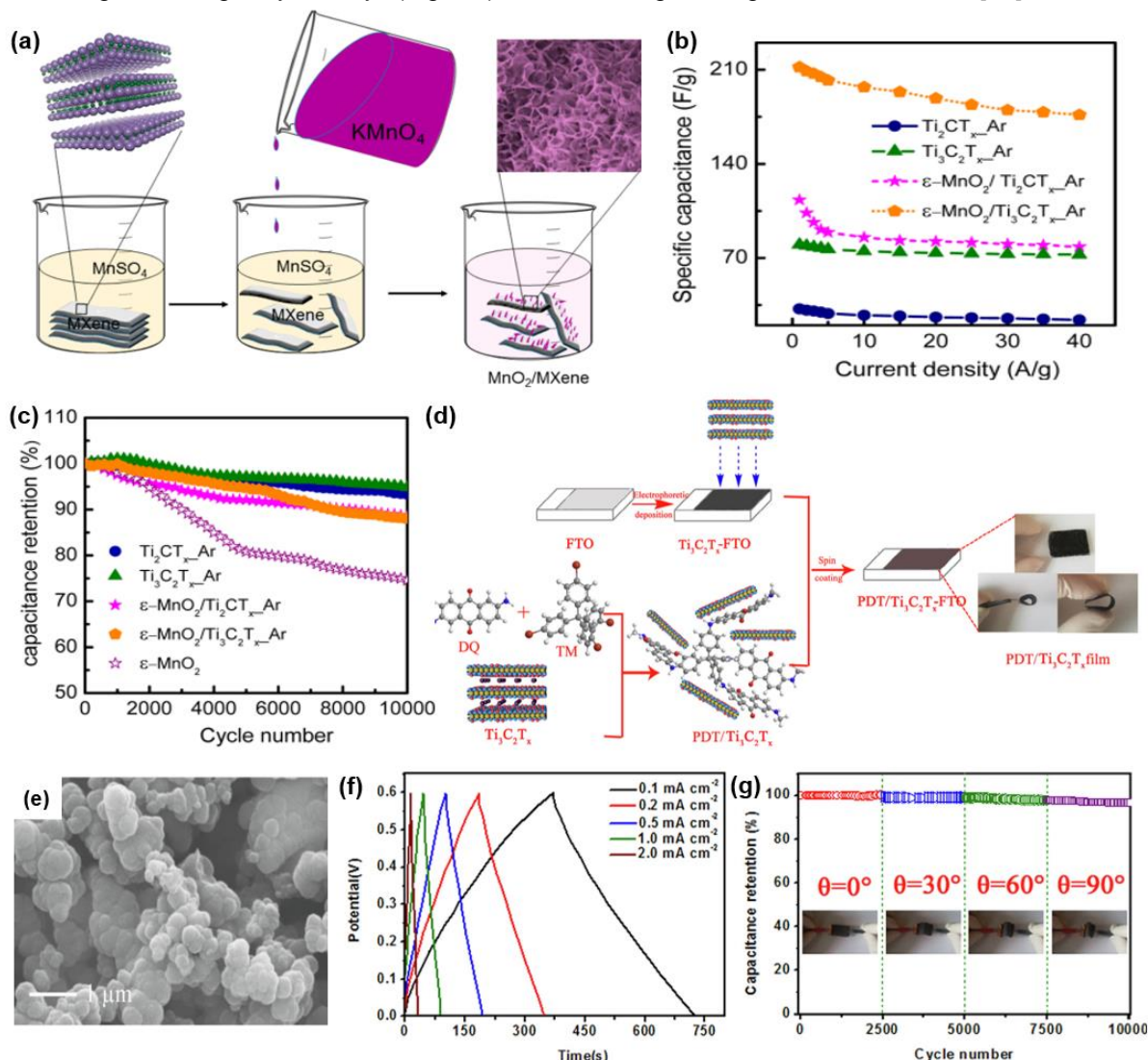
Figure 5. (a) MnO₂/MXene composite synthesis schematic, (b) specific capacitances of MXene and metal oxide/MXenesupercapacitors at various current densities, (c) cycling performance of supercapacitors at 5 A/g over 10,000 cycles. (a-c) (Reprinted with permission from Ref. [64]. Applied Materials & Interfaces, © 2016 American Chemical Society). (d) PDT/Ti₃C₂Tₓ film electrode fabrication schematic, (e) SEM images of PDT/Ti₃C₂Tₓ film, (f) GCD curves of PDT/Ti₃C₂Tₓsupercapacitor, (g) cycling performance under 10,000 bends at four angles. (d-g) (Reprinted with permission from Ref. [65]. Chemical Engineering Journal, Copyright © 2019, Elsevier).

4.2. Battery

MXene-based batteries represent a cutting-edge development in energy storage technologies, leveraging the unique properties of MXenes—two-dimensional transition metal carbides, nitrides, and carbonitrides. These materials boast high electrical conductivity, robust mechanical strength, and customizable surface chemistries, making them exceptional candidates for battery electrodes. The layered structure of MXenes enables efficient ion intercalation, significantly enhancing charge storage capacity. Recent advancements in this field have focused on optimizing MXene performance through the development of composite materials, surface modifications, and structural engineering, addressing key challenges such as scalability and long-term stability. Consequently, MXene-based batteries show immense potential for advancing lithium-ion, sodium-ion, potassium-ion, and zinc-ion battery technologies, positioning them as crucial

components in the future landscape of sustainable energy storage solutions.

$Ti_3C_2T_x$ has gained attention as an anode material for LIBs. For the first time, Ti_2CO_xMXene's Li-ion storage capability was demonstrated, showing about five times higher reversible capacity than Ti_2AlC MAX at 0.1C. Its higher surface area is key

to its enhanced capacity [66]. Furthermore, $Ti_3C_2T_x$ anodes for LIBs were prepared using HF alone and HF followed by DMSO intercalation. DMSO-treated $Ti_3C_2T_x$ had a first discharge capacity of 264.5 mAh/g at 1C, compared to 107.2 mAh/g for untreated $Ti_3C_2T_x$, highlighting the improved Li-ion storage with increased interlayer spacing [67].
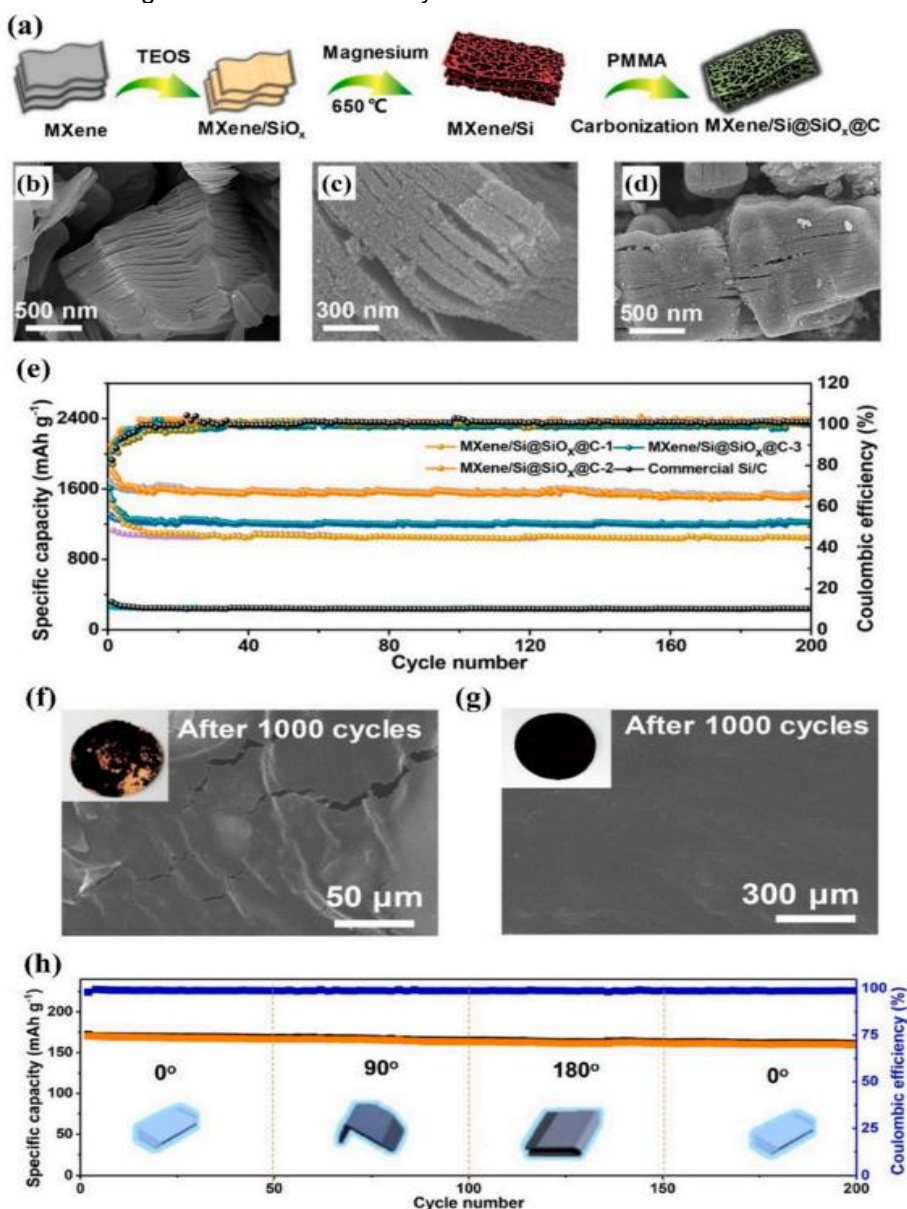
Figure 6. (a) Schematic of $Ti_3C_2T_x$/Si/SiO$_x$/C synthesis process, (b) SEM image of MXene, (c) SEM image of $Ti_3C_2T_x$/Si composite, (d) SEM image of $Ti_3C_2T_x$/Si/SiO$_x$/C composite, (e) cyclic stability at 0.2C, (f) SEM image of Si/C electrode after 1000 cycles at 10C, (g) SEM image of $Ti_3C_2T_x$/Si/SiO$_x$/C after 1000 cycles at 10C, and (h) cyclic stability. (a-h) (Reprinted with permission from Ref. [68]. ACS Nano, © 2019 American Chemical Society).

A recent study developed a $Ti_3C_2T_x$/Si/SiO$_x$/C anode for LIBs. Fig. 6 shows its preparation and performance. $Ti_3C_2T_x$ mixed with TEOS, heat-treated under H_2/Ar, and PMMA pyrolysis formed the composite (Fig. 6a). The 74.3 wt% Si

composite achieved 1674 mAh/g at 0.2C and 1547 mAh/g after 1000 cycles at 10C (Fig. 6d). SEM images showed $Ti_3C_2T_x$/Si/SiO$_x$/C maintained its structure, unlike Si/C which cracked (Fig. 6f-g). The NCM cathode displayed high retention (Fig. 6h),

and full-cell batteries reached 485 Wh/kg. MXene/Si and MXene/graphene anodes maintained over 1000 mAh/g after 100 cycles at 1 A/g[68].

Although LIBs are widely used, limited lithium resources pose challenges for meeting growing global demand. Developing alternative energy storage solutions is crucial. Sodium-ion batteries (SIBs) share similar electrochemical principles with LIBs and benefit from abundant sodium resources. SIBs could replace LIBs in applications such as large-scale power grids and renewable energy storage. A heterolayerMXene composite (MoS_2-in-Ti_3C_2) has shown promise as a Na-ion battery electrode, delivering a specific capacity of 450 mAh/g at 0.05 A/g and excellent cycling performance. This supports previous DFT results and literature, suggesting that expanded and functionalized MXenes are more effective at storing Na ions [69].

Future research on MXenes should explore their use in Na-ion and K-ion batteries, which offer advantages like abundant materials and lower costs. MXenes, with their excellent conductivity and high surface area, could be optimized for these chemistries to address challenges like larger ionic sizes and different interaction dynamics. Research should focus on how MXene-based anodes and cathodes impact energy density, cycling stability, and overall performance, potentially leading to more sustainable and cost-effective energy storage solutions.

5. METHODOLOGY

The scientific investigation requires, reliable data must be gathered from a reputable database to guarantee the accuracy of the analysis and the data used as input for the software. The available databases for record-keeping include Scopus, Dimension AI, ISI Web of Science, PubMed, and Google Scholar.

The Web of Science Core Collection database (http://apps.webofknowledge.com), which has extensive coverage and thorough content, was selected as the primary information source for this investigation. The **"MXene energy storage"** system was used to initiate the data collecting approach with "ALL" search fields. The data collection timeframe was set to 2012–2024, and 4371 documents were found using the search tools. The bibliometric information for the collected articles is processed by employing theMS Excel software.VOSviewersoftware was used for bibliometric analysis and computational mapping.Fig. 7.illustrates the complete search strategy, including the search string and keywords.The primary criteria used as the framework for the analysis are analysing the annual count of literature, type of literature, country wise contribution, Institute wise contribution, author contribution, most cited literature, journals and key words. A statistical technique used to group subjects that are similar and named cluster analysis.
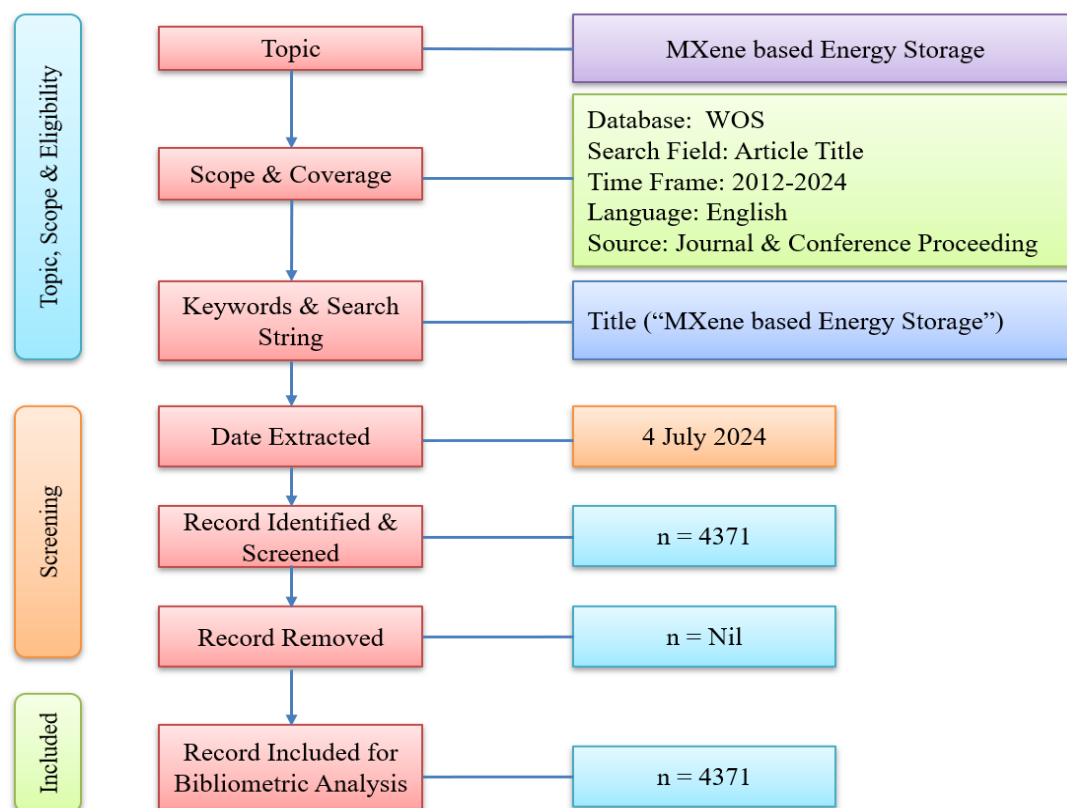
Figure 7. Flow chart of the search process.

6. RESULT AND DISCUSSION

6.1. An overview of scientific documents

The data set used for this study is gathered for the time frame from 2012 to 2024, and atotal of 4371 records were found. There are 73 contributing nations in total, 12216 authors across 376 journals, and 1846 participatinginstitutions.The frequently utilized words in this database were identified as 200 with 25 minimum number of occurrences of a keyword out of 7874 keywords. Fig. 8 illustrates a schematic representation of the annual growth of publications, which clearly shows the progressive establishment of the MXene-based energy storage research field.
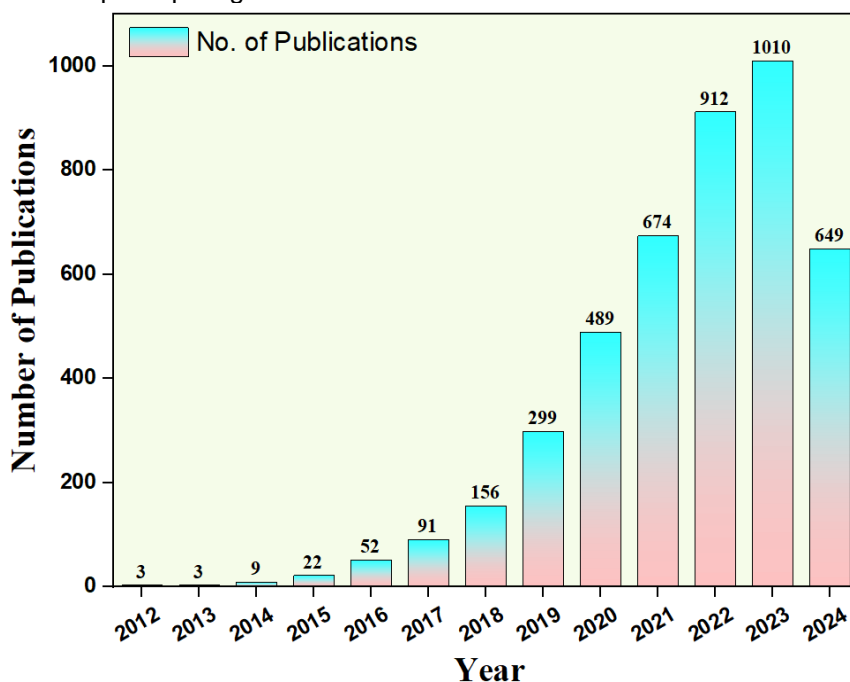
Figure 8. Number of Publications on topic "MXene based energy storage". Source: (http://apps.webofknowledge.com) (data accessed on 04 July 2024).

6.2. Assessment based on contributing nations

The top 10 nations fascinated by MXene-based energy storage devices are ordered according to the number of documents produced and are shown in Table 1. The top three nations identified are China, USA and India with 3003,559 and 360 documents produced, respectively. The number of citations gained by China is 141941, USA gained 86074 and India achieved 7298. China has a lower ratio of citations to documents (47) than the United States (154), which is relatively higher. The higher the number of citations to documents exhibits the quality of research produced by the involving countries in this state-of-the-art research going on MXene-based energy storage devices. The network visualisation of nations with minimum 5 publications are shown in Fig.9(a).

Table 1.Publication of MXene based energy storage research papers - top countries.

S. No.	Country	documents	citations	Citations to doc. Ratio
1	Peoples r china	3003	141941	47
2	USA	559	86074	154
3	India	360	7298	20
4	South Korea	331	11956	36
5	Australia	207	14457	70
6	Saudiarabia	169	11193	66
7	Pakistan	146	2695	18
8	England	103	4764	46
9	Germany	102	8567	84
10	Singapore	82	6671	81
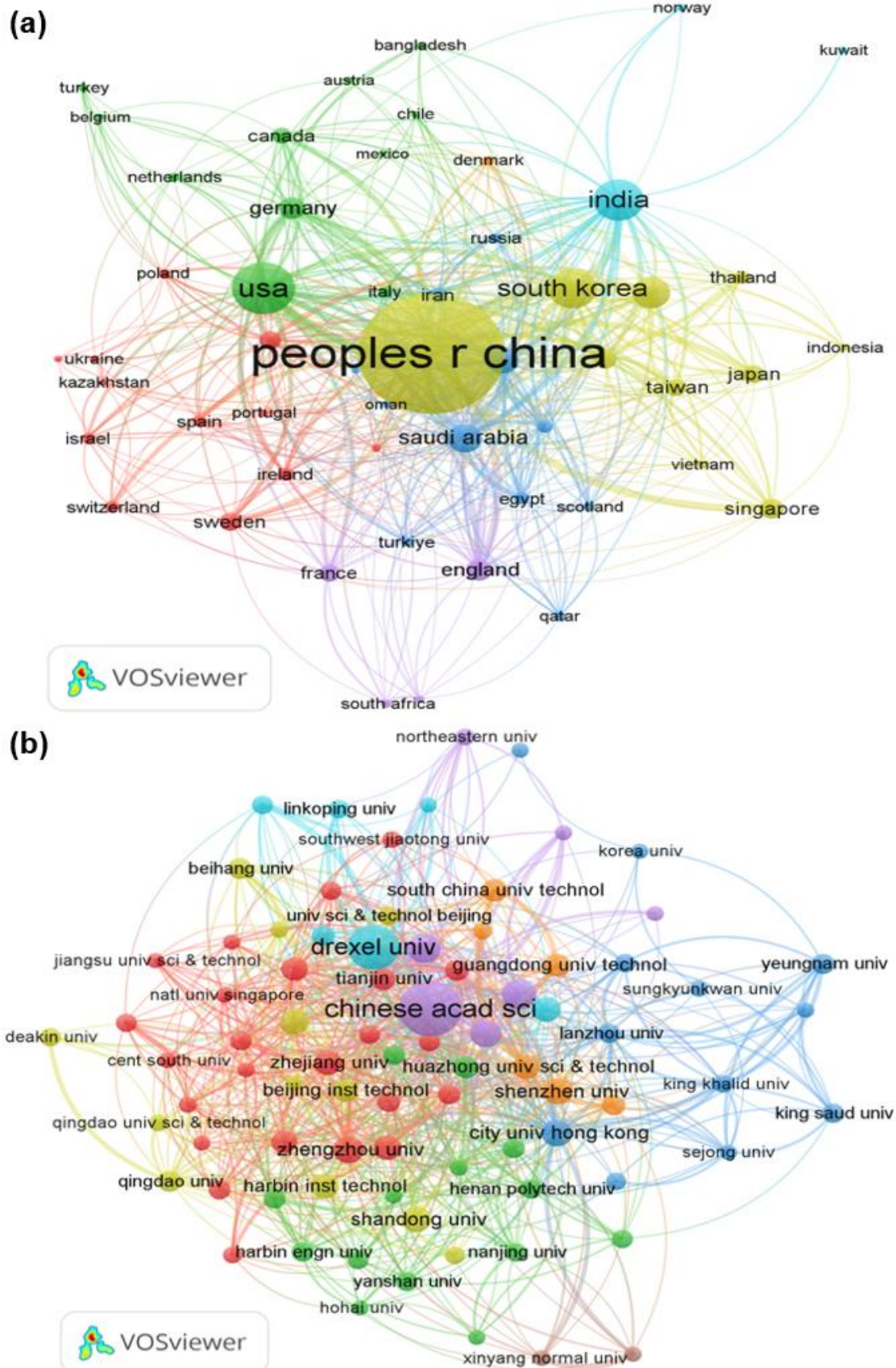
Figure 9.(a) Network visualisation map showing global collaboration among nations with minimum number of 5 documents of a country. (b) Cluster of institutions collaboration.

6.3. Assessment based on contributing Institutions

The top 10 institutions having the highest research activities that are engaged in the MXene based energy storage devices research field are tabulated in Table2. The top three institutions identified are China Acad. Sci., Drexel university and Univ.Sci.&Technol.China with 343,229 and 104 documents produced, respectively. The number of citations gained by ChinaAcad.Sci is 21072, Drexel university gained 67113 and Univ.Sci.&Technol.Chinaachieved 8535. Among them the Drexel university achieved the highest citations to document ratio as 293. Fig.9(b) illustrates a network of institutional collaboration.

Table 2.Ranking of Organizations based on MXene energy storage documents.

S. No.	Organization	documents	citations	Citations to Doc. Ratio
1	Chineseacadsci	343	21072	61
2	Drexeluniv	229	67113	293
3	Univsci&technol china	104	8535	82
4	Univ Chinese acadsci	100	8260	83
5	Jilinuniv	88	5771	66
6	City univhongkong	83	4596	55
7	Zhengzhouuniv	80	5691	71
8	Shandonguniv	79	6003	76
9	Shenzhenuniv	75	3842	51
10	Tsinghuauniv	74	4302	58

6.4. Assessment based on contributing Author

The documents based on MXene based energy storage devices are examined in accordance with the respective top 10 authors that performed these studies as tabulated in Table 3.

Table 3. Ranking of authors based on article contribution.

S.No.	Author	Documents	citations	Citations to Doc. Ratio
1	gogotsi, yury	198	63625	321
2	anasori, babak	59	24192	410
3	naguib, michael	40	15265	382
4	barsoum, michel w.	34	23613	695
5	zhang, wei	34	1605	47
6	wang, guoxiu	33	5221	158
7	zhang, peng	32	2588	81
8	wang, lei	31	1741	56
9	xu, bin	31	2830	91
10	alshareef, husam n.	30	5979	199

The authors are ranked in accordance with the number of articles published.The top three researchers in the respective field are GogotsiYury (198), Anasori,babak (59) and Naguib, Michael (40). During this bibliometric analysis, it was found that Gogotsi, Yury is top performing researcher in this field. Fig.10(a) illustrates a network of authors collaboration.

6.5. Assessment based on Keywords:

Use of relevant and appropriate keywords has a significant impact on the efficacy of document search.Among the enormous number of papers available, the keyword serves as a vital link that distinguishes the information sources. The top three keywords identified are MXene (1856), performance (975) and nanosheets (652). Top 10 keywords related to this research are tabulated in Table 4.A network of keywords occurrence is illustrated in Fig. 10(b).

Table 4. Ranking of keywords based on occurrences.

S. No.	keyword	occurrences
1	mxene	1856
2	performance	975
3	nanosheets	652
4	energy-storage	644
5	graphene	550
6	intercalation	489
7	mxenes	481
8	carbon	458
9	storage	456
10	supercapacitors	396
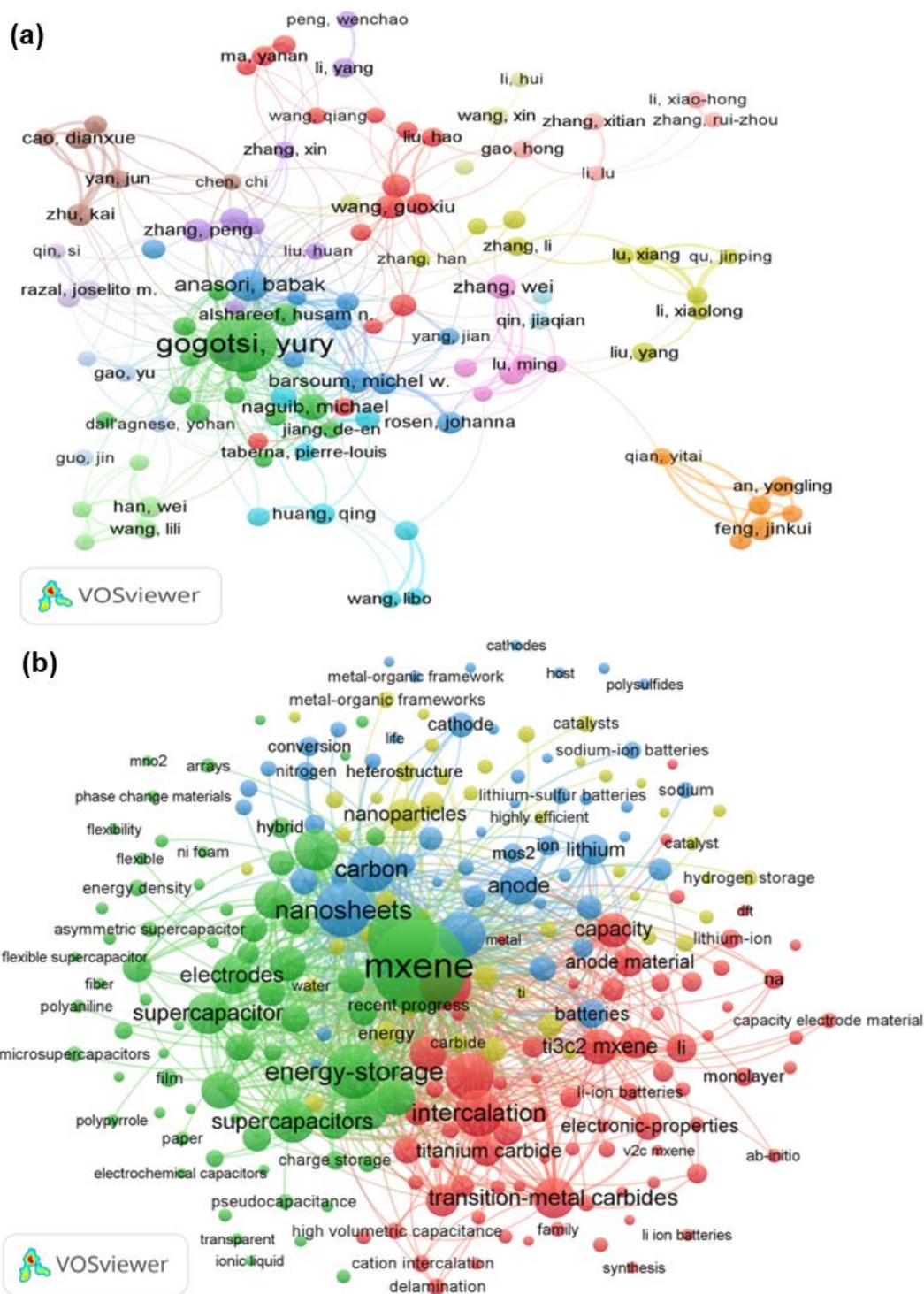
Figure 10.(a) Cluster of authors collaboration; (b) An illustration of co-occurrence of keywords.

7. CONCLUSIONS

This review comprehensively explores the field of MXenes, focusing on their synthesis methods, key properties, and applications in energy storage technologies. We have detailed various synthesis techniques and examined the unique properties of MXenes, including surface terminations, condu-

ctivity, optical and magnetic characteristics. The review further highlights the potential of MXenes in advancing energy storage solutions, particularly in supercapacitors and batteries. Despite substantial progress, a thorough scientometric study was previously lacking, and this review addresses this gap using VOSviewer software to analyze research

trends from 2012 to 2024. By examining data across countries, organizations, and authors, we reveal critical collaboration patterns and research themes. The findings underscore MXenes' promising role in meeting global energy demands and suggest future research directions to enhance their practical applications, particularly in the realms of electric vehicles and portable electronics.

8. REFERENCES

[1] P.Poonam, K. Sharma, A. Arora, S.K.Tripathi(2019) Review of supercapacitors: Materials and devices. J. Energy Storage, 21, 801–825. https://doi.org/10.1016/j.est.2019.01.010.

[2] X. Zhang, L. Hou, A.Ciesielski, P. Samorì(2016) 2D Materials Beyond Graphene for High-Performance Energy Storage Applications. Adv. Energy Mater, 6, https://doi.org/10.1002/aenm.201600671.

[3] Y. Gogotsi, P. Simon(2011) True performance metrics in electrochemical energy storage. Science, (80-.), 334, 917–918 https://doi.org/10.1126/science.1213003.

[4] F. Bonaccorso, L. Colombo, G. Yu, M. Stoller, V. Tozzini, A.C. Ferrari, R.S. Ruoff, V. Pellegrini(2015) Graphene, related two-dimensional crystals, and hybrid systems for energy conversion and storage, Science, (80-.), 347, 1246501 https://doi.org/10.1126/science.1246501.

[5] D. Larcher, J.-M. Tarascon(2015) Towards greener and more sustainable batteries for electrical energy storage. Nat. Chem., 7, 19–29, https://doi.org/10.1038/nchem.2085.

[6] Y. Sun, D. Chen, Z. Liang(2017) Two-dimensional MXenes for energy storage and conversion applications. Mater. Today Energy, 5, 22–36, https://doi.org/10.1016/j.mtener.2017.04.008.

[7] K.S. Novoselov, A.K. Geim, S. V Morozov, D. Jiang, Y. Zhang, S. V Dubonos, I. V Grigorieva, A.A. Firsov(2004) Electric field effect in atomically thin carbon films. Science, (80-.), 306, 666–669, https://doi.org/10.1126/science.1102896.

[8] E.P. Randviir, D.A.C. Brownson, C.E. Banks(2014) A decade of graphene research: production,

[9] K. Poonia, A.S. Lather, S. Jangra, R.S. Kundu, A. Nehra(2023) Analysis of structural and electrical properties of Sn modified Ca0. 6Sr0. 4TiO3 ceramics. Mater. Today Proc. http://dx.doi.org/10.1016/j.matpr.2023.06.068.

[10] J. Sharma, A. Bhandari, S. Jangra, M.S. Goyat(2024) Sol–gel derived highly hydrophobic Polystyrene/SiO2 spray coatings on polished stainless steel and textured aluminium substrates. Trans. Inst. Met. Finish., 102, 77–82 https://doi.org/10.1080/00202967.2024.2315777.

[11] Y. Gogotsi, B. Anasori(2019) The rise of MXenes. ACS Nano, 13, 8491–8494, https://doi.org/10.1021/acsnano.9b06394.

[12] S. Jangra, A. Raza, B. Kumar, J. Sharma, S. Das, K. Pandey, Y.K. Mishra, M.S. Goyat(2025) MXene decorated ZnO-tetrapod for efficient degradation of Methyl Orange, Methylene Blue, and Rhodamine B dyes. Mater. Sci. Eng. B, 311, 117832, https://doi.org/10.1016/j.mseb.2024.117832.

[13] S. Jangra, B. Kumar, J. Sharma, S. Sengupta, S. Das, R.K. Brajpuriya, A. Ohlan, Y.K. Mishra, M.S. Goyat(2024) A review on overcoming challenges and pioneering advances: MXene-based materials for energy storage applications. J. Energy Storage, 101, 113810 https://doi.org/10.1016/j.est.2024.113810.

[14] Y. Ren, Q. He, T. Xu, W. Zhang, Z. Peng, B. Meng(2023) Recent Progress in MXene Hydrogel for Wearable Electronics. BIOSENSORS-BASEL, 13, https://doi.org/10.3390/bios13050495.

[15] R. Verma, P. Thakur, A. Chauhan, R. Jasrotia, A. Thakur(2023) A review on MXene and its' composites for electromagnetic interference (EMI) shielding applications. Carbon, N. Y., 208, 170–190 http://dx.doi.org/10.1016/j.carbon.2023.03.050.

[16] M.S. Irfan, M.A. Ali, T. Khan, S. Anwer, K. Liao, R. Umer(2023) MXene and graphene coated multifunctional fiber reinforced aerospace composites with sensing and EMI shielding abilities. Compos. Part A Appl. Sci. Manuf., 165, 107351, https://doi.org/10.1016/j.compositesa.2022.107351.

[17] Y. Li, S. Huang, S. Peng, H. Jia, J. Pang, B. Ibarlucea, C. Hou, Y. Cao, W. Zhou, H. Liu(2023) Toward smart sensing by MXene. Small, 19, 2206126,https://doi.org/10.1002/smll.202206126.

[18] S.M. Majhi, A. Ali, Y.E. Greish, H.F. El-Maghraby, S.T. Mahmoud(2023) V2CTX MXene-based hybrid sensor with high selectivity and ppb-level detection for acetone at room temperature. Sci. Rep., 13, 3114,https://doi.org/10.1038/s41598-023-30002-6.

[19] Z.-Q. Wang, Y.-W. Pan, J. Wu, H.-B. Qi, S. Zhu, Z.-J.Gu(2024) A bibliometric analysis of molybdenum-based nanomaterials in the biomedical field. Tungsten, 6, 17–47 ,https://doi.org/10.1007/s42864-023-00225-1.

[20] S. Nezami, F. Moazami, M. Helmi, A. Hemmati, A. Ghaemi (2024) Properties of MXene, in: MXenes. Emerg. 2D Mater., Springer, pp, 45–56 https://doi.org/10.1007/978-981-97-4064-2_3.

[21] Y. Wang, Y. Wang(2023) Recent progress in MXene layers materials for supercapacitors: High-performance electrodes. SmartMat., 4, https://doi.org/10.1002/smm2.1130.

[22] L. Zhang, W. Song, H. Liu, H. Ding, Y. Yan, R. Chen(2022) Influencing Factors on Synthesis and Properties of MXene: A Review. Processes., 10, 1–13, https://doi.org/10.3390/pr10091744.

[23] M.A.K. Purbayanto, D. Bury, M. Chandel, Z.D. Shahrak, V.N. Mochalin, A. Wójcik, D. Moszczyńska, A. Wojciechowska, A. Tabassum, M. Naguib, A.M. Jastrzębska(2023) Ambient Processed rGO/Ti3CNTx MXene Thin Film with High Oxidation Stability, Photosensitivity, and Self-Cleaning Potential. ACS Appl. Mater. Interfaces, 15, 44075–44086
https://doi.org/10.1021/acsami.3c07972.

[24] M.R. Lukatskaya, O. Mashtalir, C.E. Ren, Y. Dall'Agnese, P. Rozier, P.L. Taberna, M. Naguib, P. Simon, M.W. Barsoum, Y. Gogotsi(2013) Cation intercalation and high volumetric capacitance of two-dimensional titanium carbide. Science, (80-.), 341, 1502–1505
https://doi.org/10.1126/science.1241488.

[25] B. Soundiraraju, B.K. George(2017) Two-dimensional titanium nitride (Ti2N) MXene: synthesis, characterization, and potential application as surface-enhanced Raman scattering substrate. ACS Nano, 11, 8892–8900
https://doi.org/10.1021/acsnano.7b03129.

[26] M. Rahman, M.S. Al Mamun(2023) Future prospects of MXenes: synthesis, functionalization, properties, and application in field effect transistors. Nanoscale Adv., 6, 367–385
https://doi.org/10.1039/d3na00874f.

[27] J. Chen, Q. Jin, Y. Li, H. Shao, P. Liu, Y. Liu, P. Taberna, Q. Huang, Z. Lin, P. Simon(2023) Molten salt-shielded synthesis (MS3) of MXenes in air, Energy Environ. Mater., 6, e12328
https://doi.org/10.1002/eem2.12328.

[28] S.A. Thomas, A. Patra, B.M. Al-Shehri, M. Selvaraj, A. Aravind, C.S. Rout(2022) MXene based hybrid materials for supercapacitors: Recent developments and future perspectives. J. Energy Storage, 55, 105765
https://doi.org/10.1016/j.est.2022.105765.

[29] S.Y. Pang, Y.T. Wong, S. Yuan, Y. Liu, M.K. Tsang, Z. Yang, H. Huang, W.T. Wong, J. Hao(2019) Universal Strategy for HF-Free Facile and Rapid Synthesis of Two-dimensional MXenes as Multifunctional Energy Materials. J. Am. Chem. Soc., 141, 9610–9616,
https://doi.org/10.1021/jacs.9b02578.

[30] P. Simon, Y. Gogotsi(2008) Materials for electrochemical capacitors. Nat. Mater., 7, 845–854, https://doi.org/10.1038/nmat2297.

[31] C. Xu, L. Wang, Z. Liu, L. Chen, J. Guo, N. Kang, X.-L. Ma, H.-M. Cheng, W. Ren(2015) Large-area high-quality 2D ultrathin Mo2C superconducting crystals. Nat. Mater., 14, 1135–1141 https://doi.org/10.1038/nmat4374.

[32] J. Jia, T. Xiong, L. Zhao, F. Wang, H. Liu, R. Hu, J. Zhou, W. Zhou, S. Chen(2017) Ultrathin N-doped Mo2C nanosheets with exposed active sites as efficient electrocatalyst for hydrogen evolution reactions. ACS Nano, 11, 12509–12518, https://doi.org/10.1021/acsnano.7b06607.

[33] C. Zhang, Y. Ma, X. Zhang, S. Abdolhosseinzadeh, H. Sheng, W. Lan, A. Pakdel, J. Heier, F. Nüesch(2020) Two-Dimensional Transition Metal Carbides and Nitrides (MXenes): Synthesis, Properties, and Electrochemical Energy Storage Applications. Energy Environ. Mater., 3, 29–55, https://doi.org/10.1002/eem2.12058.

[34] Y.A. Kumar, C.J. Raorane, H.H. Hegazy, T. Ramachandran, S.C. Kim, M. Moniruzzaman(2023) 2D MXene-based supercapacitors: A promising path towards high-performance energy storage. J. Energy Storage, 72, 108433, https://doi.org/10.1016/j.est.2023.108433.

[35] R. Ibragimova, P. Erhart, P. Rinke, H.-P. Komsa(2021) Surface functionalization of 2D MXenes: trends in distribution, composition, and electronic properties. J. Phys. Chem. Lett., 12, 2377–2384
https://doi.org/10.1021/acs.jpclett.0c03710.

[36] F. Shahzad, M. Alhabeb, C.B. Hatter, B. Anasori, S.M. Hong, C.M. Koo, Y. Gogotsi(2023) Electromagnetic interference shielding with 2D transition metal carbides (MXenes).Science, 353, 933–947,https://doi.org/10.1126/science.aag2421.

[37] F. Xia, H. Wang, D. Xiao, M. Dubey, A. Ramasubramaniam(2014) Two-dimensional material nanophotonics. Nat. Photonics, 8, 899–907, https://doi.org/10.1038/nphoton.2014.271.

[38] G.R. Berdiyorov(2016) Optical properties of functionalized Ti3C2T2 (T = F, O, OH) MXene: First-principles calculations. AIP Adv., 6, https://doi.org/10.1063/1.4948799.

[39] K. Hantanasirisakul, M. Zhao, P. Urbankowski, J. Halim, B. Anasori, S. Kota, C.E. Ren, M.W. Barsoum, Y. Gogotsi(2016) Fabrication of Ti 3 C 2 T x MXene Transparent Thin Films with Tunable Optoelectronic Properties. 1–7, https://doi.org/10.1002/aelm.201600050.

[40] E. Satheeshkumar, T. Makaryan, A. Melikyan, H. Minassian, Y. Gogotsi, M. Yoshimura(2016) One-step Solution Processing of Ag, Au and Pd@MXene Hybrids for SERS. Sci. Rep., 6, 1–9, https://doi.org/10.1038/srep32049.

[41] K. Chaudhuri, M. Alhabeb, Z. Wang, V.M. Shalaev, Y. Gogotsi, A. Boltasseva(2018) Highly Broadband Absorber Using Plasmonic Titanium Carbide (MXene). ACS Photonics, 5, 1115–1122, https://doi.org/10.1021/acsphotonics.7b01439.

[42] B. Anasori, M.R. Lukatskaya, Y. Gogotsi (2017) 2D metal carbides and nitrides (MXenes) for energy storage. Nat. Rev. Mater.
https://doi.org/10.1038/natrevmats.2016.98.

[43] M. Khazaei, M. Arai, T. Sasaki, C. Chung, N.S. Venkataramanan, M. Estili, Y. Sakka, Y. Kawazoe(2013) Novel Electronic and Magnetic

Properties of Two-Dimensional Transition Metal Carbides and Nitrides. 2185–2192, https://doi.org/10.1002/adfm.201202502.

[44] G. Gao, G. Ding, J. Li, K. Yao, M. Wu, M. Qian(2016) Monolayer MXenes: Promising half-metals and spin gapless semiconductors. Nanoscale, 8, 8986–8994 https://doi.org/10.1039/c6nr01333c.

[45] B. Anasori, M.R. Lukatskaya, Y. Gogotsi(2017) 2D metal carbides and nitrides (MXenes) for energy storage. Nat. Rev. Mater., 2, https://doi.org/10.1038/natrevmats.2016.98.

[46] A. VahidMohammadi, J. Rosen, Y. Gogotsi(2021) The world of two-dimensional carbides and nitrides (MXenes). Science, 372, eabf1581 https://doi.org/10.1126/science.abf1581.

[47] J. Sharma, A. Bhandari, N. Khatri, S. Jangra, M.S. Goyat, Y.K. Mishra(2024) A brief review of transitional wetting regimes for superhydrophobic surfaces. J. Brazilian Soc. Mech. Sci. Eng., 46, 273,https://doi.org/10.1007/s40430-024-04844-8.

[48] H. Peçenek, S. Yetiman, F.K. Dokan, M.S. Onses, E. Yılmaz, E. Sahmetlioglu(2022) Effects of carbon nanomaterials and MXene addition on the performance of nitrogen doped MnO2 based supercapacitors. Ceram. Int., 48, 7253–7260,10.1016/j.ceramint.2021.11.285.

[49] J. Nan, X. Guo, J. Xiao, X. Li, W. Chen, W. Wu, H. Liu, Y. Wang, M. Wu, G. Wang(2021) Nanoengineering of 2D MXene-Based Materials for Energy Storage Applications. Small, 17, 1–20, https://doi.org/10.1002/smll.201902085.

[50] X. Xu, Y. Zhang, H. Sun, J. Zhou, F. Yang, H. Li, H. Chen, Y. Chen, Z. Liu, Z. Qiu(2021) Progress and perspective: MXene and MXene-based nano-materials for high-performance energy storage devices. Adv. Electron. Mater., 7, 2000967, https://doi.org/10.1002/aelm.202000967.

[51] X. Hui, X. Ge, R. Zhao, Z. Li, L. Yin(2020) Interface chemistry on MXene-based materials for enhanced energy storage and conversion performance. Adv. Funct. Mater., 30, 2005190, https://doi.org/10.1002/adfm.202005190.

[52] H. Aghamohammadi, R. Eslami-Farsani, E. Castillo-Martinez(2022) Recent trends in the development of MXenes and MXene-based composites as anode materials for Li-ion batteries. J. Energy Storage, 47, 103572,https://doi.org/10.1016/j.est.2021.103572.

[53] A.G. Olabi, Q. Abbas, A. Al Makky, M.A. Abdelkareem(2022) Supercapacitors as next generation energy storage devices: Properties and applications. Energy, 248, 123617, https://doi.org/10.1016/j.energy.2022.123617.

[54] X. Zhang, Z. Zhang, Z. Zhou(2018) MXene-based materials for electrochemical energy storage. J. Energy Chem., 27, 73–85 https://doi.org/10.1016/j.jechem.2017.08.004.

[55] Y. Zhou, L. Yin, S. Xiang, S. Yu, H.M. Johnson, S. Wang, J. Yin, J. Zhao, Y. Luo, P.K. Chu(2024) Unleashing the Potential of MXene-Based Flexible Materials for High-Performance Energy Storage Devices. Adv. Sci., 11, 2304874 https://doi.org/10.1002/advs.202304874.

[56] Y. Anil, C. Jayprakash, H.H. Hegazy, T. Ramachandran, S. Cheol(2023) 2D MXene-based supercapacitors : A promising path towards high-performance energy storage. J. Energy Storage, 72, 108433 https://doi.org/10.1016/j.est.2023.108433.

[57] K. Maleski, C.E. Ren, M.-Q. Zhao, B. Anasori, Y. Gogotsi(2018) Size-dependent physical and electrochemical properties of two-dimensional MXene flakes, ACS Appl. Mater. Interfaces, 10, 24491–24498 https://doi.org/10.1021/acsami.8b04662.

[58] M. Sajjad, M.I. Khan, F. Cheng, W. Lu(2021) A review on selection criteria of aqueous electrolytes performance evaluation for advanced asymmetric supercapacitors. J. Energy Storage, 40, 102729, http://dx.doi.org/10.1007/s43939-023-00065-3.

[59] A. Patra, S. Kapse, R. Thapa, D.J. Late, C.S. Rout(2022) Quasi-one-dimensional van der Waals TiS3 nanosheets for energy storage applications: Theoretical predications and experimental validation. Appl. Phys. Lett., 120, https://doi.org/10.1063/5.0080346.

[60] M. Naguib, O. Mashtalir, M.R. Lukatskaya, B. Dyatkin, C. Zhang, V. Presser, Y. Gogotsi, M.W. Barsoum(2014) One-step synthesis of nano-crystalline transition metal oxides on thin sheets of disordered graphitic carbon by oxidation of MXenes. Chem. Commun., 50, 7420–7423, https://doi.org/10.1039/C4CC01646G.

[61] Z. Lin, P. Rozier, B. Duployer, P.-L. Taberna, B. Anasori, Y. Gogotsi, P. Simon(2016) Electroche-mical and in-situ X-ray diffraction studies of Ti3C2Tx MXene in ionic liquid electrolyte. Electrochem. Commun., 72, 50–53, http://dx.doi.org/10.1016/j.elecom.2016.08.023.

[62] M. Ghidiu, M.R. Lukatskaya, M.-Q. Zhao, Y. Gogotsi, M.W. Barsoum(2014) Conductive two-dimensional titanium carbide 'clay'with high volumetric capacitance. Nature, 516, 78–81,https://doi.org/10.1038/nature13970.

[63] H. Hwang, S. Byun, S. Yuk, S. Kim, S.H. Song, D. Lee(2021) High-rate electrospun Ti3C2Tx MXene/carbon nanofiber electrodes for flexible supercapacitors. Appl. Surf. Sci., 556, 149710, https://doi.org/10.1016/j.apsusc.2021.149710.

[64] R.B. Rakhi, B. Ahmed, D. Anjum, H.N. Alshareef(2016) Direct Chemical Synthesis of MnO2 Nanowhiskers on Transition-Metal Carbide Surfaces for Supercapacitor Applications. ACS Appl. Mater. Interfaces, 8, 18806–18814, https://doi.org/10.1021/acsami.6b04481.

[65] X. Wu, B. Huang, R. Lv, Q. Wang, Y. Wang(2019) Highly flexible and low capacitance loss supercapacitor electrode based on hybridizing decentralized conjugated polymer chains with MXene. Chem. Eng. J., 378, 122246, https://doi.org/10.1016/j.cej.2019.122246.

[66] M. Naguib, J. Come, B. Dyatkin, V. Presser, P.L. Taberna, P. Simon, M.W. Barsoum, Y. Gogotsi(2012) MXene: A Promising Transition Metal Carbide Anode for Lithium-Ion Batteries. Electrochem. Commun., 16, 61-69, https://doi.org/10.1016/j.elecom.2012.01.002.

[67] D. Sun, M. Wang, Z. Li, G. Fan, L.-Z. Fan, A. Zhou(2014) Two-dimensional Ti3C2 as anode material for Li-ion batteries. Electrochem. Commun., 47, 80–83, https://doi.org/10.1016/J.ELECOM.2014.07.026.

[68] Y. Zhang, Z. Mu, J. Lai, Y. Chao, Y. Yang, P. Zhou, Y. Li, W. Yang, Z. Xia, S. Guo(2019) MXene/Si@ SiO x@ C layer-by-layer superstructure with autoadjustable function for superior stable lithium storage, ACS Nano, 13, 2167–2175,doi:10.1021/acsnano.8b08821.

[69] K. Ma, H. Jiang, Y. Hu, C. Li(2018) 2D nanospace confined synthesis of pseudocapacitance-dominated MoS2-in-Ti3C2 superstructure for ultrafast and stable Li/Na-ion batteries. Adv. Funct. Mater., 28, 1804306, https://doi.org/10.1002/adfm.201804306.

[70] M. Naguib, M. Kurtoglu, V. Presser, J. Lu, J. Niu, M. Heon, L. Hultman, Y. Gogotsi, M.W. Barsoum(2011) Two-dimensional nanocrystals produced by exfoliation of Ti 3AlC 2. Adv. Mater., 23, 4248–4253, https://doi.org/10.1002/adma.201102306.

[71] M. Alhabeb, K. Maleski, B. Anasori, P. Lelyukh, L. Clark, S. Sin, Y. Gogotsi(2017) Guidelines for synthesis and processing of two-dimensional titanium carbide (Ti3C2T x MXene). Chem. Mater., 29, 7633–7644, https://doi.org/10.1021/acs.chemmater.7b02847.

IZVOD

MXenes: SINTEZA, SVOJSTVAIAPLIKACIJE U NAPREDNIMTEHNOLOGIJAMASKLADIŠTENJAENERGIJE

MXSenes su se pojavili kao veoma obećavajući materijali u oblasti naprednih tehnologija skladištenja energije, zahvaljujući svojim karakterističnim svojstvima i raznovrsnim primenama. Ovaj pregled nudi sveobuhvatnu analizu MXSena, fokusirajući se na njihove metode sinteze, osnovna svojstva i primene u punjivim baterijama i superkondenzatorima. Kao odgovor na sve veće globalne potrebe za energijom, MXSenes predstavljaju ubedljiva rešenja zbog svojih izuzetnih električnih i elektrohemijskih karakteristika. To uključuje visoku provodljivost, veliku površinu, hidrofilnost i jedinstvenu dvodimenzionalnu strukturu koja se sastoji od metalnih karbida, nitrida i karbonitrida. Pored toga, ovaj pregled uključuje detaljnu bibliometrijsku analizu korišćenjem računarskih alata kao što je VOSviever, koji ispituje globalni pejzaž MXSene istraživanja u periodu od 2012. do 2024. Ova analiza identifikuje trendove saradnje između različitih zemalja, institucija, autora i časopisa, naglašavajući vodeće oblasti istraživanja. Sve u svemu, ovaj pregled naglašava značajan potencijal MXSenes-a u unapređenju tehnologija za skladištenje energije. Pruža uvid u buduće pravce istraživanja i praktične primene koje bi mogle efikasno da zadovolje rastuće potrebe za energijom koje pokreću električna vozila i prenosiva elektronika.

Ključne reči: *MXSene; 2D materijali; skladištenje energije; supercapacitor; bibliometrijska analiza*

Sahil Jangra: https://orcid.org/0009-0004-6217-9496
Bhushan Kumar: https://orcid.org/0009-0006-8870-5962
Subhankar Das: https://orcid.org/0000-0002-1724-2722
Manjeet Singh Goyat: https://orcid.org/0000-0002-0668-6512
JaishreeSharma: https://orcid.org/0000-0001-9954-2202

Velumani Murugesan[1], Mohanraj Rajendran[2],
Loganathan Pattusamy[3],Sakthieswaran Natarajan[4]*

[1]*Department of Civil Engineering, K S Rangasamy College of Techno-
logy, Namakkal, Tamilnadu, India, [2]Department of Civil Engineering,
Faculty of Engineering & Technology, SRM University, Delhi-NCR,
Sonipat, Haryana, India, [3]Civil Engineering, Excel Engineering College,
Komarapalayam, Namakkal, Tamilnadu, India, [4]Department of Civil
Engineering, P.S.R. Engineering College, Sivakasi, Tamilnadu, India*

Enhancing corrosion resistance in concrete structures using *Euphorbia Tortilis* cactus extract by non-destructive testing

ABSTRACT

This research investigates the corrosion resistance of reinforced concrete structures, a crucial aspect for ensuring their long-term performance and sustainability. Utilizing both the half-cell potential method and an accelerated corrosion test, the study introduces a novel approach by incorporating Euphorbia Tortilis Cactus (ETC) extract as an organic additive in concrete. The half-cell potential method involves measuring potential differences between steel reinforcement and an external electrode in a Cu/CuSO$_4$ solution, revealing varied corrosion inhibition levels in different specimens. Notably, the introduction of ETC extract demonstrates unprecedented resistivity, showcasing a mere 10% probability of corrosion, even in atmospheric conditions. The accelerated corrosion test further emphasizes the novelty of the research. ETC concrete exhibits lower applied current and mass loss percentages compared to control mixes, indicating superior corrosion resistance and reduced porosity. This novel use of ETC extract in concrete enhances its durability and sustainability, providing valuable insights for developing resilient concrete structures amid increasing concerns about corrosion-induced deterioration in reinforced concrete constructions.
Keywords: *Corrosion Resistance, Concrete Structures, Euphorbia Tortilis Cactus, Organic Additive,Sustainability*

1. INTRODUCTION

The durability and longevity of reinforced concrete structures are critical considerations in civil engineering [1]. One of the primary challenges that compromise the performance of these structures is the insidious and pervasive impact of corrosion on steel reinforcement [2-5]. Corrosion-induced deterioration weakens the structural integrity of concrete elements and poses significant economic and environmental concerns [6]. In light of these challenges, this researchendeavors to address the issue of corrosion in reinforced concrete by exploring innovative and sustainable solutions [7]. The introduction of organic additives in concrete technology represents a promising avenue for enhancing corrosion resistance [8]. In this context, the study focuses on the incorporation of Euphorbia Tortilis Cactus (ETC) extract as a novel and environmentally friendly admixture [9-13].

ETC, a readily available plant in certain regions, has shown promising properties that make it a potential candidate for mitigating corrosion in concrete structures [14]. Javaherdashti et al. [16] explores five mechanisms of microbiologically influenced corrosion and deterioration of reinforced concrete by algae. Microorganisms, including bacteria, algae, fungi, and lichens, significantly impact mineral materials' biodeterioration, especially stone, concrete, and glass, via aggressive biogenic acids and biofilms. Biotests, unlike chemical tests, reveal material resistance to microbial attack, showing notable weight loss variations and aiding in material selection for durability [17]. The use of bio-concrete for enhancing durability against aggressive conditions, motivated by insufficient data on its performance in extreme environments [18].Key processes include chemical absorption from cement paste, biofilm formation attracting corrosive organisms, and photosynthetic-driven electrochemical cells, each contributing to concrete drying, cracking, and corrosion of both concrete and reinforcement steel [19].This research embarks on a comprehensive investigation, employing both the half-cell potential method and an accelerated corrosion test, to assess the corrosion resistance of concrete

*Corresponding author: Mohanraj Rajendran

E-mail: rsrirammohan@srmuniversity.ac.in

enhanced with ETC extract [20]. Agboola et al. [21] examines corrosion of reinforcing steel in marine concrete, emphasizing the role of corrosion-inhibiting admixtures. It discusses classifications, applications, and the integration of functional nanostructured materials, highlighting their effectiveness in mitigating corrosion and enhancing durability in new constructions and repairs within the marine industry, alongside future research directions [22]. The study aims to provide quantitative insights into the effectiveness of ETC as a corrosion inhibitor and evaluate its potential as a sustainable alternative to traditional synthetic additives [23]. Through rigorous experimentation and analysis, this research seeks to contribute to the advancement of concrete technology, offering practical solutions to enhance the durability of structures in the face of corrosion challenges [24]. By exploring the unique properties of Euphorbia Tortilis Cactus, this study aligns with the broader objectives of promoting sustainability and eco-friendly practices in the construction industry [25-28]. Variations in soil composition, climate, and seasonal growth conditions can alter the concentrations of key active compounds, such as flavonoids, tannins, and saponins, within the plant [29]. These fluctuations may impact the extract's effectiveness, as changes in the levels of antioxidative and film-forming constituents could affect the protective properties provided to the concrete [30].

Monteny et al. [31] reviews recent advancements in testing methods for biogenic sulfuric acid corrosion in concrete, highlighting differences between biogenic and chemical corrosion. It discusses various research approaches, including chemical tests, microbial simulations, and in situ exposure tests to assess material resistance [32]. Xu et al. [33] investigate the self-healing potential of ureolytic microbes embedded in ceramsite particles for repairing cracks in reinforced concrete. Results show complete healing of cracks up to 450 µm in 120 days, enhancing mechanical properties and effectively inhibiting reinforcement corrosion. Kanwal et al. [35] evaluates the impact of the calcifying bacterium *Bacillus safensis* and biochar on the mechanical and transport properties of cementitious composites. Results show significant enhancements in flexural and compressive strength, a healing degree increase, and 95.18% corrosion inhibition, suggesting a sustainable approach for improving durability in reinforced concrete.

2. RESEARCH SIGNIFICANT

The significance of this research lies in its multifaceted contributions to the field of concrete technology, addressing critical challenges associated with corrosion in reinforced concrete structures. The primary objectives of this study are intricately connected to the broader significance, offering solutions to enhance durability, sustainability, and environmental friendliness in construction practices.

Corrosion Mitigation: The research aims to provide concrete structures with improved resistance to corrosion, a pervasive issue that compromises the longevity and structural integrity of reinforced concrete. By investigating the potential of Euphorbia Tortilis Cactus (ETC) extract as an organic additive, the study seeks to offer an innovative and eco-friendly solution to mitigate corrosion-related deterioration.

Novel Organic Additive: The incorporation of ETC extract represents a novel approach to concrete admixtures. The research strives to establish the efficacy of this organic additive in enhancing the corrosion resistance of concrete, providing an alternative to traditional synthetic additives, and contributing to the development of sustainable construction materials.

Half-Cell Potential Method Evaluation: The utilization of the half-cell potential method serves as a key objective, offering a quantitative assessment of the probability of corrosion in different concrete specimens. The significance lies in providing a reliable and standardized technique to evaluate the effectiveness of corrosion inhibition, enabling comparisons and insights into the performance of diverse concrete mixes.

Accelerated Corrosion Test: Through the accelerated corrosion test, the research aims to simulate and assess the performance of ETC concrete under harsh environmental conditions. The outcomes will contribute valuable data on the material's resistance to corrosion, aiding in the formulation of durable concrete mixes suitable for aggressive environments.

Sustainable Construction Practices: The broader significance of this research extends to the promotion of sustainable construction practices. By exploring environmentally friendly alternatives, such as ETC extract, the study aligns with global efforts to reduce the ecological footprint of construction activities and advance the development of green building materials.

This research's significance lies in its potential to revolutionize concrete technology by introducing a natural, sustainable, and effective corrosion mitigation strategy. The outlined objectives collectively contribute to the advancement of construction materials, fostering durability, resilience, and environmental responsibility in the built environment.

3. MATERIALS AND METHODOLOGY

In this research, Ordinary Portland cement, grade 53, conforming to IS: 12269 – 2013, IS: 4032-2013, and IS:4031-2013, was utilized. The cement underwent various tests to ensure its suitability, including fineness, normal consistency, setting time, soundness, and compressive strength at different curing periods [36]. The results indicated that the selected cement met the requirements, ensuring the desired properties of the ETC concrete [37]. Aggregates, accounting for 70 to 80 percent of concrete volume, play a crucial role in the material's production [38]. Fine aggregates, sourced from the locally available Karur River, were subjected to tests outlined in IS: 2386 (Part 3 & 4) [39].

The results confirmed that the fine aggregates met the specifications, falling under Zone III. Coarse aggregates, chosen for durability and low permeability, were tested according to IS: 2386-2012 and IS 383-2012 [40, 41]. The properties showcased the suitability of the coarse aggregates for ETC concrete [42]. Water, another vital component, should be free from salts and impurities that could adversely affect the chemical reactions in concrete. The water used in this study, sourced from the Cauvery River, adhered to the specifications of IS: 456-2000 [43]. A unique aspect of this study involved the use of Euphorbia Tortilis Cactus extract as a natural organic additive. Collected from Pallakapalayam in Tamilnadu, the cactus extract underwent thorough analysis, revealing its composition of fats, proteins, polysaccharides, and water [44]. The extract was added to the water at varying concentrations (1%, 3%, 5%, 7%, and 9%) to explore its impact on the ETC concrete [45]. With 5.2% polysaccharides and 1.9% proteins, the organic additive offers a unique and environmentally friendly alternative to synthetic additives [46]. Finally, steel reinforcement is a critical component in concrete construction, providing strength and durability [47]. In this study, Fe415 grade steel was chosen for its favorable characteristics in flexural strength and deflection tests. The primary constituents, Flavonoids, Tannins, Alkaloids, Saponins and Lipid-like Waxes are contributing to corrosion inhibition in ETC extract [48]. Thus, the Euphorbia Tortilis Cactus concrete in this study is meticulously designed, considering the properties of cement, aggregates, water, organic additives, and steel reinforcement [49]. The comprehensive testing and analysis of each component ensure that the ETC concrete meets the specified standards for strength, durability, and environmental sustainability. This research contributes to the ongoing efforts to explore eco-friendly alternatives in the field of concrete technology.

4. EXPERIMENTAL STUDY

Steel reinforcement provides the tensile qualities needed in structural concrete. Wind, traffic, dead loads, and thermal cycling do not induce the breakdown of concrete structures subjected to tension and flexural stresses. However, when the reinforcement corrodes, connection is lost, which causes the concrete to rust and eventually spall and delaminate. If not stopped, the structure's integrity can be compromised. The strength capability of the structure decreases as a result of the reduction in steel's cross-sectional area.

4.1. Corrosion process

Corrosion is a term used to describe the degradation of a metal or alloy brought on by oxidation, a chemical process that creates iron oxides and leads them to break away from the base. Concrete deteriorates due to reinforcing corrosion, which causes spots, cracks, and spalling, reducing the material's strength and dimensions [50]. As a result, in recent years more emphasis has been paid to the steel reinforcement in ETC concrete. The thermal power plant's operational state and the calibre of the coal utilised both affect the ETC quality [51]. Ingress of carbonization and chloride ions is the main cause of corrosion in ETC concrete. In ETC concrete, the corrosion of the reinforcing steel occurs electrochemically in the presence of oxygen and water [52]. Corrosion is prevented on the steel reinforcement by the highly alkaline atmosphere [53]. Rust (Ferric hydroxides and Ferric oxides) that are present at the interface between concrete and reinforcement and have a volume 3 to 6 times greater than Fe ions are the cause of concrete deterioration [54]. Internal tensions caused by rusting in a concrete part cause fractures to appear on the exterior of the cement composite, which then causes harm to the structure and, ultimately, causes the collapse of the entire structure [55].

Figure 1 shows the Galvanic Corrosion Cell. It takes flow current and several other chemical processes to prevent steel reinforcement corrosion in concrete, which is an electrochemical process. An electrochemical cell is set up when the potential on the concrete reinforcement changes. A galvanic cell of corrosion must have the following three components.
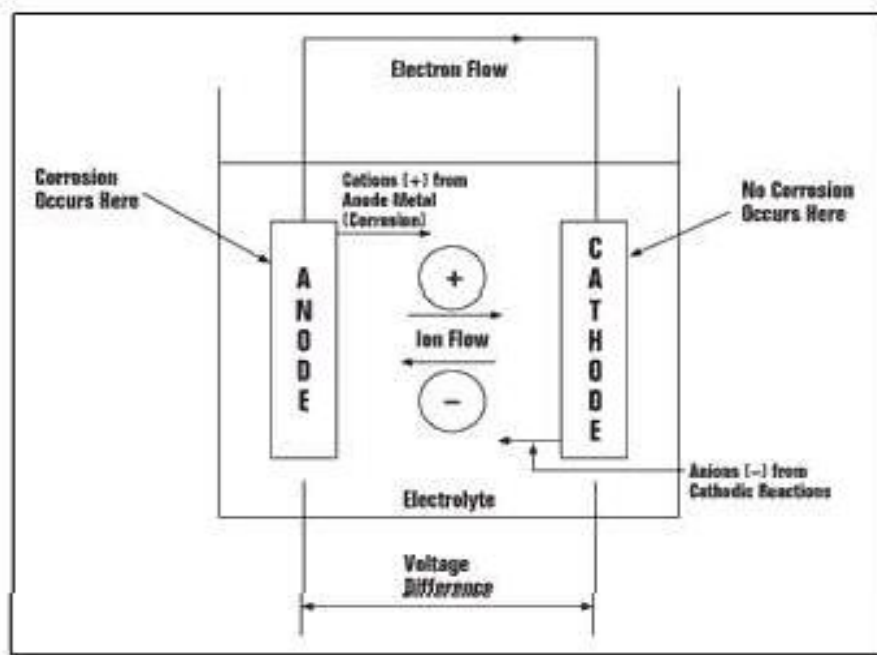
Figure 1. Galvanic corrosion cell

Anode

The anode is the area on a steel bar inserted in concrete where negatively charged electrons enter the cathode through the steel reinforcement and ferrous ions from the steel are lost to the solution. The anodic reaction is the name for the aforementioned process.

Cathode

The location of a steel reinforcement embedded in concrete is also known as the cathode. Anywhere the electrolytes (water and oxygen) negatively charged electrons, or e⁻, are absorbed, they join with the water and oxygen to form hydroxyl group ions or OH^-. The reaction described above is referred to as a cathodic reaction.

Through the electrolyte, this hydroxyl group ion OH^- combines with ferrous ions Fe^{2+} to form ferrous hydroxide Fe $(OH)_2$. Fe $(OH)_3$ is produced when they react with the solution's water (H_2O) and oxygen (O). More oxidation transforms this into rust.

Electrolyte

Between the anode and cathode, current (electron) can flow more easily through this material. Concrete can act as an electrolyte when it has sufficient conduction after being subjected to wet and dry cycles. The anode and cathode are frequently placed close together or can be separated by a certain amount of space. The corrosion process requires both cathodic and anodic reactions to take place. The responses happen at the same time.

4.2. Corrosion mechanism

Concrete reinforcement corrosion is challenging. Similar to a basic battery, this electrochemical process uses electricity. An electrochemical cell is established within the reinforcement when the potential for steel reinforcement in concrete changes. The anode is the portion of the steel that is the most negatively charged, and the cathode is the opposite (positively charged). With the reinforcement completing the circuit and the concrete acting as the electrolyte, the concrete can conduct current positively charged ferrous ions generated by the anode combine with the ions of the cathode's hydroxyl group (OH^-) in the presence of water and oxygen. Once in the electrolyte, they move through it and interact with ferrous ions to form Fe (OH), which is further oxidised to form rust [56]. This expansive reaction results in ai volume of rust that is six times larger than the initial volume of ferrous ion. The collected amount of rust causes internal tensions in the concrete, which results in cracking, spalling, or delamination of the concrete on the cap. Concrete loses its integrity in these things. The entire structure collapsed as a result of the concrete member's altered cross section. Figure 2 depicts the rebar corrosion.

In a newly built structure, the concrete's alkalinity is sufficient to establish that the steel is in a passive state and will not corrode. If specific ions don't attack the steel, these chemicals, with a p^H scale of 13–14, provide a passive coating that will protect the metal. In this film, it is demonstrated that chloride ions exchange hydroxyl group ions,

causing localised pitting and the onset of the corrosion process. In order to identify the corrosion mechanism in various reinforced concrete types that contain ETC and steel bar, extensive experimental tests were undertaken, and the results are reported in this work. It also informs on the research done to determine how corrosion attacks on ETC concrete structures affected the various curing conditions. With 20 percent, 30 percent, and 40 percent of the weight of cement (Dalmia), concrete mixes were made using samples made of 16 mm diameter steel bars (TATA Tiscon) that were 100 mm long and had a 25 mm clear cover. In embedded steel bars, the corrosion process was examined. Using ACM Instruments, half-cell potential and Accelerated corrosion techniques were conducted.
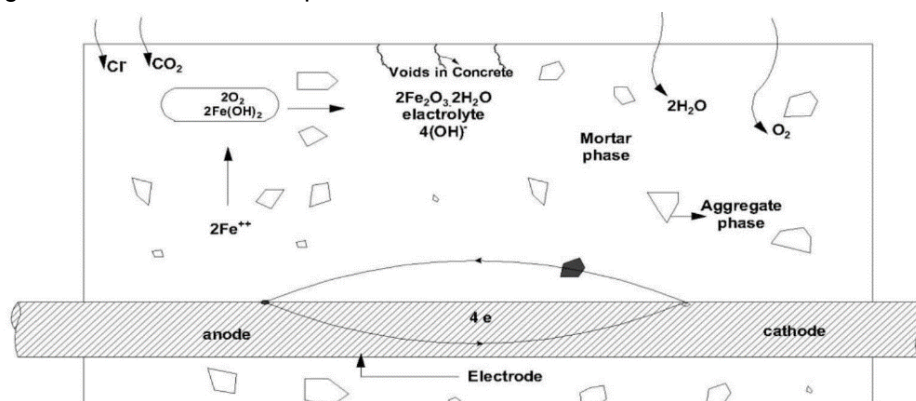
Figure 2. Rebar corrosion

4.3 Half-cell potential method

To make sure the concrete is still strong and durable enough, it is frequently necessary to inspect and test existing concrete structures. Anodic and cathodic activity will be encouraged at various locations throughout the reinforcement if the steel is de-passivated by carbonation or intrusion of chlorides [57]. At the anodes, where metal ion oxidation occurs, metal is dissolved, leading to the formation of metal oxide corrosion products. A reduction process takes place simultaneously with the release of electrons, which are then carried by an electrical current via the metallic reinforcement to the cathodic site. An appropriate half-cell electrode can be used to detect this fluctuation in electrical potential throughout the length of the corroding reinforcement that is connected to the flow of current. Anodic regions for steel in concrete often have higher negative potentials than cathodic zones, which have lower negative potentials. Half-cell probes are made of an electrolyte and conductor that may be held up to the concrete surface; the concrete and reinforcing make up the other half of the cell. They work as a unit to create a full electrical cell that produces a mill voltmeter-measurable voltage. The schematic view of the half-cell potential method is shown in Figure 3.

Figure 3. Typical Half-cell potential measurement arrangement

Table 1 Corrosion probability percentage

Half-cell potential (mV) relative to	Chance of corrosion (in %)
< 200	10 %
200 to 350	50 %
> 350	90 %

A voltmeter was used to measure the potential difference between the steel reinforcement and the external electrode in this procedure. A metal rod is immersed in Cu/CuSO$_4$ solution in the half-cell. A voltmeter connects the metal rod to the reinforcement steel. To generate an exact value, steel reinforcement, and outside electrodes were connected through wet concrete protection. The availability of oxygen, concrete resistivity, and cover thickness all stimulus the outcome of a half-cell potential test. Half-cell potential measurements only provide a "probability" of rebar corrosion occurring; they do not provide an estimate of its rate.

4.4 Accelerated corrosion test

According to ASTM C 876 criteria, the corrosion test measures how steadily steel degrades while exposed to external current. Since the corrosion analysis is based on a quick examination of the performance of steel without waiting for a long time, this test is also known as an accelerated corrosion test. The beams of 1 m in length and cross-section 150 × 200 mm were cast for each optimum ETC mix and the control mix (totalof 6 numbers). The tension reinforcement was wound with wires at two points so that uniform corrosion was initiated in the rebars [58]. After that, the specimen is submerged in a container containing water that has been thoroughly diluted with 5 percent sodium chloride (NaCl). The RCC specimen under investigation is perfectly enclosed by a steel sheet of extremely thin thickness.

The supply was connected so that the positive end went to the steel sheet and the negative to the steel embedded in concrete. After passing a 12V external supply to the connection, six days of behaviour analysis follow. The embedded steel then corrodes over time as a result of the power source and a reaction to the temperature of the environment. The output of the rusted steel in the concrete was then observed using a half-cell potential metre. In a half-cell potential metre, a glass tube containing a copper rod is filled with diluted copper sulphate solution. The sponge will be near the bottom of the tube, below the porous stopper. Over the concrete, the sponge-like arrangement was put, and the steel was attached to the point's other end. Figure 4 displays concrete corrosion and its interpolation analysis.

Figure 4. CorrosionTestAnalysisasperASTMC876specifications

Calculation of Corrosion

Based on the Faraday law, the theoretical mass of rust (M_{th}) is determined as follows

$$M_{th} = \frac{WI_{app}T}{F} \quad (1)$$

Where M_{th} is the theoretical mass of rustormassloss (g); W–the equivalent weight of steel (27.925g); I_{app} – the current applied (A); T– the period of induced corrosion (s); F – the Faraday constant (96487 A$_s$).

After the corrosion test, by breaking the specimens and rebars were extracted. According to the gravimetric test (ASTM G1), the actual mass (M_{ac}) of rust is calculated:

$$M_{ac} = \frac{W_i - W_f}{\pi D L} \quad (2)$$

Where W_i is the initial weight of the rebar; W_f – the weight of the rebar after corrosion; D – the diameter of the rebar, and L – the length of the rebar.

Assuming that the actual and theoretical mass of rust are equal (i.e., $I_{corr} = I_{app}$) and by equating M_{ac} and M_{th} the equivalent corrosion current (I_{corr}) is calculated:

$$I_{corr} = \frac{W_i - W_f}{W_t} \qquad (3)$$

The percentage weight loss (ρ) is calculated as:

$$P = \frac{W_i - W_f}{W_i} \times 100 \qquad (4)$$

5. CORROSION TEST RESULTS ON ETC CONCRETE

5.1. Half-cell potential method

The fundamental disadvantage of RC concrete structures is that their performance deteriorates when they are exposed to the action of corrosion. To evaluate the probability of corrosion in concrete, the half-cell potential approach was used. A voltmeter was used to measure the potential difference between the steel reinforcement and the external electrode in this procedure. A metal rod is immersed in $Cu/CuSO_4$ solution in the half-cell. A voltmeter connects the metal rod to the reinforcement steel. The high-accelerated corrosion experiment's driving force, external voltage, was maintained at a constant level throughout. To generate an exact value, steel reinforcement, and outside electrodes were connected through wet concrete protection. The availability of oxygen, concrete resistivity, and cover thickness all stimulus the outcome of a half-cell potential test. For determining the possibility of corrosion, the potentials were measured an average of many measurements obtained from different sites on the same surface or at any place on the surface was used. According to ASTM C876, the half-cell potential test was carried out; the graphical variations are shown in Figure 5 and Figure 6 for M 20 and M 25, respectively. For the M20 concrete, the half-cell potential measurements were as follows: -2715mV, -216mV, -178mV, -142mV, -121mV, and -97mV; and for the M25 concrete, -255mV, -196mV, -157mV, 126mV, -

98mV, and -76mV. This shows that various specimens have variable corrosion inhibition. After obtaining the results, the contour was plotted on a graph to identify the high corrosion activity. Concrete with ETC showed the highest level of resistivity. Hence regarding the test result, it shows that the corrosion on the ETC Concrete was not affected by any corrosion agent even after placing it in atmospheric conditions and the probability of corrosion was 10% in the concrete.

5.2. Accelerated corrosion test

For the current capacity of the circuit, the current applied to the fiber specimens was found to be lesser than that of the control specimens. From Table 1, it can be understood that the conductance of the ETC concrete specimens was lesser compared to control specimens, which in turn indicates higher porosity of control specimens. In the accelerated corrosion test, three distinct concrete mixes were subjected to corrosion evaluation, with results outlined in Table 1. The reference concrete exhibited an average applied current (I_{app}) of 1.02 As, experiencing a weight loss of 120g over the testing period. The theoretical weight loss, calculated at 126.56g, resulted in a 4.22% weight loss and a corresponding equivalent corrosion current (I_{corr}) of 0.95 As. The ETC9M20 concrete mix, incorporating Euphorbia Tortilis Cactus (ETC) extract, demonstrated an I_{app} of 1.19 As, with a weight loss of 193g, yielding a 5.06% weight loss and an I_{corr} of 1.14 As. Similarly, for the ETC9M25 mix, the I_{app} was 1.57 As, accompanied by a weight loss of 179g, translating to a 6.24% weight loss and an I_{corr} of 1.42 As. These results collectively highlight the variations in weight loss percentages and equivalent corrosion currents among the concrete mixes, emphasizing the potential of ETC extract in enhancing corrosion resistance, particularly in the M20 mix where the inhibitory effect is most pronounced. Thus, it can be concluded that ETC concrete has higher corrosion resistance and it can effectively be used in an aggressive environment. The mass loss percentages of ETC concrete specimens were found to be lesser than the control mix cast without ETC

Table 1. Accelerated corrosion test results

Beam ID	Average I_{app}(A$_s$) (g)	Initial weight (g)	Final weight (g)	Weight loss (g)	Theoretical Weight loss (g)	Weight loss (%)	Weight loss (%)	Equivalent corrosion current I_{corr}(A$_s$)
Reference Concrete	1.02	2823	2703	120	126.56	4.22	4.48	0.95
ETC9 M 20	1.19	2858	2665	193	150.11	5.06	5.35	1.14
ETC9 M 25	1.57	2836	2657	179	97.84	6.24	6.98	1.42
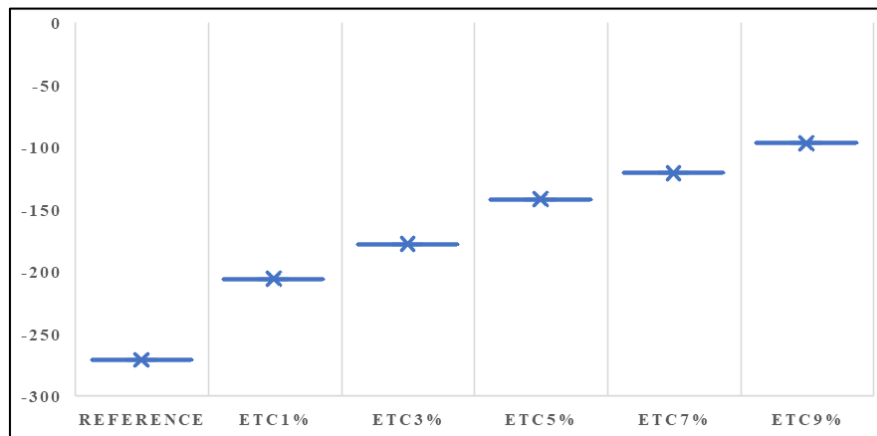
Figure 5. Rate of corrosion in M20 concrete
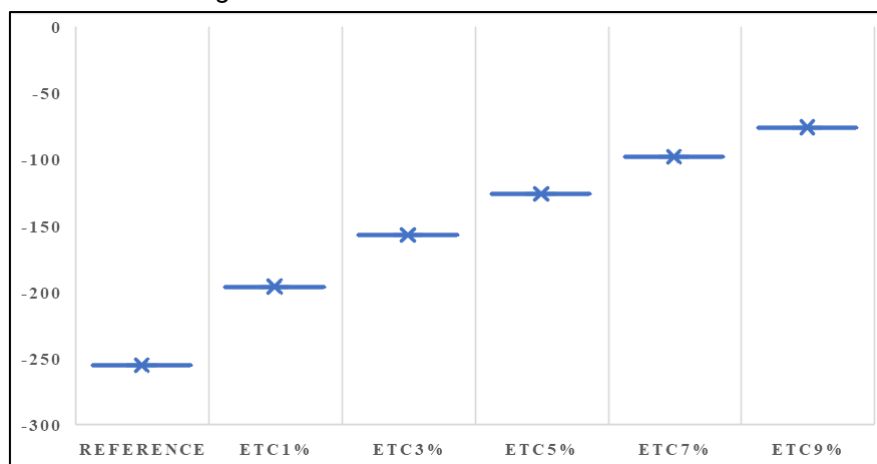
Figure 6. Rate of corrosion in M25 concrete

5.3. Chemical interactions and mechanisms by which Euphorbia Tortilis cactus extract enhances corrosion resistance in concrete structures

Euphorbia Tortilis extract contains a high concentration of flavonoids, alkaloids, and tannins, which possess antioxidative properties. These compounds can neutralize free radicals and reduce oxygen availability at the steel-concrete interface, which is essential for the initiation and progression of corrosion, equation 5. The extract effectively slows down the electrochemical reactions that drive corrosion by diminishing the oxygen concentration. The bioactive compounds in ETC extract can adsorb onto the steel reinforcement surface, forming a thin protective layer (Eqn. 6). This film acts as a physical barrier, reducing the interaction between the steel and corrosive agents such as chloride ions and water. The protective film is enhanced by the presence of tannins and saponins, which are known for their film-forming and adhesive properties.ETC extract contains waxy and lipid-like compounds (Eqn. 7) that increase the hydrophobicity of the concrete matrix. This reduces water permeability within the concrete, thereby minimizing the migration of moisture and dissolved ions to the steel reinforcement. Lower permeability reduces the concrete's porosity and its potential to conduct ions, directly decreasing the likelihood of corrosion initiation. Euphorbia Tortilis contains certain alkaline compounds that help stabilize the pH levels within concrete. A stable, high pH environment within the concrete prevents the passivation layer on the steel from dissolving, which is critical for corrosion protection (Eqn. 8). This buffering effect also maintains the basicity of the surrounding concrete, further deterring acidic conditions that might accelerate corrosion.

$$Flavonoid\ (reduced) + \cdot OH \rightarrow Flavonoid\ (oxidized) + H_2O \qquad (5)$$

$$Tannin + Fe^{2+} \rightarrow Tannin\text{-}Fe\ complex\ (protective\ film) \qquad (6)$$

$$C_nH_2n + 2O + H_2O \rightarrow Hydrophobic\ layer\ (repels\ water) \qquad (7)$$

$$K^+ + Cl^- \rightarrow KCl\ (reduced\ chloride\ concentration) \qquad (8)$$
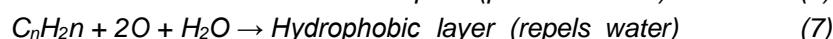
Ion Exchange and Chelation

Some compounds within the Euphorbia Tortilis extract exhibit chelating abilities, binding to metal ions that might otherwise catalyze the breakdown of the passivating film on the steel. Chelation of chloride ions or other aggressive ions reduces their free concentration, thus decreasing their availability to participate in the corrosive process (Eqn. 9).

Tannin + Cl − → Tannin - Cl complex (chelated form)
$$(9)$$
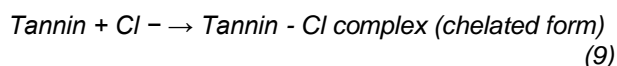
The complex mix of bioactive compounds in the ETC extract likely acts synergistically to enhance corrosion resistance. While individual compounds have their protective roles, their combined effect can produce a stronger, more cohesive inhibition mechanism. This may include the combination of antioxidative actions, film formation, and hydrophobic effects, offering comprehensive protection against multiple corrosion factors.

Outcomes-based on the observed improvements in corrosion resistance include the improved corrosion resistance of ETC-treated concrete, as evidenced by lower weight loss percentages and lower corrosion currents (Icorr) compared to untreated concrete, indicating a slower degradation rate of steel reinforcement. This slowdown could extend the concrete's service life by reducing the frequency of corrosion-induced damage, potentially extending the lifespan by 10-20% or more, depending on the exposure environment. ETC extract's hydrophobic properties reduce water permeability and chloride ion ingress, both critical factors in corrosion initiation. With lower chloride diffusion rates, the initiation phase of corrosion could be significantly delayed, particularly in marine or de-icing salt environments, potentially adding another 5-10 years to the concrete's expected lifespan. For structures in harsh climates or industrial settings, the antioxidative and passivating effects of the extract could extend service life even further. In such environments, ETC-treated concrete might show an extended service life of 15-30% beyond untreated concrete, translating to an additional 10-15 years in typical reinforced concrete structures exposed to these conditions.Reduced maintenance requirements due to delayed corrosion initiation and progression mean fewer repairs or replacements, further contributing to the longevity of structures and offering significant cost savings over the structure's lifetime.

6. CONCLUSION

The possibility of corrosion occurrence was evaluated by the half-cell potential method and accelerated corrosion test. The following conclusions are reached based on the outcomes of the experimental tests:

- The minimum possibility of corrosion (36%) was observed at an optimum level of dosage when compared to reference concrete. Results showed a better inhibiting effect of corrosion rate on steel rods and reduced weight loss.

- In conclusion, the scientific investigation has yielded compelling numerical evidence supporting the enhanced corrosion resistance of concrete structures through the incorporation of Euphorbia Tortilis Cactus (ETC) extract. The half-cell potential method, conducted according to ASTM C876, revealed notable variations in corrosion inhibition across specimens. For M20 concrete, half-cell potential measurements ranged from -2715mV to -97mV, and for M25 concrete, values ranged from -255mV to -76mV. Significantly, ETC concrete consistently exhibited the highest resistivity, with a mere 10% probability of corrosion.

- The accelerated corrosion test further substantiates these findings, emphasizing the novel and sustainable nature of ETC concrete. In the case of ETC9M20, the weight loss percentage was 5.06%, and for ETC9M25, it was 6.24%. In comparison, the reference concrete showed a weight loss percentage of 4.22%. This numerical evidence underscores the superior corrosion resistance and reduced porosity of ETC concrete, indicating its efficacy in aggressive environments.

- The study's quantitative results contribute to the scientific understanding of corrosion mitigation strategies in concrete, emphasizing the numerical advantages of incorporating Euphorbia Tortilis Cactus extract. These findings bear significant implications for the development of durable and sustainable concrete structures in the construction industry. Further exploration and application of these numerical insights could drive advancements in eco-friendly construction practices.

7. REFERENCE

[1] Y.Song, K.Chetty, U.Garbe, J.Wei, H.Bu, L. O'moore,...G.Jiang (2021) A novel granular sludge-based and highly corrosion-resistant bio-concrete in sewers. *Science of The Total Environment*, *791*, 148270.
https://doi.org/10.1016/j.scitotenv.2021.148270

[2] N.Roghanian, N. Banthia (2019) Development of a sustainable coating and repair material to prevent bio-corrosion in concrete sewer and waste-water pipes. *Cement and Concrete Composites*, *100*, 99-107. https://doi.org/10.1016/j.cemconcomp.2019.03.026

[3] S. Fedosov, S. Loginova (2020) Mathematical model of concrete biological corrosion. *Magazine of Civil Engineering*, 7, 9906-9906.
doi: 10.18720/MCE.99.6

[4] R. Mohanraj, S.Senthilkumar, P.Padmapoorani (2022) Mechanical properties of RC beams With AFRP sheets under a sustained load. *Materials and Technology*, 56, 4, 365–372. https://doi.org/10.17222/mit.2022.481

[5] J. Strigáč, P. Martauz, A. Eštoková, N. Števulová, A.Luptáková (2016) Bio-corrosion resistance of concretes containing antimicrobial ground granulated blastfurnace slag BIOLANOVA and novel hybrid H-CEMENT. *Solid State Phenomena*, 244, 57-64. https://doi.org/10.4028/www.scientific.net/SSP.244.57

[6] K. Yuvaraj, S. Ramesh, M. Velumani (2023) Predicting the mechanical strength of coal pond ash based geopolymer concrete using linear regression method. *Materials Today: Proceedings.* https://doi.org/10.1016/j.matpr.2023.04.514

[7] M.Kanwal, F.Adnan, R. A.Khushnood, A. Jalil, H. A.Khan, A. G.Wattoo, S. Rasheed (2023) Biomineralization and corrosion inhibition of steel in simulated bio-inspired self-healing concrete. *Journal of Building Engineering*, 108224. https://doi.org/10.1016/j.jobe.2023.108224

[8] V.Shubina, L.Gaillet, T.Chaussadent, T.Meylheuc, J. Creus (2016) Biomolecules as a sustainable protection against corrosion of reinforced carbon steel in concrete. *Journal of Cleaner Production*, 112, 666-671. https://doi.org/10.1016/j.jclepro.2015.07.124

[9] R.Mohanraj, S. Senthilkumar, S. Shanmugasundaram, P. Padmapoorani (2022) Torsional performance of reinforced concrete beam with carbon fiber and aramid fiber laminates. *Revista de la Construcción. Journal of Construction*, 21(2), 329-337. https://doi.org/10.7764/RDLC.21.2.329

[10] H. Mohammed, M.Ortoneda-Pedrola, I. Nakouti, A. Bras (2020) Experimental characterisation of non-encapsulated bio-based concrete with self-healing capacity. *Construction and Building Materials*, 256, 119411.https://doi.org/10.1016/j.conbuildmat.2020.119411

[11] K. Kawaai, T. Nishida, A. Saito, T. Hayashi (2022) Application of bio-based materials to crack and patch repair methods in concrete. *Construction and Building Materials*, 340, 127718.

[12] S. V. Fedosov, V. E. Roumyantseva, S. A. Loginova, I. N. Goglev (2021) Experimental Research of the Process Bio-corrosion of Cement Concrete for Inspection of Building Structures. *International Conference Industrial and Civil Construction* (pp. 168-175). Cham: Springer International Publishing. https://doi.org/10.1007/978-3-030-68984-1_25

[13] R. Vasanthi, R. Baskar (2017) Corrosion Based Durability Study in Concrete Using Biomineralization. *Int J CivEngTechnol*, 8(9), 680-91.

[14] R. Jakubovskis, A.Jankutė, J.Urbonavičius, V. Gribniak (2020) Analysis of mechanical performance and durability of self-healing biological concrete. *Construction and Building Materials*, 260, 119822. https://doi.org/10.1016/j.conbuildmat.2020. 119822

[15] M.Velumani, R.Mohanraj, R.Krishnasamy, K. Yuvaraj (2023) Durability Evaluation of Cactus-Infused M25 Grade Concrete as a Bio-Admixture. *PeriodicaPolytechnica Civil Engineering*,67(4). https://doi.org/10.3311/PPci.22050

[16] Y.Yogeswaran, M. I.Juki (2022) The Effect of Bacteria to Steel Corrosion in Concrete: A Systematic Review. *Recent Trends in Civil Engineering and Built Environment*, 3(1), 272-280.

[17] R.Javaherdashti, H.Nikraz, M.Borowitzka, N. Moheimani, M.Olivia, (2009) On the impact of algae on accelerating the biodeterioration/ biocorrosion of reinforced concrete: a mechanistic review. *European Journal of Scientific Research*, 36(3), 394-406.

[18] J. M.Irwan, T. Teddy (2017) An overview of bacterial concrete on concrete durability in aggressive environment. *Pertanika J SciTechnol*, 25, 259-264.

[19] C. C.Gaylarde, B. O. Ortega-Morales (2023) Biodeterioration and Chemical Corrosion of Concrete in the Marine Environment: Too Complex for Prediction. *Microorganisms*, 11(10), 2438. https://doi.org/10.3390/microorganisms11102438

[20] D. Merachtsaki, E. C. Tsardaka, E. K. Anastasiou, H. Yiannoulakis, A. Zouboulis (2021) Comparison of different magnesium hydroxide coatings applied on concrete substrates (sewer pipes) for protection against bio-corrosion. *Water*, 13(9), 1227. https://doi.org/10.3390/w13091227

[21] O.Agboola, K. W.Kupolati, O. S. I.Fayomi, A. O.Ayeni, A.Ayodeji, J. J.Akinmolayemi, ...K. M. Oluwasegun (2022) A Review on corrosion in concrete structure: inhibiting admixtures and their compatibility in concrete. *Journal of Bio-and Tribo-Corrosion*, 8(1), 25. https://doi.org/10.1007/s40735-021-00624-2

[22] G. Fytianos, V.Baltikas, D.Loukovitis, D.Banti, A.Sfikas, E. Papastergiadis, P. Samaras (2020) Biocorrosion of concrete sewers in Greece: current practices and challenges. *Sustainability*, 12(7), 2638.https://doi.org/10.3390/su12072638

[23] R. Mohanraj, R.Krishnasamy(2024) Enhancing Concrete Flexural Behaviour with Euphorbia Tortilis Cactus: Sustainable Additive for Improved Load-Carrying Capacity and Ductility. *Indian Journal of Engineering & Materials Sciences*, 31(3), 388-396. https://doi.org/10.56042/ijems.v31i3.6667

[24] K.M.Gopalakrishnan,R.Mohanraj, S. Southamirajan, S. Ramkumar (2024) Characterization of Euphorbia Tortilis Cactus Concrete Specimen by 3D X-ray Tomography. *Russian Journal of Nondestructive Testing*, 60(6), 692–698. https://doi.org/10.1134/S1061830924601892

[25] M.Seifan, A. K.Samani, A. Berenjian (2016) Bioconcrete: next generation of self-healing concrete. *Applied microbiology and biotechnology*, 100, 2591-2602. https://doi.org/10.1007/s00253-016-7316-z

[26] R.Mohanraj, K. Vidhya (2024) Evaluation of compressive strength of Euphorbia tortilis cactus infused M25 concrete by using ABAQUS under static load. *Materials Letters*, 356, 135600. https://doi.org/10.1016/j.matlet.2023.135600

[27] R. P.George, V.Vishwakarma, S. S.Samal, U. K. Mudali (2012) Current understanding and future approaches for controlling microbially influenced concrete corrosion: a review. *Concrete research letters*, 3(3), 491-506.

[28] S. V.Reddy, A. K.Satya, S. M.Rao, M.Azmatunnisa (2012) A biological approach to enhance strength and durability in concrete structures. *International journal of advances in engineering & technology*, 4(2), 392.

[29] Y. Kandasamy, B.Thangavel, K.K.Sukumar, B. Ravi (2024) Strength properties of engineered cementitious composites containing pond ash and steel fiber. *Matéria (Rio de Janeiro)*, 29(1), e20230277. https://doi.org/10.1590/1517-7076-rmat-2023-0277

[30] K. Yuvaraj, S. Ramesh (2022) Performance study on strength, morphological, and durability characteristics of coal pond ash concrete. *International Journal of Coal Preparation and Utilization*, 42(8), 2233-2247. https://doi.org/10.1080/19392699.2022.2101457

[31] J. Monteny, E.Vincke, A.Beeldens, N.De Belie, L.Taerwe, D.Van Gemert, W.Verstraete (2000) Chemical, microbiological, and in situ test methods for biogenic sulfuric acid corrosion of concrete. *Cement and Concrete Research*, 30(4), 623-634. https://doi.org/10.1016/S0008-8846(00)00219-2

[32] P.Padmapoorani, S.Senthilkumar, R.Mohanraj (2023) Machine Learning Techniques for Structural Health Monitoring of Concrete Structures: A Systematic Review. *Iranian Journal of Science and Technology, Transactions of Civil Engineering*, 47(4), 1919-1931. https://doi.org/10.1007/s40996-023-01054-5

[33] J. Xu, Y. Tang, X. Wang, Z. Wang, W. Yao (2020) Application of ureolysis-based microbial CaCO3 precipitation in self-healing of concrete and inhibition of reinforcement corrosion. *Construction and Building Materials*, 265, 120364. https://doi.org/10.1016/j.conbuildmat.2020.120364

[34] K. Ravikumar, C. J. Singaram, S. Palanichamy, M.Rajendran(2024) Testing and Evaluation of Buckling and Tensile Performance of Glass Fiber–reinforced polymer Angle Section with Different Joints/Connections. *Journal of Testing and Evaluation*, 52(1). http://doi.org/10.1520/JTE20230010

[35] M. Kanwal, R. A. Khushnood, A. G. Wattoo, M.Shahid (2023) Improved anti-corrosion and mechanical aspects of reinforced cementitious composites with bio-inspired strategies. *Journal of Building Engineering*, 70, 105930. https://doi.org/10.1016/j.jobe.2023.105930

[36] B. Huber, H. Hilbig, J. E. Drewes, E. Müller (2017) Evaluation of concrete corrosion after short-and long-term exposure to chemically and microbially generated sulfuric acid. *Cement and Concrete Research*, 94, 36-48. https://doi.org/10.1016/j.cemconres.2017.01.005

[37] R. Mohanraj, S. Senthilkumar, Prince Goel, Ronak Bharti (2023) A state-of-the-art review of Euphorbia Tortilis cactus as a bio-additive for sustainable construction materials. *Materials Today: Proceedings* https://doi.org/10.1016/j.matpr.2023.03.762

[38] X. Sun, O. W.Wai, J. Xie, X. Li (2023) Biomineralizationto Prevent Microbially Induced Corrosion on Concrete for Sustainable Marine Infrastructure. *Environmental Science & Technology* https://doi.org/10.1021/acs.est.3c04680

[39] M. B. E. Khan, L.Shen, D. Dias-da-Costa (2021) Self-healing behaviour of bio-concrete in submerged and tidal marine environments. *Construction and Building Materials*, 277, 122332. https://doi.org/10.1016/j.conbuildmat.2021.122332

[40] E.Vincke, S. Verstichel, J. Monteny, W. Verstraete (1999) A new test procedure for biogenic sulfuric acid corrosion of concrete. *Biodegradation*, 10, 421-428. https://doi.org/10.1023/A:1008309320957

[41] Y. Kandasamy, V.Kumarasamy, P.Thirumoorthy, S.Murugan, R. Subramani(2021) Mechanical, Mineralogical and Durability Properties of Pulverized Pond Ash Based Concrete. *Materials Science*. doi: 10.15244/pjoes/170852

[42] M. Mirshahmohammad, H. Rahmani, M.Maleki-Kakelar, A. Bahari (2022) Effect of sustained service loads on the self-healing and corrosion of bacterial concretes. *Construction and Building Materials*, 322, 126423. https://doi.org/10.1016/j.conbuildmat.2022.126423

[43] T. Noeiaghaei, A.Mukherjee,N.Dhami,S. R. Chae (2017) Biogenic deterioration of concrete and its mitigation technologies. *Construction and Building Materials*, 149, 575-586. https://doi.org/10.1016/j.conbuildmat.2017.05.144

[44] S. Joshi, S. Goyal, M. S. Reddy(2021) Bio-consolidation of cracks with fly ash amended biogrouting in concrete structures. *Construction and Building Materials*, 300, 124044. https://doi.org/10.1016/j.conbuildmat.2021.124044

[45] K. Ravikumar, S. Palanichamy, C. J. Singaram,M. Rajendran (2023) Crushing performance of pultruded GFRP angle section with various connections and joints on lattice towers. *Matéria (Rio de Janeiro)*, 28, e20230003. https://doi.org/10.1590/1517-7076-RMAT-2023-0003

[46] C. S. S.Durga, N. Ruben, M. S. R. Chand, C.Venkatesh (2020) Performance studies on rate of self healing in bio concrete. *Materials Today: Proceedings*, 27, 158-162. https://doi.org/10.1016/j.matpr.2019.09.151

[47] B. Chaudhari, B.Panda, B. Šavija, S. Chandra Paul (2022) Microbiologically Induced Concrete Corrosion: A Concise Review of Assessment Methods, Effects, and Corrosion-Resistant Coating Materials. *Materials*, 15(12), 4279. https://doi.org/10.3390/ma15124279

[48] C. Grengg, F. Mittermayr, N.Ukrainczyk, G. Koraimann, S.Kienesberger, M.Dietzel (2018) Advances in concrete materials for sewer systems affected by microbial induced concrete corrosion: A review. *Water research*, 134, 341-352. https://doi.org/10.1016/j.watres.2018.01.043

[49] T.Haile, G.Nakhla, E.Allouche, S. Vaidya(2010) Evaluation of the bactericidal characteristics of nano-copper oxide or functionalized zeolite coating for bio-corrosion control in concrete sewer pipes. *Corrosion Science*, 52(1), 45-53. https://doi.org/10.1016/j.corsci.2009.08.046

[50] M. Wu, T. Wang, K. Wu, L. Kan (2020) Microbiologically induced corrosion of concrete in sewer structures: A review of the mechanisms and phenomena. *Construction and Building Materials*, 239, 117813. https://doi.org/10.1016/j.conbuildmat.2019.117813

[51] K. Chetty, S. Xie, Y. Song, T. McCarthy, U. Garbe, X. Li, G. Jiang (2021) Self-healing bioconcrete based on non-axenic granules: A potential solution for concrete wastewater infrastructure. *Journal of Water Process Engineering*, 42, 102139. https://doi.org/10.1016/j.jwpe.2021.102139

[52] L.Pattusamy, M.Rajendran, S.Senthilkumar, R. Krishnasamy (2023) Confinement effectiveness of 2900psi concrete using the extract of Euphorbia tortilis cactus as a natural additive. *Matéria (Rio de Janeiro)*, 28(1). https://doi.org/10.1590/1517-7076-RMAT-2022-0233

[53] P. Loganathan, R. Mohanraj, S. Senthilkumar, K. Yuvaraj (2022) Mechanical performance of ETC RC beam with U-framed AFRP laminates under a static load condition. *Revista de la Construcción. Journal of Construction*, 21(3), 678- 691. https:/doi.org/10.7764/RDLC.21.3.678

[54] K. M. Gopalakrishnan, R, Mohanraj, P. Swaminathan, R. Saravanan (2024) Enhancing concrete beam performance with PVAfibers, coal ash, and graphene fabric: a comprehensive structural analysis. *International Journal of Coal Preparation and Utilization*. https://doi.org/10.1080/19392699.2024.2407604

[55] R. Krishnasamy, S. C. Johnson, P. S. Kumar, R. Mohanraj (2024) Experimental Investigation of Lateral Load Test on Diagonal Braced 3M Glass Fiber Reinforced Polymer Transmission Tower. *Power Research - A Journal of CPRI*, 19(2), 225–231. https://doi.org/10.33686/pwj.v19i2.1150

[56] K. Yuvaraj, M.Sakthivel, M.D.Karthick, T.Pradeep, M.Veerapathran, S.Gowtham(2024) Mechanical performance of mono and hybrid synthetic fibers engineered cementitious composites with silica fume. *Journal of Ceramic Processing Research*, 25(2), 254-260.

[57] Y. Kandasamy, M.E.Krishnasamy, K.Moongilpatti Krishnasamy, K.S. Navaneethan (2024) Investigating the influence of various metakaolin combinations with different proportions of pond ash and Alccofine 1203 on ternary blended geopolymer concrete at ambient curing. *Environmental Science and Pollution Research*, 1-12. https://doi.org/10.1007/s11356-024-35397-x

[58] D. Velumani, P. Mageshkumar, K.Yuvaraj(2024) Properties of Binary and Ternary Blended Cement Containing Pond Ash and Ground Granulated Blast Furnace Slag. *Polish Journal of Environmental Studies*, 33(1).

IZVOD

POVEĆANJE OTPORNOSTI NA KOROZIJU U BETONSKIM KONSTRUKCIJAMA KORIŠĆENJEM EKSTRAKTA KAKTUSA *Euphorbia Tortilis* ISPITIVANJEM BEZ RAZARANJA

Ovo istraživanje istražuje otpornost armirano betonskih konstrukcija na koroziju, što je ključni aspekt za obezbeđivanje njihovih dugoročnih performansi i održivosti. Koristeći imetodu polućelijskog potencijala i ubrzani test korozije, studija uvodi novi pristup ugradnjom ekstrakta kaktusa Euphorbia Tortilis (ETC) kao organskog aditiva u beton. Metoda polućelijskog potencijala uključuje merenje potencijalnih razlika između čelične armature i spoljne elektrode u rastvoru Cu/CuSO₄, otkrivajući različite nivoe inhibicije korozije u različitim uzorcima. Primetno je da uvođenje ETC ekstrakta pokazuje otpornost bez presedana, pokazujući samo 10% verovatnoće korozije, čak i u atmosferskim uslovima. Ubrzani test korozije dodatn onaglašava novinu istraživanja. ETC beton pokazuje niže procente primenjene struje iqubitka mase u poređenju sa kontrolnim mešavinama, što ukazuje na superiornu otpornost na koroziju i smanjenu poroznost. Ova nova upotreba ETC ekstrakta u betonu povećava njegovu izdržljivost i održivost, pružajući dragocene uvide u razvoj otpornih betonskih konstrukcija usred sve veće zabrinutosti zbog propadanja armirano betonskih konstrukcija izazvanih korozijom.

Ključnereči: *otpornost na koroziju, betonske konstrukcije, kaktus Euphorbia Tortilis, organski aditiv, održivost*

Dr. M. Velumani   - https://orcid.org/0000-0001-8123-3751
Dr. R. Mohanraj   -https://orcid.org/0000-0002-1795-616X
Dr. P. Loganathan   -https://orcid.org/0000-0002-4154-7593
Dr. N. Sakthieswaran   - https://orcid.org/0000-0001-9926-2390

Jasmina Popović*

University of Belgrade-Faculty of Forestry, Belgrade, Republic of Serbia

Hot water pretreatment in wood biorefining processing

ABSTRACT

Wood can be processed to create various products or components that can cover a wide range of purposes. As a natural reservoir of organic matter, wood is also an important raw material for the production of chemicals and fuels. The limited reserves of fossil resources, environmental pollution and climate change make it necessary to obtain energy and chemicals from renewable raw materials. In this context, there is a growing demand for wood as a renewable and available raw material, which also emphasizes the importance of its optimal use. Namely, the end products made from wood often contain elements that do not significantly enhance the quality of these products, or may even have negative effects. In addition, degradation and permanent loss of valuable wood components can occur during the chemical processing. The introduction of hot water pretreatment in wood processing can be a way to biorefine wood and a solution for a more rational use of its ingredients. In this way, some valuable products such as hemicelluloses, saccharides or extractives (e.g. tannins) and other compounds can be extracted from the wood before the main process. The type and amount of products separated depend on a number of factors such as the wood species and the pretreatment conditions (temperature, pressure and duration of the process). At the same time, changes in its chemical composition can improve some properties of the wood after pretreatmentor facilitate its further processing. This paper shows the influence of hot water pretreatment on some properties of wood, such as dimensional stability and heating value. The possibilities of using water-treated wood for the production of wood products with improved properties are also shown.
Keywords: wood, hot water pretreatment, dimensional stability, heating value

1. WOOD AS A RAW MATERIAL

Wood is a natural raw material with a wide range of uses. Wood is used for the manufacture of numerous products, such as structural elements, windows and doors, furniture, veneers, particle boards and fiberboards and others. Wood is also used as an energy source, in its natural form (logs) or in modified form, as charcoal, briquettes and pellets. Chemical processing of wood can produce cellulose and carbohydrates with different molecular weights such as glucose and xylose and their derivatives,aromatic compounds from the lignin, tannins, turpentine, acetic acid, tar and many other products [1]. The properties and use of wood depend on its anatomical and chemical composition.

*Corresponding author: Jasmina Popović

E-mail: jasmina.popovic@sfb.bg.ac.rs

1.1. Chemical composition and wood properties

The cell walls of wood consist of three biopolymer compounds: cellulose, hemicelluloses and lignin. Cellulose, hemicelluloses, and lignin have completely different structures and properties [2]. Wood also contains a large number of different organic compounds with a lower molecular weight, such as fats, waxes, polyphenols, alkaloids, monosaccharide's, proteins and others. These compounds are referred to as extractives. Their content in wood is usually 3 to 5%, but can be higher in some species. Wood contains up to 1% inorganic substances. After burning the wood, they remain as a non-combustible residue (ash) [2].

Cellulose is the structural material of the cell walls of wood and other plants. Cellulose is a linear homopolymer of β-D-glucose that makes up half namely 40 – 50% of the dry mass of wood [3]. In the cell walls of wood cellulose molecules group into bundles called microfibrils and fibrils. Within the microfibrils, there are highly ordered (crystalline) and less ordered (amorphous) regions [3]. Due to its high crystallinity, cellulose is more

resistant to the effects of chemical reagents than other structural components [4]. **Hemicelluloses** are heteropolymers (hetero-polysaccharides). Hemicelluloses contain many different mono-saccharides as well as their derivatives. The content of hemicelluloses in woodis 20 – 35% [2]**.** Hemicelluloses have no crystalline structure, and are therefore the most reactive component of the cell wall [5]. The hydroxyl groups (-OH) of hemicelluloses contribute greatly to the hydrophilic properties of wood [6-8]. **Lignin** is complex, branched, cross-linked phenolic biopolymer with a high molecular weight. Depending on the wood species, the lignin content in wood is 17 – 35% [3].

The content and properties of the structural cell wall molecules and the relationships between them have a significant influence on the wood properties [9,10].

Hemicelluloses and amorphous regions of cellulose microfibrils contain a large number of available -OH groups, which make the wood hygroscopic. As a result, wood exchanges moisture with itsenvironment. Changes in the moisture content of wood lead to changes in the dimensions of the wood. The hemicelluloses are the most hygroscopic component of wood, while lignin has the lowest hygroscopicity [8]. In addition, the available hydroxyl groups of woodplay an important role in the chemical aspect of adhesion and the formation of an adhesive bond [11,12].

The heating value (HV) of wood is a combination of the heating values of its components and their proportions [13]. The heating value of lignin is the highest (26.7 MJ/kg) [14]. The heating value of cellulose is 17.3 MJ/kg, while hemicelluloses have the lowest heating value at 16.2 MJ/kg [13]. Therefore, the chemical composition of wood has a major influence on the heating value of wood [13]. A high content of mineral substances and high moisture content have a negative effect on the HV of wood [13,14].

2. BIOREFINING

Nowadays, chemicals and energy are obtained by processing fossil raw materials, such as oil. The consequence of the high consumption of fossil raw materials is everincreasing environmental pollution, global warming and other climate changes. This is the reason why the production of chemicals and energy from renewable sources is necessary, as well as the increasing demand for energy and materials in modern society.

Biomass, such as forest and agricultural biomass, is the only renewable resource from which solid, liquid and gaseous fuels, as well as chemicals, can be produced [1,15-20]. Wood, as the most abundant renewable source of

lignocelluloses, has a high potential for utilizationin a biorefinery for the production of chemicals and fuels [3,15,17, 19,21,22]. For these reasons, the demand for wood as a raw material is constantly growing and it's more efficient and rational use is necessary.

In the traditional chemical processing of wood, the components of wood are not optimally utilized (Fig. 1). When chemical processes are used to produce pulp, for example, the wood components are not optimally utilized. The hydrolysis products of the hemicelluloses are found in the black liquor together with the degradation products of lignin and together with small amounts of extractives [23-28]. Black liquor, containing dissolved degradation products of hemicelluloses and lignin, is combusted in the regeneration of chemicals and energy process, although the heating value of carbohydrates and their degradation products is low compared to that of lignin[1].

Figure 1. Diagram of traditional wood processing

By applying biorefining in the chemical processing of wood, wood components such as hemicelluloses or extractives (e.g. tannins) are removed before the main process [23-28]. In this way, the wood components can be more optimallyused. Biorefining is an approach that offers the possibility of producing not only the main product, but also a wide range of valuable secondary products such as fuels (e.g. ethanol), chemicals (such as carbohydrate derivatives and also lignin-based chemicals), extractives andothers [1,15,17,28].

2.1. Pretreatments

Various chemical pretreatments play an important role in biorefinery processes based on lignocellulosic feedstocks [17,29-32]. The application of pretreatments usually aims to change the original chemical composition of the wood and thus enable further processing (e.g. hydrolytic decomposition) and at the same time a more optimal utilization of the wood. Depending on the conditions of the treatment applied (pH value, temperature and treatment duration) the following effects can be achieved in addition to the partial removal of hemicelluloses, removal of part of lignin [29], reduction of crystallinity and degree of cellulose polymerization [33],removal of acetyl groups, etc. [6,29].

Chemical pretreatments include two phases: solid,resulting in wood with an altered chemical composition and properties, and liquid resulting in

hydrolysate or extract resulting in dissolved wood degradation products that can be further converted into the desired chemicals, biomaterials or biofuels (Fig. 2) [15,34-38].

Figure 2. Diagram of wood processing with pretreatment

2.2. Water pretreatments of wood

Water pretreatments have the greatest utilizationpotential because water is non-toxic and non-flammable, inexpensive and available; it is a good solvent, easy to handle and environmentally friendly [1,4,22]. Water pretreatments causes less corrosion to equipment compared to utilizationwith other chemicals [4] and does not require special equipment, so the costs are not high. In addition, no significant cellulose degradation occurs during treatment [1,39,40].

The effects of water pretreatments depend on the treatment parameters, such as temperature, which is the most important parameter, pressure and extraction time, as well as on the properties of the wood samples, such as chemical composition, porosity, surface area to volume ratio, size and mass [1,4,22,41]. Water pretreatments at high temperatures, or *Hot water extraction under pressure* (HWE), or *Pressurized hot-water extraction* (PHWE) is carried out at temperatures ranging from 100 to 374 °C and is the most commonly used pretreatment [16,42,43]. During this process polar and non-polar wood components are dissolved,and the main reaction in this process is the depolymerization and removal of significant amounts of hemicelluloses from the wood [30,44-46]. Higher temperatures and a longer extraction time at HWE lead to degradation of the hemicelluloses [47].

2.3. Possible uses of the resulting extractafter pretreatment

Increased energy consumption due to the introduction of pretreatment can be compensated for by the production of numerous valuable products from the hydrolysate. The hydrolysate contains mono-, oligo- and polysaccharides from hemicelluloses, which account for up to 60 – 80% of the total dissolved organic material, phenolic, aldehydic and other aromatic compounds from lignin, as well as various degradation products, extractives and acetic acid [1,15,34,48-51].

Various aromatic compounds resulting from lignin fractionation can be directly burned as fuel or converted into many valuable products, such as activated carbon or adhesives. Hemicelluloses can be used in polymeric form such as biopolymers or hydrogels [50]. Degradation products of carbohydrates can be converted into ethanol, xylitol, glycerol, sorbitol, arabinitol, furfural, hydroxymethylfurfural, acids such as fumaric, aspartic or levulinic acid, biobased protective films, stabilizers, emulsions and other derivatives that are used in the food, pharmaceutical and cosmetics industries [15,17,20,34,50,52].

3. PROPERTIES OF TREATED WOOD

Changes in the chemical composition of wood are reflected in changes in the physical, mechanical, thermal and biological properties of the original material [53,54]. Popović et al. [55]found that the mass loss of narrow-leaved ash (*Fraxinus angustifolia* Vahl. ssp. *Pannonica* Soó & Simon) wood panels (5 x 20 x 150 mm) during water pretreatments at 100 °C and 120 °C for 1 h was low, 0.90% and 0.92%, respectively. These values indicate that the water treatments at these temperatures did not lead to degradation of the structural compounds of the cell wall [55]. However, the mass loss of narrow-leaved ash wood particles (0.5 - 1 mm) treated at 100 °C of 4.90% is higher than the mass loss of panels treated under the same conditions [56]. The reason for this is the smaller dimensions and the larger contact surface of the wood particles with water during treatment. This leads to faster and more complete chemical reactions [4,22,41]. The mass loss of beech particles (≤ 1.2 mm) treated at 150 °C for 1 h is higher, 10.56% [57]. This indicates significant degradation of wood cell wall polymers (mainly hemicelluloses, but also lignin and cellulose) during treatment. As a result of the loss of mass during pretreatment, the density of the treated wood is lower, which is reflected in its lower mechanical properties [58,59]. However, some other properties of the wood can be improved, which can result in better properties of the final product.

3.1. Wateruptakeandvolumetricswelling

The degradation of hemicelluloses during water pretreatment reduces the number of accessible -OH groups. This leads to a reduction in the hygroscopic character, lower water absorption and higher dimensional stability of the treated wood samples [6,7,48,60].

Popović [56] investigated water uptake as a function of time during 48 hours immersion in water (20 °C) of water-treated (100 and 120 °C, 1 h) narrow-leaved ash wood panels, as well as volumetric swelling. In the first 10 hours of immersion, both groups of treated samples absorb larger amounts of water compared to the control samples. After the first hour, the water uptake of the samples treated with water at 100 °C increased by 25.51% compared to the control samples [56]. The more intense water uptake of the treated samples during the first 10 hours indicates that the treatments increased the permeability and porosity of the ash wood. The reason for this could be the removal of extractives from the wood structure during the treatment[56]. After 10 hours of immersion, the intensity of water uptake decreases. The samples treated at 100 °C absorbed the least amount of water after 48 hours. This indicates that the applied treatments did not lead to a significant disruption of the cell wall structure and the appearance of new cavities of significant size, which is consistent with a low mass loss during the treatment [55].

Mohebby and Sanaei [61] found an increased moisture absorption of beech wood samples (*Fagus orientalis*) after hydrothermal treatment at 180 °C, as well as by Zhang et al. [60], who noted increased water absorption of pine strand samples after hot water extraction. Zhang et al. [60]and Paredes [62]explain the increased water absorption of the treated samples by the increase in the number and volume of pores and the appearance of micropores in the cells, which promote the capillary movement of water in the treated samples.

However,Hornus et al. [63] found that the equilibrium moisture content (EMC) of water treated (120, 140 and 160°C, 45 min) southern yellow pine (Pinus spp.) strands was reduced compared to control samples. Sattler et al. [64]investigated the effects of water treatment at 120, 140 and 160 °C for 20, 40 and 60 min on the physical and chemical properties of loblolly pine (*Pinus taeda*) wood flakes. They found that the EMC of flakes decreasedwith increasesin temperature and treatment duration, indicating an increase in the dimensional stability of the samples[64]. Paredes et al. [48] also found that the EMC of OSB boards made from water-treated red maple chips at 160 °C was reduced, but that the water absorption of these boards was increased during immersion. The authors explained this disagreement with the consequences of the treatment [48].

Popović [56]also investigated the volumetric swelling of water-treated (100 and 120 °C, 1 h)

narrow-leaved ash wood panels during immersion in water for 48 h (20 °C). During the entire immersion, the control group of samples showed higher swelling compared to both treated groups of samples, even though their water absorption was lower. Water absorption and swelling are usually strongly correlated, but the relationship changes when extracted wood is used[48]. Popović [56]concluded that pretreatments with water at 100 and 120 °C led to an increase in the dimensional stability of ash wood panel samples, despite more intensive water absorption in the first hours of immersion [56]. After the first hour of immersion, the samples treated with water at 100 °C showed 5.87% less swelling compared to the control samples. These samples showed a maximum decrease in volumetric swelling of 20.27% compared to the control samples after 24 hours of immersion [56]. An increase in dimensional stability indicates a decrease in the content of available –OH groups as a result of the treatment. During hydrothermal treatment, wood degradation processes already start at temperatures of 100 °C, during which small amounts of amorphous areas of the cellulose dissolve [65,66], but also glucomannans [66].

3.2. Adhesion properties

The adhesion properties of wood are important for all processes that involve bonding, such as the manufacture of wood-based panels. Some of the factors that affect the chemical interaction between the wood and the adhesive can also change during pretreatment. Hydroxyl groups are potential sites for the formation of bonds between the wood and the adhesive [11]. Thus, as the number of available -OH groupsdecreases the number of bonds between the wood and the adhesive also decreases. In this way, the pretreatments affect the changes in the adhesion properties of the wood and the strength of the bond [67]. The removal of acetyl groups and extractives during pretreatment changes the pH value of the wood, which can also affect the curing of the adhesive.

Popović et al. [55] examined the tensile shear strength in the lap joint of water-treated (100 and 120 °C, 1 h) narrow-leaved ash wood panels. They found that the shear strength of the control and treated samples did not differ significantly. This indicatedthat the applied pretreatments did not have a significant influence on the structural compounds of the wood [55]. A slight decrease in the shear strength of the treated samples compared to the control is probably due to aslight decrease in the content of available –OH groups, which is due to the dissolution of small amounts of amorphous regions of cellulose and glucomannans [65,66].

Based on the results shown, it can be assumed that water pretreatment at temperatures of 100 and 120 °C did not significantly change the adhesion properties of the ash wood panels[55]. These results indicate that the applied treatments do not significantly affect the interaction of wood and adhesive in wood-based panels made from water-treated ash wood at 100 and 120 °C.

3.3. Heatingvalue

The removal of hemicelluloses, whose heating value is low compared to lignin, can increase the heating value of treated wood [14,26]. Popović [56] found that heating value (HV) of ash wood particles increased slightly(by 0.17%), after water treatment at 100 °C. Laurová and Kačík [66] state that during hydrothermal treatment in the temperature range of 100-140 °C, glucomannans and the amorphous region of cellulose undergo autohydrolysis. Mamoňová et al. [65] also find that during hydrothermal treatment, wood degradation begins at temperatures as low as 100 °C, when small amounts of the amorphous region of cellulose dissolve, while xylans are stable at these temperatures.

Water treatment at higher temperaturesresulted in more significant changes in the chemical structure [63-66]. Laurová and Kačík [66] and Sattler et al. [64] found that the concentration of carbohydrate degradation products in the hydrolysate increases with increasing temperature and treatment duration. However, Hornus et al. [63] found that the cellulose content in southern yellow pine (Pinus spp.) strands increases with increasing water treatment temperature from 120 to 160°C, while a significant loss of hemicelluloses occurs only at 160° C. The intensive hydrolysis of xylan starts at 140 °C [64,65] and is the dominant reaction at a temperature of 160 °C [66]. According to Pu et al. [26] and Runge et al. [14] the HV of wood increases after the removal of hemicelluloses. However, depending on the conditions, lignin degradation reactions also occur in the water medium. Laurová and Kačík [66] found that the concentration of lignin degradation products (syringaldehyde and vanillin) in the hydrolysate from hydrothermal treatment increases slowly with an increase in temperature from 100 to 140°C. owever, with increasing temperature (and duration of hydrolysis), the proportion of these substances in the hydrolysate increases and reaches maximum values at 160 °C [66]. Sattler et al. [64]reported a lignin loss of 1.24% during the 60 minute water extraction of loblolly pine (Pinus taeda) flakes at 160 °C. The decomposition of lignin at high treatment temperatures has an effect on the reduction of the HV of the samples. Popović et al. [57] found that the content of hemicelluloses decreased and the content of cellulose in beech wood particles increased after treatment with water at 150 °C, while the content of lignin did not change significantly. These changes in the content of wood constituents led to an increase in carbon (C) content by 1.4% and a decrease in oxygen (O) content by about 1.4% in the treated samples. As a result, the C/O ratio and HV increased by 2.8% and 2.5% [57].

3.4. Viscoelastic properties of wood

The degradation of hemicelluloses, which contribute significantly to the viscoelastic properties of wood, reduces the elasticity of the wood and it becomes brittle and stiff. This facilitates the compression of wood particles in processes involving pressing, such as particleboards or the productionof pellets. This improves the contact between the particles, which promotes the formation of bonds and increases the strength and stiffness of the product, while the lower elasticity of the wood influences the reduction of the springback effect [68].

4. UTILIZATION POSSIBILITIES OF WATER-TREATED WOOD

Water-treated wood can be used to produce wood-based boards with improved properties, such as oriented strand boards (OSB) [48,63], particleboards (PB) [56,68], fiberboards [69] or wood-plastic composites (WPCs) [70,71]. A lower EMC value for 6.2% of OSB made of red maple (*Acer rubrum* L.) strands extracted with water at 160 °C compared to the moisture content of control boards of 10.2% was established by Paredes et al.[48]. At the same time, water uptake was increased while the thickness swelling of OSB from treated strands was reduced [48].OSB from of southern yellow pine strands treated with water (120, 140, and 160 °C, 45 min) showed lower water absorption and thickness swelling compared to control OSB while increasing modulus of elasticity (MOE) and bending strength (MOR) [63].

Popović [56]found that particleboards made from narrow-leavedash particles treated with water at 100 °C for 1 h had a lower density as well as a lower EMC at all applied ambient moisture conditions (32%, 65% and 90%, 20 °C) compared to control panels. This led to a reduction in thickness swelling of about 23% compared to the control panels [56]. Pelaez-Samaniego et al. [68] investigated the effects of HWE (160 °C, 90 min) of ponderosa pine (*Pinus ponderosa* Dougl. Ex Laws.) and sugar maple (*Acer saccharum* Marsh.) chips on the properties of particleboard. They find that HWE increases compressibility and reduces springback by 34% for maple chips and 44% for pine chips. The water absorption of PB panels from

HWE samples was reduced by 35% (pine) and 30% (maple). This resulted in a reduction in thickness swelling by 39% for pine PB and 56% for maple PB after 24 hours of immersion in water. At the same time, the mechanical properties were not significantly affected [68].

The dimensional stability of wood-plastic composites (WPCs) made from polypropylene and extracted southern yellow pine (Pinus spp.) wood flour in cold water for 1, 3 and 5 days and in boiling water for 1, 3 and 5 hours was significantly improved compared to the corresponding WPCs made from untreated flour. In all treatment conditions applied, the water absorption and thickness swelling of the WPCs were lower than those of WPCs made from non-extracted wood [71].

Medium-density fiberboard (MDF) made from hydrothermally treated fibers at 120, 150 and 180 °C for 30 and 90 minutes showed increased dimensional stability. Although the hydrothermal treatment of the fibers did not affect water absorption, the thickness swelling of MDF made from treated fibers was significantly reduced. However, the mechanical properties were also reduced [69].

Wood particles with increased HV after HWE can be used for the production of wood biofuels such as pellets. Pellets produced from beech particles water-treated at 150 °C (with a MC of 10%) showed a 5.84% higher HV and 24.24% lower ash content compared to control pellets [57]. In addition, due to the reduction of the springback effect caused by the loss of hemicelluloses, the diameter of pellets from treated wood particles showed a lower deviation from the nominal value, the density of pellets after conditioning (68%, 20.1 °C) increased by 15.70%, which resulted in an increase in bulk density by 20.57% compared to control pellets [57]. A pellet made from water-treated (170 °C, 60 min) poplar wood (*Populus maximowiczii x nigra*) chips showed a 5.8% higher HV, 12.1% higher density and 18.5% higher energy density compared to a pellet made from untreated wood chips of this type. The compressive strength and durability of pellets made from poplar chips treated with liquid hot water were also significantly higher [14].

5. CONCLUSION

Depending on the conditions of the process, water treatment leads to greater or lesser degradation of the wood. If the water treatments take place at lower temperatures, there is no significant degradation of the structural molecules of the cell wall.With an increase in the treatment temperature, the cell wall structural compounds - primarily hemicelluloses and amorphous areas of cellulose microfibrils, but also lignin, are degraded.The products of wood decomposition are in the liquid phase of the treatment - the hydrolyzate, and they can be used to produce numerousvalue added products.

The changes that occur in the chemical composition are reflected in the physical, mechanical, thermal and other properties of wood. The degradation of hemicelluloses during water pretreatment reduces the number of accessible -OH groups.This results in a decrease in hygroscopic character and an increase in dimensional stability, despite the higher water absorption of water-treated wood samples, as well as an increase in thermal power. In addition, the elasticity of wood decreases, whichis significant for wood products produced by pressing.Water treatments can also affect the adhesive properties of wood.

Water treatments at certain parameters can be applied for wood products with improved properties, such as wood-based panels (OSB, PB, MDF, WPCs) with improved dimensional stability, as well as for solid fuels such as pellets, with improved combustion properties (HV, ash and moisture content).

Considering the above, it can be concluded that liquid hot water pretreatment in wood biorefining processing can result in more efficient use of wood, with the simultaneous production of wood products with improved properties.

6. REFERENCES

[1] J.T.Lehto, R.J.Alén (2014) Chemical Pretreatments of Wood Chips Prior to Alkaline Pulping - A Review of Pretreatment Alternatives, Chemical Aspects of the Resulting Liquors, and Pulping Outcomes, Bio Resources 10(4), 8604-8656.
doi: 10.15376/biores.10.4.lehto.

[2] E.Sjöström (1993)Wood Chemistry – Fundamentals and Applications, 2nd edition, Academic Press, San Diego, CA, USA.

[3] T.Stevanovic (2016) Chemical Composition and Properties of Wood, book Lignocellulosic Fibers and Wood Handbook: Renewable Materials for Today's Environment. Belgacem, N. Pizzi, A.Eds.; Wiley: Hoboken, NJ, USA, p. 49-106.
doi: 10.1002/9781118773727.ch3.

[4] J.Krogell(2015) Intensification of Hemicellulose Hot-water Extraction from Spruce Wood by Parameter Tuning, Doctoral Thesis, Laboratory of Wood and Paper Chemistry, Åbo Akademi University, Turku, Finland.

[5] G.Hu, J.A.Heitmann, O.J.Rojas (2008) Feedstock pretreatment strategies for producing ethanol from wood bark and forest residues, BioResources, 3(1), 270-294.
doi: 10.15376/BIORES.3.1.270-294.

[6] O.Hosseinaei, S.Wang, G.T.Rials, C.Xing, A.M. Taylor, S.Kelley(2011) Effect of hemicellulose extraction on physical/mechanical properties and mold susceptibility of flakeboard, Forest Products Journal, 61(1), 31-37.
doi: 10.13073/0015-7473-61.1.31.

[7] O.Hosseinaei, S.Wang, T.G.Rials, Y.Hing, Y.Zhang (2011) Effects of decreasing carbohydrate content on properties of wood strands, Cellulose, 18, 841-850. doi: 10. 1007/s10570-011-9519-x.

[8] S.Hou, J.Wang, F.Yin, C.Qi, J.Mu (2022) Moisture sorption isotherms and hysteresis of cellulose, hemicelluloses and lignin isolated from birch wood and their effects on wood hygroscopicity. Wood Science and Technology, 56, 1087–1102. doi: 10.1007/s00226-022-01393-y.

[9] J.J.Paredes, S.M.Shaler, C.Howell, J.Jakes (2017) Influence of hot water extraction on cell wall and OSB strand mechanics, Wood Sci. Technol., 51, 1307–1319. doi: 10.1007/s00226-017-0951-4.

[10] L.Cheng, P.Zhao, Y.Di, J.Dai, W.Wang (2023) Correlation of wood properties with chemical composition and microstructure of wood components. Research Square
doi:10.21203/rs.3.rs-2611726/v1. (*preprint*)

[11] B.H.River, C.B.Vick, R.H.Gillespie (1991) Wood as an adherend,book: Treatise on Adhesion and Adhesives. Vol. 7. J.D.Minford (Ed.), CRC Press, Marcel Dekker, New York, p. 1-238.

[12] R.C.Frihart (2006) Wood Structure and Adhesive Bond Strength, book: Characterization of the Cellulosic Cell Wall, D.D.Stokke, L.H.Groom, Blackwell Publishing, p. 241-253.

[13] S.Döring (2013) Power from Pellets: Technology and Applications, Springer-Verlag Berlin Heidelberg. doi: 10.1007/978-3-642-19962-2.

[14] T.Runge, P.Wipperfurth, C.Zhang (2013) Improving biomass combustion quality using a liquid hot water treatment, Biofuels, 4(1), 73-83.
doi: 10.4155/bfs.12.70.

[15] T.E.Amidon, C.D.Wood, A.M.Shupe, Y.Wang, M.Graves, S. Liu (2008) Biorefinery: conversion of woody biomass to chemicals, energy and materials. J. Biobased Mater. Biol., 2,100–120.
doi: 10.1166/jbmb.2008.302.

[16] A T.E.midon, S.Liu (2009) Water-based woody biorefinery, Biotechnol. Adv., 27(5), 542-550. doi: 10.1016/j.biotechadv.2009.04.012.

[17] F.Carvalheiro, L.C.Duarte, F.M.Gírio, (2008) Hemicellulose biorefineries: A review on biomass pretreatments,J. Sci. Ind. Res., 67, 849-864.

[18] S.Liu, L.P.Abrahamson, G.M.Scott (2012) Biorefinery: Ensuring biomass as a sustainable renewable source of chemicals, materials and energy, Biom. Bioen.,39, 1-4.
doi: 10.1016/j.biombioe.2010.12.042.

[19] S.Liu, H.Lu, R.Hu, A.Shupe, L.Lin, B.Liang (2012) A sustainable woody biomass biorefinery, Biotechnol. Adv., 30(4),.785-810.
doi: 10.1016/j.biotechadv.2012.01.013.

[20] B.M.Bujanovic, M.J.Goundalkar, T.E.Amidon(2012) Increasing the value of a biorefinery based on hot-water extraction: Lignin products, Tappi J., 11(1), 19-26.

[21] S.Liu (2010) Woody biomass: Niche position as a source of sustainable renewable chemicals and energy and kinetics of hot-water extraction/ hydrolysis, Biotechnol. Adv.,28(5), 563-582. doi: 10.1016/j.biotechadv.2010.05.006.

[22] J.Krogell, E.Korotkova, K.Eränen, A.Pranovich, T.Salmi, D.Murzin, S.Willför (2013) Intensification of hemicellulose hot-water extraction from spruce wood in a batch extractor – Effects of wood particle size. Bioresource Technology, 143, 212–220. doi: 10.1016/j.biortech.2013.05.110.

[23] M.S.Tunc, A.R.P.van Heiningen (2008) Hydrothermal dissolution of mixed southern hardwoods, Holzforschung, 62(5), 539-545.
doi: 10.1515/HF.2008.100.

[24] M.S.Tunc, A.R.P.van Heiningen (2008) Hemicellulose extraction of mixed southern hardwood with water at 150 °C: Effect of time, Ind. Eng. Chem. Res., 47(18), 7031-7037.
doi: 10.1021/ie8007105.

[25] W.W.Al-Dajani, U.W.Tschirner (2010) Pre-extraction of hemicelluloses and subsequent ASA and ASAM pulping: Comparison of autohydrolysis and alkaline extraction, Holzforschung, 64(4), 411-416. doi: 10.1515/hf.2010.064.

[26] Y.Pu, T.Treasure, R.Gonzalez, R.Venditti, H.Jameel (2011) Autohydrolysis pretreatment of mixed hardwoods to extract value prior to combustion, BioResources, 6(4), 4856-4870.
doi:10.15376/biores.6.4.4856-4870.

[27] W.Liu, Z.Yuan, C.Mao, Q.Hou, K.Li(2012) Extracting hemicelluloses prior to aspen chemi-thermomechanical pulping: Effects of pre-extraction on pulp properties, Carbohydr. Polym., 87(1), 322-327. doi: 10.1016/j.carbpol.2011.07.050.

[28] R.Martin-Sampedro, M.E.Eugenio, J.A.Moreno, E.Revilla, J.C.Villar (2014) Integration of a kraft pulping mill into a forest biorefinery: Pre-extraction of hemicellulose by steam explosion versus steam treatment, Bioresour. Technol., 153, 236-244. doi: 10.1016/j.biortech.2013.11.088.

[29] N.Mosier, C.Wyman, B.Dale, R.Elander, Y.Y.Lee, M.Holtzapple, M.Ladisch (2005) Features of promising technologies for pretreatment of lignocellulosic biomass, Bioresour. Technol., 96(6), 673-686. doi: 10.1016/j.biortech.2004.06.025.

[30] S.H.Yoon, K.Macewan, A.van Heiningen (2008) Hot-water pre-extraction from Loblolly pine (Pinus taeda) in an integrated forest products biorefinery, Tappi J., 7(6), 27-32.

[31] S.H.Yoon, A.van Heiningen (2008) Kraft pulping and papermaking properties of hot-water pre-extracted loblolly pine in an integrated forest products biorefinery,TAPPI J., 7(7), 22-27.

[32] S.H.Yoon, A.van Heiningen (2010) Green liquor extraction of hemicelluloses from southern pine in an Integrated Forest Biorefinery, J. Ind. Eng. Chem., 16(1), 74-80.
doi: 10.1016/j.jiec.2010.01.018.

[33] E. Rojo, M.V. Alonso,J.C. Domínguez,B.Del Saz-Orozco, M.Oliet, F.Rodriguez (2013) Alkali treatment of viscose cellulosic fibers from eucalyptus wood: Structural, morphological, and thermal analysis, Journal of Applied Polymer Science, 130(3), 2198–2204.
doi: 10.1002/app.39399.

[34] H Wikberg, V. Grönberg, J. Jermakka, K. Kemppainen, M.Kleen, C. Laine, V. Paasikallio, A. Oasmaa (2015) Hydrothermal refining of biomass: An overview and future perspectives. Tappi Journal, 14(3), 195-207.

[35] O.J.Sánchez,C.A.Cardona (2008) Trends in biotechnological production of fuel ethanol from different feedstocks. Bioresour. Technol., 99(13), 5270-5295. doi: 10.1016/j.biortech.2007.11.013

[36] P.Alvira,E.Tomás-Pejó,M.Ballesteros,M.J.Negro (2010) Pretreatment technologies for an efficient bioethanol production process based on enzymatic hydrolysis: a review. Biores. Technol., 10, 4851–4861.doi: 10.1016/j.biortech.2009.11.093.

[37] J.Y.Zhu, X.J.Pan (2010) Woody Biomass Pretreatment for Cellulosic Ethanol Production: Technology and Energy Consumption Evaluation. Bioresource Technology, 101, 4992-5002. doi: 10.1016/j.biortech.2009.11.007.

[38] C.Gong,B.M.Bujanovic (2014) Impact of Hot-Water Extraction on Acetone-Water Oxygen Delignification of Paulownia Spp. and Lignin Recovery, Energies, 7(2), 857-873.doi: 10.3390/en7020857.

[39] G.Garrote, H.Domínguez, J.C.Parajó(1999) Hydro-thermal processing of lignocellulosic materials, Holz als Roh- und Werkst., 57(3), 191-203.
doi: 10.1007/s001070050039.

[40] Y.Lei, S.Liu, J.Li, R.Sun (2010) Effect of hot-water extraction on alkaline pulping of bagasse, Biotechnol. Adv., 28(5), 609-612.
doi: 10.1016/j.biotechadv.2010.05.009.

[41] M.A.Kleen, T.M.Liitiä, M.M.Tehomaa (2011) The effect of the physical form and size of raw materials in pressurized hot water extraction of birch, 16. International Symposium on Wood, Fibre and Pulping Chemistry, ISWFPC, Tianjin, China, proceedings, p. 1013-1018.

[42] Y.Kim, R.Hendrickson, N.S.Mosier, M.R.Ladisch (2009) Liquid hot water pretreatment of cellulosic biomass, book: Biofuels – Methods and Protocols, J.R.Mielenz(ed.), Humana Press Springer, New York, NY, USA, p. 93-102.

[43] R.Singh, A.Shukla, S.Tiwari, M.Srivastava (2014) A review on delignification of lignocellulosic biomass for enhancement of ethanol production potential, Renew. Sustain. Energy Rev., 32, 713-728. doi: 10.1016/j.rser.2014.01.051.

[44] T.E.Amidon, T.S.Bolton, R.C.Francis, K.Gratien (2006) Effect of Hot Water Pre-Extraction on Alkaline Pulping of Hardwoods. In Tappi Engine-ering, Pulping and Environmental Conference, Atlanta, p. 156.

[45] G.Garrote, H.Domínguez, J.C.Parajó (2001) Generation of xylose solutions from *Eucalyptus globulus* wood by autohydrolysis-posthydrolysis processes: Posthydrolysis kinetics, Bioresour. Technol., 79(2), 155-164. doi: 10.1016/s0960-8524(01)00044.

[46] C.Liu, C.E.Wyman (2005) Partial flow of compres-sed-hot water through corn stover to enhance hemicellulose sugar recovery and enzymatic digestibility of cellulose, Bioresour. Technol., 96, 1978–1985. doi: 10.1016/j.biortech.2005.01.012.

[47] M.Borrega, K.Nieminen, H.Sixta(2011) Degradation kinetics of the main carbohydrates in birch wood during hot water extraction in a batch reactor at elevated temperatures, Bioresour. Technol., 102 (22),10724-10732.
doi: 10.1016/j.biortech.2011.09.027.

[48] J.J.Paredes, R.Jara, S.M.Shaler, A.van Heiningen (2008) Influence of hot water extraction on the physical and mechanical behavior of OSB, For. Prod. J., 58(12), 56-62.

[49] P.Kilpeläinen, K.Leppänen, P.Spetz, V.Kitunen, H.Ilvesniemi, A.Pranovich, S.Willför (2012) Pressurised hot water extraction of acetylated xylan from birch sawdust, Nord. Pulp Pap. Res. J., 27(4), 680-688.
doi: 10.3183/NPPRJ-2012-27-04-p680-688.

[50] M.Fišerová, E.Opálená (2012) Hemicelluloses extraction from beech wood with water and alkaline solutions, Wood research, 57(4), 505-514.

[51] L.Cruz-Lopes, Y.Dulyanska, I.Domingos, J.Ferreira, A.Fragata, R.Guiné, B.Esteves (2022) Influence of Pre-Hydrolysis on the Chemical Composition of Prunus avium Cherry Seeds, Agronomy, 12(2), 280. doi: 10.3390/agronomy12020280.

[52] C.G.Yoo (2012) Pretreatment and fractionation of lignocellulosic biomass for production of biofuel and value-added products, Doctoral dissertation, Iowa State University.

[53] C.A.S.Hill (2006) Wood modification: chemical, thermal and other processes, John Wiley & Sons, New York.

[54] J.Kúdela (2009) Permanent changes to structure and properties of beech and ash wood after hydro-thermal plasticization. Part I. Changes to selected properties.Folia Forestalia Polonica, 40, 3-14.

[55] J.Popović, M.Popović, M.Điporović-Momčilović, I. Gavrilović - Grmuša (2015) Effects of the Chemical Treatment Conditions of the Narrow-Leaved Ash (Fraxinus angustifolia Vahl. ssp. Pannonica Soo & Simon) on the Lap Shear Strength, Wood Research,60(4), 543-554.

[56] J.Popović (2015) Efekti nekih predtretmana na hemijski sastav juvenilnog i zrelog drveta poljskog jasena (*Fraxinus angustifolia* Vahl. ssp. *Pannonica* Soó & Simon) i mogućnosti primene tako modifikovanog drveta, Doktorska disertacija, Univer-zitet u Beogradu - Šumarski fakultet, Beograd, Srbija.

[57] J.Popović, M.Popović, M.Điporović-Momčilović, A. Prahin, V.Dodevski, I.Gavrilović-Grmuša (2021) Effects of Water Pretreatment on Properties of Pellets Made from Beech Particles, Hem. Ind. 75(1), 39-51. doi: 10.2298/HEMIN191224007P.

[58] R.M.Kellog, G.Ifju (1962) Influence of specific gravity and certain other factors on the tensile properties of wood. Forest Prod. *J.* 12(10), 463-470.

[59] P.R.P.Blankenhorn, Jr.L.Labosky, R.Stover, D. Nicholls (1989) Selected chemical modifications of red oak and hard maple flakes for flakeboard manufacturing. Wood Fiber Sci., 21(2), 169-176.

[60] Y.Zhang,O.Hosseinaei, S.Wang, Z.Zhou (2011) Influence of hemicelluloses extraction on water uptake behavior of wood strands, Wood and Fiber Science, 43(3), 244-250.

[61] B.Mohebby, I.Sanaei (2005) Influence of hydrothermal treatment on physical properties of beech wood. The International Research Group on

Wood Protection, 36. Annual Meeting, Bangalore, India,IDocument No IRG/WP 05- 40303. p. 2-9.

[62] J.J.Paredes,(2009) The influence of hot water extraction on physical and mechanical properties of OSB, Doctoral Thesis, The University of Maine, Orono,USA.

[63] N.Hornus, G.Cheng, I.Erramuspe, M.Peresin, T.Gallagher, B.Via, (2020) Oriented strand board with improved dimensional stability by extraction of hemicelluloses, Wood and Fiber Science, 52, 257-265. doi: 10.22382/wfs-2020-024.

[64] C.Sattler,N.Labbe,D.Harper,T.Elder,T.Rials (2008) Effects of hot water extraction on physical and chemical characteristics of oriented strand board (OSB) wood flakes. Clean-Soil Air Water,36(8), 674-681. doi: 10.1002/clen.200800051.

[65] M.Mamoňová, M.Laurová, V.Nemčoková (2002) Analysis of structure of beech wood subjected to hydrothermal treatment, 4. IUFRO Symposium, Zvolen, Slovakia. Proceedings - Wood structure and properties, p. 51-55.

[66] M.Laurová, F.Kačík (2009)Permanent changes to structure and properties of beech and ash wood after its hydrothermal plasticization. Part II. Chemical changes, Folia Forestalia Polonica, 40, 15-22.

[67] M.Šernek, M.Humar, M.Kumer, F.Pohleven (2007) Bonding of thermally modified spruce with PF and UF adhesives, 5. COST E34 International workshop on bonding of modified wood, Bled, Slovenia, Proceedings, p. 31-37.

[68] M.R.Pelaez-Samaniego,V.Yadama,T.Garcia-Perez,E.Lowell,T.Amidon (2014) Effect of hot water extracted hardwood and softwood chips on particleboard properties, Holzforschung, 68(7), 807–815. doi: 10.1515/hf-2013-0150.

[69] B.Mohebby, F.Ilbeighi, S.Kazemi-Najafi (2008) Influence of hydrothermal modification of fibers on some physical and mechanical properties of medium density fiberboard (MDF), Holz als Roh- und Werkstoff, 66, 213-218.
doi:10.1007/s00107-008-0231-y.

[70] M.Pelaez-Samaniego, V.Yadama, E.Lowell, T.Amidon, T.Chaffee (2013) Hot water extracted wood fiber for production of wood plastic composites (WPCs), Holzforschung, 67(2), 193-200. doi: 10.1515/hf-2012-0071.

[71] F.Ozdemir, A.Kaymakci, J.H.Kwon (2014) Improving dimensional stability of injection molded wood plastic composites using cold and hot water extraction methods, Maderas: Ciencia y Tecnologia, 16(3), 365-372.
doi: 10.4067/S0718-221X2014005000029.

IZVOD

PRIMENA PREDTRETMANA VRELOM VODOM U BIORAFINACIJI DRVETA

Drvo se može preraditi u razne proizvode ili poluproizvode sa širokim spektrom primene. Kao prirodni rezervoar organskih materija, drvo je, takođe, važna sirovina za proizvodnju hemikalija i goriva. Ograničenost rezervi fosilnih resursa, zagađenje životne sredine i klimatske promene nameću potrebu za proizvodnjom energije i hemikalija iz obnovljivih sirovina. U tom kontekstu potražnja za drvetom kao obnovljivom i dostupnom sirovinom sve više raste, a time i potreba za njegovim optimalnijim iskorišćenjem. Naime, u krajnjim proizvodima od drveta često se nalaze sastojci koji ne utiču značajno na njihov kvalitet, ili čak mogu imati negativan uticaj. Pored toga, tokom hemijskih procesa prerade može doći do degradacije i trajnog gubitka vrednih sastojaka drveta. Uvođenje predtretmana vrelom vodom u procese prerade drveta može biti jedan od načina biorafinacije drveta i racionalnijeg iskorišćenja njegovih sastojaka. Tako se, pre glavnog procesa prerade, iz drveta mogu izdvojiti vredni proizvodi kao što su hemicelulozni šećeri ili ekstraktivi (na primer tanini), ali i druga jedinjenja. Vrsta i količina izdvojenih proizvoda zavise od brojnih faktora kao što su vrsta drveta i uslovi izvođenja predtretmana (temperatura, pritisak i trajanje procesa). Istovremeno, usled promena u hemijskom sastavu, posle predtretmana mogu biti poboljšana neka svojstva drveta, ili se može olakšati njegova dalja prerada. U ovom radu prikazan je uticaj predtretmana vrelom vodom na neka svojstva drveta, kao što su dimenzionalna stabilnost i toplotna moć. Takođe su prikazane mogućnosti upotrebe drveta tretiranog vodom za proizvodnju proizvoda od drveta poboljšanih svojstava.

Ključne reči: *drvo, predtretman vrelom vodom, dimenzionalna stabilnost, toplotna moć*

JasminaPopović: https://orcid.org/0000-0003-2122-7311

Prabin Kumar Mahato[1]*, Swarat Choudhuri[2],
Shristi Chaudhary[3], Prashanta Patra[4], Deepak Gupta[5]

[1]*Department of Physics, Ranchi University, Ranchi, India,* [2]*Department of Physics, St. Xavier College, Ranchi, India,* [3]*Department of Physics, Chandigarh University, Gharuan, Mohali, Punjab, India,* [4]*Department of Physics, Kolhan University, Chaibasa, India,* [5]*School of Basic and Applied Sciences, Galgotias University, Greater Noida, India*

Morphological, size-dependent field emission investigation of GO and rGO nanosheet

ABSTRACT

Here, we report the role of surface morphologies and grain size on electron field emission characteristics of GO and rGOnanosheets, synthesized through the modified Hummer method. The plasmon peaks were observed at 290nm -310nm for both samples. Here, a plasmonicenergy-associated effective mass model was used to calculate the crystal size of the nanosheet, which is 3.56nm and 4.79nm for GO and rGOnanosheet, which confirms the confinement behavior. Raman data recorded for GO and rGO nanosheet confirm the presence of D and G bands, suggesting growth of GO and rGO, in addition, the Crystal size is calculated by Raman data, which is comparable to Bohr exciton radius size, indicating the GO and rGO are quantum dots. The electron field emission parameters of synthesized GO and rGOnanosheets have been investigated and parameters are calculated by the Fowler–Nordheim (F-N) equation. Among them, the GO sample exhibits the best electron field emission properties with the minimum turn-on voltage of 8.2 V/µm and the field enhancement factor of 1200 due to possessing the smallest emitter tip radius(size) and the varying surface morphologies.
Keywords: Graphene oxide, Raman, Band gap, Field Emission

1. INTRODUCTION

Graphene and its derivatives, such as graphene oxide (GO) and reduced graphene oxide (rGO) are said to be effective and promising materials for many applications. Graphene shows a 2D structure, where a uniform, homogeneous single layer of carbon (Z=6) atoms are set in a hexagonal lattice plane and play a significant role in emission properties [1]. Moreover, graphene and its derivatives(GO and rGO) are usually flat with better transmission and efficient charge transfer [2]. Since graphene is getting attraction in nano and tech. fields. Graphene shows high surface area, a variable energy gap, extraordinary thermal as well as electrical conductivity, and excellent mobility at room temperature [3]. The GO is a carbon layer with the presence of oxygen functional, that is attached to both sides of the carbon layer and the carbon edges of the plane [4].GO could be a single or multilayer sheet. A2-dimensional sheet with a single layer is GO; two double layers of GO are named two-layered GO[5]. Moreover, the 2-dimensional GO layer in between two to five layers is called a few-layered GO sheet, and more than five layers are said to be multilayer GO[6]. GO nanosheets are synthesized by the modified Hummer method [7] that controls the morphology and size of nanostructure, which play an important role in electron field emission properties [8].

Electron field emission is the important characteristic of electron emission by the emitter surface height barrier of a structure through the principle of quantum tunnel phenomenon[9]. In the basic theory of thermionic emission(TE), the emitter(GO and rGO) are annealed at extreme temperatures to transfer enough energy to excited electrons, which is needed to discuss the work function of the emitter of the nanosheet [10]. While, the electron field emission is produced under the most intense external applied electricfield to an emitter surface(as cathode), called cold cathode emission [12]. These electron emissions are used for various applications including microwave

generation devices, gas sensors, field emission displays, and medical imaging [13]. Various groups made an effort to investigate the field emission properties of different nanostructures [9,14,15]. The majority of previously reported investigations on electron field emission of graphene, GO and rGOnanosheetshave not focused in detail. However, the correlation between morphologies and grain size(calculated from the EMA model) with electron field emission propertieshasbeen rarely reported yet.

This investigation reports the role of morphology and grain size on the performance of electron field emission of GO and rGO. The theoretical effective mass models are used to calculate the size using different absorption plasmonic energy. A correlation between morphologies and grain size and electron field emission properties exhibits that the turn-on field is effectively impacted by the size quantum effect in GO and rGOnanosheets.

2. MATERIALS AND METHODS

Graphene oxide (GO) is synthesized through the improved Hummers' method. In the Hummers' method, graphite is oxidized using a mixture of concentrated sulfuric acid (H_2SO_4), sodium nitrate ($NaNO_3$), and potassium permanganate ($KMnO_4$). H_2O_2 is used to stop the reaction. The resultant solution is centrifuged using HCl, and dried in the presence of IR at 85°. Finally, GO is obtained by exfoliating using heat treatment. The oxidation process introduces oxygen-containing functional groups such as hydroxyl (-OH), epoxide (-O-), and carboxyl (-COOH) onto the graphene layers, resulting in the formation of GO.After obtaining GO, reduced graphene oxide (rGO) is prepared by reducing the oxygen-containing functional groups in GO using sodium Borohydride[16-17]. The reduction process removes some of the oxygen groups and partially restores the sp^2 carbon network, leading to the formation of rGO. The schematic of synthesis process is shown in Fig 1.
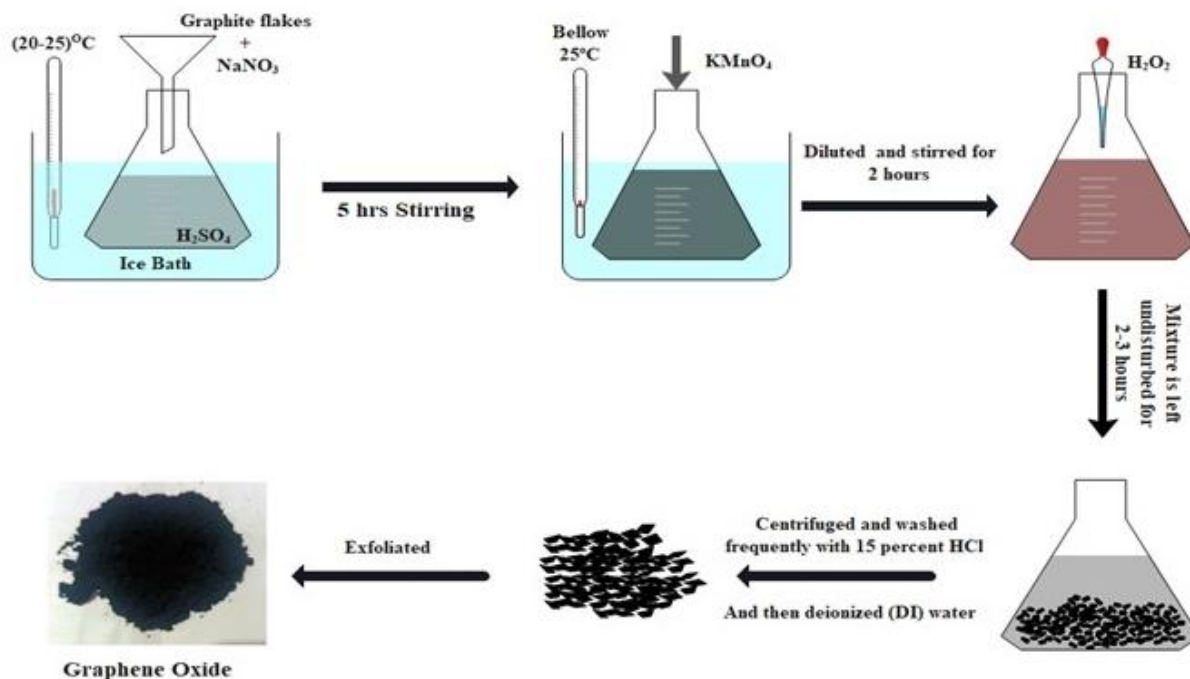
Figure 1. Schematic diagram of synthesis of GO

3. RESULTS AND DISCUSSION

3.1. Morphological and elemental composition of GO and rGO

Figure 2(a-b) displaysthe FESEM micrograph of graphene oxide (GO) and reduced graphene oxide (rGO) samples. Figure 2(a) shows the presence of crumple and spherical type structure, because of the exfoliation of graphite sheet, which becomes to GO nanosheet and results in reduction or deformation onthe exfoliation. Fig. 2(b) displays

the micrograph of reduced graphene oxide (rGO), the folded and wrinkled nanostructure has been found. This folding rGOnanosheetis observed on the surface and the edge of rGO due to the losses of the presence of oxygen functional groups[18]. More folded and wrinkled nanosheet is produced when the reduction is quite stronger. A layered sheet with few defects is found in both samples, indicating their polycrystalline behavior. Relatively, the rGOnanosheet shows more aggregation than

the GO. The ratio of C:O for GO and rGO nanosheetshas been investigated through EDS measurement, as shown in Figure 2(c-d). The ratiosof C:O of GO and rGO are 1.48 and 2.53, respectively. The EDS result confirms the reduction of rGO from the GO nanosheet [19].
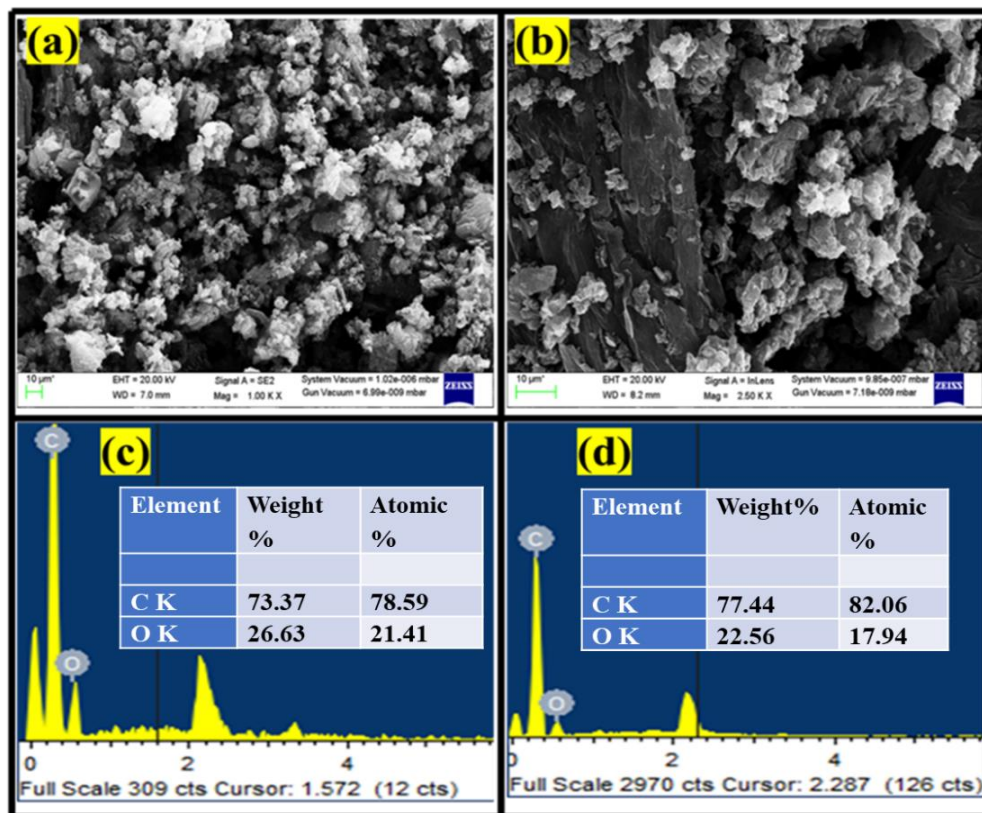
Figure 2. FESEM and EDS spectra,(a-c) GO, (b-d) rGO

3.2. XRD study of GO and rGO

XRD spectra were recorded by using Cu (Kα) radiation (0.154 nm) and intensity was collected in range of 2θ = 5–40∘ for GO and rGOnanosheetto evaluate the structural and elastic properties, as shown in Figure 3. The observed peaks corresponding to reflection planes (001) at 2θ = 11.8 assigned to GO phase and observed peaks corresponding to reflection planes (002) at 2θ = 26.8 assigned to rGOphase [JCPDS card no. 77-2306] .The structural parameters such as crystal size (D), lattice strain (ε), and dislocation density (δ) have been studied corresponding to (001) and (002) reflection peak of GO and rGOnanosheetare estimated using the Scherer equation [20].

$$D = \frac{k\,\lambda}{\beta_D \cos\theta} \qquad (1)$$

$$\varepsilon = \frac{\beta_{hkl}}{4\,\tan\theta} \qquad (2)$$

Here β_D is full-width at half maximum (FWHM). The estimated average values of D of GO and rGOnanosheetusing Scherrer's formula are 2.9 nm and 6.6 nm. The analysis of disorderness, non-uniformity, non-homogeneity, irregularities and crystal defects present in samples has been carried out using dislocation density (δ), calculated through following equation [21]:

$$\delta = \left(\frac{\beta_D \cos\theta}{k\,\lambda}\right)^2 = \frac{1}{D^2} \qquad (3)$$

The estimated average value of dislocation density of GO and rGOnanosheet are 0.1228 and 0.0229 respectively.
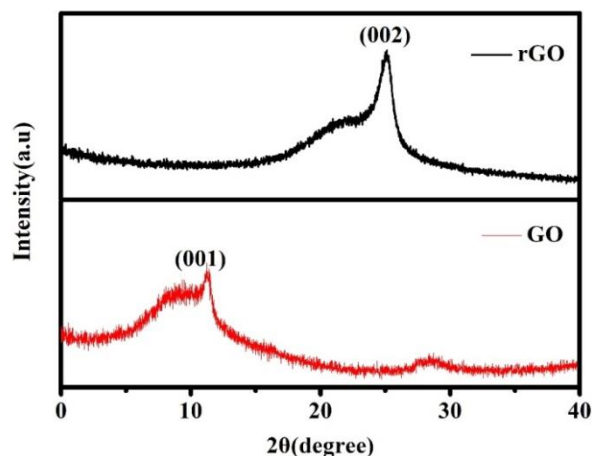
Figure 3. XRDof GO and rGOnanoseet

3.3. Optical and Raman study of GO and rGO

The optical absorption properties of the GO and rGOare shown in Fig. 4(a), The GO exhibits the peak position at 290 nm indicating the p–n* absorption band, on the other hand, the rGO exhibits the peak position at 298 nm indicate the p–n* absorption band, suggest that some groups on the GO nanosheet are eliminated and the conjugated nanostructures have been restored. The surfaceplasmonic position centered at 230 nm for the GO nanosheet is red-shifted(shifting towards a higher wavelength) with increasing reduction i.e GO to rGO samples. Further, red shifting can be explained through the quantum confinement effect through various theoretical models using optical absorption. Here we will use the effective mass model to compute the size, which is expressed as[22-24].

$$E_g^* = E_g^{bulk} - \frac{1.8e^2}{4\pi\epsilon.\epsilon_r} + \frac{\hbar^2\pi^2}{2r^2}\left(\frac{1}{m_e^*} + \frac{1}{m_h^*}\right) \qquad (4)$$

Where r is the crystallite radius.The calculated size from this model are3.56nm and 4.79 nm respectively for both the samples. Besides the effective mass model, another model called the Hyperbolic Band approximation(HBA) model, is used to estimate the size of GO and rGO. The HBA model is expressed as[25-26].

$$E_g^2 = E_{bulk}^2 + \left(\frac{2\hbar^2 E_{bulk}}{\mu}\right)\left(\frac{\pi}{r}\right)^2 \qquad (5)$$

The estimated crystallite size from this model is8.45nm and 11.76 nm.

Raman spectroscopy is used to investigate the defects and disorders present in synthesized samples of GO and rGO. Figure 4(b) displays the Raman spectra for both samples, which exhibit two significant bands namely the G band and D band. In the recorded GO and rGO samples, the G band centered at ~1540-1545 cm^{-1}, indcates the perfect GO and rGO nanostructure of a carbon atom with sp^2 hybridization mode and is assigned to E2g-symmetry phonons. The D band is centered at 1350-1380 cm^{-1}, indicating the A1g-symmetry phonons and which confirm the presence of defects in samples. The defect (D) band suggests the disorder in samples arises because of microstructural imperfections and irregularities by the presence of functional groups in the 2-dimensional. graphene sheets. The G-band comes in our samples because of lattice plane vibration of sp^2 hybridized mode of carbon atoms. In the case of the GO nanosheet, the functional groups are fond of the carbon atoms by shifting the hybridization mode from sp2 to sp3mode. On the other hand, the rGO shows the red shifting of the G band than the GO nanosheet. The Raman intensity ratio of D-band (I_D) and G-band (I_G) is also estimated, which gives the information of qualitative assessment of the presence of disorder, defects in the GO and rGO samples. The I_D/I_G ratio decreases from 0.81 to 0.92 for the samples. The I_D/I_Gratio of Raman band decreases with the reduction of graphene oxide. To estimate the grain size from recorded Raman spectra through expression [27]

$$L_a = \frac{560}{E^4}\left(\frac{I_D}{I_G}\right)^{-1}$$

Where E is laser energy and expression $L_a = 2.4*10^{-10}\,\lambda^4\left(\frac{I_D}{I_G}\right)$ is used to calculate the size. The estimated Size was 17 and 23 nm for GO and rGO.
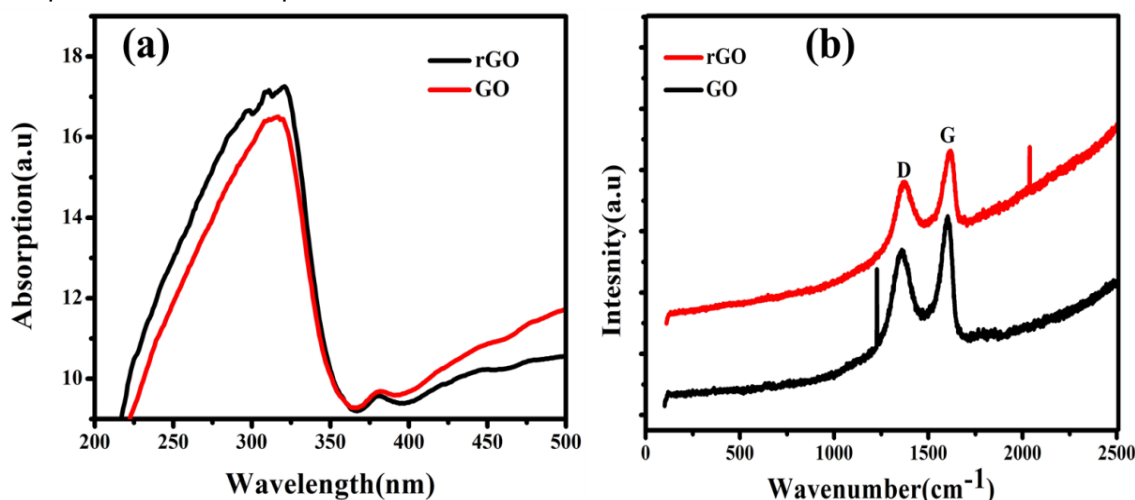
Figure 4. (a) absorption, (b) Raman spectra of GO and rGO

3.4. Field emission properties of GO and rGO

Graphene and its derivatives show promising electron field emission behavior and are examined for application in devices. To understand the emission properties of nanosheets, the electron emissions testing is carried out with diode assembly inside the chamber at a minimum pressure, and the separation between the cathode and anode was0.025cm.A schematic diagram of field emission geometry is shown in Figure 5.
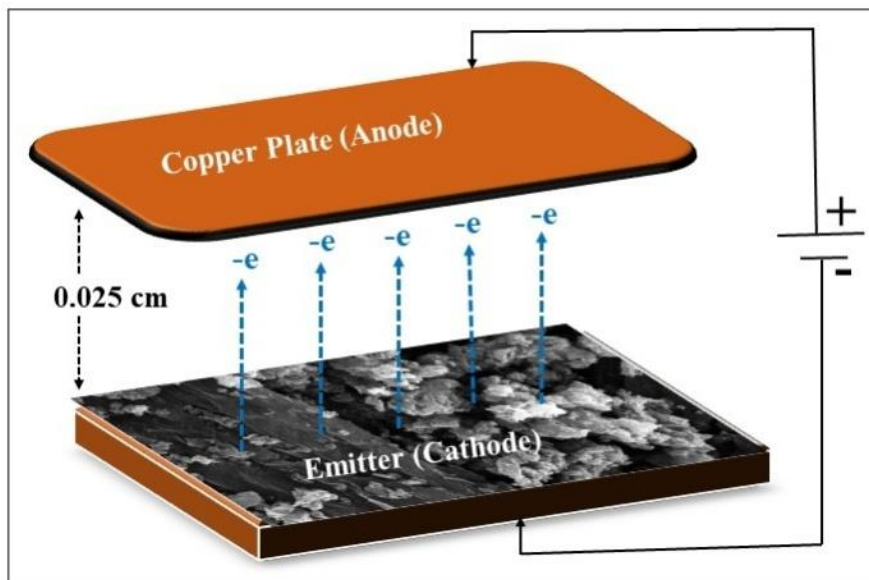
Figure 5. Schematic diagram of field emission geometry

The process of field emission depends on the principle of quantum tunneling phenomenon. Figure 6(a-b) displays the current density (J) versus applied electric field (E) curve plotsfor bothsamples. The turn-on voltage for collection of GO is usually expressed as the electric field needed to create the emission current densities of 15 mA-cm^{-2}. The turn on voltage valuesis found to be 8.67 V/μmand 9.2V/μmfor both the samples. A morphology and size dependent on turn on voltage, indicate that turn-on fields are possibly tailored through tailoring the GO and rGO diameter. A minimum turn on voltage is required for electron field emission from synthesized GO and rGO samples are used for minimal power operation-based devices. It is evidence that the emission behavior of nanosheetis effectively impacted with size. It is required to turn on voltage of GO and rGO shows minimum size because of larger applied external field at the tip of the nanosheet.
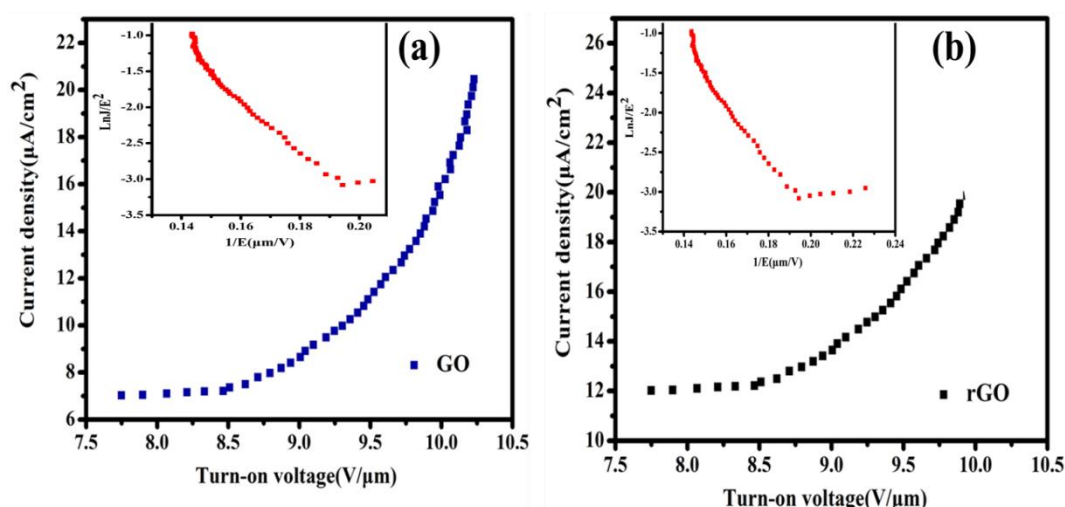
Figure 6. Electron emission current–voltage plot(inset FN plot) of (a) GO, (b) rGO nanosheet

The electron field emission data have been investigated through the Fowler–Nordheim (FN) model which tells about the electron emission current density through barrier tunneling phenomenon, electron field emission current as a function of the applied external electric field and are expressed as follows [28-29].

$$J = \frac{K\beta^2 V^2}{\varphi} exp\left(-\frac{PW^{\frac{3}{2}}}{\beta V}\right) \qquad (6)$$

where K (= 1.541×10^{-6} AV^{-2}eV) is a constant, P = 6831 eV^{-32}µm^{-1} V, V is the applied electric field, φ is the work function and β is the field-enhancement factor. The plot of ln (J/E^2) with (1/E) is defined as FN plot, whose gradient is expressed as.

$$Gradient = -\frac{P\,\varphi^{\frac{3}{2}}}{\beta} \qquad (7)$$

where, β is field-enhancement factor, which is sued to investigate the degrees of emission enhancement of tips. Various group reported the field-enhancement factor is most significant characteristic, which depends on the surface geometry of the GO and rGO(in our case), and the distance between the emitter(nanosheet) and anode plate. As the effective electron emission area and the φ (work function) for GO and rGO are quite impossible to estimate, field-enhancement factor are calculated by the slope of the fitting FN plot. Inset Figure 5 (a and b)display the FN plot of GO and rGO, which well fitted and the gradient of the linear portion, and further estimated values of field-enhancement factor are 1200 and 1160 for both samples. A size dependent change in turn-on field suggest that electron field emission parameters are also be tailored as a result of size confinement in GO and rGO nanosheet.

4. CONCLUSIONS

This investigation demonstrated the synthetization of GO and rGO through a modified hummer method. XRD pattern confirm the formation of GO and rGO phase. The plasmon peaks were observed at 290 nm to 310 nm for both the samples. Here, a plasmonic energy associated effective mass model was used to calculate the crystal size of nanosheet, which is 3.56nm and 4.79nm for GO and rGOnanosheet, which confirm the confinement behavior. The G band is centered at ~1540-1545 cm^{-1}, and the D band is centered at 1350 to 1380 cm^{-1}, indicating the A1g-symmetry phonons and which confirm the presence of defects in samples. An excellent field emission for GO was found withminimum turn-on voltage of 6 V/µm. The synthesized GOhas proved to be an excellent electron field emitter. On the other hand, the field enhancement factors are 1200 and 1160 for both samples. A maximum field enhancement factor was found for a smaller crystal size sample. A size dependent change in turn-on field suggests that electron field emission parameters are also be tailored as a result of size confinement in GO and rGO nanosheets.

5. REFERENCE

[1] T. M.Magne, T.de Oliveira Vieira, L. M. R.Alencar, F. F. M.Junior, S.Gemini-Piperni, Carneiro, R. Santos-Oliveira(2022)Graphene and itsderivatives: understandingthemainchemical and medicinal chemistry roles forbiomedicalapplications. Journal of nanostructure in chemistry, 12, 693-727. https://doi.org/10.1007/s40097-021-00444-3

[2] R. S.Krishna, J.Mishra, B.Nanda, S. K.Patro, A. Adetayo, T. S.Qureshi(2021) The role of graphene and its derivatives in modifying different phases of geopolymer composites: A review. Construction and Building Materials, 306, 124774. https://doi.org/10.1016/j.conbuildmat.2021.124774

[3] V. B.Mbayachi, E.Ndayiragije, T.Sammani, S.Taj, E. R. Mbuta (2021) Graphene synthesis, characterization and its applications: A review. Results in Chemistry, 3, 100163. https://doi.org/10.1016/j.rechem.2021.100163

[4] J.Liu, S.Chen, Y.Liu, B.Zhao (2022) Progress in preparation, characterization, surface functional modification of graphene oxide: A review. Journal of Saudi Chemical Society, 26(6), 101560. https://doi.org/10.1016/j.jscs.2022.101560

[5] T. R.Mignoli, T. L.Hewer, R. A.Antunes, R. M.Alves, M.Schmal (2021) Synthesis of few-layered graphene sheets as support of cobalt nanoparticles and its influence on CO hydrogenation. Materials Science and Engineering: B, 273, 115388. https://doi.org/10.1016/j.mseb.2021.115388

[6] Y.Cao (2024) Rhombohedral graphene goes correlated at four or five layers. Nature Nanotechnology, 19(2), 139-140. https://doi.org/10.1038/s41565-023-01566-1

[7] N. I.Zaaba, K. L.Foo, U. Hashim, S. J.Tan, W. W. Liu, C. H.Voon (2017) Synthesis of graphene oxide using modified hummers method: solvent influence. Procedia engineering, 184, 469-477. https://doi.org/10.1016/j.proeng.2017.04.118

[8] S.Santandrea, F.Giubileo, V.Grossi, S.Santucci, M. Passacantando, T.Schroeder,... A. Di Bartolomeo (2011) Field emission from single and few-layer graphene flakes. Applied Physics Letters, 98(16). https://doi.org/10.1063/1.3579533

[9] V.Kashyap, C.Kumar, N.Chaudhary, K.Saxena (2022) The role of quantum crystal radius on electron field emission properties of fractal silicon nanowire arrays. Materials Letters, 314, 131842. https://doi.org/10.1016/j.matlet.2022.131842

[10] I.Lahiri, V. P.Verma, W.Choi(2011) An all-graphene based transparent and flexible field emission device. Carbon, 49(5), 1614-1619. https://doi.org/10.1016/j.carbon.2010.12.044

[11] C.Kumar, V.Kashyap, A.Kumar,A. K.Sharma, D.Gupta, D. P.Singh, K.Saxena (2023) Reframe of Fowler-Northeim Approach for Electron Field Emission of a Vertical Silicon Nanowires. Silicon, 15(15), 6591-6602. https://doi.org/10.1007/s12633-023-02505-4

[12] V.Kashyap, C.Kumar, N.Chaudhary, K. Saxena (2023) Quantification of deviation of size dependent field enhancement factor of silicon nanowires array through theoretical modeling. Silicon, 15(3), 1203-1210. https://doi.org/10.1007/s12633-022-02068-w

[13] S.Nirantar, T.Ahmed, M.Bhaskaran, J. W.Han, S. Walia, S. Sriram(2019)Electron emission devices for energy-efficient systems. Advanced Intelligent Systems, 1(4), 1900039. https://doi.org/10.1002/aisy.201900039

[14] Y. W. Zhu, H. Z.Zhang, X. C.Sun, S. Q.Feng,J.Xu, Q. Zhao, ... D. P.Yu (2003) Efficient field emission from ZnOnanoneedle arrays. Applied Physics Letters, 83(1), 144-146. https://doi.org/10.1063/1.1589166

[15] L.Chen, H.Yu, J.Zhong, J.Wu, W.Su (2018) Graphene based hybrid/composite for electron field emission: a review. Journal of Alloys and Compounds, 749, 60-84. https://doi.org/10.1016/j.jallcom.2018.03.100

[16] S. N.Alam, N.Sharma, L. Kumar(2017) Synthesis of graphene oxide (GO) by modified hummers method and its thermal reduction to obtain reduced graphene oxide (rGO). Graphene, 6(1), 1-18. http://dx.doi.org/10.4236/graphene.2017.61001

[17] T. K.Kuanyshbekov, K.Akatan, S. K. Kabdrakhma-nova, R.Nemkaeva, M.Aitzhanov, A.Imasheva, E. Kairatuly (2021)Synthesis of graphene oxide from graphite by the hummers method. Oxidation Communications, 44 (2).

[18] N.Sharma, V.Sharma, Y.Jain, M.Kumari, R.Gupta, S. K. Sharma, K.Sachdev (2017) Synthesis and characterization of graphene oxide (GO) and reduced graphene oxide (rGO) for gas sensing application. In Macromolecular symposia. 376(1), 1700006. https://doi.org/10.1002/masy.201700006

[19] N.Aslan, B.Aksakal (2021) Effect of graphene reinforcement on hybrid bioceramic coating deposited on the produced porous Ti64 alloys. Journal of Porous Materials, 28(4), 1301-1313. https://doi.org/10.1007/s10934-021-01081-5

[20] C. Kumar, M.Shrivastav, J.Escrig, L. P.Campos,A. I. Martinez, H.Silva, A. Zarate (2024) The investiga-tion of thickness-dependent mono-fractal, optical and optoelectronics properties of sputtered silver thin film for silicon solar cell. Vacuum, 225, 113247.

https://doi.org/10.1016/j.vacuum.2024.113247

[21] V.Kashyap, H.Pawar,I.Sihmar, C.Kumar, A.Kumar, S.Kumar, ... K.Saxena (2024) X-ray analysis of Ag nanoparticles on Si wafer and influence of Ag nano-particles on Si nanowire-based gas sensor. Applied Physics A, 130(4), 238. https://doi.org/10.1007/s00339-024-07379-w

[22] V.Kashyap,C.Kumar, N.Chaudhary, N.Goyal, K. Saxena (2021) The correlation of resistivity with the crystal size present in silicon nanowires through confinement-based models. Materials Letters, 301, 130312. https://doi.org/10.1016/j.matlet.2021.130312

[23] P.Patra, R.Kumar, C.Kumar, P. K.Mahato (2022)Ni-incorporated cadmium sulphide quantum dots for solar cell: an evolution to microstructural and linear-nonlinear optical properties. Journal of Crystal Growth, 583, 126542. https://doi.org/10.1016/j.jcrysgro.2022.126542

[24] S.Pathak, S.Chaudhary, M.Shrivastav, N.Kumar, S. Varshney, M.Kumar, ... C. Kumar(2024) The effects of air-annealing on the performance of optical-electrical assessment of sputtered CdS film towards the Ag/n-CdS/p-Si (100)/Al photodetectors. Optical Materials, 150, 115117. https://doi.org/10.1016/j.optmat.2024.115117

[25] C.Kumar, V.Kashyap, M.Shrivastav, F.Guzman, D. P.Singh, K.Saxena (2023) In-depth opto-electrical analysis of Ni: CdS film towards the performance as Ag/Ni:CdS/FTOSchottky diode. Optical Materials, 143, 114226. https://doi.org/10.1016/j.optmat.2023.114226

[26] P.Patra, R.Kumar, C.Kumar, K.Pandey, P. K.Mahato (2023)Exploration of impact of thermal condition on microstructural-optical-electrical properties of Ni doped CdS thin films. Materials Today: Proceedings.

[27] https://doi.org/10.1016/j.matpr.2023.07.018

[28] P. K.Mahato, S.Choudhuri, C.Kumar, S.Roy, P. Patra (2023) Evaluation of crystal size present in graphene oxide quantum dots using optical and Raman spectroscopy. Materials Today: Proceedings, 80, 668-673.

[29] V.Kashyap, C.Kumar, V.Kumar, N.Chaudhary, K.Saxena(2022) Induced quantum-Fano effect by Raman scattering and its correlation with field emission properties of silicon nanowires. Applied Physics A, 128(4), 312. https://doi.org/10.1007/s00339-022-05415-1

[30] C.Kumar, V.Kashyap, J. M.Shrivastav, V.Kumar, F.Guzman, K.Saxena(2024) The dopant (n-and p-type)-, band gap-, size-and stress-dependent field electron emission of silicon nanowires. Physical Chemistry Chemical Physics, 26(25), 17609-17621. doi:10.1039/D4CP00825A

IZVOD

MORFOLOŠKO ISTRAŽIVANJE EMISIJE GO i rGO NANOLISTA ZAVISNO OD VELIČINE

Ovde izveštavamo o ulozi morfologije površine i veličine zrna na karakteristike emisije elektronskog polja GO i rGO nanolistova, sintetizovanih modifikovanom Hamerovom metodom. Plazmonski vrhovi su primećeni na 290 nm -310 nm za oba uzorka. Ovde je korišćen model efektivne mase povezan sa plazmonično energijom za izračunavanje veličine kristala nanolima, koja je 3,56 nm i 4,79 nm za GO i rGOnanolist, što potvrđuje ponašanje zatvaranja. Ramanovi podaci snimljeni za GO i rGOnanosheet potvrđuju prisustvo D i G traka, što sugeriše rast GO i rGO, pored toga, veličina kristala se izračunava Ramanovim podacima, koji je uporediv sa veličinom radijusa Borovog eksitona, što ukazuje da su GO i rGO kvantne tačke. Istraženi su parametri emisije elektronskog polja sintetizovanih GO i rGOnano listova i parametri su izračunati pomoću Fauler–Nordhajmove (F-N) jednačine. Među njima, GO uzorak pokazuje najbolja svojstva emisije elektronskog polja sa minimalnim naponom uključivanja od 8,2 V/mm i faktorom poboljšanja polja od 1200 zbog posedovanja najmanjeg radijusa (veličine) vrha emitera i različite morfologije površine.
Ključne reči: Grafen oksid, raman, pojasni razmak, emisija polja

Prabin Kumar Mahato: http://orchid.org/0000-0001-6718-4893
PrashantaPatra: http://orchid.org/0000-0002-2425-1037
DeepakGupta: http://orchid.org/0000-0002-4228-2523

*Pooja Singh[1,2, *], Avshish Kumar[1], Vinod Kumar Jain[1]*

[1]*Amity Institute for Advanced Research and Studies (Materials & Devices), Amity University Uttar Pradesh, Noida, 201313, India,* [2]*MaharajaSurajmal Institute of Technology, New Delhi 110058, India*

Development of UV Photodetector using SnO₂/AuNPs@SiNWs hetero junction on Si chip

ABSTRACT

In this study, we present the development of a hybrid nanostructure based on silicon nanowires (SiNWs) and tin oxide (SnO₂) and Au nanoparticles, which was utilized to develop a UV photodetector. Metal assisted chemical etching (MACE) was used to create SiNWs on p-Si (1 1 1) substrate, while reduction synthesis and co-precipitation techniques were used to create AuNPs and SnO₂ nanoparticles, respectively. These AuNPs and SnO₂ nanoparticles were then deposited on top of SiNWs. Using an X-ray diffractometer (XRD), UV-Visible spectrophotometer, and scanning electron microscopy (SEM), the synthesized SnO₂/AuNPs@SiNWs hybrid nanostructure was examined. The synthesized SnO₂ nanoparticles were subjected to TEM examination as well. At room temperature, the UV photocurrent response of SnO₂/AuNPs@SiNWs was studied at varying UV light intensities as 1, 1.5, and 2 mW/cm².

The hybrid nanostructure of SnO₂/AuNPs@SiNWs was found to have a photocurrent response time to be very fast (1.32 s). As we turned off the UV source, the sensor reached to its initial state in ~0.77 s. The sample was checked continually for three on/off sets of illumination at a regular interval of 60 s. Therefore, the work disclosed here has great promise for the advancement of highly effective miniature UV photodetectors with unique features.

Keywords:Photodetector, ultra-violet, gold nanoparticles, silicon nanowires, tin oxide.

1. INTRODUCTION

A device that transforms light energy into a measured electrical reaction is called a photodetector (PD). All solid state photodetectors operate on the same fundamental concept. When a photon with enough energy interacts with a semiconductor material, the distribution of electron energies within the material is momentarily altered [1,2]. An electron can become energetically conducting when it has enough energy to do so, allowing it to freely move within the crystal. A vacancy, or hole, is left behind by the migrating electron and is free to move within the crystal. They are together known as electron hole pair and in photodetector, one such pair is created for every absorbed photon.

*Corresponding author: Pooja Singh

E-mail: psingh126@gmail.com

If the electron hole pair left in material long enough, they will recombine and give up extra energy in the form of heat. The time scale during which it happens is called recombination lifetime, τ_r. While excited, the electron and hole will drift in the presence of an electric field, creating electric current. This current can be detected by connecting the active area of the semiconductor into an electric circuit. Here, however we are specifically interested in PDs for the detection of UV wavelength [3,4].

UV PDs find wide applications in various fields like industrial, environmental, military and commercial fields [5]. In the domains of solar astronomy, water sterilization, flame detection, and safe space communication, they are frequently employed to detect UV light [6,7]. Particularly, UV PDs have garnered a lot of attention lately because of the growing demands from the military and civic sectors to develop UV equipment that can function in high temperatures [8]. Commercially available PDs are utilized in various applications such as atmospheric clock transfer using femtosecond

frequency combs, measuring speckle motion to monitor ultrasonic vibrations, measuring the polarization state of a weak signal field by homodyne detection, and remote optical diagnostics of non-stationary aerosol media in a wide range of particle sizes [9].

There are three bands in the UV spectrum. Three wavelength ranges are identified: UVA, UVB, and UVC. The wavelength range from ~ 320 nm to 400 nm is assigned to the band UVA, while the wavelength range from 280 nm to ~ 320 nm is assigned to the band UVB and the wavelength range from 100 nm to 280 nm is assigned to the band UVC[10]. UVA makes up 95% of the UV light that reaches the earth and is located in the visible region among these bands.

In this investigation, we developed a silicon nanowire-based heterojunction p-n device. The devices obtained as a p-n heterojunction may give photodetectors functioning in a larger wavelength range due to the wavelength constraint of silicon homojunction in terms of photodetector performances. Moreover, heterojunctionphotodetectors are created by combining several materials with nearly matched lattice characteristics but distinct band gaps [11]. This absorbs various wavelengths, enabling the photodetector to be employed in a broad spectral range. There are opportunities for high-performance photodetectors using lattice-matched heterojunctions. As a result, creating p-n heterojunctions is frequently more advantageous than creating homojunctions since they are cheap, simple to fabricate, and have good performance. In optical devices, metal oxide semiconductors play a crucial role because of their intriguing opto-electronic features.

The wide gap semiconductors for example, SnO_2[12], GaN [13], Ga_2O_3[14], TiO_2 [15], ZnMgO [16] and ZnO [17], are attracting significant research and commercial owing to their improves thermal stability, high breakdown voltage, low cost and favourable sensitivity to UV radiation. Here, in this work we choose SnO_2nanoparticles which is a wide band gap semiconducting material. SnO_2 found interesting electrical and optical application. MSM UV photodetectors based on SnO_2 have been demonstrated recently, but they have a lot of issues. Interstitial Sn atoms, numerous oxygen vacancies, and other defects are common in SnO_2 material. These flaws provide a huge amount of background carriers, which in turn cause a high dark current. Another reason is that some of these defects function as trap centers, which prevent photogenerated electrons and holes from recombining, slowing down the response time [12]. But the forbidden dipole transition among its valence band and conduction band limits its applicability in photodetectors. The performance of

UV PDs enhances with incorporation of nobel metal nanoparticles due to the generation of Localized Surface Plasmon Resonance (LSP). LSP encourages the confinement of optical fields directly affecting the increase in the intensity of the optical energy inside the SnO_2 [18]. This lead to better optical and electrical performances of the photodetector.Keeping in view above considerations, for the first time, we have used AuNPs/SnO$_2$ heterojunction for UV detection and experimental data depicts good results that to the best of our knowledge has not been reported so far by this nanostructure.

2. EXPERIMENTAL WORK

2.1. Materials Procurement

For the synthesis of SiNWs, hydrogen peroxide (30%), hydrogen flouride (40%), IPA(99%) were purchased from Rankem, Fisher Scientific SRL respectively. Sulphuric acid (99%) and nitric acid procured from Merck. Silver nitrate (99.9%) was procured from Qualikems. For the synthesis of Gold nanoparticles, gold hydrogen chloride acquired from Sisco Research Laboratories pvt. Ltd. and trisodium citrate dehydrate (98%) from LobaChemiePvt. Ltd and for the synthesis of SnO$_2$ NPs, Tin chloride dihydrateSnCl$_2$.2H$_2$O (98%, Sigma Aldrich), ammonia hydroxide (NH$_4$OH), Hydrochloric acid (HCl) and distilled water. The chemicals were used without any further purification.

2.2 Synthesis of SiNWs on Si chip

We choose n-type Si substrate and ultrasonicated it 10 mins with DI water, 10 mins with acetone and 10 mins with isopropyl alcohol to remove dust and oxides layer deposited over substrate. The substrate was then dipped in piranha solution (H$_2$SO$_4$:H$_2$O$_2$) taken in the ratio of 3:1 for 30 mins to remove organic and inorganic contaminations. Further cleaning the substrate by dipping in HF solution (1mlHF+9ml DI) for 2 mins, after HF dip the substrate was dipped in etching solution. Etching solution was prepared by ultrasonicatedAgNO$_3$ solution (0.068gAgNO$_3$ + 20 ml DI) with HF solution (4mlHF + 16 ml DI). We kept the substrate in etching solution for 1 hour at 60°C[19,20]. The length of SiNWs can be adjusted by changing the time for which we kept in etching solution. After that it is cleaned with HNO$_3$ solution for 5 mins to remove the Ag from the Si wafer.The oxidation-reduction takes place which is explained below.

$$Si(s) + 4Ag^+ + 6HF \rightarrow 4Ag(s) + 4H^+ + H_2SiF_6$$
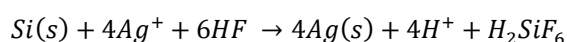
2.3. Synthesis of AuNPs

In a typical AuNPsynthesis [21], 20 ml of 1.0 mM gold hydrogen tetrachloride solution was

prepared in a flask. Independently, 2mL of (1.0 wt %) trisodium citrate dihydrate solution was prepared in a flask. Independently, 2mL of (1.0 wt %) trisodium citrate dihydrate solution was prepared. Using a hotplate, the flask holding the HAuCl$_4$ solution was heated while being vigorously and continuously stirred. A disposable Petri dish was utilized to cover the flask during the synthesis to prevent contamination and solvent evaporation. A 2 mL solution of citrate was quickly injected into the HAuCl$_4$ solution after it had reached the boiling point at room pressure. The main variable that was regulated to produce the appropriate particle size was the molar ratio of citrate to gold chloride. When the suspension turned wine red, the synthesis was finished. Depending on the molar ratio, the reaction typically took two to five minutes. The sample reached room temperature by natural cooling.

Here, gold ions react with citrate ions to form gold atoms as well as citrate acting as a reducing agent in producing the gold atoms. Citrate ions acts as shielding agent, wrapping around the cluster of atoms which constitute the nanoparticles[22]. This electrostatic sheath prevent agglomeration and stabilizes the particles.

2.4. Synthesis of SnO$_2$

The SnO$_2$ NPs were prepared by co-precipitation[23] technique where 0.85 g of SnCl$_2$.2H$_2$O was added into 100 mL of ethanol in a 500 mL beaker with continuous magnetic stirring for 1 hr to obtain a homogeneous solution. 100 mL of hydrochloric acid was then added drop wise with further stirring the solution for another 30 min to get proper mixing the solution in a clear transparent form. Further, NH$_4$OH was added drop by drop till the pH of the solution became 8.5 where a milky white solution was obtained. This solution was kept on continuous stirring for 3 hrs. Thereafter the stirring was stopped and the solution was then washed with DI water as well as ethanol multiple times so that the residual chlorine content can be removed. The resulting solution was filtered,

covered and left overnight for drying. The dried powder was then calcinated at 650°C.

Then we ultrasonicate the solution of AuNPs and SnO$_2$and then we drop casted the solution over SiNWs on Si chip and placed on PCB for making electrodes respectively.

3. CHARACTERIZATION TECHNIQUE USED

To study the stoichiometry, morphology, and structural analysis of the developed materials (SnO$_2$, AuNPs and its heterojunction nanostructure over SiNWs) various characterization techniques were used. Scanning electron microscope (SEM) of Zeiss (model: EVO-18) equipped with energy dispersive X-ray spectrometer (EDS) was used to analyse the shape and size of the prepared nanostructures. Transmission electron microscope (TEM) of (JEOL, model no. JEM-2100G) was used to get the structural analysis. For the crystallographic analysis of the heterojunction nanostructure, Ultima IV PXRD (source Cu, K = 1.54Å) X-ray diffractometer was performed. UV–Vis spectrophotometer was also used to get the absorption spectra of the SnO$_2$, AuNPs and SnO$_2$/AuNPs. For UV sensing analysis, Keithley electrometer was used to record the data.

4. RESULTS AND DISCUSSIONS

4.1.SEM Analysis

The surface morphology of the developed materials was recorded using SEM and results were analysed. The top view micrograph of SnO$_2$deposited over Si substrate has been depicted in figure 1(a) which clearly indicates uniform coverage of the substrate. Fig. 1(b) reveals the synthesis of Au nanoparticles whose particle size is in the range of 30-50 nm. Fig. 1(c) show the AuNPs and SnO$_2$ deposited over SiNWs. The micrographs showed the good coverage and a heterojunction between SnO$_2$/AuNPs and SiNWs.
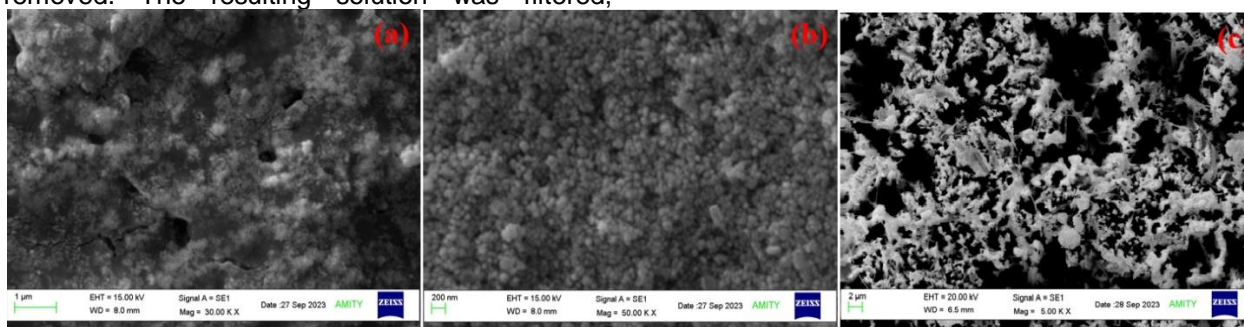
Figure 1. (a) Top view of SnO$_2$deposited over Si substrate, (b) Top view of AuNPs deposited over Si Substrate, (c) Top view of SnO$_2$/AuNPs deposited over SiNWs

4.2.EDX Analysis

In order to confirm the presence of elements in the developed SnO$_2$/AuNPs@SiNWs structure,

EDX analysis was also performed where weight% and atomic% were observed as depicted in Fig.2(a). The elemental analysis also confirms the

presence of Gold 'Au', oxygen 'O', Tin 'Sn' and silicon 'Si' species in the developed hybrid

structures. The EDX mapping of the developed structure was also recorded as shown in Figure3.

Element	Weight%	Atomic%
O K	9.08	17.91
Si K	68.90	77.47
Sn L	10.32	2.75
Au M	11.71	1.88
Totals	100.00	

Full Scale 3143 cts Cursor: 0.000   keV
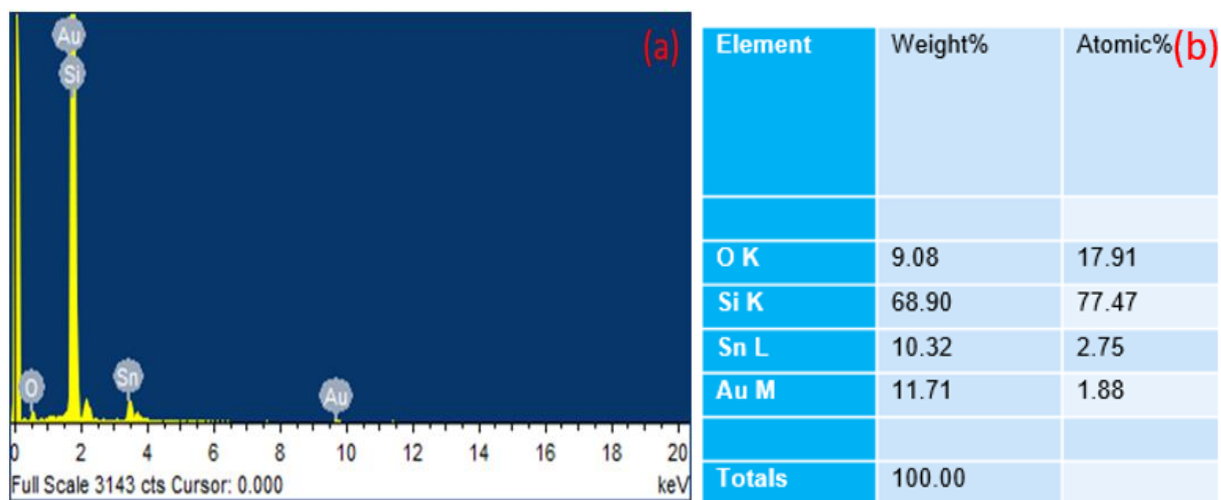
Figure 2. (a) EDX spectrum of SnO₂/AuNPs@ SiNWs, (b) Atomic percentage
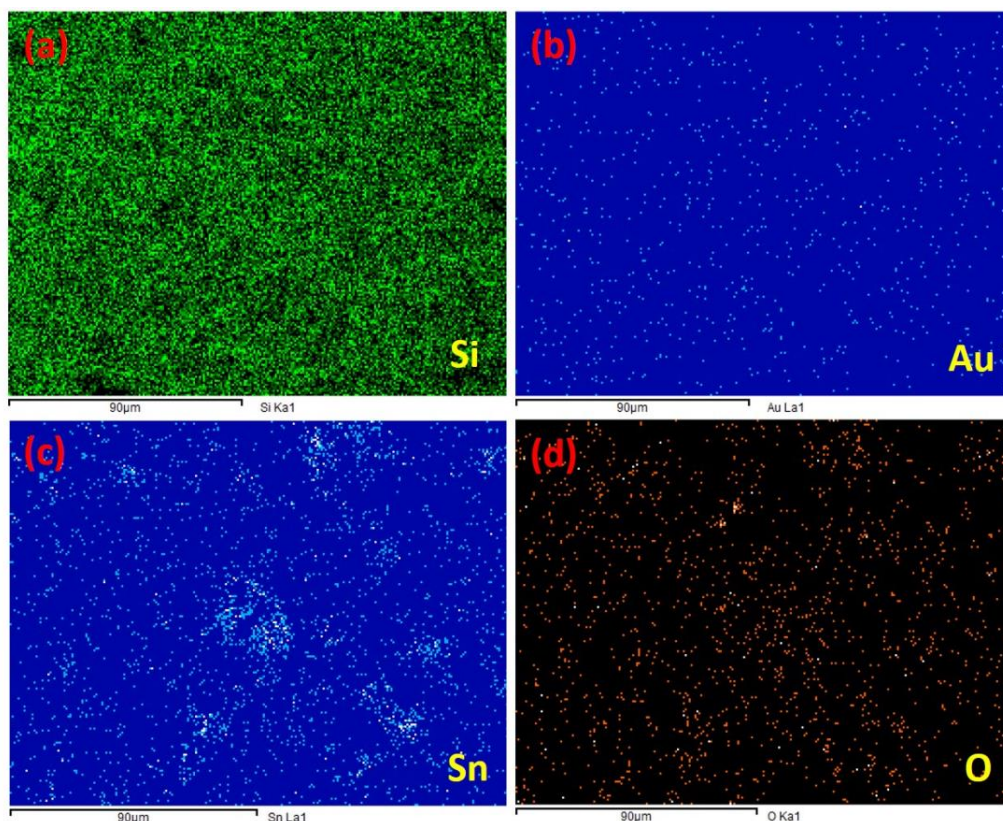
Figure 3.EDXcolour mapping of (a) Silicon (b) Gold (c) Tin (d) Oxygen

During the EDX measurement, the existence of four elements; Sn, Au, Si and O can be seen in the heterojunction nanostructure shown in colour mapping in Figure 3. The atomic and weight percentage is shown in Figure 2(b). The atomic percentage of Oxygen is 17.91%, Silicon is 77.47%, Tin is 2.75% and of Gold is 1.88%. The EDXcolour mapping of Gold, Oxygen and Tin

shown in Figure 3 show uniform coverage over the Silicon substrate.

4.3.XRDDiffractometer Analysis

XRD pattern of SnO₂ and SnO₂/AuNPs deposited over SiNWs on Si chip is shown in Fig. 4. The spectrum recorded for SnO₂ nanoparticles showed peaks at 2θ = 25.98°, 33.46°, 51.44° and

55.66° corresponding to (110), (101), (211) and (220) diffraction planes respectively[24]. The results are supported by JCPDS card no. 41-1445. The peaks of Au nanoparticles recorded at 2θ = 37.56°, 46.94° and 64.24° corresponding to (111), (200) and (220) diffraction planes respectively supported by JCPDS card no. 01-1172[25].
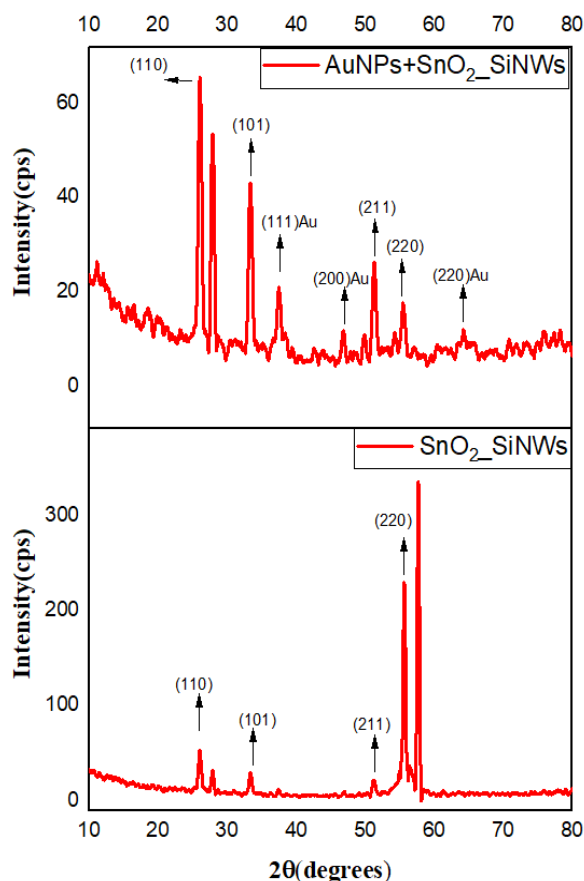
Figure 4.XRD of SnO$_2$ and SnO$_2$/AuNPs deposited over SiNWs on Si chip is shown in (a) and (b) respectively

4.4. TEM Analysis

The in-depth structural analysis of the prepared SnO$_2$ nanoparticle was done by using TEM as shown in Fig. 5(a). The samples were prepared on carbon coated copper grid after preparing the dispersion solution in ethanol where an ultrasonicator was used for ~ 45 min continuously to get a uniform distribution of the materials. Fig 5(b) shows the selected area electron diffraction patterns of the sample. The electron diffraction patterns show continuous ring patterns without any additional diffraction spots and rings of secondary phases, revealing their crystalline structure [24, 26]. XRD and TEM studies confirmed pure tetragonal structure of SnO$_2$ as evidenced from Fig. 5(a). The size of SnO$_2$ is of the order of 30-40nm.
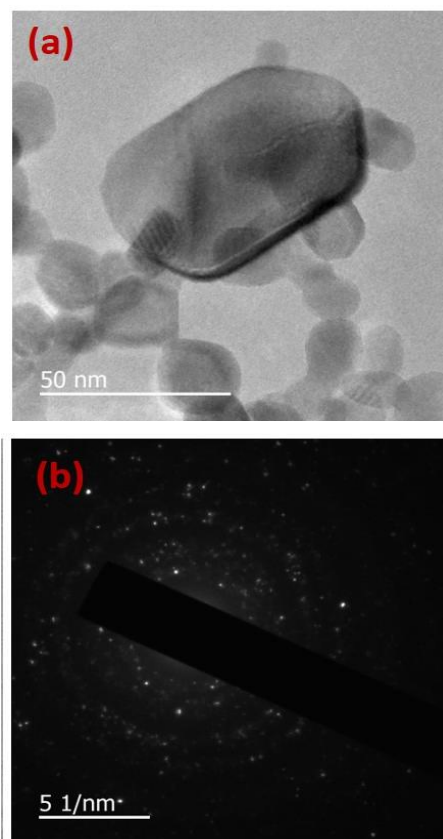
Figure 5.(a) TEM image of SnO$_2$NPs (b) SAED pattern of the SnO$_2$ NP

4.5. UV-Vis Analysis

Figure 6 shows the UV-Vis spectra of SnO$_2$/AuNPs and SnO$_2$ samples. Because of the surface plasmon absorption (SPR) of the AuNPs mixed with SnO$_2$ sample, the SnO$_2$/AuNPs sample exhibits enhanced absorption in the UV-visible region with a very broad band around 550 nm[27]. Peak observation in the UV region occurs at 280 nm.
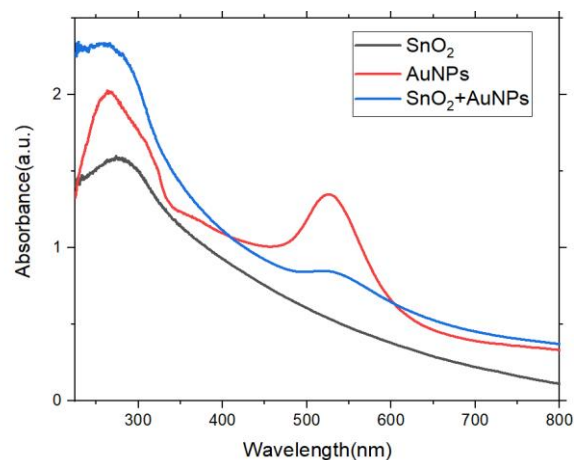
Figure 6. UV vis absorption spectra of SnO$_2$, AuNPs and SnO$_2$/AuNPs

4.6. UV response of the device

Here, in SnO_2/AuNPs deposited over SiNWs, we studied its I-V characteristics for dark condition and UV illumination condition. We can observe that in reverse bias condition the current in more than twice under UV illumination condition in comparison to dark condition shown in figure 7. Here the increase in current can be due to the SPR absorption of photons by Au nanoparticles.
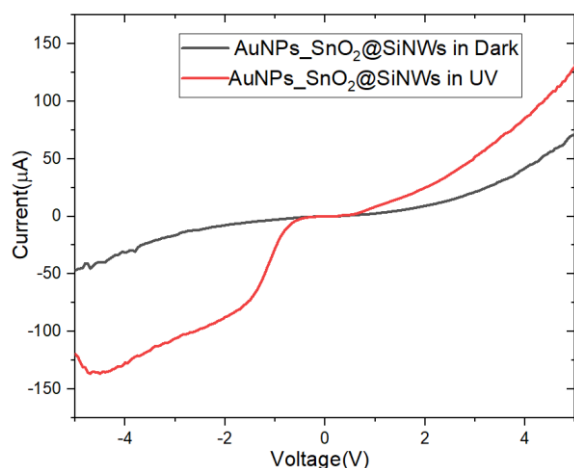
Figure 7. I-V graph of SnO_2/AuNPs@SiNWs in dark and UV illumination

According to Liu et al. [28], grapheneplasmons are generated when the energy of photons released from ZnO nanostructures is equal to the graphene surface plasmon energy. Hwang et al. [29] have reported similar results, demonstrating that improved photoemission from graphene/ZnO film architectures is caused by resonant stimulation of grapheneplasmons. In our example, surface plasmons of Au nanoparticles are resonantly excited by photons emanating from nanostructured SnO_2.

The powerful local light fields produced by these plasmons around the nanoparticles greatly intensify the incident light field [30]. These powerful electrons are transferred into the SnO_2 conduction band, increasing the conduction band electron density, and producing more UV emission as a result. Li et al. [31] examined surface plasmon effects on Au-ZnO films.

In figure 8 we recorded 3 On/Off cycle of the current. Here, as we switch on the UV illumination the current rises to ~ 58 μA and as we switch off the UV illumination very small dark current is observed. We also recorded the variation of on current with respect to time for different intensities of UV source, which is shown in Fig. 9. Here we recorded current for 2mW/cm^2, 1,5mW/cm^2 and 1mW/cm^2.
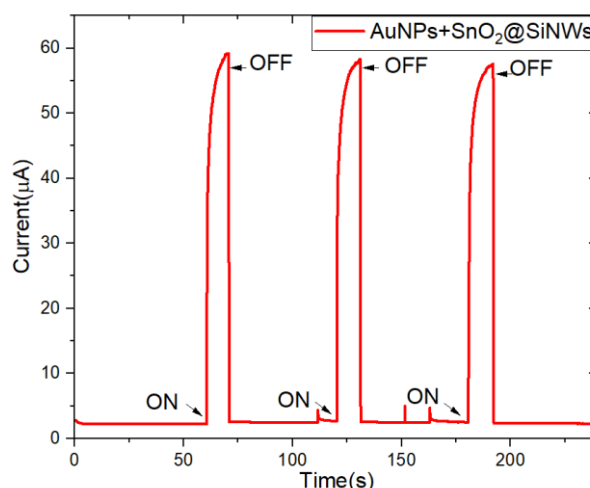
Figure 8. I-t graph of SnO_2/AuNPs@SiNWs
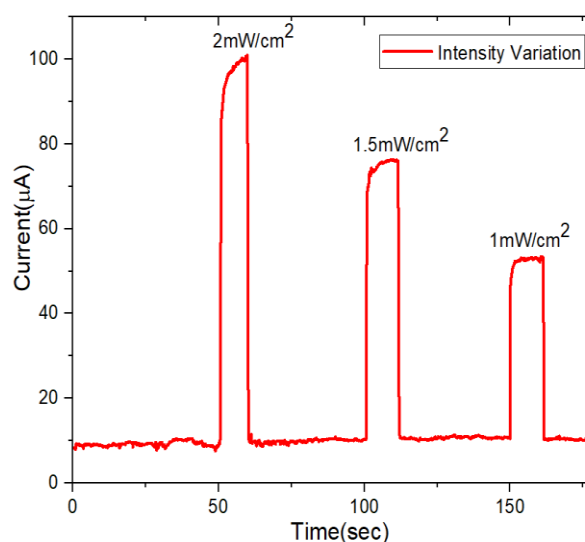
Figure 9. Current in SnO_2/AuNPs@SiNWs with varying Intensity

We calculated responsivity of the device by using formula, Responsivity (R) = $\frac{I_{ph}}{P*A}$ A/W; where I_{ph} = I_L-I_d and calculated detectivity by using, Detectivity (D) = $\frac{R*A^{1/2}}{(2qI_d)^{1/2}}$ Jones [32].

Where, I_L = 9.98×10^{-5} A which is a current in presence of UV Radiation, I_d = 8.9×10^{-6} A i.e. current in dark, P = Power (2 mW), A= Area of device (1cm^2).

By using above equations, the Responsivity and Detectivity was measured to be as, R = 45.4 × 10^{-3} A/W and D = 2.69 × 10^{10} Jones. The response time was measured to be ~ 1.32 s and decay time was ~ 0.77 s. The recovery of the device was found to be very fast. In Fig. 10, we recorded variation of responsivity with intensity. It is observed that responsivity increases with increasing intensity.
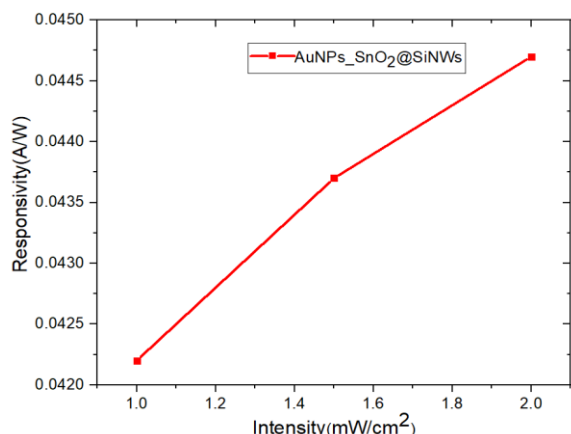
Figure 10. Intensity vs Responsivity variation for SnO₂/AuNPs deposited over SiNWs

5. CONCLUSIONS

Here, a high-performance UV photodetector has been successfully fabricated by developing a heterojunction of SnO₂/AuNPsoverSiNWs. SEM analysis depicts a uniform deposition of SnO₂/AuNPs over SiNWs which was supported by EDX color mapping and X-ray diffraction analysis. The TEM analysis of SnO₂ estimates the size of nanoparticles which is of the order of 30-40 nm. The developed UV photodetector revealed a good responsivity, detectivity and reproducibility under UV illumination where the responsivity and detectivity were estimated to be 45.4×10^{-3} A/W and 2.69×10^{10} Jones respectively with response time ~ 1.32 s and decay time ~0.77 s. Under different intensity, the photo current was observed to be decreasing with decrease intensity. Thus, developed heterojunction based device can be considered for future high-performance SiNWs based UV photodetectors that can be employed in a variety of applications due to its easy and inexpensive construction.

6. REFERENCES

[1] Z.Alaie (2015) Recent advances in ultraviolet photodetectors. Materials Science in Semiconductor Processing, 29, 16-55. https://doi.org/10.1016/j.mssp.2014.02.054

[2] Z.Li (2023) Low-dimensional wide-bandgap semiconductors for UV photodetectors. Nature Reviews Materials, 8(9),587-603. https://doi.org/10.1038/s41578-023-00583-9

[3] H. Chen (2015) New concept ultraviolet photodetectors. Materials Today, 18(9), 493-502. https://doi.org/10.1016/j.mattod.2015.06.001

[4] A.Kumar (2021) Recent advances in UV photodetectors based on 2D materials: A review. Journal of Physics D: Applied Physics, 55(13), 133002. https://iopscience.iop.org/article/10.1088/1361-6463/ac33d7/meta.

[5] Z. Lou (2016) Flexible photodetectors based on 1D inorganic nanostructures.Advanced Science, 3(6), 1500287.https://doi.org/10.1002/advs.201500287

[6] J.Son (2018) UV detectors: status and prospects. UV and Higher Energy Photonics: From Materials to Applications 2018, 10727, 12-20. https://doi.org/10.1117/12.2324105

[7] E. Munoz (2001) III nitrides and UV detection. Journal of Physics: Condensed Matter, 1(32), 7115. https://iopscience.iop.org/article/10.1088/0953-8984/13/32/316/meta

[8] L. Shi (2012) Comparative study of silicon-based ultraviolet photodetectors.IEEE Sensors Journal, 12(7), 2453-2459, doi: 10.1109/JSEN.2012.2192103

[9] F. Bouzid (2018) Numerical simulation study of a high efficient AlGaN-based ultraviolet photodetector. Superlattices and microstructures,122, 57-73. https://doi.org/10.1016/j.spmi.2018.08.022.

[10] Z. Li (2022) Application of nanostructured TiO2in UV photodetectors: A review.Advanced Materials, 34(28), 2109083. https://doi.org/10.1002/adma.202109083

[11] J. Chen (2020) Recent progress of heterojunction ultraviolet photodetectors: materials, integrations, and applications. Advanced Functional Materials, 30(16), 1909909. https://doi.org/10.1002/adfm.201909909

[12] P. Chetri (2019) Self-powered UV detection using SnO₂ nanowire arrays with Au Schottky contact. Materials Science in Semiconductor Processing, 100, 123-129. https://doi.org/10.1016/j.mssp.2019.05.003

[13] A. Gundimeda (2017) Fabrication of non-polar GaN based highly responsive and fast UV photodetector.Applied Physics Letters, 110,(10). https://doi.org/10.1063/1.4978427

[14] M. Zhong (2015) High-performance single crystalline UV photodetectors of β-Ga2O3. Journal of Alloys and Compounds, 619, 572-575. https://doi.org/10.1016/j.jallcom.2014.09.070

[15] U.M. Nayef (2016) Ultraviolet photodetector based on TiO2 nanoparticles/porous silicon hetrojunction. Optik, 127(5), 2806-2810. https://doi.org/10.1016/j.ijleo.2015.12.002

[16] J.L. Yang (2017) Recent progress of ZnMgO ultraviolet photodetector. Chinese Physics B, 26(4), 047308.https://iopscience.iop.org/article/10.1088/1674-1056/26/4/047308/meta

[17] C.A. Amarnath (2013) Nanohybridization of low-dimensional nanomaterials: synthesis, classification, and application. Critical reviews in solid state and materials sciences, 38(1), 1-56. https://doi.org/10.1080/10408436.2012.732545

[18] P. Singh (2022) Development of an ultrasensitive IR sensor using ZnO/SiNWs hybrid nanostructure. Materials Today: Proceedings, 66, 2303-2307. https://doi.org/10.1016/j.matpr.2022.06.229

[19] A. Kumar (2020) Fabrication of SiNWs/Graphene-nanocomposite for IR sensing. Materials Today: Proceedings, 32, 397-401. https://doi.org/10.1016/j.matpr.2020.02.086

[20] M. Iqbal (2016) Preparation of gold nanoparticles and determination of their particles size via different methods. Materials Research Bulletin, 79, 97-104. https://doi.org/10.1016/j.materresbull.2015.12.026

[21] T. Muangnapoh (2010) Facile strategy for stability control of gold nanoparticles synthesized by aqueous reduction method. Current Applied Physics, 10(2), 708-714. https://doi.org/10.1016/j.cap.2009.09.005

[22] M.V. Arularasu (2018) Structural, optical, morphological and microbial studies on SnO₂ nanoparticles prepared by co-precipitation method. Journal of nanoscience and nanotechnology, 18(5), 3511-3517 https://doi.org/10.1166/jnn.2018.14658

[23] X.Cui (2017) The synthesis of polyamidoamine modified gold nanoparticles/SnO2/graphene sheets nanocomposite and its application in biosensor. Colloids and Surfaces A: Physicochemical and Engineering Aspects, 520, 668-675. https://doi.org/10.1016/j.colsurfa.2017.02.030

[24] A. Borhaninia (2017) Gas sensing properties of SnO₂ nanoparticles mixed with gold nanoparticles. Transactions of Nonferrous Metals Society of China, 27(8), 1777-1784. https://doi.org/10.1016/S1003-6326(17)60200-0

[25] J.Y. Cheong (2017) In situ high-resolution transmission electron microscopy (TEM) observation of Sn nanoparticles on SnO₂ nanotubes under lithiation. Microscopy and Microanalysis, 23(6), 1107-1115. https://doi.org/10.1017/S1431927617012739

[26] Y. Wang (2016) Facile approach to synthesize uniform Au mesoporous SnO₂ yolk–shell nanoparticles and their excellent catalytic activity in 4-nitrophenol reduction. Journal of Nanoparticle Research, 18, 1-11. https://doi.org/10.1007/s11051-015-3307-8

[27] M. Ivanovskaya (2021) Effect of Au nanoparticles on the gas sensitivity of nanosizedSnO2. Materials Chemistry and Physics, 258, 123858. https://doi.org/10.1016/j.matchemphys.2020.123858

[28] R. Liu (2013) Grapheneplasmon enhanced photoluminescence in ZnOmicrowires, Nanoscale, 5, 5294.https://doi.org/10.1039/C3NR01226C

[29] S.W. Hwang (2010) Plasmon-enhanced ultraviolet photoluminescence from hybrid structures of graphene/ZnO films, Phys. Rev. Lett., 105, 127403. https://doi.org/10.1103/PhysRevLett.105.127403

[30] B. Lamprecht (2001) Surface plasmon propagation in microscale metal stripes, Appl. Phys. Lett., 79, 51–53.https://doi.org/10.1063/1.1380236 X. Li (2009) Effects of localized surface plasmons on the photoluminescence properties of Au-coated ZnO films, Optics Exp., 17, 8737–8740. https://doi.org/10.1364/OE.17.008735

[31] G. Wang (2018) Two dimensional materials based photodetectors, Infrared Physics & Technology, 88, 149–173.doi.org/10.1016/j.infrared.2017.11.009

IZVOD

RAZVOJ UV FOTODETEKTORA KOJI KORISTI SnO₂/AuNPs@SiNWs HETEROSPOJNICU NA Si ČIPU

U ovoj studiji predstavljamo razvoj hibridne nanostrukture zasnovane na silicijumskim nanožicama (SiNV) i nanočesticama kalajnog oksida (SnO₂) i Au, koja je korišćena za razvoj UV fotodetektora. Hemijsko jetkanje uz pomoć metala (MACE) korišćeno je za kreiranje SiNV na p-Si (1 1 1) supstratu, dok su tehnike redukcione sinteze i ko-precipitacije korišćene za stvaranje AuNP i SnO2 nanočestica, respektivno. Ove nanočestice AuNP i SnO₂ su zatim deponovane na SiNV. Koristeći rendgenski difraktometar (KSRD), UV-vidljivi spektrofotometar i skenirajuću elektronsku mikroskopiju (SEM), ispitana je sintetizovana hibridna nanostruktura SnO₂/AuNPs@SiNVs. Sintetizovane nanočestice SnO₂ su takođe podvrgnute TEM ispitivanju. Na sobnoj temperaturi, UV fotostrujni odgovor SnO₂/AuNPs@SiNVs je proučavan pri različitim intenzitetima UV svetlosti od 1, 1,5 i 2 mV/cm². Utvrđeno je da hibridna nanostruktura SnO₂/AuNPs@SiNVs ima vreme odziva fotostruje veoma brzo (1,32 s). Kako smo isključili UV izvor, senzor je dostigao svoje početno stanje za ~0,77 s. Uzorak je kontinuirano proveravan za tri uključena/isključena seta osvetljenja u redovnom intervalu od 60 s. Stoga, rad koji je ovde otkriven ima veliko obećanje za unapređenje visoko efikasnih minijaturnih UV fotodetektora sa jedinstvenim karakteristikama.
Ključne reči: *fotodetektor, ultraljubičasto, nanočestice zlata, silicijumske nanožice, kalaj oksid*

Pooja Singh: https://orcid.org/0000-0001-8370-5775
Avshish Kumar: https://orcid.org/0000-0003-1681-5426
V.K. Jain: https://orcid.org/0000-0002-4439-6583

Harshani Ramesh[1], Karthikeyan Ganesan[2],
Padma Rani Ramesh[3]*

[1]*Civil Department, National Engineering College, Kovilpatti, India,*
 [2]*Civil Department, Ramco Institute of Technology, Rajapalayam, India,*
[3]*Civil Department, Sri Bharathi Engineering College for women, Pudukottai, India*

A Study on mechanical behavior of Eco-friendlyLight Weight Concrete (LWC) blocks using industrial wastes

ABSTRACT

In the construction industry, concrete comes beginning due to its affordability and widespread application. One of the drawbacks of normal concrete is its substantial self-weight. This heavy self-weight of construction will lead to in unprofitable structural material. To reduce the self-weight, coarse gravel has been substituted partially / substantially by lightweight aggregate. This studyaims to investigate the production of LWC (Light Weight Concrete) by using cenosphere and pumice and subsequently evaluate their performance in terms of compressive strength, water absorption, wet density, dry density, and thermal conductivity Based on a thorough review of the relevant literature, the goal of thisstudy is to find the optimal volume of cenosphere for fine aggregates and pumice for coarse aggregates in LWC blocks. Here Cenosphere is replaced for fine aggregate in the ratios of 30% from literature review and pumice is replaced for coarse aggregate in the ratios of 20%, 40%,60%, 80%,100%. The strength properties and lightweight properties of various cenosphere and pumice concrete ratios were compared and the concrete with 30% cenosphere and 60% pumice is found as the optimal mix. The optimal mix is found based on compressive strength, wet density, dry density, water absorption, thermal conductivity for amount of density reduced in concrete. This optimal mix has a compressive strength of 21.81 N/mm^2 which is lower than conventional concrete and has a water absorption of 3.31% which is higher than conventional concrete and also greater than LWB(Lightweight Block) 40%. It also shows better results in lightweight as well as strength.
Keywords: Lightweight Concrete, Density, compression, porous, thermal conductivity

1. INTRODUCTION

LWC is produced by including a lightweight coarse aggregate, and in some cases, utilizing lightweight fine aggregates that possess a lower density compared to traditional aggregates [1]. The weight of structural lightweight concrete typically falls within the range of 1400 to 1800 kg/m^3. The density of typical weight concretes exhibits a range of 2400 to 2800 kg/m^3, but its strength must surpass 17.0 MPa to meet the requirements for structural applications. Lightweight aggregates commonly consist of shale, or basalt materials, clay that have undergone a process of combustion in a rotary-kiln furnace, resulting in the formation of a structure that exhibits impermeability. Moreover, supplementary materials, such as air-cooled blast furnace slag, are also employed.

The incorporation of waste materials into concrete results in cost reduction, and this method of addressing garbage disposal is considered environmentally conscientious [2-4]. Figure1 indicated that cenosphere are a major waste product of coal thermal power plants. At that time, the cenosphere in the concrete materials will enable effective and efficient utilization of the products while enriching what is now accessible to produce the concrete materials, such as river sand, M-sand, etc. [5]. As a result, reducing the proportion of fine aggregate has no adverse influence on strength attributes, but has a good impact on sustainability issues with an ideal suggestion of 35% fine aggregate as cenosphere. Perhaps the most valuable parts of coal fly ash are cenosphere is shown in Fig 1. Due to their excellent features, involving as low bulk density, thermal resistance, high workability, and high strength, they have a hollow shape that isspherical and may be used in a extensive set of application. [6-8] This work focuses on the creation of cenosphere, their characterization, and their effect on their strength when mixed with Pumice is shown in Fig 2.

---

*Corresponding author: Harshani Ramesh

E-mail: harshaniramesh1050@gmail.com
Paper received: 17. 09. 2024.
Paper accepted: 28. 09. 2024.
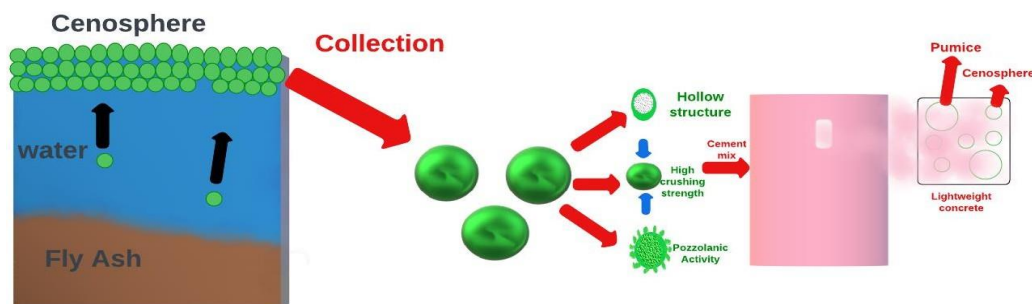
Figure 1. Cenosphere and Pumice in Lightweight Concrete

Pumice aggregates possess the physical characteristics of aggregates made from concrete and can be took advantage of proficiently as lightweight aggregates, and the concrete built with these aggregates meets the demands of low concrete that are lightweight [9]. Furthermore, the resulting concrete can be employed safely in the construction of residences because loads are low and significant durability is not required [10,11]. This country's pumice aggregates can generate commercially low concrete weight, and there is an abundance of naturally generated lightweight gravel for industrial utilization. Pumice is the kind of rock particle used in the concrete in this research, and light weight gravel is a type of material that is lower than aggregate from nature [12,13].The proposed methodology's main goal is to frame a mathematical model using optimization methods. Architectural lightweight concrete is widely employed in the construction industry, especially in skyscrapers [14]. It can only be made with lightweight stones. Pumice is an opaque component and a light porous rock that can be used in place of coarse particles in concrete, and Nanoparticles Silica can be used in substitute of cement [15-18]. Pumice was utilised as a substitute for Coarse Aggregate (CA) in proportions of 0%, 20%, and 30% by amount, and Nano Silica was substitute in 1-3% in various mixtures for estimating three output parameters: compressive force, split tensile capacity (MPa), and bending strength (MPa) [19]. According to test results, incorporating pumice to CA concrete reduces density while also diminishing all mechanical qualities. This is since pumice has a smoother surface texture and a density that is lower than Coarse Aggregate [20,21]. LWC comprising more than 20% pumice, on the other hand, turns into structural lightweight concrete with exceptional strength. Several studies indicated an overall increase in strength as well as a decrease in weight. As a result, light weight construction has the same strength as heavy- weight concrete [22,23]. Because of its utility and low cost, concrete is the most frequently prefabricated material for construction in the world. One of the drawbacks of traditional building materials is its exceptionally high its own weight. Because of the high self-weight of concrete, structural material will be uneconomical [24-26].

To reduce the own-weight of concrete, coarse material has been mainly substituted by lightweight aggregate. This is lightweight concrete with a low density, reduced dead load, and increased thermal insulation [27]. Natural lightweight gravel and artificial lightweight gravel are two distinct types of lightweight aggregate. Pumice aggregate, one of the most readily accessible natural aggregates, is utilized as a filler for coarse aggregate. Lightweight concrete is made by replacing 50%, 80%, and 100% of the coarse stones with pumice aggregate. Mix M30 with Conplast SP430 additive is used to make conventional concrete together with pumice lightweight aggregate concrete [28-30]. By performing non-destructive assessments, the mechanical and durability qualities of standard concrete as well as pumice aggregate concrete are compared, and a beneficial replacement is identified.

According to IS 1199-2018, the test using a slump cone constitutes one of the more commonly used examines for evaluating the consistency of concrete. In accordance with the outcomes of a slump cone test, pumice is lightweight. The workability of pumice with 50% replacement is very high and in comparison, to the other substitute percentages. Among the most accurate tests is the compacting factor test [31-33]. Using IS 1199-2018 as a guide, determine the mix's workability. When compared to mixes with lower replacement percentages, mixes with 50% replacement also have a high compaction factor. Analysis of the test findings leads to the following conclusions: It proves that aggregate concrete becomes lighter when the percentage of pumice aggregate increases, as the density of the concrete decreases. Using pumice aggregate instead of natural aggregate can make concrete lighter. The reduced strength and increased water absorption of pumice stone aggregate are because of its higher pore content compared to that of regular coarse aggregate. Consequently, superplasticizers are employed.

Comparing pumice with 50%, 80%, and 100% replacement in terms of split tensile strength, compressive strength, and bending strength reveals that 50% replacement provides the most

benefit. The tensile, crushing, and bending strengths at 80% and 100% gradually diminish after 50%.
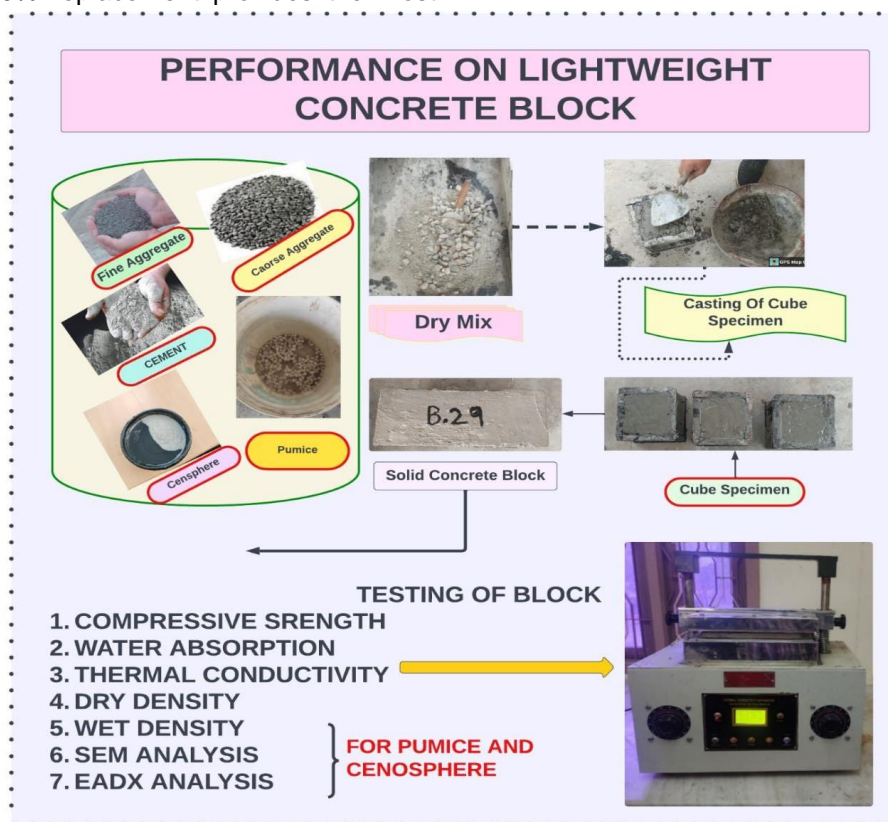
Figure 2. Methodology of LWC block

2. MATERIAL PROPERTIES

Selecting raw materials with sufficient proportioning as well as quality control is crucial for Lightweight Concrete to attain its desired strength and its density. Materials which are used in this work are cement Ordinary Portland Cement (OPC), Cenosphere, Pumice, Fine aggregate, and Coarse aggregate. Energy Dispersive x-ray Spectroscopy (EDS) is a method of analysis to identify the chemical components of a material. For chemical analysis, it utilizes the x-ray spectrum obtained from a specimen sample engaged with an electron beam. The EDS method can identify all elements with an atomic number ranging from 4 through 92. The identification of lines in the spectrum constitutes a component of qualitative analysis. The field emission scan electron microscope is a kind of non-destructive scanning technique which employs high-resolution images to examine the shape and structure of a material.

When a high-energy electron beam strikes a material, , x-rays, as well as scattered electrons are released[34,35]. A detector gathers electrons that are released and converts them into an electrical signal that appears on the screen. It recognizes

crystalline formations and displays spatial shifts in chemical structures. Topographical imaging and complete three-dimensional scanning are two of the many uses for an electron microscope scanner. It is capable of approximating particle size within certain limits. Improved spatial resolution with reduced sample charging and damage is achieved by the morphological evaluation technique.

2.1. Cement

OPC cement is main ingredient in making LWC. It also it plays a crucial role in LWC because it offers the chemical reaction required for the curing process. Hydration is the process that occurs when OPC cement is combined with water; during this time, C-S-H and (Ca (OH)2) are formed. The final product's strength and durability can be attributed to these components. By reducing the amount of water needed to reach a workable consistency while yet allowing for proper hydration and hardening, OPC cement plays a crucial part in this process [36,37]. Concrete needs ductile property to increase its breaking strength and strain hardening.

2.2.Pumice

Pumice is one of the most widespread and ancient built-in aggregates used in the manufacturing of lightweight coarse aggregates for the building industry. Pumice is a generic word for porous materials formed during the cooling effect of lava because of igneous activity; fill the gaps are caused by the expulsion of vapors from the magma. Because of the microscopic hollow spaces created by the gases, the resulting particles have an extremely porous structure, which is why pumice has a highly porous structure [38]. Multiple investigations on pumice aggregate for lightweight have been carried out throughout globe, with most studies emphasizing materials that are accessible in specific regions or nations worldwide. The Scanning Electron Microscope (SEM) for pumice was examined in 50µm, shown in Fig 3. The EDS for pumice explained that the elements present inside were O, Si, Al, K and Na which has 67.29%, 21.21%, 4.97%, 3.01% and 2.32 % of composition respectively as shown in Fig 3.
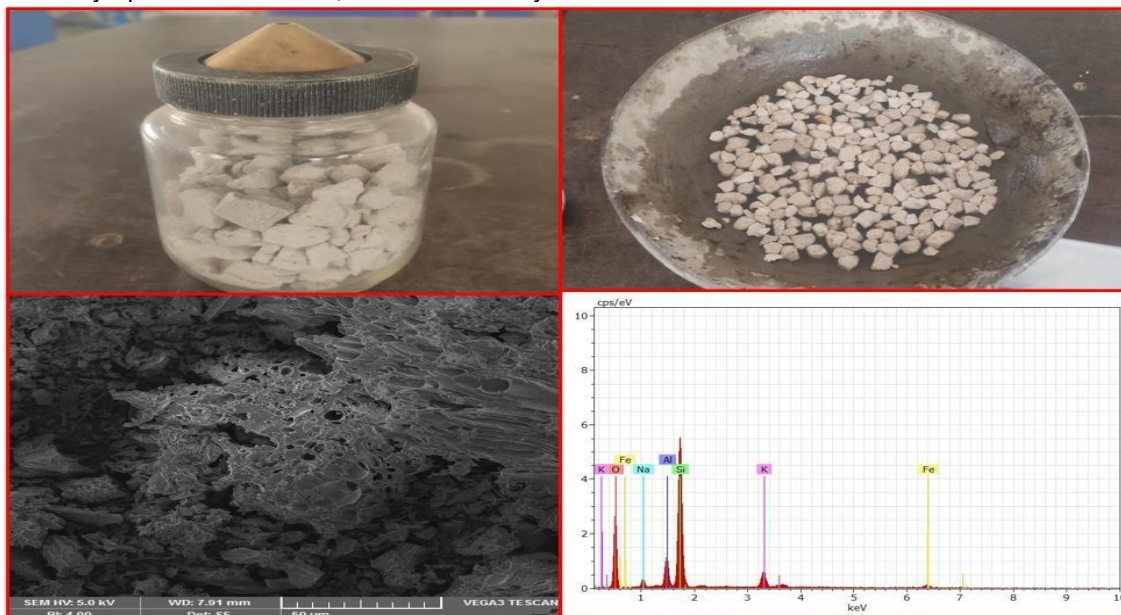
Figure 3. Physical properties and microstructural analysis of Pumice

2.3. Cenosphere

Figure 4 shows that the cenosphere are thin-walled hollow particles with a density to volume ratio of less than 1.0 that float on the water and are retrieved from the float formed by ash removal lagoons in general. They possess chemical characteristics that are comparable to fly ash and are used in a wide range of industries because of their distinctive blend of spherical form, high compression as well, low specific weight, better thermal and acoustical insulating material properties, and inertness in to acids and alkalis [39,40]. EDS is the X-ray emission from an object passing through an electron beam. The SEM for cenosphere of (400-600micron) was examined in 100µm, shown in Fig 4. EDAX for cenosphere of explained that the elements present inside were O, Al, Si, K and Fe which has 61.53%, 17.46%, 16.60%, 3.77%, and 0.64 % of composition respectively as shown in Fig 4.

2.4. Superplasticizer

Benefits of using a superplasticizer in concrete include improved workability at a constant cement concentration, easier placing and compacting, and reduced water content that results in greater strength. Incorporating superplasticizers into concrete improves fresh as well as hardened state. Standard code for Admixtures of Concrete (ASTM C494). Master Glenium SKY 8233, a high-range water-reducing superplasticizer based on a polycarboxylic ether formulation, will be employed. A minimum solids range of 32% and a specific gravity of 1.08 are required for the product.

When compared to conventional superplasticizers, Master Glenium SKY 8233 has a unique chemical structure. It is a polymer of long-chain carboxylic ethers. It starts with the identical electrostatic dispersal mechanism as typical superplasticizers at the initial stage of hydration, but the adjacent chains attached to the polymer backbone provide a steric barrier that substantially regulates the cement particles' ability to split and disperse themselves [41]. In addition to the electrostatic limitation, steric interference creates a physical barrier between the cement grains. Concrete that is flowable and has a significantly reduced amount of water content can be obtained using this technique.
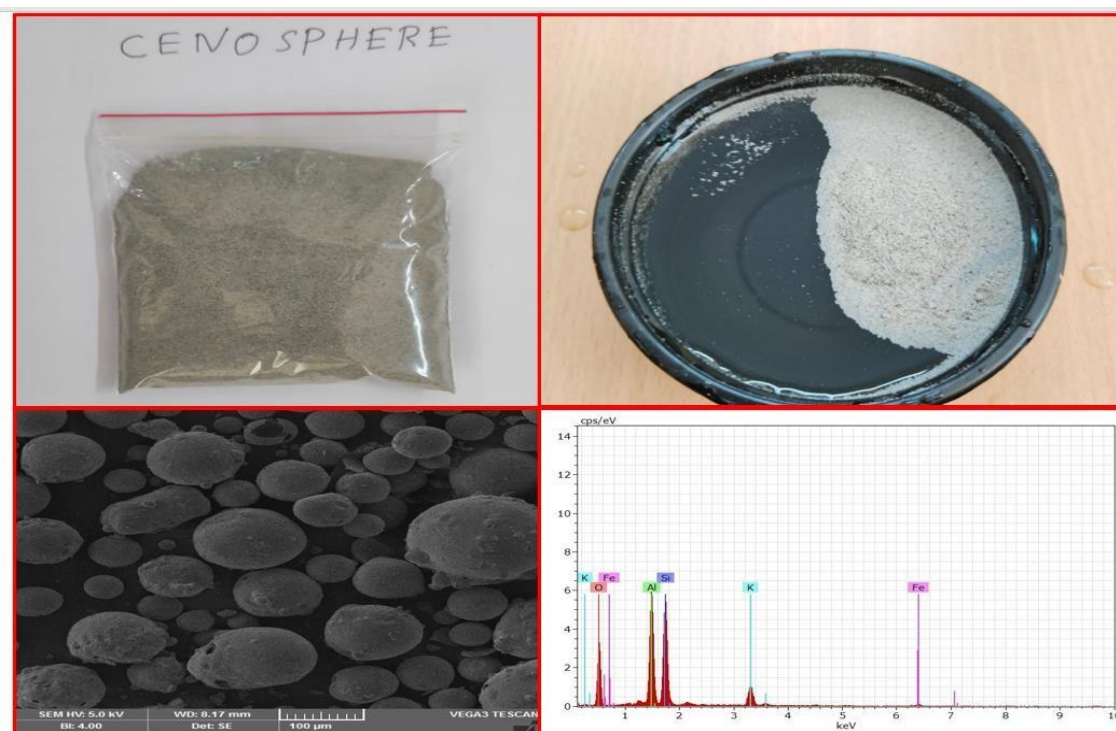
Figure 4. Physical properties and microstructural analysis of Cenosphere

3. EXPERIMENTAL WORK

Cement was subjected to tests such as the Standard consistency test, beginning and final setting time, and specific gravity test and for zeolite specific gravity test is done as per IS 1124-1974. The specific gravities of zeolite and cement were 2.8 and 3.16 respectively. Particle size distribution for fine aggregate is 0.525 and specific gravity revealed a value of 2.65. Specific gravity of coarse aggregate is found to be 2.74 and water absorption were also conducted. Utilizing the slump conetest, it is possible to determine how workable the fresh concrete is and the value is found to be 3.7 cm. The concrete mix of M35 grade was adopted in this project. Six types of concrete blocks were casted using the materials pumice, cenosphere, cement, fine aggregate, and coarse aggregate is shown in Fig 5. This study aims to investigate the production

of lightweight concrete blocks by using cenosphere and pumice and subsequently evaluate their performance in terms of compressive strength, water absorption, wet density, dry density, and thermal conductivity. Based on the findings of the literature review, it was noted that the incorporation of cenosphere in concrete blocks should be limited to a maximum of 30% is indicated in Table 1. Beyond this threshold, adverse effects on both the fresh and hardened properties of the concrete blocks were seen. Based on a thorough review of the relevant literature, the goal of this study is to find the optimal volume of cenosphere for fine aggregates and pumice for coarse aggregates in lightweight concrete (LWC) blocks [42]. Mix design for various proportion for blocks is indicated as Light Weight Block (LWB) with different volume of pumice.

Table 1. Mix ratio LWC using Cenosphere and Pumice

Mix name	Cement (Kg/m^3)	Fine aggregate (Kg/m^3)	Coarse aggregate(Kg/m^3)	Water (Kg/m^3)	Super plasticizer(By its weight of cement)	Cenosphere (Kg/m^3)	Pumice (Kg/m^3)
LWB 0%	437.77	710.22	1150	197	0%	0	0
LWB 20%	437.77	568.176	920	220	1%	142	230
LWB 40%	437.77	426.132	690	220	1%	213	460
LWB 60%	437.77	284.08	460	220	1.5%	355	690
LWB 80%	437.77	142.06	230	220	2%	497	920
LWB 100%	437.77	0	0	220	2%	639	1150

Figure 5. Casting of Conventional Block and LWC block

The Pumice and Cenosphere LWC block were cased on varying ratios as shown in Table-1. Control specimens were also casted. The casted specimens were kept in curing tank for curing and their 28th day compressive strength, water absorption, wet density, dry density, and thermal conductivity were done for all the six ratios and for the conventional blocks. Where mineral-based additives or blended cement are included in the concrete, it is advised that the following minimum periods be increased to 28 days: Specimens are demolded after 24 hours and then submerged under water for 28 days to achieve the target crushing strength.

3. RESULTS AND DISCUSSION

3.1. Compressive strength

Compressive strength commences with the preparation of concrete samples. These specimens are typically cubical in shape, with a size of 400 mmx200mmx100mm. The specimens are then placed in a mould and aged in preparation for testing by curing them under a wide range of curing condition. After a suitable period has passed, the specimens' compressive strength is evaluated is mentioned in Table 2. Typically, a hydraulic press is used to apply a force to the top of the specimen and press down until failure occurs. The load is applied at a steady rate until the specimen fails, typically at a rate of 0.6MPa per second. It is calculated by recording the highest load applied to the specimen [43]. By dividing the highest load exerted on the specimen by its c/s area, researchers may determine the concrete's compressive strength in

units of megapascals (MPa). Table 2 indicates that the crushing strength of the LWB 60% mix is 21.81 MPa, which is higher compared to LWB 20% and LWB 40% due to cenosphere and because the incorporation of pumice reduce the strength and make concrete as lighter. Due to the high pumice content in LWB 80%, itdoes not attain an enormous amount of strength compared to LWB 40% is indicated in Fig 6.
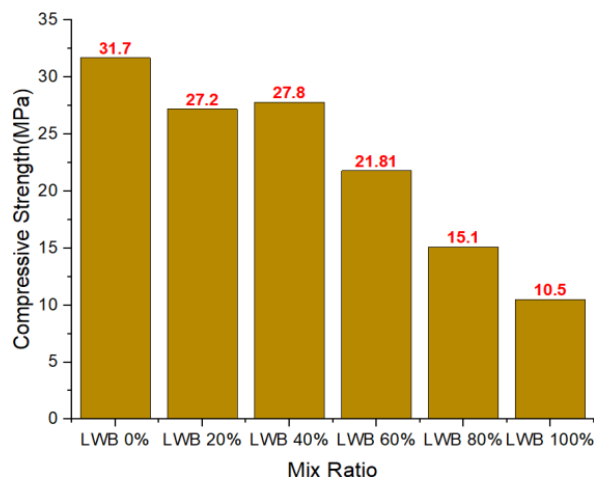
Figure 6. Compressive strength (MPa) of LWB

3.2. Water Absorption

Concrete's ability to absorb water is one of its most essential properties, and it is one of the ways that its strength and resistance to weathering are evaluated. After being cured, the specimens are weighed again, and this time the initial weight is noted. The samples are stored in water in a sealed

container to prevent loss due to evaporation. After that, the samples are left to soak for a certain amount of time, usually 60 days. After the allotted time has passed, the samples are taken out of the water and wiped off with a towel [44]. The percentage of water absorbed is found by taking the difference in weight before and after soaking and dividing it by the weight before soaking. The result of this calculation is the percentage of water that the concrete has absorbed in graphical manner in Fig 7. In addition, mix LWB 80% and LWB 100% had water absorption values lower than that of the control mix samples (mix LWB 20% and LWB 40%) is shown in Table 2.
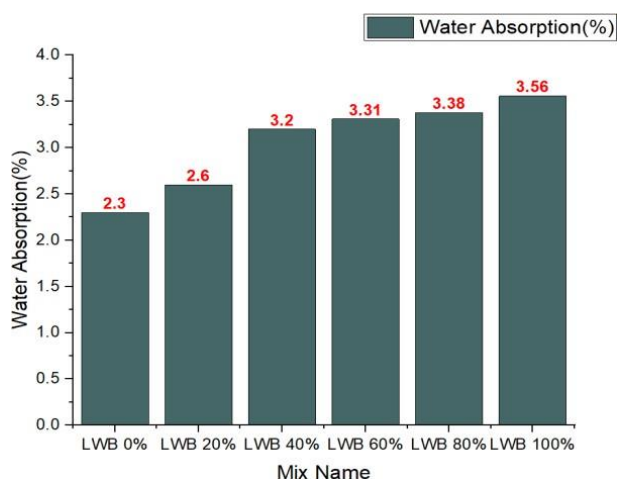
Figure 7. Water Absorption (%) of LWB

3.3. Wet density

The wet density of LWC is the mass of the mix of concrete per unit volume when it is fresh, and it is usually measured in kg/m^3. It is a critical parameter in the design of concrete mixtures and the building industry. The wet density is affected by a wide variety of things like the ratios of the concrete mix's ingredients, the volume of water utilized, and the stage of consolidation.
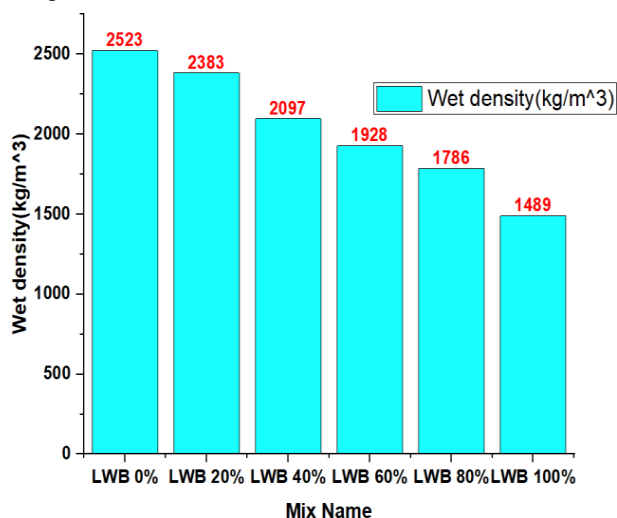
Figure 8. Wet Density (Kg/m^3) of LWB

Table 2 indicated that depend on its requirements, density, and strength wise produce a lightweight block because incorporation of pumice is above permissible limit it will affect the strength characteristics but it will drastically reduce the density of structure. Simultaneously 60% of pumice and 30% of cenosphere it will satisfy both strength and density criteria as shown in Fig 8.

3.4. Dry Density

The dry density of concrete, an important construction parameter, is the mass per volume of hardened concrete. identifying dry density requires measuring the mass and volume of the concrete after curing. When the concrete has hardened, the excess water has dissipated, and its composition has attained its dried state, the dry density can be determined using the following equation: Dry density = Mass of concrete/Volume of Concrete.
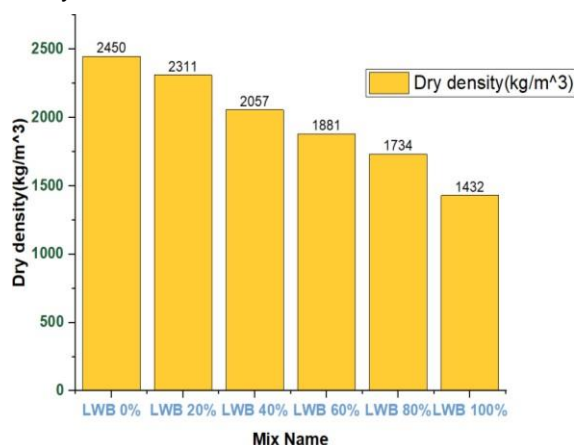
Figure 9. Dry Density (Kg/m^3) of LWB

The density of a material is critical for determining structural strength and durability. Table 2 indicated that depend on its requirements desired density lightweight blocks because incorporation of pumice within limit it will affect the strength characteristics but it will drastically reduce the density of structure. Simultaneously 60% of pumice and 30% of cenosphere it will satisfy both strength and density criteria as shown in Fig 9.

3.5. Thermal Conductivity

Thermal analysis is a branch within experimental condensed matter science that studies material properties as a function of temperature. There are plenty of thermal analysis methods accessible that offer data on different characteristics of materials such as phase changes, shift temperature, heat of response, oxidative resistance, purity, thermal endurance, creep/stress tranquilly, flexural modulus, as well

dissipation of energy, permeability, and loss factor, between others. Thermal analysis yields properties such as energy density, heat capacity, mass modifications, and the ratio of heat contraction in practice. Thermal analysis is employed in solid state chemistry to examine solid-state processes, such as thermal responses, phase transitions, and diagrams of phase. When vital, the thermal conductivity of LWA in the air state of dryness shall be assessed in accordance with EN 12664 in the event of dry LWA with a thermal conductivity value less than 0.4 W/(mK) is shown in Fig 2.

Table 2. Lightweight Concrete Block Test results

Mix name	Compressive strength(N/mm^2)	Water absorption (%)	Wet density(kg/m^3)	Dry density (kg/m^3)	Thermal Conductivity W/(mK).
LWB 0%	31.7	2.3	2523	2450	1.82
LWB 20%	27.2	2.6	2383	2311	0.38
LWB 40%	27.8	3.2	2097	2057	0.36
LWB 60%	21.81	3.31	1928	1881	0.34
LWB 80%	15.10	3.38	1786	1734	0.22
LWB 100%	10.5	3.56	1489	1432	0.18

5. CONCLUSION

Cenospheres are often mixed into concrete to make lightweight composites. Large levels of cenosphere reduce concrete weight but increase consistency, reducing hard composite strength and porosity. When pumice replaces coarse aggregate to 60% or more, compressive strength drops because load bearing capacity diminishes. Instead of cenosphere, 30% fine aggregate was used. Due to its greater aluminium and silica content, cenosphere increases heat conductivity. Compare LWB 20%, 40%, and 60%, the latter has the highest compressive strength at 31.7 N/mm^2. LWB 100% had the maximum compressive strength at 15.10 N/mm^2, surpassing ordinary concrete. Lightweight concrete with all pumice and cenosphere mixes percentages absorbs water within limits. Other ratios have higher wet density than LWB 100%. A hollow sphere is generated when cenosphere is added to a cement matrix form, indicating that axial breaking microstructures occur when compressed [45,46]. Crack form parallel to compression. Cenosphere/cement composite materials have closed porosity from cenosphere capsules and exposed permeability from inadequate packing [47].

The compressive strength of the LWB 60% mix is lower than that of the LWB 20% and LWB 40% mixes. This reduction in strength can be attributed to the higher proportion of lightweight aggregates, such as cenosphere and pumice, which, although advantageous for decreasing density and thermal conductivity, generally result in diminished strength. Here According to literature, 30% cenosphere replaces fine aggregate while 20%, 40%, 60%, 80%, and 100% pumice replaces coarse aggregate. The best blend of 30% cenosphere and 60% pumice concrete was established by comparing the strength and lightweight. For concrete density reduction, compressive strength, wet density, dry density, water absorption, and thermal conductivity determine the best combination. The compressive strength of this ideal mix is 21.81 N/mm^2, lower than ordinary concrete, while the water absorption is 3.31%, higher than LWB 40%.

6. REFERENCES

[1] S.Arivalagan, K.S.A.Dinesh (2022) Experimental Study on Light Weight Concrete by Using Light Expanded Clay Aggregate (LECA). International Journal of Research in Applied Science and Engineering Technology 10, 1091–1094. https://doi.org/10.22214/ijraset.2022.48111

[2] K.S. Elango, J. Sanfeer, R. Gopi et al. (2020) Properties of light weight concrete - A state of the art review. Materials Today: Proceedings 33, 4059–4062. https://doi.org/10.1016/j.matpr.2020.04.278

[3] R.B. Karthika, V. Vidyapriya, K.V. Nandhini Sri et al. (2020) Experimental study on lightweight concrete using pumice aggregate. Materials Today: Proceedings 22, 1606–1613. https://doi.org/10.1016/j.matpr.2019.11.232

[4] M.A.A. Alrubaie, S. Wtaife, Z.H.J. Alsafy, N.H.A. Khalid (2023) Compressive Strength of Light-Weight Concrete Material Made from Treated Wood Waste as a Coarse Aggregate. Bioresources 18, 111–130. https://doi.org/10.15376/biores.18.1.111-130

[5] M. Nomikou, V. Kaloidas, C.T. Galmpenis, G. Tzouvalas (2022) MASTER FLOOR®: The New

Application of Pumice Stone as Lightweight Floor Filling Material. Construction Materials 2, 105. https://doi.org/10.3390/constrmater2030005

[6]   N. Degirmenci, A. Yilmaz (2011) Use of pumice fine aggregate as an alternative to standard sand in production of lightweight cement mortar. Cement and Concrete Research 41, 998–1001. https://doi.org/10.1016/j.cemconres.2010.04.005

[7]   Asadi, M. Hashemi, B. Sajadi et al. (2023) Evaluating the time lag and decrement factor of mortar and concrete containing OPBC as an agricultural by-product lightweight aggregate. Case Studies in Thermal Engineering 41, 102609. https://doi.org/10.1016/j.csite.2022.102609

[8]   M. Amran, A.M. Onaizi, R. Fediuk et al. (2022) An ultra-lightweight cellular concrete for geotechnical applications – A review. Case Studies in Construction Materials 16, e01096. https://doi.org/10.1016/j.cscm.2022.e01096

[9]   M. Maghfouri, V. Alimohammadi, R. Gupta et al. (2022) Drying shrinkage properties of expanded polystyrene (EPS) lightweight aggregate concrete: A review. Case Studies in Construction Materials 16, e00919. https://doi.org/10.1016/j.cscm.2022.e00919

[10] S.K. Adhikary, D.K. Ashish, Ž. Rudžionis (2021) Expanded glass as light-weight aggregate in concrete – A review. Journal of Cleaner Production 313, 127889. https://doi.org/10.1016/j.jclepro.2021.127889

[11] K.B. Teoh, Y.S. Chua, S.D. Pang, S.Y. Kong (2023) Experimental investigation of lightweight aggregate concrete-filled cold-formed built-up box section (CFBBS) stub columns under axial compression. Engineering Structures 279, 115630. https://doi.org/10.1016/j.engstruct.2023.115630

[12] P. Pongsopha, P. Sukontasukkul, H. Zhang, S. Limkatanyu (2022) Thermal and acoustic properties of sustainable structural lightweight aggregate rubberized concrete. Results in Engineering 13, 100333. https://doi.org/10.1016/j.rineng.2022.100333

[13] C.J. Cobo-Ceacero, J.M. Moreno-Maroto, M. Guerrero-Martínez et al. (2023) Effect of the addition of organic wastes (cork powder, nut shell, coffee grounds and paper sludge) in clays to obtain expanded lightweight aggregates. Boletin de la Sociedad Española de Cerámica y Vidrio 62, 88–105. https://doi.org/10.1016/j.bsecv.2022.02.007

[14] Muhtar (2023) Performance-based experimental study into quality zones of lightweight concrete using pumice aggregates. Case Studies in Construction Materials 18, e01960. https://doi.org/10.1016/j.cscm.2023.e01960

[15] M.M. Abdelfattah, R. Géber, I. Kocserha (2023) Enhancing the properties of lightweight aggregates using volcanic rock additive materials. Journal of Building Engineering 63, 105426. https://doi.org/10.1016/j.jobe.2022.105426

[16] B.S. Thomas, J. Yang, A. Bahurudeen et al. (2022) Geopolymer concrete incorporating recycled aggregates: A comprehensive review. Cleaner Materials 3, 100059. https://doi.org/10.1016/j.clema.2022.100059

[17] A.M. Solak, J.A. Tenza-Abril, V.E. García-Vera (2022) Adopting an image analysis method to study the influence of segregation on the compressive strength of lightweight aggregate concretes. Construction and Building Materials 323, 126594. https://doi.org/10.1016/j.conbuildmat.2022.126594

[18] E. del Rey Castillo, N. Almesfer, O. Saggi, J.M. Ingham (2020) Light-weight concrete with artificial aggregate manufactured from plastic waste. Construction and Building Materials 265, 120199. https://doi.org/10.1016/j.conbuildmat.2020.120199

[19] M. Ali, A. Kumar, A. Yvaz, B. Salah (2023) Central composite design application in the optimization of the effect of pumice stone on lightweight concrete properties using RSM. Case Studies in Construction Materials 18, e01958. https://doi.org/10.1016/j.cscm.2023.e01958

[20] R. Szydlowski, M. Mieszcak (2017) Study of Application of Lightweight Aggregate Concrete to Construct Post-tensioned Long-span Slabs. Procedia Engineering 193, 1077–1085. https://doi.org/10.1016/j.proeng.2017.06.275

[21] F. Wu, Q. Yu, C. Liu (2021) Durability of thermal insulating bio-based lightweight concrete: Understanding of heat treatment on bio-aggregates. Construction and Building Materials 269, 121800. https://doi.org/10.1016/j.conbuildmat.2020.121800

[22] A.A. Abbara, A. Abdelhalim, M. Al-Ajamee et al. (2022) Uniaxial compressive stress-strain relationship for rubberized concrete with coarse aggregate replacement up to 100%. Case Studies in Construction Materials 17, e01336. https://doi.org/10.1016/j.cscm.2022.e01336

[23] S.M. Hama (2017) Improving mechanical properties of lightweight Porcelanite aggregate concrete using different waste material. International Journal of Sustainable Built Environment 6, 81–90. https://doi.org/10.1016/j.ijsbe.2017.03.002

[24] T. Jiang, Y. Wang, S. Shi et al. (2022) Compressive behavior of lightweight concrete using aerogel-reinforced expanded polystyrene foams. Case Studies in Construction Materials 17, e01557. https://doi.org/10.1016/j.cscm.2022.e01557

[25] M.K. Yew, J.H. Beh, M.C. Yew et al. (2022) Performance of surface modification on bio-based aggregate for high strength lightweight concrete. Case Studies in Construction Materials 16, e00910. https://doi.org/10.1016/j.cscm.2022.e00910

[26] T.Y. Shin, Y.H. Kim, C.B. Park, J.H. Kim (2022) Quantitative evaluation on the pumpability of lightweight aggregate concrete by a full-scale pumping test. Case Studies in Construction Materials 16, e01075. https://doi.org/10.1016/j.cscm.2022.e01075

[27] D. Waldmann, A. May, V.B. Thapa (2017) Influence of the sheet profile design on the composite action of slabs made of lightweight woodchip concrete. Construction and Building Materials 148, 887–899. https://doi.org/10.1016/j.conbuildmat.2017.04.193

[28] A.M. Rashad (2018) Lightweight expanded clay aggregate as a building material – An overview. Construction and Building Materials 170, 757–775. https://doi.org/10.1016/j.conbuildmat.2018.03.009

[29] Amran, N. Farzadnia, M. Ali (2015) Properties and applications of foamed concrete; a review. Construction and Building Materials 101, 990–1005. https://doi.org/10.1016/j.conbuildmat.2015.10.112

[30] G. Jasieńko, J. Nowik, W. Giergiczny (2019) Application of lightweight foamed concrete to strengthening of timber structures. Construction and Building Materials 228, 116739. https://doi.org/10.1016/j.conbuildmat.2019.116739

[31] T. Sedaghat, H. Barkhordari, S. Javadian (2023) Experimental investigation of the behavior of lightweight foamed concrete containing recycled PET aggregate under high-temperature conditions. Case Studies in Construction Materials 19, e02046. https://doi.org/10.1016/j.cscm.2023.e02046

[32] T.Y. Shin, C.B. Park, J.H. Kim (2023) Rheological properties and compressive strength prediction models for lightweight aggregate concrete incorporating structural fibers. Cement and Concrete Composites 142, 105567. https://doi.org/10.1016/j.cemconcomp.2023.105567

[33] C.B. Park, J.H. Kim, T.Y. Shin et al. (2023) Pumping test for high-strength lightweight concrete: Role of water-to-cement ratio and pumping distance on fresh and hardened concrete properties. Cement and Concrete Composites 144, 105683. https://doi.org/10.1016/j.cemconcomp.2023.105683

[34] M. Maghfouri, V. Alimohammadi, R. Gupta et al. (2023) Mechanical behavior and thermal properties of lightweight concrete reinforced with polypropylene fiber and expanded polystyrene. Construction and Building Materials 381, 131074. https://doi.org/10.1016/j.conbuildmat.2023.131074

[35] T.Y. Shin, Y.H. Kim, C.B. Park, J.H. Kim (2022) Rheological properties of lightweight aggregate concrete incorporating fiber-reinforced polymer reinforcement. Cement and Concrete Composites 142, 105615. https://doi.org/10.1016/j.cemconcomp.2022.105615

[36] N. Cavaleri, M. Corradi, A. La Mendola et al. (2017) Lightweight Composite Concrete Reinforced with Basalt Fiber Reinforced Polymer (BFRP) for Structural Applications. Materials 10, 1218. https://doi.org/10.3390/ma10101218

[37] G. Kalpana, A. Gurumoorthy, K. Nallusamy et al. (2020) Experimental Investigation on Strength and Durability Characteristics of Foam Concrete. Materials Today: Proceedings 33, 1306–1310. https://doi.org/10.1016/j.matpr.2020.03.426

[38] H.M. Arabi, M.E.A. Bashter, M.M. Afifi (2014) Mechanical Properties of Lightweight Concrete Incorporating Expanded Polystyrene. International Journal of Engineering Research and Applications 4, 86–90.

[39] M.S. Gadisa, B. Gudeta, A. Wassie, D. Wondimu (2023) Durability of lightweight concrete incorporating pumice aggregate and polypropylene fiber. Journal of Building Engineering 67, 106013. https://doi.org/10.1016/j.jobe.2023.106013

[40] H. Majid, A.A. Shubbar, A. Althoey et al. (2022) Influence of recycled aggregates on mechanical and durability properties of self-compacting lightweight concrete. Cleaner Materials 3, 100057. https://doi.org/10.1016/j.clema.2022.100057

[41] Koniorczyk, P. Miądlicki, Ł. Zarębski (2021) Lightweight steel-concrete composite floor slabs – Experimental tests. Journal of Building Engineering 44, 102681. https://doi.org/10.1016/j.jobe.2021.102681

[42] P. Ponsot, M. Karamanis, G. Athanasopoulos, P. Laes (2021) Strength Development and Fire Resistance of Lightweight Concretes Made with Lightweight Aggregates Produced from Waste. International Journal of Architectural, Civil and Construction Sciences 15, 71–77.

[43] S.M. Alsayed, Y.A. Al-Salloum, T.H. Almusallam et al. (2014) Lightweight Aggregate Concrete with High Compressive Strength and Low Thermal Conductivity. Energy Procedia 57, 59–65. https://doi.org/10.1016/j.egypro.2014.10.007

[44] R.B. Padhy, A. Sharma, R. Kaushik, B. Sarangi (2018) Fire performance of light weight concrete filled steel tubular columns under axial compression. Structures 14, 49–59. https://doi.org/10.1016/j.istruc.2018.02.002

[45] M.S. Kotresh, S.C. Belurkar (2014) Properties of Foam Concrete – A Review. International Journal of Scientific Research and Reviews 3, 84–92. https://doi.org/10.1016/j.conbuildmat.2021.123091

[46] A.M. Kedir, M.D. Abdulfetah (2018) Durability Characteristics of Lightweight Foamed Concrete. International Journal of Recent Technology and Engineering 7, 187–193. https://doi.org/10.1016/j.conbuildmat.2021.123091

[47] J.M. Martinez, P. Sánchez-Silva, J.M. Moreno-Maroto (2021) Behavior of lightweight concrete structures made with recycled plastic aggregate under seismic loads. Construction and Building Materials 289, 123091. https://doi.org/10.1016/j.conbuildmat.2021.123091

IZVOD

STUDIJA O MEHANIČKOM PONAŠANJU EKOLOŠKI PRIHVATLJIVIH LAKIH BETONSKIH BLOKOVA (LVC) KOJI KORISTE INDUSTRIJSKI OTPAD

U građevinskoj industriji beton se koristi zbog svoje pristupačnosti i široke primene. Jedan od nedostataka normalnog betona je njegova velika sopstvena težina. Ova velika sopstvena težina konstrukcije će dovesti do neisplativosti konstrukcijskog materijala. Da bi se smanjila sopstvena težina, krupni šljunak je delimično/značajno zamenjen lakim agregatom. Ova studija ima za cilj da istraži proizvodnju LVC-a (Light Veight Concrete) korišćenjem cenosfere i plovućca i zatim proceni njihove performanse u smislu čvrstoće na pritisak, upijanja vode, gustine mokre, suve gustine i toplotne provodljivosti. Na osnovu detaljnog pregleda relevantnih literaturi, cilj ovog istraživanja je pronalaženje optimalne zapremine cenosfere za fine agregate i plovućca za krupne agregate u LVC blokovima. Ovde je cenosfera zamenjena finim agregatom u razmerama od 30% iz pregleda literature, a plovućac je zamenjen krupnim agregatom u odnosima od 20%, 40%, 60%, 80%,100%. Upoređene su osobine čvrstoće i lake težine različitih odnosa cenosfere i plovca betona i beton sa 30% cenosfere i 60% plovućca je pronađen kao optimalna mešavina. Optimalna mešavina se nalazi na osnovu čvrstoće na pritisak, vlažne gustine, suve gustine, upijanja vode, toplotne provodljivosti za količinu smanjene gustine u betonu. Ova optimalna mešavina ima čvrstoću na pritisak od 21,81 N/mm^2 koja je niža od konvencionalnog betona i ima apsorpciju vode od 3,31% što je više od konvencionalnog betona i takođe veće od LVB (Lightveight Block) 40%. Takođe pokazuje bolje rezultate u laganoj težini i snazi.
Ključne reči: laki beton, gustina, kompresija, porozna, toplotna provodljivost.

Harshani Ramesh   https://orcid.org/0009-0006-5452 5402
Karthikeyan Ganesan   https://orcid.org/0000-0001-8007-1420
Padma Rani Ramesh   https://orcid.org/0009-0007-7186-2985

Farzet Bikić, Dejana Kasapović

Faculty of Engineering and Natural Sciences, University of Zenica, Zenica, Bosnia and Herzegovina

Investigation of general corrosion of austenitic stainless steel types 304 L and 317 L, especially from the aspect of their chemical composition

ABSTRACT

Austenitic stainless steels are among the most widely used types of stainless steel. The most commonly used grades are the American Iron and Steel Institute (AISI) 300 series of alloys. Starting from the basic 304 alloy (Fe-19Cr-10Ni), molybdenum is added to improve resistance to pitting (2-3 wt.% in the case of type 316 and 3-4 wt.% in type 317). Sensitisation due to chrome depletion during welding and other heat treatments, and the possible resultant intergranular corrosion, can be avoided through the use of low-carbon grades (304L, 316L, 317L, in which carbon is limited to 0.03 wt.% max.) or by adding titanium (type 321) or niobium and tantalum (type 347) to precipitate carbon at higher temperatures. The addition of chromealso imparts greater oxidation resistance, whilst nickel improves the ductility and workability of the material at room temperature.

In this paper, general corrosion of austenitic stainless steels, specifically low-carbon types 317 L and 304 L, was investigated. The research results are presented in the form of Tafel polarization curves, expressed through corrosion current density and open circuit potential. The results prove that the rate of general corrosion of the tested austenitic stainless steels decreases by lowering the temperature of the HCl solution, decreasing the concentration of HCl, and the presence of molybdenum in the composition of steel type 317 L.

Keywords: *austenitic stainless steels, general corrosion, 317 L, 304 L, Tafel polarization curves*

1. INTRODUCTION

Stainless steels usually excellent resistance to corrosion is down to an ultrathin layer of oxides of especially chromium and iron, and although this film is only a few nanometres thick, it is still so dense and strong that the steel is effectively 'isolated' from the surrounding environment - similarly to an ultrathin paint. If, despite all precautions, a hole occurs in the protective oxide layer, it quickly restores itself, and the steel is again protected. This mechanism is called repassivation [1]. Austenitic stainless steels are among the most widely used types of stainless steel. The most commonly used grades are the American Iron and Steel Institute (AISI) 300 series of alloys. Starting from the basic 304 alloy (Fe-19Cr-10Ni),molybdenum is added to improve resistance to pitting (2-3 wt.% in

the case of type 316 and 3-4 wt.% in type 317). Sensitisation due to chrome depletion during welding and other heat treatments, and the possible resultant intergranular corrosion, can be avoided through the use of low-carbon grades (304L, 316L, 317L, in which carbon is limited to 0.03 wt.% max.) or by adding titanium (type 321) or niobium and tantalum (type 347) to precipitate carbon at higher temperatures. The addition of chrome also imparts greater oxidation resistance, whilst nickel improves the ductility and workability of the material at room temperature[2, 3].

In this paper, general corrosion of austenitic stainless steels, specifically low-carbon types 317 L and 304 L, will be investigated. The high corrosion resistance of stainless steel is attributed to the formation of a protective passive film on its surface. Many scholars have studied the characteristics of passive film. By direct imaging of native passive film on 304 stainless steel, Hamada demonstrated the enrichment of chromium in the film and the enrichment of nickel in the matrix side closest to the passive film/matrix interface [4]. Stainless steel

*Corresponding author: Farzet Bikić
E-mail: farzet.bikic@unze.ba

has important characteristics such as versatility, durability, attractiveness and high mechanical and corrosion resistance [5].General corrosion is also called acid corrosion as it is a type of corrosion that in stainless steel is often found in very acidic, but also in very alkaline media. As opposed to the four other types of stainless steel corrosion, general corrosion is characterised by both anode and cathode reactions taking place all over the surface. This means that the whole surface is activated and thereby corrodes more or less uniformly [1]. In non-passivating metals and alloys, general corrosion is the most common type of corrosion, but for passivatable alloys it is relatively rare. Even in strong acids, stainless steel can achieve a certain level of passivity, and in practice there is a big difference between an acid that simply thins the

passive layer, but does not entirely dissolve it, and an acid that eats away the whole of the passive layer and immediately attacks the underlying steel. Relatively weak and pure acids (e.g. citric acid, acetic acid or formic acid) only thin the naturally occurring oxide layer slightly. The oxide layer is restored with the same speed, and corrosion loss is minimal - at least when the acids are pure. If the acids contain aggressive ions (especially chloride), the situation may become far worse, especially at high temperatures [1].

2. EXPERIMENTAL PART

AISI/ASTM 304 L and 317L steels were used for general corrosion testing of austenitic stainless steels. The chemical compositions of the mentioned steels are given in table 1.

Table 1. Chemical composition of tested austenitic stainless steels

AISI/ ASTM	Mas. %								
	C	Si	Mn	P_{max}	S	N	Cr	Mo	Ni
317L	$\leq 0,03$	$\leq 1,00$	$\leq 2,00$	0,045	$\leq 0,015$	$\leq 0,11$	17,5-19,5	3-4	13-16
304L	$\leq 0,03$	$\leq 1,00$	$\leq 2,00$	0,045	$\leq 0,015$	$\leq 0,11$	18 -20	-	10-12

The test of general corrosion of austenitic stainless steels was carried at temperatures of 20 ±1 °C, 30 ±1 °C and 40 ±1 °C, in 0.5% HCl and 1% HCl solutions. The Taffel extrapolation method was used to examine general corrosion of 317 L and 304 L austenitic stainless steels. The Taffel extrapolation method involves scanning the potential of the working electrode of ±250 mV in relation to its open circuit potential $E_{(I=0)}$, at a speed of 0.5 mVs^{-1}. Investigation of corrosion was conducted in a corrosion cell according to the Standard ASTM G5-94 [6], on a potentiostat/galvanostat instrument Princeton Applied Research, model 263A-2, with

PowerCORR® software, which is part of the Power Suite softwere package.

3. RESULTS AND DISCUSSION

The results of testing the general corrosion rate of selected austenitic stainless steels, using the Taffel extrapolation method, are shown in tables 2 and 3, but also in figures 1-8.

Table 2 but alsoFigures 1 and 2 show the influence of the concentration of HCl solution on the rate of general corrosion of austenitic stainless steel types 304 L 317 L.

Table 2. Corrosion rate of tested austeniticstainless steels in 0.5% and 1% HCl

AISI/ ASTM	t = 30 ±1 °C, 0,5 % HCl		t = 30 ±1 °C, 1 % HCl	
	$E_{(I=0)}$, mV	i_{cor}, µAcm^{-2} (mmpy)	$E_{(I=0)}$, mV	i_{cor}, µA cm^{-2}(mmpy)
304L	10,823	7,79(9,06·10^{-2})	-334,42	6,71·10^{1}(7,79·10^{-1})
317L	-22,314	5,907(6,86·10^{-2})	-312,90	3,854·10^{1}(4,48·10^{-1})

With an increase in the concentration of the HCl solution, there is an increase in the rate of general corrosion for both types of stainless steels, 304 L and 317 L. With an increase in the concentration of the HCl solution, there is an increase in the value of the corrosion current density $i_{cor}$for both types of stainless steels, Table 2 but also Figures 1 and 2. With an increase in the concentration of the HCl solution, the open circuit potential $E_{(I=0)}$ shifts to more negative values for

both types of stainless steels, Table 2 but also Figures 1 and 2.

One of the most aggressive ions that cause general corrosion of stainless steels are chloride ions. Chlorides are able to remove the oxide of steel and then attack the steel itself. By adding chloride to an otherwise relatively harmless acid, you get diluted hydrochloric acid which will be far more corrosive to the steel than the pure, chloride-free acid [1].
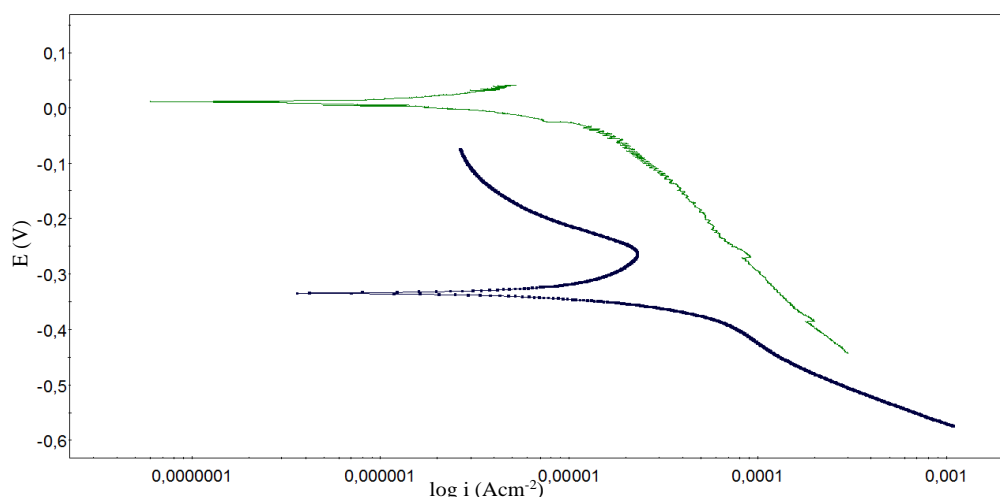
Figure 1. Tafel curves of samples ASTM 304 L (t =30 °C, ---- 1% HCl, ---- 0,5% HCl)
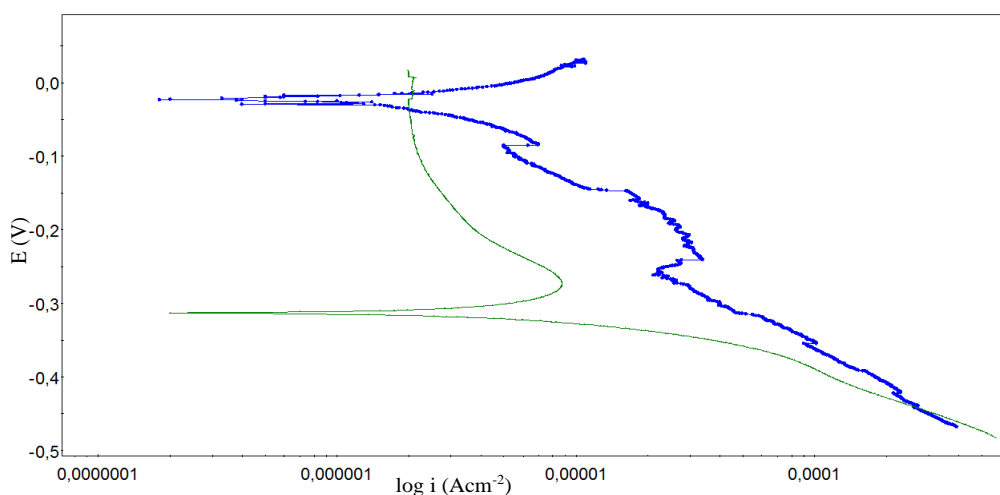
Figure 2. Tafel curves of samples ASTM 317 L (t =30 °C, ---- 1% HCl, ----0,5% HCl)

Table 3 but also Figures 3 and 4 show the influence of temperature on the rate of general corrosion of austenitic stainless steel types 304 L and 317 L.

Table 3. Corrosion rate of tested austeniticstainless steels in 0.5% HCl solution

AISI/ ASTM	t = 20 ±1 °C		t = 30 ±1 °C		t = 40 ±1°C	
	$E_{(I=0)}$, mV	i_{cor}, µAcm^{-2} (mmpy)	$E_{(I=0)}$, mV	i_{cor}, µAcm^{-2} (mmpy)	$E_{(I=0)}$, mV	i_{cor}, µAcm^{-2} (mmpy)
304L	61,07	2,33(2,71·10^{-2})	10,823	7,79(9,06·10^{-2})	-146,71	35,4(4,11·10^{-1})
317L	72,05	5,57(6,47·10^{-2})	-22,314	5,91 (6,86·10^{-2})	-55,413	9,24 (1,07·10^{-1})

With increasing temperature of the HCl solutionthere is an increase in the rate of general corrosion for both types of stainless steels 304 L and 317 L.With increasing temperature of the HCl solution, there is an increase in the value of the corrosion current density i$_{cor}$for both types of stainless steels, Table 3but also Figures 3 and 4. With increasing temperature of the HCl solution, the open circuit potential E$_{(I=0)}$ shifts to more negative values for both types of stainless steels, Table 3 but also Figures 3 and 4. Temperature has an important effect on the corrosion of stainless steels. A rise in temperature will generally lead to a decrease in the corrosion resistance [7].Escrivà suggested that the passive films formed at high temperatures should be more defective[8]. This was beneficial for the mitigation of aggressive ions inside the passive film and consequently could accelerate the dissolution process and the exchange kinetics between the electrode surface and the electrolyte [9]. BenSalah found that higher temperatures tended to promote the for mation of a porous film, thus leading to a decrease in the corrosion resistance[10].
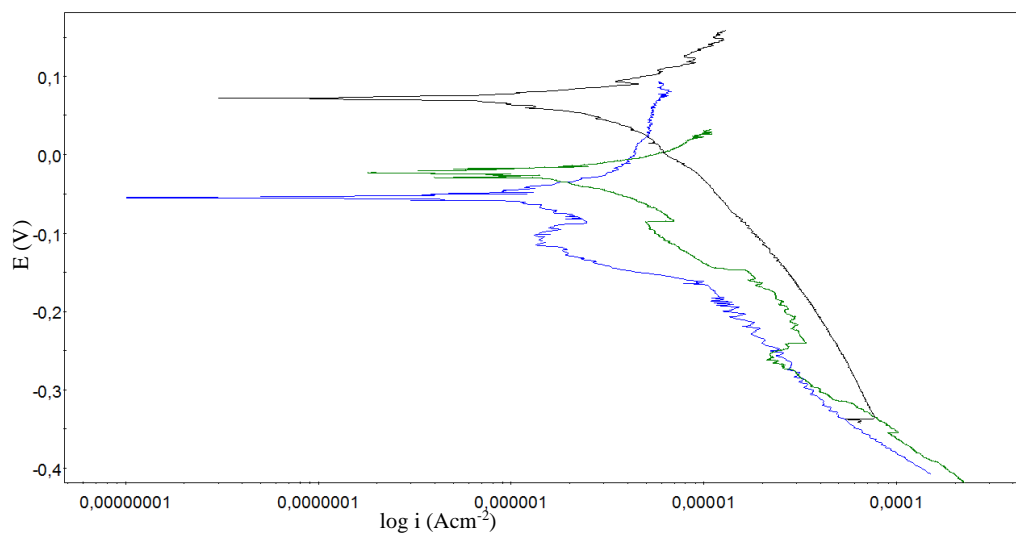
Figure 3. Tafel curves of samples ASTM 317 L tested in 0.5% HCl(---- 40℃, ---- 30 ℃, ---- 20 ℃)
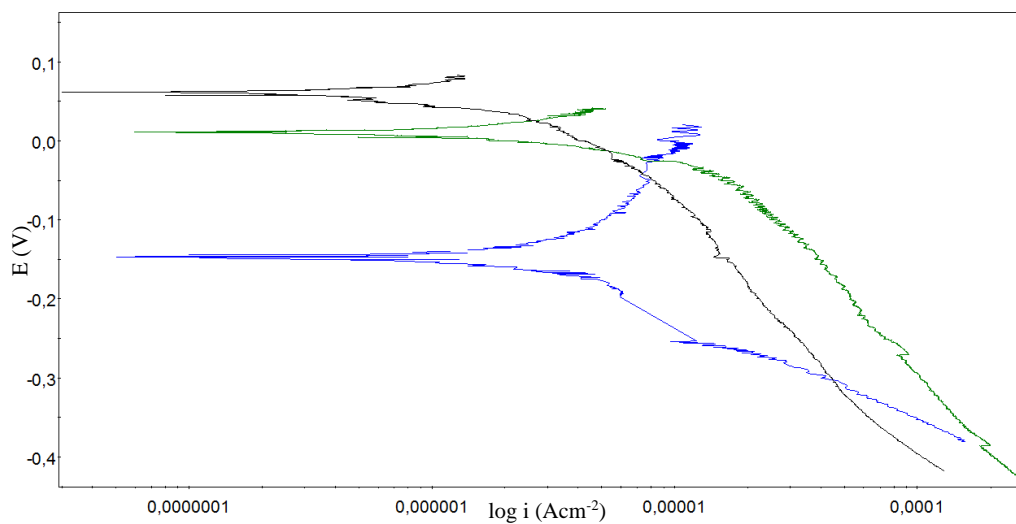
Figure 4. Tafel curves of samples ASTM 304 L tested in 0.5% HCl solution (---- 40℃, ----30 ℃, ---- 20 ℃)
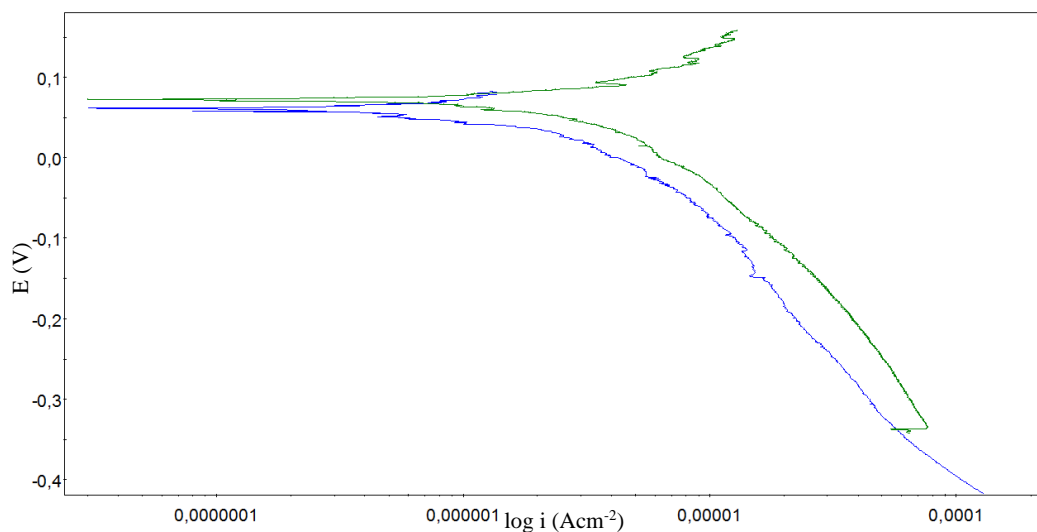
Figure 5. Tafel curves of samples tested in 0.5% HCl solution at 20 ℃ (--- 304 L, ----317 L)

Tables 2 and 3 but also Figures 5, 6, 7 and 8show the influence of chemical composition on the rate of general corrosion of austenitic stainless steel types 304 L and 317 L.
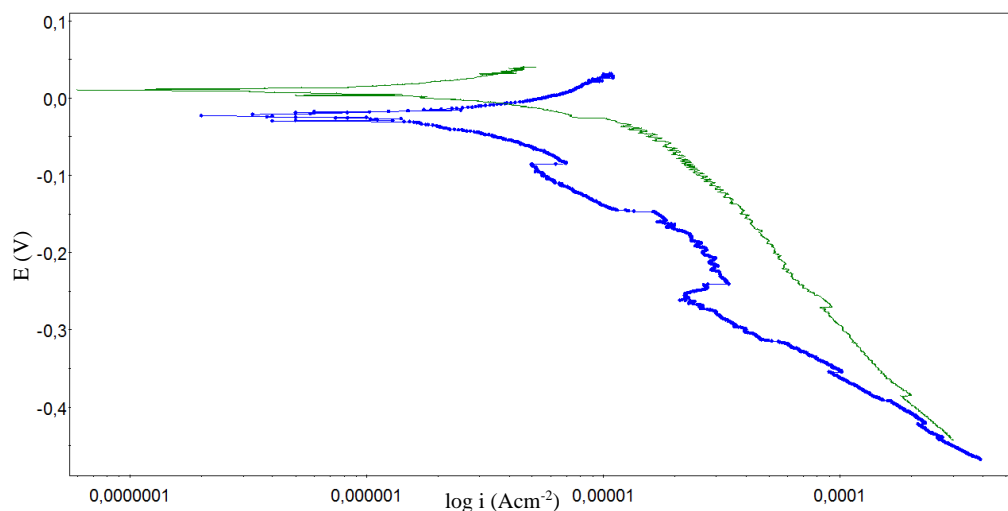
Figure 6. Tafel curves of samples tested in 0.5% HCl solution at 30 °C (---- 317 L, ---- 304 L)
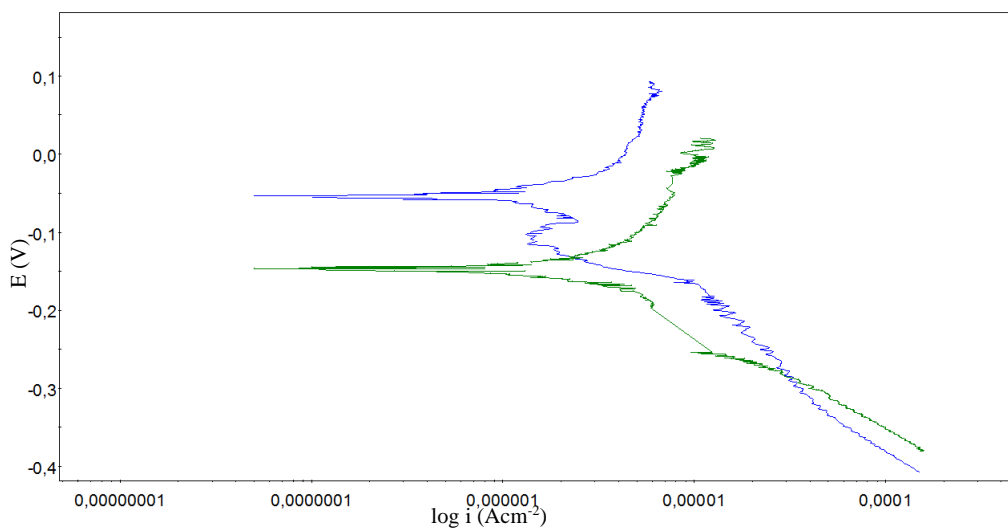
Figure 7. Tafel curves of samples tested in 0.5% HCl solution at 40 °C (---- 317 L, ---- 304 L)
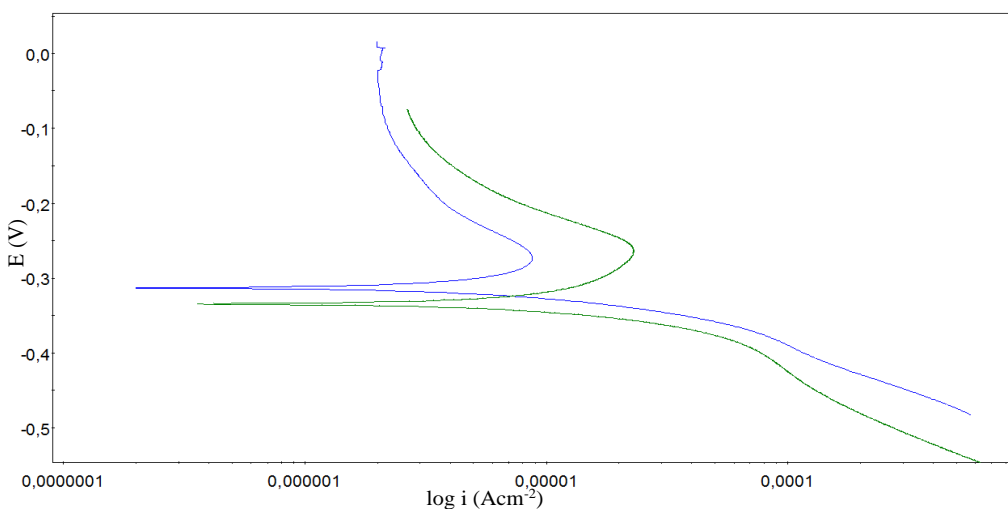
Figure 8. Tafel curves of samples tested in 1 % HCl at 30 °C (---- 317 L, ---- 304 L)

The results shown in Tables 2 and 3 but also Figures 5, 6, 7 and 8 almost undoubtedly show a higher general corrosion resistance of stainless steel type 317 L compared to stainless steel type 304 L.Samples of stainless steel type 317 L at all tested temperatures, 20 °C, 30 °C and 40 °C, as well as in both tested HCl solutions, 0.5% HCl and 1% HCl, show lower values of corrosion current density $i_{cor}$and more positive values of open circuit potential $E_{(I=0)}$ in relation to stainless steel samples of type 304 L.The only exception is the more positive value of the open circuit potential $E_{(I=0)}$ of the stainless steel sample of type 304 L compared to the sample of stainless steel of type 317 L testing of general corrosion of the mentioned stainless steels at temperature 30 °C in 0.5% HCl solution, Table 3 and Figure 7.

The reason for the increase in corrosion resistance of 317 L stainless steel compared to 304 L stainless steel, looking at their chemical composition, should be the content of molybdenum in 317 L stainless steel, because the main difference between them is the absence of molybdenum in 304L.Generally, the addition of molybdenum increases corrosion resistance of wrought austenitic stainless steels [11].Addition Mo to austenitic stainless steels allows formation of a passive film consisted of a solid solution of Mo^{6+} in chromium oxyhydroxide network, which reduces the corrosion current density in the active region for acidic solution [12].

The beneficial effects of molybdenum have been interpreted as follows: molybdenum eliminates the active surface sites through the formation of molybdenum oxy-hydroxide or molybdate on these site, on which it is difficult to form the stable passive film. This leads to the appearance of a homogeneous steel surface and to the formation of a homogeneous passive film [13].In the end, Pourbaix diagrams establish MoO_3 as the only compound formed in strongly acidic media [14].

4. CONCLUSION

Testing the influence of temperature of the HCl solution, HCl concentration and molybdenum content on the rate of general corrosion of austenitic stainless steels, it is concluded:

- With an increase in the concentration of the HCl solution, there is an increase in the rate of general corrosion for both types of stainless steels, 304 L and 317 L.
- With increasing temperature of the HCl solution there is an increase in the rate of general

corrosion for both types of stainless steels 304 L and 317 L.
- Higher general corrosion resistance of stainless steel type 317 L compared to stainless steel type 304 L. The reason for the increase in corrosion resistance of 317 L stainless steel compared to 304 L stainless steel, looking at their chemical composition, should be the content of molybdenum in 317 L stainless steel, because the main difference between them is the absence of molybdenum in 304 L. Generally the conclusion can be that the addition of molybdenum increases corrosion resistance of austenitic stainless steels.

5. REFERENCES

[1] C. Q. Jessen (2011) Stainless Steel and Corrosion, Damstahl a/s, Denmark.

[2] F. King (2009) Corrosion Resistance of Austenitic and Duplex Stainless Steels in Environments Related to UK Geological Disposal, Quintessa Limited, QRS-1384C-R1, Version 1.2, UK.

[3] F. Bikić, D. Mujagić(2014)Investigation of possibility for reducing AISI 303 stainless steel pitting corrosion by microalloying with boron or zirconium, Bulletin of the Chemists and Technologists of Bosnia and Herzegovina, 42, 41-46.

[4] E. Hamada, K. Yamada, M. Nagoshi, N. Makiishi, K. Sato, T. Ishii, K. Fukuda, S. Ishikawa, T. Ujiro (2010) Direct imaging of native passive film on stainless steel by aberration corrected STEM, Corros. Sci., 52, 3851–3854.

[5] E.Kikuti, R.Conrrado, N. Bocchi, S.R. Biaggio, R.C.Rocha-Filho (2004) Chemical and Electrochemical Coloration of Stainless Steel and Pitting Corrosion Resistance Studies, J. Braz. Chem. Soc., 15 (4), 472-480.

[6] ASTM G5 (1994) Standard Reference Test Method for Making Potentiostatic and Potenciodynamic Anodic Polarization Measurements.

[7] Z. Wang, Z. Feng, L. Zhang (2020) Effect of high temperature on the corrosion behavior and passive film composition of 316 L stainless steel in high H_2S-containing environments, Corrosion Science, 174, 108844.

[8] C. Escrivà-Cerdán, E. Blasco-Tamarit, D.M. García-García, J. García-Antón, A. Guenbour (2012) Passivation behaviour of Alloy 31 (UNSN08031) in polluted phosphoric acid at different temperatures, Corros. Sci., 56, 114–122.

[9] H. Iken, R. Basseguy, A. Guenbour, A.B. Bachir (2007) Classic and local analysis of corrosion behaviour of graphite and stainless steels in polluted phosphoric acid, Electrochim. Acta, 52, 2580–2587.

[10] M. BenSalah, R. Sabot, E. Triki, L. Dhouibi, P. Refait, M. Jeannin (2014) Passivity of Sanicro28 (UNS N-08028) stainless steel in polluted phosphoric acid at different temperatures studied by electrochemical impedance spectroscopy and Mott–Schottky analysis, Corros. Sci., 86, 61–70.

[11] A. Szewczyk-Nykiel (2015) The influence of molibdenum on corrosion resistance of sintered austenitic stainless steels, Tehnical Transactions Mechanics, 4-M (26), p. 131 – 142.

[12] K.Sugimoto, Y.Sawada (1977)The role of molybdenum additions to austenitic stainless steels in the inhibition of pitting in acid chloride solutions, Corrosion Science,17 (5), 425-445

[13] K.Hashimoto, K.Asami, K.Teramoto (1979)An X-ray photo-electron spectroscopic study on the role of molybdenum in increasing the corrosion resistance of ferritic stainless steels in HCl, Corrosion Science, 19(1), 3-14

[14] A.Pardo, M.C.Merino, A.E.Coy, F.Viejo, R.Arrabal, E.Matykina (2008)Effect of Mo and Mn additions on the corrosion behaviour of AISI 304 and 316 stainless steels in H_2SO_4, Corrosion ScienceVolume 50, Issue 3, March, p. 780-794.

IZVOD

ISPITIVANJE OPŠTE KOROZIJE AUSTENITNOG NERĐAJUĆEG ČELIKA TIPOVI 304 L I 317 L, POSEBNO SA ASPEKTA NJIHOVOG HEMIJSKOG SASTAVA

Austenitni nerđajući čelici su među najčešće korišćenim vrstama nerđajućeg čelika. Najčešće korišćene klase su legure serije 300 Američkog instituta za gvožđe i čelik (AISI). Počevši od osnovne legure 304 (Fe-19Cr-10Ni), dodaje se molibden radi poboljšanja otpornosti na piting (2-3 tež.% kod tipa 316 i 3-4 tež.% kod tipa 317). Preosetljivost usled trošenja hroma tokom zavarivanja i drugih toplotnih tretmana, kao i moguća rezultujuća intergranularna korozija, može se izbeći upotrebom niskougljeničnih razreda (304L, 316L, 317L, u kojima je ugljenik ograničen na 0,03 tež.% mak.) ili dodavanjem titanijuma (tip nital47bium) i hroma (tip nital47 i 321). taloži ugljenik na višim temperaturama. Dodatak hroma takođe daje veću otpornost na oksidaciju, dok nikl poboljšava duktilnost i obradivost materijala na sobnoj temperaturi.

U ovom radu je ispitivana opšta korozija austenitnih nerđajućih čelika, posebno niskougljeničnih tipova 317 L i 304 L. Rezultati istraživanja su predstavljeni u obliku Tafel polarizacionih krivulja, izraženih kroz gustinu struje korozije i potencijal otvorenog kola. Rezultati pokazuju da se brzina opšte korozije ispitivanih austenitnih nerđajućih čelika smanjuje snižavanjem temperature rastvora HCl, smanjenjem koncentracije HCl i prisustva molibdena u sastavu čelika tipa 317 L.

Ključne reči: *austenitni nerđajući čelici, opšta korozija, 317 L, 304 L, Tafelove polarizacione krive*

Farzet Bikić: https://orcid.org/0009-0002-9797-8883
Dejana Kasapović: https://orcid.org/0009-0003-2066-6053

Mohamed F. Atia[1], KamalShalabi[2], Mohamed A. Ismail[2], Magdy. Abd El-Khalek[2], Abd El-Aziz S. Fouda[2]*

[1]*Institute of aviation engineering and technology, Cairo, Egypt*
[2]*Department of Chemistry, Faculty of Science, Mansoura University, Mansoura 35516, Egypt*

Contribution to the corrosion inhibition of carbon steel by 5-(2-ethoxybenzylidene) 1,3-dimethylbarbituric acid in HCl solution: Experimental and theoretical study

ABSTRACT

The inhibiting impact of ecofriendly 5-(2-ethoxybenzylidene) 1,3-dimethylbarbituric acid (5-EBMB) in 1 M HCl on the corrosion of C-steel has been examined via weight loss (WL) method, potentiodynamic polarization (PDP), electrochemical impedance spectroscopy (EIS), electrochemical frequency modulation (EFM) techniques". The obtained results demonstrate that the studied chemical is good 5-EBMB and that, in both PDP and EIS methods, its inhibition efficiency (%IE) increases with increasing concentration, reaching 82.5 at 21×10^{-6} M. Conversely, when the temperature rose, the percentage of IE reduced. "The adsorption of the investigated derivative on the surface of C-steel follows Langmuir isotherm. The adsorption process of the investigated compound is spontaneous and considered as chemisorption type". PDP curves revealed that the studied derivative is mixed-type inhibitor. Furthermore, the EIS results verified that the compound under investigation had adsorbed on the C-steel surface by raising the charge transfer resistance (R_{ct}) to 139.7 ohm cm^2 and decreasing the double layer (C_{dl}) capacitance from 102 to 69 $\mu F\ cm^{-2}$. The inhibitor adsorption on the C-steel surface was confirmed by surface examination using atomic force microscopy (AFM), energy dispersive X-ray (EDX), and scanning electron microscopy (SEM). Additionally, quantum chemistry and molecular dynamic simulation were used to extensively examine the mechanism of 5-EBMB's corrosion inhibition. All tested methods gave good agreement.

***Keywords**: Corrosion inhibition, HCl, C-steel, Arylidene barbituric acid derivative, Langmuir isotherm*

1. INTRODUCTION

Acidic media are generally applied for elimination of unwanted scale and corrosion in several industrial procedures. By monitoring metal dissolution attributable to acidic exposure, so 5-EBMBs are commonly applied within this operation [1]. "Organic 5-EBMBs today do the inhibition of corrosion well than the inorganic 5-EBMBs [2]. Organic compounds are kind of acidic 5-EBMBs including hetero atoms for example oxygen , sulfur, and nitrogen. Amongst, organic 5-EBMBs have several advantages for instance low cost, low poisonousness, high inhibition efficiency, and easy to organize" [3-6].

Generally, "heterocyclic organic compounds are applied to the corrosion inhibition on Cu [7] Al [8-10], Fe [11-16] and also other metals [17-18] within diverse corrosion media". "A review of the literature on acid corrosion 5-EBMBs reveal that they work by adsorbing to the metal's surface. This effect may be caused by (i) electrostatic attraction between the charged metal and the charged 5-EBMB molecules, (ii) dipole-type interaction between uncharged electron pairs in the 5-EBMB and the metal, (iii) electron-interaction with the metal, or (iv) A combination of the aforementioned" [19]. Pyrimidine is a six-membered heterocyclic aromatic compound with two nitrogen atoms at positions 1 and 3. The chemistry of pyrimidine derivatives is crucial in medicine, agrochemicals, and a variety of biological activities. "Many well-known commercial medications contain pyrimidine derivatives, such as Uramustine, Piritrexim, Isetionate, Tegafur, Floxuridine, Fluorouracil, Cytarabine, and Methotrexate. Furthermore, the pyrimidine skeleton is found in a wide range of natural products, including nucleic acids, vitamins,

*Corresponding author: A.S. Fouda
E-mail: asfouda@mans.edu.eg

enzymes, chlorophyll, hemoglobin, and hormones". Ansari el al [20] "investigates the corrosion protection of mild steel by four PPDs in 1 M HCl solution and they found the percentage inhibition efficacy 88-97.1% at 400 mg L^{-1}. Numerous pyrimidine derivatives have been synthesized and studied their suitability for corrosion inhibition of variety of steel samples in acidic medium" [21-27]. "The efficacy of the organic compounds including hetero atoms as corrosion 5-EBMBs in acidic solutions for C-steels is well recognized" [28-32]. "Pyrimidines and their derivatives are important because they are available in nature, particularly in the nucleobases present in nucleic acids, and many of them have been discovered to be beneficial in chemotherapy" [33]. "Currently in use as anticancer, antifungal, and antibacterial medicines are pyrimidine-containing chemotherapeutics" [34]. "Furthermore, in HCl and H_2SO_4 solutions, several pyrimidine derivatives were found to be efficient corrosion inhibitors for steel" [35]. Novel cationic and non-ionic biopolyurethanes for effective inhibition of mild steel corrosion in H_2S-CO_2 environment was studied by Banan, and Asadi [36], Haruna et al [37] reported the effect of acrylic acid modified indapamide-based polymer as an effective inhibitor against carbon steel corrosion in CO_2-saturated NaCl with variable H_2S levels. Bairagi et al [38] studied the effect of polymers and their composites for corrosion inhibition application

The purpose of this work is to study the impact of 5-(2-ethoxybenzylidene)-1,3-dimethylbarbituric (5-EBMB) acid as ecofriendly inhibitor for C-steel in 1 M hydrochloric acid solution by applying WL, PDP, EIS, EFM tests. The investigated 5-EBMB is not reported as a corrosion inhibitor for steel in the literatures before".
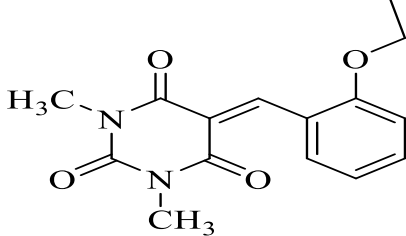
2. MATERIALS AND METHODS

"Chemical composition of C-steel coupons in weight percentage is: carbon (0.200); manganese (0.350); phosphorus (0.024); chromium; sulfur (0.003); and balance Fe".

"5-(2-Ethoxybenzylidene)-1,3-imethylbarbituric acid (5-EBMB) was prepared as outlined in scheme 1. The detailed information of 5-EBMB is reported in the literature" [39, 40] with identical melting point of 165-166°C. 5-EBMB: Adopting the same methodology used for preparation before [40], starting with 2-ethoxybenzaldehyde instead of 4-methoxybenzaldehyde. "Yield 85%, mp 165–166 °C. IR (KBr) v' 3114, 3095, 2987, 2950, 2900 (CH), 1730, 1670 (CO), 1577, 1541 (C=C) cm^{-1}." ^{1}H NMR (CDCl$_3$); δ 1.37 (t, J = 7.2 Hz, 3H), 3.28 (s, 3H), 3.35 (s, 3H), 4.07 (q, J = 7.2 Hz, 2H), 6.84 (d, J = 8.4 Hz, 1H), 6.92 (t, J = 7.2 Hz, 1H), 7.39 (t, J = 7.2 Hz, 1H), 7.98 (d, J = 8.4 Hz, 1H), 8.85 (s,

1H)". "MS (EI) m/e (rel.int.); 288 (M$^+$, 24), 243 (100).Anal. Calc. for $C_{15}H_{16}N_2O_4$ (288.30): C, 62.49; H, 5.59; N, 9.72. Found. C, 62.21; H, 5.73; N, 9.48"

Table 1. Chemical structures of tested 5-EBMB inhibitor

Molecular structures/Chemical name

5-(2-Ethoxybenzylidene)-1,3-dimethylbarbituric acid (5-EBMB)

| Chemical Formula $C_{15}H_{16}N_2O_4$, Molecular Weight 288.3 |

The aggressive solutions used were prepared from analytical grade HCl. A 1M HCl solution was prepared using bidistilled water, both with and without different concentrations of inhibitor. All experiments were conducted in stagnant, aerated solutions.

2.1. WL method

"Samples used in weight loss measurements were coupons measuring 2 cm x 2 cm x 0.2 cm. Before starting any experiment, specimens were prepared by abrading them successively with emery paper (grades 100–1200), followed by thorough washing with bidistilled water, degreasing with acetone, and drying in a stream of air. The weight loss method involved the following steps: Each coupon was weighed using an analytical balance and recorded as weight W1. The coupon was then suspended in a 100 mL beaker using a glass hook. A 100 mL of 1 M HCl was introduced into reaction beakers. Each coupon was extracted from the test medium at intervals of 3 hours. The corroded coupons were rinsed with bidistilled water and dried using acetone. The coupons were then reweighed, and the final weights, W_2, were recorded. Weight losses, $\Delta W = W_1 - W_2$, were calculated. The inhibition efficiency % IE and surface coverage θ were determined using the following equations:

$$\theta = W_0 - W_i W_0 \qquad (1)$$

$$\% IE = W_0 - W_i W_0 \times 100 \qquad (2)$$

"Where w_i and w_0 are the weight loss values in the presence and absence of the inhibitor, respectively. The experiment was repeated using various concentrations of (5-EBMB) in the 1 M HCl

medium, varying the time between 50 and 180 minutes and the temperature between 25 and 45 °C for a duration of 3 hours. The corrosion rate (k_{corr}) is expressed as an increase in corrosion depth per unit time in (mg cm^{-2} h^{-1}). The corrosion rate equation is given as:"

$$k_{corr}=\Delta W/At \qquad (3)$$

where: ΔW = weight loss of coupon, t = immersion time, and A = area of coupon

2.3. Electrochemical techniques

Electrochemical measurements are taken within traditional three electrodes glass cell include saturated calomel electrode (SCE) linked with fine "Luggin capillary, platinum counter electrode and working electrode is carbon steel with a square cut shape and surface area of 1.0×1.0 cm^2. PDP curves are established through altering the electrode potential automatically from -500 to +500 mV vs. OCP with a sweep rate of 0.2 mVs^{-1}. Stern-Geary method [43] applied the definition of corrosion current is achieved via deducing on cathodic and anodic Tafel lines to a point which provides log i_{corr} and the resulting E_{corr} for 5-EBMB free acid and to any concentration of 5-EBMB". Thereafter i_{corr} can be applied to examine of θ and IE % as subsequent:

$$IE\% = \theta \times 100 = \left[1 - \frac{i_{corr}}{i_{corr(inh)}}\right] \times 100 \qquad (4)$$

Where, "$i_{corr(free)}$ and $i_{corr(inh)}$ are the corrosion current densities at the absence and existence of 5-EBMB", separately.

EIS are applied within range of frequency from 100 kHz to 0.01 mHz and 10 mV amplitude peak-to-peak at OCP. The θ and the % IE achieved from the impedance calculation were assessed through the next equation:

$$IE\% = \theta \times 100 = \left[1 - \frac{R_{ct}^{\circ}}{R_{ct}}\right] \times 100 \qquad (5)$$

Where, "R°_{ct} and R_{ct} are the resistance of charge transfer at the absence and existence of 5-EBMB", separately.

EFM tests were accomplished via dual frequencies "2 and 5 Hz with base frequency 0.1 Hz, consequently the wave shape repeats subsequently at 1s. The large peaks located in the intermodulation spectra were utilized to assess the corrosion current density (i_{corr}), the Tafel slopes (β_a and β_c) and CF-2 & CF-3" [44, 45], the %IE and θ were assessed from Eq. (2).

All electrochemical experiments are ready solution at 25 ±1°C. The potential of electrode can be permitted until become stable 30 min prior to start the measurements. All electrochemical experiments were done at 25±1°C and accomplished via Gamry (PCI4/ 750G) Potentiostat/Galvanostat/ ZRA. This includes Gamry Framework for controlling and Echem Analyst5.58 software for data analysis and plotting.

3. RESULTS AND DISCUSSION

3.1. WL method

The WL-time diagrams for the corrosion of C-steel in 1 M hydrochloric solution before and after addition of diverse concentrations of 5-EBMB is displayed within Fig. 1. This Figure demonstrates that the values of WL for C-steel with 1M hydrochloric acid solution lies higher than in 5-EBMB and the WL decreases as 5-EBMB dose rises; It is meaning the strengthens of corrosion inhibition by increasing the 5-EBMB concentration as listed in Table 2. This explains the adsorption of 5-EBMB molecules on the C-steel surface, i.e., the C-steel surface is shielded from the aqueous media through creation of protecting film on this surface [46, 47].
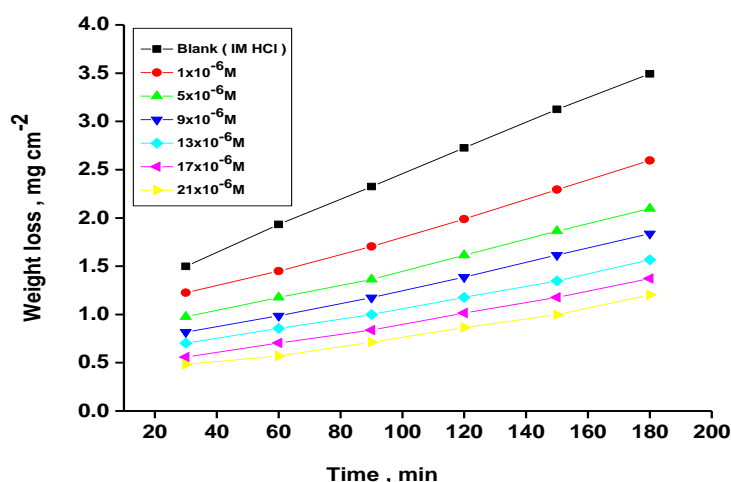
Figure 1. Time-WL bends for C-steel in 1M HCl in the absence and presence of diverse doses of 5-EBMB at 25 ºC

Conc. (M)	k_{corr} (mg cm^{-2} min^{-1})	% IE
Blank	0.028	---
1x10^{-6}	0.022	47.1
5x10^{-6}	0.017	55.8
9x10^{-6}	0.015	58.1
13x10^{-6}	0.013	62.7
17x10^{-6}	0.011	68.6
21x10^{-6}	0.009	74.7

3.2. PDP studies

Figure 2 illustrates the Tafel polarization diagrams for C-steel in 1 M hydrochloric acid in the absence and existence of 5-EBMB dose at 25oC, separately. From Fig.2, it is obvious that anodic metal dissolution and cathodic H2 reduction reactions were controlled when 5-EBMB was added to 1 M HCl solution also this inhibition was more obvious through raising the dose of the 5-EBMB. The computation of icorr is made possible by the extrapolation of Tafel straight lines. Table 3 lists the values of icorr, the corrosion potential Ecorr, θ, and the percentage of IE as well as the cathodic and anodic Tafel slopes (β_a, β_c). Table 3 illustrates that i$_{corr}$ declines via addition of the 5-EBMB and through raising its doses. Additionally, it is evident that, in the presence of different dosages of 5-EBMB in a 1 M HCl solution, there is no discernible trend in Ecorr values (15 mV). According to this finding, 5-EBMB in a 1 M HCl solution can be categorized as a mixed-type inhibitor [48, 49]. Furthermore, Tafel slopes [βa, βc] remain nearly constant, suggesting that the adsorption of 5-EBMB alters both the cathodic hydrogen evolution and anodic dissolution mechanisms. [50,51].
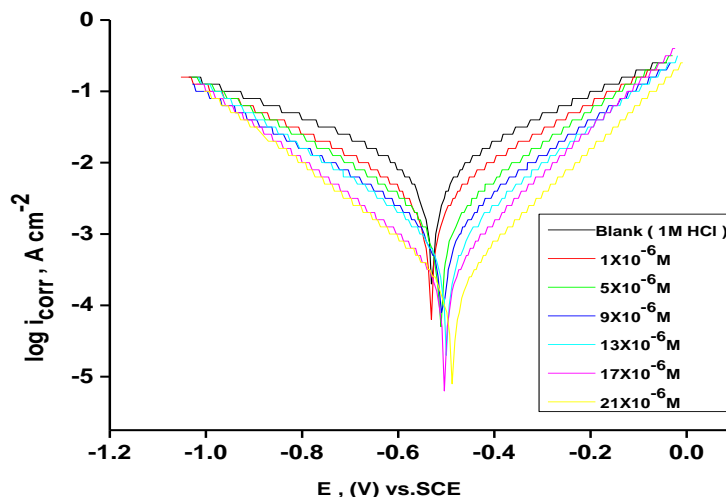
Figure 2. PDP diagrams for dissolution of C-steel in 1M HCl in the attendance and absence of altered doses of 5-EBMB at 25 ºC.

Table 3. Corrosion parameters of C-steel electrode in 1M HCl solution containing altered doses of 5-EBMB at 25℃ from PP technique

Conc., x10^6 M	-E$_{corr}$ (mV , vs. SCE)	i$_{corr}$ (mA cm^{-2})	- β_c mV dec^{-1}	β_a mV dec^{-1}	θ	%IE	k$_{corr}$ mmy^{-1}
1 M HCl	587	422	42	22	---	---	220.6
1x10^{-6}	585	369	37	36	0.378	37.8	186.5
5x10^{-6}	584	263	61	42	0476	47.6	120.1
9x10^{-6}	583	206	71	51	0.579	57.9	94.3
13x10^{-6}	580	160	80	58	0.685	68.5	73.3
17x10^{-6}	573	123	64	46	0.757	75.7	56.2
21x10^{-6}	572	96.8	122	82	0.825	82.5	44.2

3.3. EIS studies

Utilizing the EIS approach, the electrode/ electrolyte interface and the corrosion processes on the C-steel surface were examined in both the presence and absence of 5-EBMB. EIS measurements in a broad frequency range at 25 °C

were conducted at OCP to guarantee thorough characterization of the interface and surface processes. The impact of the doses of 5-EBMB on the impedance of C-steel in 1M HCl at 25 ºC is produced in Nyquist and Bode plots as shown in Fig. 3 a, b. Curves show identical kind of Nyquist bends for C-steel with existence of diverse doses of 5-EBMB. Presence of single semi-circle displayed the single charge transfer procedure through dissolution which is unaltered with the existence of 5-EBMB compound. Deviations from ideal circular form are frequently signalize to the frequency dispersal of impedance interfacial which occurs because of impurities, surface coarseness, grain limits, dislocations, forming of porous layers and adsorption of derivatives, also homogenized on the surface of electrode [52,53]. Observation of these data detected from all impedance graphs contains of large capacitive circle by only time constant of capacitive with Bode–phase graphs (Fig.3b). The electrical equivalent circuit is displayed in Fig. 4 and it applied for examine achieve impedance data.

This circuit involves R_{ct} (The corrosion rate is inversely related to the Rct value, which measures electron transmission over the surface) , C_{dl} also the solution resistance (R_s). Fit excellent through this model can be gained through experimental data. EIS outcomes in Table 4 distinguished that C_{dl} values declines as well as R_{ct} values rises by rising doses of 5-EBMB. It is because of the increasing in the thickness of the adsorbed layer and to the exchange of the adsorbed water molecules with the 5-EBMB molecules on the surface of metal, declining the metal dissolution reaction [54, 55].

The diminishing in C_{dl} can be caused by a drop in the local dielectric constant and/or a rise in the thickness of the double layer electrical suggested that 5-EBMB molecule function through adsorption at the metal and solution interface [56]. Using the chi-squared approach, the accuracy of the fitted

results was assessed; each result's minuscule chi-squared value (Table 4) shows that the fitted results and the experimental findings are in close agreement. The %IE gained from EIS studies are close to those inferred of PDP studies.

(a)

(b)
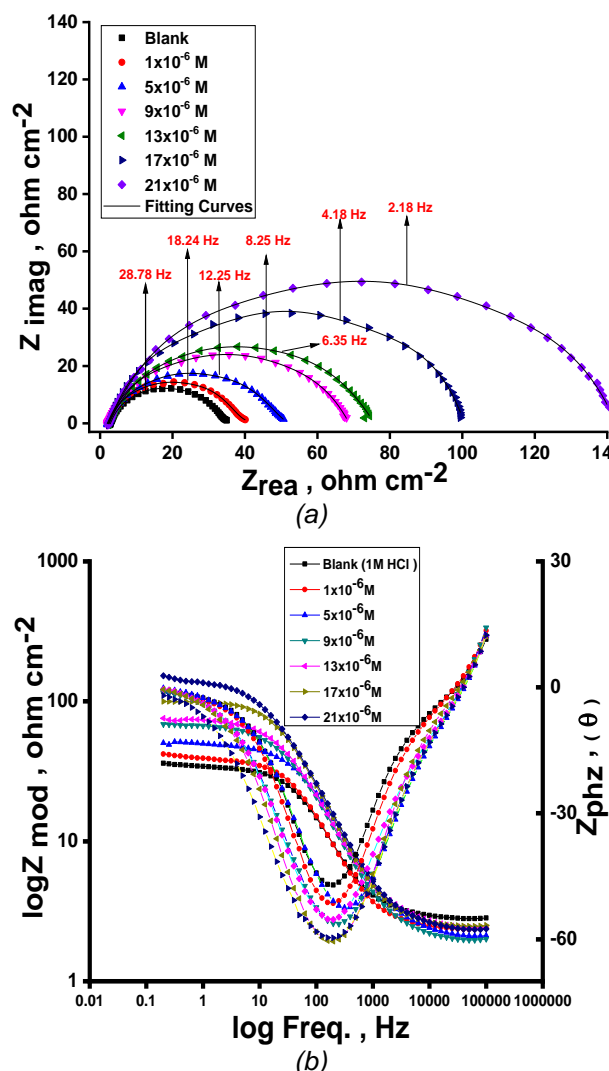
Figure 3. Nyquist plots (a) and Bode plots (b) for C-steel in 1M HCl at different concentrations of 5-EBMB at 30⁰C

Table 4. EIS data of C-steel in 1M HCl and in existence of altered doses of 5-EBMB at 25ºC

Conc., M	Yo, µΩ−1 sn cm⁻²	n	Cdl (µF cm⁻²)	Rct, (ohm cm²)	θ	%IE	Goodness of fit, (χ2)
1M HCl	129	0.995	117	31.7	---	---	17.24x10⁻³
1x10⁻⁶	118	0.989	102	37.5	0.147	14.7	13.25x10⁻³
5x10⁻⁵	103	0.984	92	47.8	0.339	33.9	14.15x10⁻³
9x10⁻⁵	97	0.981	86	66.1	0.521	52.1	12.54x10⁻³
13x10⁻⁶	88	0.976	79	72.5	0.563	56.3	16.47x10⁻³
17x10⁻⁶	86	0.968	77	97.7	0.676	67.6	17.87x10⁻³
21x10-6	74	0.961	69	139.7	0.773	77.3	12.53x10-3
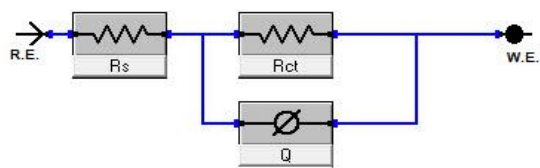
Figure 4. Electrical equivalent circuit model utilized to fit the results of impedance

3.4. EFM studies

EFM spectra intermodulation for C-steel in 1 M hydrochloric acid solution before and after adding 21x10⁻⁶M of 5-EBMB is displayed in Fig. 5. The bigger peaks were applied to examine i_{corr}, $β_c$, $β_a$, CF-2 and CF-3. Those electrochemical factors are concurrently specified then recorded in Table 5.

It can be viewed from this Table 5, the values of i_{corr} diminish with existence of various doses of 5-EBMB than with existence only of 1 M HCl in situation of C-steel. The obtained Causality factors for the examined data are in excellent quality with their theoretical (2 &3) values.
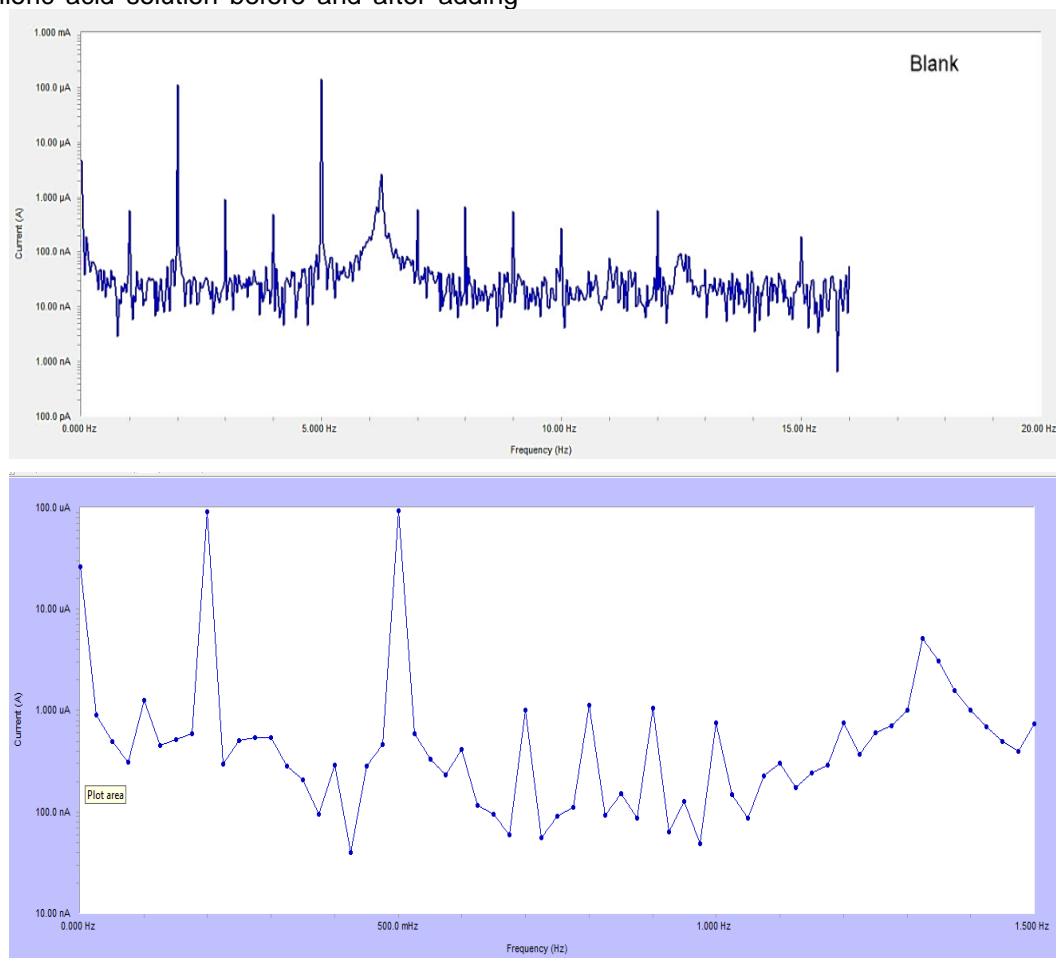
Figure 5. EFM spectra for C–steel in 1M HCl with and without 21x10⁻⁶ M of 5-ABA at 25ºC

Table 5. EFM parameters for C-steel 1M HCl solution and existence of altered doses of 5-EBMB at 25°C

Conc., (M)	i_{corr}, (µA cm⁻²)	$β_1$,(mVdec⁻¹)	$β_2$, (mVdec⁻¹)	CF-2	CF-3	k_{corr}, mmy⁻¹	% IE
1M HCl	808.5	113	164	2.09	1.75	370.2	---
1x10⁻⁶	599.9	99	137	2.04	3.23	274.1	25.8
5x10⁻⁶	453.9	101	126	1.95	3.09	207.4	43.9
9x10⁻⁶	374.5	112	118	2.05	3.08	172	53.7
13x10⁻⁶	272.7	97	101	1.73	2.61	124.6	66.3
17x10⁻⁶	233.1	92	118	1.97	2.57	106.5	71.2
21x10⁻⁶	152.6	105	111	1.49	1.83	69.7	81.1

3.5. Effectiveness of temperature

Temperature impact on the rate of corrosion of C-steel in 1 M HCl including diverse concentration of the investigated 5-EBMB can be examined via WL method at temperature ranges of 25 to 55°C

(Table 6). The Outcomes discovered that, by raising the temperature the rate of corrosion rises and decline with dose of the 5-EBMB rise for the investigated 5-EBMB.

Table 6. Data of WL measurements for C-steel in 1M HCl solution with and without altered doses of 5-EBMB at 25 – 55°C

Conc. (M)	Temp. (°C)	k_{corr} (mg cm^{-2} min^{-1})	θ	% IE
Blank (1 M HCl)	25	0.028	----	----
	35	0.033	----	----
	45	0.039	----	----
	55	0.045	----	----
1x10^{-6}	25	0.022	0.249	47.1
	35	0.026	0.196	19.6
	45	0.033	0.149	14.9
	55	0.038	0.137	13.7
5x10^{-6}	25	0.017	0.394	55.8
	35	0.022	0.314	31.4
	45	0.028	0.258	25.8
	55	0.033	0.242	24.2
9x10^{-6}	25	0.015	0.471	58.1
	35	0.019	0.405	40.5
	45	0.025	0.339	33.9
	55	0.030	0.315	31.5
13x10^{-6}	25	0.013	0.558	62.7
	35	0.017	0.475	47.5
	45	0.022	0.416	41.6
	55	0.026	0.403	40.3
17x10^{-6}	25	0.011	0.627	68.6
	35	0.014	0.554	55.4
	45	0.019	0.495	49.5
	55	0.023	0.479	47.9
21x10^{-6}	25	0.009	0.683	74.7
	35	0.012	0.627	62.7
	45	0.017	0.563	56.3
	55	0.020	0.555	55.5

The activation energy (E^*_a) can be examined by applying Arrhenius equation:

$$k = A\ e^{\dfrac{-E^*_a}{RT}} \qquad (6)$$

Where

A is Arrhenius constant and k is rate of corrosion. Straight lines are displayed in Fig. 6.and their linear regression (R²) is nearer to 1 and E^*_a can be obtained from the slope.

Table 6 displayed that the value of E^*_a for uninhibited solution is lower than inhibited solution, supposing that the dissolution of C-steel is slow

within existence of 5-EBMB [57]. This is recognized from Eq. 10 the higher values of E^*_a cause lower corrosion rate owing to construction of protecting film on the C-steel surface acting as an energy barrier of the C-steel corrosion [58-60]. Entropy and enthalpy of activation (ΔS*, ΔH*)" of the corrosion procedure were reckoned from the transition state theory:

$$k = \left[\dfrac{RT}{Nh}\right] e^{\dfrac{\Delta S^*}{R}}\ e^{\dfrac{-\Delta H^*}{RT}} \qquad (7)$$

Where

N Avogadro's number and h Planck's constant. The graphs of log k/T versus 1/ T of C-steel with 1

M hydrochloric acid solution at diverse doses from examined compound, provides straight lines as displayed in Fig.7 for 5-EBMB. The thermodynamic parameters are list in Table 6 shows that ΔH^* values are positive signalize that the steel dissolution process is endothermic process. High and negative values of ΔS^* assume that activated complex found in an association form more than dissociation form.
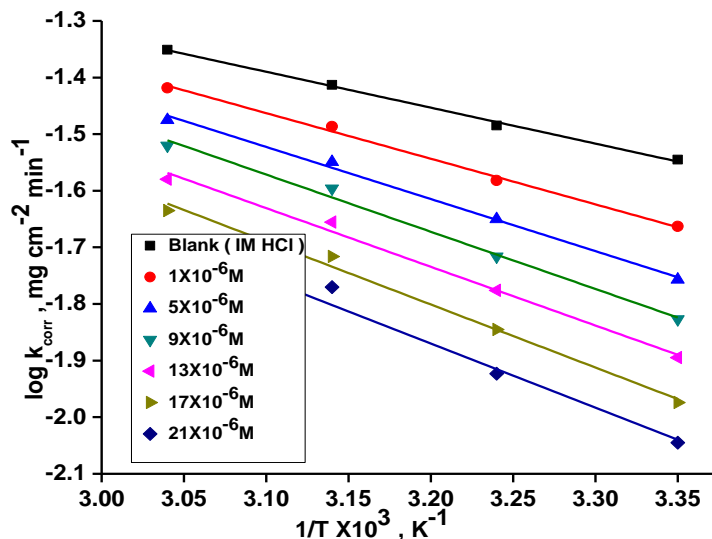
Figure 6. Log k_{corr} – 1/T curves for C-steel dissolution in 1.0 M HCl in the absence and existence of altered doses of 5-EBMB
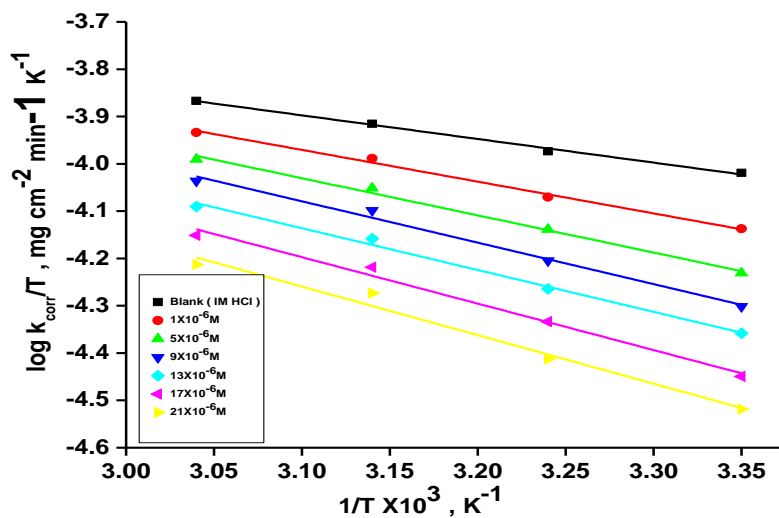
Figure 7. log k_{corr}/T – 1/T curves for C-steel dissolution in 1M HCl and existence of altered doses the investigated 5-EBM

Table 7. Activation parameters for dissolution of C-steel in the absence and existence of altered doses of 5-EBMB in 1M HCl

Activation parameters				
Conc. M	E_a^*, kJ mol^{-1}	ΔH^*, kJ mol^{-1}	ΔS^*,- J mol^{-1}K^{-1}	Regression Coefficient, (R^2)
Blank	12.2	9.6	108.6	0.9941
1x10^{-6}	15.4	12.8	99.8	0.9921
5x10^{-6}	17.6	15.1	94.1	0.9917
9x10^{-6}	19.3	16.8	89.7	0.9868
13x10^{-6}	19.9	16.9	90.3	0.9907
17x10^{-6}	21.3	18.8	85.7	0.9845
21x10^{-6}	21.7	19.6	84.2	0.9718

3.6. Adsorption Isotherm

Organic compounds are inhibited the metal corrosion through adsorption on surface of metal. The adsorption procedure is considered as single replacement process of adsorbed water molecules (x) by a single 5-EBMB molecule [61,62].

$$I_{(aq)} + xH_2O_{(sur)} \rightarrow I_{(sur)} + xH_2O_{(aq)} \qquad (8)$$
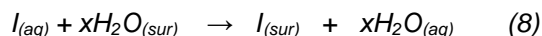
As well, the adsorption affords data about interaction between the adsorbed molecules and the surface of metal. The values of θ for diverse doses of the analyzed 5-EBMB at various temperatures have been applied to describe the most suitable adsorption isotherm to define adsorption procedure. Results of the studied derivative are suitable with Langmuir adsorption isotherm. **Fig 8** displays the plotting of C/θ versus C at 25°C to examine 5-EBMB, separately. Those schemes provided straight lines with unit slope signalized that adsorption of 5-EBMB on C-steel surface confirmed Langmuir equation [63].

$$\frac{C}{\theta} = \frac{1}{K_{ads}} + C \qquad (9)$$

where, "C is the 5-EBMB concentration and K_{ads} is adsorption equilibrium constant" associated to the free energy of adsorption ΔG_{ads} as appear [64]:

$$K_{ads} = \frac{1}{55.5} e^{\frac{-\Delta G^{\circ}_{ads}}{RT}} \qquad (10)$$

where, "T is the absolute temperature R is the universal gas constant and 55.5 is the concentration of water on the metal surface in M". The K_{ads} and ΔG°_{ads} values of 5-EBMB are 2,.08 x 10-5 M-1 and 40.3 kJ mol-1, respectively. The increase in the negative value of ΔG°_{ads} indicates that the 5-ABA was strongly adsorbed onto the C-steel surface in a stable state and that the adsorption process was spontaneous. From this data the adsorption of 5-EBMB on C-steel on C-steel surface is mixed type i.e., physisorption and chemisorption, but mainly physisorption because the E^{*}_a values increases in presence of 5-EBMB than in its absence and % inhibition decreases by raising temperature [65].
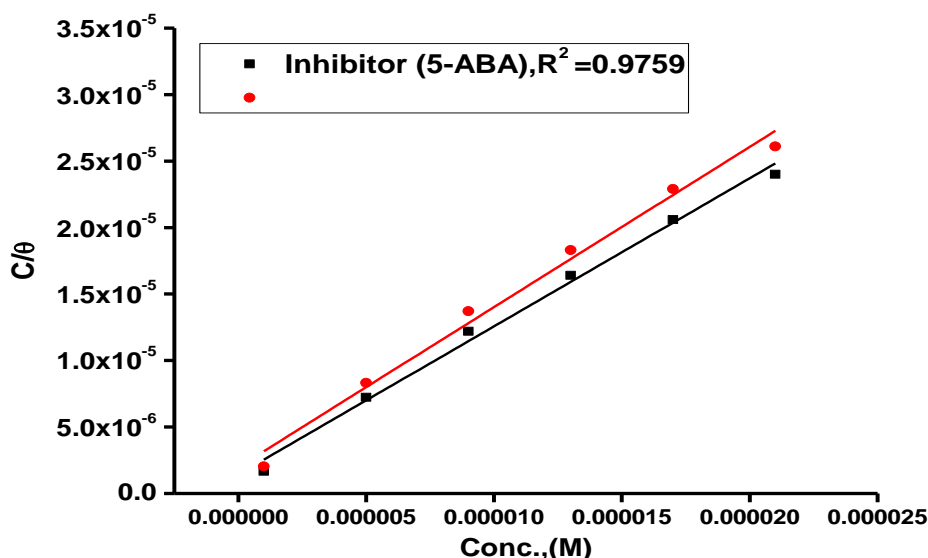
Figure 8. Langmuir isotherm plots for C-steel in 1 M HCl containing various doses of 5-EBMB at 25 °C

3.7. Surface Examination

3.7.1. SEM & EDX analysis

Figure (9a,b) describes the C-steel samples in 1M HCl acid in the lack and existence of 21×10-6 M 5-EBMB. The SEM image after C-steel exposure to 1 M HCl for 24 h, was severely scratched and destroyed (Fig. (9a) whereas, after adding the optimum dose of 5-EBMB the surface turns smoother and free slightly from corrosion product this presumed the protection action of inhibitor via restraining the active centers of the C-steel

surface. Fig. (9 c, d) implies the EDX analysis and the percentage of atomic content of blank and inhibited pieces, respectively. The strong Fe signal (Fig. 9d) implied a Fe-rich pristine C-steel surface. However, untreated C-steel surface exposed to 1M HCl as a corrosive medium exhibited O, Cl, and Fe signals (Table Fig. 9a). This might be related to strong corrosion and/or formation of iron chloride and/or iron oxide layers on the CS surface. As revealed in (Fig. 9c, d) the EDX spectrums of 5-EBMB display additional signals due to the occurrence of N and O.

(a) Blank   *(b) Compound 5-EBMB*

(c) Blank

(d) Compound 5-EBMB
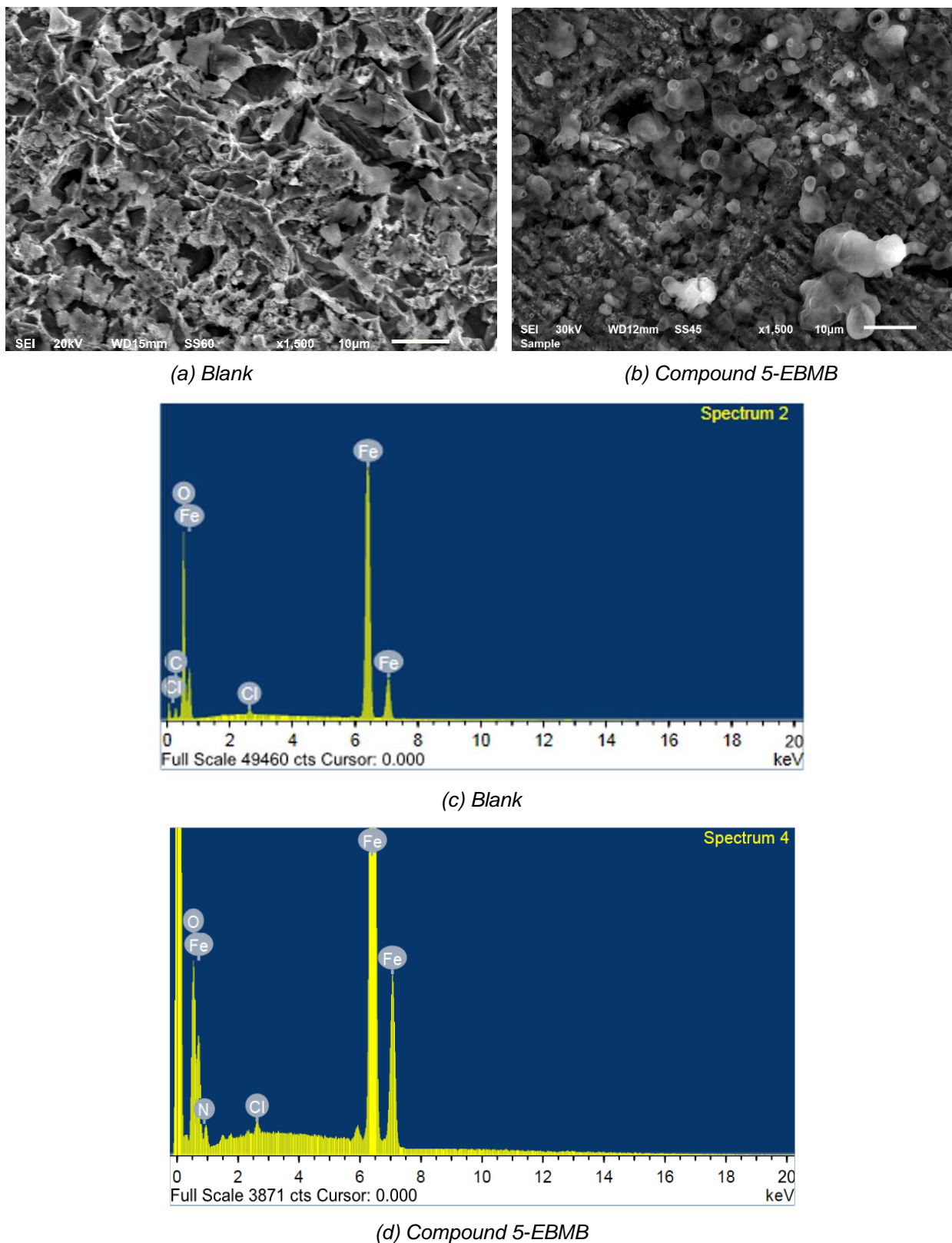
Figure 9. SEM images and EDX spectra of the C-steel surface before and after immersion in 1 M HCl in the lack and existence of 21×10⁻⁶M for 5-EBMB 24 h at 25°C

The occurrence of N and O elements in the EDX models of inhibited surface determines the inhibitor molecule is adsorbed on the C-steel interface and inhibiting from corrosion (Table 8).

Table 8. Atomic content percentage of the C-steel surface prior and after submersion in 1 M HCl in the lack and existence of 21×10⁻⁶M of 5-EBMB for 24 h at 25°C

Atomic content %	Fe	C	Cl	O	N
Free	92.16	7.84	--	--	--
Blank	63.05	11.69	2.35	22.91	--
5-EBMB	70.21	11.33	2.19	15.95	0.32

3.7.2. AFM analysis

AFM is one the most powerful method which used to detect the effect of 5-EBMB on CS surface by studying the morphology of the surface. CS surface was prepared before starting this examination by polishing its surface and immersion of CS pieces in HCl solution for 24 hrs in existence and nonexistence of 21×10⁻⁶ M of 5-EBMB **[42].** Topographic maps of CS surface are represented in Fig. 10 where 2D and 3D images were appeared. R_q (square roughness) and Ra (average roughness). R_a has a small value in presence of 5-EBMB (115.2 nm) and its value is high in case of C-steel in HCl only (161.8 nm). R_q is 179.5 nm, 150.6 nm without and with 5-EBMB, respectively.

3.8. Theoretical calculations

3.8.1. DFT studies

In the aqueous phase, the optimal structure, HOMO, and LUMO distribution of 5-EBMB molecules are revealed in Fig. 10, and the quantum chemical characteristics are included in Table 9.

| Optimized Structure | HOMO | LUMO |

(a) Blank   *(b) 5-EBMB*
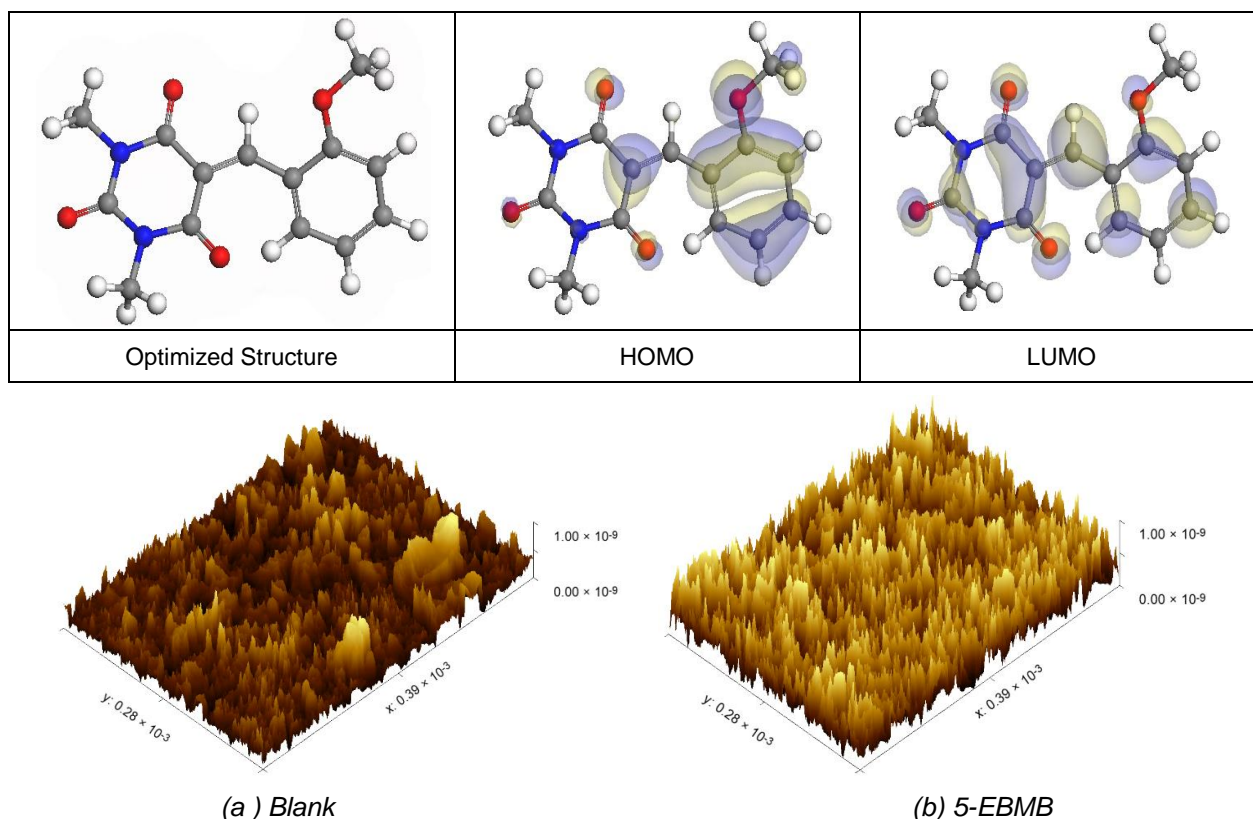
Figure 10. The optimized molecular structures, HOMO and LUMO for the utilizing DFT caculations in the aqeous phase for 5-EBMB inhibitor

Fig. 10 represents the energy diagram of the Frontier molecular orbitals for the investigated compound and its assessed ΔE. The interaction between the inhibitor molecule and the metal is directed by HOMO and LUMO energies, according to the Frontier orbital theory [66[. Where E_{HOMO} signifies the capability of a molecule to contribute electrons and E_{LUMO} signifies the capacity of a molecule to receive electrons [67]. As a result, the corrosion inhibition capability of an inhibitor molecule with high E_{HOMO} and low E_{LUMO} values improves. Similarly, high corrosion protection efficiency was proposed for an inhibitor molecule with a low energy gap between LUMO and HOMO energy (ΔE) since proffering an electron from E_{HOMO} to E_{LUMO}. According to Table 9, 5-EBMB has larger E_{HOMO} value of -5.47 eV. As exposed in Fig. 10, for the 5-EBMB molecules, we notice that the

HOMO level is identified on the phenyl, methoxy and pyrimidine moieties, implying that the O and N atoms are the desired location for electrophilic attacks on the surface of C-steel. This would enhance the adsorption capability of 5-EBMB molecules on the C-steel surface and therefore enhance the protection efficiency, which is in an excellent concurring with the empirical results. Moreover, the E_{LUMO} values are -5.47 eV for 5-EBMB (Table 9) indicating the great inhibition efficacy for 5-EBMB. Similarly, the energy gap (ΔE) is another critical aspect in approving the inhibitor molecule's corrosion prevention capability, which improves as the (ΔE) value decreases [68]. 5-EBMB exhibits lower (ΔE) values (2.66 eV), as shown in Table 9, indicating a higher propensity for 5-EBMB to be adsorbed on the C-steel surface.

Table 9. Calculated quantum chemical parameters for the structure of 5-EBMB in the aqueous phase

Compound	5-EBMB
E_{HOMO}, eV	-5.47
E_{LUMO}, eV	-2.81
ΔE, eV	2.66
I, eV	5.47
A, eV	2.81
χ, eV	4.14
η, eV	1.33
σ, eV	0.75
ΔN, e	1.08
Dipole moment, Debye	6.42
Molecular surface area, Å^2	289.05

Furthermore, because of the low electronegativity (χ), the 5-EBMB molecules have a high potential reactivity to offer electrons to the metal surface [69]. Furthermore, the global hardness η and softness σ of a molecule are important qualities that determine its consistency and reactivity. Because electrons are smoothly afforded to the C-steel surface via adsorption, soft molecules are more reactive than hard molecules [70]. The ΔN values determine the electron contributing capability of the inhibitor, and the higher the ΔN value, the larger the electron providing facility of the inhibitor molecule. According to Lukovits's study [71], when ΔN < 3.6, the % IE improves with greater electron donating ability. The calculated values of ΔN are listed is 1.08 eV. This means that 5-EBMB molecule has greater proclivities to offer electrons to the surface of C-steel. Furthermore, the dipole moment is an important indicator for forecasting the path of corrosion protection [72].The augmentation in dipole moment leads to an increase in deformation

energy and better molecule adsorption on steel surface, enhancing inhibitory activity [73]. 5-EBMB has a greater dipole moment value (6.42 debye), as shown in Table 9, indicating a strong tendency for 5-EBMB to be adsorbed on the C-steel surface and enhance inhibition effectiveness. Furthermore, the molecular size of the 5-EBMB and its tendency to protect C-steel surface in corrosive environment has a clear relationship. The inhibition efficiency upsurges with increasing of the molecular structure size because the contact area between the inhibitors molecules and the steel surface raises [74]. As mentioned in Table 10, 5-EBMB demonstrates the greater area (289.05Å^2) and for this purpose, it has greater inhibition proficiency. MEP mapping is a powerful 3D vision tool for distinguishing the net electrostatic effect established over a molecule from total charge dispersal [75]. The red colors in Fig. 11 signify the highest electron density, with MEP being the biggest negative (nucleophilic reaction). The blue colors, on the other hand, signify the most positive region (electrophilic reaction) [76]. The largest negative (red color) regions in methoxy and pyrimidine moieties are generally over N and O atoms, whereas the lower density (yellow color) regions in 5-EBMB molecules are mostly over phenyl moieties. In keto form, MEP, on the other hand, showed the most positive (blue hue) area over oxygen". "The locations in 5-EBMB molecules with the highest electron density may be the furthermost proper for interactions with the C-steel surface".
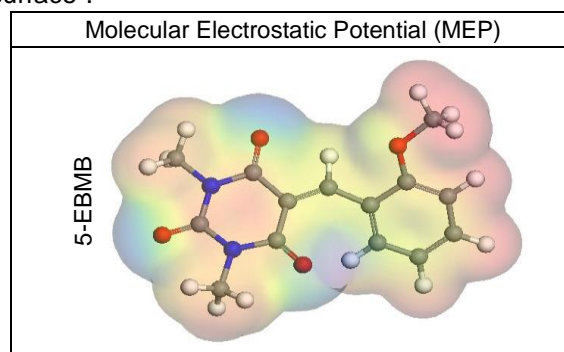
Figure 11. Graphical presentation of the MEP for the 5-EBMB utilizing DFT caculations in the aqeous phase

3.8.2 Monte Carlo (MC simulation)

"MC simulations are theoretical approaches for comprehend the nature of the interaction between the 5-EBMB molecules and the C-steel surface thru the adsorption procedure by retaining the adsorption locator module". Therefore, "Fig. 12 divulges the highest appropriate adsorption configurations for the 5-EBMB molecules on the C-steel surface which located in nearly parallel or flat disposition, designating an increase in the scope of adsorption and greatest surface coverage" [77].

"Table 10 also lists the results of the Monte Carlo simulation, including the adsorption energy for relaxed adsorbate molecules, the rigid adsorption energy for unrelaxed adsorbate molecules, and the deformation energy for relaxed adorbate molecules" [78]. "Table 10 shows that 5-EBMB (-3467.07 kcal mol^{-1}) has a higher adsorption energy, implying that 5-EBMB has a strong adsorption on the C-steel surface, creating stationary adsorbed layers that protect the C-steel from corrosion, which is concurred with the empirical results". Furthermore, the findings in Table 10 and after the geometry optimization process, indicating that 5-EBMB have a higher inhibitory efficiency."When one of the adsorbate is abolished, the dE_{ads}/dN_i

values explain the energy of metal-adsorbate conformation"[79]. The dE_{ads}/dN_i value for 5-EBMB (-196.17kcal mol^{-1}) is higher indicating that 5-EBMB molecules have better adsorption molecules. Furthermore, the dE_{ads}/dN_i values for water are close to -14.15 kcal mol-1, which is low indicating that 5-EBMB"molecules have a more durable adsorption than water molecules, indicating that water molecules can be replaced by 5-EBMB molecules". As a result, the 5-EBMB molecules are forcefully adsorbed on the C-steel surface and form a robust adsorbed defensive layer, resulting in a corrosion shield for the C-steel surface in destructive conditions, as demonstrated by both empirical and theoretical research.

Table 10. Data and descriptors calculated by the Mont Carlo simulation (MC) for the adsorption of the 5-EBMB on iron" (110)

Structures	Adsorption energy/ kcal mol^{-1}	Rigid adsorption energy/ kcal mol^{-1}	Deformation energy/kcal mol^{-1}	dE$_{ads}$/dN$_i$: nhibitor kcal mol^{-1}	dE$_{ads}$/dN$_i$: Water, kcal mol^{-1}
Fe (110)					
IV	-3467.07	-3615.28	148.21	-196.17	-14.15
Water					

Figure 12. The most appropriate adsorption shape for 5-EBM on Fe (110) substrate obtained from adsorption locator module

4. MECHANISM OF CORROSION AND ADSORPTION

One way to propose an inhibitory mechanism is to employ the inhibitor's adsorption on the steel surface. Because of the complexity involved in both adsorption and inhibition of a particular inhibitor, it is generally not feasible to have a single adsorption mode between the inhibitor and the metal surface. The 5-arylidene barbituric acid derivative (5-EBMB) may adsorb on a C-steel surface's active site in the

current system, according to its chemical structure. Consequently, the following adsorption may have an impact on the inhibitory phenomenon:

(i) 5-EBMB can be protonated in an acidic solution due to its neutral O atoms: (5-EBMB) + xH+ → [5-EBMBH]$^{x+}$. Thus, in acidic solutions, 5-EBMB exist as [5-EBMB H]$^{x+}$. "They give an excess negative charge in the solution, encouraging cation adsorption since Cl–may adsorb on metal surfaces [80]". A metal surface that is negatively charged could absorb [5-EBMB Hx]$^{x+}$. Stated

differently, adsorbed Cl⁻ and protonated inhibitor may have a synergistic interaction [81].

(ii) 5-EBMB can also be adsorbed on metal surfaces through chemisorption, which strengthens the tension between the inhibitor molecule and the electrode surface by forming coordinate bonds between the lone electron pairs of the O and N atoms and the empty orbital of the Fe atoms. This process occurs in addition to physical adsorption.

(iii) The heterocyclic ring is generally accepted to be the main site of adsorption for heterocyclic compounds. "5-EBMB contains a lot of π-electrons due to the heterocyclic ring, and these electrons may be adsorbed on the metal surface due to donor–acceptor interactions between the unoccupied d-orbitals of Fe and the π-electrons of the heterocyclic ring."

5. CONCLUSIONS

Researchers also investigated how well this substance, which has a variable chemical makeup, performed in lowering the pace at which C-steel corroded in a 1 M HCl solution at various exposure temperatures (25–45 °C). The above conversation leads to the following conclusions:

1. The inhibitory process increased with rising 5-EBMB concentrations, but it decreased with increasing temperature, according to values from WL measurements.

2. In a 1 M HCl solution, this chemical had a maximum inhibitory performance of 82.5% at a concentration of 2.1×10^{-6} M.

3. The 5-EBMB adhered to the Langmuir adsorption isotherm and had a mixed adsorption nature on the C-steel surface, with physical adsorption predominating.

4. Measurements of potentiodynamic polarization reveal that this substance functions as a mixed-type inhibitor.

5. The charge transfer resistance (R_{ct}) increased and the double layer capacitance values (C_{dl}) decreased at varying concentrations of 5-EBMB, according to the electrochemical impedance spectroscopy data. This is because the inhibitor molecules of 5-EBMB have adsorbed on the metal surface.

6. Theoretical calculations show that the structural characteristics and quantum chemistry parameters, such as energy gap (ΔE), the E_{LUMO}, and chemical softness, are related to the tested drugs' inhibitory efficacy and are compatible with many experimental findings.

7. All of the techniques yielded results that were very consistent with one another.

Acknowledgements

Competing interests

The authors declare no competing interests

6. REFERENCE

[1] H.B. Fan, C.-Y. Fu, H.-L. Wang, X.-P. Guo, J.-S. Zheng (2002) Inhibition of corrosion of mild steel by sodium n, n-diethyl dithiocarbamate in hydrochloric acid solution, Br. Corros. J., 37, 122–125.

[2] Y.K. Agrawal, J.D. Talati, M.D. Shah, M.N. Desai, N.K. Shah (2004) Schiff bases of ethylenediamine as corrosion inhibitors of zinc in sulphuric acid, Corros. Sci., 46, 633–651.

[3] G. Trabanelli (1991) Whitney award lecture: inhibitors—an old remedy for a new challenge, Corrosion, 47, 410–419.

[4] D.D.N. Singh, A.K. Dey (1993) Synergistic effects of inorganic and organic cations on inhibitive performance of propargyl alcohol on steel dissolution in boiling hydrochloric acid solution, Corrosion, 49, 594–600.

[5] G. Banerjee, S.N. Malhotra (1992) Contribution to adsorption of aromatic amines on mild steel surface from HCl solutions by impedance, UV, and Raman spectroscopy, Corrosion, 48, 10–15.

[6] S.T. Arab, E.A. Noor (1993) Inhibition of acid corrosion of steel by some S-alkylisothiouronium iodides, Corrosion, 49, 122–129.

[7] A. Frignani, V. Grassi, F. Zanotto, F. Zucchi (2012) Inhibition of AZ31 Mg alloy corrosion by anionic surfactants, Corros. Sci., 63, 29–39.

[8] R.F. V Villamil, P. Corio, S.M.L. Agostinho, J.C. Rubim (1999) Effect of sodium dodecylsulfate on copper corrosion in sulfuric acid media in the absence and presence of benzotriazole, J. Electroanal. Chem., 472, 112–119.

[9] T. Zhao, G. Mu (1999) The adsorption and corrosion inhibition of anion surfactants on aluminium surface in hydrochloric acid, Corros. Sci., 41, 1937–1944.

[10] S.S. Abd El Rehim, H.H. Hassan, M.A. Amin (2001) Corrosion inhibition of aluminum by 1, 1 (lauryl amido) propyl ammonium chloride in HCl solution, Mater. Chem. Phys., 70, 64–72.

[11] I.A. Raspini (1993) Influence of sodium salts of organic acids as additives on localized corrosion of aluminum and its alloys, Corrosion, 49, 821–828.

[12] N. Hajjaji, I. Rico, A. Srhiri, A. Lattes, M. Soufiaoui, A. Ben Bachir (1993) Effect of N-alkylbetaines on the corrosion of iron in 1 M HCl solution, Corrosion, 49, 326–334.

[13] M. Elachouri, M.S. Hajji, S. Kertit, E.M. Essassi, M. Salem, R. Coudert (1995) Some surfactants in the series of 2-(alkyldimethylammonio) alkanol bromides as inhibitors of the corrosion of iron in acid chloride solution, Corros. Sci., 37, 381–389.

[14] H. Luo, Y.C. Guan, K.N. Han (1998) Inhibition of mild steel corrosion by sodium dodecyl benzene sulfonate and sodium oleate in acidic solutions, Corrosion, 54.

[15] M.A. Migahed, E.M.S. Azzam, A.M. Al-Sabagh (2004) Corrosion inhibition of mild steel in 1 M sulfuric acid solution using anionic surfactant, Mater. Chem. Phys., 85, 273–279.

[16] M.M. Osman, A.M.A. Omar, A.M. Al-Sabagh (1997) Corrosion inhibition of benzyl triethanol ammonium chloride and its ethoxylate on steel in sulphuric acid solution, Mater. Chem. Phys. 50, 271–274.

[17] S.S. Abd El Rehim, H.H. Hassan, M.A. Amin (2003) The corrosion inhibition study of sodium dodecyl benzene sulphonate to aluminium and its alloys in 1.0 M HCl solution, Mater. Chem. Phys., 78, 337–348.

[18] R. Guo, T. Liu, X. Wei (2002) Effects of SDS and some alcohols on the inhibition efficiency of corrosion for nickel, Colloids Surfaces A Physicochem. Eng. Asp., 209, 37–45.

[19] D.P. Schweinsberg, G.A. George, A.K. Nanayakkara, D.A. Steinert (1988) The protective action of epoxy resins and curing agents—inhibitive effects on the aqueous acid corrosion of iron and steel, Corros. Sci., 28, 33–42.

[20] K.R. Ansari, Sudheer, A. Singh, M.A. Quraishi (2015) Some pyrimidine derivatives as corrosion inhibitor for mild steel in hydrochloric acid, J. Dispers. Sci. Technol., 36, 908–917.

[21] G.Y. Elewady (2008) Pyrimidine derivatives as corrosion inhibitors for carbon-steel in 2M hydrochloric acid solution, Int. J. Electrochem. Sci., 3, 1149.

[22] A. Espinoza-Vazquez, G. Negrón-Silva, D. Angeles-Beltrán, M.E. Palomar-Pardavé, M.A. Romero-Romo, H. Herrera-Hernández (2011) Electro-chemical impedance evaluation of uracil and thymine pyrimidine derivatives and its nucleosides compounds as a non-toxic corrosion inhibitors of steels in 1M HCl, ECS Trans., 36, 217.

[23] H. Jafari, K. Sayin, Sulfur containing compounds as corrosion inhibitors for mild steel in hydrochloric acid solution, Trans. Indian Inst. Met. 69 (2016) 805–815.

[24] A. Samide (2013) A pharmaceutical product as corrosion inhibitor for carbon steel in acidic environments, J. Environ. Sci. Heal. Part A., 48, 159–165.

[25] H. Ashassi-Sorkhabi, B. Shaabani, D. Seifzadeh (2005) Effect of some pyrimidinic Shciff bases on the corrosion of mild steel in hydrochloric acid solution, Electrochim. Acta., 50, 3446–3452.

[26] A.S. Fouda, M.A. Ismail, M.A. Khaled, A.A. El-Hossiany (2022) Experimental and computational chemical studies on the corrosion inhibition of new pyrimidinone derivatives for copper in nitric acid, Sci. Rep., 12, 1–19.

[27] S. Lahmidi, A. Elyoussfi, A. Dafali, H. Elmsellem, N.K. Sebbar, L. El Ouasif, A.E. Jilalat, B. El Mahi, E.M. Essassi, I. Abdel-Rahman (2017) Corrosion inhibition of mild steel by two new 1, 2, 4-triazolo [1, 5-a] pyrimidine derivatives in 1 M HCl: Experimental and computational study, J. Mater. Environ. Sci., 8, 225–237.

[28] Z.D. Stanković, M. Vuković (1996) The influence of thiourea on kinetic parameters on the cathodic and anodic reaction at different metals in H2SO4 solution, Electrochim. Acta., 41, 2529–2535.

[29] M.A. El Khalek Khaled, K. Shalabi, M.A. Ismail, F. El Aziz Abd S (2022) Adsorption and inhibitive impact of 5-[4-(dimethylamino) benzylidene]-1, 3-dimethylbarbituric acid on carbon steel corrosion in molar hydrochloric acid solution, Zast. Mater., 63, 238–250.

[30] I. Lukovits, I. Bakó, A. Shaban, E. Kálmán (1998) Polynomial model of the inhibition mechanism of

[31] E.E. Ebenso, U.J. Ekpe, B.I. Ita, O.E. Offiong, U.J. Ibok (1999) Effect of molecular structure on the efficiency of amides and thiosemicarbazones used for corrosion inhibition of mild steel in hydrochloric acid, Mater. Chem. Phys., 60, 79–90.

[32] M.A. Quraishi, F.A. Ansari, D. Jamal (2003) Thiourea derivatives as corrosion inhibitors for mild steel in formic acid, Mater. Chem. Phys. 77, 687–690.

[33] E.G. Brown, E.G. Brown (1998) Pyrimidines, Ring Nitrogen Key Biomol. Biochem. N-Heterocycles, 88–127.

[34] C. Macilwain (1993) Activists now urge caution on approval of new AIDS drug, Nature. 365, 378.

[35] M.A. Khaled, M.A. Ismail, A.A. El-Hossiany, A.S. Fouda (2021) Novel pyrimidine-bichalcophene derivatives as corrosion inhibitors for copper in 1 M nitric acid solution, RSC Adv., 11, 25314–25333.

[36] A. Banan, S. Asadi (2024) Novel cationic and non-ionic biopolyurethanes for effective inhibition of mild steel corrosion in H2S-CO2 environment, Ind. Crops Prod., 221, 119320.

[37] K. Haruna, T.A. Saleh, A. Lawal (2024) Acrylic acid modified indapamide-based polymer as an effective inhibitor against carbon steel corrosion in CO2-saturated NaCl with variable H2S levels: An electrochemical, weight loss and machine learning study, Surfaces and Interfaces, 105065.

[38] H. Bairagi, P. Vashishth, J. Gopal, S.K. Shukla, E.E. Ebenso, B. Mangla (2024) Polymers and their composites for corrosion inhibition application: Development, Advancement, and Future Scope–a critical review, Corros. Commun.

[39] M.A. Ismail, S. Al-Shihry, R.K. Arafa, U. El-Ayaan (2013) Synthesis, antimicrobial activity and molecular modeling study of substituted 5-aryl-pyrimido [5, 4-c] quinoline-2, 4-diones, J. Enzyme Inhib. Med. Chem. 28, 530–538.

[40] K.A. Krasnov, V.G. Kartsev, A.S. Gorovoi (2000) Chemical modification of plant alkaloids. I. Aminomethylation of barbituric acid derivatives by cytisine, Chem. Nat. Compd. 36, 192–197.

[41] G.N. Mu, T P Zhao, M. Liu, T. Gu (1996) Effect of metallic cations on corrosion inhibition of an anionic surfactant for mild steel, Corrosion, 52.

[42] R.G. Parr, R.A. Donnelly, M. Levy, W.E. Palke (1978) Electronegativity: the density functional viewpoint, J. Chem. Phys., 68, 3801–3807.

[43] A.S. Fouda, S.A.A. El-Maksoud, A. El-Hossiany, A. Ibrahim (2019) Evolution of the corrosion-inhibiting efficiency of novel hydrazine derivatives against corrosion of stainless steel 201 in acidic medium, Int. J. Electrochem. Sci., 14, 6045–6064. https://doi.org/10.20964/2019.07.65.

[44] K. Aramaki, M. Hagiwara, H. Nishihara (1987) The synergistic effect of anions and the ammonium cation on the inhibition of iron corrosion in acid solution, Corros. Sci., 27, 487–497.

[45] A.S. Fouda, E. Abdel-Latif, H.M. Helal, A. El-Hossiany (2021) Synthesis and Characterization of Some Novel Thiazole Derivatives and Their Applications as Corrosion Inhibitors for Zinc in 1 M

thiourea derivatives, Electrochim. Acta., 43, 131–136.

Hydrochloric Acid Solution, Russ. J. Electrochem., 57, 159–171. https://doi.org/10.1134/S1023193521020105.

[46] J. Aljourani, K. Raeissi, M.A. Golozar (2009) Benzimidazole and its derivatives as corrosion inhibitors for mild steel in 1M HCl solution, Corros. Sci. 51, 1836–1843.

[47] M. Finšgar, J. Jackson (2014) Application of corrosion inhibitors for steels in acidic media for the oil and gas industry: A review, Corros. Sci., 86, 17–41.

[48] A.S. Fouda, R.E. Ahmed, A. El-Hossiany (2021) Chemical, Electrochemical and Quantum Chemical Studies for Famotidine Drug as a Safe Corrosion Inhibitor for α-Brass in HCl Solution, Prot. Met. Phys. Chem. Surfaces, 57, 398–411.

[49] M.A. Migahed, E.M.S. Azzam, S.M.I. Morsy (2009) Electrochemical behaviour of carbon steel in acid chloride solution in the presence of dodecyl cysteine hydrochloride self-assembled on gold nanoparticles, Corros. Sci., 51, 1636–1644.

[50] M.N.H. Moussa, A.A. El-Far, A.A. El-Shafei (2007) The use of water-soluble hydrazones as inhibitors for the corrosion of C-steel in acidic medium, Mater. Chem. Phys., 105, 105–113.

[51] A.S. Fouda, H. Ibrahim, S. Rashwaan, A. El-Hossiany, R.M. Ahmed (2018) Expired drug (pantoprazole sodium) as a corrosion inhibitor for high carbon steel in hydrochloric acid solution, Int. J. Electrochem. Sci., 13, 6327–6346.

[52] E. Bayol, K. Kayakırılmaz, M. Erbil (2007) The inhibitive effect of hexamethylenetetramine on the acid corrosion of steel, Mater. Chem. Phys., 104, 74–82.

[53] O. Benali, L. Larabi, M. Traisnel, L. Gengembre, Y. Harek (2007) Electrochemical, theoretical and XPS studies of 2-mercapto-1-methylimidazole adsorption on carbon steel in 1 M HClO4, Appl. Surf. Sci. 253, 6130–6139.

[54] I. Epelboin, M. Keddam, H. Takenouti (1972) Use of impedance measurements for the determination of the instant rate of metal corrosion, J. Appl. Electrochem., 2, 71–79.

[55] B.B. Damaskin, O.A. Petrii, V.V. Batrakov, E.B. Uvarov, R. Parsons (1971) Adsorption of organic compounds on electrodes, Springer.

[56] A.S. Fouda, M. Eissa, A. El-Hossiany (2018) Ciprofloxacin as eco-friendly corrosion inhibitor for carbon steel in hydrochloric acid solution, Int. J. Electrochem. Sci., 13, 11096–11112. https://doi.org/10.20964/2018.11.86.

[57] S. Da Costa, S.M.L. Agostinho (1989) Electrochemical behavior of copper in 0.5 M H2SO4 solutions in the absence and presence of Fe (III) and benzotriazole, Corrosion, 45, 472–477.

[58] A.S. Fouda, S.E.H. Etaiw, A.M. Ibrahim, A.A. El-Hossiany (2023) Insights into the use of two novel supramolecular compounds as corrosion inhibitors for stainless steel in a chloride environment: experimental as well as theoretical investigation, RSC Adv., 13, 35305–35320.

[59] A.S. Fouda, M.A.A. El-Ghaffar, M.H. Sherif, A.T. El-Habab, A. El-Hossiany (2020) Novel Anionic 4-Tert-Octyl Phenol Ethoxylate Phosphate Surfactant as Corrosion Inhibitor for C-steel in Acidic Media, Prot.

Met. Phys. Chem. Surfaces, 56, 189–201. https://doi.org/10.1134/S2070205120010086.

[60] R.W. Bosch, J. Hubrecht, W.F. Bogaerts, B.C. Syrett (2001) Electrochemical frequency modulation: a new electrochemical technique for online corrosion monitoring, Corrosion, 57, 60–70.

[61] H.A. Ali, A.A. El-Hossiany, A.S. Abousalem, M.A. Ismail, A.S. Fouda, E.A. Ghaith (2024) Synthesis of new binary trimethoxyphenylfuran pyrimidinones as proficient and sustainable corrosion inhibitors for carbon steel in acidic medium: experimental, surface morphology analysis, and theoretical studies, BMC Chem., 18, 182.

[62] H. Ashassi-Sorkhabi, N. Ghalebsaz-Jeddi (2005) Inhibition effect of polyethylene glycol on the corrosion of carbon steel in sulphuric acid, Mater. Chem. Phys., 92, 480–486.

[63] K.F. Khaled, N. Hackerman (2003) Investigation of the inhibitive effect of ortho-substituted anilines on corrosion of iron in 1 M HCl solutions, Electrochim. Acta., 48, 2715–2723.

[64] Y. Feng, S. Chen, W. Guo, Y. Zhang, G. Liu (2007) Inhibition of iron corrosion by 5, 10, 15, 20-tetraphenylporphyrin and 5, 10, 15, 20-tetra-(4-chlorophenyl) porphyrin adlayers in 0.5 M H2SO4 solutions, J. Electroanal. Chem., 602, 115–122.

[65] Y.M. Abdallah, K. Shalabi, N.M. Bayoumy (2018) Eco-friendly synthesis, biological activity and evaluation of some new pyridopyrimidinone derivatives as corrosion inhibitors for API 5L X52 carbon steel in 5% sulfamic acid medium, J. Mol. Struct., 1171, 658–671.

[66] S.K. Gupta, R.K. Mitra, M. Yadav, O. Dagdag, A. Berisha, B.B. Mamba, T.T.I. Nkambule, E.E. Ebenso, S.K. Singh (2023) Electrochemical, surface morphological and computational evaluation on carbohydrazide Schiff bases as corrosion inhibitor for mild steel in acidic medium, Sci. Rep., 13, 15108.

[67] G. Gece, S. Bilgiç (2009) Quantum chemical study of some cyclic nitrogen compounds as corrosion inhibitors of steel in NaCl media, Corros. Sci., 51, 1876–1878.

[68] N. Palaniappan, I.S. Cole, A.E. Kuznetsov (2020) Experimental and computational studies of graphene oxide covalently functionalized by octylamine: electrochemical stability, hydrogen evolution, and corrosion inhibition of the AZ13 Mg alloy in 3.5% NaCl, Rsc Adv., 10, 11426–11434.

[69] I.B. Obot, D.D. Macdonald, Z.M. Gasem (2015) Density functional theory (DFT) as a powerful tool for designing new organic corrosion inhibitors. Part 1: an overview, Corros. Sci., 99, 1–30.

[70] D. Romani, S.A. Brandan (2020) Investigating the behaviors of corticosterone hormone in different solvents by using DFT calculations and experimental data, Biointerface Res. Appl. Chem., 10, 4876–4892. https://doi.org/10.33263/BRIAC101.876892.

[71] I. Lukovits, E. Kalman, F. Zucchi (2001) Corrosion inhibitors—correlation between electronic structure and efficiency, Corrosion, 57, 3–8.

[72] I.B. Obot, S. Kaya, C. Kaya, B. Tüzün (2016) Density Functional Theory (DFT) modeling and Monte Carlo simulation assessment of inhibition

performance of some carbohydrazide Schiff bases for steel corrosion, Phys. E Low-Dimensional Syst. Nanostructures, 80, 82–90.

[73] K. Shalabi, A.A. Nazeer (2019) Ethoxylates nonionic surfactants as promising environmentally safe inhibitors for corrosion protection of reinforcing steel in 3.5% NaCl saturated with Ca (OH) 2 solution, J. Mol. Struct., 1195, 863–876.

[74] K. Shalabi, O.A. El-Gammal, Y.M. Abdallah (2021) Adsorption and inhibition effect of tetraaza-tetradentate macrocycle ligand and its Ni (II), Cu (II) complexes on the corrosion of Cu10Ni alloy in 3.5% NaCl solutions, Colloids Surfaces A Physicochem. Eng. Asp., 609, 125653.

[75] Y.S. Mary, C.Y. Panicker, M. Sapnakumari, B. Narayana, B.K. Sarojini, A.A. Al-Saadi, C. Van Alsenoy, J.A. War (2015) FT-IR, NBO, HOMO–LUMO, MEP analysis and molecular docking study of 1-[3-(4-Fluorophenyl)-5-phenyl-4, 5-dihydro-1H-pyrazol-1-yl] ethanone, Spectrochim. Acta Part A Mol. Biomol. Spectrosc., 136, 483–493.

[76] S. Ramalingam, P.D.S. Babu, S. Periandy, E. Fereyduni (2011) Vibrational investigation, molecular orbital studies and molecular electrostatic potential map analysis on 3-chlorobenzoic acid using hybrid computational calculations, Spectrochim. Acta Part A Mol. Biomol. Spectrosc., 84, 210–220.

[77] L.H. Madkour, S. Kaya, I.B. Obot (2018) Computational, Monte Carlo simulation and experimental studies of some arylazotriazoles (AATR) and their copper complexes in corrosion inhibition process, J. Mol. Liq., 260, 351–374.

[78] K. Shalabi, A.M. Helmy, A.H. El-Askalany, M.M. Shahba (2019) New pyridinium bromide mono-cationic surfactant as corrosion inhibitor for carbon steel during chemical cleaning: Experimental and theoretical studies, J. Mol. Liq., 293, 111480.

[79] M. Özcan, İ. Dehri, M. Erbil (2004) Organic sulphur-containing compounds as corrosion inhibitors for mild steel in acidic media: correlation between inhibition efficiency and chemical structure, Appl. Surf. Sci., 236, 155–164.

[80] C. Verma, E.E. Ebenso, M.A. Quraishi (2020) Molecular structural aspects of organic corrosion inhibitors: Influence of–CN and–NO2 substituents on designing of potential corrosion inhibitors for aqueous media, J. Mol. Liq., 316, 113874.

[81] M.A. Migahed (2005) Electrochemical investigation of the corrosion behaviour of mild steel in 2 M HCl solution in presence of 1-dodecyl-4-methoxy pyridinium bromide, Mater. Chem. Phys., 93, 48–53.

IZVOD

DOPRINOS INHIBICIJI KOROZIJE UGLJENIČNOG ČELIKA POMOĆU 5-(2-ETOKSIBENZILIDEN) 1,3-DIMETILBARBITURNE KISELINE U RASTVORU HCl: EKSPERIMENTALNA I TEORIJSKA STUDIJA

Inhibirajući uticaj ekološki prihvatljive 5-(2-etoksibenziliden) 1,3-dimetilbarbiturne kiseline (5-EBMB) u 1 M HCl na koroziju ugljeničnog čelika je ispitan metodom gubitka težine (VL), potenciodinamičke polarizacije (PDP), spektroskopija elektrohemijske impedanse (EIS), tehnike elektrohemijske frekvencijske modulacije (EFM). Dobijeni rezultati pokazuju da je proučavana hemikalija dobra 5-EBMB i da, kako u PDP tako iu EIS metodi, njena efikasnost inhibicije (%IE) raste sa povećanjem koncentracije, dostižući 82,5 na 21k10⁻⁶ M. Nasuprot tome, kada temperatura raste, smanjen je procenat IE. „Adsorpcija ispitivanog derivata na površini C-čelika prati Langmuirovu izotermu. Proces adsorpcije ispitivanog jedinjenja je spontan i smatra se tipom hemisorpcije. PDP krive su pokazale da je proučavani derivat inhibitor mešovitog tipa. Štaviše, rezultati EIS-a su potvrdili da se jedinjenje koje se ispituje adsorbovalo na površini C-čelika podizanjem otpora prenosa naelektrisanja (Rct) na 139,7 ohm cm² i smanjenjem kapacitivnosti dvostrukog sloja (Cdl) sa 102 na 69 μF cm⁻². Adsorpcija inhibitora na površini C-čelika je potvrđena ispitivanjem površine primenom mikroskopije atomske sile (AFM), energetski disperzivnog Ks zraka (EDKS) i skenirajuće elektronske mikroskopije (SEM). Pored toga, kvantna hemija i molekularna dinamička simulacija su korišćene da se opširno ispita mehanizam inhibicije korozije 5-EBMB. Sve testirane metode dale su dobru saglasnost.

Ključne reči: *Inhibicija korozije, HCl, C-čelik, derivat ariliden barbiturne kiseline, Langmuirova izoterma*

Mohamed F. Atia: https://orcid.org/0009-0003-5907-8304
Kamal Shalabi: https://orcid.org/0000-00015478-6369
Mohamed A. Ismail: https://orcid.org/0000-0001-5855-3714
Abd El-Aziz S. Fouda: https://orcid.org/0000-0002-3239-4417

Jonida Tahiraj[1], Ridvana Mediu[2], Sonila Shehu[1],
Esmeralda Halo[1], Bledar Murtaj[1], Elda Marku[1], Aurel Nuro[1]*

[1]*Department of Chemistry,Faculty of Natural Sciences, University of Tirana, Albania,* [2]*Department of Medical Science, Faculty of Applied Science, University College LOGOS, Tirana, Albania*

Levels, distribution, and potential sources of polycyclic aromatic hydrocarbons in surface sediments of Petrolifera and Porto Romano ports in Albania

ABSTRACT

This study reports the levels, distribution,and sources of polycyclic aromatic hydrocarbons (PAHs) analyzed in surface sediment samples from Petrolifera and Porto Romano ports. They are well known for their industrial activity and good transportation.A total of 17 samples were collected from both ports in December 2023. A gas chromatography/flame ionization detector (GC/FID) was used to analyse the 13PAHs. The total concentrations of PAHs in sediments at PetroliferaPort varied from 102.9ngg^{-1} to 358.3ng g^{-1}, with an average value of 226.6ng g^{-1}. Similarly, the quantities in sediments from Porto Romano Port varied from 135ng g^{-1}to 1241ng g^{-1}, with an average value of 556ng g^{-1}. Sites within the ports have the highest concentrations of PAHs. Approximately 40% of the Σ13PAHs in Petrolifera and 39% in Porto Romano were attributed to 3-ringed PAHs within the analyzed areas. About 60% of the PAHs with rings between 4 and 6 were found in Petrolifera Port, and 61% in Porto Romano Port. The isomeric diagnostic ratio showed that PAHs in surface sediments in both areas originated from both sources, but mainly dominatedby pyrogenic sources. The results were compared with different sediment quality guidelines.

Keywords*: port, PAHs, 3-ring, sediments, diagnostic ratio*

1. INTRODUCTION

Increasing urbanization and industrialization, the import and export of petroleum and related goods, and the positioning of cities close to ports are thought to be the primary causes of the increasing levels of organic pollutants in port areas [1]. Ports are very important to the development of country's trade and economy [2]. Their development has led to an increase of several contaminants [3]. Albania's major industrial ports are Petrolifera and Porto Romano, which are situated in Vlora and Durrësi Bay, respectively. Petrolifera Port is known for handling and transportation of crude oil and refined petroleum products. The port is equipped with specialized infrastructure for the loading and unloading of oil tankers, including storage tanks and pipelines for efficient transfer.

The proximity to refineries in Greece and Italy is its main advantage. Porto Romano serves as a vital port for shipping and trade, facilitating the movement of goods (construction materials, consumer goods, agricultural products, fisheries), in and out of Albania. This port is involved in handling liquefied natural gas (LNG) and byproducts from the oil and gas industry along the coast. The construction of Porto Romano seaport is now underway. One class of organic compounds commonly analyzed in marine sediments is polycyclic aromatic hydrocarbons or PAHs[4,5]. Due to hydrophobicity, low solubility in water, and high vapor pressure, the sediment samples are considered the last sink of PAH[6].Numerous literature have reported that carcinogenic and mutagenic PAHs are widely present in marine environments [7,8].Therefore, seawater contamination may be reflected in the PAH quantities found in sediments over a prolonged time. Many sources, including marine fuels and oils, vessel operations, cargo handling, stormwater runoff, industrial activities, sediment resuspension, atmospheric deposition, and waste disposalreleased PAHs in

*Corresponding author: JonidaTahiraj
E-mail: jonida.tahiraj@fshn.edu.al

the marine environment [2,4,5]. Their anthropogenic sources are divided intopetroleum-associatedPAHs and pyrogenic-associated PAHs[9,10]. Petroleum-associated hydrocarbons are produced during crude oil maturation.They can be present to port areas during their storage, transportation, utilization, production, and leakage. Pyrogenic-associated PAHs are mainly produced during the incomplete combustion of petroleum fuels, coal, biomass, and other hydrocarbons. Also, they can be transported to port areas via different pathways, including atmospheric transport, wet and dry deposition, surface runoff, and river discharges [11,12]. Referred to other studies, the origin of PAHs is defined using different diagnostic ratios. The ratios of "anthracene/anthracene + phenanthrene, benz(a)anthracene/ benz(a)anthracene+ chrysene, and indeno(1,2,3-c,d)-pyrene/indeno (1,2,3-c,d)+benzo[g,h,i]perylene are the most used in literature[13]. The main objectives of this study were: i) to determine the levels of PAHs in both areas; ii) to define the potential sources of PAHs

and evaluate the results using sediment quality guidelines (SQGs).

2. MATERIALS AND METHODS

Sampling sites

A total of 17 stations were established throughout the two industrial ports, in Albania, with 8 stations atPertoliferaPort and 9 stations at Porto Romano Port, during May 2023. Eight surface sediment samples were taken from various stations, both inside and outside Petrolifera Port, labeled SP-1 to SP-8. Samples SP-1, SP-2, SP-7, and SP-8 were collected from outside the port, while the remaining samples were gathered within the port area. The same methodology was applied to the nine sediment samples collected in Porto Romano Port. The samples (SPR-1, SPR-2, SPR-8, and SPR-9) were collected outside the port. All sampling stationswere selected to cover all the areas impacted by shipping and industrialactivities. The locations of the sampling sites are illustrated in Fig. 1.
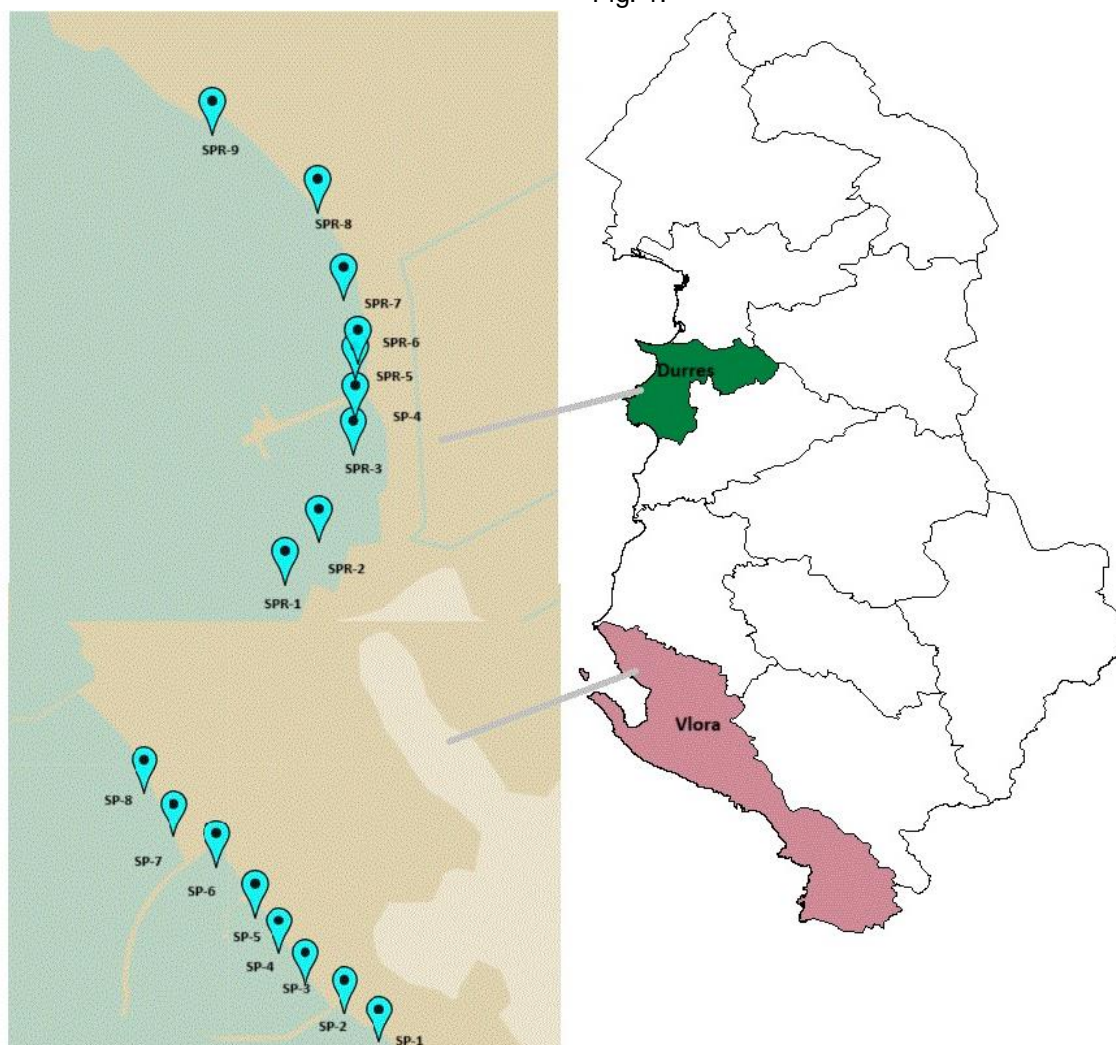
Figure 1. Map of sampling area and the sampling station: a)Porto Romano Port, and b) Petrolifera Port

Sample treatment

A van grab was used to collect the sediment samples in both sites. After the sampling, all the samples were kept in ice boxes for further analysis in the laboratory. The sediment samples were air dried, crushed with a mortar, andsieved through a 63 mesh to remove debris and obtain awell-mixed sample.The detailed procedure ofextraction and qualitative and quantitative analysis of PAHs in sediment samples is describedbyNuro et al. 2024 [14]. In this study, theindividual PAH analyzed in the sediment samples were anthracene (ANT), acenaphthylene (ANP), phenanthrene (PHE), fluorene (FLU), pyrene (PYR), benzo[a]anthracene (BaA), chrysene (CHR), perylene, benzo[b]fluo-ranthene (BbF), benzo[k] fluoranthene (BkF), indene[1,2,3-cd]pyrene (IcP), dibenzo[a,h] ant-hracene (DhA),benzo[ghi]perylene (BgP).A gas chromatography/flame ionization detector (GC/FID) was used to analyse the 13PAHs.

3. RESULTS AND DISCUSSION

Descriptive analyses were performed to determine the distributions of the data. Some individual PAHs were not detected, and during the descriptive analysis their value was set to zero. All the statistical analysis was done using MiniTab (version 22) and Excel software.

Concentration of PAHs in sediment samples

The measured concentrations of 13 priority PAHs and the total sum (Σ13PAHs) analyzed in the surface sediments from Petrolifera and Porto Romano Ports are shown in Tab. 1. The level of individual PAH ranged widely in both investigated areas. Sediment samples from PetroliferaPort showed thatthe total concentration of 13 PAHs ranged from 102.9 to 358.3 ng g^{-1}, with a mean value of 226.6 ng g^{-1}. In Porto Romano, the total PAH concentration ranged from 135 to 1241 ng g^{-1}, with a mean value of 556 ng g^{-1}. The PAH concentration in sedimentscollected inside ports showed higher levels than those analyzed outside the areas. The same finding was reported in other studies [15,16].Sediment from Porto Romano Port recorded the highest total PAHs concentration, which could be due to the intense activities of ships.

Table 1. The mean, median, minimum, and maximum of individual PAHs and the total PAHs levels in Petrolifera and Porto Romano ports. The values used as guidelines according to CCME

Analytes	Petrolifera Port				Porto Romano Port				CCME	
	Mean ng/g	Median ng/g	Min ng/g	Max ng/g	Mean ng/g	Median ng/g	Min	Max ng/g	ISQGs	PEL
Acenaphthylene (ANP)	17.84	18.43	n.d	51.30	**144**	1.10	n.d	1098	6.71	88.9
Fluorene (FLU)	16.23	18.45	0.25	37.90	**106**	39.85	n.d	652	21.2	144
Phenanthrene (PHE)	20.84	23.50	2.10	34.90	0.613	0.181	n.d	3.535	86.7	544
Anthracene (ANT)	**31.3**	26.6	0.7	100.3	**0.704**	0.280	n.d	4.022	46.9	245
Pyrene (PYR)	17.78	10.13	n.d	48.50	**74.7**	4.10	n.d	599	153	1398
Benzo(a)anthrax-cene, (BaA)	**18.79**	16.27	n.d	37.95	**63.7**	40.10	n.d	332	74.8	63
Chrysene (CHR)	16.92	10.10	n.d	46.90	28.5	n.d	n.d	179	108	846
Perylene	4.29	n.d	n.d	33.55	5.817	n.d	n.d	28.55	-	-
Benzo[b]fluorant-hene(BbF)	21.19	12.07	n.d	65.60	5.522	n.d	n.d	35.80	-	-
Benzo[k]fluorant-hene(BkF)	21.51	25.19	n.d	41.80	**49.30**	n.d	n.d	287.6	-	-
Indeno[1,2,3-cd]pyrene (IcP)	**22.45**	16.32	n.d	79.35	7.36	n.d	n.d	37.50	-	-
Dibenzo[a,h] anthracene (DhA)	12.44	0.0	n.d	68.85	4.100	n.d	n.d	36.90	6.22	135
Benzo[ghi]perylene (BgP)	4.98	0.0	n.d	39.80	n.d	n.d	n.d	n.d	-	-
ΣPAHs	**226.6**	**195.2**	**102.9**	**358.3**	**491.4**	**422**	**84.6**	**1237**	**-**	**16700**

n.d –no detected, CCME- Canadian Council of Ministers of the Environment, ISQGs-Canadian interim marine sediment quality guidelines, PEL-Probable Effects Level

In both areas,Perylene, Dibenzo [a,h] anthracene, and Benzo[g,h,i]perylene represented in most stations were non-detected. The highest concentration of PAH was found for ANT in station SP-1 (Petrolifera) and ANP was found with the highest concentration in SPR-7 (Porto Romano). The high abundance of low molecular weight PAHs in some stations suggests relatively recent local PAH sources that entered the seawater[17].

The findings revealed that the light PAHs were present in both areas, whereas the heavy PAHs were mostly present in Porto Romano Port. Numerous sources, including accidental oil spills, ship activities, emissions from fuel burning, discharged waters, closeness to the cities, and human activities can contribute to the difference in PAH content along the examined locations.

The Canadian interim marine sediment quality guidelines (ISQGs) is widely applied, to find out the PAH pollution in marine environment. (Tab. 1). The results from Petrolifera samples showed that some of the PAHs contents in sediments of this port were lower than the levels reported by CCME. Acenaphthylene and Dibenzo[a,h]anthracene were found in higher levels than those reported in ISQGs. The results from Porto Romano samples showed that Acenaphthylene and Fluorene were found at higher levels than those reported from ISQGs. Based on this guideline, the sediment samples from both areas have less potential for negative effects. The results found in both areas are lower than the values of Probable-Effects Level (PEL).

The levels of PAHs in sediments are frequently used to classify an area as polluted or not. In Tab. 2, are given the range of PAHs quantities, indicating the level of pollution in sediments.

Table 2. The range values for the classification of pollution [18]

PAHs quantities (range)	Level of pollution
0–100 ng/g	light pollution
100–1000 ng/g	moderate pollution
1000–5000 ng/g	high pollution
> 5000 ng/g	extreme pollution

The range of PAHs content in the sediments from Petrolifera Port (ΣPAHs 102.9-358 ng g^{-1}) and Porto Romano Port (ΣPAHs 105.4-1241 ng g^{-1}) indicated light to moderate pollution,except the station SPR-6 and SPR-7 that were considered as highly polluted, according to the total PAHs concentration. The main factors that have increased the concentration of PAHs in both areas are their geographical location, export of goods, ship repair, and incoming fuel from ships. The individual plot of PAH concentration in both areas is shown in Fig. 2.
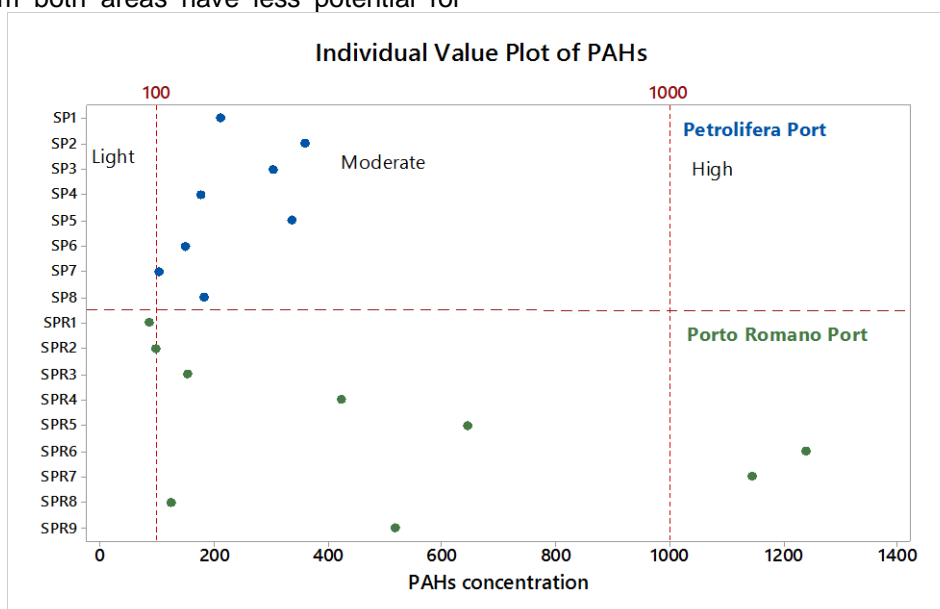
Figure 2. The plot of individual PAHs in both areas

According to USEPA [19], the possible carcinogenic PAHsare BaA,CHR,BaP, BbF, BkF, Ba, hA, BgP, and IcP. The sum of carcinogenic PAHs labeled as Carc_PAHs, was calculated. BaP is not analyzed, and the sum is calculated for the rest of the PAHs. In sediments from Petrolifera Port, Carc_PAHsranged from 5.2 to 232 ng g^{-1}, and in Porto Romano Port ranged from 5.2 to 577 ng g^{-1}. The ratio of ΣCarc/ΣPAHs expressed in %, ranged from 3% to 76 % for samples in Petrolifera Port and

1% to 76 % for Porto Romano. Another parameter that has been calculated in this study is the total amount of the main combustion-specific PAH. The Comb_PAH (BbF; BaA; CHY; PYR; FLU; BgP; BaP; IcP; and BkF), ranged from 63 to 239 ng g^{-1} and 21.9 to 1273 ng g^{-1} in Petrolifera and Porto Romano,respectively.The percent of the ratio Comb_PAH to ΣPAHs ranged from 36% to 76%, and in PortoRomano ranged from 2% to 99%.

Distribution of PAHs

The composition pattern of PAHs by ring size in sediment samples from Petrolifera and Porto Romano Ports are shown in Fig. 3. The compositionof the sediment samples from Petrolifera Port were found in the order; 3-ring PAHs > 4-ring PAHs > 5-ring PAHs >6-ring PAHs (Figure 3).On average, the 3-ring PAHs were the most predominant compound accounting 40 % and 4-ring PAHs accounting 26 % of the total PAHs. In Porto Romano Port the distribution were found in the order: 4-ring PAHs > 3-ring PAHs > 5-ring PAHs >6-ring PAHs. The 4-ring PAHs contributed with 44 % and 3-ring PAHs with 40% of the total PAH concentrations.
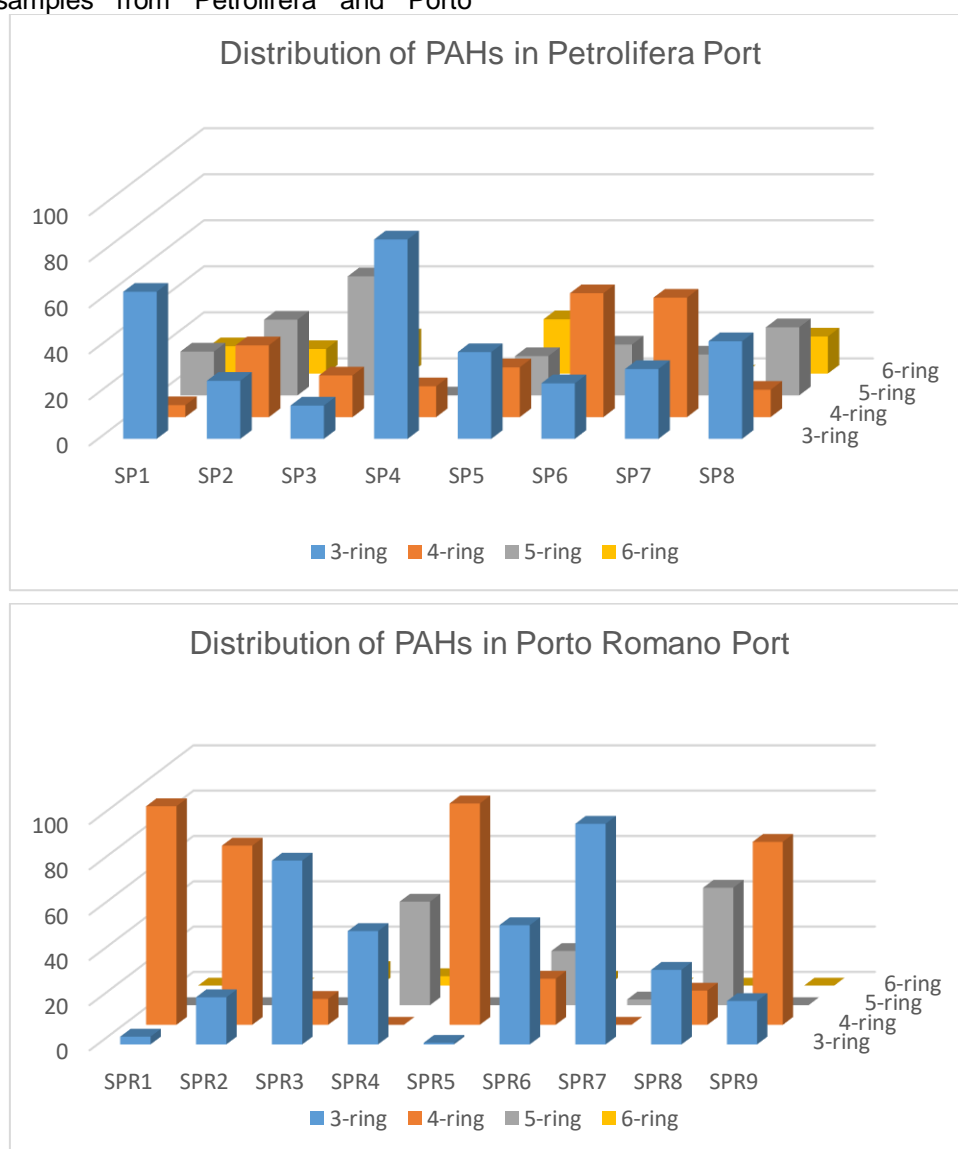
Figure 3. The composition profile of different ring numbers in surface sediments from Petrolifera and Porto Romano Ports

PAHs sources using diagnostic ratio

The measured PAHs were categorized using Low molecular weight rings (LMW, up to 3-rings, MW<202) and Heavy molecular weight rings (HMW, 4-rings and above, MW>202). In Petrolifera Port, the LMW PAHs dominated the surface sediment sampleswith 41 %, whereas in Porto Romano, the LMW PAHs dominated the sediment samples with 40 %. The source of PAH fractions can be identified by comparing the ratio between

Low molecular weight rings (LMW) and heavy molecular weight rings (HMW). The ratio of LMW to HMW >1 indicates dominance of petrogenic sources and lower than 1, indicates pyrolytic sources. The sediment samples from both areas indicated the dominance of pyrolytic sources.

To investigate the potential sources of PAHs were calculated the most used ratio of BaA/(BaA + CHR) and ANT/(ANT + PHE), and IcP/(IcP + BgP)[13]. The distribution of the ratios BaA/(BaA + CHR) versus ANT/(ANT + PHE), and IcP/(IcP +

BgP) versus ANT/(ANT + PHE) are shown in Fig.4. In both areas, the ratios of ANT/(ANT+ PHE) were higher than 0.1 with a mean value of 0.5 in Pertolifera and 0.43 in Porto Romano, indicating that PAHs derived from different combustion sources (pyrolytic sources). In this study, the BaA/(BaA+CHY) fluctuated between 0 and 1 with an average value of 0.56 which indicates petroleum combustion (0.20–0.50), and fossil fuel combustion (>0.35). Our results are shown in Fig.4, where the major stations pointedto pyrolytic sources.
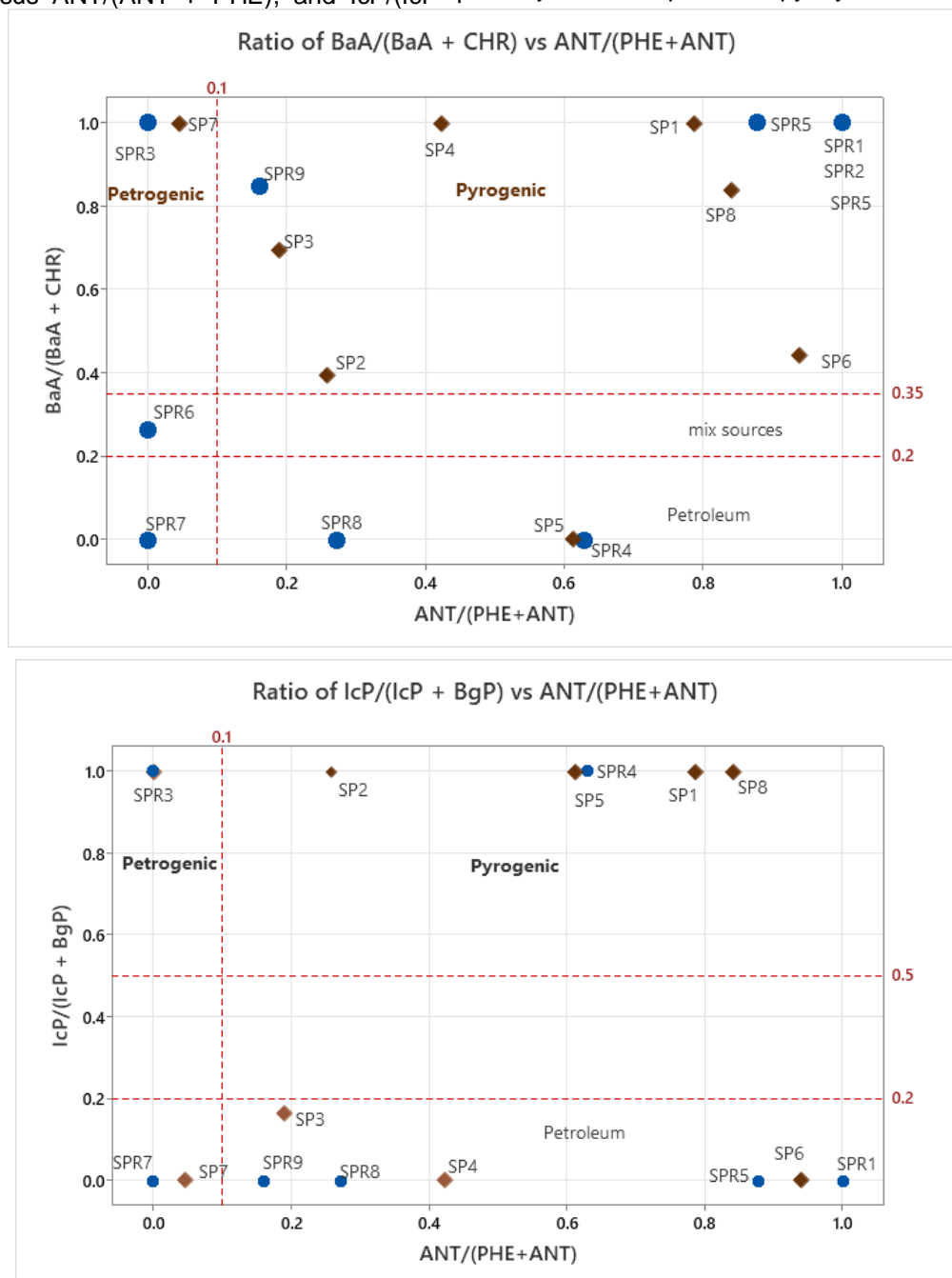
Figure 4. Possible sources of PAHs, identified using diagnostic ratio of BaA/(BaA + CHY) a and IcP/(IcP + BgP) versus ANT/(ANT + PHE) in both areas.

The distribution of the ANT/(ANT + PHE) and BaA/(BaA + CHR) ratios showed that the PAHs in the sediments of both areas originated mainly from combustion and/or pyrolysis sources.The ratios of ANT/(ANT + PHE) and IcP/(IcP + BgP) showed that PAHs in the sediments were mainly contributed by the combustion of petroleum. PetrogenicPAHs have frequently entered the environment through the usage, storage, and transportation of crude oil and its derivatives, storage tank breaches, oil spills, motor oil and gasoline leaks, and small gasoline.All release petroleum-based PAHs into the marine environment. Pyrogenic PAHs are formed by incomplete combustion or pyrolysis of the organic matter at very high temperatures. The main contributors are the incomplete combustion of carbonaceous matter, burning and pyrolysis of coal, oil, gas, trash, wood, vehicular emissions, and industrial processes. The dominance of 3- and 4-ring PAHs is indicative of the potential sources of low-temperature combustion/pyrolysis of biomass (coal, wood, and straw) or petroleum-related fuels [20,21].

Ecosystem Risk Assessment

To assess the ecological risk of PAHs in sediments from Petrolifera and Porto Romano Ports, total and individual PAH levels were compared to effects-based guidelines, including two target values: the effects range-low (ERL) and effects range-median (ERM) [22]. Total PAH concentrations at study sites were below the sediment quality guidelines (SQGs) for both the ERL (3442 ng g−1) and ERM (24290 ng g−1), suggesting that the sediments were not toxic to local organisms. However, some stations showed elevated levels of Acenaphthylene, Fluorene, Anthracene, and Benzo(a)anthracene, exceeding the ERL but remaining below the ERM values. This indicates that occasional biological effects could occur. The sediment quality guidelines values for PAHs and the relative percentage of samples within each SQG range are summarized in Table 3.Although some stations had individual PAH concentrations exceeding the ERL but still below the ERM, the overall results indicate no significant toxic effects. However, these elevated levels at certain stations could lead to occasional negative impacts on the ecosystem.

Table 3. Sediment quality guidelines values for PAHs and relative percentage of samples amongst ranges of ERL and ERM values.

| PAH | SQGs | | % of stations | | | % of stations | | |
| | ERL ng g⁻¹ | ERM ng g⁻¹ | Petrolifera Port | | | Porto Romano Port | | |
			<ERL	ERL-ERM	>ERM	<ERL	ERL-ERM	>ERM
NP	44	500	87.5	12.5	-	66.7	33.3	-
FLU	19	540	75	25	-	44.4	55.6	-
PHE	240	1500	100	-	-	100	-	-
ANT	85.3	1100	87.5	12.5	-	100	-	-
PYR	665	2600	100	-	-	100	-	-
BaA	261	1600	100	-	-	88.9	11.1	-
CHR	385	2800	100	-	-	100	-	-
Perylene	-	-	-	-	-	-	-	-
BbF	-	-	-	-	-	-	-	-
BkF	-	-	-	-	-	-	-	-
IcP	240	950	100	-	-	100	-	-
DhA	63.4	260	100	-	-	100	-	-
BgP	85	330	100	-	-	100	-	-

Concentration <ERL- Biological effects are rare

ERL ≤Concentration ≤ ERM -Biological effects may occasionally occur

Concentration >ERM -Negative biological effects are frequent

4. CONCLUSIONS

This study reports the levels, distribution, and potential sources of PAHs in the surface sediments from 17 stations in total, from two major industrial ports in Albania, Petrolifera and Porto Romano. The sediment samples from Petrolifera Port showed light pollution compared with samples from Porto Romano, which showed light to moderate pollution, except two stations that showed a high level of pollution. The primary sources of PAHs in the sediments of both ports were found to be pyrogenic, such as from incomplete and complete

combustion of petroleum products, including emissions from boats, ships, and vehicle engines. Total PAH concentrations in the sediments were found to be below the Effects Range-Low (ERL) and Effects Range-Median (ERM) values, suggesting that there is no significant toxicity to the local organisms.The study offers useful baseline information on PAH pollution in these ports, emphasizing the need for ongoing observation to better understand the situation and inform future environmental management strategies.

5. REFERENCES

[1] S. M. S. Shaikh, J. P. Tagde , P. R. Singh, S. Dutta, L. N. Sangolkar , M. Suresh Kumar(2021) Impact of port and harbour activities on plankton distribution and dynamics: a multivariate approach. Mar. Pollut. Bull. 165, 112105.

[2] C.F.Chen, Y.C. Lim, Y.R. Ju, F.P.J.B. Albarico , J.W. Cheng, C.W. Chen, C.D.Dong (2022) Method development for low-concentration PAHs analysis in seawater to evaluate the impact of ship scrubber washwater effluents. Water 14 (3), 287.

[3] C.F. Chen, Y.R. Ju, C.W.Chen, C.D. Dong (2019) Changes in the total content and speciation patterns of metals in the dredged sediments after ocean dumping: Taiwan continental slope. Ocean Coast. Manag. 181, 104893.

[4] B.O.Botwe, P.Kelderman, E.Nyarko, P.N.L. Lens (2017) Assessment of DDT, HCH and PAH contamination and associated ecotoxicological risks in surface sediments of coastal Temaharbour (Ghana). Mar. Pollut. Bull. 115, 480–488.

[5] Ch. F. Chen, Y.R.Ju, Y.Ch. Lim, M.-H. Wang,F. P. J. B. Albarico, Ch.-W. Chen, Ch.-D. Dong, (2022) Potential sources and toxicity risks of polycyclic aromatic hydrocarbons in surface sediments of commercial ports in Taiwan. Marine Pollution Bulletin 181 113924 0025

[6] Y.M. Nellier, M.E. Perga, N. Cottin, P. Fanget, E.I M alet, E. Naffrechoux (2015) Mass budget in two high altitude lakes reveals their role as atmospheric PCB sinks. Sci. Total Environ. 511, 203–213.

[7] A.R. Jafarabadi, A. RiyahiBakhtiari, Z. Yaghoobi, C. K. Yap, M. Maisano, T. Cappello, (2019) Distribu-tions and compositional patterns of polycyclic aromatic hydrocarbons (PAHs) and their derivatives in three edible fishes from Kharg coral Island, Persian Gulf, Iran. Chemosphere 215, 835–845.

[8] M. Honda, N. Suzuki (2020) Toxicities of polycyclic aromatic hydrocarbons for aquatic animals. Int. J. Environ. Res. Public Health 17, 1363

[9] E. Y. Zeng and C. L. Vista (2009) Organic pollutants in the coastal environment off San Diego, California. 1. Source identification and assessment by compositional indices of polycyclic aromatic hydrocarbons, Environmental Toxicology and Chemistry, 16(2), 179–188,

[10] R. Boonyatumanond, M. Murakami, G. Wattayakorn, A. Togo, H. Takada (2007) Sources

[11] A.L.C Lima, J.W. Farrington, C.M. Reddy (2005) Combustion-Derived Polycyclic Aromatic Hydrocarbons in the Environment—A Review. Environmental Forensics,6, 109–131. https://doi.org/10.1080/15275920590952739

[12] A.L. Blanchard, D.G. Shaw (2021) Multivariate analysis of polycyclic aromatic hydrocarbons in sediments of Port Valdez, Alaska, 1989–2019. Marine Pollution Bulletin 171, 112906. https://doi.org/10.1016/j.marpolbul.2021.112906

[13] M.B. Yunker, S.M. Backus, E. Graf Pannatier, D.S. Jeffries, R.W. Macdonald (2002). Sources and significance of alkane and PAH hydrocarbons in Canadian arctic rivers. Estuar. Coast. Shelf Sci., 55, 1–31.

[14] A. Nuro, B. Murtaj, J. Tahiraj, S. Shehu, E. Halo, E. Marku, I. Boçi (2024) Priority substances in water and sediments of Albanian Ports. JNS 35

[15] F. Vitali, M. Mandalakis, E. Chatzinikolaou, T. Dailianis, G. Senatore, E. Casalone, G. Mastromei, S.Sergi, R.Lussu, Ch.Arvanitidis, E. Tamburini (2019) Benthic prokaryotic community response to polycyclic aromatic hydrocarbon chronic exposure: importance of emission sources in Mediterranean ports. Front. Mar. Sci., 6, 590.

[16] D. Merhaby, B. Ouddane, S. Net, J. Halwani (2020) Assessment of persistent organic pollutants in surface sediments along lebanese coastal zone. Mar. Pollut. Bull., 153,110947.

[17] R. J. Law, V. J. Dawes, R. J. Woodhead, P. Matthiessen (1997) Polycyclic aromatic hydro-carbons (PAH) in seawater around England and Wales," Marine Pollution Bulletin, 34(5), 306–322,

[18] P.Baumard, H.Budzinski, P.Garrigues, J.C.Sorbe, T. Burgeot, J.Bellocq(1998) Concentrations of PAHs (polycyclic aromatic hydrocarbons) in various marine organisms in relation to those in sediments and to trophic level. Mar. Pollut. Bull., 36, 951–960.

[19] United States Environmental Protection Agency (USEPA) (1993).Provisional Guidance for Quantitative Risk Assessment of Polycyclic Aromatic Hydrocarbons. EPA/600/R-93/ 089 (Office of Research and Development, 1993).

[20] M.S. Garcia-Falcon, B. Soto-Gonzalez, J. Simal-Gandara (2006) Evolution of the concentrations of polycyclic aromatic hydrocarbons in burnt woodland soils. Environ. Sci. Technol., 40, 759–763.

[21] C.W .Chen, C.F. Chen, C.D. Dong, Y.T. Tu (2012) Composition and source apportionment of PAHs in sediments at river mouths and channel in Kaohsiung Harbor Taiwan. J. Environ. Monit, 14, 105–115.

[22] E. R. Long, D. D. Macdonald, S. L. Smith, F. D. Calder (2016)Incidence of adverse biological effects within ranges of chemical concentrations in marine and estuarine sediments," Environmental Management, 19(1), 81–97

[10] R. Boonyatumanond, M. Murakami, G. Wattayakorn, A. Togo, H. Takada (2007) Sources of polycyclic aromatic hydrocarbons (PAHs) in street dust in a tropical asian mega-city, Bangkok, Thailand, Science of the Total Environment, 384 (1–3), 420–432,.

IZVOD

NIVOI, DISTRIBUCIJA I POTENCIJALNI IZVORI POLICIKLIČNIH AROMATIČNIH UGLJOVODONIKA U POVRŠINSKIM SEDIMENTIMA LUKA PETROLIFERA I PORTO ROMANO U ALBANIJI

Ova studija prikazuje nivoe, distribuciju i izvore policikličnih aromatičnih ugljovodonika (PAH) analiziranih u uzorcima površinskih sedimenata iz luka Petrolifera i Porto Romano. Poznati su po svojoj industrijskoj aktivnosti i dobrom saobraćaju. Ukupno 17 uzoraka je prikupljeno iz obe luke u decembru 2023. Za analizu 13 PAH-ova korišćen je gasna hromatografija/detektor plamene jonizacije (GC/FID). Ukupne koncentracije PAH u sedimentima u luci Petrolifera varirale su od 102,9 ng g^{-1} do 358,3 ng g^{-1}, sa prosečnom vrednošću od 226,6 ng g^{-1}. Slično tome, količine u sedimentima iz luke Porto Romano varirale su od 135 ng g^{-1} do 1241 ng g^{-1}, sa prosečnom vrednošću od 556 ng g^{-1}. Lokacije unutar luka imaju najveću koncentraciju PAH. Približno 40% S13PAH-a u Petroliferi i 39% u Porto Romanu pripisano je PAH-ovimasa 3 prstena unutar analiziranih oblasti. Oko 60% PAH-ova sa prstenovima između 4 i 6 pronađeno je u luci Petrolifera, a 61% u luci Porto Romano. Izomerni dijagnostički odnos je pokazao da PAH u površinskim sedimentima u oba područja potiču iz oba izvora, ali uglavnom dominiraju pirogeni izvori. Rezultati su upoređeni sa različitim smernicama za kvalitet sedimenta.
Ključnereči: luka, PAH, 3-prsten, sedimenti, dijagnostički odnos

Jonida Tahiraj   https://orcid.org/0000-0002-2539-6430
Ridvana Mediu   https://orcid.org/0000-0001-6568-9003
Sonila Shehu   https://orcid.org/0000-0002-0863-2331
Esmeralda Halo   https://orcid.org/0009-0003-3569-2553
Bledar Myrtaj   https://orcid.org/0009-0008-3518-4424
Elda Marku   https://orcid.org/0000-0003-1199-8737
Aurel Nuro   https://orcid.org/0000-0003-1875-2430

Vanela Gjeci[1]*, Xhuljeta Hamiti[2], Flora Qarri[3], Pranvera Lazo[2]

[1]*National Environmental Agency, Directory of Environmental Data Management, Chemicals, Laboratory Analyses and Innovation, Tirana, Albania,* [2]*University of Tirana, Faculty of Natural Sciences, Department of Chemistry, Tirana, Albania,* [3] *University of Vlora, Faculty of Technical Sciences, Department of Chemistry, Vlora, Albania*

Water quality of Shkumbini River, Albania, evaluated by physical-chemical parameters and nutrient content

ABSTRACT

Water is an important natural resource that supports the lives of humans and the environment.Monitoring the quality of fresh water is important for water quality assessment and for ensuring a good quality objective. It is very necessary to test the nutrient and physical-chemical parameters of water in respect of national and/or EU standards before it is used for different purposes, such as drinking, domestic, agricultural, and industrial water. This study deals with the water quality assessment of the Shkumbini River based on the distribution and level of physical-chemical parameters and nutrients along the river. The study was performed in March 2022 by applying in-situ measurements of water quality parameters combined with chemical analysis of nutrient content. The results revealed the geographical position, the related urbanization and human activity, as well as weather variation along the river catchment as primary factors affecting the changes in river water quality. Although the number of sampling sites is small (N=4), it is noted that the measured results for all parameters obey the normal distribution (tested by Anderson-darling test, p > 0.05) and were characterized by low variation (CV% < 25%), except TSS which showed a moderate variation (CV% = 49%). The water quality parameters resulted in a lower level than the permitted values, by indicating good water quality in the Shkumbini River. It is confirmed by the WQI index, which ranged in a good water quality status (71 < WQI < 90) for all monitoring stations. It is probably related to low water temperatures and a rainy period in March. The outcomes demonstrate the effectiveness of the water quality parameters and the model employed for assessing water quality.

Keywords:*river water, sampling, water quality,physical-chemical parameters,nutrient.*

1. INTRODUCTION

The surrounding environment is a complex system that consists of land, water, air, and living organisms that are influenced by various natural and human factors, establishing certain balances between them. As a result of intense human activity, these balances have changed, which has caused the destruction of natural ecosystems. Pollution is a serious problem as it passes into the soil, water, and air and then passes into the food chain, posing a risk to human health and living organisms. Water is a key resource for the development of every human activity and is the most important natural resource of life throughout the world. The world's freshwater resources are very unevenly distributed, compared to the world population density [1]

*Corresponding author: Vanela Gjeci

E-mail: vanelagjeci2006@yahoo.com

Regional and seasonal differences in the study area, land use and erosion processes, the spatial scale of sampling sites, the extent and type of human activities in the catchment, and the time of sampling all affect river water quality [2,3]. Urban areas with intensive human activity and rapid land use change are vulnerable to water degradation [4]. As a result of human activity in the downstream regions of most river basins, the water quality of these basins exhibits significant changes that have a detrimental impact on the rivers' health, particularly in terms of their water supply for daily life, industry, and agriculture[5].

Limited water resources and water quality have become major problems throughout the world, resulting in a global water crisis for billions of people [1, 6]. Water quality monitoring following the Water Framework Directive (WFD) shows that the study of the environmental situation and water quality is complex, including various biological, chemical, and physical-chemical parameters. The balance between water demands, water quantity,

and water quality is a critical problem in many regions of the world, increasing the demand for a sustainable water resources management approach [6]. Waste disposal and the use of various chemicals in urban, industrial, and agricultural processes can cause serious water pollution. Water eutrophication is an important environmental issue in surface water, groundwater, and marine systems that is strongly related to the increase of nutrient content in water, mainly affected by human activities and atmospheric deposition [7].

The presence of macronutrients like carbon, nitrogen, and phosphorus is essential for the growth of aquatic life in freshwater [8], but high levels are dangerous for aquatic life. In addition to natural sources, manmade inputs and erosion carried out by runoff are the main sources of nutrients in fresh water [8]. Changes in nutrient flux in heavily populated areas can induce spatial and temporal variations in nutrient and physical-chemical parameters in water. The level and the technology used for sewage treatment and nutrient removal are significant factors contributing to the fluctuations in nutrient and physical-chemical parameters in water [4] that cause the eutrophication of water ecosystems. Eutrophication of waters is associated with the enrichment of nitrogen (N) compounds like nitrite (NO_2^-), nitrate (NO_3^-), ammonium (NH_4^+), and phosphate (PO_4^{3-}) content in water that can cause the presence of algal blooms and macrophytes in certain waters, depletion of dissolved oxygen in water, degradation of aquatic ecosystems, and loss of key aquatic species. EPA 2001 water quality standards [9] include several parameters, such as chemical, physical, and biological parameters, that directly affect the water quality.

This study is focused on the water quality of the Shkumbini River, an important river located in the central part of Albania. Water quality assessment was based on water physical-chemical parameters such as temperature, pH, dissolved oxygen (DO), TSS, nutrients ($N-NO_2^-$, $N-NO_3^-$, $N-NH_4^+$, $P-PO_4^{3-}$).

2. MATERIAL AND METHODS

General view of Shkumbin River

The Shkumbin River i is positioned in central Albania, originating from the mountainous area of Valmara (Korce), and flows into the Adriatic Sea near the Karavastase Lagoon. Since it passes through areas with high chrome, nickel, and iron minerals, the industrial area of Elbasan with high industrial activity of chrome, nickel, and iron metallurgy, as well as cement, as well as urban and industrial area of Elbasan, it is affected by various manmade factors.

Four monitory sites along the Shkumbin River were selected in this study (Fig. 1). The selection of the monitoring sites was carried out by taking into account the geographical position, urban, industrial, and agricultural pollution factors, erosion conditions, etc. The hydrological parameters of the Shkumbini River are shown in Table 1, and the map of the area and sampling positions are shown in Fig. 1.

Figure 1. The position of sampling sites: St.1- Qukes; St.2 – Fushe Labinot; St.3 - Mjekes; St.4 - Rogozhina

Table 1. Hydrological parameters of the Shkumbin River [10]

Length	Surface	Altitude	Flow	Modulus of flow	Average amount of mineralization
km	km^2	m	m^3/sec	l/sec/km^2	mg/L
181.4	2445	753	61	25.2	317

St. 1 is located close to the Qukes, a small village with only 650 inhabitants, which is selected as a clean area. Shkumbini River passes at a significant thickness of topsoil area in this zone, which is characterized by moderate erosion.

St. 2 is located next to the Qukes area. It is characterized by relatively flat mountainous terrain.

The area is relatively sparse in population settlements. It is a rural area with activities in agriculture, farming, and tourism.

St. 3 is located in Mjeke, just in the exit to Elbasan town with 100,903 inhabitants. The river runs through the Shkumbini valley. The river water of this station is heavily impacted by urban and industrial activity in this area.

St. 4 is located at the exit of Rogozhina town. Shkumbin River runs approximately 2 km from the Rrogozhina center. This station is located at the end of the river, between Rogozhina and the river-mouth. The area is characterized by flooding, river erosion, and massive exploitation without criteria of the inert materials.

Table 2. Description of demographic and economic situation of sampling areas

Sites	Qukes	Labinot-Fushe	Mjekes - Elbasan	Rogozhin
Geographical	41.07773, 20.45920	41.13463, 20.15593	41.08056, 20.04315	41.06439, 19.65285
Population (2012 Census)	650	7,058	More than 110,000 inhabitants	22,148
Agriculture activity	Rural area, Agriculture, farming	Rural area, Agriculture, farming	Urban area, Agriculture, farming	Urban area
Industrial activity	No	No	Metallurgy, Cement production, etc	Small enterprices

Water sampling method

Sampling was performed based on the standard methods "Standard Methods for the Examination of Water and Wastewater" with the APHA(1998) standard method [11] and ISO Standard 5667-1: 2006 [12]. The samples were filtered with 0.45 µm Millipore nitrocellulose filters. To clean the membrane, the initial part of the filtered water was poured. Water samples for metal analysis were taken in 0.5 PET bottles pre-cleaned in the laboratory. Water samples for nutrient analysis were taken in 100 ml glass bottles. For metals, the PET bottles were washed with 10% v/v nitric acid, and then rinsed several times with pure deionized water. The samples were transported during the same day to the laboratory using cold boxes to maintain the temperature of +4 °C. The samples were stored under standard conditions until analysis. During transportation, the water samples were treated with chemicals to maintain the stability of the parameters taken in the study, as shown in Table 3.

Table 3. Samples storage conditions

Parameter	BOD	NH_3, NO_2^-, NO_3^-	DO
Consevation conditions	4° C, dark bottles	pH<2, H_2SO_4	In the presence of chemical fixation reagents for DO, dark bottles

Determination of physico-chemical parameters

Physical-chemical parameters such as water temperature, pH, dissolved oxygen (DO), total dissolved solids (TDS), salinity and electrical conductivity were measured in situ using a portable multiparameter apparatus (HACH type sension 156). Suspended solids (TSS) were determined by filtration on a pre-weighed filter with a pore size of 0.42 µm. The filter was weighed again after drying at 105℃ for 2 hours to constant weight. Nutrient content (N-NO_3^-, N-NO_2^-, NNH_4^+, P-PO_4^{3-}) was determined according to standard APHA (1998) procedures [11] using UV-Vis spectrophotometric methods using a Specord 40 spectrophotometer.

Data analysis

Water quality index (WQI) was used to assess the water quality of Shkumbini River. In order to measure the pressures of natural and anthropogenic effects to water bodies, the aquatic classification system, which covers rivers, estuaries, coastal and groundwater bodies [13], is used. Classification of water quality means the categorization of water bodies based on water quality parameters, which have a certain effect on the pollution level of water bodies. Classification takes into consideration two main criteria: the destination of use, like as drinking water, for aquatic life, agricultural, or industrial use, and commercial, industrial, navigational, recreational, wildlife conservation and aesthetic purposes, and the second, taking into consideration the environmental health of water bodies.

The simple water quality index (WQI), which is based on five water quality parameters, temperature, biological oxygen demand (BOD), total suspended sediment (TSS), dissolved oxygen (DO), and conductivity, is used in this study. A higher value of WQI indicates better water quality. Surface water bodies are classified using a system of five quality classes that vary from 0 to 100, with five different ranges from 91 to 100 as excellent water quality, 71 to 90 as good water quality, 51 to 70 as average water quality, 26 to 50 as fair water quality, and 0 to 25 as poor water quality [13].WQI is calculated by the following equation[14]:

$$WQI = \frac{\sum qn * Wn}{\sum Wn}$$

Where

qn = Quality rating of nth water quality parameter. Wn= Unit weight of water quality parameter. All WQI data of this study were calculated through the online simple index calculator.

Cluster analysis was used to better understand the relationships and behavior of multivariate data. Sorting a data collection of observations and/or variables into comparable group variables that differ from one another [15, 16]. Cluster analysis is a data-separating method groups of different observations and/or variables into different clusters that differ from each other [15]. The obtained clusters consist of variables with high similarity and as high as possible distances between the clusters

[15, 16]. The correlation distance, calculated as d=1-r (r represents the correlation coefficient), is mentioned as the most appropriate distance measure [15, 17]. In addition, the Euclidean distance that evaluates the similarity between two objects based on the squared distances between the data points is also used in cluster distance calculation [17]. Cluster analysis is widely used to group together the parameters with high similarity and to assess the factors affecting the complexity of the environment.

3. RESULTS AND DISCUSSIONS

Chemical-physical parameters

The experimental results of the chemical-physical parameters of the Shkumbin River samples are given in Table 4.

Table 4. Experimental results of chemical-physical parameters

Sampling Sites	Temperature	pH	Alkalinity	EC	TSS	DO	BOD	WQI
	°C		(mg/l)	(µs/cm)	(mg/l)	(mg/l)	(mg/l)	
St1	13.7	7.82	187	315	38.2	10.6	3.5	87
St2	16.4	8.01	203	348	69.5	9.1	4.7	78
St3	17.8	7.77	192	323	137	9.3	4.2	73
St4	17.6	8.18	265	344	97	8.9	5.1	74

Table 5. Results of the statistical analysis performed by "descriptive statistics" (in mg/l)*

Variable	Temp (°C)	pH	Alkalinity*	EC (µs/cm)	TSS*	DO*	BOD*	WQI
Mean± StDev	16.4 ± 1.9	7.9 ± 0.19	212 ± 36	333 ± 16	85 ± 42	9.8 ± 0.8	4.4 ± 0.7	78 ± 6
CV%	12	2	17	5	49	8	16	8
Minimum	13.7	7.8	187	354	38.2	8.9	3.5	73
Median	17	7.9	198	333	83.3	9.8	4.5	76
Maximum	17.8	8.2	265	348	137	10.7	5.1	87

Although the number of sampling sites is small (N=4), it is noted that the measured results for all parameters obey the normal distribution (tested by Anderson-darling test, p > 0.05). With the exception of TSS (CV% = 49%), all other parameters result in a fairly low variation (CV% < 25%), and vary in a narrow range. Quite important are the results of the WQI index, which show a good water quality (71 < WQI < 90) for all monitoring stations, which is probably affected by low water temperatures and a rainy period of March.

Temperature

The temperature level depends mainly on the temperature of the environment and the speed of the water flow. The temperature of the samples taken in the study ranged from 13.7 to 17.8 ºC. The minimum temperature (13.7 ºC) was measured at station St1, followed by station St2 (16.4º C). Both of these stations are located in mountainous areas with different geographical heights, which has affected the temperature of the environment in

these areas and the speed of water flow in these areas. The other two stations (St3 and St4), positioned in plain areas and closer to the Adriatic Sea, show higher temperatures. Changes in the temperature values of water systems are caused by changes in various chemical processes in water, such as the dissolution of oxygen in water, in various chemical reactions, or in the activity of organisms or microorganisms in water that affect the fermentation of pollutants and the eutrophication of natural waters. With all that, the level of temperature variance is low (CV% = 12 %), which is not the main reason for the level of pollution in the Shkumbin River during the spring when the monitoring was carried out.

pH

Monitoring the pH of water systems is of particular importance as it is a very important parameter which mainly depends on the nature of the ions dissolved in them, with a tendency of basic values mainly in carbonate areas. On the other

hand, pH is an indicative parameter of the degree of eutrophication of waters when it goes to acidic values, indicating the presence of urban discharges, urban waste, industrial discharges, or biological processes of plants or aquatic algae such as photosynthesis or respiration of algae. The pH values of the samples taken in the study fluctuate in a fairly narrow range (7.8 to 8.2) with values within the range of normal values (6 to 9) recommended by the EPA for surface waters [18].

Alkilinity

The alkalinity of Shkumbin river samples fluctuated from 187 to 265 mg/l (CaCO3). The minimum value was observed at station St1 and the maximum value at station St4. The alkalinity of natural water samples is related to the presence of carbonate salts, hydrogen carbonate, or oxide-hydroxides in the water. It indicates the presence of carbonate, bicarbonate, or hydroxide in water. It shows how able the water is to neutralize the acids.

Elektrical Conductivity (EC)

The EC values of the samples taken in the study fluctuate in a fairly narrow range, from 315 µS/cm (St4) to 348 µS/cm (St2) accompanied by a very low variation (CV% = 5%), showing a stable situation during the monitoring period. High conductivity values are thought to be influenced by industrial, agricultural, and rural activities. The conductivity value in water is affected by the presence of dissolved solids such as anions or cations, and higher salinity in water indicates higher water conductivity.

Total suspended matter(TSS)

The TSS values of the samples taken in the study fluctuate in a wide range, from 37.2 mg/l (St1) to 137 mg/l (St3), associated with a very high variation (CV% = 49%). The TSS values in the samples taken in the study are higher than the values recommended by the European Community (< 10 mg/L). Such a situation can be caused by different conditions of erosion in different areas, by different parameters of the speed of water flow in areas with high slopes, as well as by the conditions of anthropogenic pollution in areas where spills can be identified as solid in water.

Disolved oxygen (DO)

The DO content in Shkumbini river water varies from 8.9 mg/l in summer (S4) to 10.6 mg/l (ST1). The content of DO in surface waters is related to the dissolution of oxygen present in the air and the process of photosynthesis in water. The level of DO in surface waters depends on a number of factors, such as water temperature (the amount of DO increases with increasing temperature), the speed of water flow, which positively affects the values of DO, the level of pollution, which negatively affects the values of DO, etc. The DO

level is essential for the survival of aquatic creatures and an important indicator of surface water pollution or eutrophication. The highest levels of DO were found in the first station (St1), which is favored by a high flow rate due to the area's fraction as well as by low levels of pollution as it is located far from urban and rural areas.

Biological oxygen demand (BOD)

The content of BOD in the Shkumbini River water varies from 3.5 mg/l to 5.1 mg/l. The lowest BOD content was found at station St1, near the source of the Shkumbin River, which is associated with a fairly low level of pollution in it. The highest value of BOD was found in station St4 (Rrogozhina), a rural area with high agricultural activity.

WQI

Based on the WQI results presented in Table 3, the water quality of Shkumbini River showed good level (71 < WQI < 91). Water quality is strongly related with population and land use along the water bodies [19]. It is verified in our result which consisted with higher WQI values near the river spring in mountain area with scarce population, and an increase in lowland characterized by relatively high populatin and industrial, agricultural, and dayly life.

Nutrients

The content of nutrients (mg/l) in the water of the Shkumbin River is given in Table 6, while the results of the statistical analysis in "descriptive statistics" are given in Table 7.

Table 6. The content of nutrients (mg/l) in the water of the Shkumbin River

Sampling Sites	NH_4^+-N	NO_2^--N	NO_3^--N	$P-PO_4^{3-}$-P
St1	0.062	0.004	0.45	0.023
St2	0.187	0.006	0.31	0.039
St3	0.275	0.011	0.23	0.034
St4	0.386	0.014	0.29	0.048

Table 7. Results of the statistical analysis performed by "descriptive statistics"

	NH_4^+-N	NO_2^--N	NO_3^--N	$P-PO_4^{3-}$
Mean	0.228	0.0088	0.320	0.0360
Median	0.231	0.0085	0.300	0.0365
St. Deviation	0.137	0.0046	0.093	0.0104
CV %	60	52	29	29
Minimum	0.062	0.004	0.230	0.0230
Maximum	0.386	0.014	0.450	0.0480

From the results of the statistical analysis, it is noted that the average values of each parameter are quite close to the median values, accompanied

by relatively low variation for NO_3^--N and P-PO_4^{3-} (CV % = 29 %) and moderate for NH_4^+-N and NO_2^--N (CV % resulted 60 % and 52 % respectively). This shows that the values of NO_3^--N and P-PO_4^{3-} are more stable than those of NH_4^+-N and NO_2^--N.

Nitrate (N-NO_3^-)

Based on the WQI results presented in Table 3, the water quality of the Shkumbini River showed a good level (71 < WQI < 91). Discussion of water quality is strongly related to population and land use along the water bodies (Pu et al. 2019). It is verified in our result, which consisted of higher WQI values near the river spring in mountain areas with scarce population and an increase in lowland characterized by relatively high population and industrial, agricultural, and daily life.

Nitrite (N-NO_2^-)

The concentration of NO_2^- - N (mg/l) in the Shkumbini river water samples is relatively low and fluctuates in the levels from 0.004 mg/l to 0.014 mg/l, with an average concentration of 0.0088 mg/l. According to the results shown in Table 5, it turns out that the profile of the change in the concentration of NO_2^- - N increases by passing from the source (St1) with minimum content to other stations, which, for the same reason as for nitrates, may have been influenced by levels of different discharges of urban waste and livestock waste in these areas. Another possible source of nitrites could be hydroplankton and sewage discharges, which are also related to the degree of urbanization of the areas where the samples were taken. On the other hand, nitrites in fresh waters are found as intermediate compounds obtained through the microbial reduction of nitrates or from the process of ammonium oxidation. The level of nitrites in unpolluted waters is usually lower than 0.01 mg/l [18] expressed as nitrogen (N) content. The level of NO_2^- - N content in the water samples of stations St1 and St2 was lower than 0.01 mg/l, while in stations ST3 and St4, it was higher than this level. As expected, this shows different levels of pollution at these stations. Stations St3 and St4 located in urban and urban-rural areas present a higher level of pollution than stations St1 and St2 located in residential areas.

Ammonium (N-NH_4^+)

Ammonium present in water systems originates from the microbiological decomposition of nitrogenous compounds, organic matter, and secretion by various aquatic organisms. Ammonium also derives from anthropogenic sources, such as industrial processes, urban sewage discharge, animal stables, or fermentation of urban waste discharged into the environment. Unpolluted natural waters contain relatively small amounts of ammonium, usually at a level lower than 0.02 mg/l NH_4^+ - N [18]. Ammonium content in Shkumbini river water ranges from 0.062 mg/l to 0.386 mg/l NH_4^+ - N. The lowest level was found at station ST1, and the highest level was found at station S4. The profile of the change of ammonium content in the station obtained in the study varies according to the order NH_4^+ - N of ST1toNH_4^+ - N of ST4 which is related to the degree of urban emissions and livestock in these areas. The levels of NH_4^+ - N in the samples taken in the study are several times higher than normal values, which indicates a high level of pollution. This can be caused by eutrophication of water.

Phosphate (PO_4^{3-}-P)

The content of phosphates in the studied stations along the Shkumbin River varies in values from 0.023 to 0.048 mg/l PO_4^{3-}—P. All measured values are lower than the recommended level (0.1 mg/l PO_4^{3-}—P) [18]. The phosphate concentration values show a low variation (CV% = 29 %), which indicates a stable state along the Shkumbin River. Phosphates in water come mainly as a result of human activity, among the main sources of phosphates in the environment, we can mention sewage discharges in urban areas, urban water discharges with phosphorus content from the use of different detergents, etc. The monitoring period (March) is characterised by abundant rainfall; therefore, pollution from areas with high agricultural activity is another factor of anthropogenic phosphate pollution. Likewise, the erosion or washing away of soils and rocks in the areas where the river passes is another source of phosphates in the water. Mention that the two extremes of minimum and maximum phosphate values were found, respectively, in stations St1 (a clean area near the source of the Shkumbin River) and St4 (a rural area with agricultural and industrial activity).

Multivariate analysis

There are few data, only four monitoring sites, for performing a Pearson correlation analysis and detecting the associations between the investigated parameters. For this reason, the similarity in the spatial distribution of each parameter was compared, as well as the cluster analysis of the measured variables was performed, which is precisely based on the similarity between the parameters used to evaluate the water quality of the Shkumbin River. The spatial distribution of physical-chemicaland and nutrients data are shown in Figure 2.

Only five pairs of parameters showed very high and significant correlations (p < 0.05). Cluster analysis was performed based on correlation coefficient distances (Figure 3).
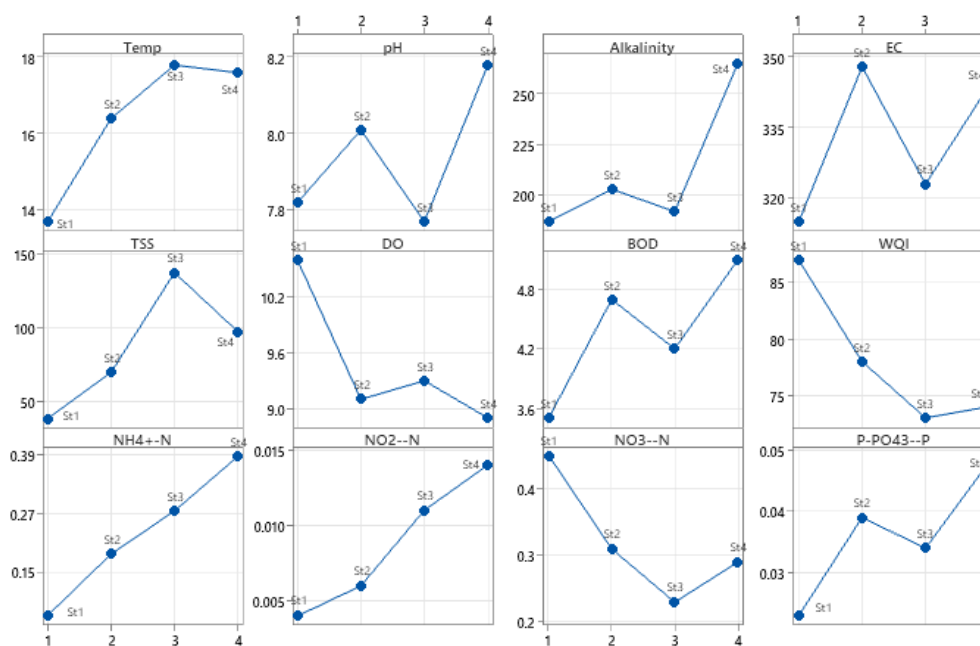
Figure 2. Spatial distribution of physical-chemicaland and nutrients data
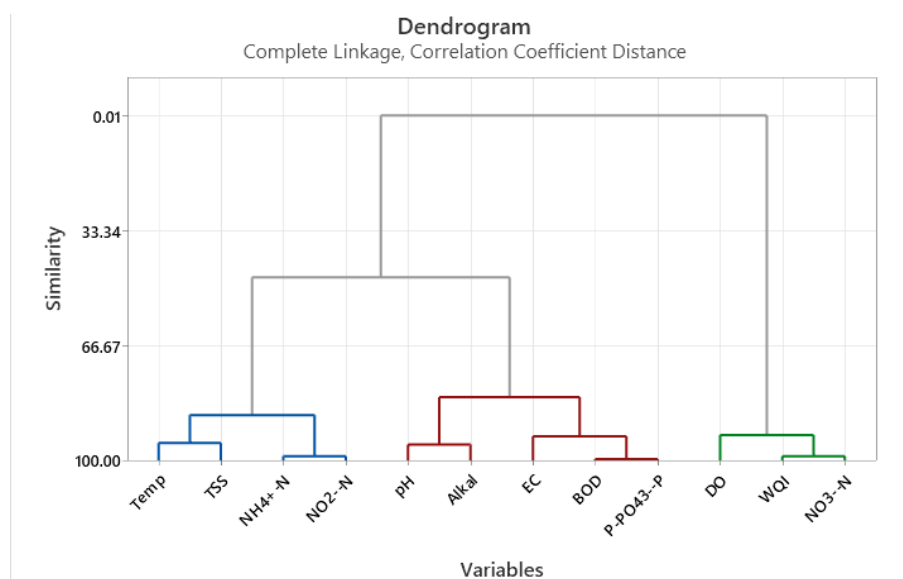
Figure 3. Dendrogram of cluster analysis

Final Partition

	Variables
Cluster 1	Temperature, TSS, NH_4^+-N, NO_2^--N
Cluster 2	pH, Alkalinity, EC, BOD, $P-PO_4^{3-}$-P
Cluster 3	DO, WQI, NO_3^--N

Present data yielded three main clusters with relatively high distances between them, i.e., similarity of 47% between the first and second clusters and 0.01% between the two first clusters and cluster 3. The moderate similarity (47%) between clustrs 1 and 2 could be explained by the behaviors and origin of their parameters, which are primary affected by anthropogenic factors and the water temperature.

Cluster 1 is composed of four parameters: temperature, TSS, NH_4^+-N, and NO_2^-N. The measured temperature ranged from 13.6 to 17.8 °C. In such a narrow range, it could appear to have small effects on the water parameters. According to Zhu et al. (2023), the temperature could affect the internal release of NH4-N that is gradually accelerated as the temperature rises, followed by a biogeochemical transformation of N, which is an important factor affecting the N content of a water body. In addition, temperature affects the nitrogen flux rate at the interface of sediment and water [20].

Cluster 2 contains pH, alkalinity, EC, BOD, P-PO_4^{3-}–P. The acidity of the water impacts the phosphorus content in the water. P retention from the sediment decreased as pH increased [21]. The phenomenon is adverse in desorption of phosphate radical ions from the ferric hydroxide colloid and the release of more phosphate into water [22]. Domestic waste was a dominant source of BOD in the Mediterranean area [23]. The same as BOD, PO_4^{3-}—P is an indicator of untreated domestic waste contamination in areas with high urban density.

Cluster 3 is composed by three water quality parameters, DO, WQI, and NO_3—N. Nitrates in water represent the oxide state of nitrogen nutrients, which have a direct effect on oxygen content in water bodies. In addition, DO content in surface water indicates directly the water quality. Higher DO content and WQI show a better water quality.

4. CONCLUSIONS

This study revealed that the nutrients and physical - chemical parameters are the basis for the environmental assessment of surface water quality.

Parameters such as temperature, pH, electrical conductivity, BOD, and nutrients are mostly varied according to the position of the stations in relation to urbanisation and human activity in them.

The investigated water quality parameters resulted in lower levels than the permitted values. The concentrations of nitrate and nitrite were generally lower than the level established by WHO, 2004 [24] for surface water (50 mg/l for nitrates and 1.0 mg/l for nitrites). On the other hand, ammonium has high concentration levels, which exceed the recommended level of surface water (0.3 mg/l) set by WHO (2004). Statistical analysis can be successfully used in the interpretation of environmental data as it highlights the phenomena that lead to the classification of the environmental status of the studying object.

Water quality in the Shkumbini River was found to be good, with a WQI value of 71 to 90. Low water temperatures and high precipitation during the March monitoring period most likely have an impact on it. It is an efficient method for monitoring of fresh quality.

For the near future, it will remain the responsibility of local authorities to increase measures for the treatment of urban and industrial waste waters particularly near urban areas.

5. REFERENCES

[1] Water UN (2007) Coping with water scarcity: Challenge of the twenty-first century. Report for World Water Day 2007. https://openknowledge. fao.org/server/api/core/bitstreams/f1100f37-2a84-4abb-a661-90ff7aa0b648/content

[2] H.Wang, X,Xiong, K.Wang, X.Li, H.Hu, Q.Li, H.Yin, C.Wu (2023) The effects of land use on water quality of alpine rivers, A case study in Qilian Mountain, China. Science of the Total Environment. 875, 162696. https://doi.org/10.1016/j.scitotenv. 2023. 162696.

[3] A.Lintern, J.A.Webb, D.Ryu, S.Liu, U.Bende-Michl, D.Waters, P.Leahy, P.Wilson, A.W.Western(2 018)Key factors in fluencing differences in stream water quality across space. WIREs Water. 5, e1260. https://doi.org/10.1002/wat2.1260.

[4] C.Cheng,F.Zhang, J.Shi, H.T.Kung(2022) What is the relationship between land use and surface water quality? A review and prospects from remote sensing perspective. Environmental Sciences and Pollution Research. 29, 56887–56907. https://doi.org/10.1007/St11356-022-21348-x.

[5] S.Wolf, V.Esser, H.Schüttrumpf, F.Lehmkuhl (2021) Influence of 200 years of water resource management on a typical central European river. Does industrialization straighten a river? Environmental Sciences Europe. 33, 15-24. https://doi.org/10.1186/St12302-021-00460-8

[6] N.Mancosu, R.L.Snyder, G.Kyriakakis, D.Spano (2015) Water Scarcity and Future Challenges for Food Production. *Water*. 5(*7*), 975-992; doi: 10.3390/w7030975

[7] D.M.Anderson, J.M.Burkholder, W.P.Cochlan, P.M.Glibert, C.J.Gobler, C.A.Heil, R.Kudela, M.L.Parsons, J.E.Rensel, D.W.Townsend, V.L.Trainer, G.A.Vargo (2008) Harmful algal blooms and eutrophication: Examining linkages from selected coastal regions of the United States. Harmful Algae, 8(1), 39-53. doi: 10.1016/j.hal.2008.08.017

[8] K.L.Reinl, T.D.Harris, I.Elfferich, A.Coker, Q.Zhan, L.N.De Senerpont Domis, A.M.Morales-Williams, R. Bhattacharya, H.P.Grossart, R.L.North, J.N. Sweetman (2022) The role of organic nutrients in structuring freshwater phytoplankton communities in a rapidly changing world. Water Research. 19, 118573.
https://doi.org/10.1016/j.watres.2022.118573.

[9] EPA 2001. PARAMETERS OF WATER QUALITY, Interpretation and Standards ISBN 1-84096-015-3

[10] S.Duka, B.Pepa, E.Keci, A.Paparisto, P.Lazo (2017) Biomonitoring of water quality of the Osumi, Devolli, and Shkumbini rivers through benthic macroinvertebrates and chemical parameters. Journal of Environmental Sciences and Health A. 52(5), 471-478.
doi:10.1080/10934529.2016.1274167.

[11] APHA, (1998). Standard methods for the examination of water and wastewater. 20th edition, American public health Association, American water works association, Water environment federation, Washington DC

[12] SO 5667-1:2006. Water quality -- Sampling -- Part 1: Guidance on the design of sampling programmes and sampling techniques. 2006.

[13] https://www.sepa.org.uk/environment/water/aquatic-classification/

[14] D.S.Chandra, S.S.Asadi, Raju MVS (2017) Estimation of water quality index by weighted arithmetic water quality index method: amodel

study. International Journal of Civil Engineering and Technology (IJCIET). 8(4),1215–1222. Article ID: IJCIET_08_04_136 Available online at http://iaeme.com/Home/issue/IJCIET?Volume=8&Issue=4

[15] **O.**Yim, K.T.Ramdeen (2015) Hierarchical Cluster Analysis: Comparison of Three Linkage Measures and Application to Psychological Data. The quantitative methods of psychology. 11, 8-21. Doi: 10.20982/tqmp.11.1.p008

[16] **A.**Michalik (2008) The Use of Chemical and Cluster Analysis for Studying Spring Water Quality in Świętokrzyski National Park. Polish J. of Environ. Stud. 17(3), 357-362

[17] F.D.Gibbons, F.P.Roth (2002) Judging the quality of gene expression-based clustering methods using gene annotation. Genome Research. 12, 1574-81. doi: 10.1101/gr.397002

[18] https://www.epa.ie/pubs/reports/water/waterqua/iwqmolou/App%207.pdf**Appendix 7**: Information On Water Quality Parameters

[19] F.Pu, C.Ding, Z.Chao, Y.Yu, X.Xu (2019) Water-Quality Classification of Inland Lakes Using Landsat8 Images by Convolutional Neural Networks. Remote Sensing. 11(14), 1674-1681. https://doi.org/10.3390/rSt11141674

[20] D.Zhu, D.J.Sample, Q.Qiao, Z.Liu (2023) Effect of water temperature on internal nitrogen release from sediments in the Pearl River Delta region, China. Hydrology Research. 54(9), 1055–1071. https://doi.org/10.2166/nh.2023.056

[21] P.Temporetti, G.Beamud, D.Nichela, G.Baffico, F.Pedrozo (2019) The effect of pH on phosphorus sorbed from sediments in a river with a natural pH gradient. Chemosphere. 228. 287-299. https://doi.org/10.1016/j.chemosphere.2019.04.134

[22] S.Zhao, X.Shi,B.Sun, Y.Liu, Z.Tian, J.Huotari (2022) Effects of pH on phosphorus form transformation in lake sediments. Water Supply. (2), 1231–1243. https://doi.org/10.2166/ws.2021.356

[23] O.Vigiak, B.Grizzetti, A.U.Moinelo, M.Zanni, C.Dorati, F.Bouraoui, A.Pistocchi(2019) Predicting biochemical oxygen demand in European freshwater bodies. Sci Total Environ. 666, 1089–1105. doi: 10.1016/j.scitotenv.2019.02.252

[24] World Health Organization (WHO) (2004) Guidelines for Water Quality (3rd ed.), World Health Organization (WHO), Geneva

IZVOD

KVALITET VODE REKE ŠKUMBINI, ALBANIJA, PROCENJEN PREMA FIZIČKO-HEMIJSKIM PARAMETRIMA I SADRŽAJU HRANLJIVIH MATERIJA

Voda je važan prirodni resurs koji podržava živote ljudi i životne sredine. Praćenje kvaliteta slatke vode je važno za procenu kvaliteta vode i za obezbeđivanje cilja dobrog kvaliteta. Veoma je neophodno ispitati hranljive i fizičko-hemijske parametre vode u skladu sa nacionalnim i/ili EU standardima pre nego što se ona upotrebi u različite svrhe, kao što su voda za piće, domaćinstva, poljoprivredna i industrijska voda. Ova studija se bavi procenom kvaliteta vode reke Škumbini na osnovu distribucije i nivoa fizičko-hemijskih parametara i hranljivih materija duž reke. Studija je izvedena u martu 2022. primenom in situ merenja parametara kvaliteta vode u kombinaciji sa hemijskom analizom sadržaja hranljivih materija. Rezultati su otkrili geografski položaj, povezanu urbanizaciju i ljudske aktivnosti, kao i vremenske varijacije duž rečnog sliva kao primarni faktori koji utiču na promene kvaliteta rečne vode. Iako je broj mesta uzorkovanja mali (N=4), primećuje se da izmereni rezultati za sve parametre poštuju normalnu distribuciju (testirano Anderson-Darling testom, p > 0,05) i da ih karakteriše mala varijacija (CV% < 25%), osim TSS koji je pokazao umerenu varijaciju (CV% = 49%). Parametri kvaliteta vode su rezultirali nižim nivoom od dozvoljenih vrednosti, ukazujući na dobar kvalitet vode u reci Škumbini. To potvrđuje VKI indeks, koji se kretao u dobrom statusu kvaliteta vode (71 < VKI < 90) za sve stanice za praćenje. Verovatno je to povezano sa niskim temperaturama vode i kišnim periodom u martu. Rezultati pokazuju efikasnost parametara kvaliteta vode i modela korišćenog za procenu kvaliteta vode.
Ključne reči: rečna voda, uzorkovanje, kvalitet vode, fizičko-hemijski parametri, hranljiva materija

Vanela Gjeci   https://orcid.org/0000-0002-0008-8685
Xhuljeta Hamiti   https://orcid.org/0000-0002-0008-8685
Flora Qarri   https://orcid.org/0009-0000-2763-401X
Pranvera Lazo   https://orcid.org/0000-0002-7202-4058

Ifeyinwa C. Ekeke[1]*, Chukwuebuka E. Mgbemere[2],
Charity N. Nwanze[1], Chinedu F. Aniukwu[1], Chigoziri N. Njoku[2]

[1]Chemical Engineering Department, Federal University of Technology, Owerri, Imo State, Nigeria. [2]Environmental, Composite and Optimization Research Group, Department of Chemical Engineering, Federal University of Technology, Owerri, Imo State, Nigeria.

Musa Paradisiaca stem sap extract as corrosion inhibitor for aluminum protection in acidic environment

ABSTRACT

This study investigates the efficacy of Musa paradisiaca stem sap extract (MPSSE) as a green corrosion inhibitor for aluminum in hydrochloric environment. Gas chromatography-mass spectroscopy (GC-MS) identified compounds in the extract. The corrosion inhibition potential was assessed through gravimetric analysis (weight loss measurements), and electrochemical impedance spectroscopy (EIS). Surface analysis was conducted using atomic force microscopy (AFM) to examine the surface morphology of aluminum before and after treatment. Adsorption Isotherm studies were performed to understand the interaction mechanism between the extract and the aluminum surface, employing Langmuir, Temkin, Frumkin, and Freundlich isotherms. The results indicate that the extract exhibits corrosion inhibition potential. GC-MS analysis identified compounds like long-chain alkanes, phthalic acid esters, and fluorinated compounds, contributing to corrosion resistance by forming protective barriers on metal surfaces. Gravimetric analysis indicated that the extract, particularly at 20 V/V% concentration, achieved up to 90.73% inhibition efficiency over 30 days, significantly reducing weight loss and corrosion rates. Adsorption studies revealed a strong adherence to the Temkin Isotherm model, suggesting effective adsorption of the extract on the aluminum surface. Atomic force microscopy showed a decrease in surface roughness with increasing extract concentration, confirming the inhibitor's protective effect. Electrochemical impedance spectroscopy demonstrated higher charge transfer resistance and pronounced inductive behavior with the inhibitor, indicating the formation of a protective layer on aluminum. The findings highlight the potential of MPSSE as an eco-friendly alternative for corrosion protection in industrial applications.
Keywords*: Corrosion inhibitor: gravimetric analysis; Musa paradisiaca; electrochemical impedance spectroscopy, eco-friendly alternative*

1. INTRODUCTION

Aluminum is a very useful metal that is known for having a special blend of beneficial qualities. Its remarkable flexibility and lightweight design are two of these that stick out. Aluminum has remarkable reflectivity, excellent ductility, and electrical and thermal conductivity [1. 2]. Because of these qualities, it is an essential material for many applications, such as the production of shell and tube heat exchangers [3]. Aluminum's excellent thermal conductivity makes it ideal for producing heat exchangers with exceptional efficiency since it facilitates efficient heat transfer between various mediums [4].

Shell and tube heat exchangers are essential in the food, chemical, and oil and gas industries [5 - 7]. Heat recovery from exhaust gases and its transfer to liquids is the purpose of this device. This procedure is crucial for condensate recovery, waste heat recovery, and energy recovery [8 – 10]. It also greatly reduces energy consumption and expenses associated with industrial processes. Aluminum performs well in these applications because it can withstand a wide range of temperatures without losing structural integrity.

These heat exchangers are essential in the chemical industry for controlling reaction temperatures, product separation, and energy recovery from process streams [11, 12]. They are employed in the food business to regulate temperature, sterilize, and pasteurize a variety of items. Heat exchangers are essential to the oil and gas sector for the manufacturing of petrochemicals, gas processing, and refining [13]. Heat exchangers

in these various industries encounter many difficulties despite the advantages, one of them being corrosion which has become one ubiquitous problem that jeopardizes the equipment's integrity and performance [14]. This equipment works in harsh conditions with high temperatures, corrosive fluids, and chemical interactions, all of which can hasten the corrosion process [15]. Corrosion raises maintenance costs and downtime by causing material degradation, decreased thermal efficiency, and possible system breakdowns [16].

The main causes of corrosion in heat exchangers are specific chemical agents and exposure to corrosive conditions [17]. Corrosive reactions can occur when aluminum interacts with other compounds, particularly acids. For example, hydrochloric and sulfuric acids are frequently used in industrial processes and can seriously corrode aluminum surfaces when they come into touch with them [18]. Secondly, the pace of chemical reactions, especially those that lead to corrosion, is accelerated by high temperatures. High operating temperatures in heat exchangers can accelerate material degradation by aggravating the corrosion process [19]. Also, these heat exchangers can be severely impacted by fluids with high degrees of acidity, salinity, or other corrosive qualities [20] For instance, saltwater used for cooling in some industrial processes has high concentrations of salts that can cause corrosion. Lastly, industrial cleaning processes, such as pickling and acid cleaning, involve the use of hydrochloric acid (HCl) to remove oxides, scale, and rust from metal surfaces [21]. While these processes are essential for maintaining efficiency, they also expose aluminum to aggressive acidic environments, which can initiate and propagate corrosion over time.

Numerous mitigating measures have been devised and put into practice to counteract corrosion in heat exchangers. These tactics seek to preserve effective operation, increase the equipment's longevity, and safeguard the metal surfaces. Typical ways for mitigating include applying protective coatings to aluminum surfaces [22, 23],cathodic protection techniques using sacrificial anodes made of a more reactive metal to protect aluminum surfaces prevent corrosion [24], choosing corrosion-resistant materials for heat exchanger construction to reduce the risk of corrosion [25], and corrosion inhibitors which are added to the fluid streams to reduce the rate of corrosion [26, 27].

The application of corrosion inhibitors is unique among corrosion prevention techniques for a number of reasons. Chemical substances known as corrosion inhibitors are added to a fluid and dramatically lower the pace at which metals exposed to the fluid corrode [28]. Inhibitors are known to be cheap, highly efficient as they provide continuous protection by forming a dynamic protective layer that adapts to changes in the operating environment, and better ease of application as they can be added directly to the process fluids, making them easy to apply and integrate into industrial processes [39, 30]. In recent years, there has been a growing interest in using plant extracts as corrosion inhibitors [31]. Plant extracts offer a sustainable and eco-friendly alternative to conventional chemical inhibitors. They are derived from natural sources and contain a variety of compounds, including phytochemicals, that contribute to their inhibitory properties [32 - 34]. Plant extracts contain key phytochemical compounds that make them effective corrosion inhibitors for instance: alkaloids, which are nitrogen-containing compounds that can adsorb onto metal surfaces and form a protective barrier that prevents corrosion [35]; flavonoids, which are known for their antioxidant properties and can neutralize reactive species that contribute to corrosion [36]; tannins, which are polyphenolic compounds that can form complexes with metal ions, reducing their reactivity and preventing corrosion [37, 38]; and saponins, which are surface-active agents that can form a protective film on metal surfaces, all of which can inhibit corrosion [39].

Musa Paradisiaca, commonly known as plantain, is a type of banana plant that is widely cultivated in tropical regions, including Nigeria. It is a significant crop in Nigerian agriculture, valued for its nutritional and economic contributions [40, 41]. The plantain plant is characterized by its large, green leaves and clusters of fruit, which are typically cooked before consumption. In Nigeria, plantains are a staple food and are grown in various regions, including the southeastern and southwestern parts of the country [42]. *Musa paradisiaca*'s natural phytochemicals are used in an inventive way when used as a corrosion inhibitor. Research has indicated that a range of chemicals with possible anti-corrosion effects can be found in plantain plant extracts [43, 44]. These substances can adsorb onto metal surfaces, creating a layer of defense that lessens the metal's reactivity and prevents corrosion. *Musa paradisiaca* has several benefits when used as a corrosion inhibitor, including affordability, ease of use, and environmental friendliness. Because they are widely cultivated, plantains are readily available, making their extracts an affordable option for industrial applications. Furthermore, the use of inhibitors derived from plants is consistent with the increasing focus on sustainability and the mitigation of chemical pollutants in industrial processes.

Herein, a combined analytical and electrochemical approach is adopted to evaluate the inhibition properties of *Musa paradisiaca* stem sap extract (MPSSE). The compounds contained in the MPSSP were identified using Gas Chromatography-Mass Spectrometry (GC-MS) analysis. The inhibition efficiencies and corrosion rates were assessed through gravimetric analysis (weight loss) and Electrochemical Impedance Spectroscopy (EIS) techniques. The best adsorption isotherm for the inhibition process was determined by studying the interaction between the MPSSE molecules and the aluminum surface. Additionally, surface analysis of the aluminum coupons before and after inhibition was conducted using Atomic Force Microscopy (AFM) to evaluate the extent of surface roughness and corrosion inhibition. Thermodynamic calculations were employed to understand the inhibitory mechanism, and Langmuir, Temkin, Frumkin, and Freundlich isotherms were used to further study the adsorption behavior of the MPSSE molecules on the metal surface. This study aims to provide a current understanding of the principles driving corrosion inhibition and offer new methods for developing more efficient and environmentally friendly metal corrosion prevention systems.

2. EXPERIMENTAL

2.1. Preparation of the Aluminum Samples

The aluminum (Al) plate obtained from Owerri, Imo State, Nigeria was used as test material. Sample coupons of 1 cm x 1cm x 1cm were cut to assemble the working electrodes to be used in the electrochemical studies, while sample coupons of varied dimensions such as D_2(6 cm $\times$ 1.2 cm $\times$ 0.05 cm); D_4(5.9 cm x 1.1 cm x 0.1 cm); D_7(6 cm $\times$ 1 cm $\times$0.05 cm);); D_9(5.8 cm $\times$ 1.1 cm $\times$ 0.1 cm); D_{11}(6.2 cm $\times$ 1.1 cm $\times$ 0.05 cm); D_{12}(6 cm $\times$ 1.1 cm $\times$ 0.07 cm) were used for weight loss tests. The aluminum coupons were cleaned by dry polishing using emery paper before being degreased with acetone, then dried at room temperature before use.

2.2. Preparation of the Extract

The MPSSE was prepared in two ways which are, the mechanical/manual extraction, and the solvent extraction method (using a Soxhlet extractor). The *Musa paradisiaca* stems were obtained commercially in Owerri, Imo State. The stems were cut into smaller pieces, ground and mashed with lab. mortar, then placed in a sanitized bag filter with micro-size pores. The liquid extract was afterwards pressed into a clean basin at room temperature.

The second method made use of a Soxhlet extractor. The extractor included an extraction chamber, condenser, thimble, siphon arm, and glass body with a round bottom distillation flask. The plantain stems were washed with distilled water, sliced into smaller pieces, and exposed to the sun for seven days. 12.9 g of the stems were extracted in a Soxhlet apparatus with 250 ml of n-hexane at 78°C till exhaustion solvent was recovered; extracts were concentrated and allowed to dry at room temperature [45].

2.3. Preparation of the Inhibitor Concentrations

Different concentrations of the MPSSE were prepared from the stock solution. Five inhibitor concentrations (25ml, 50ml, 75ml, 100ml, and 125ml of the extract in HCl solution) were prepared using volume per volume method to give 5.88 V/V%, 11.11 V/V%, 15.79 V/V%, 20 V/V%, and 23.81 V/V% of extract concentration.

2.4. Gas Chromatography-Mass Spectroscopy

The chemical composition of the *Musa Paradisiaca* extract was characterized using Gas Chromatography-Mass Spectrometry (GC-MS). The analysis was performed with an Agilent 5977B GC/MSD system coupled with an Agilent 8860 auto-sampler. The GC-MS system was equipped with an Elite-5MS fused capillary column. For the GC-MS detection, an electron ionization system was operated in electron impact mode with an ionization energy of 70 eV. High-purity helium gas (99.999%) was used as the carrier gas at a constant flow rate of 1 ml/min. An injection volume of 1 µl was used, with a split ratio of 10:1. The injector temperature was set at 300 °C, while the ion-source temperature was maintained at 250 °C. The oven temperature program was as follows: starting at 100 °C (isothermal for 0.5 min), increasing at a rate of 20 °C/min to 280 °C, and holding at this final temperature for 2.5 min. Mass spectra were acquired at 70 eV, with a scanning interval of 0.5 s, and mass fragments were detected in the range of 45 to 450 Da. The solvent delay was set from 0 to 3 min to avoid interference from the solvent peak.

2.5. Gravimetric Analysis

The gravimetric tests were performed at different inhibitor concentrations, and time intervals. The weight loss measurements were conducted by placing the Al coupons in separate cylindrical plastic containers with 400 ml of 0.5 M HCl solution. Then the Al coupons were also individually submerged in cylindrical containers with 400 ml of the different concentrations of MPSSE (5.88 V/V%, 11.11 V/V%, 15.79 V/V%, 20 V/V%, and 23.81 V/V%).

First, the coupons were suspended in the container after being weighed with an electronic balance. Over the course of thirty (30) days, the coupons were recovered every three days, carefully cleaned with a brush, rinsed several times in water, dried and then reweighed. The weight losses were obtained by the differences between the initial and final weights. The weight loss (ΔW), corrosion rate (CR), inhibition efficiency (%IE) and surface coverage (θ) were calculated by using the following Eqs. (1-4):

$$\triangle W = W_i - W_f \qquad (1)$$

$$CR = \frac{\triangle W}{A \, x \, t} \qquad (2)$$

$$\% \, IE = \frac{CR_O - CR_i}{CR_O} \quad x \, 100 \qquad (3)$$

$$\theta = \frac{IE}{100} \qquad (4)$$

Where:

ΔW is the weight loss of coupon (g), W_i is the initial weight loss (g), W_f is the weight of coupon at any time of observation (g), CR is the corrosion rate (g/cm^2day), A is the area of coupon (cm^2), t is the time of immersion (day), % IE is the inhibition efficiency, CR_O is the corrosion rate of coupon before inhibition (g/cm^2day), CR_i is the corrosion rate of coupon after inhibition (g/cm^2day), θ is the surface coverage.

2.6. Adsorption Isotherms

The method by which inhibitors adsorb on the metal surface is described by adsorption isotherm investigations [46]. By fitting the concentration (V/V%) and surface coverage (θ) of the inhibitor into the various adsorption isotherm models (Langmuir, Temkin, Frumkin, and Freundlich adsorption isotherms), the adsorption isotherm model that best described the adsorption of MPSSE on aluminum in 0.5MHCl medium was determined. The relationship between surface coverage (θ) and concentration (V/V%) is provided by the following equations of the various isotherms' Eqs. (5 -8):

Langmuir isotherm:

$$\frac{C_{inh}}{\theta} = C_{inh} + \frac{1}{K_{ads}} \qquad (5)$$

Temkin isotherm:

$$\theta = \frac{2.303}{\alpha}(log \, K_{ads} + log \, C_{inh}) \qquad (6)$$

Frumkin isotherm:

$$\frac{\theta}{1-\theta} = K_{ads}C_{inh}e^{2a\theta} \qquad (7)$$

Freundlich isotherm:

$$log \, \theta = nlog C_{inh} + log K_{ads} \qquad (8)$$

Where

C_{inh} is the concentration of the inhibitor, K_{ads} is the adsorption constant, α and a are constants. n is a slope.

2.7. Electrochemical Impedance Spectroscopy (EIS) Analysis

A three-electrode cell with an aluminum working electrode, a platinum auxiliary electrode, and a saturated calomel electrode (SCE) as the reference electrode was used for the electrochemical studies. In this study, all potential values are stated in relation to the SCE. The trials were conducted both with and without the MPSSE.

EIS measurements were carried out in the frequency range of 100 kHz to 20 MHz, by applying 5mV amplitude.

2.8. Atomic Force Microscopy (AFM) Analysis

6 of the aluminum coupons used for the weight loss analysis; the first from the blank HCl solution, and each of the rest from the five inhibitor solutions (I,e, the solutions containing 5.8 V/V%, 11.11 V/V%, 15.89 V/V%, 20 V/V%, 23.81 V/V%) were employed for the AFM analysis. An atomic force microscope (Stromlingo DIY AFM model) was used to observe the metal surfaces.

3. RESULTS AND DISCUSSION

3.1. Gas Chromatography Mass Spectroscopy Analysis

The extract from the *Musa paradisiaca* stem sap showed twenty-four (24) identified compounds as seen in Table 1.

The GC-MS analysis of the MPSSE revealed a diverse array of compounds with significant potential for corrosion inhibition. Each peak and its corresponding retention time represent a specific component of the sample quantified in their percentage composition. Long chain alkanes (such as Eicosane, Octacosane, Hentriacosane, and Tricosane with abundant composition in the sap extract) are commonly found in plant waxes and cuticles [47]. They can form protective layers on metal surfaces, shielding them from corrosive agents. These compounds also contribute to the overall effectiveness of the sap in inhibiting corrosion. Phthalic acid, pentadecyl-2-propylphenyl ester present in the extract, can adsorb onto the metal surface and form a protective barrier. The long hydrophobic alkyl chain (pentadecyl) allows the molecule to adsorb onto the metal surface, creating a barrier that shields the metal from corrosive agents. Additionally, the aromatic phenyl group and the phthalic acid moiety may interact with the metal surface, further enhancing the protective effect. Moreover, Hexatriacontylpenta fluoropropionate, Octatriaconty ltrifluoroacetat

ecyclotetradecane, and Octatriacontyl pentaf luoropropionate present in the sap extract are long-chain fluorinated compounds used as a corrosion inhibitor. Their effectiveness in inhibiting corrosion is primarily attributed to the presence of fluorine atoms in the molecule. Fluorine is highly electronegative, which means it can form strong bonds with other atoms, making the compound less susceptible to oxidation and corrosion. Additionally, the long carbon chain in these compounds provides a hydrophobic barrier, preventing water and other corrosive substances from reaching the surface of the metal, further inhibiting corrosion.

Table 1: Volatile Phytochemical Composition (GC-MS) of Musa ParadisiacaStem Sap

S/N	RT	Area%	Compound Name	% Composition
1	7.058	2.99	Phthalic acid, pentadecyl 2-propylphenyl ester	2.99
2	8.918	3.91	Eicosane	3.91
3	11.121	7.66	2-methyltetracosane	7.66
4	11.499	5.19	Octacosane	5.19
5	12.18	3.17	Tetrapentacontane	3.17
6	12.912	5.42	Octadecane	5.42
7	14.148	3.42	Octatriacontylpentafluoropropionate	3.42
8	14.245	3.71	Tetrapentacontane	3.71
9	14.388	2.87	Hexacosane	2.87
10	14.526	4.2	Octatriacontylpentafluoropropionate	4.20
11	14.571	4.87	Nonacosane	4.87
12	14.846	2.78	Hentriacontane	2.78
13	15.167	4.93	Hentriacontane	4.93
14	15.51	4.36	Heptacosane	4.36
15	15.55	3.8	Octacosane	3.80
16	15.756	5.41	Tricosane	5.41
17	16.179	3.9	Octacosane	3.90
18	16.74	2.81	Octacosane	2.81
19	16.912	3.39	Hexatriaconylpentafluoropropionate	3.39
20	17.083	5.32	Tetracosane	5.32
21	17.101	5.42	Hentriacontane	5.42
22	17.57	3.12	Octatriacontyltrifluoroacetatecyclotetradecane	3.12
23	18.857	4.27	Octacosane	4.27
24	19.864	3.09	Hexacosane	3.08

In summary, the inhibitive nature of MPSSE can be attributed to the presence of Phthalic acid esters, fluorinated compounds, long-chain alkanes, and other organic compounds. These compounds, which possess relatively high molecular weights and consist of long chains of carbon atoms bonded together, have non-polar characteristics that enable them to form protective films on metal surfaces.

3.2. Gravimetric Analysis

Results of weight loss measurements in the acid media without and with the addition of various concentrations of MPSSE are shown below in Fig. 1a.

The graph of weight losses clearly reveals that the control sample experienced the highest weight losses over the experimental period, though it shows lower values before the 8th day. This is also evident in the corrosion rate versus time graph. The sample containing 100ml of the inhibitor had the lowest weight loss and corrosion rates over the period of observation. This invariably means that this sample also had the highest inhibition efficiency values as can be seen in Fig. 1c, though it occurred from somewhere about the 12th day. The 125ml sample experienced the next lower weight loss values and hence the next values of inhibition efficiency after the 100ml sample. This trend also became obvious from the 12th day of the experimentation. The inhibition efficiency graphs show that, generally, inhibition efficiency values above 50% were obtained for this extract from the 12th day to the end of the experiments for all the concentrations. These results prove the extract's ability to significantly reduce the corrosion rate of the aluminum metal in HCl medium.
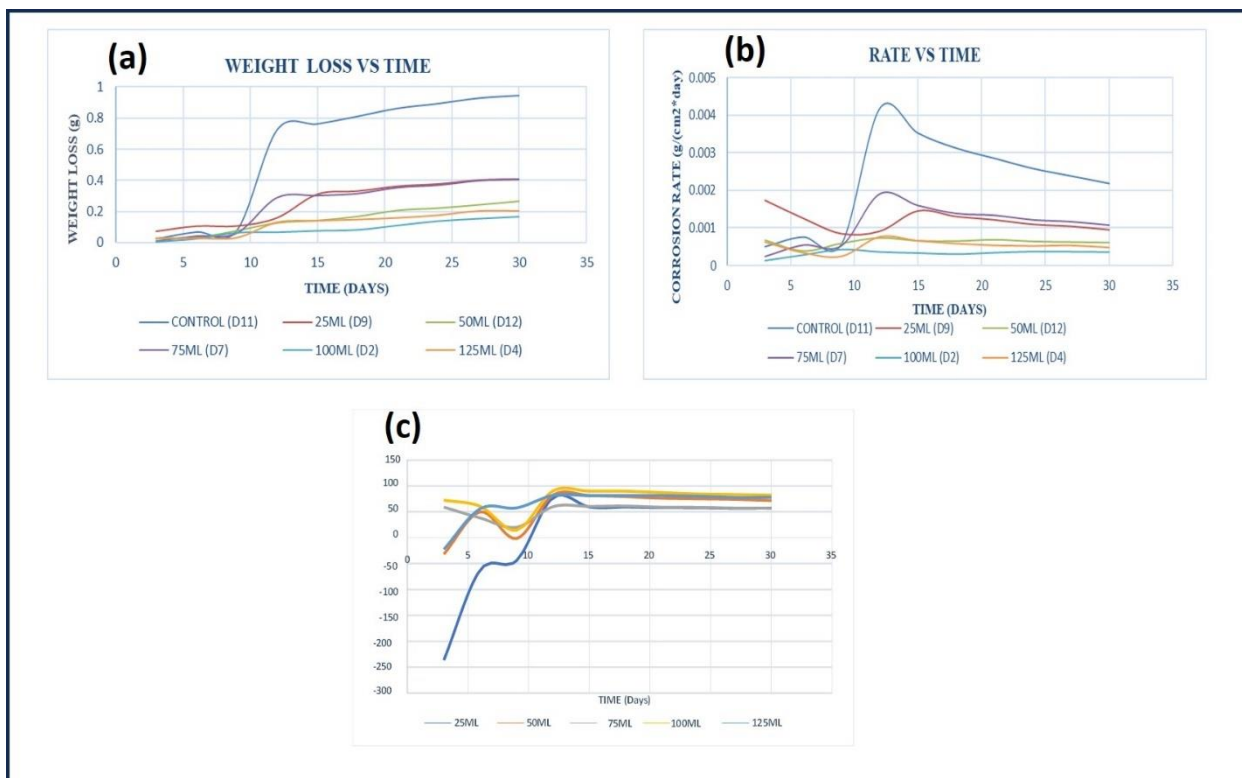
*Figure 1. Plotsof aluminum coupons in 0.5MHCL solution for; (a) weightloss (g) vs.time(day);
(b)Corrosionrate vs.time and (c) Inhibition Efficiency (%)vs time*

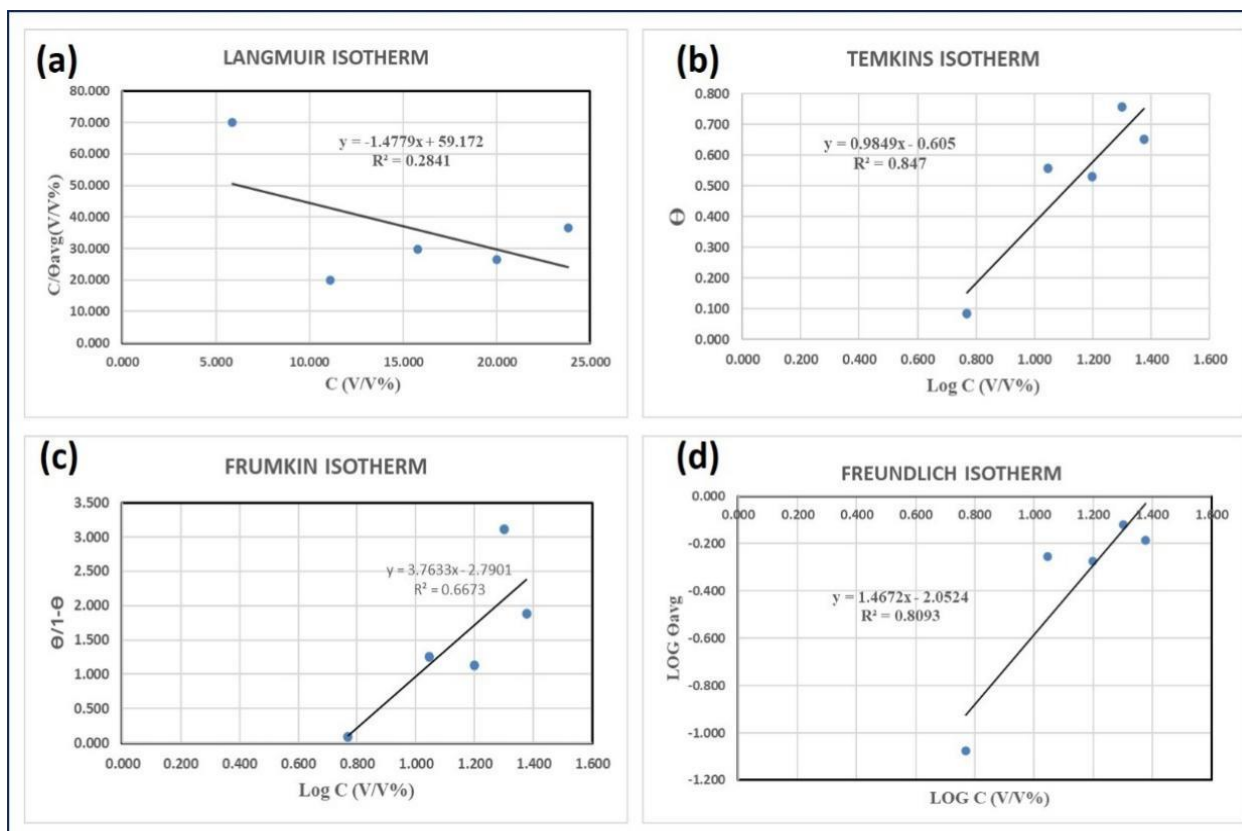*Figure 2. Different isotherm plots of MPSSE for the corrosion of Al in HCl for; (a) Langmuir,
(b)Temkin (c) Frumkin, and (d) Freundlich*

3.3. Adsorption Isotherm Parameters

The adsorption mechanism of the inhibitors was examined through the application of Langmuir, Temkin, Frumkin, and Freundlich isotherms. The graph of C/θ_{avg} vs C for Langmuir adsorption is displayed by the isotherm, as shown in Fig. 2a. The correlation coefficient (R^2) was utilised to find the best fit and ascertain the mode of adsorption of the *Musa paradisiaca* stem sap extract onto the aluminum surface. The surface coverage data were easily fitted into the selected adsorption isotherms. With a low regression coefficient of 0.2841, the graph could not fit the Langmuir adsorption isotherm, indicating limited adherence to the isotherm. Fig. 2b displays the Temkin isotherm graph. The graph reveals a strong adherence to the isotherm as evidenced by a best fit with the linear plot regression coefficient (R^2) with a value of 0.847. Fig. 2c shows the graph of Frumkin isotherm. The graph shows a slightly much better adherence to the isotherm than the Langmuir adsorption Isotherm resulting from a best fit with the linear plot regression coefficient (R^2) with a value of 0.6673. Fig. 2d represents the graph of the Freundlich Isotherm, showing log average vs. Log C. An R^2 value of 0.8093 was obtained suggesting a good fit. A comparison of the various isotherms shows that the Temkin adsorption isotherm gave the best linear relationship which indicates that the inhibitor was strongly adsorbed on the metal surface following the Temkin model as its R^2 value was closest to unity (1).

3.4. Electrochemical Impedance Spectroscopy Analysis

EIS measurements were performed to examine the corrosion inhibition process at the metal/solution interface, which allows us to gain deeper insight into the inhibition processes. Figs. 3 and 4 display impedance spectra collected at room temperature and MPSSE concentration.

In the high-frequency region, both curves start near the origin, indicating that the solution Resistance (R_s) is low and similar for both cases (Fig. (3a)). In the mid-frequency region, the black curve (Al Blank) shows a semicircle that peaks around 80 ohms on the imaginary axis. In contrast, the red curve (Al Inhibited) exhibits a semicircle that peaks around 100 ohms on the imaginary axis, suggesting a different electrochemical behavior when the inhibitor is present (refer to Fig. (3b)). In the low-frequency region, after the main semicircle, the black curve (Al Blank) dips downward and shows small fluctuations. This behavior is indicative of inductive effects, often associated with the adsorption of intermediates or relaxation processes on the electrode surface (refer to Fig. 3c).
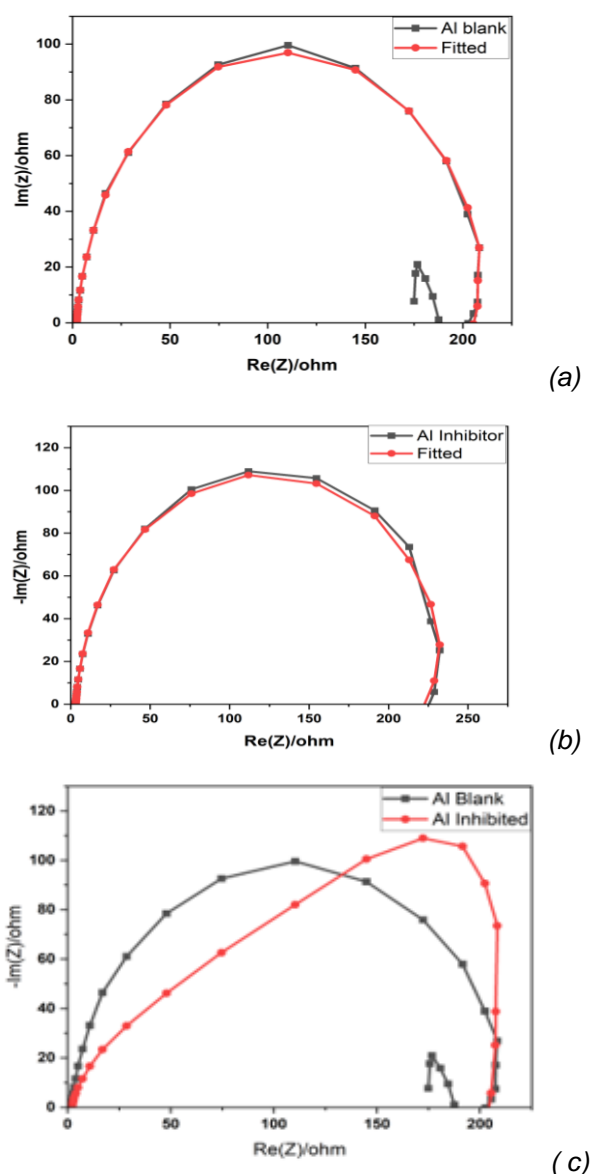

(a)

(b)

(c)

Figure 3. Nyquist representations of experimental data and results of electrode impedance for Al/0.5 M HCl in the absence and the presence of the inhibitor.

Similarly, the red curve (Al inhibited) dips down after the main semicircle, showing a more pronounced dip compared to the blank, which is also indicative of inductive behavior. The charge transfer resistance (R_{ct}) can be analyzed based on the semicircle sizes in the EIS spectra. For the Al Blank sample, the smaller semicircle indicates a lower charge transfer resistance, suggesting a more active corrosion process in the absence of the inhibitor. Conversely, for the Al inhibited sample, the larger semicircle indicates a higher charge transfer resistance. This suggests that the inhibitor effectively increases the resistance to charge transfer, likely by forming a protective layer on the aluminum surface, which slows down the

corrosion process. The double layer capacitance (Q1) can be inferred from the size of the semicircles in the EIS spectra. For the Al Blank sample, the smaller semicircle may indicate a lower double-layer capacitance. In contrast, the Al Inhibited sample shows a larger semicircle, which may suggest a higher double-layer capacitance due to the formation of a more stable and possibly thicker protective layer. The inductive behavior observed at low frequencies is characterized by a downward dip in both the Al Blank and Al Inhibited curves, forming what is referred to as an inductive loop. This behavior is typically caused by the adsorption of species onto the electrode surface or relaxation processes in the system. For the Al Blank sample, the presence of a small inductive loop suggests some degree of adsorption or relaxation processes taking place without the inhibitor. In comparison, the Al inhibited sample exhibits a larger inductive loop, indicating more significant adsorption or relaxation effects when the inhibitor is present. This could be due to the inhibitor causing the formation of intermediate species that adsorb onto the electrode surface.
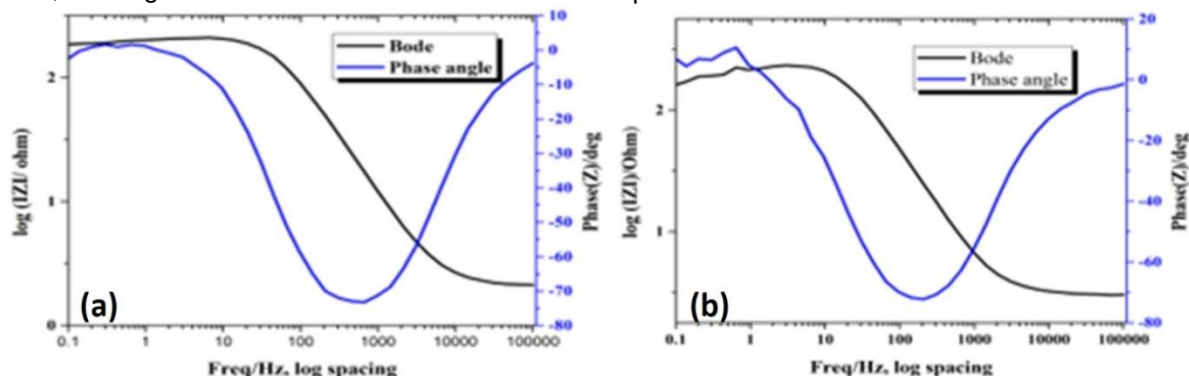

Figure 4. Graphical representation showing the Bode plot and Phase angle of Aluminum Coupon immersed in (a) blank solution and (b) solution containing inhibitor

From Fig. 4a, at low frequencies (around 0.1 Hz to 1 Hz), the magnitude remains relatively high and stable, indicating that the impedance is relatively high. As the frequency increases (from around 10 Hz to 1 kHz), the magnitude decreases significantly, showing a drop in impedance. Beyond 1 kHz, the magnitude levels off, indicating that the impedance becomes less frequency-dependent at higher frequencies. At low frequencies (around 0.1 Hz to 1 Hz), the phase angle is around 0°, indicating that the voltage and current are in phase. As the frequency increases (from around 1 Hz to 10 Hz), the phase angle decreases, reaching around -10°, indicating a slight lag of current behind voltage. From 10 Hz to 1 kHz, the phase angle drops more steeply, reaching around -80°, indicating a significant lag of current behind voltage. From Fig. 4b, at low frequencies (around 0.1 Hz to 1Hz), the magnitude is relatively high and stable, indicating that the impedance is relatively high. As frequency increases, the magnitude decreases significantly, showing a drop in impedance. And, at low frequencies (0.1 Hz to 1 Hz), the phase angle starts around -20°, indicating some lag of current behind voltage. As the frequency increases, the phase angle decreases, reaching around -70°.

The high and stable impedance at low frequencies suggests a capacitive or resistive nature, where the system can store charge. The significant drop in impedance and steep decline in phase angle in the mid-frequency range indicate the presence of reactive elements (inductive or capacitance) that dominates the response. Inhibition in the Al inhibitor sample is evident through the distinct changes in both the magnitude and phase plots compared to the Al Blank sample. In the magnitude plot, as the frequency increases, the impedance for the Al inhibitor decreases significantly from 1 Hz to 100 Hz, compared to a more gradual decrease for Al Blank from 10 Hz to 1 kHz. From the phase plot, as frequency increases, the phase angle for Al inhibitor decreases more gradually to around 70° from 1 Hz to 100 Hz, whereas for Al Blank, it drops steeply to around -80° from 10 Hz to 1 kHz. At high frequencies, the phase angle for Al inhibitor approaches 0°, indicating more resistive behavior.
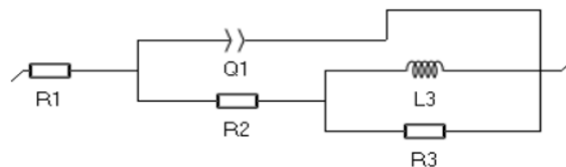

Figure 5. Equivalent Circuit Model

Fig. 5 shows that for this system, an appropriate equivalent circuit model would include elements to represent the solution resistance (R_s), charge transfer resistance (R_{ct}), double-layer capacitance (C_{dl}), and an inductance (L) to account for the inductive behavior observed at low frequencies. Overall, the inhibitor increases the charge transfer resistance and introduces more pronounced

inductive behavior, suggesting the formation of a protective layer and more complex electrochemical interactions on the aluminum surface.

3.5. Surface morphology

AFM is an effective instrument for examining surface morphology at the nano-to-micro scale, and it is now a popular option for determining how inhibitors affect the rate at which corrosion occurs at the metal/solution interface [48]. Fig. 6 shows the three-dimensional (3D) AFM morphologies of the aluminum surface immersed in hydrochloric acid solution with varied concentrations of the extract, the aluminum surface immersed in hydrochloric acid (without inhibitor), and the aluminum surface immersed in hydrochloric acid

containing varied concentrations of the MPSSE. The findings from the AFM image analysis comprised the following: the average roughness (average deviation of all point roughness profile from a mean line over the evaluation length) [49] , the maximum height (Sz) values (vertical distance between the highest peak and the lowest valley within the analyzed area of the surface) [50], (and the root-mean-square roughness (Sq) (the average of the measured height deviations taken within the evaluation length and measured from the mean line). These values are compiled in Table 2 for the various aluminum surfaces immersed in different environments.

Table 2. AFM data for aluminum surface immersed in uninhibited and inhibited environment.

| Samples	RMS Roughness	Average Roughness	Maximum height (Sz)
1. Aluminum coupon (D_{11}) immersed in HCl acid solution (blank)	183.917 pm	0.56355 nm	1.34769 nm
2. Aluminum coupon (D_9) immersed in HCl acid solution containing 5.88 V/V% of extract	53.8324 pm	0.56355 nm	1.20639 nm
3. Aluminum coupon (D_{12}) immersed in HCl acid solution containing 11.11 V/V% of extract	29.1348 nm	326.284 nm	1.19735 nm
4. Aluminum coupon (D_7) immersed in HCl acid solution containing 15.89 V/V% of extract	53.5673 pm	0.59384 nm	1.21586 nm
5. Aluminum coupon (D_2) immersed in HCl acid solution containing 20 V/V% of extract	38.5951 pm	0.51183 nm	1.03233 nm
6. Aluminum coupon (D_4) immersed in HCl acid solution containing 23.81 V/V% of extract	21.2896 pm	395.437 pm	957.682 pm
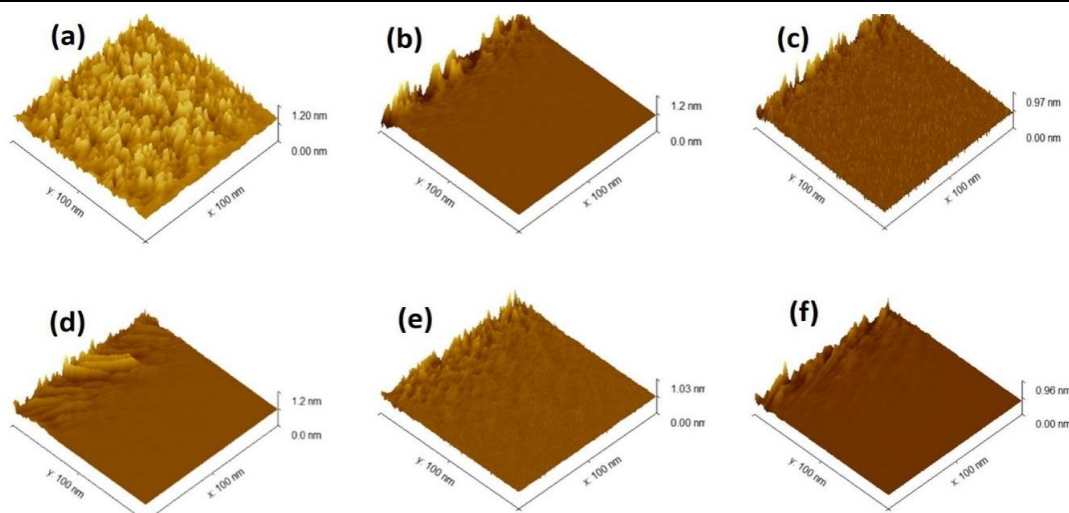
Figure 6. Image of aluminum coupon after immersion in 0.5 M HCl solution (a) without inhibitor, (b) in the presence of 5.81 V/V% of MPSSE, (c) in the presence of 11.11 V/V% of MPSSE, (d) in the presence of 15.89 V/V% of MPSSE, (e) in the presence of 20 V/V% of MPSSE, (f) in the presence of 23.81 V/V% of MPSSE

Significant variations in surface roughness characteristics are shown by the AFM results in Table 2 for the aluminum coupons immersed in HCl solution and different doses of the MPSSE demonstrating the extract's potency as a corrosion

inhibitor. The highest values of RMS roughness (183.917 pm), average roughness (0.56355 nm), and maximum height (1.34769 nm) were displayed by the submerged sample in HCl solution without the extract, showing significant corrosion. This is

also demonstrated in Fig. 6a. On the other hand, the samples that were immersed in HCl media containing the extract showed lower values of these parameters. This is observed in Fig. 3b – Fig. 3f, which display flatter, more homogenous and uniform surfaces than that of the surface without the inhibitor. The results further reveal a general improvement in the surface characteristics of the samples immersed in the inhibitor as the concentration of the inhibitor increased. These findings further prove the efficacy of the MPSSE in inhibiting the corrosion of aluminum metal in hydrochloric acid solution.

4. CONCLUSION

This study evaluated the MPSSE as a potential corrosion inhibitor for aluminum. The GC-MS analysis identified several key compounds ranging from long-chain alkanes to fluorinated compounds, which play a crucial role in corrosion inhibition. These compounds form protective layers on metal surfaces, effectively shielding them from corrosion agents. Weight loss measurements demonstrated that the MPSSE significantly reduced corrosion rates, with the highest inhibition efficiency of 90.73% observed at a 20 V/V% concentration on the 12th day of experimentation. This shows the extract's potent ability to minimize weight loss and corrosion rates compared to the control. The Temkin adsorption isotherm indicated strong adherence of the extract to the metal surface. AFM analysis further confirmed that increasing extract concentrations resulted in smoother metal surfaces. EIS analysis indicated a stable protective layer on the metal surface resulting from increased charge transfer resistance and inductive behavior in the presence of the extract. Overall, the *Musa paradisiaca* stem sap extract shows considerable promise as an eco-friendly and effective corrosion inhibitor.

Acknowledgement

5. REFERENCES

[1] S.Mridha (2016) Metallic Materials. In Reference Module in Materials Science and Materials Engineering.Elsevier. https://doi.org/10.1016/B978-0-12-803581-8.040972

[2] K.Sathyanarayana, M.Puttegowda, S..Rangappa, S.Siengchin, P.Shivanna, S.Nagaraju, M. Somashekara, P.Girijashankar, Y.Girijappa (2023) 3 – Metallic lightweight materials: Properties and their applications. In S. Rangappa, S.Doddamani, S. Siengchin, M.Doddamani (Eds.), Lightweight and Sustainable Composite Materials (pp. 47–67). Woodhead Publishing. https://doi.org/10.1016/B978-0-323-95189-0.00003-2

[3] E.Fernandes, S.Krishanmurthy (2022) Design and analysis of shell and tube heat exchanger. *Int. J. Simul*, *13*, 15. https://doi.org/10.1051/smdo/2022005.

[4] A.Hamadouche, A.Azzi, S.Abboudi, R.Nebbali (2018) Enhancement of heat exchanger thermal hydraulic performance using aluminum foam. Exp. Therm. Fluid Sci, *92*, 1–12. https://doi.org/10.1016/j.expthermflusci.2017.10.035.

[5] A.Prasad, K.Anand (2020) Design & Analysis of Shell & Tube Type Heat Exchanger. Int. J. Eng. Res. Technol *9*(01). https://doi.org/10.17577/IJERTV9IS010215.

[6] P.andakumar, D.Loganathan, D.Nataraja, P. Manikandan (2023) 6—Shell and tube heat exchangers in the food industry. In S. M. Jafari (Ed.), *Thermal Processing of Food Products by Steam and Hot Water* (pp. 153–179). Woodhead Publishing. https://doi.org/10.1016/B978-0-12-818616-9.00004-3

[7] P.Wildi-Tremblay, L.Gosselin (2007). Minimizing shell-and-tube heat exchanger cost with genetic algorithms and considering maintenance. Int. J. Energy Res, *31*(9), 867– 885. https://doi.org/10.1002/er.1272

[8] S.Bari, S.Hossain (2013). Waste heat recovery from a diesel engine using shell and tube heat exchanger. Appl. Therm. Eng, *61*(2), 355–363. https://doi.org/10.1016/j.applthermaleng.2013.08.020

[9] V.Pandiyarajan, M.ChinnaPandian, E.Malan, R. Velraj, R.Seeniraj 2011) Experimental investigation on heat recovery from diesel engine exhaust using finned shell and tube heat exchanger and thermal storage system. Appl. Energy *88*(1), 77–87. https://doi.org/10.1016/j.apenergy.2010.07.023

[10] R.Thakar, S.Bhosle, S.Lahane (2018). Design of Heat Exchanger for Waste Heat Recovery from Exhaust Gas of Diesel Engine.*Procedia Manufacturing*, *20*, 372 – 376. https://doi.org/10.1016/j.promfg.2018.02.054

[11] B.Kilkovsky, P.Stehlik, Z.Jegla, L.Tovazhnyansky, O.Arsenyeva, P.Kapustenko (2014) Heat exchangers for energy recovery in waste and biomass to energy technologies – I. Energy recovery from flue gas. Appl. Therm. Eng., *64*(1), 213–223. https://doi.org/10.1016/j.applthermaleng.2013.11.041

[12] R.Shah, B.Thonon, D.Benforado (2000) Opportunities for heat exchanger applications in environmental systems. Appl. Therm. Eng., *20*(7), 631–650. https://doi.org/10.1016/S1359-4311(99)00045-9

[13] M.Mehdizadeh, F.Pourfayaz, A.Kasaeian, M. Mehrpooya (2017) A practical approach to heat exchanger network design in a complex natural gas refinery. Nat. Gas Sci. Eng., *40*, 141–158. https://doi.org/10.1016/j.jngse.2017.02.001

[14] W.Faes, S.Lecompte, Z.Ahmed, J.Bael, R. Salenbien, K.Verbeken, M.Paepe(2019) Corrosion and corrosion prevention in heat exchangers. Corros. Rev., *37*(2), 131–155. https://doi.org/10.1515/corrrev-2018-0054.

[15] M.Ali, A.Ul-Hamid, T.Khan, A.Bake, H.Butt, O. Bamidele, A.Saeed (2021) Corrosion-related failures in heat exchangers.Corros. Rev., *39*(6), 519–546. https://doi.org/10.1515/corrrev-2020-0073

[16] J.Stringer (2004) High temperature corrosion issues in energy-related systems. Mater.,*7*, 01–19. https://doi.org/10.1590/S1516-14392004000100002

[17] K.Li, Y.Zeng (2022) Corrosion of heat exchanger materials in co-combustion thermal power plants. Renew. Sust.Energ.Rev, *161*, 112328. https://doi.org/10.1016/j.rser.2022.112328

[18] J.Kaufman (2019) Corrosion of Aluminum and Aluminum Alloys. In K. Anderson, J. Weritz, & J. G. Kaufman (Eds.), *Properties and Selection of Aluminum Alloys* (pp. 96–129) .ASM International. https://doi.org/10.31399/asm.hb.v02b.a0006546.

[19] S.Addepalli, D.Eiroa, S.Lieotrakool, A-L.François, J.Guisset, D.Sanjaime, M.Kazarian, J.Duda, R.Roy, P.Phillips (2015) Degradation Study of Heat Exchangers. *ProcediaCIRP*, *38*, 137–142. https://doi.org/10.1016/j.procir.2015.07.057

[20] C.Penot, D.Martelo, S.Paul (2023) Corrosion and Scaling in Geothermal Heat Exchangers. Appl. Sci.*13*(20), Article 20. https://doi.org/10.3390/app132011549.

[21] G.khan, S.Newaz, W..Basirun, H.Ali, F.Faraj, G.Khan (2015) Application of Natural Product Extracts as Green Corrosion Inhibitors for Metals and Alloys in Acid Pickling Processes-A review. Int. J. Electrochem. 10(8), 6120–6134. https://doi.org/10.1016/S1452-3981(23)06707-X

[22] J-W.Lee, W.Hwang (2018) Fabrication of a superhydrophobic surface with fungus-cleaning properties on brazed aluminum for industrial application in heat exchangers. Appl. Surf. Sci, *442*, 461–466.
https://doi.org/10.1016/j.apsusc.2018.02.170

[23] R.Naderi, M.Fedel, T.Urios, M.Poelman, M-G.Olivier, F.Deflorian (2013) Optimization ofsilane sol–gel coatings for the protection of aluminium components of heat exchangers. Surf. Interface Anal, *45*(10), 1457–1466.
https://doi.org/10.1002/sia.5249

[24] Y-S.Kim, I-J.Park, J-G.Kim (2019) Simulation Approach for Cathodic Protection Prediction of Aluminum Fin-Tube Heat Exchanger Using Boundary Element Method.*MTL*, *9*(3), Article 3. https://doi.org/10.3390/met9030376

[25] A.Patel (2023) Heat Exchanger Materials and Coatings: Innovations for Improved Heat Transfer and Durability. Int. J. Eng. Res. Appl*s*, *13*, 131–142. https://doi.org/10.9790/9622-1309131142

[26] I.Obot, A.Meroufel, I.Onyeachu, A.Alenazi, A.Sorour (2019) Corrosion inhibitors for acid cleaning of desalination heat exchangers: Progress, challenges and future perspectives. J. Mol. Liq., *296*, 111760. https://doi.org/10.1016/j.molliq.2019.111760

[27] I.Onyeachu, M.Solomon, S.Umoren, I.Obot, A.Sorour (2020) Corrosion inhibition effect of a benzimidazole derivative on heat exchanger tubing materials during acid cleaning of multistage flash desalination plants. *Desalination*, *479*, 114283. https://doi.org/10.1016/j.desal.2019.114283

[28] H.Assad, A.Thakur, A.Bharmal, S.Sharma, R.Ganjoo, S.Kaya (2022) 2 Corrosion inhibitors: Fundamental concepts and selection metrics. In *2 Corrosion inhibitors: Fundamental concepts and selection metrics* (pp. 19–50). De Gruyter. https://doi.org/10.1515/9783110760583-002

[29] S.Abo El-Enin, A.Amin (2020) Review of Corrosion Inhibitors for Industrial Applications.3, 127–145.

[30] M.Chigondo, F.Chigondo (2016) Recent Natural Corrosion Inhibitors for Mild Steel: An Overview. J. Chem, *2016*, 6208937. https://doi.org/10.1155/2016/6208937

[31] Z.Shang, J.Zhu (2021) Overview on plant extracts as green corrosion inhibitors in the oil and gas fields. J. Mater. Res. Technol., *15*, 5078–5094. https://doi.org/10.1016/j.jmrt.2021.10.095

[32] R.Haldhar, D.Prasad, I.Bahadur, O.Dagdag, S.Kaya, D.Verma, S.Kim (2021) Investigation of plant waste as a renewable biomass source to develop efficient, economical and eco-friendly corrosion inhibitor. J. Mol. Liq., *335*, 116184. https://doi.org/10.1016/j.molliq.2021.116184

[33] A.Thakur, H.Assad, S.Kaya, A.Kumar (2022) Chapter17—Plant extracts as environmentally sustainable corrosion inhibitors II. In L. Guo, C. Verma, & D. Zhang (Eds.), *Eco-Friendly Corrosion Inhibitors* (pp. 283–310). Elsevier. https://doi.org/10.1016/B978-0-323-91176-4.00017-9

[34] C.Verma, H.Ebenso, I.Bahadur, M.Quraishi (2018) An overview on plant extracts as environmental sustainable and green corrosion inhibitors for metals and alloys in aggressive corrosive media. J. Mol. Liq., *266*, 577–590. https://doi.org/10.1016/j.molliq.2018.06.110.

[35] C.Verma, E.Ebenso, M.Quraishi (2019) Alkaloids as green and environmental benign corrosion inhibitors: An overview. Int. J. Corros. Scale Inhib.,*8*(3), 512–528. https://doi.org/10.17675/2305-6894-2019-8-3-3

[36] M.Shamsuzzaman, K.Kalaiselvi, M.Prabakaran (2021) Evaluation of Antioxidant and Anticorrosive Activities of Ceriopstagal Plant Extract. Appl. Sci., *11*(21), Article 21. https://doi.org/10.3390/app112110150.

[37] A.Rahim, J.Kassim (2008) Recent Development of Vegetal Tannins in Corrosion Protection of Iron and Steel. Recent Pat.Mater. Sci., *1*(3), 223–231.

[38] Y.Shirmohammadli, D.Efhamisisi, A.Pizzi (2018) Tannins as a sustainable raw material for green chemistry: A review. Ind Crop Prod, *126*, 316–332. https://doi.org/10.1016/j.indcrop.2018.10.034.

[39] A.Pal, R.Sarkar, K.Karmakar, M.Mondal, B.Saha (2022). Surfactant as an anti-corrosive agent: A review. *Tenside Surfactants Detergents*, *59*(5), 363–372. https://doi.org/10.1515/tsd-2022-2434

[40] K.Ajijolakewu, A.Ayoola, T.Agbabiaka, F.Zakariyah, N.Ahmed, O.Oyedele, A.Sani (2021) A review of the ethnomedicinal, antimicrobial, and phytochemical properties of Musa paradisiaca (plantain). Bull. Natl. Res. Cent. *45*(1), 86. https://doi.org/10.1186/s42269-021-00549-3.

[41] B.Oyeyinka, A.Afolayan (2019) Comparative Evaluation of the Nutritive, Mineral, and Antinutritive Composition of Musa sinensis L. (Banana) and Musa paradisiaca L. (Plantain) Fruit Compartments. *Plants*, *8*(12), Article 12. https://doi.org/10.3390/plants8120598.

[42] S.Akinyemi, I.Aiyelaagbe, E.Akyeampong (2010) Plantain (Musa Spp.) Cultivation In Nigeria: A Review of Its Production, Marketing And Research In the Last Two Decades. *Acta Horticulturae*, *879*, 211–218.

https://doi.org/10.17660/ActaHortic.2010.879.19.

[43] S.Uzairu, M.Kano (2021) Assessment of phytochemical and mineral composition of unripe and ripe plantain (Musa paradisiaca) peels. Afr. j. food sci., *15*(3), 107–112. https://doi.org/10.5897/AJFS2017.1680/

[44] I.Ekeke, S.Umosah, A.Nkwocha (2021) *Musa Paradisiaca*(Plantain) Stem Sap Extract as a Potential Corrosion Inhibitor on Mild Steel in Acid Medium. Int. J. Innov. Sci. Res. Technol*., 6 (12), 659 - 664.*

[45] K.Amutha, U.Selvakumari (2016) Wound healing activity of methanolic stem extract of Musa paradisiaca Linn. (Banana) in Wistar albino rats. Int. Wound J., *13*(5), 763. https://doi.org/10.1111/iwj.12371

[46] E.Ituen, O.Akaranta, A.James (2016) Evaluation of performance of corrosion inhibitors using adsorption isotherm models: An overview. Am. Chem. Sci. J.. https://doi.org/10.9734/ACSJ/2016/28976

[47] S.Mitra, N.Sarkar, A.Barik (2017) Long-chain alkanes and fatty acids from Ludwigia octovalvis weed leaf surface waxes as short-range attractant and ovipositional stimulant to Alticacyanea (Weber) (Coleoptera: Chrysomelidae). B. Entomol. Res. *107*(3), 391–400. https://doi.org/10.1017/S0007485316001012.

[48] P.Dohare, K.Ansari, M.Quraishi, I.Obot (2017) Pyranpyrazole derivatives as novel corrosion inhibitors for mild steel useful for industrial pickling process Experimental and Quantum Chemical study. In Y.Qiang, S.Zhang , B.Tan, S.Chen (2017) Evaluation of Ginkgo leaf extract as an eco-friendly corrosion inhibitor of X70 steel in HCl solution. Corrs. Sci., 133, 6 – 16. https://doi.org/10.1016/j.corsci.2018.01.008

[49] V.Banu, S.Rajendran, S.Abuthahir (2017). International Journal of Chemical Concepts Corrosion Inhibition by Self-assembling Nano films of Tween 60 on Mild steel surface. International Journal of Chemical Concepts, *03*, 161–173.

[50] J.Smith, S.Breakspear, S.Campbell (2003) AFM in surface finishing: Part II. Surface roughness. Trans. Inst. Met. Finish.,*81*, B55–B58. https://doi.org/10.1080/00202967.2003.11871499

IZVOD

EKSTRAKT SOKA STABLJIKE *Musa Paradisiaca* KAO INHIBITOR KOROZIJE ZA ZAŠTITU ALUMINIJUMA U KISELOJ SREDINI

Ova studija istražuje efikasnost ekstrakta stabljike Musa paradisiaca (MPSSE) kao zelenog inhibitora korozije za aluminijum u hlorovodoničnom okruženju. Gasna hromatografija-masena spektroskopija (GC-MS) identifikovala je jedinjenja u ekstraktu. Potencijal inhibicije korozije je procenjen gravimetrijskom analizom (merenja gubitka težine) i spektroskopijom elektrohemijske impedanse (EIS). Analiza površine je sprovedena korišćenjem mikroskopije atomske sile (AFM) da bi se ispitala morfologija površine aluminijuma pre i posle tretmana. Studije izoterme adsorpcije su sprovedene da bi se razumeo mehanizam interakcije između ekstrakta i površine aluminijuma, koristeći Langmuir, Temkin, Frumkin i Freundlich izoterme. Rezultati pokazuju da ekstrakt pokazuje potencijal inhibicije korozije. GC-MS analiza identifikovala je jedinjenja kao što su dugolančani alkani, estri ftalne kiseline i fluorovana jedinjenja, koja doprinose otpornosti na koroziju formiranjem zaštitnih barijera na metalnim površinama. Gravimetrijska analiza je pokazala da je ekstrakt, posebno pri koncentraciji od 20 V/V%, postigao efikasnost inhibicije do 90,73% tokom 30 dana, značajno smanjujući gubitak težine i stope korozije. Studije adsorpcije su otkrile snažno pridržavanje Temkin Isotherm modela, što sugeriše efikasnu adsorpciju ekstrakta na površini aluminijuma. Mikroskopija atomske sile pokazala je smanjenje hrapavosti površine sa povećanjem koncentracije ekstrakta, potvrđujući zaštitni efekat inhibitora. Spektroskopija elektrohemijske impedanse pokazala je veću otpornost na prenos naelektrisanja i izraženo induktivno ponašanje sa inhibitorom, što ukazuje na formiranje zaštitnog sloja na aluminijumu. Nalazi ističu potencijal MPSSE-a kao ekološki prihvatljive alternative za zaštitu od korozije u industrijskim aplikacijama.
Ključne reči: inhibitor korozije: gravimetrijska analiza; Musa paradisiaca; elektrohemijska impedansna spektroskopija, ekološki prihvatljiva alternativa

Ifeyinwa C. Ekeke   https://orcid.org/0000-0002-8165-4449
Chukwuebuka E. Mgbemere https://orcid.org/0009-0004-5165-460X
Charity N. Nwanze   https://orcid.org/0000-0002-7585-9050
Chinedu F. Aniukwu   https://orcid.org/0009-0008-5376-7148
Chigoziri N. Njoku   https://orcid.org/0000-0002-8999-3912

Richa Sharma[*1], *Vijaylaxmi Mishra*[2] *, Supyar Kumawat*[1], *Gajanand Sharma*[3]

[1]*Department of Microbiology, Mahatma Gandhi University of Medical Sciences & Technology, Jaipur,* [2]*Department of Quality Control, Bharat Biotech International Pvt Limited, Hyderabad,* [3]*Department of Chemistry, MPS International, Jaipur*

Medicinal Importance of *Emblica officinalis* leaf extract nanoparticles and their biological evaluation

ABSTRACT

Green Synthesis of Nanoparticles is a novel field of nanotechnology that outperforms both biological and chemical approaches in terms of biocompatibility, cost-efficiency, scalability and environmental friendliness. Bacteria, fungi, plant and algae have lately been used to produce metals and metal oxide nanoparticles as an alternate method. In the present study, the green synthesis of Silver and copper nanoparticles was carried out using leaf extract of Emblica officinalis as a reducing agent and their antibacterial activity against human pathogens. Biosynthesis of nanoparticles were carried out using methanolic leaves extract of Emblica officinalis. Nanoparticles were characterized by UV-Visible Spectroscopy, X-ray Diffraction patterns(XRD), Scanning Electron Microscopy (SEM) and Transmission Electron Microscopy (TEM). These biogenic particles were tested for antimicrobial activity by disc diffusion method against Escherichia coli & Staphylococcus aureus. Biosynthesized nanoparticles showed potent biological activity and effective radicals scavenging activity. Methanolic leaf extract of Emblica officinalis acts as an excellent capping agent for the formation of silver & copper nanoparticles and demonstrates immense biological activities. Hence, these particles can be used as antibacterial, antioxidant as well as cytotoxic agent in treating many medical complications. It can be concluded that the silver and copper nanoparticles constitute an effective antimicrobial agent against common pathogenic bacteria. This could be a significant achievement in contending with many dynamic pathogens.
Keywords: *Nanoparticles, Green synthesis**, XRD, Emblica officinalis, Biological agents*

1. INTRODUCTION

Green particles is the ideal approach to minimize the effectively of nanomaterial manufacturing and application while also reducing the risk of problems associated with other methods [1]. Biogenic nanoparticles have potential applications and have gained considerable interest in different fields such as biomedical filed, agriculture information technology, optical, environment, energy, and sensors [2]. These metals particles include Silver Copper Zinc and Iron [3]. Ultimately, our aim is to provide a strategy for "green" synthesis and associated components that will help researchers working in this area while also serving as a useful reference for readers interested in the subject in general [4]. Green synthesis methods utilize biological activity such as bacteria, algae, viruses, fungi and plants that are used for the

synthesis of nanoparticles are non-pathogenic in nature because they should not interfere with the application of synthesized nanoparticles [5]. Bacterial infections most illnesses caused by bacteria are associated with the consumption of infected fresh products. The U.S. Center for Disease Control and Prevention (CDC) estimates that forty-eight million people get sick from a food borne illness each year [6], meaning, that microbial pathogens are responsible for one of the leading causes of life-threatening illnesses around the world. Among the most common food borne disease-causing bacteria, in the United States, are *E. coli* and *S. aureus* [7]. The consumption of food contaminated with these pathogenic bacteria could cause diarrhea, abdominal cramps and nausea. However, it could also lead to chronic illnesses such as cancer, brain and neural disorders, kidney and liver failure [8]. Hence, the attention has been focused on the production of novel nanoparticles-based on materials with enhanced antimicrobial properties[9]. It is well-known that Silver and copper is a potent antimicrobial agent whose properties have been exploited to inhibit bacterial growth and destroy the cellular structure of

*Corresponding author: Richa Sharma
E-mail: richa.phd.15@gmail.com

microorganisms [10]. In this paper, we present synthesis of silver and copper nanoparticles produced using a biological method. This synthesis route provides an enhanced alternative to conventional synthesis method as it leads to the formation of smaller and monodisperse metallic nanoparticles in a shorter time, thus decreasing the use and quantity of toxic reagents [11]. UV-Vis analyses were carried out to confirm the presence of Silver and Copper in the nanoparticles form. The NPs were characterized in terms of crystallinity through XRD, and morphology and nanoparticle size distribution by TEM and SEM [12].The antibacterial activity of the nanoparticles was tested against *E. coli* and *S. aureus*, all of which are well known to be responsible of the most common food borne illnesses [13]. To the best of our knowledge, the use of E. officinalis plant extract for greener synthesis of Copper & Silver nanoparticles has not been reported. Hence the present study was carried out to synthesize and characterize the copper & silver nanoparticles using E. officinalis plantextract. The aim of the present study is the green synthesis, characterization, and applications of plant-derived Nanoparticles using E. officinalis leaf extract as a reducing/stabilizing agent and to investigate their antibacterial activity against human pathogenic bacteria.

2. MATERIAL AND METHODS

Collection of Plant Material

Healthy, disease-free leaves of *E.officinalis* were collected during the month of August from Jaipur, Rajasthan India. The collected leaves were washed thoroughly in tap water and then in detergent water and were finally rinsed with distilled water until no foreignmaterial remained. The freshly cleaned leaves were left todry in sun light for approximately 10 days after dried leaves used for further experiment.

Preparation of Plant Extract

Take 500 gm of dried leaves were washed twice in tap water and rinsed thrice in distilled water. Then they were surface sterilized by 70% isopropyl alcohol for 1 min, cut into small pieces, dried in the micro-oven, and ground into powder using an electronic blender. About 100 g of leaf powder material was uniformly packed into a thimble and run in soxhlet extractor. It was extracted with methanol for the period of about 5–6 cycles. After that extracts were filtered with the help of Whatman No. 1 filter paper. The filtrates were then evaporated under reduced pressure and dried using a rotary evaporator at 55ºC. Then the extract was kept in refrigerator at 4ºC for future experiments [14].

Synthesis of Silver and Copper oxide Nanoparticles

For reduction of silver ions, 10 ml of collected filtrate was treated with 90 ml of silver nitrate aqueous solution (21 gm of AgNO3 powder in 125 ml of Milli Q water) and incubated at room temperature for 10 mins. Similarly for reduction of copper ions, 15 ml of collected filtrate was treated with 85 ml of copper sulphate aqueous solution (21 gm of $CuSO_4$ powder in 125 ml of Milli Q water) and incubated at room temperature for 10 mins. After 8 hours of incubation, the solution was centrifuged with 12,000 rpm for 20 min, and their pellets were redispersed in sterile distilled water. The centrifugation and redispersion were repeated three times to ensure the complete separation of nanoparticles. After drying, purified nanoparticles were resuspended in de-ionized water and stored in a freezer for further study [15].

Characterization of Nanoparticles

Purified nanoparticles were characterized for their morphology using a UV-Visible Spectroscopy, ZEISS EVO series Scanning Electron Microscopy model EVO-50 (SEM), IIT Delhi, Philips CM200 model of Transmission Electron Microscopy and X-Ray Diffraction (XRD) Rigaku Miniflex 600 model [16].

Antibacterial Activity

Copper and silver oxide nanoparticles synthesized using *E. officinalis*leaves extract were tested for antimicrobial activity by agar well diffusion method against different pathogenic microorganisms *E. coli* and *S. aureus*. Each strain was swabbed uniformly onto the individual plates using sterile cotton swabs. The sterile disc approximately 6mm in diameter of Whatman filter paper discs were prepared by applying 50µg/ml and 100µg/ml of synthesized nanoparticles for bacterial cultures and also applying for Standard antibiotics streptomycin sulphate. The disc was dried in hot air oven until it gets fully dry. The pure cultures of bacteria were subculture on Muller Hinton Agar. The agar suspension is poured into sterile petri-plates and allowed to solidify. Than the pathogenic bacterial strains *E. coli* and *S. aureus* fresh overnight cultures were spreaded evenly over the entire surface of the plate by swabbing in three directions.The sterile discs so prepared were kept in the centre of all petri plates after they were fully dried and incubated at 37°C for bacterial cultures. The standard antibiotic discs Streptomycin sulphate purchases from CDH (laboratory reagent) New Delhi were used. The activity was clearly visible after 24-48 hrs. for bacterial cultures. The zone of inhibition was noted for all the petri plates [17].

3. RESULTS AND DISCUSSION

In the present study, *E. Officinalis* leaf methanolic extract is used to produce silver and copper oxide nanoparticles. The color change from green to dark brown and the absorbance peak at about 439 nm indicated the formation of nano-particles. Reduction is followed by an immediate change in colour from light brown to black and change in pH of the solution. On mixing, E. officinalisleaf methanolic extract with the aqueous $AgNO_3$, solution and $FeCl_3$, it changed the color of the solution immediately and reducing the pH, which indicates the formation of silver and copper nanoparticles. It was observed that the pH changed from high acidic to low acidic. For reduction of copper ions, 15 ml of collected filtrate was treated with 85 ml of copper sulphate aqueous solution (21 gm of $CuSO_4$ powder in 125 ml of Milli Q water) and incubated at room temperature for 10 min, resulting in the formation of sea green to dark navy brown color indicating the synthesis of silver nanoparticles. From the leaf extract of *Eugenia jambolana,* silver nanoparticles synthesis was carried out and their phytochemical screening was evaluated [18]. Earlier, reports are available regarding the formation of AgNPs and their biological applications from *Syzygium cumini* [19] *Eugenia caryophyllata* [20]. From the leaf extract of *Eugenia uniflora,* silver nanoparticle formation was carried out and their antibacterial and antidiabetic potential were evaluated [21]. It is essential that these NPs be precisely and thoroughly chara-cterized in order to ensure reproducibility in their production, biological activity, and safety. For this purpose, a wide range of physicochemical methods are used to very precisely characterized the synthesized NPs including ultraviolet-visible spectroscopy, Fourier transform infrared spectroscopy (FTIR), attenuated total reflection (ATR), Raman spectroscopy, photoluminescence analysis (PL), dynamic light scattering (DLS), UV-visible diffuse reflectance spectroscopy (UV-DRS), transmission electron microscopy (TEM), scanning electron microscopy (SEM), atomic force micro-scopy (AFM), field emission scanning electron microscopy (FE-SEM), X-ray diffractometer (XRD), X-ray photoelectron microscopy (XPS), energy dispersion analysis of X-ray (EDAX), thermal gravimetric differential thermal analysis (TG-DTA), or nuclear magnetic resonance (NMR) [22-24].

UV-Vis Spectroscopy Analysis

Formation and stability of silver and copper oxide nanoparticles in sterile distilled water is conformed using UV-Vis spectroscopy in a range of wavelength from 300nm to 800nm as shown in Figure 1. The synthesis of silver and copper oxide nanoparticles of the surface Plasmon resonance of silver occurs at 331nm and 451nm where as copper wavelength showed 310nm and 561nm, steadily increasing with the time of reaction without much change in the peak wavelength. In this study, after mixing of extract and silver nitrate solutions a color change of extract was observed over the progression of time which may be due to the reduction of the silver ions leading to the excitation of Surface Plasmon Resonance (SPR) of the AgNPs [25]. To confirm this, UV spectra analysis was carried out and a peak was observed at 451nm & 561nm of silver & copper nanoparticles which showed a stable range for nanoparticles formation. In *Syzygium cumini* the UV spectra of synthesized nanoparticles was observed at~450 nm with particle size 3.5 nm from the XRD analysis [26] and also in Eugenia unifora UV spectra of synthesized nanoparticles was observed at 44 nm having its particle size was ranging from 25 to 50 nm. [27]

X-ray diffraction pattern (XRD) Analysis

X-ray diffraction pattern (XRD) was recorded for the synthesized Silver Nanoparticles and Copper Nanoparticles. Three distinct diffraction peaks at 35.04°, 43.23°, and 64.37° were indexed with the planes (111), (200), and (220) for the face-centered cubic silver as per (20). The X-ray diffraction pattern of as prepared copper nanoparticles is shown in Figure 2. Three peaks are observed at 2θ values of 39.46°, 45.65° and 65.73° and indexed as (111), (200) and (220) respectively, which confirmed the monophasic nature of pure copper with face centered cubic symmetry. The peaks are broad with fair intensity indicating the nanocrystalline nature of copper powder. The well resolved and intense XRD pattern clearly showed that the Ag NPs formed by the reduction of Ag+ ions using *Emblicaofficinalis* leaf extract are crystalline in nature. Similar results were reported for Silver Nanoparticles in the literature [14-17, 28, 32-35]. The low intense peak at 77.34 belongs to (311) plane [28]. The result indicated that the formation of a typical monoclinic structure for all weight fraction of copper oxide & iron oxide nanoparticles. Moreover, sharp peaks confirmed CuO Nps is highly crystalline nature which is good agreement with (JCPDS card no. 801268 [29-30].
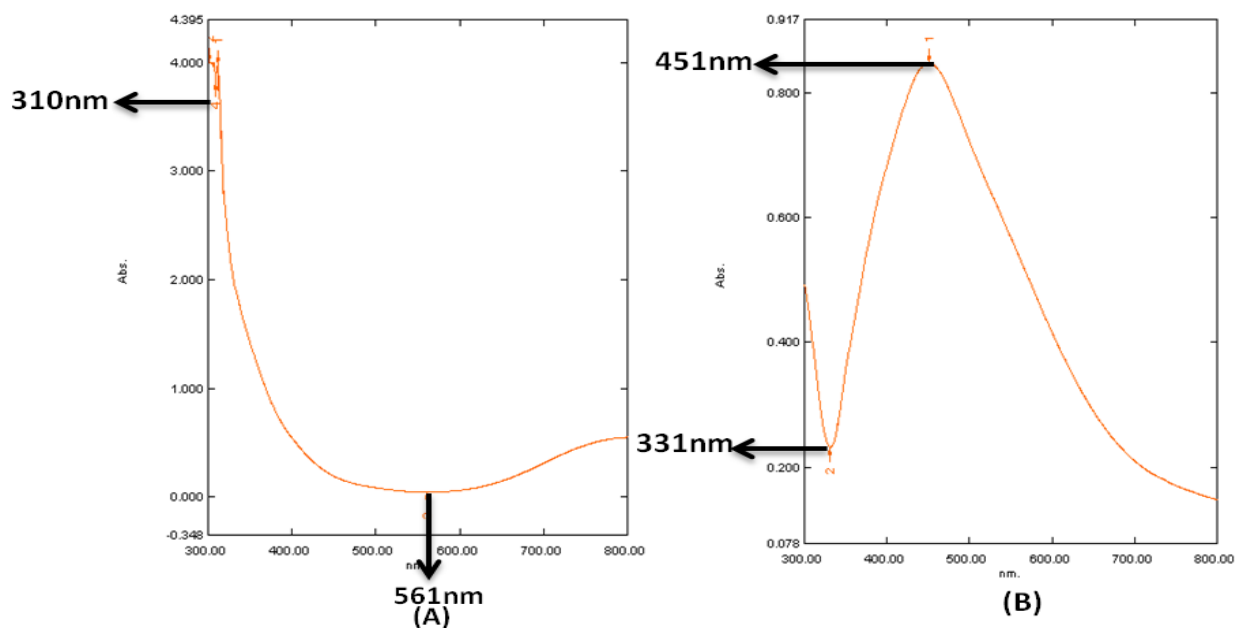
Figure 1. 1 UV – Vis absorption spectra of copper nanoparticles (A) silver nanoparticles sinthesized by biological method
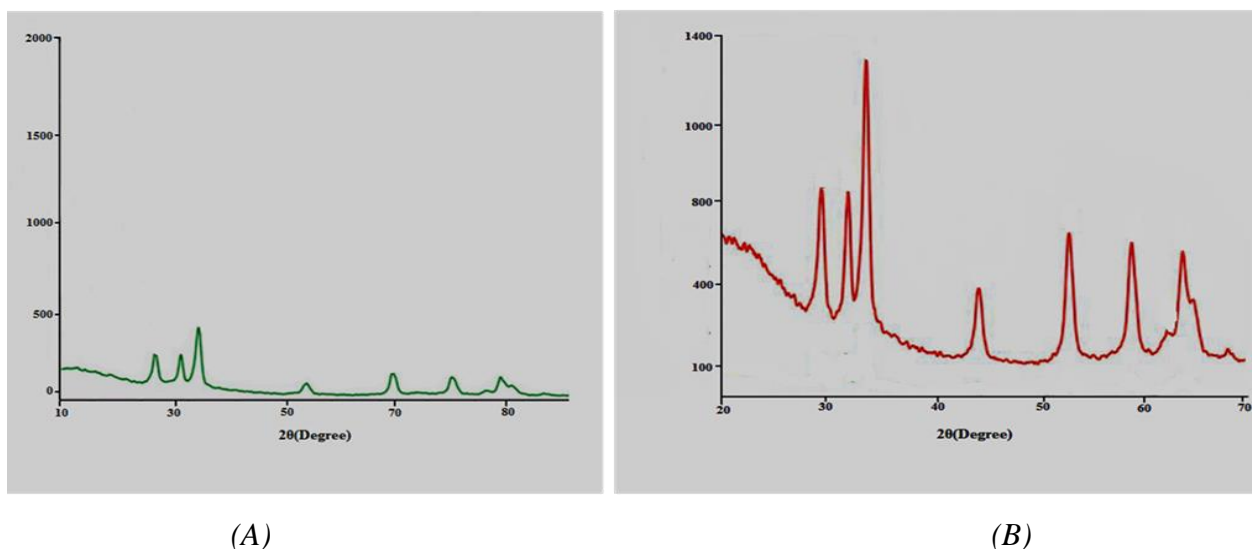

(A)   *(B)*

Figure 2. XRD patern of sinthesized copper nanoparticles (A) and silver nanoparticles (B)

Scanning Electron Microscopy Analysis

Scanning Electron Microscopy analysis was done using ZEISS EVO series SEM model EVO-50 machine. Thin films of synthesized and stabilized copper and silver nanoparticles powder was placed on carbon tape coated very small amount of the sample on the grid extra solution was removed using blotting paper and then the film on the SEM grid were allowed to dry by putting it under a mercury lamp for 15min. and sample was analyzed for morphology and size of the copper and silver nanoparticles. The SEM image showed relatively crystalline spherical shape nanoparticles formed with diameter range 50-1000 nm. SEM analysis shows uniformly distributed copper and silver nanoparticles on the surface of the cells, because those dispersing in the solution may also deposit on to the surface of the cells whereas they showed only change of particles surface due to increased permeability.

Transmission Electron Microscopy Analysis

Transmission Electron Microscopy analysis of copper and silver nanoparticles sample was dispersed in double distilled water a drop of thin dispersion is placed on a "staining mat", carbon tape coated grid is inserted in to the drop with the

coated side upwards. After about 15 minutes, the grid is removed and air dried. Then screened in Philips CM-200 model of transmission electron microscopy at an accelerating voltage of 80kv. The abstained nanoparticles are in the range of size 50-200nm and few particles are agglomerated; it is evident that there is variation in particles size and the average size estimated. It was found that the average size and distribution by taking micrograph from drop coated films of the copper and silver nanoparticles shows that most of them are crystalline spherical with the average size range from 200nm which correlated with the morphology of the nanoparticles which is highly variable, with crystalline spherical and occasionally triangular nanoparticles observed in micrograph. Moreover, the nanoparticles were not in direct contact even within the aggregates, indicating stabilization of the particles by a capping agent.

Analysis of Antimicrobial Activity

The antibacterialassay was performed against two bacterial pathogens using green-synthesized silver and copper nanoparticles. Silver and Copper oxide nanoparticles at concentration of 150µg/ml showed excellent antibacterial activity against S. aureus & E. coli. as compared to standard antibiotics Figure 3. In previous studies, it was reported that nanoparticles the green antibacterial synthesized silver activity against Staphylococcus aureus, Escherichia coli, Proteus vulgaris showed the maximum inhibition of bacterial zone.Silver & Copper Nanoparticles exhibit a high antibacterial effect due to their well developed surface which provides the maximum contact with the environment. Furthermore, toxicity is presumed to be size and shape dependent because small size of nanoparticles may pass through cell membranes. Insides a bacterium, nanoparticles can interact with DNA, thus losing its ability to replicate which may lead to the cell death. Green synthesized nanoparticles also have the more effective antimicrobial zone inhibition of the pathogens. To enhance the antimicrobial activity of the leaf extract we have tried to prepare AgNPs from the extract to access the effect of the nanoparticles, we have used it to inhibit the growth of biofilms by S. aureus. As it has been seen that nanomaterial is better at combating microbes than normal crude extracts, our present investigation will help evaluate the antimicrobial effect of Emblica officinalis AgNPs. Adhesion or attachment of microorganisms to a substrate is the first step towards colonization and this strategy has been used for microbial biofilm production [31]. In this study, a new approach was undertaken by synthesizing nanoparticles from biomaterial and using them against biofilm-producing micro-organisms to test their effects on them. Silver and Copper oxide nanoparticles synthesized at various concentrations showed higher antimicrobial activity as compared to standard antibiotics (Table 1 & 2).

The reason could be that the smaller size of particles which lead to increased membrane permeability and cell destruction.. The zone of inhibition increases with increasing concentration of silver and copper nanoparticles as the nano-particles bind with cytoplasmic membrane and killed the bacterial cell. As compare to copper nanoparticles, electrostatic attraction of silver nanoparticles causes damage of bacterial cell membrane to the formation of pits on the surface, and these structural changes take place due to cell expiration [32-35]. Previous studies have demon-strated the antimicrobial effect of iron oxide nanoparticles. Naseem and Farrukh evaluated the antimicrobial efficiency of IONPs by five different plants [36]. They observed that the iron oxide nanoparticles synthesized via Lawsonia inermis and Gardenia jasminoides have good antimicrobial effect against Salmonella enterica, Proteus mirabilis, Escherichia coli and Staphylococcus aureus.Our results are in agreement with Chifiriuc et al (2012) who reported Fe3O4 nanoparticles covered with Rosmarinus officinalis essential oil had strong inhibitory activity on biofilm-forming C.tropicalis and C. albicans [37]. The present results coincides with Beher etal who reported ZnO and CuO NPs had best antibacterial behavior against both Gram-positive and Gram-negative bacteria compared with Fe2O3 NP. The antimicrobial activity of the IONPs closely correlates to the oxidative stress generated by reactive oxygen species (ROS). ROS including hydrogen peroxide, superoxide radicals (O2–), hydroxyl radicals (–OH) and singlet oxygen could cause damage to DNA and proteins in pathogenic organisms such as bacteria and fungi [38].Silver oxide and Copper oxide nanoparticles interfere with the bacterial cell membrane and bind with mesosome cell organelle and after that reduce the mesosomal function and increase the ROS generation. Nanoparticles interact with thiol groups in protein which induced the inactivation of the bacterial protein synthesis as well as DNA replication [39-40]. Similarly, oxygen associates with silver and copper reacts with the sulfhydryl (−S-H) groups on cell wall to remove the hydrogen atoms causing the sulfur atoms to form an R-S-S-R bond, blocked the respiration, and causing the lethal effect of bacterial cells [41]. Nanoparticles naturally interact with the membrane of bacteria

and disrupt the membrane integrity; silver ions and copper ions bind to sulfur, oxygen, and nitrogen of essential biological molecules and inhibit the bacterial growth.

*Table 1. Screening of Silver nanoparticles against bacterial strains tested*

Bacterial cultures	Silver nanoparticles			Streptomycin sulphate		
	50 μg/ml	100 μg/ml	150 μg/ml	50μg/ml	100 μg/ml	150 μg/ml
Staphylococcus aureus	20 mm	32mm	40mm	18mm	27mm	37 mm
Escherichia coli	22 mm	37 mm	45mm	15mm	30mm	35 mm

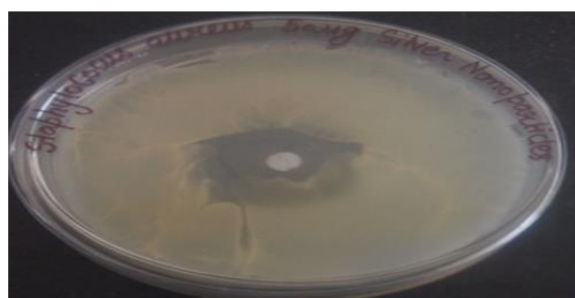*Table 2. Screening of Copper nanoparticles against bacterial strains tested*

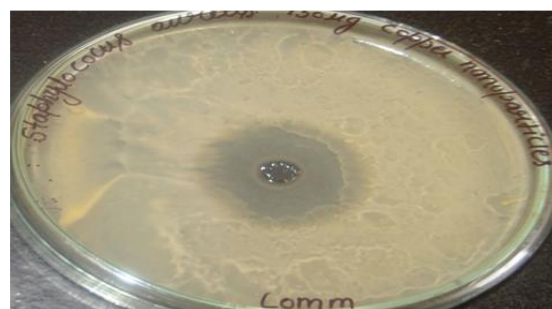| Bacterial cultures	Copper nanoparticles			Streptomycin sulphate		
	50μg/ml	100μg/ml	150μg/ml	50μg/ml	100μg/ml	150μg/ml
Staphylococcus aureus	22 mm	34 mm	46mm	18mm	27mm	37 mm
Escherichia coli	25 mm	39 mm	49mm	15mm	30mm	35 mm
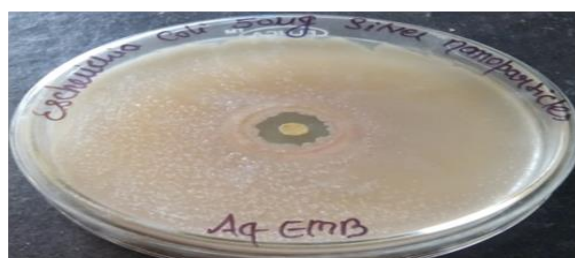
Escherichia Coli
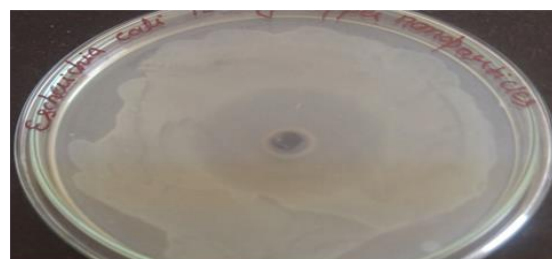
Escherichia Coli

Stephylococus aureus

Stephylococus aureus

(A)   *(B)*

Figure 3. Antimicrobial activity studies on two selected bacteril culture against (A) silver nanoparticles (B) copper nanoparticles

4. CONCLUSIONS

The growing demand for green chemistry and nanotechnology has pushed for the development of green synthetic methods for the production of nanomaterials using plants, microbes and other natural resources. The silver and copper nanoparticles prepared from *E.officinalis* leaf extract were observed under UV–Vis Spectroscopy monitored at 451 nm & 561 nm and their crystallinity nature was confirmed from their XRD study. The antimicrobial activity depends upon the concentration of silver and copper nanoparticles to produce the most significant effects against the pathogenic bacterial growth. AgNPs are found to be very effective against biofilm production by bacteria. Toxicological studies are also required to eradicate any kind of intoxication in a mouse model or human being. Once the NP is found nontoxic or safe in vivo studies, the nanoparticles can be utilized for the treatment of various diseases such as diabetes, arthritis, hypertension, etc.

This green-synthesized method is rapid, facile, convenient, less time consuming, environmentally safe, and can be applied in a variety of existing applications. This plant leaf extract compounds can be extended to the synthesis of other metal and

metal oxide nanoparticles. This study springs a new approach for synthesizing nanoparticles from the leaves of *E. officinalis* which is found out to be inhibiting biofilm production and bacterial colonies can be a significant achievement in contending many dynamic pathogens. So, the present work can be considered an attempt to exploit the active principle present in the leaf of *E. officinalis* to cure various ailments.

Ethics approval

This article does not contain any studies with human participants performed by any of the authors.

5. REFERENCES

[1] H.M. Ahmed, A. Roy, M. Wahab, M. Ahmed, G. Othman-Qadir, B.H. Elesawy, T.B. Emran (2021) Applications of Nanomaterials in Agri food and Pharmaceutical Industry, J. Nano. 1472096, 1-10. doi:10.1155/j.jnano.2021.1472096.

[2] A.A Ahmed, H. Hamzah and M. Maaroof (2018) Analyzing formation of silver nanoparticles from the filamentous fungus *Fusarium oxysporum* and their antimicrobial activity, Turk. J. Biol. 42, 54-62. doi:10.3906/biy-1710-2.

[3] Malavi, N. Karimi (2018) Characterization, antibacterial, total antioxidant, scavenging, reducing power and ion chelating activities of green synthesized silver, copper and titanium dioxide nanoparticles using *Artemisia haussknechtii* leaf extract, Artif. Cells Nanomed. Biotech. 46, 2066-2081. doi: 10.1080/j.artcnb.21691401.2017.1408121.

[4] S. Arokiyaraj, V.D. Kumar, V. Elakya, T. Kamala, S.K. Park, M. Ragam, S. Vincent (2015) Biosynthesized silver nanoparticles using floral extract of Chrysanthemum indicum L. potential for malaria vector control, Environ. Sci. Pollut. Res. 22, 9759-9765. doi: 10.1007/j.espr.11356-015-4148-9 .

[5] M.S. Khan, S.S. Habib, A. Memic (2012) Antimicrobial activity of metal oxide nanoparticles against Gram-positive and Gram-negative bacteria: a comparative study, Int. J. Nanomed.7, 60001-60005.
doi.org/10.2147/IJN.S35347.

[6] Y.Y. Liu, Y. Wang, T.R. Walsh(2016) Emergence of plasmid-mediated colistin resistance mechanism MCR-1 in animals and human beings in China: a microbiological and molecular biological study, Lancet Infect Dis. 16, 161-168.

[7] T. Alam, R.A.A. Khan, A. Ali, H. Sher, Z. Ullah, M. Ali (2019) Biogenic synthesis of iron oxide nanoparticles via *Skimmia laureola* and their antibacterial efficacy against bacterial wilt pathogen *Ralstonia solanacearum*, Mater. Sci. Eng. 98, 101-108.doi: org/10.1016/j.msec.2018.12.117.

[8] T. Hayashida, M. Tsutsui, H. Kawakubo (2015) Comprehensive screening of genes resistant to an anticancer drug in esophageal squamous cell carcinoma, Int. J. Onco. 47, 867- 874. doi:10.3892/ijo.2015.3085.

[9] R. Singh, M.S. Smitha, S.P. Singh (2014) The role of nanotechnology in combating multi-drug resistant bacteria, J. Nano. Sci. Nano. Technol. 14, 4745-4756. doi:10.1166/j.jnsnt.2014.9527.

[10] L.P. Silva, A.P. Silveira, C.C. Bonatto, I.G. Reis, P.V. Milreu (2017) Nanostructures for Antimicrobial Therapy: Nanostructures in Therapeutic Medicine Series. Elsevier; Amsterdam, The Netherlands, Silver Nanoparticles as Antimicrobial Agents: Past, Present, and Future, Elsevier. 577-596.

[11] E.D. Cavassin, L.F. Figueiredo de, J.P. Otoch (2015) Comparison of methods to detect the in vitro activity of silver nanoparticles (AgNP) against multidrug resistant bacteria, J. Nanobiotechnology. 13-64.doi:10.1186/s12951-015-0120-6.

[12] K.S. Siddiqi, A. Husen, R.A.K. Rao (2018) A review on biosynthesis of silver nanoparticles and their biocidal properties, J. Nanobiotechno. 16, 1-28. doi:10.1186/j.jnabt.12951-018-0334-5.

[13] N.A. Al-Dhabi, A.K.M. Ghilan, G.A. Esmail, M.V. Arasu, V. Duraipandiyan, K. Ponmurugan (2019) Environmental friendly synthesis of silver nanomaterials from the promising *Streptomyces parvus* strain Al-Dhabi-91 recovered from the Saudi Arabian marine regions for antimicrobial and antioxidant properties, J. Photochem. Photobiol. 197-201. doi: 10.1016/j.jphotobiol.2019.111529.

[14] D.S. Balaji, S. Basavaraja, R. Deshpande, D.B. Mahesh, B.K. Prabhakar, A. Venkataraman (2009) Extracellular biosynthesis of functionalized silver nanoparticles by strains of *Cladosporium cladosporioides* fungus, Colloids Surf. Bio interfaces. 68, 88-92.
doi:10.1016/j.colsurfb.2008.09.022.

[15] M.J. Mehdipour Moghaddam, A.A. Mirbagheri, Z. Salehi, S.M. Habibzade (2015) Prevalence of class 1 integrons and extended spectrum beta lactamases among multi-drug resistant *Escherichia coli* isolates from north of Iran, Iran Biomed. J. 19, 233-239.
doi: 10.7508/j.ibj.2015.04.007.

[16] M.K. Swamy, K.M. Sudipta, K. Jayanta, S. Balasubramanya (2015) The green synthesis, characterization, and evaluation of the biological activities of silver nanoparticles synthesized from

Leptadenia reticulata leaf extract, Appl. Nano. sci. 5, 73-81.

doi:10.1007/j.jans13204-014-0293-6.

[17] J.L. Graves, M. Tajkarimi, Q. Cunningham, A. Campbell, H. Nonga, S.H. Harrison, J.E. Barrick (2015) Rapid evolution of silver nanoparticle resistance in *Escherichia coli*, Front. Genet. 5:42. doi.org/10.3389/fgene.2015.00042

[18] S.A. Khan, S. Shahid, B. Shahid, U. Fatima, S.A. Abbasi (2020) Green Synthesis of MnO Nanoparticles Using Abutilon indicum Leaf Extract for Biological, Photocatalytic, and Adsorption Activities, Biomole. 10, 785.

doi: 10.3390/biom10050785

[19] A.A. Alshehri, M.A. Malik (2020) Phytomediated Photo-Induced Green Synthesis of Silver Nano-particles Using Matricaria chamomilla L. and Its Catalytic Activity against Rhodamine, B. Biomole. 10, 1604. doi: 10.3390/biom10121604.

[20] R. Singh, C. Hano, G. Nath, B. Sharma (2021) Green Biosynthesis of Silver Nanoparticles Using Leaf Extract of Carissa carandas L. and Their Antioxidant and Antimicrobial Activity against Human Pathogenic Bacteria, Biomole.11, 299.

doi.org/10.3390/biom11020299

[21] A. Zaeem, S. Drouet, S. Anjum, R. Khurshid, M. Younas, J.P. Blondeau, D. Tungmunnithum, N. Giglioli-Guivarc'h, C. Hano, B.H. Abbasi, (2020) Effects of Biogenic Zinc Oxide Nanoparticles on Growth and Oxidative Stress Response in Flax Seedlings vs. In Vitro Cultures: A Comparative Analysis, Biomole.10, 918.

doi: 10.3390/biom10060918.

[22] M.A. Ansari, M. Murali, D. Prasad, M.A. Alzohairy, A. Almatroudi, M.N. Alomary, A.C. Udayashankar, S.B. Singh, S.M.M. Asiri, B.S. Ashwini (2020) Cinnamomum verum Bark Extract Mediated Green Synthesis of ZnO Nanoparticles and Their Antibacterial Potentiality, Biomole.10, 336.

doi: 10.3390/biom10020336

[23] K. Perveen, F.M. Husain, F.A. Qais, A. Khan, S. Razak, T. Afsar, P. Alam, A.M. Almajwal, M.M.A. Abulmeaty (2021) Microwave-Assisted Rapid Green Synthesis of Gold Nanoparticles Using Seed Extract of Trachyspermum ammi: ROS Mediated Biofilm Inhibition and Anticancer Activity, Biomole.11, 197.

doi:10.3390/biom11020197

[24] S. Mickymaray (2019) One-step Synthesis of Silver Nanoparticles Using Saudi Arabian Desert Seasonal Plant Sisymbrium irio and Antibacterial Activity Against Multidrug-Resistant Bacterial Strains, Biomole. 9, 662.

doi: 10.3390/biom9110662.

[25] P. Mulvaney (1996) Surface plasmon spectroscopy of nanosized metal particles, Langmuir,12, 788-800. doi.org/10.1021/la9502711.

[26] J.L. Banerjee (2011) Biosynthesis of silver nanoparticles from syzygium cumini (l.) seed extract and evaluation of their in vitro antioxidant activities. Digest J Nano Bio. 6, 961-968.

[27] G.K. Dugganaboyana, C.K. Eranna (2017) Green synthesis of silver nanoparticles by using Simarouba amara aubl. Fruit extract and their antioxidant and antibacterial activities, Int. J. Drug Deliv. Technol. 7, 137-145.

doi: : 10.25258/ijddt.v7i03.9557

[28] J. Carrola, V. Bastos, I. Jarak, R. Oliveira-Silva, E. Malheiro, A.L. Daniel-da-Silva, H. Oliveira, C. Santos, A.M. Gil, I.F. Duarte (2016) Metabolomics of silver nanoparticles toxicity in HaCaT cells: Structure–activity relationships and role of ionic silver and oxidative stress, Nanotoxicol. 10, 1105-1117. doi:10.1039/j.nt.2na00534d.

[29] P. Kumari, P.K.Panda, E.Jha, K.Kumari, K.Nisha, M.A.Mallick, S.K.Verma (2017) Mechanistic insight to ROS and apoptosis regulated cytotoxicity inferred by green synthesized CuO nanoparticles from Calotropis gigantea to embryonic zebrafish, Sci. Rep. 7, 16284.

[30] M.Ghashang,M.Kargar,M.R.Shafiee,S.S.Mansoor,A.Fazlinia,H. Esfandiari (2015) CuO nano-structures prepared in Rosmarinus officinalis leaves extract medium: efficient catalysts for the aqueous media preparation of dihydropyrano [3, 2-c] chromene derivatives. Recent Pat. Nanotechnol., 9 (3), 204-211. doi: 10.2174/1872210510999151126110657.

[31] N. Dror, M. Mandel, Z. Hazan, G. Lavie (2009) Advances in microbial biofilm prevention on indwelling medical devices with emphasis on usage of acoustic energy, Sensors (Basel).9, 2538–2554.

[32] E.Z. Gomaa (2017) Silver nanoparticles as an antimicrobial agent: A case study on *Staphylococcus aureus* and *Escherichia coli* as models for Gram-positive and Gram-negative bacteria, J. Gen. Appl. Microbiol. 63, 36-43.

doi:10.2323/jgam.2016.07.004 .

[33] G. Cheng, M. Dai, S. Ahmed, H. Hao, X. Wang, Z. Yuan (2016) Antimicrobial drugs in fighting against antimicrobial resistance, Front. Microbiol. 7, 461-470. doi:10.3389/fmicb.2016.00470.

[34] A. Abbaszadegan, Y. Ghahramani, A. Gholami, B. Hemmateenejad, S. Dorostkar, M. Nabavizadeh, H. Sharghi (2015) The Effect of Charge at the Surface of Silver Nanoparticles on Antimicrobial Activity against Gram-Positive and Gram-Negative Bacteria: A Preliminary Study, J. Nanomater. 7, 1-10. doi:10.1155/2015/720654.

[35] M. Mühling, A. Bradford, J.W. Readman, R.D. Somerfield, P.G.R.D Handy (2009) An investigation into the effects of silver nanoparticles on antibiotic resistance of naturally occurring bacteria in estuarine sediment, Mar Environ Res. 68, 278-283. doi: 10.1016/j.marenvres.2009.07.001 .

[36] T. Naseem, M.A. Farrukh (2015) Antibacterial activity of green synthesis of iron nanoparticles using Lawsonia inermis and Gardenia jasminoides leaves extract, J. Chem. 2015, 1-7.

doi:10.1155/j.chem.2015/912342.

[37] C. Chifiriuc, V. Grumezescu, A.M. Grumezescu (2012) Antifungal activity of chemotypes essential

oil from rosemary against *Candida albicans*, Nanoscale Res. Lett. 7, 1-7. doi:10.4236/ojst.2013.32031.

[38] S.S. Behera, J.K. Patra, K. Pramanik (2012) Characterization and Evaluation of Antibacterial Activities of Chemically Synthesized Iron Oxide Nanoparticles. World. J. Nano. Sci. & Eng. 2, 196-200. doi:10.4236/wjnse.2012.24026.

[39] M.S Aung, H. Zi, K.M. Newb (2016) Drug resistance and genetic characteristics of clinical isolates of *Staphylococci* in Myanmar: high prevalence of PVL among methicillin-susceptible *Staphylococcus aureus* belonging to various sequence types, New Microbes New Infect. 10, 58-65. doi:10.1016/j.nmni.2015.12.007.

[40] A. Kędziora, M. Speruda, E. Krzyżewska, J. Rybka, A. Łukowiak, G. Bugla-Płoskońska (2018). Similarities and differences between silver ions and silver in nanoforms as antibacterial agents, Int. J. Mol. Sci. 19, 432-444. doi:/10.3390/ijms19020444.

[41] N.Y. Lee, W.C. Ko, P.R. Hsueh (2019) Nanoparticles in the treatment of infections caused by multidrug-resistant organisms, Front. Pharmacol. 10, 1145-1153. doi:/10.3389/fphar.2019.01153.

IZVOD

LEKOVITI ZNAČAJ NANOČESTICA EKSTRAKTA LISTA *EMBLICA OFFICINALIS* I NJIHOVA BIOLOŠKA PROCENA

Zelena sinteza nanočestica je nova oblast nanotehnologije koja nadmašuje i biološke i hemijske pristupe u smislu biokompatibilnosti, ekonomičnosti, skalabilnosti i ekološke prihvatljivosti. Bakterije, gljive, biljke i alge se u poslednje vreme koriste za proizvodnju metala i nanočestica metalnih oksida kao alternativne metode. U ovoj studiji, zelena sinteza nanočestica srebra i bakra je sprovedena korišćenjem ekstrakta lista Emblica officinalis kao redukcionog agensa i njihove antibakterijske aktivnosti protiv ljudskih patogena. Preliminarna fitohemijska analiza metanolnog ekstrakta E.officinalis pokazala je prisustvo tanina, saponina, flavanoida i fenola, od kojih su flavonoidi i saponini najinhibitivniji prema svim patogenima. Emblica officinalis definitivno poseduje snažno antimikrobno dejstvo protiv bakterijskih patogena i može se koristiti u lečenju različitih bolesti izazvanih ovim organizmima. Biosinteza nanočestica je sprovedena korišćenjem metanolnog ekstrakta listova Emblica officinalis. Nanočestice su okarakterisane UV-vidljivom spektroskopijom, uzorcima difrakcije rendgenskih zraka (XRD), skenirajućom elektronskom mikroskopijom (SEM) i transmisijskom elektronskom mikroskopijom (TEM). Ove biogene čestice su testirane na antimikrobnu aktivnost metodom disk difuzije protiv Escherichia coli i Staphilococus aureus. Biosintetizovane nanočestice pokazale su snažnu biološku aktivnost i efikasnu aktivnost uklanjanja radikala. Metanolni ekstrakt lista Emblica officinalis deluje kao odlično sredstvo za zatvaranje za formiranje nanočestica srebra i bakra i pokazuje ogromne biološke aktivnosti. Stoga se ove čestice mogu koristiti kao antibakterijski, antioksidativni, kao i citotoksični agens u lečenju mnogih medicinskih komplikacija. Može se zaključiti da nanočestice srebra i bakra predstavljaju efikasan antimikrobni agens protiv uobičajenih patogenih bakterija.
Ključne reči: *nanočestice, Green sinteza, KSRD, Emblica officinalis, Biološki agensi.*

Dr.Richa Sharma: https://orcid.org/0000-0001-9747-0700
Dr.Vijaylaxmi Mishra: https://orcid.org/0000-0001-9129-104X
SupyarKumawat: https://orcid.org/0009-0006-6794-6804
Dr.Gajanand Sharma: https://orcid.org/0000-0003-3771-3197

*Nilavan Anitha[1], Joseph Ignatius Navis Karthika[2],
Micheal Velankanni Jeevitha Clara[1], Arockiam Roslin[1],
Arockiaraj Little Jewelcy[1], Susai Rajendran[1,3,]**

[1]*Corrosion Research Centre, Department of Chemistry, St Antony's College
of Arts and Sciences for Women, Dindigul, Tamil Nadu, India (Affiliated to
Mother Teresa Women's University, Kodaikanal), Tamil Nadu, India,
[2]Department of Chemistry, PSNA College of Engineering and Technology,
Dindigul, Tamil Nadu, India, [3]Centre for Nanoscience and Technology,
Pondicherry University, ChinnaKalapet, Kalapet, Puducherry, India*

Corrosion resistance of Ever Silver vessel in the presence of rasam-a light South Indian traditional soup

ABSTRACT

Food packaging serves purposes of food product safety and easy handling and transport by preventing chemical contamination and enhancing shelf life, which provides convenience for consumers. Various types of materials, including plastics, glass, metals, and papers and their composites, have been used for food packaging. However, owing to consumers' increased health awareness, the significance of transferring harmful materials from packaging materials into foods is of greater concern. In the present study corrosion resistance of Ever Silver vessel in the absence and presence of rasam recipe, a light South Indian traditional soup made with basic spices, ripe tomatoes, tamarind and herbs. AC impedance spectra have been used to measure the corrosion resistance. It is observed that the corrosion resistance of Ever Silver vessel increases in the presence of rasam recipe. This is due to the presence of various molecules present in the ingredients of rasam. So it is concluded that rasam recipe can be stored in Ever Silver vessel and also rasam can be served in Ever Silver vessel during dining.
Keywords: *Corrosion resistance, Ever Silver vessel, rasam, AC impedance spectra, electrochemical study*

1. INTRODUCTION

Food packaging systems have been widely studied [1-13]. Food packaging is a packaging system specifically designed for food and represents one of the most important aspects among the processes involved in the food industry, as it provides protection from chemical, biological and physical alterations [1]. The main goal of food packaging is to provide a practical means of protecting and delivering food goods at a reasonable cost while meeting the needs and expectations of both consumers and industries [1]. Additionally, current trends like sustainability, environmental impact reduction, and shelf-life extension have gradually become among the most important aspects in designing a packaging system [2].

History

Packaging of food products has seen a vast transformation in technology usage and application from the Stone Age to the industrial revolution:

Year	Description	Ref.
7000 BC	The adoption of pottery and glass which saw industrialization around 1500 BC.	[3]
1700s	The first manufacturing production of tinplate was introduced in England (1699) and in France (1720). Afterwards, the Dutch navy start to use such packaging to prolong the preservation of food products.[4]	[4]
1804	Nicolas Appert, in response to inquiries into extending the shelf life of food for the French Army, employed glass bottles along with thermal food treatment. Glass has been replaced by metal cans in this application. However, there is still an ongoing debate about who first introduced the use of tinplates as food packaging.	[4],5
1870	The use of paper board was launched and corrugated materials patented.	[6]
1880s	First cereal packaged in a folding box by Quaker Oats.	[7]
1890s	The crown cap for glass bottles was patented by William Painter.	[8]

1950s	The bag-in-box system was invented by American chemist William R. Scholle – initially for acid liquids, but quickly also used for food liquids.	
1960s	Development of the two-piece drawn and wall-ironed. Metal cans in the US, along with the ring-pull opener and the Tetra Brik Aseptic carton package.	[9]
1970s	The barcode system was introduced in the retail and manufacturing industry. PET plastic blow-mold bottle technology, which is widely used in the beverage industry, was introduced.	[10]
1990s	The application of digital printing on food packages became widely adopted.	
	Plastic packaging saw its inaugural use during World War II, even though materials employed in its manufacturing (such as cellulose nitrate, styrene and vinyl chloride) were discovered in the 1800s.	[11]

Food packaging alloys

There are several metals which have been used as food packaging materials including; aluminum (Al), stannous or tin (Sn), Sn free steel (SFS), and rustles steel (RS) commonly known as stainless steel. These metals provide hard food packaging such as cans and flexible food packaging in the form of foil and bags.

Various metals are commonly used in food packaging. Here are the main ones:

1. *Aluminum:* Aluminum is widely used for food packaging. It's used to make cans, as well as thin aluminum foils and coatings. Aluminum packaging is lightweight, corrosion-resistant, and easily recyclable.

2. *Steel:* Steel is primarily used to make rigid cans. These steel cans are commonly used for packaging food items. Steel cans are durable and provide good protection for the contents.

3. *Tinplate:* Tinplate, also known as tin-coated steel or electrolytic chromium-coated steel, is another metal used in food packaging. It's often used for items like cans and lids. Direct contact between the metal and food can be prevented by coating the metal with an organic polymer to maintain packaging integrity and food properties.

4. *Stainless Steel:* While less common, stainless steel is sometimes used for specific food packaging applications. It offers excellent durability and resistance to corrosion.

These metals play a crucial role in preserving food quality, safety, and shelf life.

Rasam recipe

Rasam is a light South Indian traditional soup made with basic spices, ripe tomatoes, tamarind and herbs. It is very soothing to the tummy and helps in digestion. Usually rasam recipe is kept in Ever Silver vessel and served Figure 1. The present work is undertaken to investigate the corrosion resistance of Ever Silver vessel in the absence and presence of rasam recipe. The corrosion resistance is measured by AC impedance spectra.

Figure 1 .Rasam RecipeinEver Silver vessel

2. EXPERIMENTAL METHOD

Ever SilverComposition

Ever Silver is an alloy of silver that consists of 92.5% pure silver and and 7.5% other metal, usually copper. The other metals in the alloy increase hardness, so the material will be durable. Ever silver was purchased in the vessel marts.

Preparationofrasamrecipe

The recipe was prepared in the usual way. Rasam a soup of spices is a traditional South Inian Food. It is traditionally prepared using tamarind juice as a base with the addition of Indian seasame oil, turmeric, tomato, chilly, pepper, garlic, cumin, curry leaves, mustard, coriander, asafoetida, sea salt and water. There are many ingredients such as tartaric acid, curcumin and many vitamins and amino acids present in the rasam soup

Electrochemicalstudy

ACimpedancespectra

A three-electrode cell assembly was used to record AC impedance spectra. Wehave taken the various test solutions like water and rasamin Ever Silver. AC impedance spectral studies were carried out in aCHI – Electrochemical works tation with impedance. The corrosion resistance of Ever Silver electrode immersed in various test solutions have been measured. A three – electrode cell assembly was used. The working electrode was Ever Silver electrode. A saturated calomel electrode (SCE) was the reference electrode and platinum was the counter electrode (Figure 2).
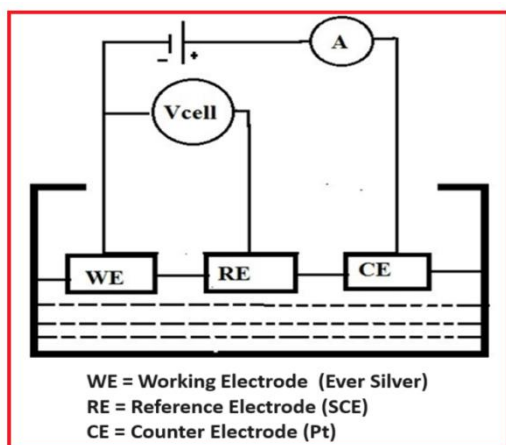
WE = Working Electrode (Ever Silver)
RE = Reference Electrode (SCE)
CE = Counter Electrode (Pt)

Figure 2. Three-electrode cell assembly

The real part (Z') and imaginary part (-Z'') of the cell impedance were measured in ohms at various frequencies. Values of the charge transfer resistance (R_t) and the double layer capacitance (C_{dl}), impedance value and phase angle were calculated from Nyquist plots and Bode plots.

3. RESULTS AND DISCUSSION

Ever Silver is popularly used for cookware, kitchen utensils and cutlery. Thisis because it is hardwearing, corrosion resistant and it doesnot affect the flavour of the food when used for food storage or production. Due to the resistance levels, foods with high acidity will not cause damage. Usually, students take many varieties rice and interesting recipes in stainless steel. In this project we have taken water and rasam recipe in a stainless steel to identify whether Ever Silver undergoes corrosion or not. We have undertaken AC impedance spectra study. They have been employed to investigate the corrosion resistance of Ever Silver electrode when it is immersed in various test solutions like water and rasam recipe.

Analysis of results of AC impedance Spectra [Electrochemical Impedance

Spectra (EIS)]

AC impedance spectra have been used to detect the formation of the film formed on the metal surface. If a protective film is formed, the charges transfer resistance (R_t) increases, impedance value increases, phase angle value increases and double layer capacitance (C_{dl}) value decreases.

The AC Impedance spectra of Ever silver electrode immersed in various solutions are shown in Figures 4, 5 (Nyquist), Figures 6, 7 (Bode plots) and Figures 8, 9 (Interactive 3D plot-log freq). The corrosion parameters are compared in Figure 10.

The AC Impedance parameters, namely, charge transfer resistance (R_t), impedance value, phase angle value and double layer capacitance (C_{dl}) are given in Table 1.

Tabje 1. Corrosion parameters of Ever Silver electrode immersed in various test solutions, obtained from AC Impedance spectra

System	Rt, Ohm.cm2	Cdl, F/cm2	Impedance, Log (Z/Ohm)	Phaseangle
Water	9.96	5.12×10^{-7}	1.518	0.1036
Rasam	47.10	1.08×10^{-7}	1.905	4.773
Observation	increases	decreases	increases	increases
Inference	Corrosion resistance increases	Corrosion resistance increases	Corrosion resistance increases	Corrosion resistance increases
Implication	Rasam recipe can be stored in Ever Silver vessels without any hesitation			

EIS (AC Impedance Spectra)

- Corrosion resistance Increases
- C_{dl} value Decreases
- Impedance value Increases
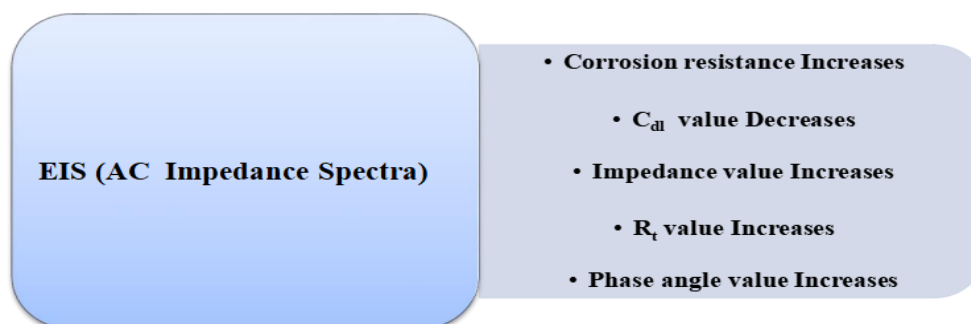- R_t value Increases
- Phase angle value Increases

Figure 3. Correlation among corrosion parameters of AC impedance spectra

Letusrecollect the principles of Acimpedance spectra and corrosion inhibition study. "Ifaprotective film is formed on the metal surface, thecharges transfer resistance (R_t) increases, impedance value increases, phase angle value increases and double layer capacitance (C_{dl}) value

decreases" Figure 3. Interesting conclusions are derived from Table 1. When Ever Silver electrode is immersed in water, the charge transfer resistance (R_t) is 9.96 Ohm.cm^2. Double layer capacitance (C_{dl}) value is 5.12 x 10^{-7} F/cm^2.
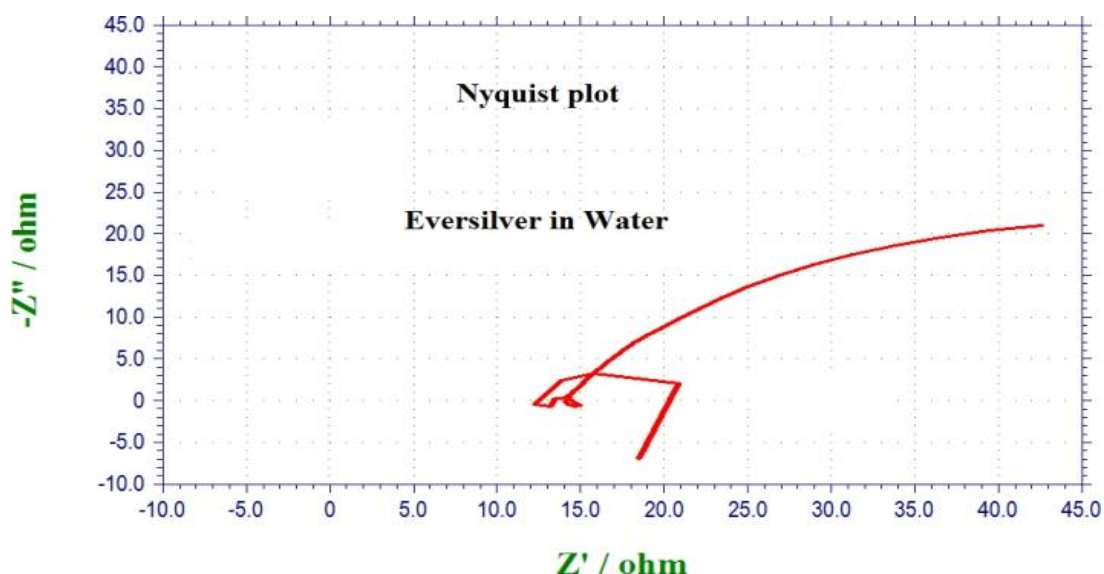

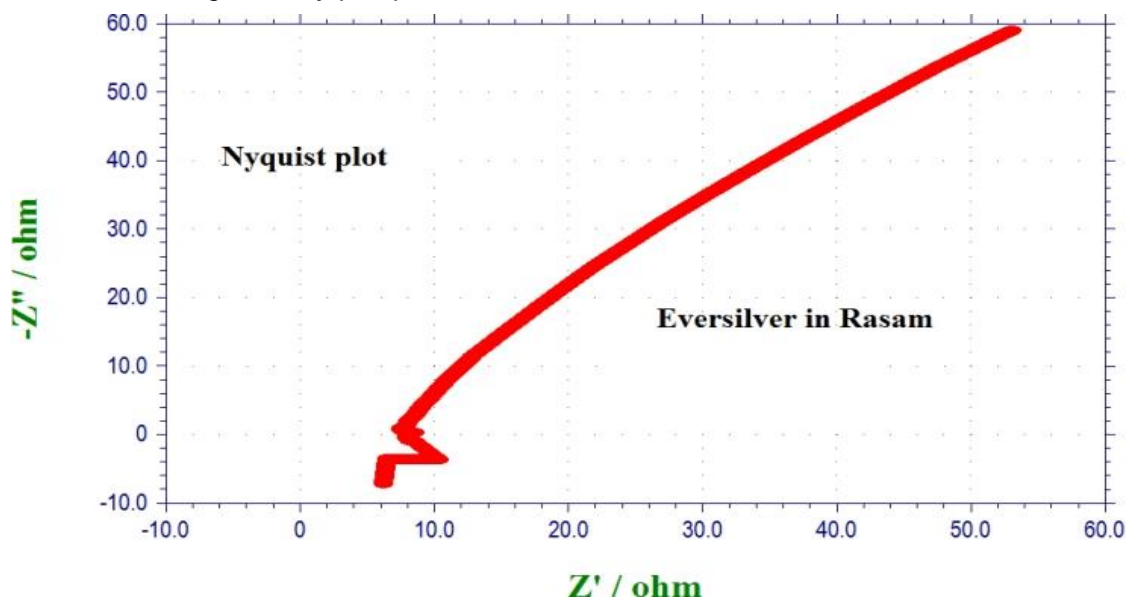*Figure 4. Nyquist plot of Ever Silver electrode immersed in Water*

Figure 5. Nyquist plot Ever Silver electrode immersed in Rasam system

When Ever Silver electrode is immersed in rasam system, the corrosion resistance of Ever Silver electrode increases. This is due to the adsorption of molecules of the ingredients present in rasam system. When Ever Silver is electrode immersed in rasam system the charge transfer resistance (R_t) increases to 47.103 Ohm.cm^2. Double layer capacitance (C_{dl}) value decreases to is1.0827x10^{-7}F/cm^2. Impedance value increases to 3.217 and phase angle increases to 5.678^0.

When Ever silver electrode is immersed in rasamsystem, the corrosion resistance ofEver silver electrode increases. This is due to the presence of molecules of the incredients introduced by the rasam system

Implication

Corrosion resistance of Ever Silvervessel increases, when it comes in contact with rasam system . This conclusion is drawn when compared with water system used..
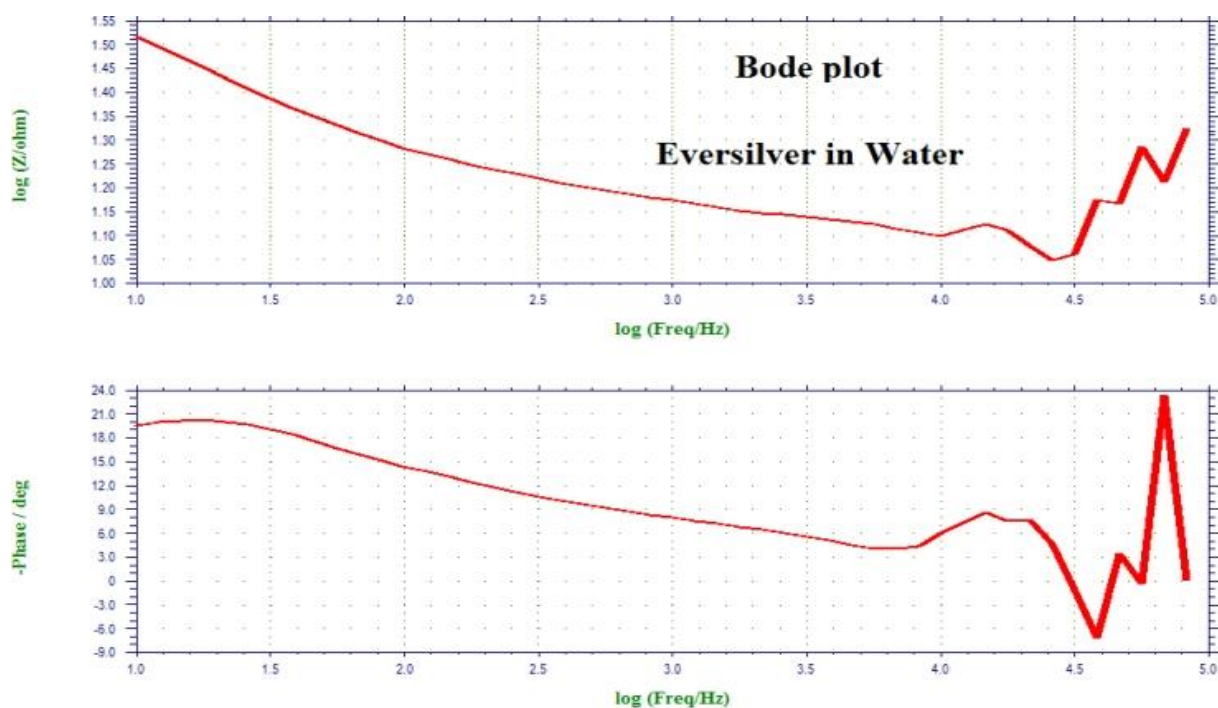
Figure 6. Bode plot of Ever Silve relectrode immersed in Water
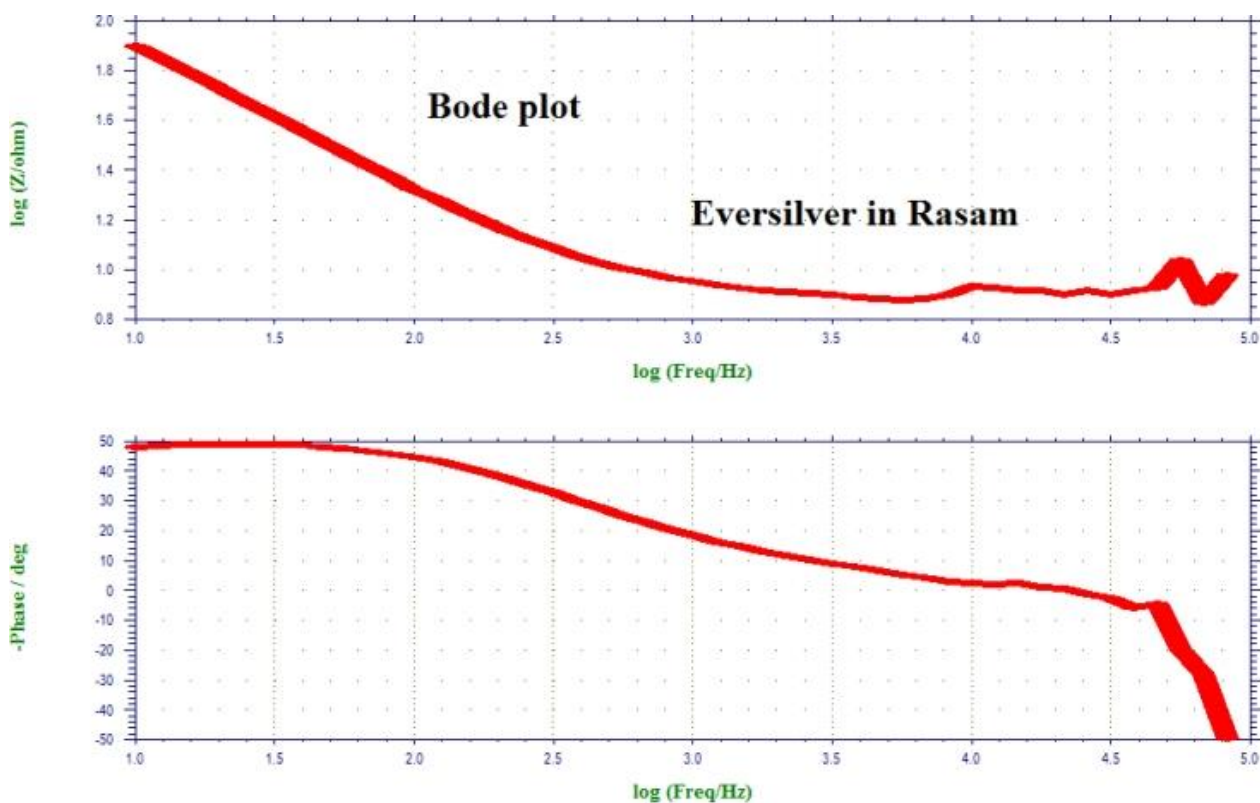

Figure 7. Bode plots Ever Silver electrode immersedin Rasam system
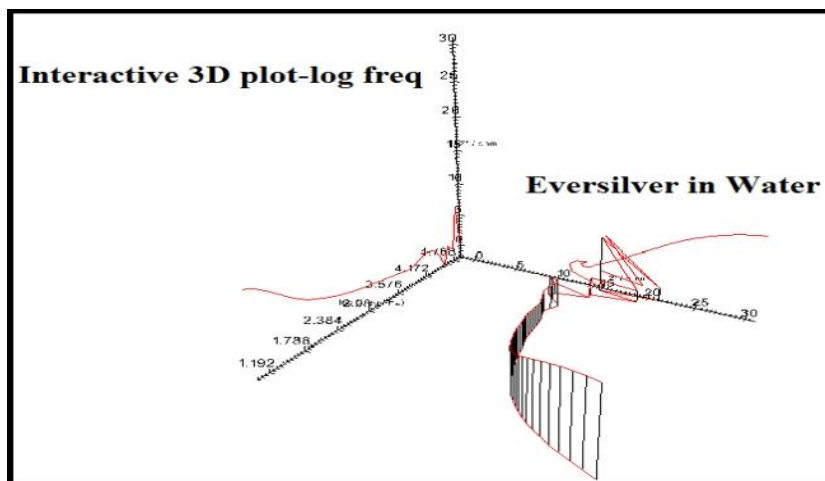
Figure 8. Interactive 3D plot-log frequency of Ever Silver electrode immersed in Water
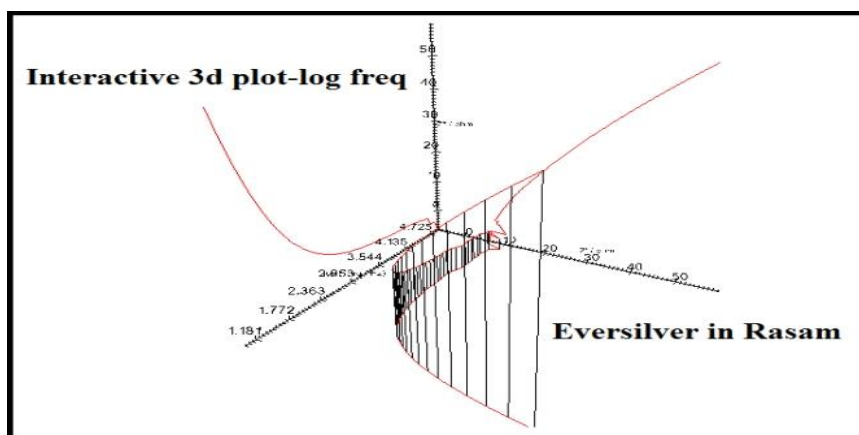

Figure 9. Interactive 3D plot-log of Ever Silver electrode immersed in Rasam system
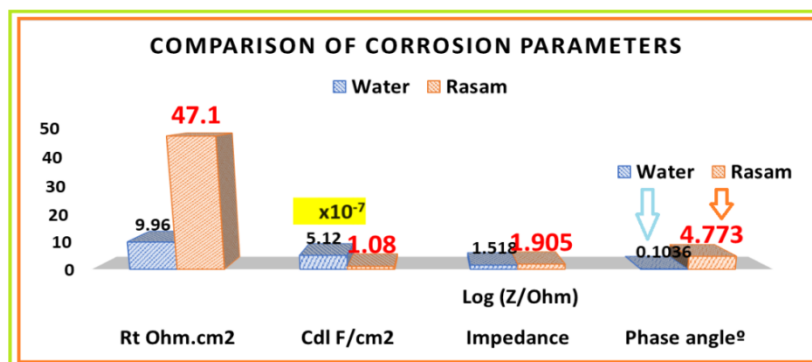

Figure 10. Comparison of corrosion parameters

4. CONCLUSION

This project is undertaken to know ifEver Silver vessels undergo corrosion or not, when they come in contact with some food items (recipes).

AC impedance spectra have been employed to investigate the corrosion resistance of Ever Silver electrode when it is immersed in various test solutions like water and also rasam recipe.

If a protective film is formed, the charge transfer resistance increases, impedance value increases, phase angle value increases and double layer capacitance (C_{dl}) value decreases.

When Ever Silver electrode is immersed in rasamsystem, the corrosion resistance ofEver Silver electrode increases. This is due to the presence of molecules of the ingredients introduced into the rasam system. The active ingredients are adsorbed on the metal surface.

The corrosion resistance decreases in the following order: rasam recipe>water

Scope for furthe rstudies

The present work is undertaken to investigate the corrosion inhibition of Ever Silver inthe presence of water, and rasam recipe. The corrosion resistance has been evaluated by electrochemical study such as AC impedance spectra. In future the following studies can be under taken

Instead of rasam other food item such as sambar recipe etc., can beused. Instead of Ever Silver other metals can be used. Surface analysis such as AFM, EDAX, contact angle etc., can beem ployed.

5. REFERENCES

[1]   Marsh, Kenneth; Bugusu, Betty (April 2007). "Food Packaging?Roles, Materials, and Environmental Issues". Journal of Food Science. **72** (3): R39–R55. doi:10.1111/j.1750-3841.2007.00301.x. PMID 17995809. S2CID 12127364.

[2]   Licciardello, Fabio (4 May 2017). "Packaging, blessing in disguise. Review on its diverse contribution to food sustainability". Trends in Food Science & Technology. **65** (65): 32–39. doi:10.1016/J.TIFS.2017.05.003. hdl:11380/1163967

[3]   A Brief History of Packaging. ufdc.ufl.edu. Retrieved 22 May 2019.

[4]   Gordon L. Robertson (18 January 2013). Food Packaging: Principles and Practice (3rd ed.). p. 736. doi:10.1201/B21347. ISBN 978-1-4398-6241-4, OL 28758289M. Wikidata Q112797468.

[5]   Francis, Frederick John (2000). Encyclopedia of food science and technology (2nd. ed.). New York: Wiley. ISBN 0471192856. OCLC 41143092.

[6]   Bi, Liu Ju (June 2012). "Research on Corrugated Cardboard and its Application". Advanced Materials Research. 535–537: 2171–2176. doi:10.4028/www.scientific.net/AMR.535-537.2171. ISSN 1662-8985. S2CID 110373839.

[7]   Hine, Thomas, 1947- (1995). The total package : the evolution and secret meanings of boxes, bottles, cans, and tubes (1st ed.). Boston: Little, Brown. ISBN 0316364800. OCLC 31288019.

[8]   Opie, Robert, 1947- (1989). Packaging source book. Macdonald Orbis. ISBN 0356176657. OCLC 19776457.

[9]   Arvanitoyannis, IS (2005). "Food packaging technology. Edited by R Coles, D McDowell and MJKirwan. Blackwell Publishing, CRC Press, Oxford, 2003. 346 pp ISBN 0-8493-9788-X". Journal of the Science of Food and Agriculture. **85** (6): 1072. Bibcode:2005JSFA...85.1072A. doi:10.1002/jsfa.2089. ISSN 0022-5142.

[10] Arvanitoyannis, Is (30 April 2005). "Food packaging technology. Edited by R Coles, D McDowell and MJKirwan. Blackwell Publishing, CRC Press, Oxford, 2003. 346 pp ISBN 0-849-39788-X". Journal of the Science of Food and Agriculture. **85** (6): 1072. Bibcode:2005JSFA...85.1072A. doi:10.1002/jsfa.2089. ISSN 0022-5142.

[11] Risch, Sara J. (23 September 2009). "Food Packaging History and Innovations". Journal of Agricultural and Food Chemistry. **57** (18): 8089–8092. doi:10.1021/jf900040r. ISSN 0021-8561. PMID19719135.

[12] Food packaging - Wikipedia

[13] food packaging alloys - Search (bing.com)

IZVOD

OTPORNOST NA KOROZIJU POSUDE EVER SILVER U PRISUSTVU RASAMA – LAGANE JUŽNOINDIJSKE TRADICIONALNE SUPE

Ambalaža za hranu služi u svrhu bezbednosti prehrambenih proizvoda i lako grukovanja i transporta sprečavajući hemijsku kontaminaciju i produžavajući rok trajanja, što pruža pogodnost za potrošače. Za pakovanje hrane korišćene su različite vrste materijala, uključujući plastiku, staklo, metale i papire i njihove kompozite. Međutim, zbog povećane zdravstvene svesti potrošača, značaj prenošenja štetnih materijala iz materijala za pakovanje u hranu izaziva veću zabrinutost. U ovoj studiji otpornost na koroziju posude Ever Silver u odsustvu i prisustvu recepta za rasam, lagane južno indijske tradicionalne supe napravljene od osnovnih začina, zrelog paradajza, tamarinda i začinskog bilja. Spektri impedanse naizmenične struje korišćeni su za merenje otpornosti na koroziju. Primećeno je da se otpornost na koroziju Ever Silver posude povećava u prisustvu rasam recepture. To je zbog prisustva različitih molekula prisutnih u sastojcima rasama. Zaključuje se da se recept za rasam može čuvati u Ever Silver posudi, a takođe se rasam može poslužiti u Ever Silver posudi tokom večere.
Ključne reči: *otpornost na koroziju, Ever Silver posuda, rasam, AC impedansni spektri, elektrohemijska studija*

Susai Rajendran   https://orcid.org/0000-0002-0040-2435

Sundus M. Ahmed[1], Nageeb S. Abtan[2], Ali H. Alwazir[3], Hakim S. Aljibori[3],Firas F. Sayyid[1], Ali M. Mustafa[1], Ahmed A. Alamiery[4,5], Abdul Amir H. Kadhum[6]

[1]Production Engineering and Metallurgy, University of Technology, Baghdad,Iraq, [2]Department of Mechanical Engineering, Tiktit University, College of Engineering, Tikreet, Salah Al Deen, Iraq, [3]College of Engineering, University of Warith Al-Anbiyaa, Karbalaa, Iraq, [4]I-Ayen Scientific Research Center, Al-Ayen Iraqi University, AUIQ, An Nasiriyah, Thi Qar, Iraq,[5]Department of Chemical and Process Engineering, Faculty of Engineering and Build Environment, Universiti Kebangsaan Malaysia, Bangi, Selangor, Malaysia, [6]Al-Ameed University College, Karbala, Iraq

Investigation of FPM as a corrosion Inhibitor for mild steel in HCl solution: Insights from electrochemical, weight loss and theoretical approaches

ABSTRACT

In this study, we investigate the efficiency of furan-2-yl-piperazin-1-yl-methanone (FPM) as a corrosion inhibitor for mild steel in HCl environment. Our study combines electrochemical techniques, weight loss measurements and Density Functional Theory (DFT) calculations. Regarding weight loss experiments, we find that a concentration of 0.5 mM of FPM provides maximum protection efficacy, reaching 91.8% at 303 K after 30 minutes of immersion and observed that the inhibition efficiency rises with increasing concentration of FPM but declines with higher temperatures. Based on the Langmuir isotherm and experimental analysis, it can be suggested that FPM can adhere to the surface of mild steel through physical and chemical interactions. Moreover, our theoretical studies reveals correlations between the structure of FPM and its effectiveness in inhibiting corrosion, shedding light on the underlying mechanisms. Experimental and theoretical results both are in agreement. Our findings underscore the potential of FPM as a corrosion inhibitor in industrial applications, offering new avenues for corrosion control techniques.
Keywords: *Furan, corrosion, steel, potentiodynamic polarization, DFT*

1. INTRODUCTION

Corrosion is now a very difficult problem that is present in every industry. It has great and farreaching consequences in terms of both economics and safety. Not only are costs related to the direct degradation and replacement of materials incurred, but also the cost of other things that may include production losses, environmental damage, or simply safety compromised [1-3]. Mild steel certainly cuts across all these challenges as it can be totally relied upon. The attributes come with almost complete availability, good physical and chemical properties, and of course, affordability [4,5]. Hence, it forms the basis for almost all the industrial applications imaginable-from construction and infrastructure to different forms of manufacturing and the transport sector. Affordability and resilience are general characteristics that put mild steel into many different fields of engineering and different applications where it is needed for mechanical strength and ease of welding [6-9]. This notwithstanding, mild steel isknown to be corrosive especially in high-acid and moisture-laden environments. Effective corrosion control measures are effective in addressing the vulnerability. This emphasizes the continued research and innovation in discovering new corrosion inhibitors as well as protective coatings [10,11]. These strategies are capable of either saving valuable assets from damage or even improving the entire operational efficiency and health standards along with overall sustainability in the industries against corrosion damages to metallic structures and equipment [12-15].

In environments one encounters with hydrochloric acid (HCl)-containing gas, such as cleaning, pickling, metal etching, and chemical synthesis, corrosion in mild steel is found to be

much more hazardous [16-18]. Among the special strategies investigated for corrosion mitigation agents are corrosion inhibitors. Such inhibitors are categorized based on their chemical form, mechanisms of internal action, and other relevant characteristics [19,20]. The copper-chromates and phosphate bases designed for purposes like corrosion inhibition have been the longtime backbone of any historic inorganic inhibitor [21-23]. But the problem of their environmental and health issue has led to investigations in other directions for organic inhibitors-their exactly current catching wave. Organic inhibitors are ornamented in a much more effective, multipurpose, and less harmful environmental and human impact. Compounds containing heteroatoms like nitrogen, oxygen, sulfur, and phosphorus show promising corrosion inhibition activity as these heteroatoms contribute to coordination bond formations where electrons from the heteroatoms are transferred to the free d-orbitals of iron atoms on the surface of mild steel. Corrosion inhibition ability decreases among these heteroatoms in the following order: oxygen (O), nitrogen (N), sulfur (S), and phosphorus (P) [24-27]. It is the electron density of the donor atom in the functional group of the inhibitor and polarizability of the functional group that affects the strength of chemisorption bond between the inhibitor molecules and the metal surface. Apart from these, electrostatic interactions between the inhibitor molecules and metal surface actually primarily accentuate the importance of such interactions with respect to corrosion inhibition mechanism [28,29].

Density Functional Theory (DFT), an extremely potent computation tool has already attracted great attention and created a strong demand for corrosion inhibition studies. DFT gives insights into the molecular structure, electronic properties, and adsorption behavior of inhibitor molecules that provide understanding of corrosion inhibition mechanisms at atomic levels [30-32]. This opens up FPM: furon-2-yl-piperazin-1-yl-methanone as a new interesting alternative for corrosion inhibition using its original structure combined with heteroatoms oxygen and nitrogen, as well as its heterocyclic rings. Those things together give an appropriate condition for favorable interactions with the metal surface to act in favor of the corrosion inhibition efficiency of FPM. This study aims to analyze the inhibition efficiency of this compound FPM (Figure 1) as an inhibitor of mild steel corrosion in 1N HCl solution. Through a holistic and synergistic collection of experimental techniques such as potentiodynamic polarization and theoretical methods like Density Functional Theory (DFT), we endeavor to explain the mechanism of corrosion inhibition by FPM. The whole originality

of the research depends upon its comprehensive study, in which experimental and theoretical data will be combined to understand the corrosion inhibition potentiality of FPM in more nuanced detail. These studies aim primarily at understanding the inhibition characteristics of FPM, detailing its adsorption characteristics on mild steel surface, and correlating the experimental with the theoretical results. These studies will thus contribute to the advancement of corrosion control strategies applicable in achieving sustainable industrial practices and alleviating the harmful effects of corrosion on infrastructure and equipment.
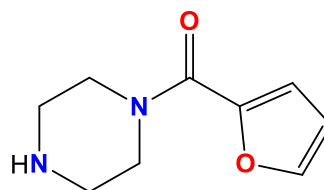

Figure 1. The chemical structure of FPM

2. METHODOLOGY

2.1. Materials

All chemicals utilized in this study were of reagent grade and procured from Sigma-Aldrich, Selangor, Malaysia. These chemicals were used without further purification. The purity of the compounds was confirmed through thin-layer chromatography (TLC) on silica gel G plates.

2.2. Electrochemical measurement

The experimental setup involved the preparation of mild steel samples, which were then immersed in hydrochloric acid (HCl) solution containing varying concentrations of FPM, the corrosion inhibitor under investigation. Potentiodynamic polarization measurements were conducted to evaluate the corrosion inhibition efficiency and to characterize the electrochemical behavior of the system. Mild steel specimens obtained from the Metal Samples Company were utilized as the working electrodes throughout the experimentation. The composition (wt%) of the mild steel was as follows: Fe, 99.21; C, 0.21; Si, 0.38; P, 0.09; S, 0.05; Al, 0.01. The specimens were cleaned in accordance with ASTM standard G1-03. The measurements were conducted in aerated, non-stirred 1.0 M HCl solutions at temperatures 303 K, with a FPM concentration range of 0.1–0.5 mM as the corrosion inhibitor [33-35]. Electrochemical measurements were performed using a Gamry water-jacketed glass cell containing three electrodes: the working, counter, and reference electrodes. These electrodes were composed of mild steel, a graphite bar, and a calomel electrode (SCE), respectively. A Gamry Instrument

Potentiostat/Galvanostat/ZRA model Ref 600, along with DC105 and EIS300 software by Gamry, was utilized for potentiodynamic scans. The potentiodynamic current-potential curves were swept from −0.25 to +0.25 VSCE at a scan rate of 0.5 mV•s^{-1}. Measurements were initiated approximately 30 minutes after immersing the working electrode in the solution to stabilize the steady-state potential. All measurements were conducted in triplicate, and average values were reported [36,37].

2.3. Weight-loss analysis

Weight-loss analysis involved immersing predetermined Mild Steel samples in 100 mL of HCl solution for 120 hours at an ambient temperature of 303 K. After every 24-hour interval, the samples were withdrawn from the acid solution, rinsed thoroughly with distilled water and acetone, dried, and re-weighed following ASTM G31-12a guidelines. Corrosion rate (C_R mm/y) and percentage inhibition efficiency (IE%) were computed based on the weight loss data collected during the exposure period [33-35]. The corrosion rate (CR) was calculated using Eq. (1)

$$C_R = \frac{87.6W}{dat} \tag{1}$$

Where W represents the weight loss in milligrams, d is the density in grams per cubic centimeter, a denotes the total area in square centimeters, t signifies the exposure time in hours, the constant 87.6 is included in the formula.

Percentage inhibition efficiency (IE) was determined using the Eq. (2):

$$IE = \frac{w_1 - w_2}{w_1} \times 100 \tag{2}$$

w_1 and w_2 represent the weight loss of specimens in the presence and absence of specific concentrations of FPM, respectively.

The inhibition efficiency was calculated for each FPM concentration throughout the exposure duration. Surface coverage (θ) was evaluated using the equation:

$$\theta = \frac{w_1 - w_2}{w_1} \tag{3}$$

Where θ denotes the quantitative amount of FPM compound adsorbed per gram on the steel specimens.

2.4. Computational Studies

The theoretical component of this study employed Density Functional Theory (DFT) calculations to investigate the molecular structure, electronic properties, and adsorption behavior of FPM on the mild steel surface. DFT simulations provided insights into the interaction mechanisms between FPM molecules and the metal surface,

elucidating the underlying principles of corrosion inhibition [38,39]. Quantum chemical computations were performed using ChemOffice software. Becke's three-parameter hybrid functional (B3LYP) level within Gaussian 03 version, with 6–31G as the reference set, was utilized to investigate the chemical reactivity of the FPM molecule. Quantum parameters such as energy gap (ΔE), fraction of electron transfer (ΔN), dipole moment (μ), ionization energy (I), electron affinity (A), absolute electronegativity (χ), hardness (η), and softness (σ) were determined for FPM in the gas phase [40].

The quantum chemical parameters, including χ, η, σ, and ΔN, were calculated using Equations (4)–(9) [41]:

$$I = -E_{HOMO} \tag{4}$$

$$A = -E_{LUMO} \tag{5}$$

$$\chi = (I + A)/2 \tag{6}$$

$$\eta = (I - A)/2 \tag{7}$$

$$\sigma = 1/\eta \tag{8}$$

$$\Delta N = (\chi_{Fe} - \chi_{inh})/2(\eta_{Fe} - \eta_{inh}) \tag{9}$$

3. RESULTS AND DISCUSSION

3.1. Potentiodynamic Polarization Analysis

As a result, the most valuable results of the potentiodynamic polarization tests are those on the efficiency achieved by different concentrations and immersions of Furan-2-yl-piperazin-1-yl-methanone (FPM) in terms of inhibiting corrosion. Deriving these tests also made it possible to determine other precious electrochemical parameters such as corrosion potential, corrosion current density, and polarization resistance. In addition, surface analysis techniques provided visual evidence of the protective film formed on the mild steel surface in the presence of FPM. They are associated with the anodic and cathodic polarization behavior, showing the electrochemical effect of FPM on mild steel corrosion in 1 M HCl acid solution, as pictorially shown in Figure 2. Table 1 presents the outcomes derived from the polarization scans [42]. Notably, the corrosion rates displayed in Table 1 demonstrate a substantial difference between FPM inhibited and uninhibited mild steel samples. At 0.0 mM FPM concentration, significant anodic dissolution of the mild steel sample occurred, accompanied by the formation of pores, pits, and channels within the porous oxide layer [43,44]. This corrosion was primarily instigated by Cl− ions present in the acid solution, facilitating corrosion reactions on the steel surface. A remarkable decrease in corrosion rate was observed as FPM concentration increased from 0.1 to 0.5 mM. This reduction can be attributed to the complex and non-homogeneous nature of metallic corrosion,

characterized by numerous anodic and cathodic reaction cells. Corrosion inhibiting compounds such as FPM tend to interact with these cells, either by retarding the redox electrochemical process or inhibiting the diffusion of active corrosive anions from the acid solution to the mild steel surface. Furthermore, variations in FPM concentration significantly impacted the inhibition efficiency values. It was observed that FPM's inhibition performance is dependent on its concentration. For instance, at 0.5 mM FPM concentration, the inhibition efficiency reached 90.7%, while at 0.1 mM FPM, the inhibition efficiency was 65.3%. The potentiodynamic polarization parameters calculated from Tafel curves for mild steel in both uninhibited and inhibited acidic solutions at 303 K are summarized in Table 1. These parameters provide quantitative data regarding the electrochemical behavior of mild steel in the presence of FPM, further elucidating its corrosion inhibition mechanism [45,46].
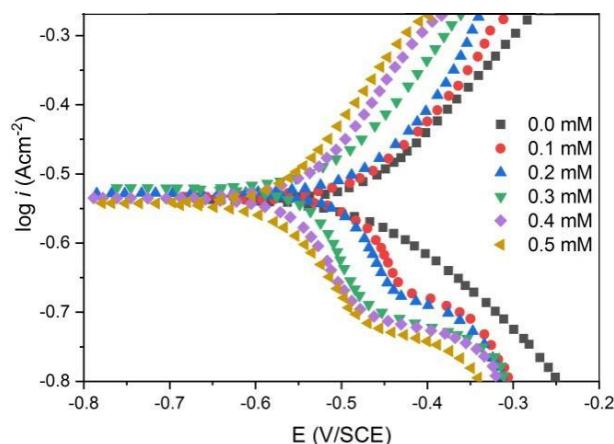

Figure 2. Potentiodynamic Polarization curves of the mild steel in the uninhibited and inhibited corrosive solution of various inhibitor concentrations

Table 1. Potentiodynamic Polarization Parameters for Mild Steel in Acidic Solution, with and without Inhibition, at 303 K

Conc.	−Ecorr (V vs. SCE)	−βc (mV dec−1)	icorr (μAcm−2)	IE(%)
0.0	503	147	602	0
0.1	492	196	62.7	65.3
0.2	495	180	89.3	73.5
0.3	497	168	121.5	80.1
0.4	507	150	142.6	84.6
0.5	510	143	175.7	90.7

3.2. Weight loss measurements

3.2.1. Effect of Inhibitor Concentrations

Figure 3 provides insights into the influence of inhibitor concentrations on the corrosion behavior of mild steel during a 24-hour immersion period at 303 K. It is evident that increasing the concentration of the inhibitor (FPM) from 0.0 mM to 0.5 mM leads to a significant reduction in the corrosion rate. For instance, at 0.0 mM inhibitor concentration, the corrosion rate is recorded at 1.294 mg/cm²·h. However, with increasing inhibitor concentrations, the corrosion rate steadily decreases. At 0.5 mM inhibitor concentration, the corrosion rate reaches its lowest value of 0.121 mg/cm²·h, representing an impressive reduction in corrosion rate compared to the uninhibited sample [47]. This observed decrease in corrosion rate with increasing inhibitor concentration highlights the effectiveness of FPM in mitigating corrosion of mild steel. As the concentration of FPM increases, more inhibitor molecules are available to form a protective barrier on the metal surface, thereby hindering corrosive processes. Furthermore, the inhibition efficiency exhibits a corresponding increase with rising inhibitor concentrations [48]. At 0.1 mM inhibitor concentration, the inhibition efficiency is measured at 54.9%, which steadily increases to 91.7% at 0.5 mM inhibitor concentration. The significant enhancement in inhibition efficiency with increasing inhibitor concentration underscores the potent corrosion inhibition properties of FPM. Higher inhibitor concentrations result in greater coverage of the metal surface by inhibitor molecules, leading to more effective corrosion protection.
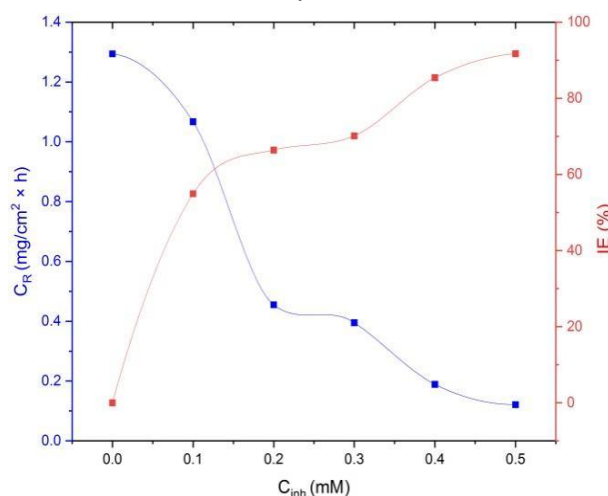

Figure 3. Effect of inhibitor concentrations for 24 hours as immersion time and 303 K

Overall, the data presented in Figure 3 demonstrate the strong correlation between inhibitor concentration, corrosion rate reduction, and inhibition efficiency improvement. These findings underscore the potential of FPM as a highly effective corrosion inhibitor for mild steel, particularly at elevated concentrations [49,50].

3.2.2. Effect of Temperature

The influence of temperature and concentrations of inhibitors on the inhibition of mild steel corrosion is presented in figure 4. Inhibition efficiency decreases with increased temperature. Increasing temperature curbs inhibition efficiency, which states that it is difficult to control corrosion at higher temperatures. Penetrating cause corrosion rates steadily increases and increases temperature for inhibition efficiency because several situations are involved [51,52]. The first is that high temperature accelerates the kinetics of reactions such that they have greater rates of dissolution for metals. Higher temperature may affect adsorption of inhibitor molecules on the metal surface, thus making their efficiency in forming protective barriers against diffusing corrosive agents less effective. Data reaction, therefore, gives an insight into how temperature is critical in determining the corrosion behavior of mild steel in the presence of inhibitors. Temperatures, therefore, should be considered when developing strategies or putting together a protocol for their use in corrosion control. This is particularly true for application at high temperatures, as they offer a likelihood of increasing corrosion rates [53,54].
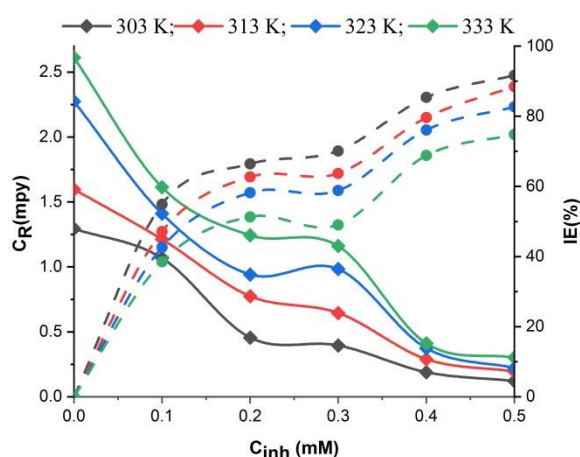

Figure 4. Impact of Temperature and Inhibitor Concentrations on Corrosion Rate and Inhibition Efficiency of Mild Steel Samples Immersed in 1 M HCl Solution for 24 Hours

3.2.3. Effect of Duration Periods

The evolution of immersion time and inhibitor concentrations on the corrosion behavior of mild steel is represented by Figure 5. It indicates that

with increase in the immersion period, there is a significant increase in corrosion rate at all inhibitor concentrations [55]. Furthermore, it was also found that at all immersion periods as the concentration of inhibitor increases, the corrosion attack decreases. The trend continues throughout different immersion periods showing that higher concentrations of inhibitors are better for corrosion control. Over time as the immersion period increases, there is a gradual decrease in inhibition efficiency for all concentrations of inhibitors [56]. Inhibition efficiency decreases as immersion time increases suggesting that the protective barrier created by the inhibitor molecules on the metal surface weaken with prolonged exposure [57]. The increase in corrosion rate with immersion time and decrease in inhibition efficiency with immersion time is due to the slow degradation and depletion of the inhibitor molecules from the surface of the metal. As time of immersion increases, the inhibitor molecules lose their activity due to desorption or chemical degradation which leads to low corrosion prevention. Overall, the data in Figure 5 speaks of how dynamic the corrosion processes are and how the rates and effectiveness of inhibition are impacted by concentrations of the inhibitors and immersion durations. This information presents approaches to the development of corrosion control methodologies with consideration for the continuous monitoring and optimization aspects of concentration and immersion durations in effective corrosion control practices for extended times [58].
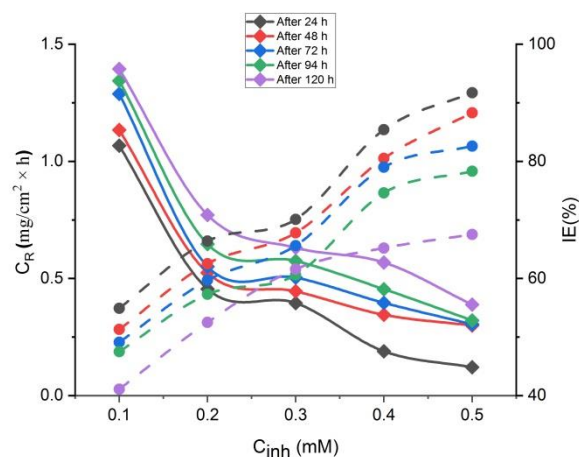

Figure 5. Impact of Immersion Periods and FPM Concentrations on C_R and IE% of Mild Steel Samples Immersed in 1 M HCl at 303 K

3.3. Adsorption Isotherm

The formation of a protective layer on the electrode surface, denoted as θ, is intimately linked with the adsorption phenomenon. Various adsorption isotherm models, including Temkin, Frumkin, Flory-Huggins, and Langmuir, have been employed to analyze weight loss data by

establishing the relationship between inhibitor concentration (C_{inh}) and surface coverage (θ) [59]. Among these models, the Langmuir adsorption isotherm demonstrated superior fitting capability, characterized by a high correlation coefficient (R^2), as depicted in Figure 6. This model effectively describes the inhibitor adsorption process through Equation 10 [60]:

$$\frac{C}{\theta} = \frac{1}{K_{ads}} + C \qquad (10)$$

Here, θ represents the surface coverage, K_{ads} denotes the adsorption constant, and C signifies the inhibitor concentration. To further elucidate the inhibitor adsorption process, the adsorption free energy (ΔG^0_{ads}) was calculated utilizing the K_{ads} value with Equation 11:

$$\Delta G^0_{ads} = \frac{1}{55.5} exp(-K_{ads}/RT) \qquad (11)$$

In this equation, the molar concentration of water (55.5 M) and the gas constant (R) under standard conditions are considered. This calculation provides valuable insights into the thermodynamic aspects of inhibitor adsorption, aiding in the comprehensive understanding of the corrosion inhibition mechanism.
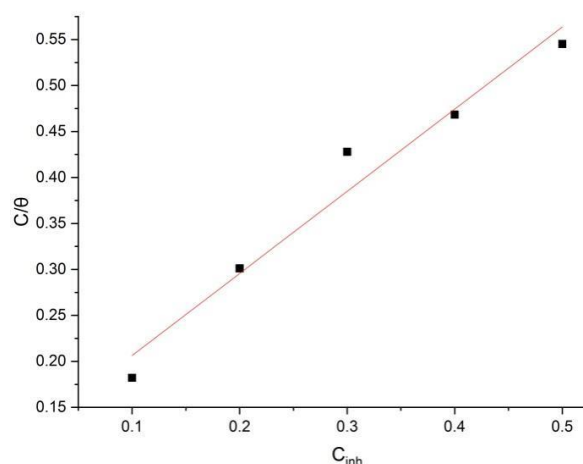

Figure 6. Langmuir isotherm adsorption of FPM on the mild steel surface in 1 M HCl at 303 K from the weight loss analysis

The Langmuir isotherm parameters throw light on the adsorption behaviour of the inhibitor molecules on the mild steel surface in 1 M HCl at 303 K. The Langmuir isotherm parameters derived from the weight loss analysis are shown in Table 2. By Langmuir adsorption constant (K_{ads}) we mean the strength of inhibitor adsorption on the metal surface. Higher value of K_{ads} means stronger adsorption of inhibitor molecules onto the mild steel surface. In this case, the calculated K_{ads} value of 11.20 × 10^5 L/mg indicates that adsorption strength

is quite significant and inhibition is very effective [61].

Table 2. Langmuir Isotherm Parameters: Adsorption of Tested Inhibitor Molecules on the Mild Steel Surface in 1 M HCl at 303 K from Weight Loss Analysis.

Parameter	Weight loss
Intercept	0.116
R^2	0.96569
slope	0.893
K	11.20 (L/mg) × 10^5
ΔG	-40.75 kJ/mol

Moreover, the adsorption free energy, denoted as (ΔG^0_{ads}) eveals the spontaneity of the adsorption process. A negative value of ΔG^0_{ads} points towards the spontaneous nature of the adsorption process, which indicates that the inhibitor molecules are favorably adsorbed on the mild steel surface. The observed value of -40.75 kJ/mol under ΔG^0_{ads} proves that the adsorption process is highly spontaneous further reaffirming the competence of the inhibitor in curbing corrosion [62].

The high value of ΔG^0_{ads} shows that the inhibitor molecules are strongly chemically adsorbed by the acid. The electrons are moved from the high electron centers to the empty 3d orbital of iron (Fe) to form a covalent bond between the metal surface and the inhibitor molecules. Such covalent bond formation strengthens the protective layer over the mild steel surface, which effectively inhibits the corrosion rate. It can be summarized that the parameters of the Langmuir isotherm show that these inhibitors tested can be adsorbed strongly and they spontaneously adsorb onto the mild steel surface, demonstrating their efficiency in corrosion inhibition. These findings show that the inhibitor molecules definitely have high potential for practical applications in corrosion control approaches.

3.4. DFT Analysis

This is revealed through frontier molecular orbital theory (FMOT) coupled with Density Functional Theory (DFT) software, which explains the adsorption ability of their molecules in their associated mild steel surfaces. The quantum chemical parameters summarized in Table 3 will serve as significant insight into the efforts to extricate the relationship between molecular properties and inhibition efficiency of Furan-2-yl-piperazin-1-yl-methanone (FPM) as a corrosion inhibitor. The HOMO and LUMO energies are indicative of the electron donation and acceptance abilities of the molecule FPM, respectively [63,64].

Here, the HOMO energy of FPM is fairly low at -10.026eV indicating a strong tendency to donate electrons, while the LUMO energy is 0.463eV which suggests it can accept electrons. Absolute electron negativity values (measured as χ) and hardness (η) further characterized by FPM's intrinsic quality with calculated values. A low value of χ (-4.282eV) indicates FPM is a very strong electron Lovelock, while a high hardness value (-5.244eV) suggests FPM's resistance to any variations in density of electrons. Moreover, the softness (σ) parameter, calculated to be -0.190 eV^{-1}, signifies FPM's propensity for electron donation or acceptance. A higher value of σ

indicates greater reactivity of the molecule. The dipole moment (μ) and Fraction of Electron Transfer (ΔN) provide additional insights into FPM's interaction with the metal surface. The negative dipole moment (-5.14) suggests a nonuniform charge distribution over the molecule, facilitating its adsorption onto the metal surface. Furthermore, the negative ΔN value (-0.2114) indicates electron transfer from FPM to the metal surface, which correlates with enhanced inhibition efficiency [65,66]. In accordance with Lukovit's study, inhibition performance correlates positively with the fraction of electron transfer (ΔN), with optimal inhibition observed when ΔN is less than 3.6 [67].

Table 3. Quantum Chemical Parameters for FPM as a Corrosion Inhibitor

HOMO (eV)	LUMO (eV)	χ (eV)	η (eV)	σ (eV^{-1})	μ	ΔN
-10.026	0.463	-4.282	-5.244	-0.190	-5.14	-0.2114

Based on Figure 7, the distribution of HOMO electron density is predominantly observed over the aromatic benzene ring and the carbonyl group of the inhibitor molecule. This spatial distribution indicates potential sites for interaction between the inhibitor and the metal surface. When the inhibitor molecule adsorbs onto the metal surface, it is likely that charge donation from the inhibitor molecules to the vacant d-orbitals of the iron atoms will occur. This charge transfer process is crucial for forming a protective layer on the metal surface, thereby inhibiting corrosion. The interaction between the HOMO of the inhibitor and the metal surface promotes the formation of stable bonds, contributing to the inhibition efficiency [68,69].

The electron density in LUMO is spread over the inhibitor molecule. This indicates that possible back-donation from the occupied orbitals of the metal to the inhibitor will involve various regions of

the inhibitor molecule for interaction. This is essential to getting the inhibitor molecule adsorbed on the metal substrate. The back-donation process, it may be noted, is necessary for stabilizing the adsorbed inhibitor molecule on the metal surface. By getting electrons back from the metal surface, it can hold itself really well and inhibit the corrosion. The wider distribution of electron density in the LUMO suggests that it is indeed versatile in that respect; it contributes to the overall effectiveness of corrosion inhibition as well in interaction of that inhibitor molecule under metal surface. Hence, it can be inferred that the electron density distribution on both these HOMO and LUMO orbitals is of paramount importance concerning the interaction between the inhibitor molecule and the metal surface. All of these include charge transfer processes, which are necessary to produce a protective layer and inhibit the corrosion [70].
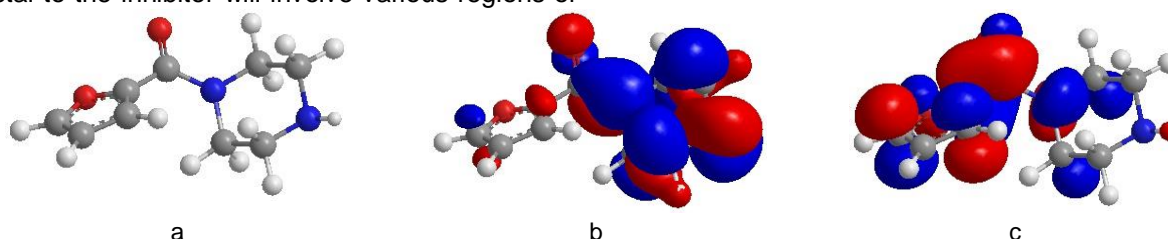

a   b   c

Figure 7. Various aspects of the tested inhibitor: (a) the optimized structure, (b) the highest occupied molecular orbitals (HOMO), and (c) the lowest unoccupied molecular orbitals (LUMO)

In considering the effects of atomic charges on the inhibition of corrosion, Figure 8 offers valuable insights'. The data indicate that the negative charges on oxygen atoms O8 and O9 are -0.85 eV and -0.28 eV, respectively. Similarly, nitrogen atoms N3 and N6 carry negative charges of -0.66 eV and -0.2 eV, respectively. The above values

suggest that there is a surplus of electrons around these atoms, making these regions electron-rich within the inhibitor molecule. These electron-rich regions further indicate that they play a vital role in corrosion inhibition by facilitating the interaction between the metal surface with the molecule. Oxygen and nitrogen, particularly, have a high

affinity for positively charged metal ions at the surface [71,72]. By forming coordination bonds with these metal ions, the inhibitor molecules can adsorb onto the metal surface, thereby forming a protective barrier against corrosive agents. Having negatively charged surfaces further enhances electron donation to the substrate. This process of electron donation works towards stabilizing the adsorbed inhibitor molecules as they promote passive film formation, inhibiting corrosion. Overall, it is significantly useful against corrosion in that negative atomic charges on the oxygen and nitrogen atoms of the inhibitor molecule contribute towards their different functions in corrosion inhibition. These functions include facilitating adsorption and electron transfer processes at the metal surface, which further improve the corrosion effectiveness of the inhibitor [73].
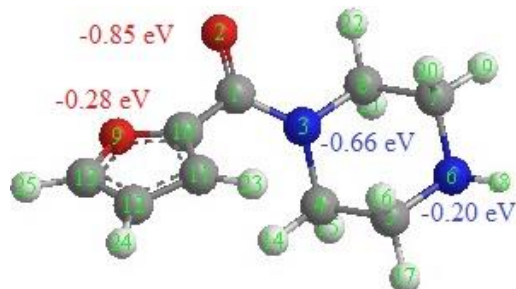

Figure 8. The atomic charges of tested inhibitor molecule

3.5. Mechanism of inhibition action

FPM inhibition mechanism on mild steel in HCl showed in figure 9. The elucidation of the adsorption mechanism of the inhibitor is vital to understand its inhibitive action, whether ionic or molecular. The major modes of adsorption can depend mainly on the nature of the chemical species of the inhibitor and the type of acid anion

present. FPM contains chemical components such as carbonyl groups, double bonds, as well as oxygen and nitrogen heteroatoms, aligning with the general characteristics of corrosion inhibitors. Chloride ions are known for their high absorptivity, suggesting their potential impact on inhibitor adherence, particularly in halide-containing solutions. Thermodynamic and kinetic parameters obtained from the study indicate the physical adsorption of FPM on the mild steel surface in acidic solutions. The increased efficacy of the inhibitor, as evidenced by weight loss measure-ments, suggests more efficient adsorption on the mild steel substrate, effectively covering the surface-active sites and thereby significantly reducing the corrosion rate. In acidic solutions, FPM likely undergoes protonation, leading to a positive surface charge on the corroded mild steel surface, which may affect its adsorption behavior. Initially, adsorption of chloride acid anions occurs, introducing additional negative charges to the solution, thereby facilitating the adsorption of cations. Subsequently, through van der Waals interactions, the protonated inhibitor accumulates on the negatively charged metal surface, forming coordinate bonds by partially transferring electrons from the nitrogen and oxygen heteroatoms and multiple bonds to the unfilled d-orbitals of iron. FPM may also interact with Fe^{2+} ions formed on the steel surface due to the presence of unshared electron pairs on nitrogen and oxygen atoms, forming metal-inhibitor complexes. These com-plexes adhere to the steel surface through van der Waals forces, creating a protective layer that effectively inhibits corrosion. In summary, the inhibition mechanism of FPM involves its adsor-ption on the mild steel surface through a combi-nation of ionic and molecular interactions, forming protective complexes that prevent corrosion.
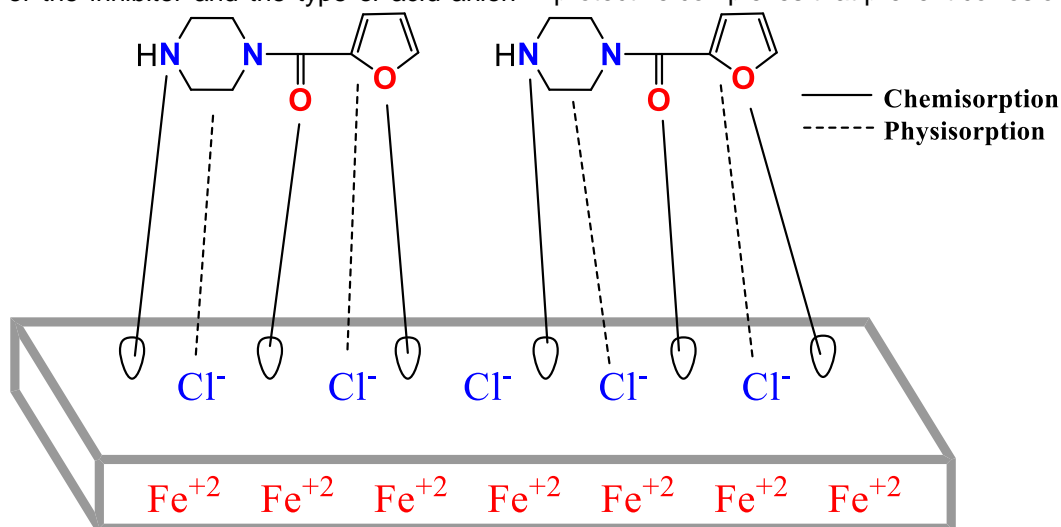

Figure 9. Schematic illustrative diagram of corrosion inhibition mechanism of FPMin acid solution

4. CONCLUSION

The study was aimed at determining the corrosion inhibition efficiency of furan-2-yl-piperazin-1-yl-methanone (FPM) for low carbon steel in hydrochloric acid (HCl) solution. Both experimental and theoretical techniques contributed significantly to understanding FPM's corrosion inhibition mechanism. Experimental results also reaffirmed that FPM is quite an efficient inhibitor, the most protection efficiency being 91.8% at 303 K after holding the specimen for 30 minutes. The increase in FPM concentration improved the inhibition efficiency, but it decreased as the temperature increased, indicating that both factors played roles in the inhibition effectiveness.

From the prediction, FPM may be adsorbed on the mild steel surface through physical and chemical bonds, following the Langmuir adsorption isotherm model. Theoretical investigations using Density Functional Theory (DFT) have shown a better understanding of the molecular structure of FPM and its relationship with the experimental inhibition efficiency. The adsorption ability of FPM as deduced by quantum chemical parameters like HOMO and LUMO energy values implied proper interaction with the mild steel surface and contributed to its action against corrosion [74]. Overall, the complete combination of experimental and theoretical methods hold bright future prospects for the application of FPM as a corrosion inhibitor in industrial settings. FPM will definitely help realize the much needed improvements in corrosion control strategies for attaining durable and safe as well as sustainable industrial applications by providing mild steel with effective protection against corrosion.

5. REFERENCES

[1] N.S. Abtan, M.A.I. Al-Hamid, L.A. Kadhim, F.A. Sayyid, F.T.M. Noori, A. Kadum, A. Alamiery, W.K. Al-Azzawi (2024) Unlocking the Power of 4-Acetamidoantipyrine: A Promising Corrosion Inhibitor for Preserving Mild Steel in Harsh Hydrochloric Acid Environments. Prog. Color Colorants Coat., 17(1), 85–96,

https://doi.org/10.30509/pccc.2023.167147.1223.

[2] A.N. Jasim, A. Mohammed, A.M. Mustafa, F.F. Sayyid, H.S. Aljibori, W.K. Al-Azzawi, A.A. Al-Amiery, E.A. Yousif (2024) Corrosion Inhibition of Mild Steel in HCl Solution by 2-acetylpyrazine: Weight Loss and DFT Studies on Immersion Time and Temperature Effects. Prog. Color Colorants Coat., 17(4), 333–350,

https://doi.org/10.30509/pccc.2024.167231.1261.

[3] A.F. Hamood, H.S. Aljibori, M.A.I. Al-Hamid, A.A. Alamiery, W.K. Al-Azzawi (2024) MOP as a Corrosion Inhibitor for Mild Steel in HCl Solution: A Comprehensive Study. Prog. Color Colorants Coat., 17(3), 207–226,

https://doi.org/10.30509/pccc.2023.167176.1237.

[4] M.M. Taha, S.A. Nawi, A.M. Mustafa, F.F. Sayyid, M.M. Hanoon, A.A. Al-Amiery, A.A.H. Kadhum, W.K. Al-Azzawi (2024) Revolutionizing Corrosion Defense: Unlocking the Power of Expired BCAA. Prog. Color Colorants Coat., 17(2), 97–111,

https://doi.org/10.30509/pccc.2023.167156.1228.

[5] A.M. Resen, A.N. Jasim, H.S. Qasim, M.M. Hanoon, A.A. Al-Amiery, W.K. Al-Azzawi, A.M. Mustafa, F.F. Sayyid (2024) Investigating the Corrosion Inhibition Performance of Methyl 3H-2,3,5-triazole-1-formate for Mild Steel in Hydrochloric Acid Solution: Experimental and Theoretical Insights. Prog. Color Colorants Coat., 17(2), 185–205,

https://doi.org/10.30509/pccc.2023.167189.1245.

[6] M.K. Abbass, K.M. Raheef, I.A. Aziz, M.M. Hanoon, A.M. Mustafa, W.K. Al-Azzawi, A.A. Al-Amiery, A.A.H. Kadhum (2024) Evaluation of 2-Dimethylaminopropionamidoantipyrine as a Corrosion Inhibitor for Mild Steel in HCl Solution: A Combined Experimental and Theoretical Study. Prog. Color Colorants Coat., 17(1), 1–10,

https://doi.org/10.30509/pccc.2023.167081.1197.

[7] H.S. Aljibori, O.H. Abdulzahra, A.J. Al-Adily, W.K. Al-Azzawi, A. Al-Amiery, A.A.H. Kadhum (2023) Corrosion inhibition effects of concentration of 2-oxo-3-hydrazonoindoline in acidic solution, exposure period, and temperature. Int. J. Corr. Scale Inhib., 12(2), 438–457,

https://doi.org/10.17675/2305-6894-2023-12-2-4.

[8] S. Junaedi, A.A.H. Kadhum, A. Al-Amiery, A.B. Mohamad, M.S. Takriff (2012) Synthesis and characterization of novel corrosion inhibitor derived from oleic acid: 2-Amino-5-Oleyl 1,3,4-Thiadiazol (AOT). Int. J. Electrochem. Sci., 7(4), 3543–3554.

[9] H.S. Aljibori, A.H. Alwazir, S. Abdulhadi, W.K. Al-Azzawi, A.A.H. Kadhum, L.M. Shaker, A.A. Al-Amiery, H.Sh. Majdi (2022) The use of a Schiff base derivative to inhibit mild steel corrosion in 1 M HCl solution: a comparison of practical and theoretical findings. Int. J. Corr. Scale Inhib., 11(2), 1435–1455.

[10] W.K. Al-Azzawi, S.M. Salih, A. Hamood, R.K. Al-Azzawi, M.H. Kzar, H.N. Jawoosh, L.M. Shakier, A. Al-Amiery, A.A.H. Kadhum, W.N.R.W. Isahak, M.S. Takriff (2022) Adsorption and theoretical investigations of a Schiff base for corrosion inhibition of mild steel in an acidic environment. Int. J. Corr. Scale Inhib., 11(2), 1063–1082.

[11] D.M. Jamil, A. Al-Okbi, M. Hanon, K.S. Rida, A. Alkaim, A. Al-Amiery, A. Kadhum, A.A.H. Kadhum (2018) Carbethoxythiazole corrosion inhibitor: as an experimentally model and DFT theory. J. Eng. Appl. Sci., 13(11), 3952–3959.

[12] A. Alobaidy, A. Kadhum, S. Al-Baghdadi, A. Al-Amiery, A. Kadhum, E. Yousif, A.B. Mohamad (2015) Eco-friendly corrosion inhibitor: experimental studies on the corrosion inhibition performance of creatinine for mild steel in HCl complemented with

quantum chemical calculations. Int. J. Electrochem. Sci., 10(3), 3961–3972.

[13] A.A. Alamiery (2022) Study of corrosion behavior of N'-(2-(2-oxomethylpyrrol-1-yl)ethyl)piperidine for mild steel in the acid environment. Biointerface Res. Appl. Chem., 12(3), 3638–3646.

[14] A. Alamiery, A.B. Mohamad, A.A.H. Kadhum, M.S. Takriff (2022) Comparative data on corrosion protection of mild steel in HCl using two new thiazoles. Data Brief, 40, 107838, https://doi.org/10.1016/j.dib.2022.107838.

[15] A.M. Mustafa, F.F. Sayyid, N. Betti, L.M. Shaker, M.M. Hanoon, A.A. Alamiery, A.A.H. Kadhum, M.S. Takriff (2022) Inhibition of mild steel corrosion in hydrochloric acid environment by 1-amino-2-mercapto-5-(4-(pyrrol-1-yl)phenyl)-1,3,4-triazole. S. Afr. J. Chem. Eng., 39(4), 42–51, https://doi.org/10.1016/j.sajce.2021.11.009.

[16] A.A. Alamiery (2022) Investigations on corrosion inhibitory effect of newly quinoline derivative on mild steel in HCl solution complemented with antibacterial studies. Biointerface Res. Appl. Chem., 12(4), 1561–1568.

[17] I.A.A. Aziz, I.A. Annon, M.H. Abdulkareem, M.M. Hanoon, M.H. Alkaabi, L.M. Shaker, A.A. Alamiery, W.N.R.W. Isahak, M.S. Takriff (2021) Insights into corrosion inhibition behavior of a 5-mercapto-1,2,4-triazole derivative for mild steel in hydrochloric acid solution: experimental and DFT studies. Lubricants, 9(12), 122, https://doi.org/10.3390/lubricants9120122.

[18] A. Alamiery (2021) Short report of mild steel corrosion in 0.5 M H2SO4 by 4-ethyl-1-(4-oxo-4-phenylbutanoyl) thiosemicarbazide. J. Tribologi, 30, 90–99.

[19] A.A. Alamiery, W.N.R.W. Isahak, M.S. Takriff (2021) Inhibition of mild steel corrosion by 4-benzyl-1-(4-oxo-4-phenylbutanoyl)thiosemicarbazide: gravimetrical, adsorption and theoretical studies. Lubricants, 9(9), 93, https://doi.org/10.3390/lubricants9090093.

[20] M.A. Dawood, Z.M.K. Alasady, M.S. Abdulazeez, D.S. Ahmed, G.M. Sulaiman, A.A.H. Kadhum, L.M. Shaker, A.A. Alamiery (2021) The corrosion inhibition effect of a pyridine derivative for low carbon steel in 1 M HCl medium: complemented with antibacterial studies. Int. J. Corr. Scale Inhib., 10(5), 1766–1782.

[21] A. Alamiery (2021) Corrosion inhibition effect of 2-N-phenylamino-5-(3-phenyl-3-oxo-1-propyl)-1,3,4-oxadiazole on mild steel in 1 M hydrochloric acid medium: insight from gravimetric and DFT investigations. Mater. Sci. Energy Technol., 4, 398–406, https://doi.org/10.1016/j.mset.2021.09.002.

[22] A.A. Alamiery (2021) Anticorrosion effect of thiosemicarbazide derivative on mild steel in 1 M hydrochloric acid and 0.5 M sulfuric acid: gravimetrical and theoretical studies. Mater. Sci. Energy Technol., 4, 263–273, https://doi.org/10.1016/j.mset.2021.07.004.

[23] A.A. Alamiery, W.N.R.W. Isahak, H.S.S. Aljibori, H.A. Al-Asadi, A.A.H. Kadhum (2021) Effect of the structure, immersion time and temperature on the corrosion inhibition of 4-pyrrol-1-yln-(2,5-dimethyl-pyrrol-1-yl)benzoylamine in 1.0 M HCl solution. Int. J. Corr. Scale Inhib., 10(6), 700–713, https://doi.org/10.17675/2305-6894-2021-10-2-14.

[24] A. Alamiery, E. Mahmoudi, T. Allami (2021) Corrosion inhibition of low-carbon steel in hydrochloric acid environment using a Schiff base derived from pyrrole: gravimetric and computational studies. Int. J. Corr. Scale Inhib., 10(4), 749–765.

[25] A.J.M. Eltmimi, A. Alamiery, A.J. Allami, R.M. Yusop, A. Kadhum, T. Allami (2021) Inhibitive effects of a novel efficient Schiff base on mild steel in hydrochloric acid environment. Int. J. Corr. Scale Inhib., 10(3), 634–648.

[26] A.L. Alamiery, L.M. Shaker, T. Allami, A.H. Kadhum, M.S. Takriff (2021) A study of acidic corrosion behavior of furan-derived Schiff base for mild steel in hydrochloric acid environment: Experimental, and surface investigation. Materials Today: Proceedings, 44(6), 2337–2341.

[27] B.S. Mahdi, H.S.S. Aljibori, M. Abbass, W.K. Al-Azzawi, A.H. Kadhum, M.M. Hanoon, W.N.R.W. Isahak, A.A. Al-Amiery, H.Sh. Majdi (2022) Gravimetric analysis and quantum chemical assessment of 4-aminoantipyrine derivatives as corrosion inhibitors. International Journal of Corrosion and Scale Inhibition, 11(9), 1191–1213.

[28] S. Junaedi, A.A. Al-Amiery, A. Kadihum, A.A.H. Kadhum, A.B. Mohamad (2013) Inhibition effects of a synthesized novel 4-aminoantipyrine derivative on the corrosion of mild steel in hydrochloric acid solution together with quantum chemical studies. International Journal of Molecular Sciences, 14(6), 11915–11928, https://doi.org/10.3390/ijms140611915.

[29] S.B. Al-Baghdadi, A.A. Al-Amiery, T.S. Gaaz, A.A.H. Kadhum (2021) Terephthalohydrazide and isophthalohydrazide as new corrosion inhibitors for mild steel in hydrochloric acid: Experimental and theoretical approaches. Koroze a ochrana materiálů, 65(8), 12–22.

[30] S. Al-Baghdadi, T.S. Gaaz, A. Al-Adili, A.A. Al-Amiery, M.S. Takriff (2021) Experimental studies on corrosion inhibition performance of acetylthiophene thiosemicarbazone for mild steel in HCl complemented with DFT investigation. International Journal of Low-Carbon Technologies, 16(6), 181–188, https://doi.org/10.1093/ijlct/ctaa050.

[31] M.S. Abdulazeez, Z.S. Abdullahe, M.A. Dawood, Z.K. Handel, R.I. Mahmood, O. Osamah, A.H. Kadhum, L.M. Shaker, A.A. Al-Amiery (2021) Corrosion inhibition of low carbon steel in HCl medium using a thiadiazole derivative: weight loss, DFT studies and antibacterial studies. Int J Corr Scale Inhib, 10(6), 1812–1828.

[32] A.M. Mustafa, F.F. Sayyid, N. Betti, M.M. Hanoon, A. Al-Amiery, A.A.H. Kadhum, M.S. Takriff (2021) Inhibition evaluation of 5-(4-(1H-pyrrol-1-yl)phenyl)-2-mercapto-1,3,4-oxadiazole for the corrosion of

mild steel in an acid environment: thermodynamic and DFT aspects. Tribologia, 38(4), 39-47. https://doi.org/10.30678/FJT.105330

[33] ASTM International, Standard Practice for Preparing, Cleaning, and Evaluating Corrosion Test, 2011, 1–9.

[34] NACE International, Laboratory Corrosion Testing of Metals in Static Chemical Cleaning Solutions at Temperatures below 93°C (200°F), TM0193-2016-SG, 2000.

[35] M.M. Hanoon, A.M. Resen, L.M. Shaker, A.A.H. Kadhum, A.A. Al-Amiery (2021) Corrosion investigation of mild steel in aqueous hydrochloric acid environment using N-(naphthalen-1yl)-1-(4-pyridinyl)methanimine complemented with antibacterial studies. Biointerface Res. Appl Chem, 11(6), 9735–9743.

[36] A.A. Al-Amiery, W.K. Al-Azzawi, W.N.R.W. Isahak (2022) Isatin Schiff base is an effective corrosion inhibitor for mild steel in hydrochloric acid solution: gravimetrical, electrochemical, and computational investigation. Sci Rep, 12(4), 17773. https://doi.org/10.1038/s41598-022-22611-4

[37] A. Al-Amiery, W.N.R.W. Isahak, W.K. Al-Azzawi (2023) Multimethod evaluation of a 2-(1,3,4-thiadiazole-2-yl)pyrrolidine corrosion inhibitor for mild steel in HCl: combining gravimetric, electrochemical, and DFT approaches. Sci Rep, 13(4), 9770. https://doi.org/10.1038/s41598-023-36252-8

[38] A.A. Al-Amiery (2021) Anti-corrosion performance of 2-isonicotinoyl-N-phenylhydrazinecarbothioamide for mild steel hydrochloric acid solution: Insights from experimental measurements and quantum chemical calculations. Surf Rev Lett, 28(3), 2050058. https://doi.org/10.1142/S0218625X20500584

[39] Y.M. Abdulsahib, A.J.M. Eltmimi, S.A. Alhabeeb, M.M. Hanoon, A.A. Al-Amiery, T. Allami, A.A.H. Kadhum (2021) Experimental and theoretical investigations on the inhibition efficiency of N-(2,4-dihydroxytolueneylidene)-4-methylpyridin-2-amine for the corrosion of mild steel in hydrochloric acid. Int J Corr Scale Inhib, 10(6), 885–899.

[40] M.J. Frisch, G.W. Trucks, H.B. Schlegel, G.E. Scuseria, M.A. Robb, J.R. Cheeseman, J.A. Montgomery, T. Vreven, K.N. Kudin, J.C. Burant, J.M. Millam, S.S. Iyengar, J. Tomasi, V. Barone, B. Mennucci, M. Cossi, G. Scalmani, N. Rega, N. Petersson, H. Nakatsuji, H. Hada, M. Ehara, R. Toyota, R. Fukuda, J. Hasegawa, M. Ishida, T. Nakajima, Y. Honda, O. Kitao, H. Nakai, M. Klene, X. Li, J.E. Knox, H.P. Hratchian, J.B. Cross, V. Bakken, C. Adamo, J. Jaramillo, R. Gomperts, R.E. Stratmann, O. Yazyev, A.J. Austin, R. Cammi, C. Pomelli, J.W. Ochterski, J.W. Ayala, P.Y. Morokuma, G.A. Voth, P. Salvador, J.J. Dannenberg, V.G. Zakrzewski, S. Dapprich, A.D. Daniels, M.C. Strain, O. Farkas, D.K. Malick, A.D. Rabuck, K. Raghavachari, J.B. Foresman, J.V. Ortiz, Q. Cui, A.G. Baboul, S. Clifford, J. Cioslowski, B.B. Stefanov, G. Liu, A. Liashenko, P. Piskorz, I. Komaromi, R.L. Martin, R.L. Fox, T. Keith, M.A. Al-Laham, C.Y. Peng, A. Nanayakkara, M. Challacombe, P.M.W. Gill, B. Johnson, W. Chen, M.W. Wong, C. Gonzalez, J.A. Pople (2004) Gaussian 03, Revision B. 05, Gaussian, Inc., Wallingford, CT.

[41] T. Koopmans (1934) Ordering of wave functions and eigenenergies to the individual electrons of an atom. Physica, 1(4), 104–113 (In German).

[42] A.A. Al-Amiery, F. Binti Kassim, A.A.H. Kadhum (2016) Synthesis and characterization of a novel eco-friendly corrosion inhibitor for mild steel in hydrochloric acid. Sci Rep, 6(3), 19890. https://doi.org/10.1038/srep19890

[43] A.K. Khudhair, A.M. Mustafa, M.M. Hanoon, A.A. Al-Amiery, L.M. Shaker, T. Gazz, A.B. Mohamad, A.H. Kadhum, M.S. Takriff (2022) Experimental and theoretical investigation on the corrosion inhibitor potential of N-MEH for mild steel in HCl. Prog Color Colorant Coat, 15(2), 111–122.
https://doi.org/10.30509/pccc.2021.166815.1111

[44] D.S. Zinad, R.D. Salim, N. Betti, L.M. Shaker, A.A. Al-Amiery (2022) Comparative investigations of the corrosion inhibition efficiency of a 1-phenyl-2-(1-phenylethylidene)hydrazine and its analog against mild steel corrosion in hydrochloric acid solution. Prog Color Colorant Coat, 15(1), 53–63. https://doi.org/10.30509/pccc.2021.166786.1108

[45] R.D. Salim, N. Betti, M. Hanoon, A.A. Al-Amiery (2021) 2-(2,4-Dimethoxybenzylidene)-N-phenylhydrazinecarbothioamide as an efficient corrosion inhibitor for mild steel in acidic environment. Prog Color Colorant Coat, 15(1), 45–52.
https://doi.org/10.30509/pccc.2021.166775.1105

[46] A.A. Al-Amiery, L.M. Shaker, A.H. Kadhum, M.S. Takriff (2021) Exploration of furan derivative for application as corrosion inhibitor for mild steel in hydrochloric acid solution: Effect of immersion time and temperature on efficiency. Mater Today: Proc, 42(6), 2968–2973.

[47] A.M. Resen, M.M. Hanoon, W.K. Alani, A. Kadhim, A.A. Mohammed, T.S. Gaaz, A.A.H. Kadhum, A.A. Al-Amiery, M.S. Takriff (2021) Exploration of 8-piperazine-1-ylmethylumbelliferone for application as a corrosion inhibitor for mild steel in hydrochloric acid solution. Int J Corr Scale Inhib, 10(2), 368–387.

[48] M.M. Hanoon, A.M. Resen, A.A. Al-Amiery, A.A.H. Kadhum, M.S. Takriff (2022) Theoretical and experimental studies on the corrosion inhibition potentials of 2-((6-methyl-2-ketoquinolin-3-yl)methylene) hydrazinecarbothioamide for mild steel in 1 M HCl. Prog Color Colorant Coat, 15(1), 11–23.
https://doi.org/10.30509/pccc.2020.166739.1095.

[49] F.G. Hashim, T.A. Salman, S.B. Al-Baghdadi, T. Gaaz, A.A. AlAmiery (2020) Inhibition effect of hydrazine-derived coumarin on a mild steel surface in hydrochloric acid. Tribologia, 37(3), 45–53, https://doi.org/10.30678/FJT.95510.

[50] A.M. Resen, M. Hanoon, R.D. Salim, A.A. Al-Amiery, L.M. Shaker, A.A.H. Kadhum (2020) Gravi-

metrical, theoretical investigations, and surface morphological investigations of corrosion inhibition effect of 4-(benzoimidazole-2-yl)pyridine on mild steel in hydrochloric acid. Koroze Ochr Mater, 64(1), 122–130, https://doi.org/10.2478/kom-2020-0018.

[51] A.Z. Salman, Q.A. Jawad, K.S. Ridah, L.M. Shaker, A.A. AlAmiery (2020) Selected bisthiadiazole: synthesis and corrosion inhibition studies on mild steel in HCl environment. Surf Rev Lett, 27(3), 2050014.

[52] A.A. Alamiery, W.N.R.W. Isahak, H.S.S. Aljibori, H.A. Al-Asadi, A.A.H. Kadhum (2021) Effect of the structure, immersion time and temperature on the corrosion inhibition of 4-pyrrol-1-yl-N-(2,5-dimethyl-pyrrol-1-yl)benzoylamine in 1.0 M HCl solution. Int J Corr Scale Inhib, 10(5), 700–713.

[53] S.B. Al-Baghdadi, F.G. Hashim, A.Q. Salam, T.K. Abed, T.S. Gaaz, A.A. Al-Amiery, A.A.H. Kadhum, K.S. Reda, W.K. Ahmed (2018) Synthesis and corrosion inhibition application of NATN on mild steel surface in acidic media complemented with DFT studies. Results Phys, 8(6), 1178–1184.

[54] W.K. Al-Azzawi, A.J. Al Adily, F.F. Sayyid, R.K. Al-Azzawi, M.H. Kzar, H.N. Jawoosh, A.A. Al-Amiery, A.A.H. Kadhum, W.N.R.W. Isahak, M.S. Takriff (2022) Evaluation of corrosion inhibition characteristics of an N-propionanilide derivative for mild steel in 1 M HCl: Gravimetrical and computational studies. Int J Corr Scale Inhib, 11(3), 1100–1114.

[55] A.K. Al-Edan, W.N.R.W. Isahak, Z.A.C. Ramli, W.K. Al-Azzawi, A.A.H. Kadhum, H.S. Jabbar, A. Al-Amiery (2023) Palmitic acid-based amide as a corrosion inhibitor for mild steel in 1M HCl. Heliyon, 9(4), e14657, https://doi.org/10.1016/j.heliyon.2023.e14657.

[56] F.F. Sayyid, A.M. Mustafa, M.M. Hanoon, L.M. Saker, A.A. Alamiery (2022) Corrosion protection effectiveness and adsorption performance of schiff base-quinazoline on mild steel in HCl environment. Corros Sci Tech, 21(4), 77–88.

[57] A.A. Al-Amiery, A.B. Mohamad, A.A.H. Kadhum (2022) Experimental and theoretical study on the corrosion inhibition of mild steel by nonanedioic acid derivative in hydrochloric acid solution. Sci Rep, 12(6), 4705, https://doi.org/10.1038/s41598-022-08146-8.

[58] A.A. Al-Amiery, W.N. Isahak, W.K. Al-Azzawi (2024) Sustainable corrosion inhibitors: A key step towards environmentally responsible corrosion control. Ain Shams Engineering Journal, 102672, https://doi.org/10.1016/j.asej.2024.102672.

[59] I. Obot, N. Obi-Egbedi, S. Umoren (2009) Adsorption characteristics and corrosion inhibitive properties of clotrimazole for aluminium corrosion in hydrochloric acid. Int. J. Electrochem. Sci, 4, 863–877

[60] M.H. Sliem, N.M. El Basiony, E.G. Zaki, M.A. Sharaf, A.M. Abdullah (2020) Corrosion Inhibition of Mild Steel in Sulfuric Acid by a Newly Synthesized Schiff Base: An Electrochemical, DFT, and Monte Carlo Simulation Study. Electroanalysis, 32, 3145–3158, DOI: 10.1002/elan.202060461.

[61] I. Obot, N. Obi-Egbedi, S. Umoren (2009) Antifungal drugs as corrosion inhibitors for aluminium in 0.1 M HCl. Corros. Sci, 51, 1868–1875, doi: 10.1016/j.corsci.2009.05.017.

[62] M. Quraishi, F. Ansari, D. Jamal (2003) Thiourea derivatives as corrosion inhibitors for mild steel in formic acid. Mater. Chem. Phys, 77, 687–690, DOI: 10.1016/S0254-0584(02)00130-X.

[63] J. Fu, H. Zang, Y. Wang, S. Li, T. Chen, X. Liu (2012) Experimental and theoretical study on the inhibition performances of quinoxaline and its derivatives for the corrosion of mild steel in hydrochloric acid. Ind. Eng. Chem. Res, 51, 6377–6386, DOI: 10.1021/ie202832e.

[64] S.K. Saha, P. Ghosh, A. Hens, N.C. Murmu, P. Banerjee (2015) Density functional theory and molecular dynamics simulation study on corrosion inhibition performance of mild steel by mercapto-quinoline Schiff base corrosion inhibitor. Physica E, 66, 332–341, DOI: 10.1016/j.physe.2014.10.035.

[65] A.S. Fouda, M.A. Ismail, A.M. Temraz, A.S. Abousalem (2019) Comprehensive investigations on the action of cationic terthiophene and bithiophene as corrosion inhibitors: experimental and theoretical studies. New J. Chem, 43, 768–789, DOI: 10.1039/C8NJ04330B.

[66] S.K. Saha, P. Banerjee (2018) Introduction of newly synthesized Schiff base molecules as efficient corrosion inhibitors for mild steel in 1 M HCl medium: an experimental, density functional theory and molecular dynamics simulation study. Mater. Chem. Front, 2, 1674–1691, doi: 10.1039/C8QM00162F.

[67] I. Lukovits, E. Kalman, F. Zucchi (2001) Corrosion inhibitors—correlation between electronic structure and efficiency. Corrosion, 57(1), 3–8.

[68] L. Guo, I.B. Obot, X. Zheng, X. Shen, Y. Qiang, S. Kaya, C. Kaya (2017) Theoretical insight into an empirical rule about organic corrosion inhibitors containing nitrogen, oxygen, and sulfur atoms. Appl. Surf. Sci, 406, 301–306, doi: 10.1016/j.apsusc.2017.02.134.

[69] M. Masoud, M. Awad, M. Shaker, M. El-Tahawy (2010) The role of structural chemistry in the inhibitive performance of some aminopyrimidines on the corrosion of steel. Corros. Sci, 52, 2387–2396, DOI: 10.1016/j.corsci.2010.04.011.

[70] B.D. Mert, A.O. Yüce, G. Kardaş, B. Yazıcı (2014) Inhibition effect of 2-amino-4-methylpyridine on mild steel corrosion: experimental and theoretical investigation. Corros. Sci, 85, 287–295, DOI: 10.1016/j.corsci.2014.04.032.

[71] N. Labjar, F. Bentiss, M. Lebrini, C. Jama, S. El hajjaji (2011) Study of Temperature Effect on the Corrosion Inhibition of C38 Carbon Steel Using Amino-tris(Methylenephosphonic) Acid in Hydrochloric Acid Solution. Int. J. Corros, 2011, 548528, DOI: 10.1155/2011/548528.

[72] A. Al-Sabagh, N. El Basiony, S. Sadeek, M. Migahed (2018) Scale and corrosion inhibition performance of the newly synthesized anionic surfactant in desalination plants: experimental, and theoretical investigations. Desalination, 437, 45–58, DOI: 10.1016/j.desal.2018.01.036.

[73] E.E. Ebenso, T. Arslan, F. Kandemirli, N. Caner, I. Love (2010) Quantum chemical studies of some rhodanine azosulpha drugs as corrosion inhibitors for mild steel in acidic medium. Int. J. Quantum Chem, 110, 1003–1018, DOI: 10.1002/qua.22249.

[74] B.G. Bedir, M. Abd El-raouf, S. Abdel-Mawgoud, N.A. Negm, N.M. El Basiony (2021) Corrosion inhibition of carbon steel in hydrochloric acid solution using ethoxylated nonionic surfactants based on schiff base: electrochemical and computational investigations. ACS omega, 6(6), 4300–4312.

IZVOD

ISTRAŽIVANJE FPM-A KAO INHIBITORA KOROZIJE ZA BLAGI ČELIK U RASTVORU HCl: UVIDI IZ ELEKTROHEMIJE, GUBITAK TEŽINE I TEORIJSKI PRISTUPI

U ovoj studiji istražujemo efikasnost furan-2-yl-piperazin-1-yl-metanona (FPM) kao inhibitora korozije za blagi čelik u okruženju HCl. Naša studija kombinuje elektrohemijske tehnike, merenja gubitka težine i proračune teorije funkcionalne gustine (DFT). Što se tiče eksperimenata sa gubitkom težine, otkrili smo da koncentracija od 0,5 mM FPM-a obezbeđuje maksimalnu efikasnost zaštite, dostižući 91,8% na 303 K nakon 30 minuta potapanja i primetili smo da efikasnost inhibicije raste sa povećanjem koncentracije FPM-a, ali opada sa višim temperaturama. Na osnovu Langmuirove izoterme i eksperimentalne analize, može se sugerisati da FPM može da prianja na površinu mekog čelika putem fizičkih i hemijskih interakcija. Štaviše, naše teorijske studije otkrivaju korelacije između strukture FPM-a i njegove efikasnosti u inhibiciji korozije, bacajući svetlo na osnovne mehanizme. I eksperimentalni i teorijski rezultati se slažu.Naši nalazi naglašavaju potencijal FPM-a kao inhibitora korozije u industrijskim primenama, nudeći nove mogućnosti za tehnike kontrole korozije.
Ključne reči: *Furan, korozija, čelik, potenciodinamička polarizacija, DFT*

Sundus M. Ahmed   https://orcid.org/0009-0008-2586-5218
Ali H. Alwazir   https://orcid.org/0009-0007-9399-142X
Hakim S. Aljibori   https://orcid.org/0000-0002-5815-8148
Firas F. Sayyid   https://orcid.org/ 0000-0002-6817-335XV
 Ali M. Mustafa   https://orcid.org/ 0000-0002-5226-0926
Ahmed A. Alamiery   https://orcid.org/ 0000-0003-1033-4904
Abdul Amir H. Kadhum   https://orcid.org/0000-0003-4074-9123

Aleksandar Petričević[1], Susanne Holmin[2], John Gustavsson[2], Lena Sundberg[2], Erik Zimmerman[2], Vladimir D. Jović[1, ∗]

[1]*Institute for Multidisciplinary Research University of Belgrade, Belgrade, Serbia,* [2]*Permascand, Folkets Husvägen 50, SE-841 99 Ljungaverk, Sweden*

Additional accelerated service life test for testing Ni-Sn coatings under the conditions of industrial hydrogen production

ABSTRACT

The accelerated service life test (ASLT), developed by PERMASCAND and applied in aspecially designed flow cell, is presented for the first time in the literature in this work. This test involves the application of six sequences of very high current densities, followed by zero current density, in 5.0 M NaOH at 50 °C.The test is performed on Ni-Sn coatings electrodeposited onto Ni mesh,which serves as the substrate for catalytic coatings used by PERMASCAND.The results demonstrate that the overpotential (η) for hydrogen evolution reaction (HER) on several Ni-Sn samples is practically unaffected by the test sequences, remaining approximately -180 mV at j = -1000 mA cm^{-2}. The same test was applied toPERMASCAND's commercial cathode, and the results were compared. Additionally, the Ni-Sn samples were tested in a stationary electrolyte H-cell configuration using polarization curves and electrochemical impedance spectroscopy (EIS) measurements. Nyquist plots recorded at four different values of η were characterized by the presence of two semi-circles, indicating the presence of charge transfer reaction and intermediate adsorption reaction. Comparing polarization curves recorded in PERMASCAND's test cell after the ASLT and in the stationary H-cell after the EIS measurements suggests that long-term performance should be assessed using the ASLT developed by the industry.
Key words: *ASLT, Ni-Sn coatings, hydrogen evolution, alkaline solution, Nyquist plots.*

1. INTRODUCTION

Chlor-alkali electrolysis represents one of the most widely used industrial processes for the production of chlorine and caustic soda [1-6]. Industrial electrolysis relies on the use of "dimensionally stable anodes" (DSA) for chlorine production in the anodic compartment, and noble metalcoated cathodes for the HER, actually caustic soda production, in the cathodic compartment. Several largeindustries in Europe produce chlorine and caustic soda throughchlor-alkali electrolysis (Arkema, Boregaard, Covestro,InovynKemira, Kemone, Vynova),each of them using different conditions for this process: different anodes and cathodes, different base materials for applying anodic and cathodic catalysts, different cell constructions (mono-polar, bi-polar, zero-gap configuration),different concentration and temperatureof NaOH, differentflow rates of

electrolyte, different diaphragm (membrane) materials, etc. Regardinganode materials, they are all based on Ti plates or meshes, which are activated by applying mixture of Ti, Ru and Ir, mostly through thethermal decomposition of their salts.This process forms a thin layerof TiO_2, RuO_2 and IrO_2 on the Ti surface. The largest producers of DSA'sin Europe are IndustryDe Nora S.p.A.and PERMASCAND. Forcathode materials, a variety of materials are used, bothas base materials andcatalytic layers.For example, Industry De Nora S.p.Aemploys cathodes with anelectrodeposited thin layer of Ni-RuO_2 coating onto Ni mesh 40, whilePERMASCAND's cathodes contain catalytic layer of noble metals on much ticker Ni mesh substrate.

The main components of the chlor-alkali cells used in the industrial processes are summarized in Table 1 [7].

The stability of commercial DSA'sin industrial chlor-alkali electrolysis is known to be very high, primarily determined by the thickness of the catalytic coating and is practically insensitive to the eventual interruption in electrolysis [1-6].

---

*Corresponding author: Dr. Vladimir D. Jović
E-mail: vladajovic@imsi.bg.ac.rs

Table 1.Characteristics of Various Chlorine/Sodium Hydroxide Electrolysis Cells

Component	Diaphragm Cell	Mercury Cell	Membrane Cell
Cathode	Steel/steel coating with nickel	Mercury flowing over steel	Steel or nickel with a nickel-based coating
Anode	DSA	DSA	DSA
Diaphragm/ Membrane Material	Asbestos and fibrous polytetrafluoroethylene	None	Ion-exchange membrane (fluorinated polymers)

However, cathodes have been observed to lose their catalytic activity during electrolysis, especially during the replacement of old electrodes with new onesinelectrolyzerwithzero-gap membrane configuration cells. During such replacements,a phenomenon known as polarity inversion of the electrodesoccurs, asanodes and cathodes in the rest of cells within the industrial plant are short-circuited. Depending on the type of cells used in the industrial plant, cathode manufacturers can predict the frequency and duration of reverse polarization and develop an appropriate ASLT, simulating certain period of time of their use in industrial plant.However, it is important to note that different industries apply different conditions for chlor-alkali electrolysis, including variations in cell types, cathode materials, and electrolyte concentration and temperature. As a result, their research and development teams create tailored ASLT's for these unique conditions.Unfortunately,the application of these ASLT's is missing in the literature and in almost all papers describing the behavior of certain catalyst for the HER, the "long-term performance" is typically based on electrolysis durations of 50 – 100 hours in a stationary electrolyte setup [8].

The only ASLT for commercial cathodes, developed by Industry De NoraS.p.A., has been partially disclosed in the literature to date [9]. The procedure involves a sequence of galvanostatic polarizations inthe HER range, followed bycyclic voltammetry (CV) at 50 mV s^{-1}, withthe HER as the negative limit and oxygen evolution as the positive limit. Thisspecific ASLT,with slight modifications, has been applied in our previousworks [10-15] on Ni-Snand Ni-MoO$_x$coatings, and the results were compared with those of the commercial Ni-RuO$_2$ (De Nora's) cathode.

In this work,the ASLT developed by PERMASCAND is presented. Since these two companies are the largest producers of cathodes for chlor-alkali electrolysis, presenting their ASLT's is crucial for researchers analyzing catalysts for the HER in alkaline solution. PERMASCAND's test is based on the application of sequences of very high current densities, followed by zero current density. The test is applied on Ni-Sn coatings electrodeposited under various conditions onto Ni mesh substrate used for the application of catalytic coating in PERMASCAND, as well as on the commercial PERMASCAND's cathode (PSC), with the obtained results beingcompared.

2. EXPERIMENTAL

2.1. Investigations in a stationary H-cell configuration

P.a. chemicals (Sigma - Aldrich, Merck) and extra pure UV water(Smart2PureUV, TKA) were used for solutions preparation.All potentials are referenced vs. thereversible hydrogen electrode (RHE)as η. Ni mesh was pre-cleaned usingthe procedure described in our previous workonNi foams [16].

The electrodeposition of the Ni-Sn coating for testing in PERMASCANDwas carried out galvanostatically at two current densities using two different solutions: solution A(0.60 MK$_4$P$_2$O$_7$ + 0.30 M Glycine + 0.10 M NiCl$_2$ + 0.03 M SnCl$_2$, j = -80 mA cm^{-2}, t = 1250 s) and solution B(0.60 M K$_4$P$_2$O$_7$ + 0.30 M Glycine + 0.20 M NiCl$_2$ + 0.06 M SnCl$_2$, j = -100 mA cm^{-2}, t = 1000 s).Two types of Ni mesh substrates were used: sand-blasted and non-blasted. Two larger counter electrodes (Pt-Ti expanded meshes) were positioned in parallel with the working electrode.

Polarization curves andEIS measurements were performed in a H-cell with stationary electrolyte, where the working and counter electrode compartments were separatedby aZirfon^{TM} Perl UTP 500membrane. A reversible hydrogen electrode (RHE) – HydroFlex (Gaskatel GmbH), connected to the working electrode compartment via bridge and a Luggin capillary, served as the reference electrode.Potentiostat Interface 1010E (Gamry Instruments Inc.) was used for polarization curves and EIS measurements. All measurements were carried out in 5.0 M NaOH at a temperature of 50 ^{o}C.

Nyquist plots for all investigated electrodes were recorded at four different η values (-60 mV, -75 mV, -90 mV and -105 mV) within the frequency range of 20 kHz to 0.01 Hz, with 20 points per decade and an amplitude of 5 mV RMS. Prior to

each measurement, the electrodes were held at the desired η for 100 s to establish a stable current density response. The current densities and solution resistance (R_s) valuesobtained from EIS measurements were used to calculate the real η_{corr} by correcting the applied η valuesfor jR_s.

2.2. Investigations in a PERMASCAND'stest cell

The HERon larger samples was tested in a specially developed PERMASCAND's test flow cell. The working electrodes for the test cell were larger (3.0 x 3.5 cm), while those used for polarization curves and EIS measurements in the H-cell were smaller (1.0 x 1.0 cm).For the testing procedure in PERMASCAND, the following equipment was used: potentiostat/galvanostat Iviumstat.XRi (Ivium)for electrochemical measurements;the electrolyte was heated in a custom-built tank and pumping station; the tank had a volume of 100 liters, and pumipng was achieved by a centrifugal pump.Sodium hydroxide (Analytical reagent grade, Fischer Scientific) was used in the PERMASCAND's test flow cell.

2.3. ASLT proceduredeveloped by PERMASCAND

The ASLT procedure, developed by PERMASCAND and performed in their laboratory,contained 7 steps schematically presented in Figure 1. The procedure begins by recording a polarization curve (corrected for ohmicdrop) from -1.0 A cm^{-2} to -0.1 A cm^{-2}and back.The first step, lasting for 1 hour is applied as follows:j =-3.0 A cm^{-2} for 54 s followed by j = 0.0 A cm^{-2} for 6 s (repeated 60 times). Before the second step, another polarization curve was recorded, and this process continues until the 6th step, after whichthe final 7th polarization curve is recorded.

Figure 1. Schematic presentation of the ASLT procedure developed by PERMASCAND

Coating amount for Ni-Sn samples was measured before and after electrolysis with X-ray Fluorescence(NITON XL3t handheld instrument from Thermo Scientific) three times on each sample in electrolyzed spot.

3. RESULTS AND DISCUSSION

3.1. Results of thetest procedure developed by PERMASCAND

A total of five Ni-Sn coatings were testedin the PERMASCAND test cell, alongsidea Ni blasted mesh and a commercial PERMASCAND cathode (PSC) under the standardized procedure. The coatings were prepared under varying conditions, as detailed below:

Ni-Sn(1) – electrodeposited onto Ni blasted mesh from solution A at$j$ = -80 mA cm^{-2} for 1250 s;

Ni-Sn(2) – electrodeposited onto Ni blasted mesh from solution B at$j$ = -100 mA cm^{-2} for 1000 s;

Ni-Sn(3) – electrodeposited onto Ni mesh from solution A at$j$ = -80 mA cm^{-2} for 1250 s;

Ni-Sn(4) – electrodeposited onto Ni mesh from solution B at$j$ = -100 mA cm^{-2} for 1000 s;

Ni-Sn(5) – electrodeposited onto Ni blasted mesh from solution B at$j$ = -100 mA cm^{-2} for 1000 s.

The corresponding U vs. t dependences for the electrodeposition of these samples are presented in Figure 2. All U vs. t dependences exhibit well-defined voltage plateaus, with differences involtage values due to different current densities of electrodeposition.
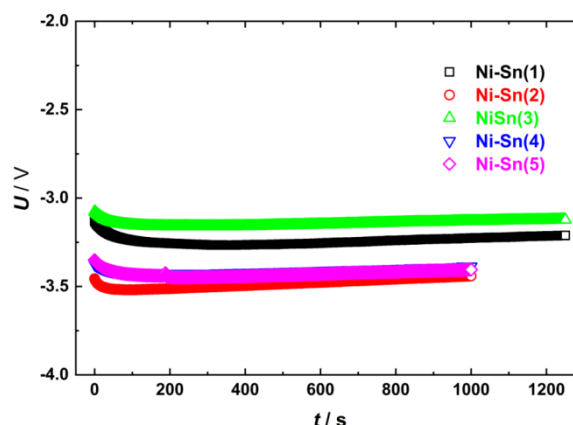

Figure 2.U vs. t dependences for the electrodeposition of all Ni-Sn tested samples

Polarization curves corrected for the ohmic drop (η_{corr}) obtained prior to the test (1) and after each subsequent step (2-7) are presented in Figure 3, as follows: (a) Blasted Ni mesh; (b) Commercial PSC cathode; (c) Ni-Sn(3)sample; (d) Ni-Sn(4) sample; (e) Summary of polarization curves corrected for the ohmic drop (η_{corr}) recorded after all test steps (2-7).

Investigated cathodes exhibited varying behavior during the test. Blasted Ni mesh (Figure 3(a)) showed clear signs of deactivation, with the η_{corr}values in the final polarization curve (7) approximately 130 mV higher than those recorded before the test (1). Commercial PERMASCAND's cathode (PSC) demonstrated activation during the test (Figure 3(b)), particularly during the first step, while Ni-Sn(3) and Ni-Sn(4) coatings (Figure 3(c) and (d) respectively)exhibited only minor sensitivity to the applied stress steps, suggesting relatively stable performance.
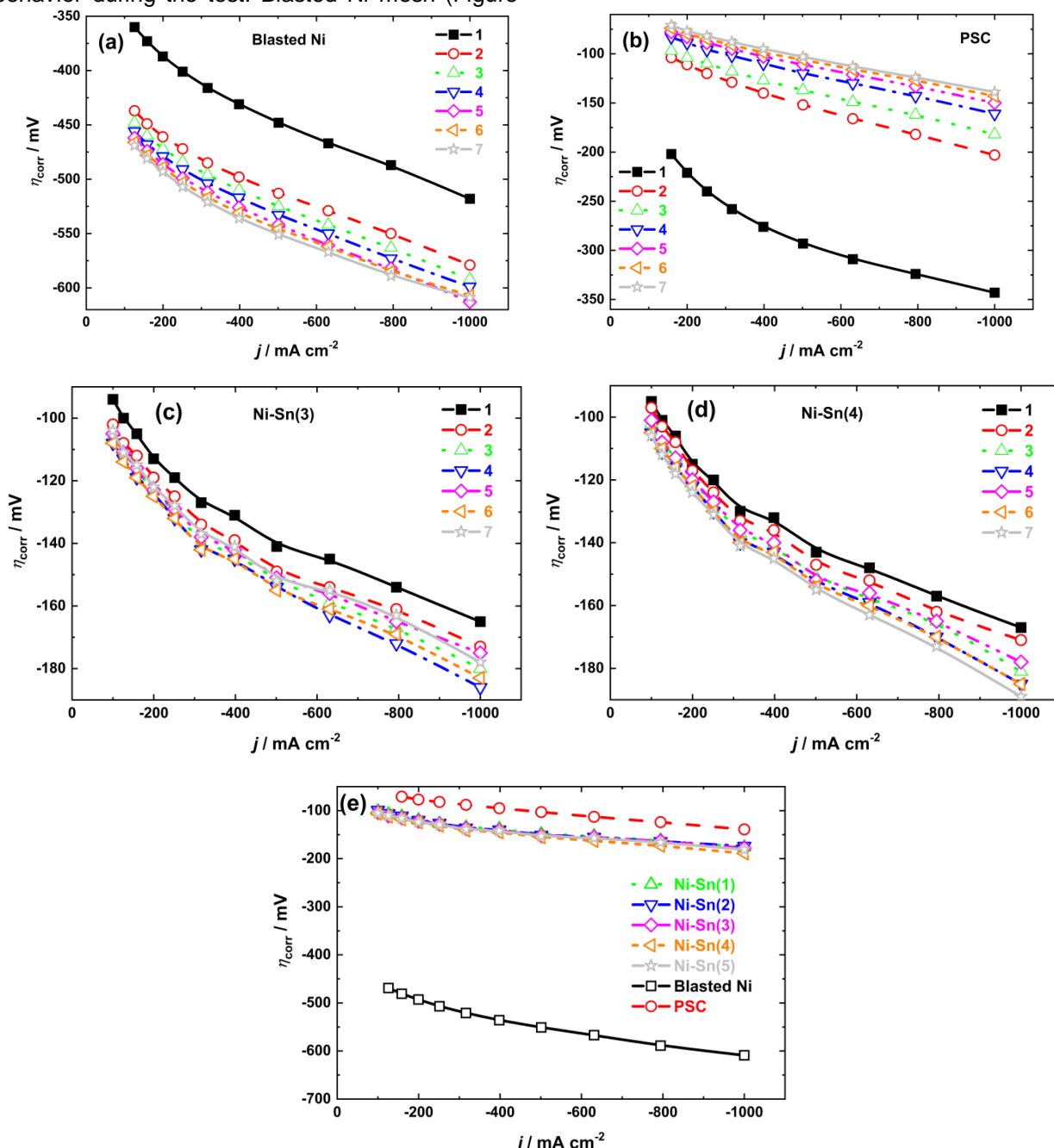

Figure 3. Polarization curves corrected for the ohmic drop (η_{corr}) obtained before the test (1) and after each subsequent step (2-7): (a) For blasted Ni mesh; (b) For commercial PSC cathode; (c) For Ni-Sn(3) coating; (d) For Ni-Sn(4) coating; (e) Comparison of the final polarization curves no. 7 for all investigated samples

As can be seen the lowest η_{corr} values recorded after the test (polarization curve 7) were obtained for the commercial PSC cathode, amounting approximately -140 mV (Figure 3(b)). In contrast, the blasted Ni mesh exhibited significantly higher overpotentials, with η_{corr} values about 500 mV higher. All Ni-Sn coatings demonstrated almost identical polarization characteristics, with a maximum variation in η_{corr} values of only about 10 mV. Among them, the characteristics of Ni-Sn(3) and Ni-Sn(4) are shown in Figures 3(c and d) respectively. An interesting observation was made for the Ni-Sn(3) sample (Figure 3(c)), where η_{corr} values increased during steps 2,3 and 4, followed by decrease through the steps 5 to 7.
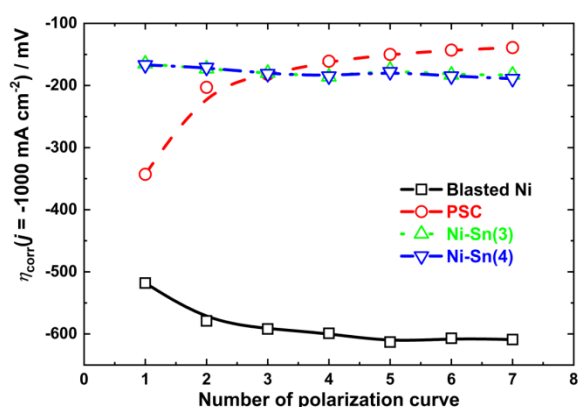
Figure 4. Overpotentials corrected for the ohmic drop(η_{corr}) recorded at j = -1000 mA cm^{-2} as a function of the polarization curve number

This trend is more clearly illustrated in Figure 4, which shows the values of η corrected for the ohmic drop recorded at the highest applied current density ($\eta_{corr}(j = -1000$ mA cm^{-2})) as a function of the polarization curve number.

An interesting observation is that the $\eta_{corr}(j = -1.0$ A cm^{-2}) values for the Ni-Sn coatings remain practically unaffected by the applied test procedure. This suggests that the alternating steps of high and zero current densities do not induce any significant changes in the coating composition. In contrast, the Ni blasted mesh exhibited a noticeable increase in η_{corr} over the course of the test, with values rising by approximately 130 mV from step 1 to step 6 (point 7). The PSC cathode showed a clear activation trend, with the $\eta_{corr}(j = -1.0$ A cm^{-2}) values decreasing sharply during the step 1 from -330 mV to -190 mV and then decreasing slowly to ~ -140 mV at the end of test. Such behavior could be explained by the change of coating composition during the first step producing surface more active towards the HER.

The Sn content in the coatings, measured by X-ray florescence (XRF) at the spot of analysis before and after the test, is presented in Figure 5. As can be seen, the loss of Sn is practically negligible. Based on the findings from our previous study[16], the small amount of Sn that dissolved during the ASLT procedure likely corresponds to the fraction of Sn in the electrodeposit that exist either as free Sn or is incorporated in secondary phases present in the Ni-Sn alloy(Ni_3Sn, Ni_3Sn_4) [17]. This is consistent with the fact that the dominant phase in the coating is Ni_3Sn_2. According to Ref. [16], Ni_3Sn_2 phase is primarily responsible for the high catalytic activity of Ni-Sn coatings towards the HER.
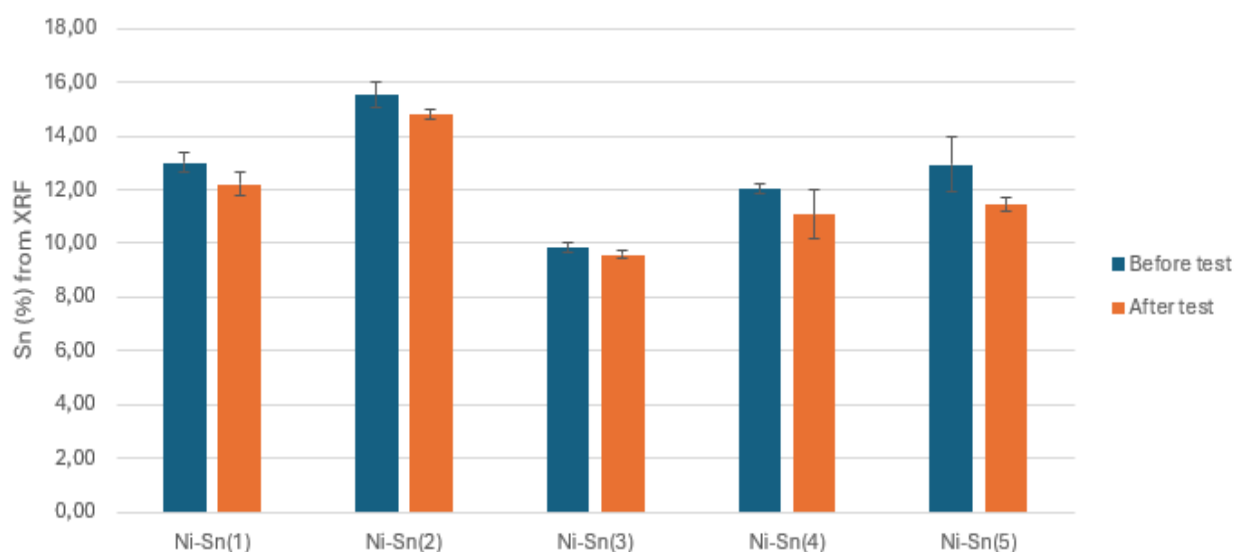

Figure 5. XRF at the spot of analysis before and after the test

3.2. Results obtained in the stationary H-cell configuration

Before and after the EIS measurements, polarization curves were recorded using linear sweep voltammetry (LSV) at a sweep rate of 1 mV s^{-1},in combination with the current interrupt technique. Figure 6 shows the polarization curves obtained before and after EIS measurements for

sample Ni-Sn(3) (a), and sample Ni-Sn(4) (b). Given that the EIS measurements lasted 4 h, a slight change in the polarization curves is to be expected. Interestingly, sample Ni-Sn(3) exhibited slightly lower η_{corr} values after the EIS measurements (a), while sample Ni-Sn(4) showed a slight increase in η_{corr} values after the EIS measurements (b).
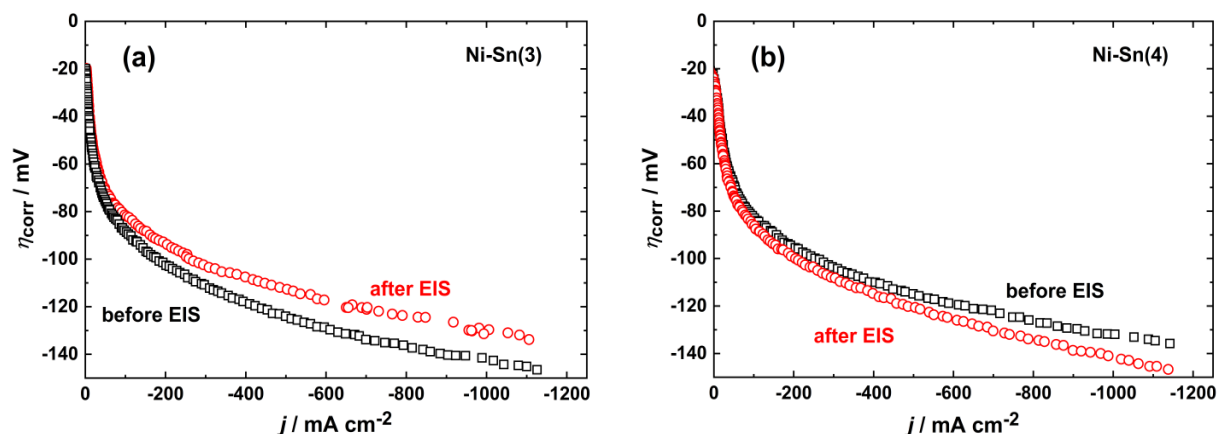

Figure 6. Polarization curves for HER at sample Ni-Sn(3) (a) and sample Ni-Sn(4) recorded before and after the EIS measurements

Nyquist plots recorded at four different values of η are shown in Figure 7. All plots are characterized by the presence of two semi-circles: the first one (at high frequencies) corresponding to the charge transfer reaction, and the second one

corresponding to the intermediate adsorption reaction. As expected, an increase in η leads to the smaller semi-circles, reflecting higher values of j and therefore faster kinetics of the HER.
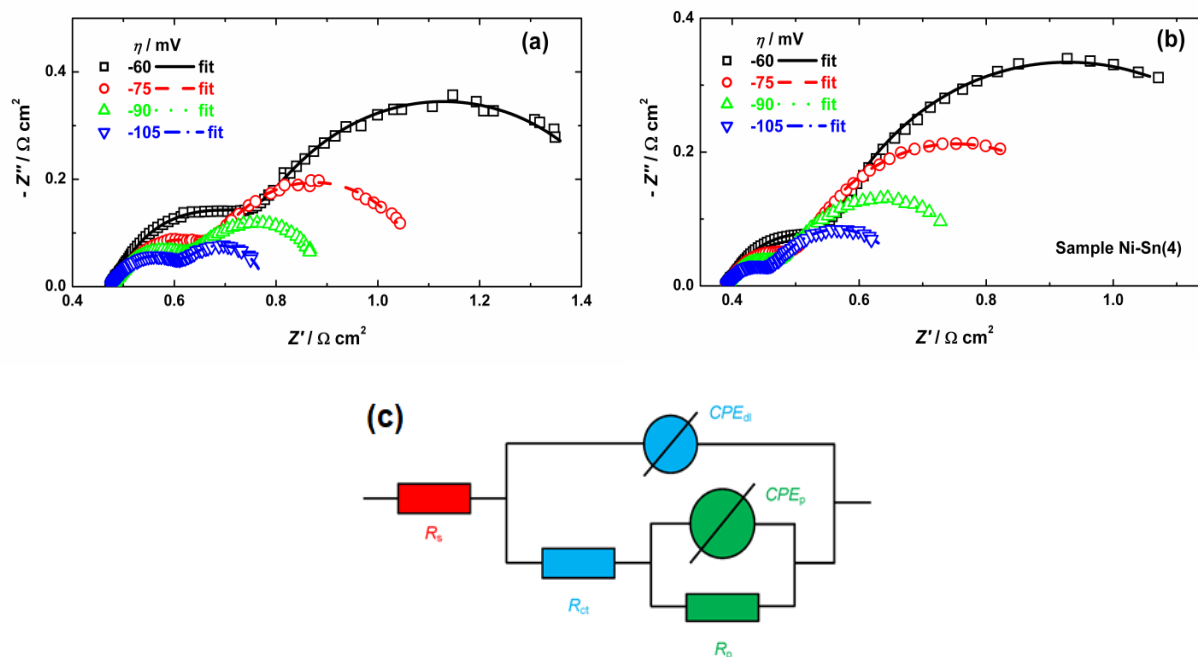

Figure 7. Nyquist plots recorded at different η values (designated in the figure) for Ni-Sn(3)sample (a) and Ni-Sn(4) sample (b). Squares, circles and triangles represent the experimental data points, while the lines correspond to the fitting results obtained using the equivalent circuit shown in Figure 7(c)

R_s – solution resistance; R_{ct} – charge transfer resistance; CPE_{dl} – constant phase element corresponding to the double layer capacitance;

R_p – resistance of the electrosorption/ electrodesorption of intermediate; CPE_p – constant phase element corresponding to the adsorption pseudo capacitance.

As reported in Ref. [15], the exchange current densities for the charge transfer reaction ($j_{o,ct}$), intermediate adsorption reaction ($j_{o,ads}$) and overall (total) HER ($j_{o,tot}$) can be determined by analyzing dependences η_{corr} vs. $\log(R_{ct}^{-1})$, η_{corr} vs. $\log(R_p^{-1})$ and η_{corr} vs. $\log(R_F^{-1})$, specifically from the intercepts of those linear dependences at $\eta_{corr.} = 0$. Similarly, the transition time τ_o at the reversible potential for HER can be obtained from the intercept of the $\log(\tau)$ vs. η_{corr} linear dependence at

$\eta_{corr.} = 0$. All respective dependences for samples Ni-Sn(3) and Ni-Sn(4) are represented in Figure 8, with the corresponding values of $j_{o,ct}$, $j_{o,ads}$, $j_{o,tot}$ and τ_o indicated in the figure. It can be observed that the slopes of η_{corr} vs. $\log(R_{ct}^{-1})$, η_{corr} vs. $\log(R_p^{-1})$ and η_{corr} vs. $\log(R_F^{-1})$ dependences are practically identical for both samples, except for that of η_{corr} vs. $\log(R_p^{-1})$ dependence of sample NiSn(4) (Figure 8(b)). Although the values of $j_{o,ct}$ and $j_{o,ads}$ are different, the linear η_{corr} vs. $\log(R_F^{-1})$ dependences for both samples are identical, resulting in the same $j_{o,tot}$ of -1.57 mA cm^{-2}. This indicates that the charge transfer and intermediate adsorption steps are sensitive to the composition (or morphology) of the Ni-Sn coatings, while the overall HER is identical for both samples being in accordance with the polarization curves.
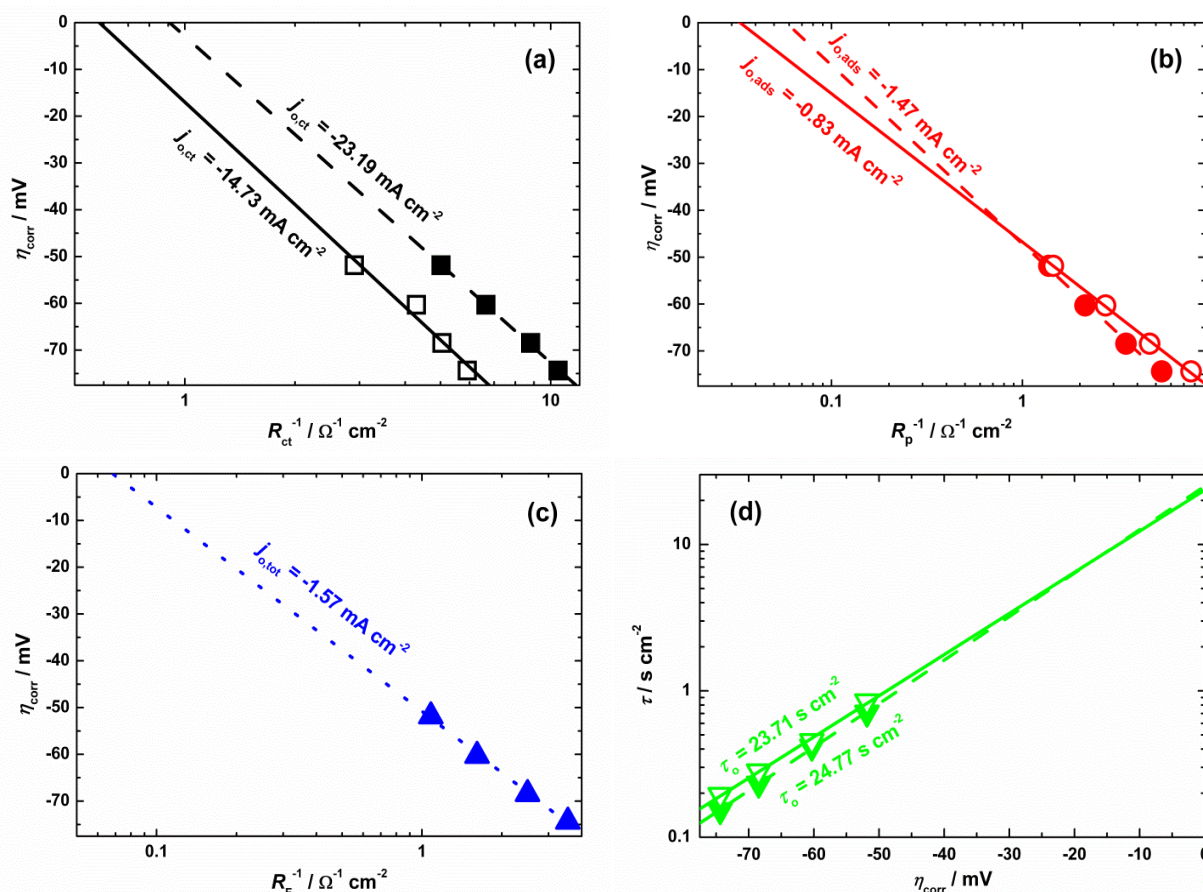

Figure 8. (a) The dependences η_{corr} vs. $\log(R_{ct}^{-1})$, (b) dependences η_{corr} vs. $\log(R_p^{-1})$, (c) dependences η_{corr} vs. $\log(R_F^{-1})$ and (d) dependences $\log(\tau)$ vs. η_{corr} for samples Ni-Sn(3) (□○△▽) and Ni-Sn(4) (■●▲▼)

3.3. Comparison of the results obtained in the flow test cell and in the stationary H-cell

Figure 9 compares the polarization curves for samples Ni-Sn(3) and Ni-Sn(4), recorded both in the PERMASCAND's flow cell and in a stationary H-cell. It should be emphasized that the samples

tested in the flow cell were analyzed 10 months after electrodeposition, while the samples tested in the H-cell were investigated immediately after the electrodeposition.

Considering presented polarization curves, it can be concluded that the samples tested in the

stationary electrolyte exhibit slightly better performance, with lower η_{corr} values across the entire current density range. Of course, comparison of presented polarization curves is not realistic, since those recorded in a stationary electrolyte were not exposed to the 6 steps ofPERMASCAND's test procedure. Hence, it should be stressed that electrodes, even if smaller than those used in full-scale industrial plants, must be tested under conditions simulating real industrial process,within a smaller pilot plant.

As previously stated [8],the commonly accepted "long-term test" used in the literatureto evaluate the catalytic behavior of electrodes for the HER is useless and this statement is confirmed by the results presented in Figure 9.
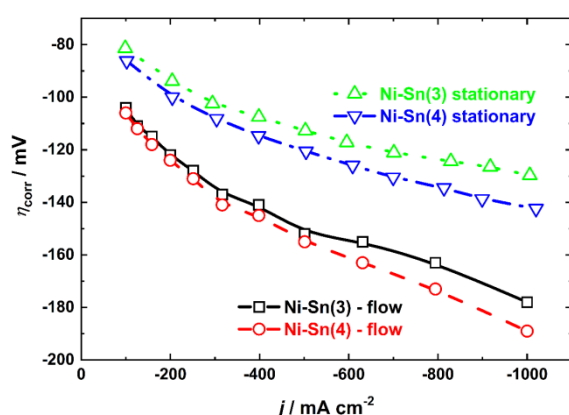

Figure 9. Polarization curves for the HER at Ni-Sn(3) sample and Ni-Sn(4) samplerecorded in the PERMASCAND's test flow cell and in stationary H-cell

4. CONCLUSIONS

1. The ASLT proceduredeveloped by PREMASCAND and applied in a specially designed flow cellusing 5.0 M NaOH at 50 °C on Ni-Sn coatings electrodeposited onto Ni mesh, used as substrate for applying catalytic coatings in PERMASCAND, has been presented in this work for the first time in the literature.

2. The η_{corr} values for the HER on several Ni-Sn samples werefound to be practically insensitive to the test sequences, maintaining valuesaround -180 mV at j = -1000 mA cm^{-2}.

3. The commercial PERMASCAND's cathode exhibited 30-40 mV lower η_{corr} values at the highest current density after the test.

4. Nyquist plots recorded at four different η_{corr} values were characterized by the presence of two semi-circles, indicating the presence of charge transfer reaction and intermediate (H_{ads}) adsorption process.

5. Comparison of the polarization curves recorded in thePERMASCAND's test cell and the stationary H-cell confirmed that long-term electrodeperformanceshould be tested using industrial-grade ASLT procedures.

3. REFERENCES

[1] J.S. Sconce (1962) Chlorine, its manufacture, properties and uses, New York, London: Reinhold Publishing Corporation, Chapman & Hall, Ltd.

[2] S. Lakshmanan, T. Murugesan (2014) The chlor-alkali process: Work in Progress, Clean Techn. Environ. Policy, 16, 225-234.

[3] I. Moussallem, J. Jörissen, U. Kunz, S. Pinnow, T. Turek (2008) Chlor-alkali electrolysis with oxygen depolarized cathodes: history, present status and future prospects, J. Appl. Electrochem., 38, 1177-1194.

[4] S. Lakshmanan, T. Murugesan (2013) The Chlor-Alkali Process – Work in Progress, Clean Technol. Environ. Policy, 16, 225-234.

[5] H. Khasawneh, M.N. Saidan, M. Al-Addous (2019) Utilization of hydrogen as clean energy resource in chlor-alkali process, Energy Explor. &Exploit., 37, 1053-1072.

[6] I. Garcia-Herrero, M. Margallo, R. Onandía, R. Aldaco, A. Irabien (2017) Life Cycle Assessment model for the chlor-alkali process: A comprehensive review of resources and available technologies, Sustain. Prod. Cons., 12, 44-58.

[7] Department of Energy (.gov), USA, https://www1.eere.energy.gov, ch. 6

[8] V.D. Jović (2024)The long time performance of catalysts usually used in the literature, Zastita Materijala, 65, 797-800.

[9] A.L.Antozzi, C. Bargioni, L. Iacopetti, M. Musiani, L. Vazquez-Gomez(2008)EIS study of the service life of activated cathodes for the hydrogenevolution reaction in the chlor–alkali membrane cell process, Electrochim. Acta, 53, 7410–7416.

[10] C. Iwakura, M. Tanaka, S. Nakamatsu, H. Noue, M. Matsuoka, N. Furukawa (1995) Electrochemical properties of Ni/(Ni+RuO$_2$) active cathodes for hydrogen evolution in chlor-alkali electrolysis, Electrochim. Acta, 40, 977-982.

[11] V.D. Jović, U. Lačnjevac, B.M. Jović, N.V. Krstajić (2012) Service life test of non-noble metal composite cathodes for hydrogen evolution in sodium hydroxide solution, Electrochim. Acta. 63, 124–130.

[12] V.D. Jović, U.Č. Lačnjevac, B.M. Jović, Lj.M. Gajić-Krstajić, N.V. Krstajić (2013) Ni–MoO$_2$ composite cathodes for hydrogen evolution in alkaline solution. Effect of aging of the electrolyte for their electrodeposition, J. Serb. Chem. Soc., 78, 689–700.

[13] B.M. Jović, U.Č. Lačnjevac, N.V. Krstajić, V.D. Jović (2014) Service life test of the Ni-Sn coatings as cathodes for hydrogen evolution in chlor-alkali electrolysis, Int. J. Hydrogen Energy, 39, 8947-8958.

[14] Vladimir D. Jović, Uroš Č. Lačnjevac, Borka M. Jović, Nedeljko V. Krstajić(2014) Electrodeposited, Ni-based, non-noble metal coatings as cathodes for hydrogen evolution in chlor-alkali electrolysis, ZaštitaMaterijala, 55, 111-125.

[15] A. Petričević, M.N. Krstajić Pajić, P. Zabinski, D. Kutyla, M.M. Marzec, M. Gajewska, N.R. Elezović, V.D. Jović (2025) Hydrogen evolution reaction on electrodeposited Ni-MoO$_x$ composite coatings, Electrochim. Acta, 519, 145825.

[16] J.D. Gojgić, A.M. Petričević, T. Rauscher, C.I. Bernäcker, T.Weißgärber, L. Pavko, R.Vasilić, M.N. KrstajićPajić, V.D. Jović (2023) Hydrogen evolution at Ni foam electrodes and Ni-Sn coated Ni foam electrodes, Appl. Catalysis A General, 663, 119312.

[17] Alloy Phase Diagrams (1992) in: ASM Handbook, (H. Baker, ed.), vol. 3, ASM International, USA.

IZVOD

DODATNI UBRZANI TEST ZA ISPITIVANJE Ni-Sn PREVLAKA U USLOVIMA INDUSTRIJSKE PROIZVODNJE VODONIKA

Prvi put u literaturi prikazan je ubrzani test za ispitivanje Ni-Sn prevlaka u uslovima industrijske proizvodnje vodonika razvijen u kompaniji PERMASCAND. Test je uradjen u specijalno dizajniranoj aparaturi koja simulira uslove rada u hlor-alkalnoj elektrolizi i bazira se na primeni šest sekvenci. Svaka sekvenca traje 1 sar i za to vreme se 60 puta ponavljaju j = - 3000mA cm^{-2} (54 s) i j = 0 mA cm^{-2}(6 s). Kao elektrolit koristi se 0.5 M NaOH zagrejan na 50 °C. Testirane elektrode su bile prevlake od Ni-Sn legure istaložene na Ni mrežici koja se koristi kao osnova za nanošenje komercijalnih prevlaka u kompaniji PERMASCAND. Pokazano je da je prenapetost korigovana za omski pad napona (η_{corr}) na svim testiranim elektrodama bila praktično nezavisna od broja sekvence ($\eta_{corr} \approx$ -180 mV prij = -1000mA cm^{-2}). Test je primenjen i na komercijalne PERMASCAND katode i rezultati su uporedjeni, pri čemu su Ni-Sn katode imale znatno bolje karakteristike u prvoj sekvenci, dok su u preostalim sekvencama komercijalne katode posedovale manju prenapetost za 30 - 40 mV. Ni-Sn katode su ispitivane i u stacionarnom elektrolitu (H – ćelija) merenjem polarizacionih krivih i impedansom. Nyquist-ovi dijagrami su bili okarakterisani prisustvom dva polukruga, ukazujući na prisustvo reakcije razmene naelektrisanja i adsorpcije intermedijara (H$_{ads}$). Polarizacione krive registrovane u PERMASCAND-ovoj test ćeliji nakon završenog testai u H – ćeliji su uporedjene i potvrdjeno je da se tzv. "dugovremenski test" mora raditi pod uslovima koji su definisani od strane industrijskih razvojnih instituta.

Ključnereči: *Ubrzani test, Ni-Sn prevlake, izdvajanje vodonika, alkalni rastvori, Nyquist-ovi dijagrami.*

AleksandarPetričević https://orcid.org/0000-0001-5954-3569
Erik Zimmerman https://orcid.org/0000-0002-5230-3682